POLISH SOCIETY OF THEORETICAL AND APPLIED MECHANICS

JOURNAL OF THEORETICAL AND APPLIED MECHANICS

No. 3 • Vol 54

Quarterly

WARSAW, JULY 2016

JOURNAL OF THEORETICAL AND APPLIED MECHANICS
(until 1997 Mechanika Teoretyczna i Stosowana, ISSN 0079-3701)

Beginning with Vol 45, No. 1, 2007, *Journal of Theoretical and Applied Mechanics* (JTAM) has been selected for coverage in Thomson Reuters products and custom information services. Now it is indexed and abstracted in the following:

- **Science Citation Index Expanded** (also known as SciSearch®)
- **Journal Citation Reports/Science Edition**

* * * * *

Editorial Office
Al. Armii Ludowej 16, room 650
00-637 Warszawa, Poland
phone (+48 22) 825 7180, (+48) 664 099 345, e-mail: biuro@ptmts.org.pl

www.ptmts.org.pl/jtam.html

* * * * *

Publication supported by Ministry of Science and Higher Education of Poland

(Journal of Theoretical and Applied Mechanics: 1) digitalizacja publikacji i monografii naukowych w celu zapewnienia i utrzymania otwartego dostępu do nich przez sieć Internet, 2) stworzenie anglojęzycznych wersji wydawanych publikacji, 3) wdrożenie procedur zabezpieczających oryginalność publikacji naukowych oraz zastosowane techniki zabezpieczeń – są finansowane w ramach umowy 734/P-DUN/2016 ze środków Ministra Nauki i Szkolnictwa Wyższego przeznaczonych na działalność upowszechniającą naukę)

JOURNAL OF THEORETICAL AND APPLIED MECHANICS
54, 3, pp. 679-690, Warsaw 2016
DOI: 10.15632/jtam-pl.54.3.679

EXPERIMENTAL INVESTIGATION OF AN ENERGY HARVESTING ROTARY GENERATOR-MR DAMPER SYSTEM

Bogdan Sapiński
AGH University of Science and Technology, Department of Process Control, Kraków, Poland
e-mail: deep@agh.edu.pl

The study investigates an energy harvesting system utilising rotary motion. The system has three components: a rotary MR damper to vary the damping characteristics, a rotary power generator (energy extractor) producing electrical power, and a conditioning electronics unit to interface directly with the damper and the generator. The objective of the study is to examine the system performance through experiments. The paper outlines the structure of the damper and the generator, provides selected results of examination of the system components and the whole system under idle run and under load for the assumed speed range. The results demonstrate that the system is adaptable to external excitations, does not require an extra power supply and provides a smart solution with potential applications to rotary motion control.

Keywords: MR damper, generator, conditioning electronics, experimental testing

1. Introduction

Energy harvesting from vibrations is one on the research areas that has recently attracted a great deal of scientific and engineering interest. A comprehensive overview of the state-of-the-art in vibration energy harvesting technologies has been provided by Priya and Inman (2009). The book presents the current state of knowledge and achievements of leading researchers both in academia and industry. Alongside, many articles have been published on the topic of vibration energy harvesting systems where an external power supply unit is replaced by energy extractors employing various mechanisms of energy conversion.

The present study focuses on a regenerative rotary system utilising an electromagnetic mechanism of energy conversion. The system incorporates three basic components: a rotary MR damper, a rotary power generator and a conditioning electronics unit. The MR damper is a semi-active current-driven device employing the real-time control of the torque output. The energy extractor is a rotary generator which converts mechanical energy into electrical energy. The energy harvested from external excitations via the generator is used for controlling the torque output of the damper. The conditioning electronics unit develops conditioning-processing circuits for improving the generator output signal.

The ability to convert mechanical into electrical energy to power an MR damper brings numerous benefits. The power generator-MR damper system forms a stand-alone regenerative device that seems to be a promising solution to control of motion. Such a system is capable of operation with no need for external power supply connections.

The concept of utilising energy recovered from structural vibrations to power MR dampers was first suggested in the work by Scruggs and Lindner (1999). Since then, a great number of publications have appeared, summarising the research results in this field. For example, Cho *et al.* (2007) developed a special structure of an electromagnetic generator to be used with an MR damper. Hong *et al.* (2007) investigated an MR damper-electromagnetic generator system

in seismic protection applications. Avadhany *et al.* (2008) developed a regenerative damper intended for automotive light-duty and military vehicle applications.

Major advances have been made in this field, enabling MR dampers to be self-powered (no extra power supply needed) and self-sensing, where information about relative velocity across the damper is derived basing on voltage produced by the generator. Choi and Werely (2009) embarked on the study of feasibility and effectiveness of a self-powered MR damper, using a spring-mass electromagnetic induction device. Wang and Wang (2010) developed a self-sensing MR damper to implement integrated relative displacement sensing and controllable damping. Jung *et al.* (2010) demonstrated that an electromagnetic generator incorporated in an MR damper-based system can act as a velocity-sign sensor. Sapiński (2011) investigated a self-powered and self-sensing control system comprising both a power generator and an MR damper. Chen and Liao (2012) reported on the energy-harvesting MR damper integrating energy harvesting, dynamic sensing and MR damping technologies in a single device and tested a prototype. Liao and Chen (2012) presented a conceptual design of such a device patented. Li *et al.* (2013) came up with an innovative concept of a mechanical motion rectifier which converts bidirectional into unidirectional motion. Sapiński (2014) developed a prototype of an energy-harvesting linear damper and provided the results of experimental testing.

It is worthwhile to mention that recent developments in regenerative MR actuators using the energy conversion mechanism included mostly shock absorbers. Research efforts have focused on regenerative MR shock absorbers in automobiles, railway vehicles and civil structure applications.

The present study focuses on an energy harvesting system utilising rotary motion. The system incorporates a rotary MR damper, a rotary generator and a conditioning electronics unit (Fig. 1) allowing the energy of external excitations to be recovered while the system adjusts itself to applied excitations. The structure design and experimental results obtained from the testing done on the system components and on the system as a whole are summarized. It is demonstrated that the system has the self-powered capability (operates without a need for an extra power supply).

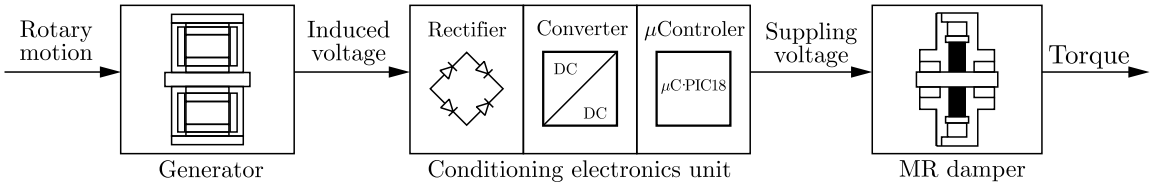

Fig. 1. Schematic diagram of the examined system

The paper is organized as follows. In Section 2, the structure of the damper is described and selected characteristics of the device are provided. In Section 3, the structure of the generator is outlined and measurement results are presented. Section 4 characterizes the conditioning electronics unit and discusses results of its experimental tests. Section 5 presents the experimental testing of the whole system. The final conclusions are given in Section 6.

2. MR damper

The structure of the MR damper is shown in Fig. 2. On shaft (2) in the damper, made of non-magnetic steel and supported on two ball bearings (3), there are four mobile and three immobile plates (4) made of magnetic steel. These plates are attached to housing (6) via closing cover (1) made of low carbon steel. Between the plates, inside the ferromagnetic core, there is control coil (5). The coil winding comprises 610 turns, wound with copper wire 0.48 mm in diameter.

The space between the plates is filled with 45 ml of MR fluid Basonetic 2040, manufactured by the BASF company. The external diameter and height of the device is 100.6 mm and 30 mm, respectively. The gap between the neighbouring plates is 0.5 mm.

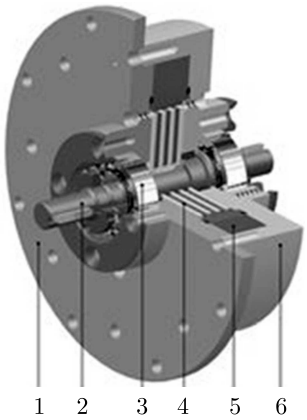

Fig. 2. Structure of the damper: 1 – cover, 2 – shaft, 3 – bearing, 4 – plates, 5 – control coil, 6 – housing

The damper described was tested experimentally. In the first step, the testing was done on the control coil. The step-like input voltages of amplitudes in the range $(2, 16)$ V were applied to the coil, and the current level in the system was measured accordingly. Figure 3 illustrates the current response of the coil to the voltage input with the amplitude 8 V. The steady state value of the current is found to be 0.55 A.

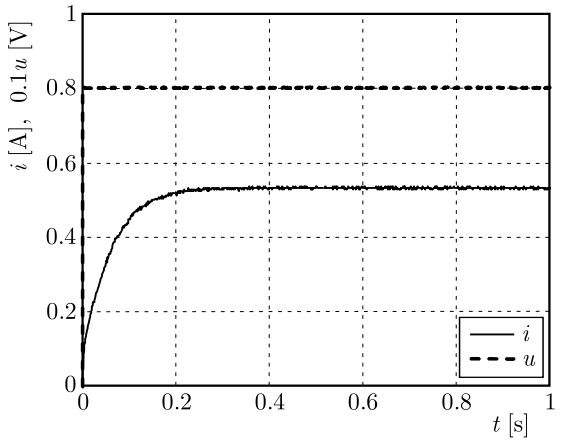

Fig. 3. Current response of the control coil to the step-like voltage input with the amplitude 8 V

The time constant of the control coil determined through the testing was found to be $\tau_d = 53$ ms. Knowing the time constant and having measured the coil resistance ($R_d = 14.67\,\Omega$), the coil inductance was derived accordingly $L_d = 0.772$ H.

Further tests were conducted to determine the relationship between the torque T and the rotational speed w for various levels of the current I in the coil and the relationship between the torque and the increasing and decreasing current level in the control coil for various speed levels. The speed range was $(10, 250)$ rpm, and the current level varied in the range $(0, 1.5)$ A. Figure 4a plots the torque vs. speed characteristics for the current values: 0, 0.2, 0.6, 1.0, 1.5 A. It is clearly apparent that the minimal torque value is 0.5 Nm ($I = 0$ A) and the maximal is equal to 10.5 Nm ($I = 1.5$ A). Figure 4b plots the dependence of the torque on the increasing and decreasing current level in the coil at the speed of 100 rpm, revealing a narrow hysteresis in the damper behaviour.

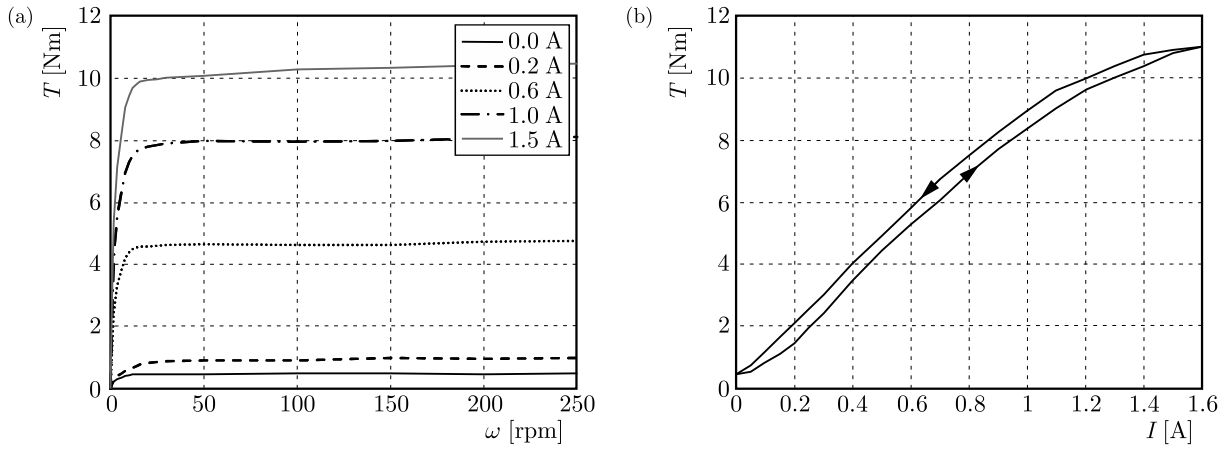

Fig. 4. (a) Torque vs. speed for various current level in the control coil. (b) Torque vs. current in the control coil; $\omega = 100\,\text{rpm}$

3. Generator

The structure of the generator is shown in Fig. 5. It comprises an axis-positioned armature and a cylindrical inductor, which acts as a housing. The inductor with external diameter of 67.5 mm, has 28 radially magnetised permanent magnets (1), forming $p = 14$ pairs of magnet poles arranged symmetrically inside its circumference, such that they face one another with their opposite poles. The armature, comprising 14 rectangular frames (2) is fixed on axis (5) with ball bearings (6). The number of frames is equal to that of the pole pairs in the inductor. The frames, made of ferromagnetic steels, are arranged radially and attached to carcass (4) made of a dielectric material. Inside the frame, there is coil (3) comprising 306 turns, wire-wound on the carcass with the copper wire 0.2 mm in diameter. The magnetic circuit in the generator is made of silicon steel laminations.

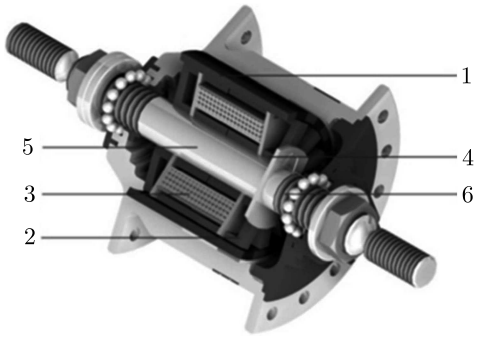

Fig. 5. Structure of the generator: 1 – magnets, 2 – frames, 3 – coil, 4 – carcass, 5 – shaft, 6 – bearing

Figure 6 illustrates how a time-variant magnetic flux is generated in a single frame of the generator. The condition when the pole pieces are positioned beneath magnets(1) with opposite poles is shown in Fig. 6a. The magnetic field having the flux density B (generated by the magnets) penetrates the frame closing the magnetic circuit. Coil (3) encompasses the resultant flux, being the sum of magnetic fluxes in all frames (2). As the inductor rotates, the pole pieces in frame move beneath the magnets with the opposite poles (see Fig. 6b). As a result, the direction of the resultant magnetic flux permeating the coil is reversed. Thus generated variable magnetic flux will then induce the emf in the coil.

The generator described was tested experimentally. In the first step, the testing was done on the coil in the generator. The step-like input voltage u of amplitudes in the range $(0, 2.5)\,\text{V}$ was applied and the current level i in the system was measured accordingly. Figure 7 illustrates

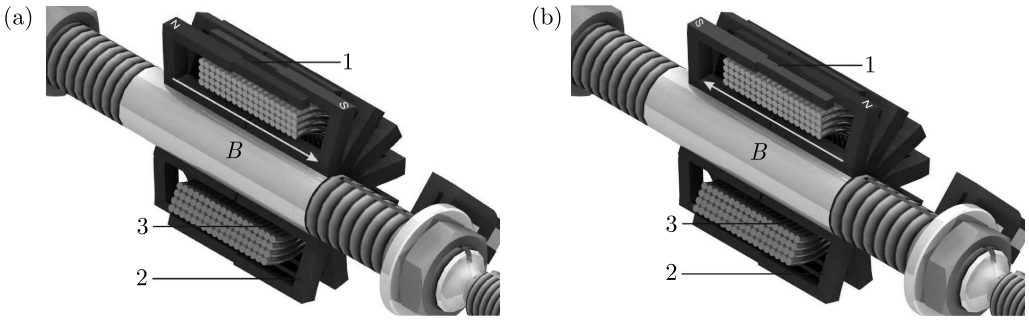

Fig. 6. Operating principle of the generator

the current response of the coil to the voltage input with the amplitude 1 V. The steady state value of current was found to be about 0.5 A. The measured current responses were utilised to derive the time constant of the control coil, which was found to be $\tau_g = 11\,\text{ms}$. With the time constant being known and the coil resistance being measured ($R_g = 2.7\,\Omega$), the coil inductance was derived accordingly $L_g = 0.031\,\text{H}$.

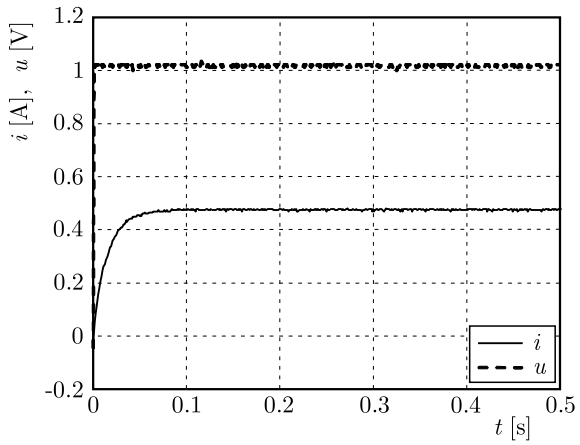

Fig. 7. Current response of the generator coil to the step-like voltage input with the amplitude 1 V

Further tests were conducted to test the generator performance under idle run and under load applied to the control coil in the MR damper, for the speed range (10, 250) rpm. The tests involved measurements of the emf in the generator (idle run) and of the voltage and the current level in the control coil (under load). The equivalent electric circuit of the generator and the damper is depicted in Fig. 8.

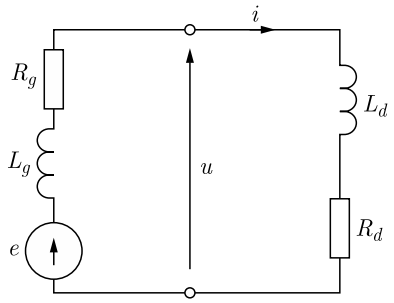

Fig. 8. Schematic diagram of the generator-MR damper circuit

Figures 9a and 9b show selected results of the experimental tests. Plots in Fig. 9a represent time patterns of the emf in the generator coil whilst plots in Fig. 9b show time patterns of the voltage and current in the damper coil (under load), obtained at 100 rpm. It appears that the

maximal value of the measured emf is 17 V and the maximal values of voltage and current in the control coil are 12 V and 0.2 A, respectively. The relationships between the *rms* value of emf, *rms* value of current and the speed, determined in the range (10, 250) mm/s, are given in Fig. 10. It is clearly apparent that these quantities in function of velocity will only slightly deviate from the linear pattern.

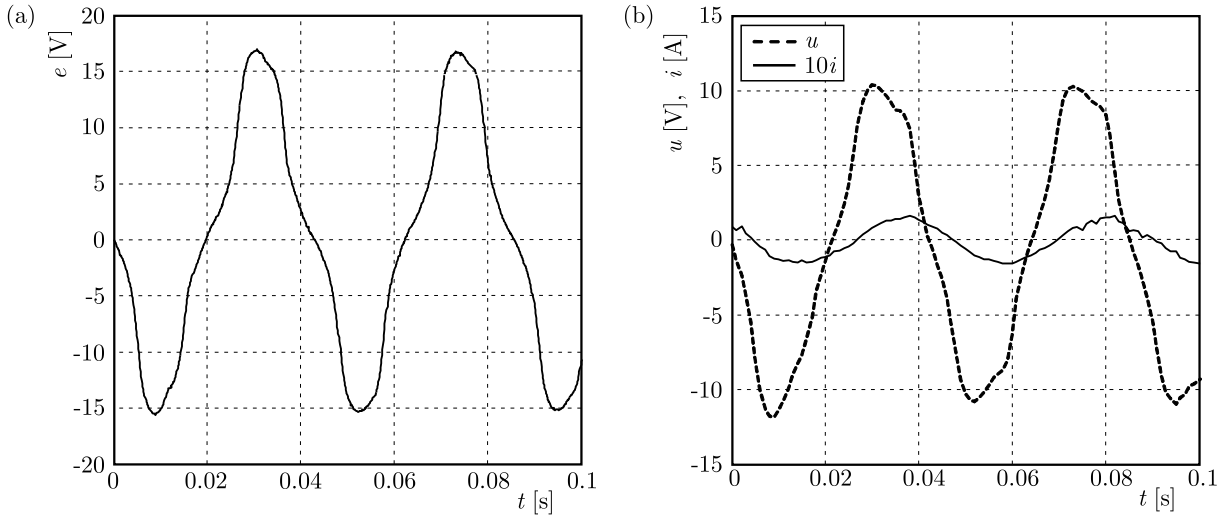

Fig. 9. Time histories of emf e (a) and of voltage u and current i (b) in the generator coil; $\omega = 100$ rpm

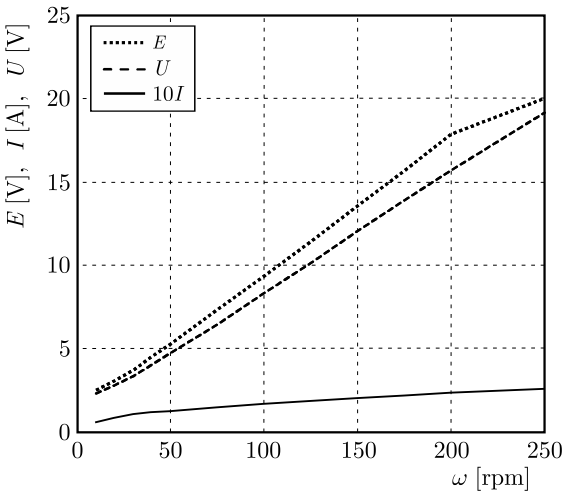

Fig. 10. *rms* values of emf in the generator coil and voltage and current in the control coil vs. speed

4. Conditioning electronics

The conditioning electronics unit creates circuits for improving the output voltage in the generator. A block diagram of the unit is shown in Fig. 11. It incorporates Graetz bridge based on the Schottky diodes (http://www.nxp.com), a converter (0.8 V/8 V), Hall sensor based on the ACS 712 system (http://www.allegromicro.com), a signal acquisition and processing block and a controller equipped with multiprocessor PIC 18 (Microchip Technology Inc., 2010). The voltage u_0 produced by the generator is rectified (voltage u_1) and delivered via the converter (voltage u_c) and the photo relay K_a to activate the damper control coil (voltage u). The controller regulates the photo relay K_a and supervises the interaction with the PC via a USB port.

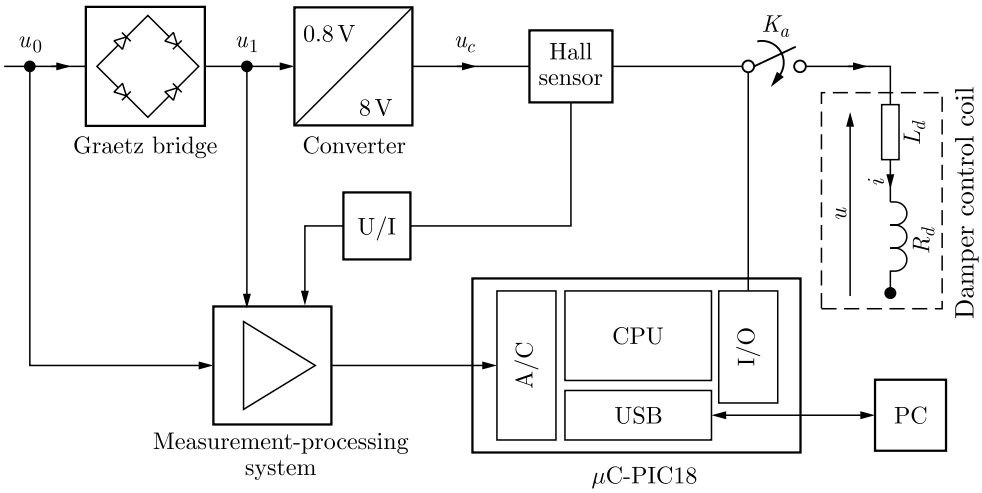

Fig. 11. Block diagram of the conditioning electronics unit

The unit described was tested experimentally. Two cases were considered in the experiments (see Fig. 12). In first case, the damper coil was not supplied (idle run) whilst in case 2, the damper coil was supplied with voltage controlled by the photo relay K_a equipped with a controller (under load).

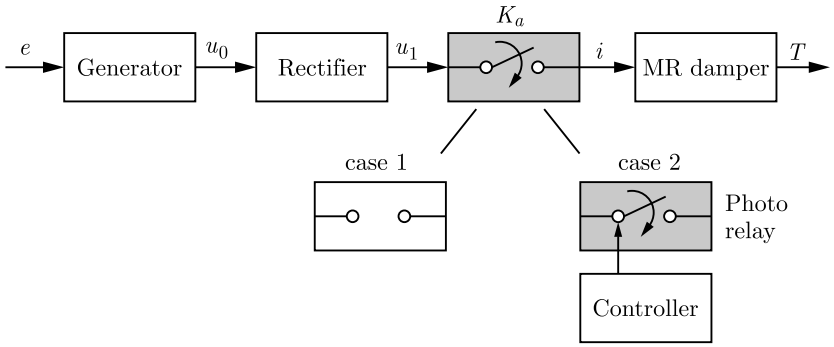

Fig. 12. Block diagram of the system in case 1 and 2

The idle-run testing began at the speed 10 rpm, and was gradually increased up to 40 rpm. Selected results are shown in Fig. 13a, plotting time histories of the emf in the generator voltage (u_0) and the output voltage from the converter u_c at speed 40 rpm. The voltage u_c reaches the value 8 V, which is the maximal admissible level for the type of converter employed in the unit.

The tests conducted under the loading conditions revealed that at speed 40 rpm the amplitude of the output voltage from the generator would go down to about 1.1 V, making the correct operation of the converter impossible. That is why the results of the tests conducted under the loading conditions are given for the speed being twice as high, i.e. 80 rpm (Figs. 13b-14b). The plots illustrate the time histories of the output voltage from the generator u_0 and voltage u and the current in the damper coil i. The voltage is found to oscillate around 6 V and the current approaches 0.2 A. The discrepancies between the calculated and measured data of the emf, voltage and current in the damper coil are attributable to differences in the values assumed for simulations and the actual parameter values of the unit components, and to the fact that the converter frequency was not included in the simulation procedure.

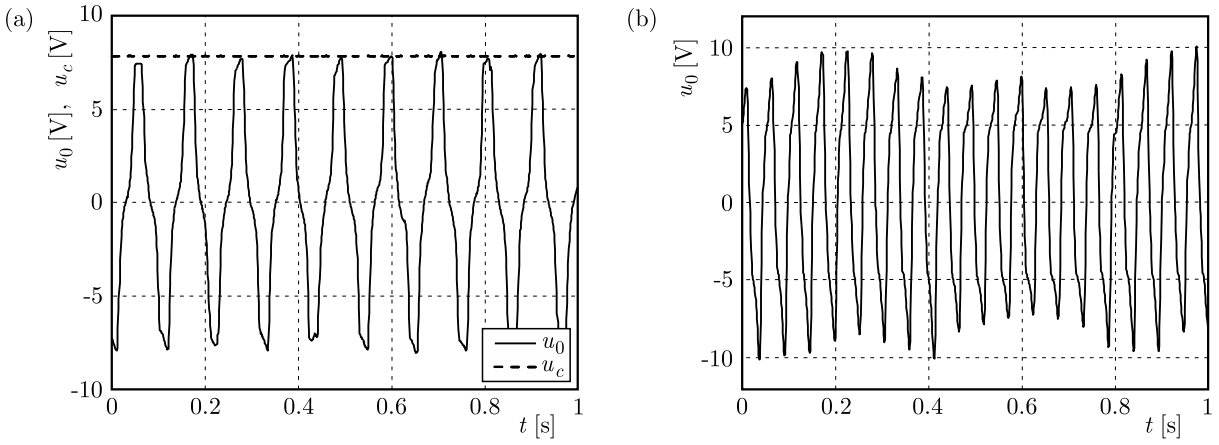

Fig. 13. Time histories of output voltage from: (a) the converter and generator in case 1 ($\omega = 40$ rpm), (b) the generator in case 2 ($\omega = 80$ rpm)

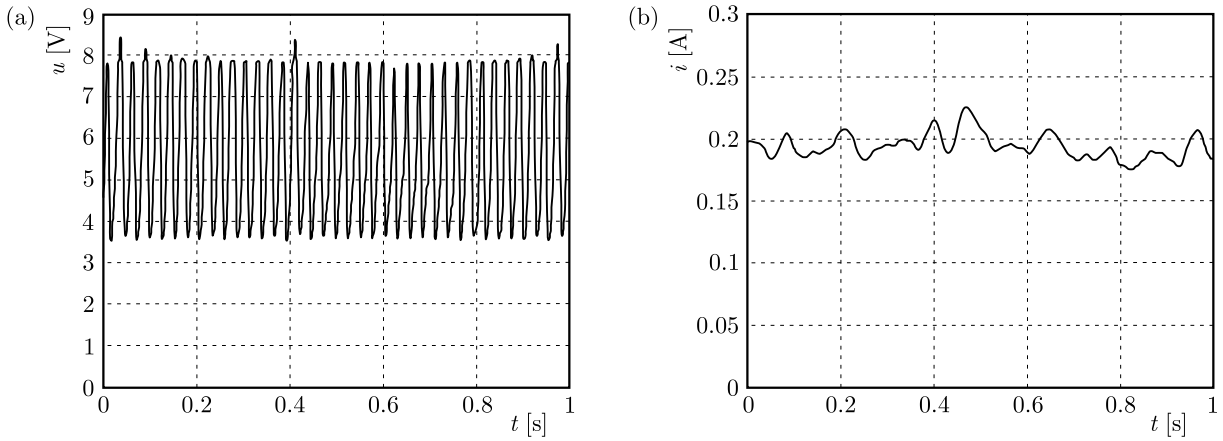

Fig. 14. Time history of voltage (a) and current (b) in the damper coil in case 2, $\omega = 80$ rpm

5. Generator-MR damper system

The tested system is indicated by a broken line in the experimental set-up shown in Fig. 15. The diagram of the measurement and control system (see Fig. 16) comprises an AD/DA board by CompacDAQ (http://sine.ni.com) connected to a PC, a drive controller (MINT Drive II) supported by Mint Workbench software (http://www.baldormotion.com) controlling the electric motor in the drive system and by LabView software operating under MS Windows. The measured quantities included the speed ω, emf in the generator e, voltage u, current i and torque T in the damper. The sampling frequency was 1 kHz.

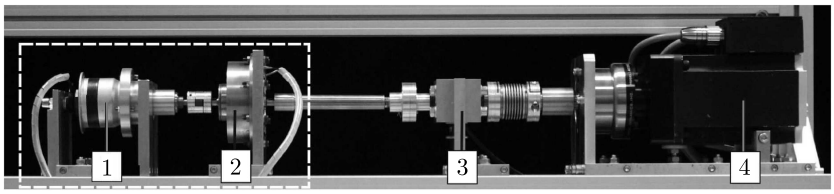

Fig. 15. Experimental set-up: 1 – generator, 2 – MR damper, 3 – torque meter, 4 – drive system

The first tests were conducted under idle run. The results are summarised in Fig. 17, showing time histories of the emf e in the generator at the speed 10, 30, 40 rpm. It seems that the emf varies over time and tends to grow with an increased speed. The variability range of emf is 0-4 V at 10 rpm and 4-6 V at 30 rpm and 6-7 V at 40 rpm.

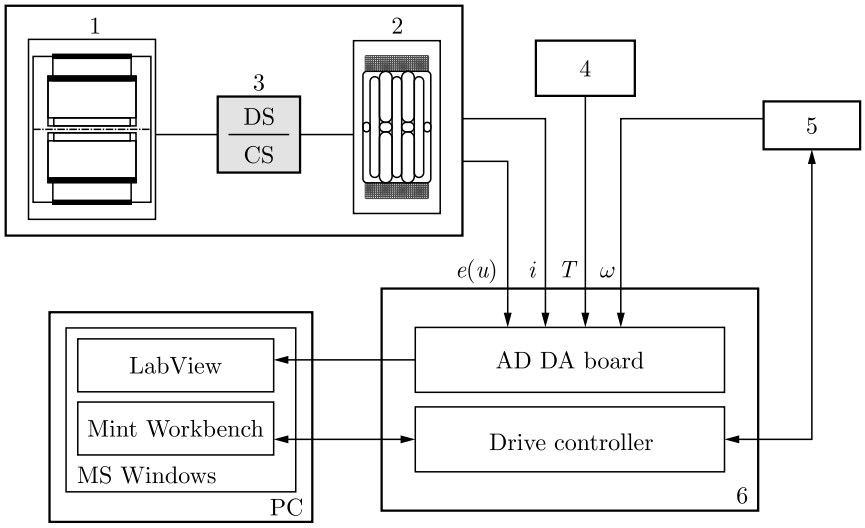

Fig. 16. Schematic diagram of the measurement and control systems: 1 – generator, 2 – MR damper, 3 – conditioning electronics, 4 – torque meter, 5 – drive system, 6 – switchbox

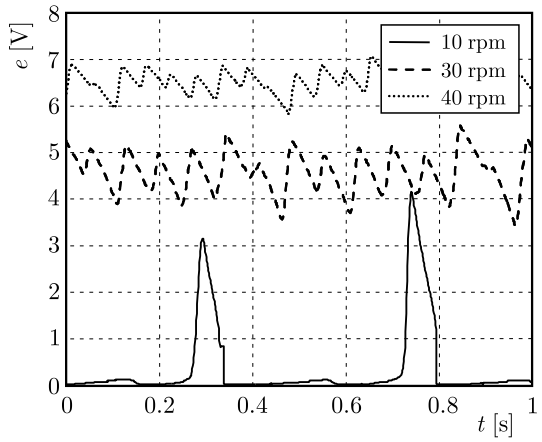

Fig. 17. Time patterns of emf in the generator at ω: 10, 30, 40 rpm

In the second stage of the experimental program, the testing was done on the system under load in the speed range $(10, 90)$ rpm. Two distinct cases were considered:

- the coil in the generator was directly connected with the damper coil (case DS),
- the coil in the generator was connected to the damper coil via the electronics unit (case CE).

Test results are shown in Fig. 18 (case DS) and Fig. 19 (case CE), plotting time histories of the voltage, current and torque in the damper at the speed 60, 80, 90 rpm. The results obtained for the two cases lead us to the following conclusions:

- in DS case, the voltage in the system increases with the speed whilst the maximal variability range is about 19 V at speed 60 rpm and 22 V at speed 90 rpm,
- in CE case, the voltage in the system also increases with speed, and its variability range is 4-8 V at speed 60 rpm and 3-7 V at speed 90 rpm,
- the largest levels of current are registered in case CE at the speed 80 rpm,
- in DS case, the torque delivered by the device does not change with the speed,
- in CE case, the torque increases with the speed.

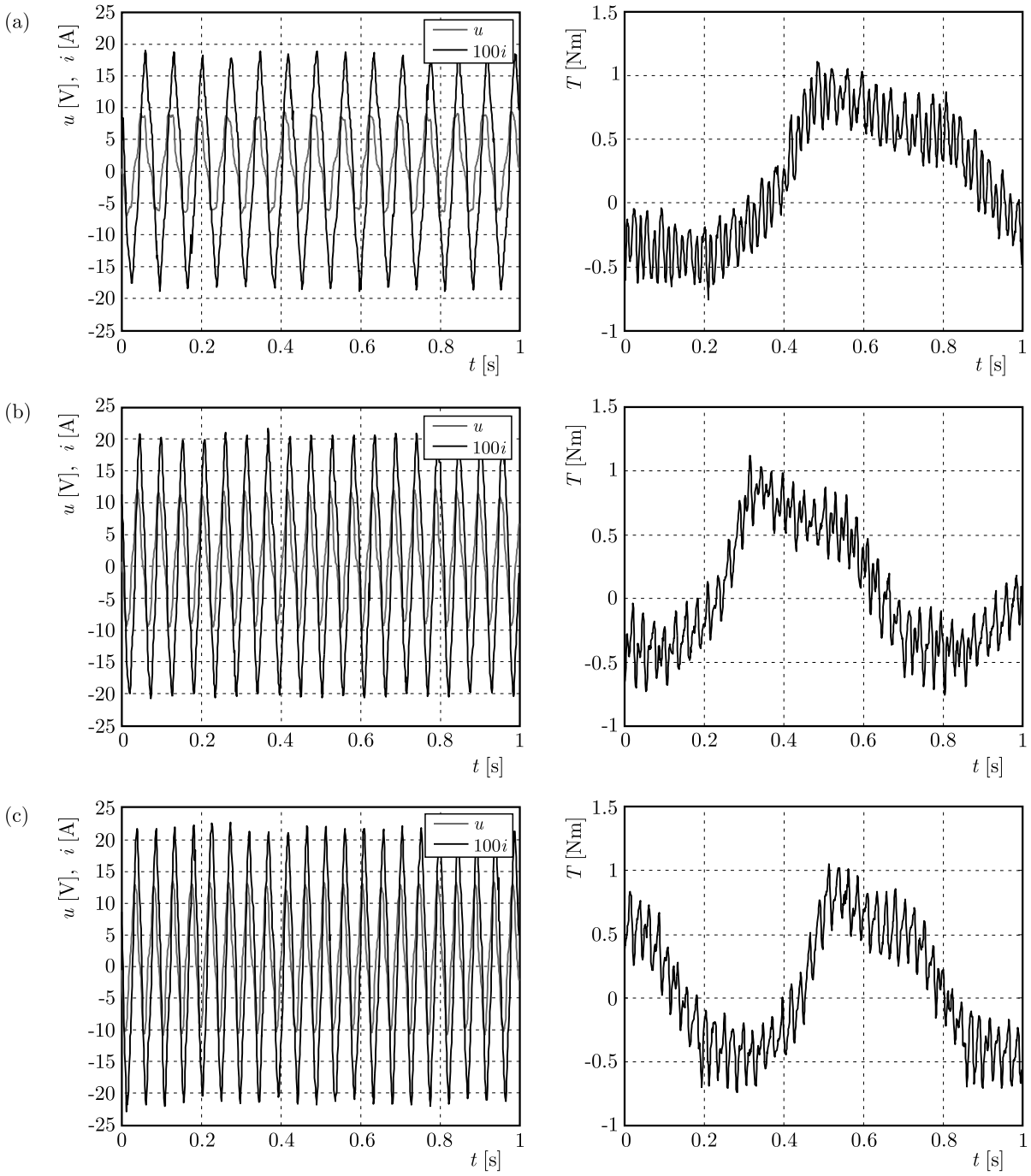

Fig. 18. Time histories of voltage, current and torque in the system in case DS: (a) $\omega = 60\,\mathrm{rpm}$, (b) $\omega = 80\,\mathrm{rpm}$, (c) $\omega = 90\,\mathrm{rpm}$

6. Summary

The study summarises research investigations of an energy harvesting system utilising rotary motion. The system is composed of: a rotary MR damper, a rotary power generator and a conditioning electronics unit. The material summarises experimental testing of each system component and the whole system.

The research investigations lead us to the following conclusions:

- a change in the speed during idle run leads to a change in the amplitude and pattern of the emf in the generator,

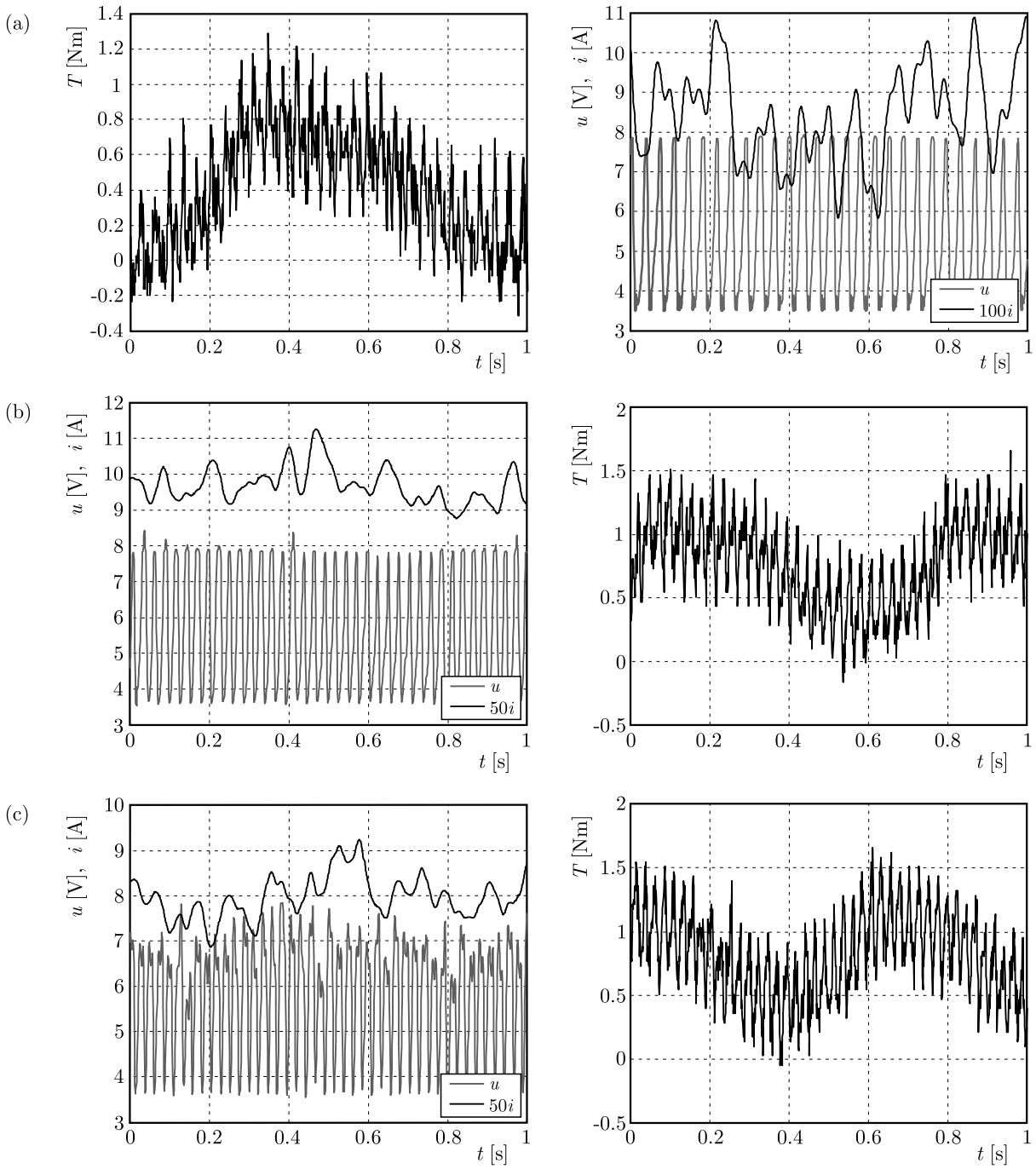

Fig. 19. Time histories of voltage, current and torque in the system in case CE: a) $\omega = 60$ rpm, (b) $\omega = 80$ rpm, (c) $\omega = 90$ rpm

- parameters of the electrical circuit models are nonlinear functions of speed,
- energy recovered by the generator is sufficient to power the device, though it may prove insufficient at velocities below 10 rpm when the generator output voltage is rather small and further reduced due to voltage drops across the diodes in the Graetz bridge,
- the voltage range handled by the converter has to be extended since the conditioning electronics unit performs better when the generator output voltage should not exceed 8 V.

The system investigated provides a smart solution with potential applications to control of rotary motion. The main advantage of the system is its easy adaptability to external excitations and the fact that no external power supply unit is required.

Further research efforts will focus on developing a different design structure of the generator and a more universal conditioning electronics unit.

Acknowledgement

This research is supported by the National Centre for Research and Development under grant No. NR03-0046-10.

References

1. Avadhany S., Abel P., Tarasov V., Anderson Z., 2008, Regenerative shock absorber, US Patent 8376100
2. Chen C., Liao W.H., 2012, A self-sensing magnetorheological damper with power generation, *Smart Materials and Structures*, **21**, 025014
3. Cho S.W., Jung H.J., Lee I.W., 2007, Feasibility study of smart passive control system equipped with electromagnetic induction device, *Smart Materials and Structures*, **16**, 2323-2329
4. Choi Y.T., Werely N.M., 2009, Self-powered magnetorhelogical dampers, *Journal of Vibration and Acoustics*, **131**, 44-50
5. Hong J.H., Choi K.M., Lee J.H., Oh J.W., Lee I.W., 2007, Experimental study on smart passive system based on MR damper, *Proceedings of the 18th KKCNN Symposium on Civil Engineering*, Taiwan
6. http://sine.ni.com; CompacDaQ Technical Information
7. http://www.baldormotion.com; Mint Workbench Technical Information
8. http://www.allegromicro.com; Allegro MicroSystems LLC, ACS712 Hall-Effect Current Sensor IC, Technical Information
9. http://www.basonetic.com; MR-Fluid Basonetic® 2040 Technical Information
10. http://www.nxp.com/documents/data_sheet/PMEG3050EP.pdf
11. Jung H.J., Jang D.D., Koo J.H., Cho S.W., 2010, Experimental evaluation of a self-sensing capability of an electromagnetic induction system designed for MR dampers, *Journal of Intelligent Material Systems and Structures*, **21**, 837-836
12. Li Z., Zhuo L., Kuang J., Luhrs G., 2013, Energy-harvesting shock absorber with a mechanical motion rectifier, *Smart Materials and Structures*, **22**, 028008
13. Liao W.H., Chen C., 2012, Self-powered, self-sensing magnetorheological dampers, US Patent Application No: 2012/0031,719
14. Microchip Technology Inc., PIC18F47J53 Family Data Sheet, 2010
15. Opera-3d version 15R2, User Guide, Cobham Technical Services, Vector Fields Software, 2011
16. Priya S., Inman D., 2009, *Energy Harvesting Technologies*, Springer Science+Business Media
17. Sapiński B., 2011, Experimental study of a self-powered and sensing MR damper-based vibration control system, *Smart Materials and Structures*, **20**, 105007
18. Sapinski B., 2014, Energy harvesting MR linear damper: prototyping and testing, *Smart Materials and Structures*, **23**, 035021
19. Scruggs J.T., Lindner D., 1999, Active energy control in civil structure, *Proceedings of SPIE Conference on Smart Systems for Bridges, Structures and Highways*
20. Wang D.H., Wang T., 2010, An integrated relative displacement self-sensing magnetorheological damper, *Smart Materials and Structures*, **19**, 105008

Manuscript received July 1, 2015; accepted for print September 30, 2015

JOURNAL OF THEORETICAL AND APPLIED MECHANICS
54, 3, pp. 691-703, Warsaw 2016
DOI: 10.15632/jtam-pl.54.3.691

CUTTING PARAMETERS AND VIBRATIONS ANALYSIS OF MAGNETIC BEARING SPINDLE IN MILLING PROCESS

Amel Bouaziz, Maher Barkallah, Slim Bouaziz
Laboratory of Mechanical Modeling and Production, National School of Engineers of Sfax, University of Sfax, Tunisia
e-mail: slim.bouaziz1@gmail.com

Jean Yves Choley
Laboratory of Engineering in Mechanical Systems and Materials, SUPMECA, Saint-Ouen, France

Mohamed Haddar
Laboratory of Mechanical Modeling and Production, National School of Engineers of Sfax, University of Sfax, Tunisia

In modern production, milling is considered the widespread cutting process in the formatting field. It remains important to study this manufacturing process as it can be subject to some parasitic phenomena that can degrade surface roughness of the machined part, increase tool wear and reduce spindle life span. In fact, the best quality work piece is obtained with a suitable choice of parameters and cutting conditions. In another hand, the study of tool vibrations and the cutting force attitude is related to the study of bearings as they present an essential part in the spindle system. In this work, a modeling of a High Speed Milling (HSM) spindle supported by two pair of Active Magnetic Bearings (AMB) is presented. The spindle is modeled by Timoshenko beam finite elements where six degrees of freedom are taken into account. The rigid displacements are also introduced in the modeling. Gyroscopic and centrifugal terms are included in the general equation. The bearings reaction forces are modeled as linear functions of journal displacement and velocity in the bearing clearance. A cutting force model for peripheral milling is proposed to estimate the tool-tip dynamic responses as well as dynamic cutting forces which are also numerically investigated. The time history of response, orbit, FFT diagram at the tool-tip center and the bearings dynamic coefficients are plotted to analyze dynamic behavior of the spindle.

Keywords: milling process, cutting forces, chip thickness, dynamic coefficients, orbit

1. Introduction

During the last years, High Speed Milling (HSM) process have become one of the most popular in the industry of shaping and producing mechanical parts and molds. It allows having complex forms thanks to the variety of cutting tools composed of several cutting edges and driven by rotational motion. There are multiple parameters that influence the forces acting on the cutter. Their knowledge and prediction become important in order to favor the adaptation of cutting tools conditions. The last researches were concentrated on studying the milling spindle with different types of bearings, especially AMB as they present many advantages deduced by Knospe (2007). He showed that AMB were characterized by their accuracy, high robustness to shock and high rotational speed, which was also proved by Kimman *et al.* (2010) and Gourc *et al.* (2011). Also, among the special feature of AMB, the possibility to vary the number of electromagnets is treated in literature. Indeed, Bouaziz *et al.* (2011, 2013) studied that variation effect on the dynamic behavior of a rigid rotor with a misalignment defect. They demonstrated that the vibratory level of the rotor decreased with an increase in the electromagnets number. Belhadj Messaoud *et al.* (2011) presented the effect of the air gap and rotor speed on electromagnetic forces. From the results obtained in that work, they concluded that the electromagnetic forces

intensity increased when the air gap decreased, but it remained unresponsive according to the rotor speed level.

In addition, it is possible to use various components of AMB such as sensors and feedback currents to predict cutting forces. In fact, Auchet *et al.* (2004) expanded a new method to measure cutting forces by analyzing command voltages of AMB. This cutting force has an influence on dimensional accuracy due to the tool and work piece deflection in peripheral milling. For this, a theoretical dynamic cutting force model was presented by Liu *et al.* (2002) including the size effect of not deformed chip thickness, the impact of the effective rake angle and the chip flow angle. Numerical simulation and prediction of cutting forces in five-axis milling processes with cutter run-out and based on tool motion analysis was presented by Sun and Guo (2011). The predicted cutting forces illustrate good accordance with experimental results that the tool orientation angle and cutting depth vary continuously for both the specified cutting conditions and milling cases. Relative to classical methods, that proposed method permits one to predict cutting forces with a higher accuracy, and it is able to be directly used in five-axis milling. Lai (2000) studied the influence of dynamic radii, cutting feed rate, and radial and axial depths of cut on milling forces. He concluded that the chip thickness presented the most significant influence. In the same context, Klocke *et al.* (2009) investigated the influence of cutting parameters in micro milling on the surface quality and tool life such as cutting speed and feed per tooth. As a results, they showed that the feed per tooth and feed rate extremely affected the surface quality in micro milling. In fact, to increase the surface quality, it is necessary to decrease the feed rate value. From an analytical prediction of the cutting force, Fontaine *et al.* (2007) presented a method to optimize the milling tools geometry. The influence of geometrical parameters like helix angle, rake angle and tool tip envelope radius was studied. The author demonstrates the ability of that type of model to provide optimization criteria for the design and selection of cutting tools. Budak (2006a,b) presented the milling force, workpiece and tool deflection, form error and stability models. From the used method, he checked the process constraints and selected the optimal cutting conditions. Concerning the machining process stability, Faassen *et al.* (2003) developed a dynamic model for milling process in which the stability lobes were generated. This model structurally predicts the stability limit slightly too conservative. Another new to the dynamical modeling of AMB to identify machining stability was presented by Gourc *et al.* (2011). From that model, the authors concluded that the machining process stability was sensitive to the position of nodes of mode of the flexible rotor. Also, they confirmed that it was important to take in consideration strong forced vibrations as they could cause loss off safety. The stability of a high speed spindle system in the presence of the gyroscopic effect was investigated by Movahhedy and Mosaddegh (2006). In that study, it has found that the stability lobe predictions based on stationary FRFs were not conservative when the gyroscopic effects were respectable and that the gyroscopic effects became significant only at very high speeds compared with conventional speeds. Also, Gagnol *et al.* (2007) developed and experimentally validated an integrated spindle finite-element model in order to characterize the dynamic behavior of a motorized machine tool spindle. They demonstrated the dependence of dynamic stiffness on spindle speed. Using this model, a new stability lobes diagram was proposed. A research performed by Zatarain *et al.* (2006) showed that mill helix angle could play an important role in instability due to repetitive impact driven chatter. In order to predict the occurrence of chatter vibrations, Lacerda and Lima (2004) applied an analytical method in which the time-varying directional dynamic milling forces coefficients were expanded in Fourier series and integrated along width of the cut bound by entry and exit angles. Wan *et al.* (2010) proposed a unified method for predicting stability lobes of the milling process with multiple delays. It was found that feed per tooth had great influence on the stability lobes when cutter run out occurred.

In this paper, a HSM spindle with AMB is modeled by the finite element method based on the Timoshenko beam theory and used by Nelson and McVough (1976) and Nelson (1980). Six

degrees of freedom are considered. Rigid displacements are also taken in account (Hentati *et al.*, 2013). AMB are presented as spring and damper elements. Peripheral milling process is modeled and cutting forces are formulated. The dynamic response at the spindle tool-tip, cutting forces in x-, y- and z- directions and the influence of some cutting parameters are predicted. The attitude of the used AMB is then investigated.

2. Modeling of AMB spindle machining

2.1. Mechanical model of the spindle

The studied spindle model is presented in Fig. 1. The modeling is based on using a new approach developed by Hentati *et al.* (2013). This method is based on coupling both elastic and rigid spindle deformations. So, the shaft is discretized into 23 Timoshenko beam elements with different circular sections, where six elastic degrees of freedom are taken in account. Six degrees of rigid motion are also considered. Thus, the gyroscopic effect and centrifugal force will be taken into account in this study. The unbalance is not treated. The tool holder and cutter are included as parts of the spindle system in the specifically developed finite element model.

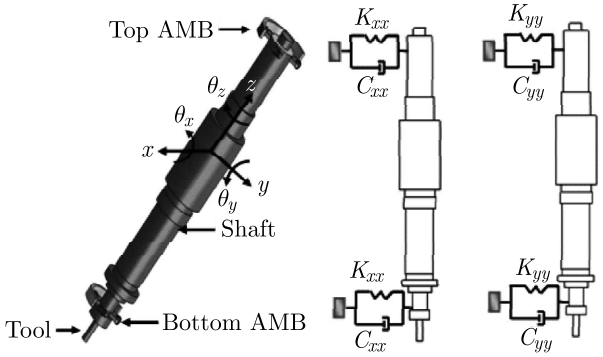

Fig. 1. Modeling of the AMB spindle machining

In this AMB spindle model we make use of a classical bearing configuration. Two radial AMBs and an axial bearing suspend the rotor in the central position. The AMB consists of four electromagnets symmetrically placed relative to the rotor. Electromagnetic forces produced by every pair of electromagnets in the x- and y-directions are presented in the following equation (Bouaziz *et al.*, 2011)

$$f_j(I_j, u_j) = -a\left[\left(\frac{I_0 - I_j}{e_0 - u_j}\right)^2 - \left(\frac{I_0 + I_j}{e_0 + u_j}\right)^2\right] \qquad j = x, y \tag{2.1}$$

where u_j represents small deformations in the j-th direction and e_0 is the nominal air gap between the shaft and the stator, a is the global magnetic permeability, and it is expressed as follows

$$a = \frac{\mu_0 S n^2 I_0^2}{4}\cos\theta$$

μ_0, n, S and θ are respectively permeability of vacuum, windings number, cross sectional area and half angle between the poles of electromagnets.

A proportional derivative controller (PD) is used to determine the control current expressed as

$$I_j = k_p u_j + k_d \dot{u}_j \qquad j = x, y \tag{2.2}$$

where $\dot{u}_j$ is the velocity corresponding to the small deformation u_j, k_p presents the proportional gain. It is assumed to be in periodic form for better stability and controllability of motion of the spindle AMB system (Bouaziz *et al.*, 2011, 2013; Amer and Hegazy, 2007)

$$k_p = k_0 + k_1 \cos \omega t + k_2 \cos 2\omega t \tag{2.3}$$

and k_d denotes the derivative gain.

In this model and as presented in Fig. 1, the electromagnetic field is modeled by stiffness and damping coefficients. The nonlinear electromagnetic forces at each bearing can be written in matrix form as follows (Bouaziz *et al.*, 2011)

$$[K_{ij}] \begin{Bmatrix} u_x \\ u_y \end{Bmatrix} + [C_{ij}] \begin{Bmatrix} \dot{u}_x \\ \dot{u}_y \end{Bmatrix} = \begin{Bmatrix} f_x \\ f_y \end{Bmatrix} \tag{2.4}$$

where $[K_{ij}]$ is the bearing stiffness matrix, $[C_{ij}]$ represents the bearing damping matrix

$$[K_{ij}] = \begin{bmatrix} K_{xx} & 0 \\ 0 & K_{yy} \end{bmatrix} \qquad [C_{ij}] = \begin{bmatrix} C_{xx} & 0 \\ 0 & C_{yy} \end{bmatrix} \tag{2.5}$$

The axial bearing consists of two magnetic actuators on each side of the thrust element. The magnetic actuators in this setup are reluctance type actuators having a circular u-shaped core with a tangentially wound coil. The resulting force, f_z of the axial bearing is linearized as

$$f_{ab} = K_{iz} I_z + K_z u_z \tag{2.6}$$

where K_{iz}, I_z and K_z are the force current dependencies, the control current of the actuator and the negative stiffness of the axial bearing respectively, u_z is the axial displacement of the shaft.

2.2. Model formulation of the cutting forces

Figure 2 presents a cross-sectional view of the cutting force model in peripheral milling. The cutting force acting on the tool and the workpiece vary depending on chip thickness, shock of engagement, specific cutting pressure and generated vibrations. They appear only when the tool is in contact with the part (cutting region). The cutting force is characterized by a tangential component F_t orthogonal to the specific segment of the cutting edge. This force is assumed to be proportional to the chip thickness and axial depth of the cut. The radial component F_r is proportional to F_t and orthogonal to both the cutting edge segment and the z-axis. The third component is the axial forc F_a. This one is typically much smaller than either F_t or F_r and does not contribute greatly to the bending moment produced on the cutter.

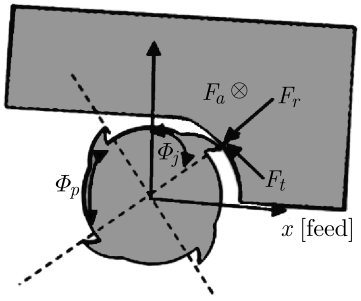

Fig. 2. Cross-sectional view of a peripheral milling process showing different forces

The milling force variation against cutter rotation can be predicted by calculating F_t, F_r and F_a for different values of ϕ_j

$$F_t = K_t a_p H(\phi_j(t)) \qquad F_r = K_r F_t \qquad F_a = K_a F_t \tag{2.7}$$

where $H(\phi_j(t))$ is the instantaneous chip thickness, $\phi_j(t)$ is the rotation angle of tooth j, measured from the positive y-axis as shown in Fig. 2. a_p, K_t, K_r and K_a are axial depth and the specific coefficients of the cut.

The resulting chip thickness $H(\phi_j(t))$ is composed of a static part (stationary part) $H_s(\phi_j(t))$ due to the rigid body motion of the cutter and a dynamic component $H_d(\phi_j(t))$ which is caused by vibrations of the tool at the present and previous tooth periods. $H_s(\phi_j(t))$ and $H_d(\phi_j(t))$ assume the following form

$$\begin{aligned} H_s(\phi_j(t)) &= f_z \sin(\phi_j(t)) \\ H_d(\phi_j(t)) &= [u_x(t) - u_x(t-\tau)] \sin(\phi_j(t)) - [u_y(t) - u_y(t-\tau)] \cos(\phi_j(t)) \end{aligned} \tag{2.8}$$

where $u_x(t)$ and $u_y(t)$ represent deflections of the tool-tip at the present time, $u_x(t-\tau)$ and $u_y(t-\tau)$ are deflections of the tool-tip at the previous time, τ is the tooth passing period time, defined as $\tau = 60/NZ$ and N, Z are respectively the spindle speed and the teeth number of the cutter.

The rotation angle $\phi_j(t)$ is expressed as follows

$$\phi_j(t) = \Omega t + j\Phi_p \qquad j = 0, 1, \ldots, Z-1 \tag{2.9}$$

where Ω is the angular velocity in rad/s and Φ_p is the angle between two subsequent teeth (pitch angle), expressed as $\Phi_p = 2\pi/Z$.

2.3. Equation of motion

As the modeling of the spindle is based on the coupling of rigid displacements and small elastic deformations, the total displacement vector is expressed as follows

$$\mathbf{Q} = [U_1, V_1, W_1, \theta_{x_1}, \theta_{y_1}, \theta_{z_1}, \ldots, U_i, V_i, W_i, \theta_{xi}, \theta_{y_i}, \theta_{z_i}, X_A, Y_A, Z_A, \alpha_x, \alpha_y, \alpha_z]^{\mathrm{T}} \tag{2.10}$$

i is the number of nodes, $(U_1, V_1, W_1, \theta_{x_1}, \theta_{y_1}, \theta_{z_1}, \ldots, U_i, V_i, W_i, \theta_{xi}, \theta_{y_i}, \theta_{z_i})$ presents nodal displacements, $(X_A, Y_A, Z_A, \alpha_x, \alpha_y, \alpha_z)$ are the displacements of rigid motion.

Applying the Lagrange formalism for kinetic and potential energies, the global equation of motion is

$$\mathbf{M}\ddot{\mathbf{Q}} + (\mathbf{G} + \mathbf{D} + \mathbf{C}_b(t))\dot{\mathbf{Q}} + (\mathbf{K} + \mathbf{K}_b(t))\mathbf{Q} = \mathbf{F}_{c(x,y,z)}(t, \mathbf{Q}) + \mathbf{f}_{ab}(t, \mathbf{Q}, \dot{\mathbf{Q}}) \tag{2.11}$$

where $\mathbf{M}$ is the global mass matrix, $\mathbf{G}$ – the global gyroscopic matrix

$$\mathbf{M} = \begin{bmatrix} \mathbf{M}_F & \mathbf{M}_{RF} \\ \mathbf{M}_{RF}^{\mathrm{T}} & \mathbf{M}_R \end{bmatrix} \qquad \mathbf{G} = 2\Omega \begin{bmatrix} \mathbf{G}_F & \mathbf{G}_{RF} \\ -\mathbf{G}_{RF}^{\mathrm{T}} & \mathbf{G}_R \end{bmatrix}$$

F and R subscripts respectively represent the flexible or rigid part. $\mathbf{D} = \alpha\mathbf{M} + \beta\mathbf{K}$ presents the damping matrix numerically constructed as a linear combination of the mass and stiffness matrix, where α and β are the damping coefficients. $\mathbf{C}_b(t)$ is the variable matrix containing the damping coefficients of bearings

$$\mathbf{C}_b(t) = \begin{bmatrix} 0 & \cdot & \cdot & 0 & \cdot & \cdot & 0 & \\ & \cdot & \cdot & \cdot & \cdot & \cdot & \cdot & 0 \\ \cdot & C_{xx} & 0 & \cdot & \cdot & \cdot & \cdot & \\ 0 & 0 & C_{yy} & \cdot & \cdot & \cdot & \cdot & \\ \cdot & \cdot & \cdot & 0 & C_{xx} & 0 & \cdot & \\ \cdot & \cdot & \cdot & \cdot & C_{yy} & 0 & & \\ 0 & \cdot & \cdot & \cdot & 0 & \cdot & 0 & \end{bmatrix}$$

$\mathbf{K}$ is the global stiffness matrix, $\mathbf{K}_c$ – the global centrifugal matrix

$$\mathbf{K} = \begin{bmatrix} \mathbf{K}_F & \mathbf{0} \\ \mathbf{0} & \mathbf{0} \end{bmatrix} - \underbrace{\Omega^2 \begin{bmatrix} \mathbf{C}_F & \mathbf{0} \\ \mathbf{0} & \mathbf{0} \end{bmatrix}}_{\mathbf{K}_c}$$

$\mathbf{K}_b(t)$ is the variable matrix containing the stiffness coefficients of bearings

$$\mathbf{K}_b(t) = \begin{bmatrix} 0 & \cdot & \cdot & 0 & \cdot & \cdot & 0 \\ \cdot & \cdot & \cdot & \cdot & \cdot & \cdot & 0 \\ \cdot & K_{xx} & 0 & \cdot & \cdot & \cdot & \cdot \\ 0 & 0 & K_{yy} & \cdot & \cdot & \cdot & \cdot \\ \cdot & \cdot & \cdot & 0 & K_{xx} & 0 & \cdot \\ \cdot & \cdot & \cdot & \cdot & 0 & K_{yy} & 0 \\ 0 & \cdot & \cdot & \cdot & 0 & \cdot & 0 \end{bmatrix}$$

and $\mathbf{F}_{c(x,y,z)}(t, \mathbf{Q})$ denotes the cutting forces in the x-, y- and z-directions, respectively, $\mathbf{f}_{ab}(t, \mathbf{Q}, \dot{\mathbf{Q}})$ is the electromagnetic force vector exerted by the axial bearing.

3. Results and discussions

In this Section, simulations are based on the spindle system with parameters listed in Tables 1 and 2. The general dynamic equation is solved by the method of resolution by Newmark coupled with Newton Raphson.

Table 1. Spindle parameters

Parameter	Symbol	Value	Unit
Permeability of vacuum	μ_0	$4\pi \cdot 10^{-7}$	Wb/Am
Air gap between stator and shaft	e_0	0.8	mm
Effective cross-sectional area of one electromagnet	S	200	mm^2
Number of windings around the core	n	300	–
Half angle between poles of electromagnet	θ	22.5	deg
Bias current	I_0	3	A
Rotor angular velocity	N	20000	rpm
Rotor length	L	651.95	mm
Stiffness coefficients	$K_{xx}, K_{xy}, K_{yx}, K_{yy}$	–	N/m
Damping coefficients	$C_{xx}, C_{xy}, C_{yx}, C_{yy}$	–	Ns/m
Derivative gain	k_d	42.4	As/m
Proportional gain constant	k_0	4520	–
	k_1	14869	–
	k_2	14869	–
Young's modulus	E	$2.1 \cdot 10^{11}$	Pa
Density	ρ	7.85	g/cm^3
Poisson's ratio	ν	0.3	–
Moment of inertia	I	0.136	kgm^2

The time responses of the tool tip are plotted in Fig. 3. From Fig. 3a, some transient effects can be observed during the first cycle while a steady state is achieved after that. Their magnitude is close. In fact, before the cutter is fully engaged, the arc of engagement increases gradually while

Table 2. Cutting parameters

Parameter	Symbol	Value	Unit
Feed per tooth	f_z	0.16	mm
Axial depth of cut	a_p	5	mm
Tangential cutting coefficient	K_t	644	N/mm^2
Radial cutting coefficient	K_r	0.38	N/mm^2
Axial cutting coefficient	K_a	0.25	N/mm^2
Teeth number	Z	2	–

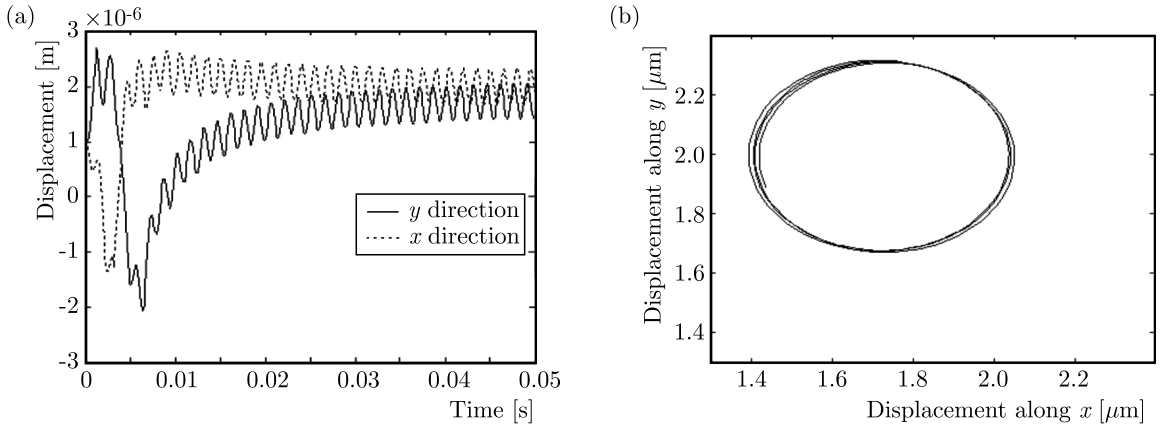

Fig. 3. The time response of the tool tip: (a) displacement of the tool tip, (b) orbit of the tool tip

the cutter is entering progressively in the cutting zone. Consequently, this leads to a gradual increase of vibrations.

The orbit of the tool tip has an elliptical shape explained by the introduction of flexible bearings (stiffness coefficient) that make the system asymmetric. Therefore, we note that vibrations in the x- and y-directions are different from the elliptic trajectory.

The Fast Fourier Transformation (FFT) diagram for the x-response of the tool-tip with two teeth at a spindle speed of 20000 rpm is shown in Fig. 4. It is found that two frequencies govern the behavior of the tool-tip response. The major peak corresponds to the frequency of $2F_r$ (666.66 Hz) which occurs with the cutting force frequency. An obvious low frequency peak, corresponding with the rotation frequency, is also found.

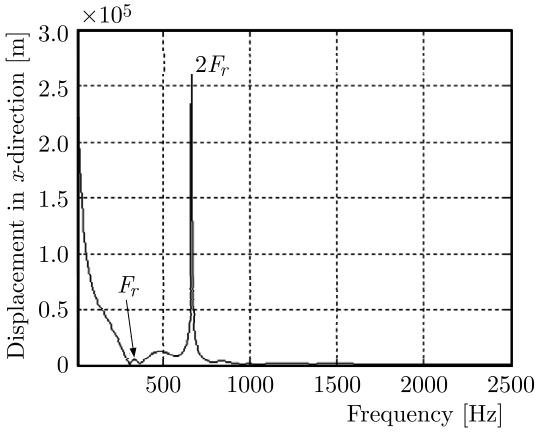

Fig. 4. Response of the tool-tip in the x-direction with 2 teeth

The dynamic cutting force in the x-, y- and z-directions for a two teeth cutter are presented in Fig. 5. It can be seen that the cutting force is constant as the cutter is always in contact with the matter and where the evolution of radial engagement is continuous. All the cutting components have periodic and sinusoidal behavior with a period of time equal to the half of the rotation period ($0.5T_r$).

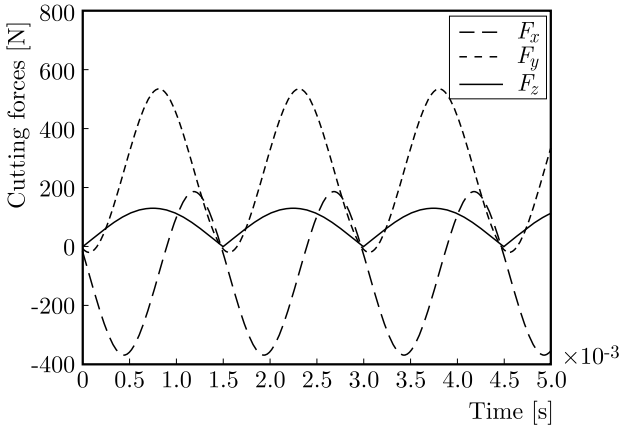

Fig. 5. Cutting forces in the x-, y- and z-directions as function of time

The following part of the study is devoted to presentation of the impact of some parameters involved in the cutting forces such as the teeth number, feed per tooth and speed rotation. Figure 6 presents variation of the cutting forces for different values of feed per tooth: 0.1, 0.2 and 0.3 mm. It appears that the components in the x- and y-directions increase with an increase in the feed. It is worth noticing that when $f_z = 0.1$ mm, the maximum value of F_y is greater than the half value as $f_z = 0.3$ mm. This evolution is logic and is explained by the fact that the feed is involved in the cut section. In fact, if the feed increases, the cutting section also increases and, therefore, the cutting force increases. This result was found by Liu *et al.* (2002) who also revealed that this variation was relative to the size effect of the chip thickness. In addition, we note that the F_y component rises with a greater rate.

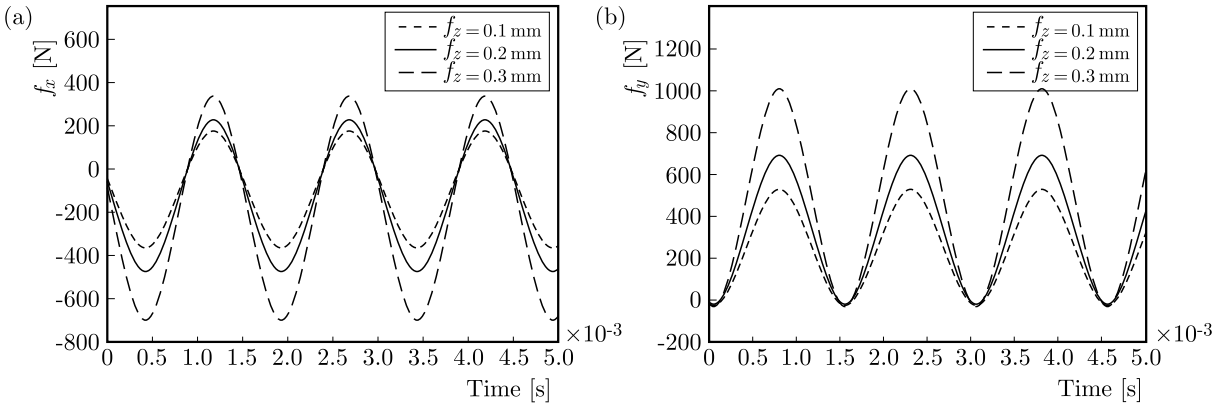

Fig. 6. Predicted cutting forces for different feed per tooth: (a) x-direction, (b) y-direction

Figure 7 shows axial depth of the cut effects the cutting force value. When this parameter changes, the cutting force vary significantly. It increases when the cutting depth increases. This raise is explained by the increase of the width of chip. For these values of axial cutting depth, we find that the cutting forces F_y are always more important than the cutting force F_x.

Figure 8a shows the instantaneous cutting forces for the tooth number $Z = 3$. It can be seen from variation of F_y that the cutting operation starts when the second tooth comes out, with the maximum value reaching 580 N.

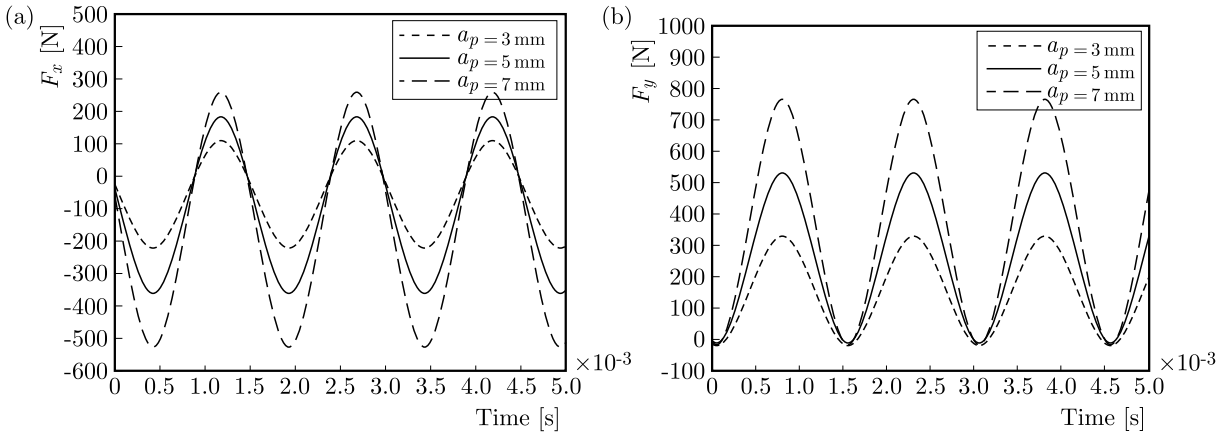

Fig. 7. Predicted cutting forces for various cutting depth: (a) x-direction, (b) y-direction

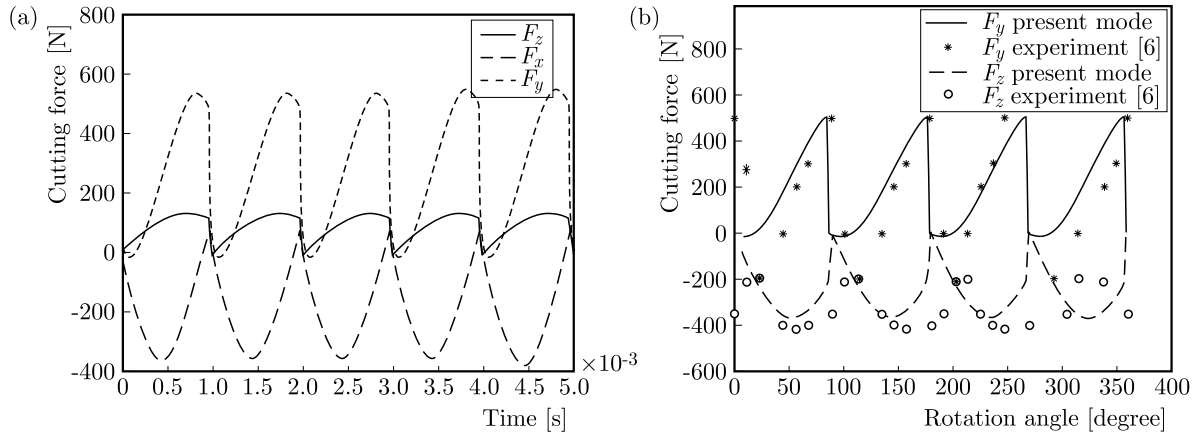

Fig. 8. Cutting force in the x-, y- and z-directions: (a) $Z = 3$ teeth, (b) $Z = 4$ teeth

Although the shape of cutting forces is affected and changed compared to that with two teeth, the distribution is still continuous. This difference is explained by the summation of cutting forces of teeth in attack with the mutter. So, it is possible that the number of teeth variation will significantly influence the accuracy of the finished part. Figure 8b also presents the predicted values of the cutting force for the same conditions but for a four teeth tool. It is noticed that the shape and values for the cutting force components F_x and F_y are similar to those of the cutter with three teeth. Also, these levels for the cutting forces, for a four flutes, seems to be typical for peripheral milling as this result is approximately close to the experimental ones found by Budak (2006a). The percentage ratio of the difference between the absolute maximum predicted and measured value relative to the measured value represents an error of 9%.

The variation of dynamic coefficients (K_{xx}, K_{yy}) is presented in Fig. 9. It is clear that the curves have a periodic form with amplitude reaching $1.8 \cdot 10^7$ N/m. The coefficient K_{xx} is less important than K_{yy}, that is why we have obtained in Fig. 3 vibrations in the x-direction more severe than in the y-direction.

The damping coefficients, presented in Fig. 10, have low amplitude varying from about $-4.1535 \cdot 10^4$ to $-4.15345 \cdot 10^4$ Ns/m with instability in the beginning.

Figure 11 shows the effect of the nominal air gap on the dynamic coefficients. This result reveals that the amplitude of both stiffness and damping coefficients decrease with an increase in the nominal air gap. This result was also proved by Bouaziz *et al.* (2011).

The impact of the bias current I0 on the dynamic coefficients is presented in Fig. 12. For different values of I_0: $I_0 = 5$ A, $I_0 = 6$ A and $I_0 = 6.5$ A, it is found that K_{xx} and C_{xx} rise when

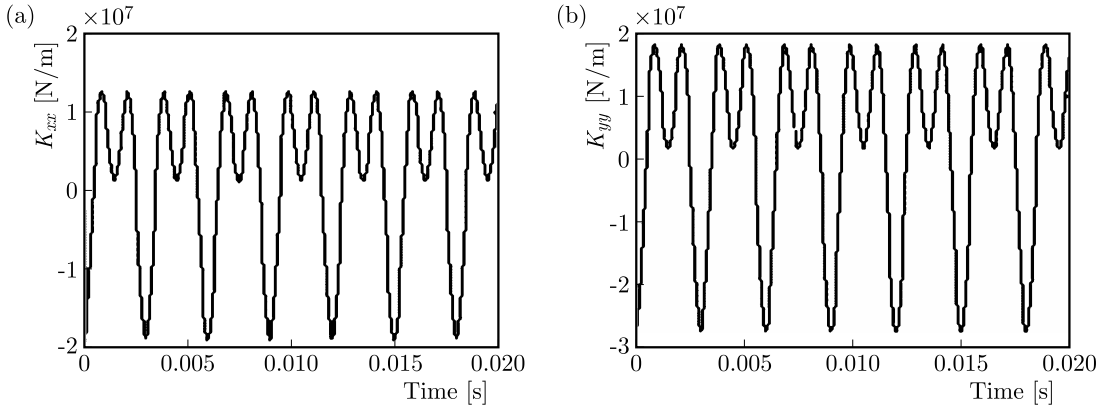

Fig. 9. Stiffness coefficients of the bottom AMB in the x- and y-directions

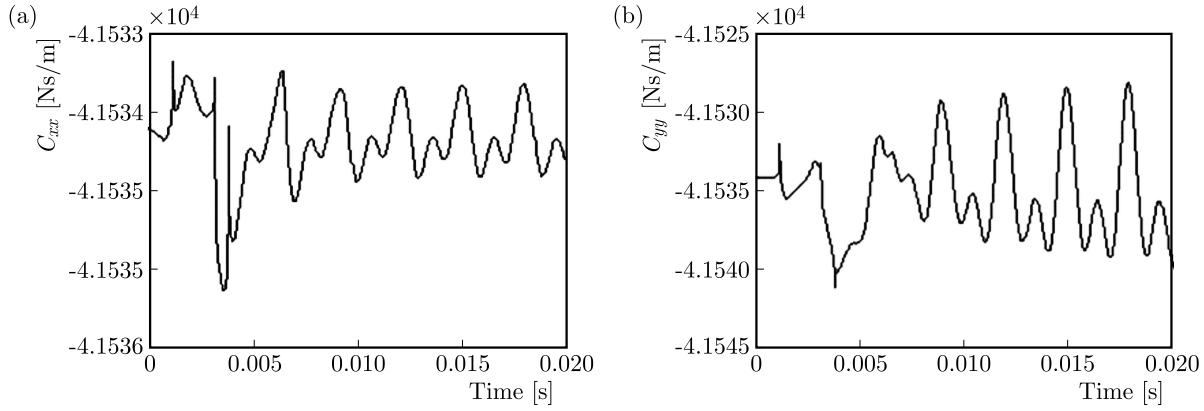

Fig. 10. Damping coefficients of the bottom AMB in the x- and y-directions

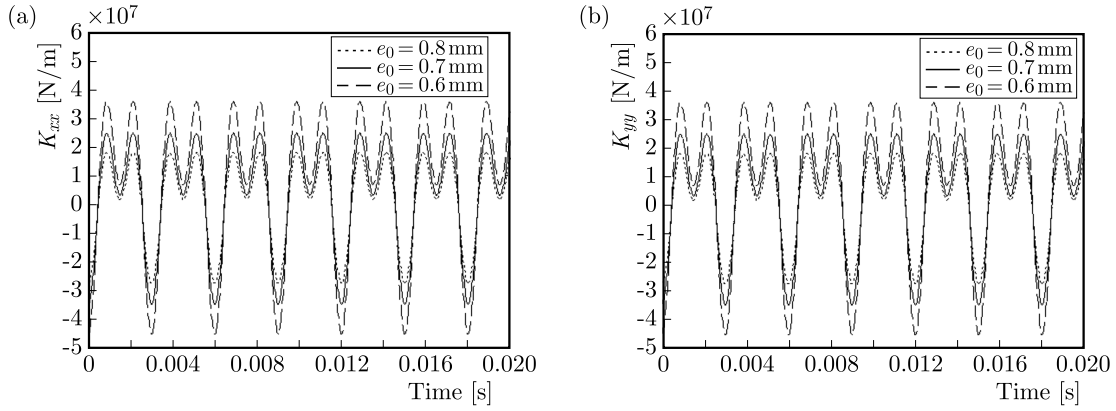

Fig. 11. Dynamic coefficients variation at the bottom AMB in the x-direction as function of e_0

I_0 increases. Indeed, equation (2.1) shows that the electromagnetic forces are proportional to the bias current. Therefore, the damping and stiffness coefficients should be increased to minimize the fluctuations.

Figure 13 presents variation of the stiffness and damping coefficients for rotational speeds of $N = 20000$ rpm and $N = 40000$ rpm, respectively. We remark that the damping coefficients increase in a noticeable way relative to the stiffness coefficients. This is explained by the fact that the vibrations generated with the highest rotational speed should be absorbed and reduced due to damping. A too small change is noted for the stiffness coefficients at the beginning.

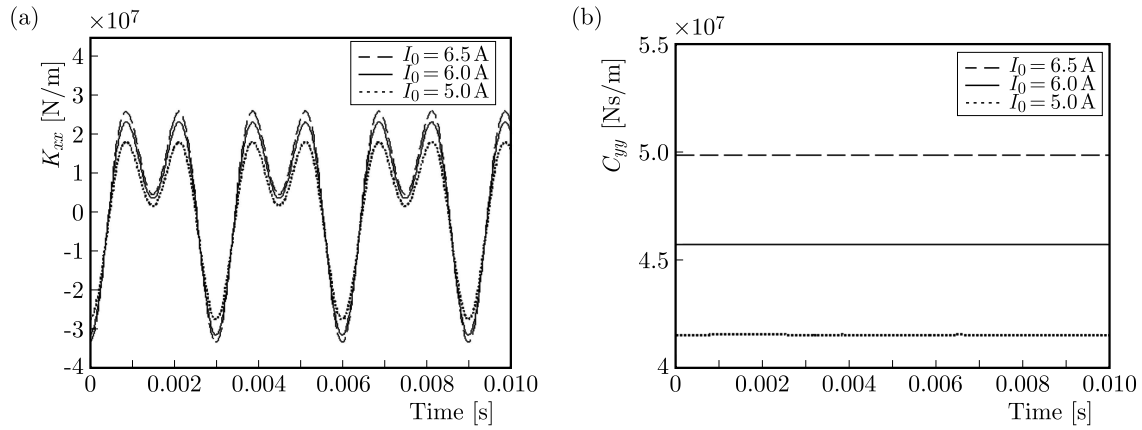

Fig. 12. Dynamic coefficients variation at the bottom AMB in the x-direction as function of I_0

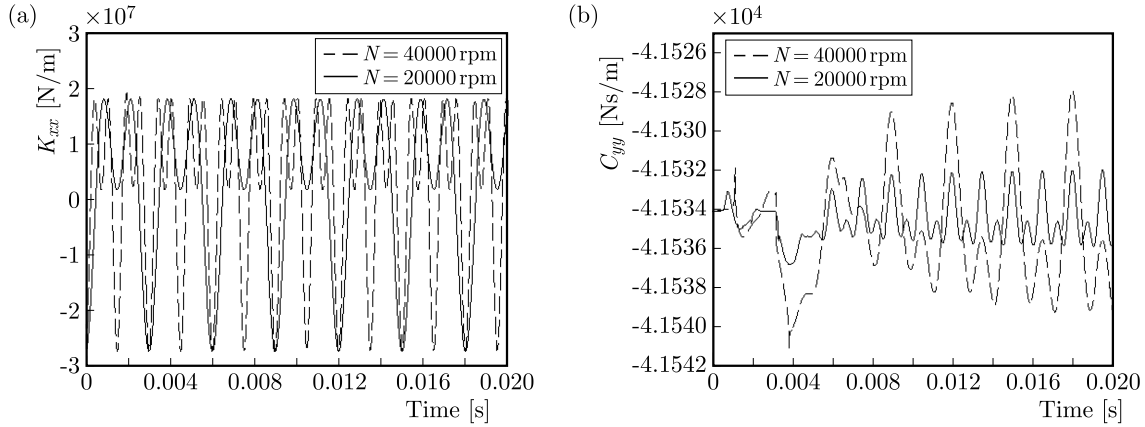

Fig. 13. Dynamic coefficients of the bottom AMB in the x-direction as function of rotation speed

4. Conclusion

This study presents dynamical analysis of a high speed AMB spindle in the peripheral milling process. The spindle rotor is modeled by finite elements using the Timoshenko beam theory. The rigid motions are also considered. A mechanistic model of the peripheral milling is presented including the influence of instantaneous chip thickness. To solve the general equations of motion, the Newmark coupled with the Newton Raphson numerical method is used. The solution gives the spindle dynamic response and explains variation of the cutting force. Analyzing this work, we conclude that the cutting force is related to the cutting parameters introduced in the modeling such as the effect of thickness of the formed chip, feed per tooth, cutting depth and the number of teeth in the cutter. So, it is necessary to select a suitable cutter with the determined flute number in order to obtain an ideal cutting force distribution. This ideality appears first, when the absolute value of the cutting force perpendicular to the feed direction during the cutting process is as small as possible; secondly, when the cutting force distribution is continuous. Concerning the modeling of the bearing, it is clear that the dynamic coefficients are influenced by the air gap as they increase when this parameter decreases. Also they increase with an increase in the rotational speed.

References

1. Amer Y.A., Hegazy U.H., 2007, Resonance behavior of a rotor-active magnetic bearing with time-varying stiffness, *Chaos, Solitons and Fractals*, **34**, 1328-1345
2. Auchet S., Chevrier P., Laccour M., Lipinski P., 2004, A new method of cutting force measurement based on command voltages of active Electro-Magnetic bearing, *International Journal of Machine Tool and Manufacture*, **44**, 1441-1449
3. Belhadj Messaoud N., Bouaziz S., Maatar M., Fakhfakh T., Haddar M., 2011, Dynamic behavior of active magnetic bearing in presence of angular misalignment defect, *International Journal of Applied Mechanics*, **3**, 1-15
4. Bouaziz S., Belhadj Messaoud N., Choley J.Y., Mataar M., Haddar M., 2013, Transient response of a rotor-AMBs system connected by a flexible mechanical coupling, *Mechatronics*, **23**,) 573-580
5. Bouaziz S., Belhadj Messaoud N., Mataar M., Fakhfakh T., Haddar M., 2011, A theoretical model for analyzing the dynamic behaviour of spatial misaligned rotor with active magnetic bearings, *Mechatronics*, **21**, 899-907
6. Budak E., 2006a, Analytical models for high performance milling. Part I: Cutting forces, structural deformations and tolerance integrity, *International Journal of Machine Tools and Manufacture*, **46**, 1478-1488
7. Budak E., 2006b, Analytical models for high performance milling. Part II: Process, dynamics and stability, *International Journal of Machine Tools and Manufacture*, **46**, 1478-1488
8. Faassen R.P.H., van de Wouw N., Oosterling J.A.J., Nijmeijer H., Prediction of regenerative chatter by modelling and analysis of high-speed milling, *International Journal of Machine Tools and Manufacture*, **43**, 1437-1446
9. Flocke F., Qwito F., Arntz K., 2009, A Study of the influence of cutting parameters on micro milling of steel with cubic boron nitride (CBN) tools, *Micro Machining and Micro Fabrication Process Technology XIV*, 7204
10. Fontaine M., Devillez A., Dudzinski D., 2007, Optimisation de la Gómtrie d'outil en fraisage à partir de la prédiction analytique des efforts de coupe, *18éme Congrès Français de Mécanique Grenoble*, 27-31
11. Gagnola V., Bouzgarroua B.C., Raya P., Barrab C., Model-based chatter stability prediction for high-speed spindles, *International Journal of Machine Tools and Manufacture*, **47**, 1176-1186
12. Gourc E., Seguy S., Arnaud L., 2011, Chatter milling modeling of active magnetic bearing spindle in high-speed domain, *International Journal of Machine Tools and Manufacture*, **51**, 928-936
13. Hentati T., Bouaziz A., Bouaziz S., Cholley J.Y., Haddar M., 2013, Dynamic behavior of active magnetic bearing spindle in high speed domain, *International Journal of Mechatronis and Manufacturing Systems*, **6**, 474-492
14. Kimman M.H., Langen H.H., Munning Schmidt R.H., 2010, A miniature milling spindle with active magnetic bearings, *Mechatronics*, **20**, 224-235
15. Knospe C.R., 2007, Active magnetic bearing for machining application, *Control Engineering Practice*, **15**, 307-313
16. Lacerda H.B., Lima V.T., 2004, Evaluation of cutting forces and prediction of chatter vibrations in milling, *Journal of the Brazilian Society of Mechanical Sciences and Engineering*, **26**, 74-81
17. Lai W.H., 2000, Modeling of cutting forces in end milling operations, *Tamkang Journal of Science and Engineering*, **3**, 15-22

18. Liu X.W., Cheng K., Webb D., Luo X.C., 2002, Prediction of cutting force distribution and its influence on dimensional accuracy in peripheral milling, *International Journal of Machine Tools and Manufacture*, **42**, 791-800

19. Movahhedy M., Mosaddegh P,, 2006, Prediction of chatter in high speed milling including gyroscopic effects, *International Journal of Machine Tools and Manufacture*, **46**, 996-1001

20. Nelson H.D., 1980, A finite rotating shaft element using Timoshenko beam theory, *Transactions on ASME Journal of Engineering for Industry*, **102**, 793-803

21. Nelson H,D., McVough J.M., 1976, The dynamic of rotor bearing system using finite element, *Transactions on ASME Journal of Engineering for Industry*, **98**, 593-600

22. Sun Y., Guo Q., 2011, Numerical simulation and prediction of cutting forces in five-axis milling processes with cutter run-out, *International Journal of Machine Tools and Manufacture*, **51**, 806-815

23. Wan M., Zangh W.H., Dang J.W., Yang Y., 2010, A unified stability prediction method for milling process with multiple delays, *International Journal of Machine Tools and Manufacture*, **50**, 29-41

24. Zatarain M., Muñoa J., Peigné G., Insperger T., 2006, Analysis of the influence of mill helix angle on chatter stability, *CIRP Annals – Manufacturing Technology*, **55**, 365-368

Manuscript received May 1, 2015; accepted for print October 9, 2015

JOURNAL OF THEORETICAL AND APPLIED MECHANICS
54, 3, pp. 705-716, Warsaw 2016
DOI: 10.15632/jtam-pl.54.3.705

COMBINED LOAD BUCKLING FOR CYLINDRICAL SHELLS BASED ON A SYMPLECTIC ELASTICITY APPROACH

Jiabin Sun

State Key Laboratory of Structure Analysis for Industrial Equipment and School of Ocean Science and Technology, Dalian University of Technology, Panjin, P.R. China; e-mail: jbsun1983@dlut.edu.cn

Xinsheng Xu

State Key Laboratory of Structure Analysis of Industrial Equipment and Department for Engineering Mechanics, Dalian University of Technology, Dalian, P.R. China

C.W. Lim

Department of Civil and Architectural Engineering, City University of Hong Kong, Hong Kong, P.R. China

Buckling behavior of cylindrical shells subjected to combined pressure, torsion and axial compression is presented by employing a symplectic method. Both symmetric and non-symmetric boundary conditions are considered. Hamiltonian canonical equations are established by introducing four pairs of dual variables. Then, solution of fundamental equations is converted into a symplectic eigenvalue problem. It is concluded that the influence of pressure on buckling solutions is more significant than that due to compressive load, in particular for a longer external pressured cylindrical shell. Besides, buckling loads and circumferential wavenumbers can be reduced greatly by relaxed in-plane axial constraints.

Keywords: buckling mode, combined loads, critical load, cylindrical shell, symplectic method

1. Introduction

In practical applications, thin-walled cylindrical shells are not usually subject to only one single loading condition but very commonly they are subject to a combination of three basic types of loads, i.e. torsional load, pressure and axial compressive load. Therefore, it is very meaningful to understand the interactive buckling behavior of cylindrical shells under the combined action of two or all of these loads. In the previous theoretical studies, various approximate methods were developed to predict the buckling loads of cylindrical shells with special boundary conditions. One common numerical approximation is to assume a suitable series expansion for the displacement, and subsequently transform the basic problem into a system of linear equations like in the Galerkin method. Kardomateas and Philobos (1996) presented benchmark solutions for instability of a thick-walled cylindrical shell under combined axial compression and external pressure by separating variables and transforming higher-order partial differential equations into ordinary differential equations. Despite obtaining more accurate results, it is necessary to assume some forms of admissible displacement expressions. The solution space is also incomplete. Another feasible approximate approach is to apply perturbation techniques to deal with the buckling of shells with more complex physical properties. Some other approaches include analytical studies by Anastasiadis *et al.* (1994) and Shen and Xiang (2008). In addition to the analytical and perturbation methods, the rapidly developing computational hardware and software also offer great opportunities to challenge the complex buckling problems. For example, Mao and Lu (2001) used the finite difference method to study plastic buckling of a thin-walled cylindrical shell subjected to combined action of general loads based on the J_2 deformation theory. Tafreshi (2006) and

Vaziri and Estekanchi (2006) investigated buckling and post-buckling cylindrical shells subjected to pressure and axial compression by means of the finite-element method. By employing the semi-analytical finite-element method, Ley *et al.* (1994) studied buckling loads of ring-stiffened anisotropic cylinders subjected to axial compression, torsion, and internal pressure.

Most of the solution methods cited above can be regarded as approximate or numerical methods, and most of the studies considered only two loads. It is very rare that three types of loads are considered. The classical analytical methods which apply a Lagrangian system involve only one type of variables. In the systems, the basic equations are expressed in higher-order partial differential equations and even after separating the variables, analytical solutions are rather difficult to be derived. In view of these shortcomings, Zhong (2004) presented a symplectic analytical theory to establish a standardized solution procedure for some fundamental problems in solid mechanics. Applying the Legendre transformation, higher-order Lagrange governing equations can be converted to lower-order Hamiltonian dual equations. Hence, analytical solutions can be subsequently obtained by separating variables in the symplectic space. This symplectic analytical method is not only rigorous, but it also establishes a rational solution procedure. In this regard, Xu *et al.* (2006) investigated local buckling and axial stress waves propagation (and reflection). They developed a Hamiltonian system for solving dynamic buckling of cylindrical shells. Recently, based on classical Donnell's shell theory, the authors (2014) presented a symplectic solving method for buckling of cylindrical shells under pressure.

The main objective of this paper is the bifurcation buckling of cylindrical shells subjected to a combination of pressure, torsion and compressive loads. Various combinations of in-plane and transverse boundary conditions at both shell edges are considered. Applying the symplectic approach, the Hamiltonian governing equations are obtained through the Hamiltonian principle of mixed energy. Then the buckling loads and buckling modes can be related to the symplectic eigenvalues and eigenvectors, respectively. The parameters which influence the shell buckling are analyzed and discussed using some numerical examples.

2. Fundamental problem and Hamiltonian system

A cylindrical shell with radius R, length l, thickness t, Young's modulus E and Poisson's ratio ν, as shown in Fig. 1, which is acted by a combination of loads including pressure P (positive for an external pressure), torque T and compressive load N is considered. A circular cylindrical coordinate with the x-axis along the shell axis is adopted, and u, v, w denote the corresponding displacements along with the x-direction, θ-direction and r-direction, respectively.

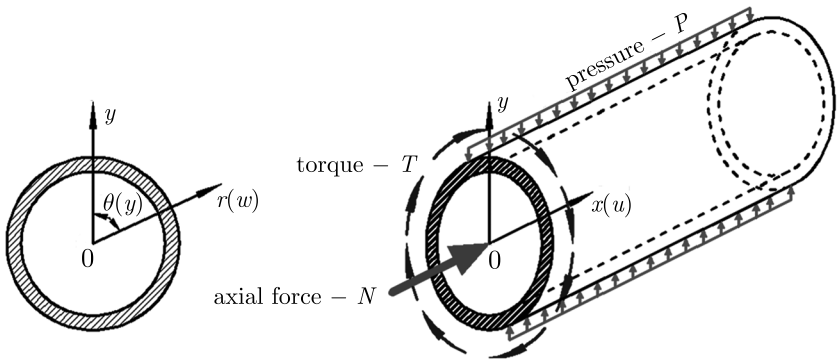

Fig. 1. Geometric parameters of a cylindrical shell subjected to combined loads

The constitutive relations are expressed as (Yamaki, 1984)

$$\begin{aligned} N_x &= K\Big[\frac{\partial u}{\partial x}+\frac{\nu}{R}\Big(\frac{\partial v}{\partial \theta}-w\Big)\Big] & M_x &= -D\Big(\frac{\partial^2 w}{\partial x^2}+\frac{\nu}{R^2}\frac{\partial^2 w}{\partial \theta^2}\Big) \\ N_\theta &= K\Big[\frac{1}{R}\Big(\frac{\partial v}{\partial \theta}-w\Big)+\nu\frac{\partial u}{\partial x}\Big] & M_\theta &= -D\Big(\frac{1}{R^2}\frac{\partial^2 w}{\partial \theta^2}+\nu\frac{\partial^2 w}{\partial x^2}\Big) \\ N_{x\theta} &= \frac{K(1-\nu)}{2}\Big(\frac{1}{R}\frac{\partial u}{\partial \theta}+\frac{\partial v}{\partial x}\Big) & M_{x\theta} &= -\frac{D(1-\nu)}{R}\frac{\partial^2 w}{\partial x\partial \theta} \end{aligned} \tag{2.1}$$

where $D = Et^3/[12(1-\nu 2)]$ and $K = Et/(1-\nu^2)$. Introducing a stress function ϕ, the membrane forces can be expressed as

$$N_x = \frac{1}{R^2}\frac{\partial^2 \phi}{\partial \theta^2} \qquad N_\theta = \frac{\partial^2 \phi}{\partial x^2} \qquad N_{x\theta} = -\frac{1}{R}\frac{\partial^2 \phi}{\partial x \partial \theta} \tag{2.2}$$

Based on Donnell's shell theory and neglecting the pre-buckling bending effect, the internal forces of the buckling state can be obtained as $N_x^0 = N/(2\pi R)$, $N_\theta^0 = -pR$ and $N_{x\theta}^0 = T/(2\pi R)$. From the variational principle, the Lagrange density function can be expressed in terms of elastic potential energy and work due to the external load, as

$$\begin{aligned} \overline{L} = {} & \frac{1}{R^2}\frac{\partial^2 \phi}{\partial \theta^2}\frac{\partial u}{\partial x}+\frac{\partial^2 \phi}{\partial x^2}\Big(\frac{1}{R}\frac{\partial v}{\partial \theta}-\frac{w}{R}\Big)-\frac{1}{R}\frac{\partial^2 \phi}{\partial x\partial \theta}\Big(\frac{1}{R}\frac{\partial u}{\partial \theta}+\frac{\partial v}{\partial x}\Big)-\frac{1}{2Eh}\Big(\frac{\partial^2 \phi}{\partial x^2}+\frac{1}{R^2}\frac{\partial^2 \phi}{\partial \theta^2}\Big)^2 \\ & +\frac{D}{2}\Big(\frac{\partial^2 w}{\partial x^2}+\frac{1}{R^2}\frac{\partial^2 w}{\partial \theta^2}\Big)^2-\frac{N_x^0}{2}\Big(\frac{\partial w}{\partial x}\Big)^2-\frac{T_{x\theta}^0}{R}\frac{\partial w}{\partial x}\frac{\partial w}{\partial \theta}-\frac{N_\theta^0}{2R^2}\Big(\frac{\partial w}{\partial \theta}\Big)^2 \end{aligned} \tag{2.3}$$

According to the variational equation $\delta\iint \overline{L}\, dS = 0$, the compatibility condition and equilibrium equation can be obtained in the Lagrange system. For simplicity, the following dimensionless terms are defined as $X = x/R$, $U = u/R$, $V = v/R$, $W = w/R$, $\Phi = \phi/(Et^3)$, $L = l/R$, $H = t/R$, $\alpha = 12(1-\nu^2)$, $\beta = \alpha H^2$, $N_{cr} = N_x^0 R^2/D$, $T_{cr} = T_{x\theta}^0 R^2/D$ and $P_{cr} = N_\theta^0/D$. An over-dot denotes differentiation with respect to θ, i.e. $\dot{W} = \partial W/\partial\theta$, in which the θ-coordinate is taken as a time-equivalent coordinate and $\partial_X W = \partial W/\partial X$. Introducing two additional variables, $\xi = -\dot{W}$ and $\varphi = -\dot{\Phi}$, the dimensionless Lagrange density function can be expressed as

$$L = -\alpha W\partial_X^2\Phi-\frac{\beta}{2}(\partial_X^2\Phi+\ddot{\Phi})^2+\frac{1}{2}(\partial_X^2 W+\ddot{W})^2-\frac{N_{cr}}{2}(\partial_X W)^2-T_{cr}\dot{W}\partial_X W-\frac{P_{cr}}{2}(\dot{W})^2 \tag{2.4}$$

Applying Legendre's transformation, a vector $\mathbf{q} = [W, \xi, \Phi, \varphi]^{\mathrm{T}}$ is introduced and the corresponding dual vector, defined as $\mathbf{p} = [p_1, p_2, p_3, p_4]^{\mathrm{T}}$, can be derived from $\mathbf{p} = \delta L/\delta\dot{\mathbf{q}}$. The elements of $\mathbf{p} = [p_1, p_2, p_3, p_4]^{\mathrm{T}}$ represent the equivalent transverse shear force, bending moment, shear stress and normal stress, in the Hamiltonian system, respectively. Then, the Hamiltonian density function is given by $H(\mathbf{q}, \mathbf{p}) = \mathbf{p}^{\mathrm{T}}\dot{\mathbf{q}} - L(\mathbf{q}, \mathbf{p})$ and the Hamiltonian canonical equations are

$$\begin{Bmatrix} \dot{\mathbf{q}} \\ \dot{\mathbf{p}} \end{Bmatrix} = \begin{Bmatrix} \dfrac{\delta H}{\delta \mathbf{p}} \\ -\dfrac{\delta H}{\delta \mathbf{q}} \end{Bmatrix} = \begin{bmatrix} \mathbf{A} & \mathbf{B} \\ \mathbf{C} & -\mathbf{A}^{\mathrm{T}} \end{bmatrix} \begin{Bmatrix} \mathbf{q} \\ \mathbf{p} \end{Bmatrix} \tag{2.5}$$

where

$$\mathbf{A}=\begin{bmatrix}0 & -1 & 0 & 0\\ \partial_X^2 & 0 & 0 & 0\\ 0 & 0 & 0 & -1\\ 0 & 0 & \partial_X^2 & 0\end{bmatrix}\qquad \mathbf{B}=\begin{bmatrix}0 & 0 & 0 & 0\\ 0 & 1 & 0 & 0\\ 0 & 0 & 0 & 0\\ 0 & 0 & 0 & -\dfrac{1}{\beta}\end{bmatrix}$$

$$\mathbf{C}=\begin{bmatrix}N_{cr}\partial_X^2 & -T_{cr}\partial_X & -\alpha\partial_X^2 & 0\\ T_{cr}\partial_X & -P_{cr} & 0 & 0\\ -\alpha\partial_X^2 & 0 & 0 & 0\\ 0 & 0 & 0 & 0\end{bmatrix}$$

Defining a state vector $\boldsymbol{\psi}=[\mathbf{q}^{\mathrm{T}},\mathbf{p}^{\mathrm{T}}]^{\mathrm{T}}$, Eq. (2.5) can be simplified as

$$\dot{\boldsymbol{\psi}}=\mathbf{H}\boldsymbol{\psi} \tag{2.6}$$

where $\mathbf{H}$ is the Hamiltonian operator matrix (Zhong, 2004).

3. Symplectic eigenvalue problem

In a symplectic system, the solution to Eq. (2.6) can be derived by separating the variables, i.e. $\boldsymbol{\psi}(X,\theta)=\boldsymbol{\eta}(X)\chi(\theta)$. Hence, Eq. (2.6) can be simplified to

$$\chi(\theta)=\mathrm{e}^{\mu\theta}\qquad \mathbf{H}\boldsymbol{\eta}(X)=\mu\boldsymbol{\eta}(X) \tag{3.1}$$

where $\boldsymbol{\eta}=[q_1',q_2',q_3',q_4',p_1',p_2',p_3',p_4']$ and μ represent the symplectic eigenvector and eigenvalue, respectively. For a shell of revolution, the continuity condition requires $\boldsymbol{\psi}(X,0)=\boldsymbol{\psi}(X,2\pi)$ and the eigenvalues are $\mu_n=n\mathrm{i}$ $(n=0,\pm1,\pm2,\ldots)$. Substituting it into Eq. (3.1), the symplectic eigenvalue equation can be expressed as

$$\mathbf{H}\boldsymbol{\eta}_n=n\mathrm{i}\boldsymbol{\eta}_n \tag{3.2}$$

The characteristic polynomial of Eq. (3.2) is

$$\lambda^8+a\lambda^6+b\lambda^5+c\lambda^4+d\lambda^3+e\lambda^2+f\lambda+g=0 \tag{3.3}$$

where $a=-4n^2+N_{cr}$, $b=2nT_{cr}\mathrm{i}$, $c=6n^4-2n^2N_{cr}-n^2P_{cr}+\alpha^2/\beta$, $d=-4n^3T_{cr}\mathrm{i}$, $e=-4n^6+n^4N_{cr}+2n^4P_{cr}$, $f=2n^5T_{cr}\mathrm{i}$ and $g=n^8-n^6P_{cr}$. Solving Eq. (3.3) in the complex domain, the n-th order eigenvector of Eq. (3.2) is given by

$$\boldsymbol{\eta}_n=\sum_{k=1}^{8}\mathbf{c}_k\mathrm{e}^{\lambda_k X} \tag{3.4}$$

where $\mathbf{c}_k=[c_{1k},c_{2k},\ldots,c_{8k}]^{\mathrm{T}}$ $(k=1,2,\ldots,8)$ is a vector which consists of eight unknown constants which can be determined from the boundary conditions. The eight characteristic roots of Eq. (3.3) are λ_k $(k=1,2,\ldots,8)$. Thus, the buckling solution can be expanded as

$$\boldsymbol{\psi}(X,\theta)=\sum_{n=1}^{\infty}\sum_{k=1}^{8}\Big(a_n\mathbf{c}_k^{(n)}\mathrm{e}^{\lambda_k(n)X}\mathrm{e}^{n\theta\mathrm{i}}+b_n\mathbf{c}_k^{(-n)}\mathrm{e}^{\lambda_k(-n)X}\mathrm{e}^{-n\theta\mathrm{i}}\Big) \tag{3.5}$$

where a_n and b_n are the undetermined coefficients, and each expansion term of Eq. (3.5) is a buckling mode.

4. Boundary conditions and buckling bifurcation condition

In a Lagrangian system, the transverse boundary conditions are generally expressed in terms of displacement components and internal forces. In a Hamiltonian system, the conditions must be expressed in terms of the Hamilton dual variables. The clamped boundary conditions are

$$W = q_1\Big|_{X=\pm L/2} = 0 \qquad \partial_X W = \partial_X q_1\Big|_{X=\pm L/2} = 0 \tag{4.1}$$

and the simply supported boundary conditions are

$$W = q_1\Big|_{X=\pm L/2} = 0 \qquad \partial_X^2 W = \partial_X^2 q_1\Big|_{X=\pm L/2} = 0 \tag{4.2}$$

In addition to transverse constraints, the in-plane boundary conditions are also necessary. From Eq. (3.1), the displacement conditions $U = 0$ and $V = 0$ can be expressed in equivalent forms as $\partial_\theta^2 U = 0$ and $\partial_\theta V = 0$ (Yamaki, 1984). Hence, the in-plane boundary conditions are:
— Case 1

$$\begin{aligned} &\partial_\theta^2 U = \Big(-(1+\nu)\partial_X^3 q_3 + \frac{2+\nu}{\beta}\partial_X p_4 + \frac{1}{H^2}\partial_X q_1\Big)\Big|_{X=\pm L/2} = 0 \\ &\partial_\theta V = \Big((1+\nu)\partial_X^2 q_3 - \frac{\nu p_4}{\beta} + \frac{q_1}{H^2}\Big)\Big|_{X=\pm L/2} = 0 \end{aligned} \tag{4.3}$$

— Case 2

$$\begin{aligned} &\partial_\theta^2 U = \Big((1+\nu)\partial_X^3 q_3 - \frac{\nu}{\beta}\partial_X p_4 + \frac{1}{H^2}\partial_X q_1\Big)\Big|_{X=\pm L/2} = 0 \\ &N_{X\theta} = \partial_X q_4\Big|_{X=\pm L/2} = 0 \end{aligned} \tag{4.4}$$

— Case 3

$$\begin{aligned} &N_X = \Big(\frac{p_4}{\beta} - \partial_X^2 q_3\Big)\Big|_{X=\pm L/2} = 0 \\ &\partial_\theta V = \Big(\partial_X^2 q_3 + \frac{q_1}{H^2}\Big)\Big|_{X=\pm L/2} = 0 \end{aligned} \tag{4.5}$$

— Case 4

$$\begin{aligned} &N_X = \Big(\frac{p_4}{\beta} - \partial_X^2 q_3\Big)\Big|_{X=\pm L/2} = 0 \\ &N_{X\theta} = \partial_X q_4\Big|_{X=\pm L/2} = 0 \end{aligned} \tag{4.6}$$

By using Eq. (3.4) and some specified boundary conditions, a homogeneous system consisting of eight linear equations can be obtained as

$$\mathbf{D}\mathbf{c}_1 = \mathbf{0} \tag{4.7}$$

where $\mathbf{c}_1 = [c_{11}, c_{12}, \ldots, c_{18}]^{\mathrm{T}}$ is the undetermined coefficients vector, and $D_{ij}(T_{cr}, N_{cr}, P_{cr}, n)$ are elements of the matrix $\mathbf{D}$ which is related to combinations of boundary cases, see Eqs. (4.1)-(4.6). For the non-trivial solution, the determinant of $\mathbf{D}$ must vanish, or

$$|\mathbf{D}|_{8\times 8} = 0 \tag{4.8}$$

Consequently, the relationship of critical loads (T_{cr}, N_{cr}, P_{cr}) and buckling mode can be determined from Eq. (4.8) and Eq. (3.4).

5. Buckling results and discussion

Here, for convenience, a curvature parameter $Z = \sqrt{1-\nu^2}L^2/H$ is adopted. In the numerical examples, the cylindrical shells have dimensionless thickness $H = t/R = 0.01$ and Poisson's ratio $\nu = 0.3$. Various combinations of transverse and in-plane boundary conditions are assumed. For two specified loads (either two of pressure P_{cr}, torque T_{cr} or axial load N_{cr}), the critical value for the remaining load can always be determined from bifurcation condition, Eq. (4.8). As an example, for some specified pressure and compressive load which act on the shell, the torsional buckling load can be obtained.

From Eq. (3.1), integer n denotes the number of buckling waves in the circumferential direction while the corresponding buckling mode can be referred as the n-th order mode. As mentioned above, torsional buckling loads for various boundary conditions are illustrated in Figs. 2 and 3 for $Z = 500$. In general, it is observed that the effect of pressure is more significant than that due to axial compression. The buckling load goes up with increasing internal pressure but decreases with growing external pressure. This observation is consistent with other published results (Yamaki, 1984; Winterstetter and Schmidt, 2002). The result indicates that a cylindrical shell loses stability more easily when acted by an external pressure. For in-plane boundary conditions, it is noted that relaxing the in-plane axial constraint greatly reduces the buckling torsional load. Comparatively, the transverse boundary conditions do have relatively limited effect on buckling solutions. In Figs. 4 and 5, the buckling modes corresponding to various boundary conditions are presented for $P_{cr} = 20$ and $N_{cr} = 200$. It also clearly shows that the in-plane boundary conditions play an important role on the relevant buckling behavior.

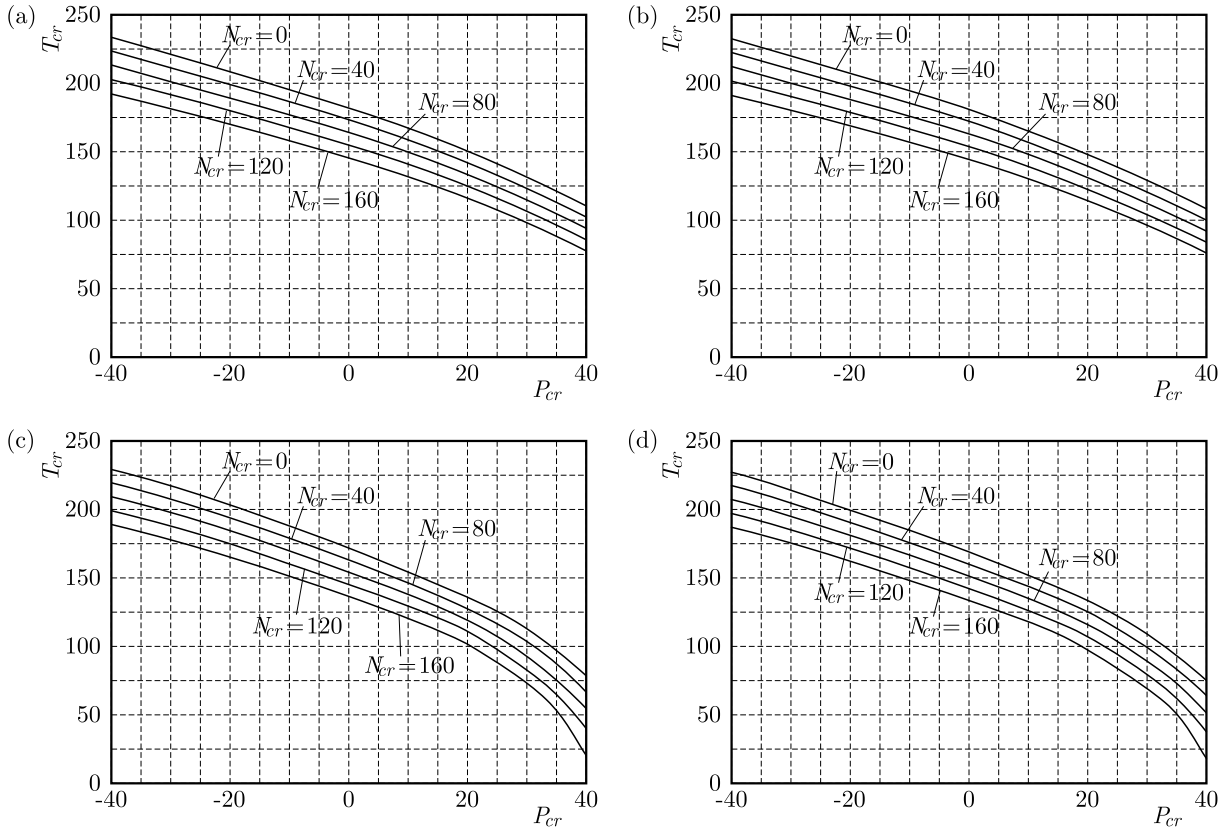

Fig. 2. T_{cr} vs. P_{cr} under clamped boundary conditions: (a) Case 1, (b) Case 2, (c) Case 3, (d) Case 4

Here, a case with clamped transverse constraints in Eq. (4.2) and Case 1 with in-plane constraints in Eq. (4.4) is considered. The buckling loads with the increasing shell length are

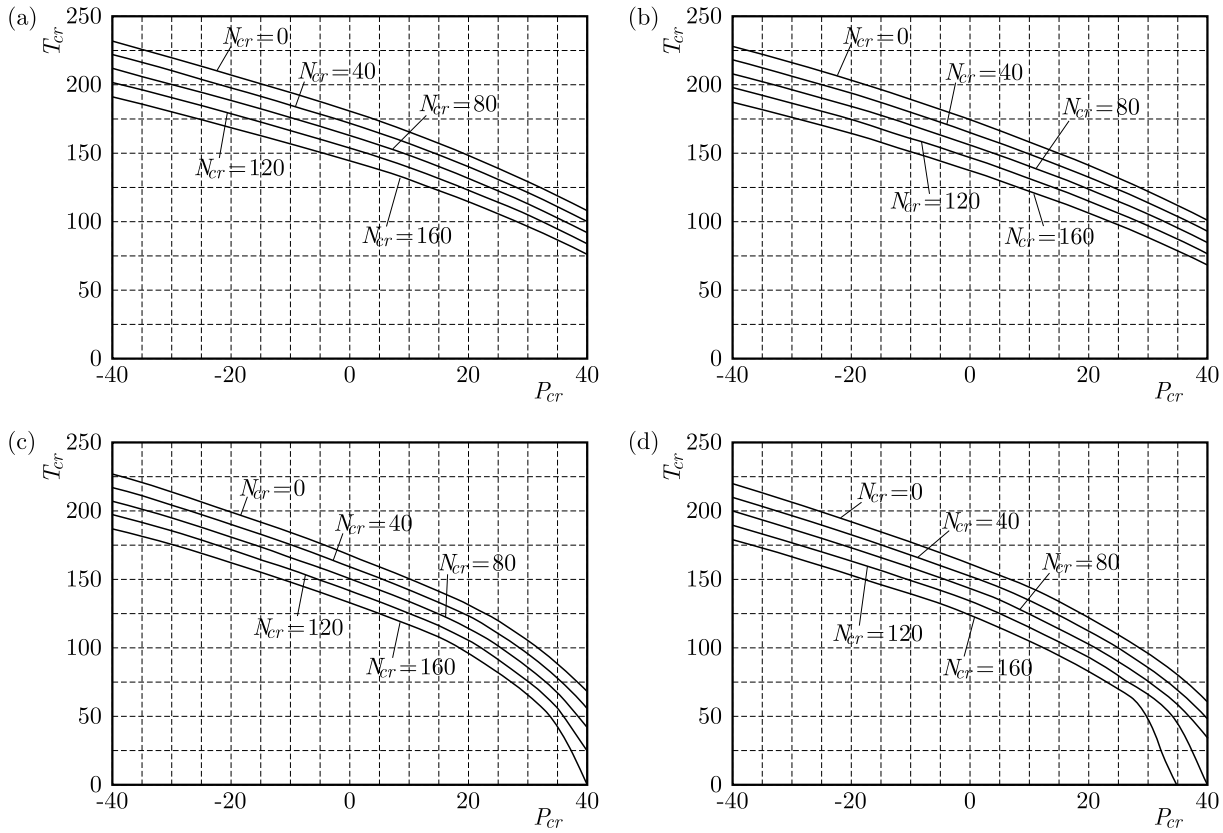

Fig. 3. T_{cr} vs. P_{cr} under simply supported boundary conditions: (a) Case 1, (b) Case 2, (c) Case 3, (d) Case 4

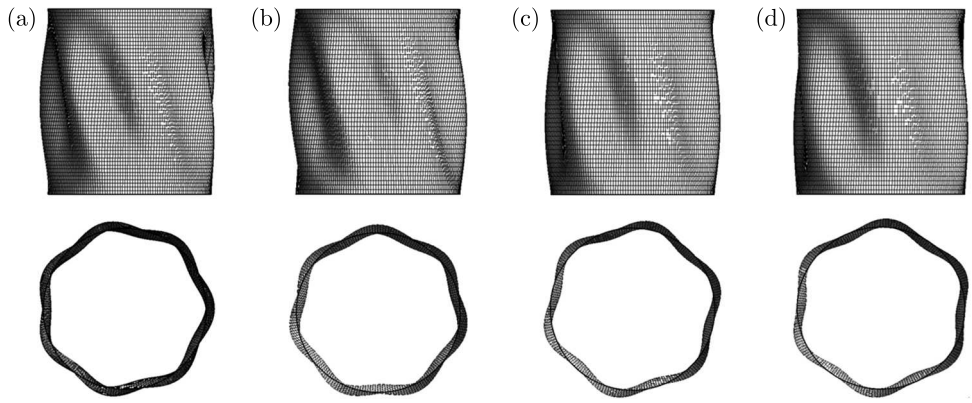

Fig. 4. Buckling modes for clamped boundary conditions: (a) Case 1, (b) Case 2, (c) Case 3, (d) Case 4

illustrated in Fig. 6. It is noticed that the buckling loads rapidly decrease with an increase in the shell length. The corresponding buckling modes for $P_{cr} = 20$ and $N_{cr} = 200$ are shown in Fig. 7. The axial waveforms which vary with Z are also observed in the figure. For a fixed axial compressive load ($N_{cr} = 200$) and curvature parameter ($Z = 1000$), the effect of buckling modes with respect to the external and internal pressure is shown in Fig. 8. It is clearly observed that the shell is twisted intensively with the increasing internal pressure. However, this effect reverses completely if the shell is acted by an external pressure. The effect of compressive load on the buckling modes is presented in Fig. 9 for $P_{cr} = 40$. It shows that an increase in the axial load have a insignificant influence on the buckling deformation.

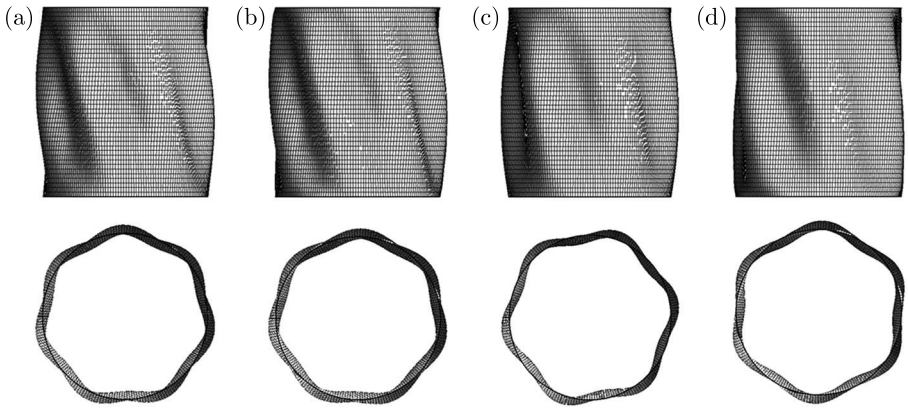

Fig. 5. Buckling modes for simply supported boundary conditions: (a) Case 1, (b) Case 2, (c) Case 3, (d) Case 4

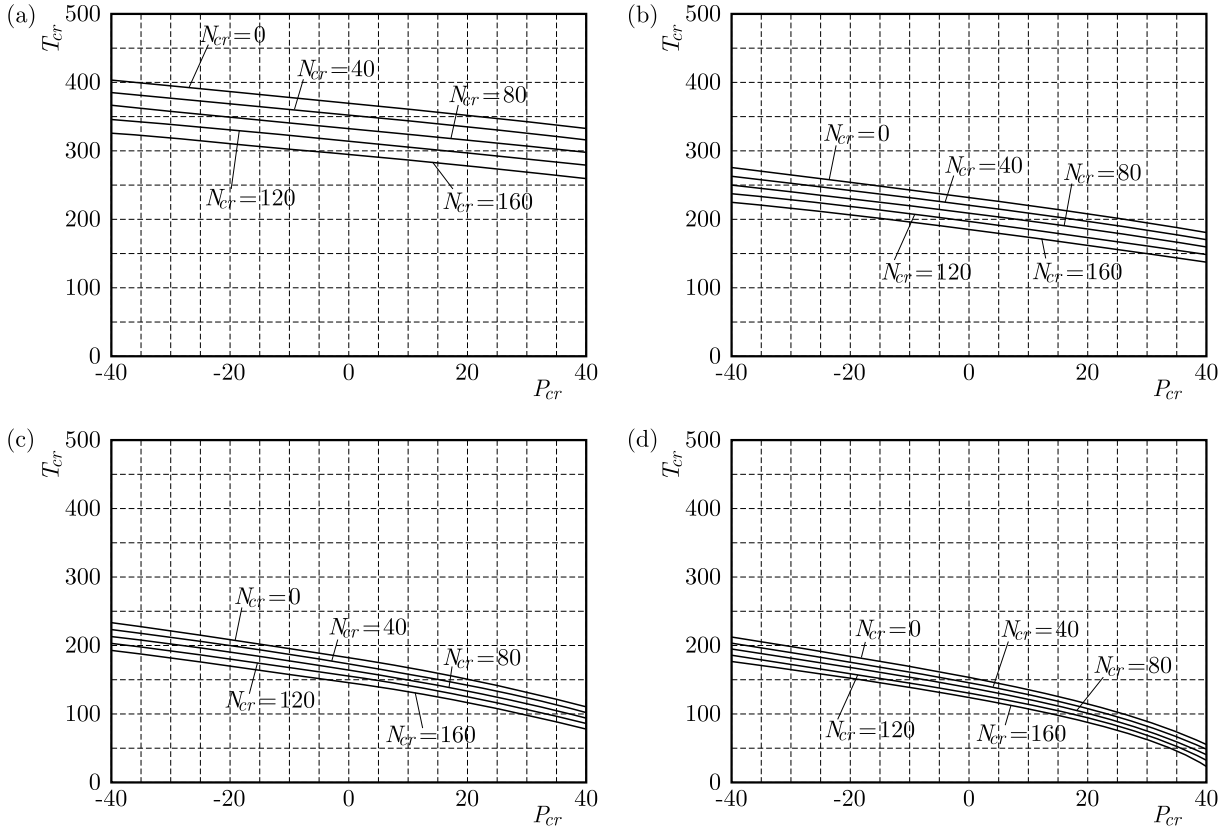

Fig. 6. T_{cr} vs. P_{cr} under different curvature parameters Z: (a) $Z = 50$, (b) $Z = 200$, (c) $Z = 500$, (d) $Z = 1000$

To study the effect of thickness on the buckling behavior, shells of thickness 0.002 and 0.005 are considered additionally. The buckling solutions for the shell with $L = 2$ are illustrated in Fig. 10. The critical load is redefined as $\overline{T}_{cr} = H^2 T_{cr}$. In the figure, it is observed that the buckling torsional load increases for a thicker shell. For similar loading conditions, the corresponding axial buckling modes are presented in Fig. 11. The figure indicates that the buckling waves become densely for a thinner shell.

Next, the buckling response of cylindrical shells subjected to non-symmetric boundary conditions is investigated. In this example, the shell has clamped transverse constraints and Case 1 in-plane constraints at $X = 0$. At the other end, the simply supported plus Case 1

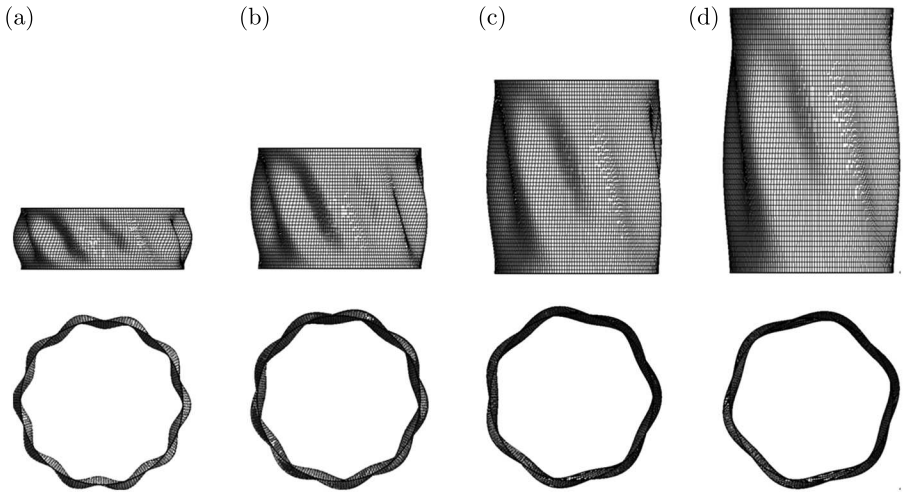

Fig. 7. Buckling mode with different curvature parameters Z: (a) $Z = 50$, (b) $Z = 200$, (c) $Z = 500$, (d) $Z = 1000$

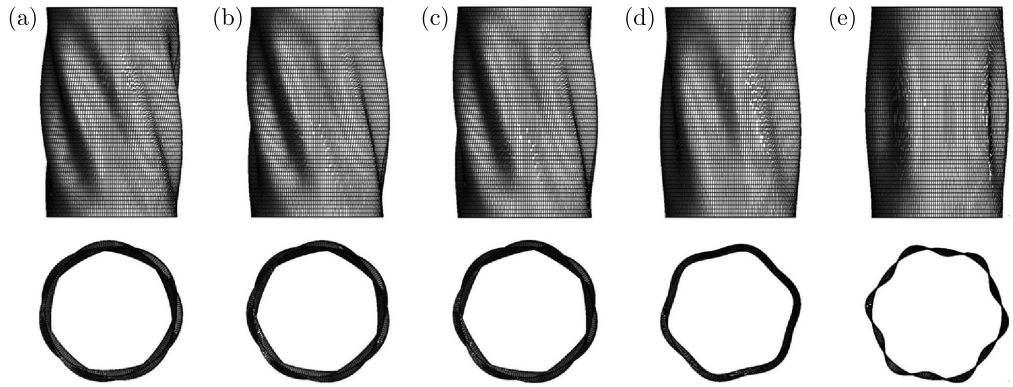

Fig. 8. Buckling modes under different pressure P_{cr}: (a) $P_{cr} = -40$, (b) $P_{cr} = -20$, (c) $P_{cr} = 0$, (d) $P_{cr} = 20$, (e) $P_{cr} = 40$

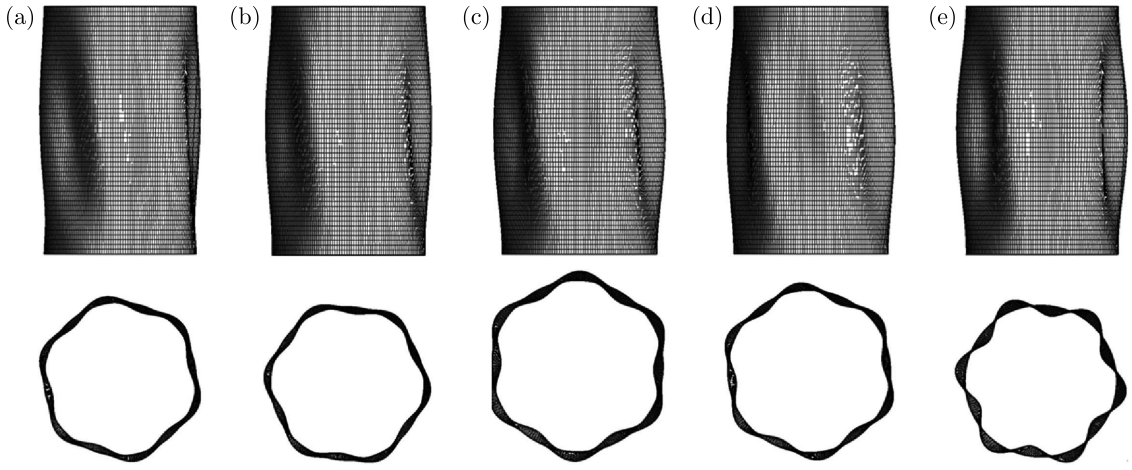

Fig. 9. Buckling modes under different compressive load N_{cr}: (a) $N_{cr} = 0$, (b) $N_{cr} = 40$, (c) $N_{cr} = 80$, (d) $N_{cr} = 120$, (e) $N_{cr} = 160$

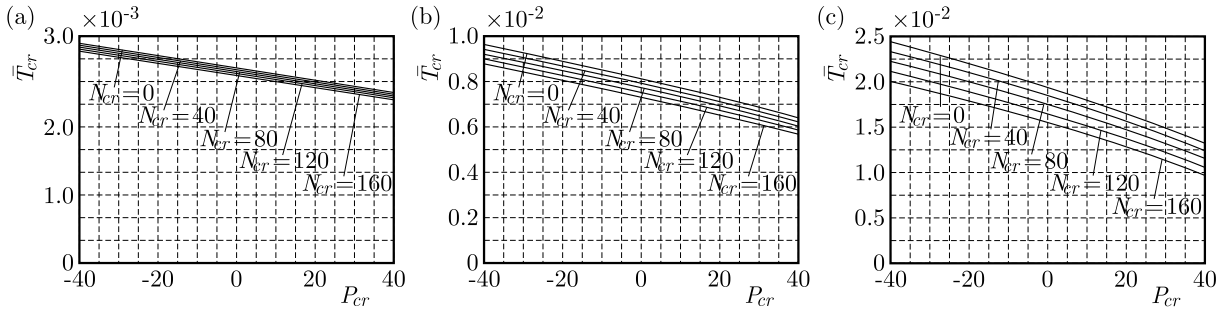

Fig. 10. $\overline{T}_{cr}$ vs. P_{cr}: (a) $H = 0.002$, (b) $H = 0.005$, (c) $H = 0.01$

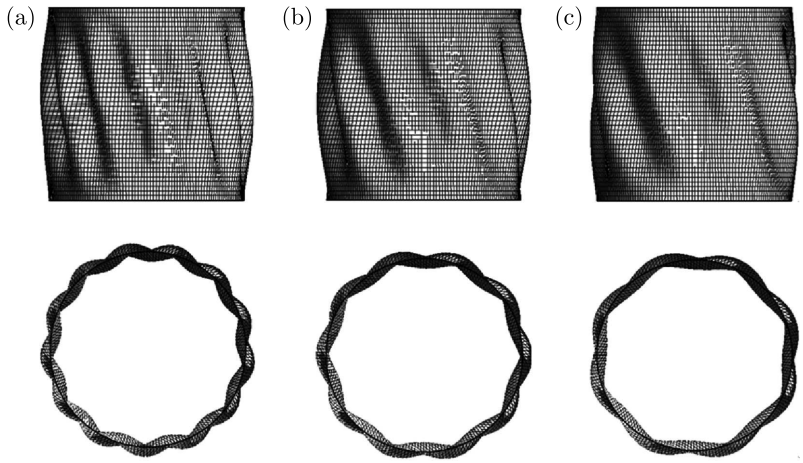

Fig. 11. Buckling modes for different shell thicknesses H: (a) $H = 0.002$, (b) $H = 0.005$, (c) $H = 0.01$

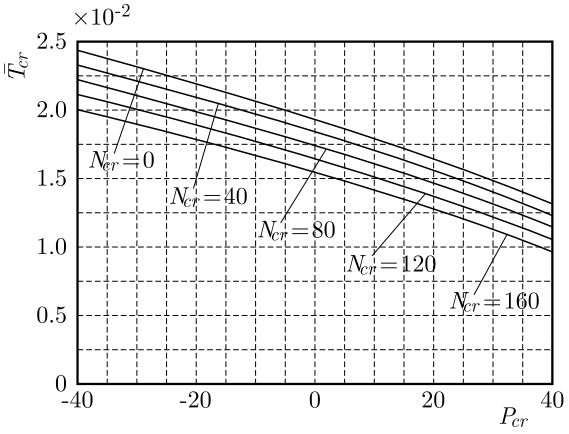

Fig. 12. T_{cr} vs. P_{cr} for the non-symmetric boundary condition (clamped at one end and simply supported at the other end)

constraints are applied. The buckling loads and buckling modes are presented in Figs. 12. The curvature parameter $Z = 500$ and thickness $H = 0.01$ are selected. Compared with Figs. 2a and 3a, it can be found that the obtained torsional loads are smaller than those of the symmetric clamped shells and larger than those of the symmetric simply supported shells.

6. Conclusion

A very effective Hamiltonian system constructed within a symplectic space for buckling of cylindrical shells subjected to a combination of pressure, torsion and axial compression is established. Applying Legendre's transformation, the Hamiltonian canonical equations are derived by introducing four pairs of dual variables. By separating the variables, the classical governing equation is converted to a symplectic eigenvalue problem where only solutions for the symplectic eigenvalues and eigenvectors are required.

Through a systematic and rational procedure, it is derived that the eigensolutions for the zero-eigenvalues and non-zero-eigenvalues represent axisymmetric and non-axisymmetric shell buckling modes, respectively. For cylindrical shells subjected to pressure and axial compression, the numerical examples concluded that: (i) buckling torsional loads should go up with an increase in the internal pressure and decline with a rise in the external pressure and compressive load. These changings induced by the applied pressure become more significant. For buckling modes, the effect of pressure load on the twisted waveforms is also more obvious that caused by axial compression; (ii) with the relaxation of the in-plane axial constraint, the downtrend of buckling loads with respect to pressure should be more dramatic. And the corresponding buckling mode also presents a slight twisted shape. Besides, the transverse boundary conditions have a limited influence on buckling results while external pressures are not extremely large; (iii) buckling torsional loads should be reduced for longer and thinner shells. The circumferential waves number of the buckling mode increases with a decrease in the thickness and length of the shell; (iv) for shells with non-symmetric boundary constrains, the buckling solutions fall in between those under the corresponding symmetric boundary conditions.

Acknowledgements

The supports of National Natural Science Foundation of China (No. 11402050), the Fundamental Research Funds for the Central Universities (No. DUT15LK46) and the Natural Science Foundation of China (No. 11372070) are acknowledged.

References

1. Anastasiadis J.S., Tabiei A., Simitses G.J., 1994, Instability of moderately thick, laminated cylindrical shells under combined axial compression and pressure, *Composite Structures*, **27**, 4, 367-378
2. Kardomateas G.A., Philobos M.S., 1995, Buckling of thick orthotropic cylindrical shells under combined external pressure and axial compression, *AIAA Journal*, **33**, 10, 1946-1953
3. Ley R.P., Johnson E.R., Guerdal Z., 1994, Buckling of imperfect, anisotropic, ring-stiffened cylinders under combined loads, *AIAA Journal*, **32**, 6, 1302-1309
4. Mao R.J., Lu G., 2001, Plastic buckling of circular cylindrical shells under combined in-plane loads, *International Journal of Solids and Structures*, **38**, 741-757
5. Shen H.S., Xiang Y., 2008, Buckling and postbuckling of anisotropic laminated cylindrical shells under combined axial compression and torsion, *Composite Structures*, **84**, 375-386
6. Sun J.B., Xu X.S., Lim C.W., 2014, Buckling of cylindrical shells under external pressure in a Hamiltonian system, *Journal of Theoretical and Applied Mechanics*, **52**, 3, 641-653
7. Tafreshi A., 2006, Delamination buckling and postbuckling in composite cylindrical shells under combined axial compression and external pressure, *Composite Structures*, **72**, 401-418
8. Vaziri A., Estekanchi H.E., 2006, Buckling of cracked cylindrical thin shells under combined internal pressure and axial compression, *Thin-Walled Structures*, **44**, 141-151

9. Winterstetter T.A., Schmidt H., 2002, Stability of circular cylindrical steel shells under combined loading, *Thin-Walled Structures*, **40**, 893-909

10. Xu X.S., Ma Y., Lim C.W., Chu H.J., 2006, Dynamic buckling of cylindrical shells subject to an axial impact in a symplectic system, *International Journal of Solids and Structures*, **43**, 3905-3919

11. Yamaki N., 1984, *Elastic Stability of Circular Cylindrical Shells*, North Holland, Amsterdam/New York/Oxford

12. Zhong W.X., 2004, *Duality System in Applied Mechanics and Optimal Control*, Kluwer Academic Publishers, Boston

Manuscript received May 7, 2015; accepted for print October 21, 2015

JOURNAL OF THEORETICAL AND APPLIED MECHANICS
54, 3, pp. 717-730, Warsaw 2016
DOI: 10.15632/jtam-pl.54.3.717

ROTATING ORBITS OF PENDULUM IN STOCHASTIC EXCITATION

Sze-Hong Teh, Ko-Choong Woo, Hazem Demrdash

University of Nottingham Malaysia Campus, Department of Mechanical, Materials and Manufacturing Engineering, Semenyih, Malaysia

e-mail: kedx1tsn@nottingham.edu.my; Woo.Ko-Choong@nottingham.edu.my; Hazem.Demrdash@nottingham.edu.my

A method to extract energy from an excitation which is stochastic in nature is presented. The experimental rig comprises a pendulum, and a vertical excitation is provided by a solenoid. The control input assumed in the form of a direct current motor, and another motor, used in reverse, acts as a generator. The stochastic excitation has been achieved by varying the time interval between switching the RLC circuit on and off according to a random distribution. Such non-linear vertical excitations act on an oscillatory system from which a pendulum is pivoted. The Pierson-Moskowitz spectrum has been chosen as the random distribution while an inverse transform technique has been used for generation of the random excitation signal in LabVIEW environment. Moreover, a bang-bang control algorithm has been implemented to facilitate rotational motion of the pendulum. Experimental observations have been made for various noise levels of vertical excitations, and their implication on energy generation has been discussed. A positive amount of energy has been extracted for a minimal amount of the control input.

Keywords: parametric pendulum, stochastic excitation, energy harvesting

1. Introduction

Energy in form of mechanical vibration generally exists everywhere, all the time, and its source can be natural (e.g. sea wave) or artificial (e.g. automobile vibration). While some vibrations may be regarded as useful and necessary, other vibrations can be suppressed or their energy can be converted into electrical energy by means of a harvester. For an instance, it can be used to vertically excite a parametric pendulum, which in turns rotates the pendulum and drives a generator to produce electrical energy. That form of vertical excitation can be chaotic or stochastic in the characteristic. Though both chaotic and stochastic excitations appear to be random and irregular, the chaotic excitation is deterministic while the stochastic excitation is characterized by using probability theory.

Various investigations have been performed on the dynamics of a parametric pendulum subjected to the stochastic excitation. For example, a stochastic forcing of Gaussian distribution was added to the forced pendulum model (Blackburn *et al.*, 1995) and its effect in stabilizing and destabilizing the periodic motion of the parametric pendulum was studied by Blackburn (2006). Influence of the Wierner phase noise in the chaotic regime of a parametrically excited pendulum was numerically studied by Litak *et al.* (2008). A numerical study was conducted to investigate how stable rotational modes of a parametric pendulum were affected by introducing a stochastic forcing of Gaussian distribution by Horton and Wiercigroch (2008). Rotation of a parametric pendulum system subjected to an excitation with the Pierson-Moskowitz wave spectrum was studied by Najdecka (2013). Rotational motion of the Mathieu equation subjected to a narrow band excitation was investigated by Yurchenko *et al.* (2013). The stochastic response of a rotating pendulum mounted on a single degree-of-freedom (SDOF) base, which was subjected to narrow band excitation, was explored numerically by Yurchenko and Alevras (2013) and

Alevras and Yurchenko (2014). Stochastic synchronization of rotating pendula mounted on a mutual elastic SDOF base subjected to narrow band excitation were numerically investigated by Alevras *et al.* (2014). Moreover, the parametric pendulum has been a subject of chaotic analysis as well. Influence of a nonlinear oscillator on an attached pendulum in the main parametric resonance region was studied by Warminski and Kecik (2006). The behavior of a parametric pendulum pivoted on a mass-spring-damper system was investigated analytically, numerically and experimentally around the principal resonance region by Warminski and Kecik (2009). The dynamics of an autoparametric pendulum-like system with a nonlinear suspension subjected to kinematic excitation was numerically and experimentally investigated by Kecik and Warminski (2011). The dynamics of a pendulum suspended on a forced Duffing oscillator was numerically explored by Brzeski *et al.* (2012).

As the rotational motion of parametric pendulum is advantageous for energy harvesting, it is desired to maintain that motion when it is subjected to any excitations. A few control strategies have been proposed for the purpose of sustaining rotational motion of the parametric pendulum. A time-delayed feedback method was employed to initiate and stabilize rotational motion of the pendulum by a feedback perturbation proportional to the difference between the present and a delayed state of the pendulum (Yukoi and Hikihara, 2011a). The tolerance of time-delayed feedback method with mistuned delay was experimentally investigated by Yukoi and Hikihara (2011b). The extended time-delayed feedback was proposed to maintain rotating solutions of the parametric pendulum to avoid bifurcations that destabilize the rotating orbit (De Paula *et al.*, 2012). The robustness and sensitivity of the time-delayed feedback method with respect to varying excitation parameters and added noise was investigated by Vaziri *et al.* (2014). In addition, a velocity control method was proposed to effect a control torque about the angular axis if the angular velocity of the pendulum droped below a threshold (Najdecka, 2013). Alternative methods of control, such as a LQR method (Dadone *et al.*, 2003) were deployed mainly for a pendulum-type system without continuous rotations.

The objective of this paper is to show an alternative mean of implementing an experimental stochastic process for facilitating investigations on the parametric pendulum for energy harvesting. In particular, the observation of rotational state of the pendulum under such an excitation is of interest in the current study. The proposed setup could exert a non-linear electromechanical force to the pendulum by means of an AC solenoid, which is powered by a solid-state-relay(SSR)-coupled RLC circuit, and it was previously reported to exhibit period-1 rotations, period-1 oscillations and period-2 oscillations (Teh *et al.*, 2015). The type of the parametric pendulum system considered belongs a special class of autoparametric systems; it has a mass-spring-damper system as the base and a pendulum is attached to it. Unlike the stochastic excitation of the parametric pendulum as the above-mentioned, the implementation of a stochastic excitation to the pendulum system in the current study is achieved by a random distribution of the input signal with respect to the duration of switching on and off the solenoid. In addition, a bang-bang control algorithm is tailored to address the problem of escaping the potential well when the noise is sufficiently destructive for positive energy generation. To implement the control algorithm and monitor potential energy generation, the experimental parametric system is enhanced with a control system by adding a rotational actuator, a generator and some necessary transducers. The main aim of this paper is to show that for stochastic energy sources commonly found in real life it is possible to introduce a minimal amount of the control input, while still harvesting more energy. This is an improvement to the previous work on periodic excitation by Teh *et al.* (2015).

The paper is organized in the following manner. The enhanced version of the experimental setup is first described in Section 2 together with its dynamic equations. The implementation of stochastic excitation for the experimental setup of the current study is described in Section 3. The bang-bang control algorithm that assists the pendulum motion is proposed in Section 4.

Some results on the pendulum system subjected to different levels of stochasticity are presented in Section 5. Finally, the paper is summarized and concluded in Section 6.

2. Experimental setup

The experimental setup of the parametric pendulum system given by Teh *et al.* (2015) has been extended to further investigation on rotations of the pendulum in the present work. The parametric pendulum system assembled for the experimental study on pendulum rotations under stochastic excitation is depicted in Fig. 1a. This configuration of the parametric pendulum system was previously described by Teh *et al.* (2015) regarding the functions and connections among the components. In the current study, the pendulum assembly has been modified by adding a L-bracket to mount the motor and the generator on to the pendulum assembly. The motor and generator are connected in parallel with the pendulum pivot by means of spur gears. The gear ratio among the pendulum pivot, motor and generator is 2:2:1. The overall assembly is suspended by means of a mechanical hook at the aluminium base plate.

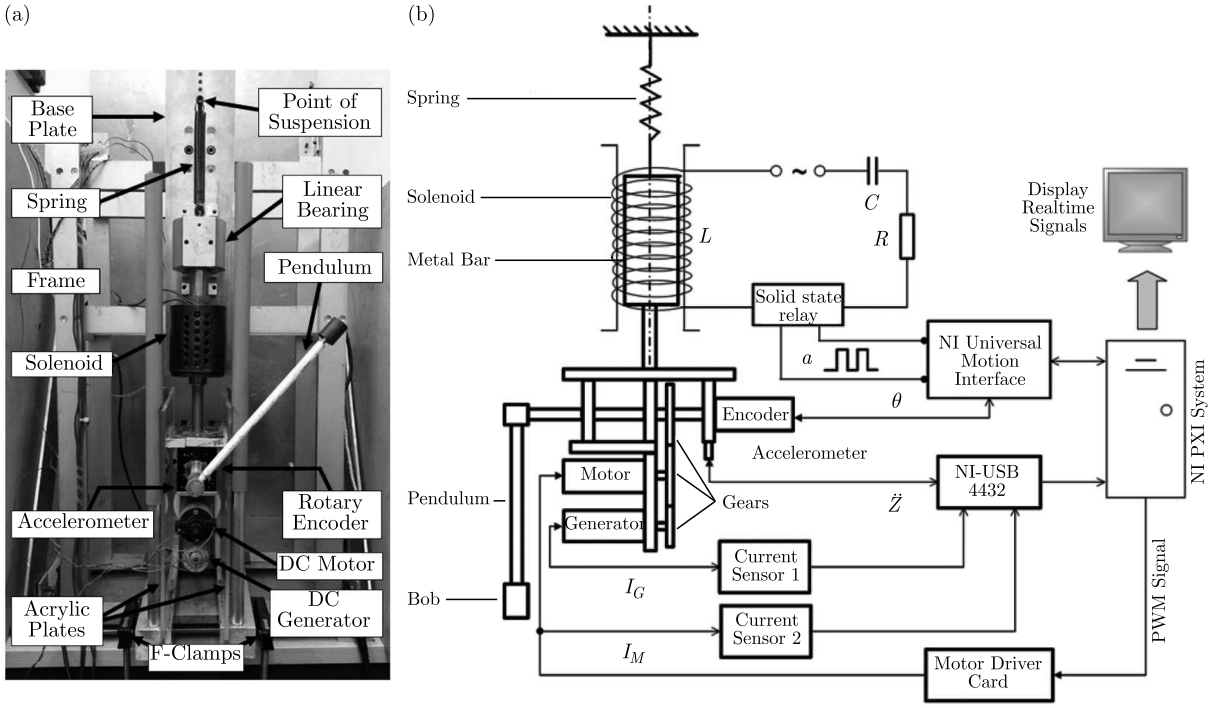

Fig. 1. (a) Experimental rig of the present work; (b) schematic of (a)

The schematic of the experimental setup is illustrated in Fig. 1b. The interface between the mechanical and electrical part of the system by Teh *et al.* (2015) has been enhanced in the present work to derive more information from the parametric pendulum setup while outputting commands simultaneously. Vertical oscillation of the pendulum assembly is achieved by exerting an electromagnetic force on the metal bar within the solenoid. The solenoid is connected in series with an external power supply and a capacitor to fulfill such forcing requirement, as depicted in Fig. 1b. It is effectively a RLC circuit and it is built in a similar way to Mendrela and Pudlowski (1992). A solid state relay is coupled with the RLC circuit to switch the solenoid on and off according to the input signal generated from the computer system. A non-linear electromechanical excitation of the pendulum assembly is generated by repeatedly switching the solenoid on and off, and a linear tension spring is used to complement the vertical oscillatory motion.

Four transducers are employed to scavenge useful data from the experimental system. The angular displacement of the pendulum is measured using an Autonics incremental optical encoder (Model: E6B2-CWZ1X), and the signal is fed to monitoring system via National Instrument (NI) universal motion interface (Model: NI UMI-7774). Besides, the vertical motion of the pendulum assembly is measured using a Brüel & Kjær piezoelectric accelerometer (Model: 4518-001). Two Allergo hall-effect based linear current sensors (Model: ACS711EX and ACS711LC) are used to respectively measure the electric current of the circuit of Crouzet DC motor (Model: 82800502) and Cytron DC generator (Model: SPG50-100K). The charge amplifier function of a NI data acquisition module (Model: NI USB-4432) is used to amplify the electrical signal generated by the accelerometer before being fed to the monitoring system. On the other hand, the analog voltage measurement function of the same data acquisition module is used to measure the voltage difference generated by the linear current sensors before being fed to the monitoring system.

The monitoring and logging of the experimental data is performed using NI PXI-embedded computer system (Model: NI PXI-8106). NI PXI-embedded computer system is also capable of simultaneously generating a signal for switching the solid state relay on-and-off and performing a control action on the pendulum axis based on the measured real-time data. LabVIEW is usedt o design a graphical user interface that could perform the above tasks based on NI PXI-embedded computer system. The NI motion controller module (Model: NI PXI-7350) of the computer system is used to generate a digital signal which is software-timed by a graphical user interface under a specific algorithm for switching the solid state relay on-and-off. Besides, the NI motion controller module is used to generate a hardware-timed pulse-width modulation (PWM) signal according to the computed control action, which is in the form of motor input voltage. The PWM signal is received by the Cytron DC motor driver card (Model: MD10C) and it draws electric current from a DC power supply to drive the DC motor according to the PWM signal.

In addition to the equations of motion for the mechanical system as well as governing equations describing the electrical circuit of the solenoid (Teh *et al.*, 2015), the variation of current flowing through the DC motor are expressed as follows

$$L_M \frac{dI_M}{dt} = U_M - R_M I_M - K_M \dot{\theta} \qquad T_M = K_M I_M \tag{2.1}$$

where L_M is the motor inductance, R_M is the motor resistance, K_M is the motor torque constant, U_M is the voltage applied to the motor armature, and I_M is the motor current. Finally, the dynamics of the DC generator is expressed using the following equations

$$L_G \frac{dI_G}{dt} = \eta K_G \dot{\theta} - R_G I_G \qquad T_G = K_G I_G \tag{2.2}$$

where L_G is the motor inductance, η is the gear ratio between the pendulum pivot and the generator, R_G is the motor resistance, K_G is the motor torque constant, and I_G is the motor current.

3. Stochastic excitation modeling

Implementation of a stochastic excitation in the parametric pendulum system of this work is described in this Section. As aforementioned, the vertical excitation of the pendulum assembly is achieved by repeatedly switching the solenoid circuit on and off via a solid state relay. Variation of the timing for switching the solenoid on and off according to a random distribution could generate a stochastic excitation on the pendulum system. An example of the input signal of the solid state relay with varying on and off timing is shown in Fig. 2. The time interval between each peak of the input signal is different, and these values are generated from a random number generator.

A frequency range from 1.2 Hz to 7.0 Hz is selected, in the first instance, as a basis for a random time period generator. The reciprocal of the upper and lower limit of frequency determines the corresponding limits of the time interval between peaks of the input signal. This frequency range has been selected such that these values can be implemented in the experiment such that the pendulum is rotated. This could maximize the transmission of vertical translational energy to the pendulum as it experiences an autoparametric resonance with the electromechanically-excited mass-spring-damper system.

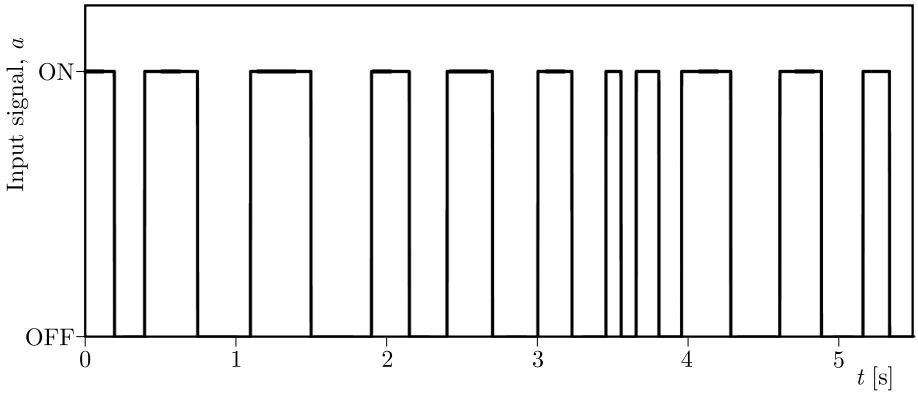

Fig. 2. Example of the input signal generated in a stochastic manner

The profile of the random distribution can be selected such that the random time period is generated according to either a set of discrete frequencies or a continuous variation of the frequency with respect to the frequency range of interest. Nonetheless, it is intended in this work to attempt emulating stochastic oscillatory motion of the pendulum assembly that could represent the sea wave excitation. The sea wave can be modeled as a stochastic process with a continuous function that can represent the state of the sea in the form of an energy spectrum; the wave spectrum. The Pierson-Moskowitz spectrum (Pierson and Moskowitz, 1964) is considered in the current study as the profile of the random distribution for the random number generator. It has been developed under the concept of a fully developed sea, and it is a one-parameter spectrum. The formulation of the Pierson-Moskowitz spectrum is given by

$$S(\omega) = A\frac{g^2}{\omega^5}\exp\Big(-\frac{16\pi^3}{\omega^4 T_z^4}\Big) \qquad T_z = B\sqrt{\frac{H_s}{g}} \tag{3.1}$$

where $A = 0.081$, $B = 11.1$, ω is the frequency, and H_s is the significant wave height which is defined as one third of the highest wave observed. From Eqs. (3.1), the profile of the wave spectrum depends solely on the parameter H_s. The same formulation was used by Najdecka (2013) to reconstruct the time history of the wave for stimulating the response of the pendulum system subjected to the sea wave excitation by means of an electro-dynamical shaker.

Figure 3a depicts the non-dimensionalized Pierson-Moskowitz spectrum.It is computed using Eqs. (3.1), and it features an asymmetric bell-shaped curve with a positive offset. It peaks at a nominal frequency, and that frequency can be expressed explicitly by equating to zero the derivative of $S(\omega)$ with respect to ω, which yields the following expression

$$\omega = \frac{2}{B}\sqrt{\frac{2g}{H_s}}\sqrt[4]{\frac{\pi^3}{5}} \tag{3.2}$$

Rearranging Eq. (3.2), one obtain an expression for H_s in terms of other parameters

$$H_s = \frac{8\pi g}{\omega^2 B^2}\sqrt{\frac{\pi}{5}} \tag{3.3}$$

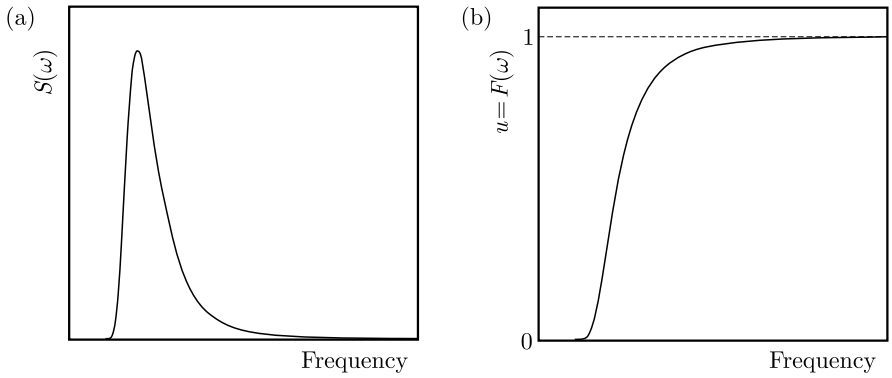

Fig. 3. Non-dimensionalized Pierson-Moskowitz wave spectrum; (b) cumulative distribution function of the Pierson-Moskowitz wave spectrum

The value of the parameter H_s can thus be determined in order to match the nominal frequency of the wave spectrum as close as possible to the operating frequency of the pendulum system.

Generation of a random time period based on the Pierson-Moskowitz spectrum is performed by using the inverse transform technique in this work. The inverse transform technique, also known as the Smirnov transform, is useful for generating random variates with an arbitrary continuous distribution function (Devroye, 1986). To utilize this technique, the selected random distribution is first integrated and then rescaled to obtain its cumulative distribution function F, such that it maps a number in the domain to a probability between $[0, 1]$, as illustrated in Fig. 3b. This technique works as follows. A random number u is generated from the standard uniform distribution in the interval of $[0, 1]$. The generated u is then interpolated with the rescaled cumulative distribution function to locate the frequency ω. In other words, the inverse function of F is sought to determine the frequency ω that corresponds to the generated random number u, with their relationship being expressed as follows

$$\omega = F^{-1}(u) \qquad \Delta t = \frac{2\pi}{\omega} - T_0 \qquad T_{new} = T_0 + C_1 \Delta t \tag{3.4}$$

In Eq. $(3.4)_2$, the random time period is decomposed into two components, namely the nominal time period T_0 and the offset time period introduced by the wave spectrum Δt. T_0 is also the inverse of the nominal frequency of the wave spectrum. Finally, a factor within the range of $[0, 1]$ C_1 is introduced to control the stochasticity of the random time period in Eq. $(3.4)_3$, which yields the new time period for that cycle.

To generate a train of square pulses with different timing for switching the solenoid on and off in the experiment continuously, the above procedure can be repeated in a timer loop. For each iteration, the timer will start counting once a new time period is generated, and a square wave and the command signal will be computed based on that time period. The command signal generated by the computer system can be written as

$$a = \begin{cases} 1 & \text{if } \ t(\text{mod } T_{new}) < \dfrac{1}{2} T_{new} \\ 0 & \text{otherwise} \end{cases} \tag{3.5}$$

where the units of the timer time t, the new time period T_{new} is in seconds. By using the equations above, the generated input signal will be a train of square pulses with a fixed duty cycle of 50%. The timer will be reset automatically once the timer counts until T_{new}. The time period for each iteration is then different, and so the on-and-off timing for each square wave in the pulse train, which is illustrated in Fig. 2. LabVIEW environment is used to program the above algorithm in this work.

Figure 4a depicts the time history of the vertical displacement of the pendulum support generated by the proposed stochastic excitation. It is observed at a root-mean-squared variac voltage of 110 V_{rms}. The nominal frequency of the spectrum is set to be 1.9 Hz, such that the corresponding value of H_s is 0.011 m. The pendulum is constrained at its downright position during the measurement, and C_1 is set to 1 to utilize the full scale of the Pierson-Moskowitz spectrum. From Fig. 4a, the amplitude of oscillation and time interval between two peaks is observed to be varying with time, which suggests that an irregular oscillation of the mass-spring-damper system could be generated by using the proposed stochastic excitation. The FFT spectrum of the time history (line 1) in Fig. 4b suggests that the vertical oscillation is stochastic in nature. The energy content of the vertical oscillation lies within a range of 1.2 Hz to 6 Hz, and it also resembles a bell-shaped curve with a positive offset. The spectrum is smoothened (line 2) and it displays a major peak in close vicinity of the nominal frequency of the Pierson-Moskowitz spectrum. By comparing it with the Pierson-Moskowitz spectrum (line 3), it can be seen that the smoothened spectrum of the time history is in good correspondence with the desired power density profile with mild slight discrepancy between the shapes of the spectra, which is representative of many vibratory systems. The above observations show the viability of the excitation mechanism in the current study to attempt emulating a stochastic excitation on a solenoid-powered mass-spring-damper system.

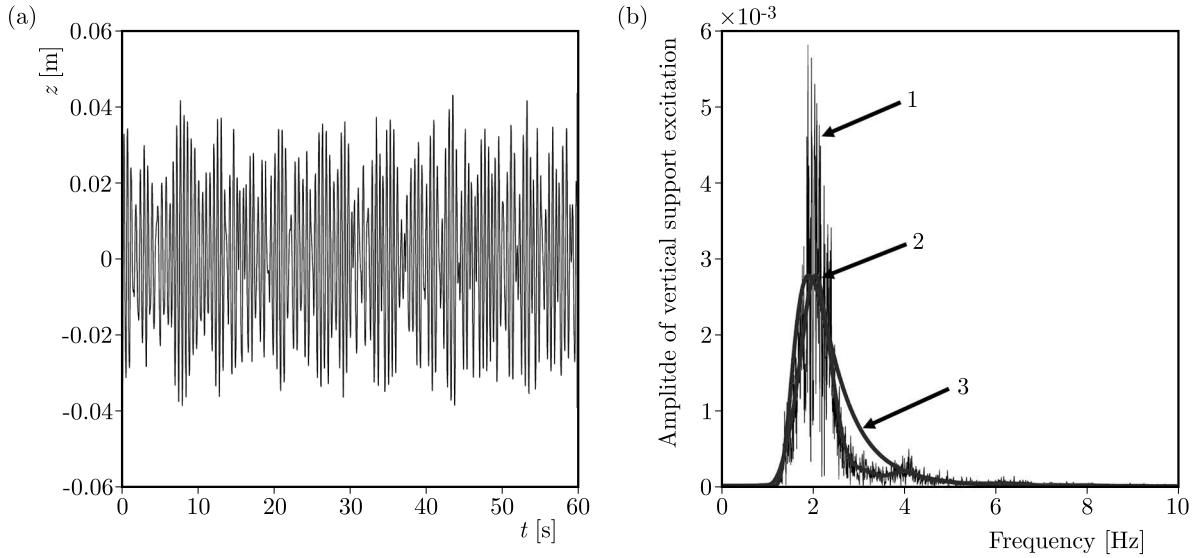

Fig. 4. (a) Time history of the vertical support excitation using the proposed stochastic excitation for $V = 130\,V_{rms}$ and $\omega_0 = 1.9$ Hz; (b) FFT spectrum of (a) compared with the Pierson-Moskowitz wave spectrum generated for $H_s = 0.011$ m

4. Rotation control of pendulum

A bang-bang control is suggested in the current study to promote rotational motion of the pendulum as it is subjected to a random excitation. The objective of control is to assist motion of the pendulum despite randomness of the vertical excitations. The nature of the control strategy is intuitive; while the pendulum is rotating, a control torque will be exerted along the rotational direction if the control system senses that the pendulum is experiencing a destructive coupling torque arisen from the pendulum support that opposes the current motion of pendulum. The real-time information of the angular displacement and velocity of the pendulum and the vertical acceleration of the pendulum support are assigned as the feedback signal of the controller and some conditions are defined based on those signals to exert control action. The function of each

signal is detailed as follows. The signal of angular displacement of the pendulum indicates the position of the pendulum from its downright equilibrium position. On the other hand, the signal of angular velocity of the pendulum indicates the direction and the rate at which the pendulum moves. Lastly, the signal of vertical acceleration of the pendulum support indicates the direction of the summation of forces acting on the pendulum support.

The rotating plane of the pendulum splits up into two halves, namely left-half plane and right-half plane, and they form control envelopes. The conditions for activating the control action is different for each plane. For the left-half plane (i.e. $2n\pi < \theta < (2n+1)\pi$, $n \in N$)

$$U_M(t) = \begin{cases} k_1 + k_2 \sin\theta & \text{if} \quad \ddot{z} > 0 \quad \wedge \quad 0 \leqslant \dot{\theta} < \dot{\theta}_{min} \\ -k_3 & \text{if} \quad \ddot{z} < 0 \quad \wedge \quad -\dot{\theta}_{min} < \dot{\theta} < 0 \\ 0 & \text{otherwise} \end{cases} \tag{4.1}$$

where U_M is the input to the DC motor, k_1 and k_2 are control parameters applied when the pendulum is climbing from its downright equilibrium, and k_3 is the control parameter applied when the pendulum is falling from its upright equilibrium position. Suppose that the pendulum is rotating in the left-half plane. The coupling torque will be destructive in that plane if the pendulum support is suddenly accelerated upwards while the pendulum is rotating in the clockwise direction, and this may cause the pendulum to lose angular velocity and fall to its downright equilibrium position. Hence, a control torque will be exerted along the clockwise direction if the pendulum support is accelerated upwards and the rate at which the pendulum is rotating is lower than the threshold angular velocity $\dot{\theta}_{min}$, as stated in the first condition of Eq.(4.1). A sinusoidal term is added to compensate for the torque due to gravity while the pendulum is climbing from its downright equilibrium position. On the other hand, the coupling torque will also be destructive in the left-half plane if the pendulum support is suddenly accelerated downwards while the pendulum is rotating in the counter-clockwise direction. A control torque of the counter-clockwise direction will then be exerted if the pendulum support is accelerated downwards and the rate at which the pendulum is rotating is greater than the negative threshold angular velocity, as stated in the second condition of Eq. (4.1). The control action will otherwise not be exerted in the left-half plane if the above conditions are not met. Likewise, for the right-half plane (i.e. $(2n+1)\pi < \theta < 2(n+1)\pi$, $n \in N$)

$$U_M(t) = \begin{cases} -(k_1 + k_2 \sin\theta) & \text{if} \quad \ddot{z} > 0 \quad \wedge \quad -\dot{\theta}_{min} < \dot{\theta} < 0 \\ k_3 & \text{if} \quad \ddot{z} < 0 \quad \wedge \quad 0 \leqslant \dot{\theta} < \dot{\theta}_{min} \\ 0 & \text{otherwise} \end{cases} \tag{4.2}$$

Due to an inequality condition at $\dot{\theta} = 0$, the control algorithm is also capable of initiating pendulum motion regardless of the initial conditions besides maintaining the rotation state of the pendulum, which is to be shown in Section 5.

5. Pendulum rotation subjected to the proposed stochastic excitation

The experimental rig, as described in Section 2, is used to implement the proposed method of varying the on-and-off timing of the solenoid to induce stochastic excitations on the pendulum system. The pendulum system is tested at different levels of stochasticity by varying the on-and-off timing, and the observation of rotational state of pendulum under such excitation is particularly of interest in view of energy scavenging. The control algorithm, as described in Section 4, is used to drive the rotational actuator in attempting to assist the rotation of the pendulum when it could not be sustained.

An AC supply voltage of $130\,\mathrm{V_{rms}}$ and a nominal frequency of 1.9 Hz is chosen to generate experimental results in the current study. The selected parameters lie within the resonance area of the pendulum system, which is advantageous for generating rotation of the pendulum. The pendulum system is first excited by switching the RLC circuit of the solenoid on-and-off with a regular time interval. The control algorithm is then activated and the pendulum is actuated from its downright equilibrium position to yield period-1 rotation. A buffer period of approximately 30 s is required to let the pendulum motion settle to period-1 rotation. After that, stochasticity is introduced to the excitation and the level of noise is controlled by manipulating C_1 in Eq. $(3.4)_3$. The pendulum system is run for a period of 300 s, and useful experimental data is logged simultaneously. As the rotational process is stochastic, the measurement for the same noise level is to be repeated for another 9 sets to obtain the average accumulated net energy. The control parameters k_1, k_2, k_3 and $\dot{\theta}_{min}$ are experimentally optimized and fixed at 8, 4, 1 and 7.5, respectively, for all noise levels throughout the experiment.

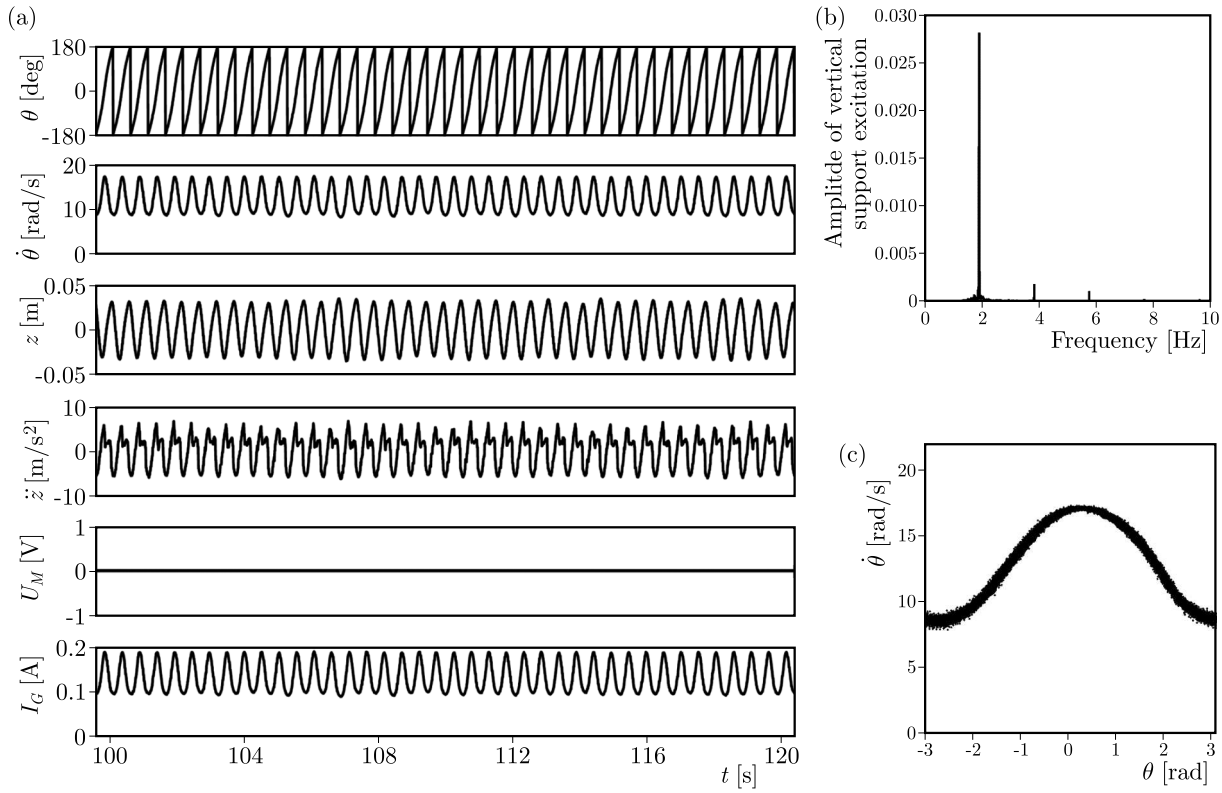

Fig. 5. (a) Time response of the pendulum system for $C_1 = 0$; (b) FFT spectrum for vertical support excitation generated using experimental results; (c) phase portrait of the pendulum axis

Figure 5a demonstrates a sample time history of the pendulum system when $C_1 = 0$ for a period of 21 s. In this case, the noise is disabled in the timer loop and the solenoid is switched on and off in a regular time interval, which is 0.526 s. Thus, the pendulum exhibits period-1 rotation as it experiences an autoparametric resonance with the vertical support excitation, which is also periodic, after it is actuated from its rest position. The quality of the periodic excitation can be assessed via its FFT spectrum, which, see Fig. 5b, shows a considerably discrete spectrum with a major peak at the fundamental frequency and subsequently minor peaks at its integer multiple with reducing the magnitude. On the other hand, it can be seen from the phase portrait of the pendulum axis in Fig. 5c that the pendulum rotates with fluctuating angular velocity, which is bounded within the range of $[7.9, 17.2]$ rad/s, under the regular excitation from the pendulum support. As the source of energy to maintain stable rotation is solely from the vertical support

excitation, no control action is required from the DC motor. The power of the generator will thus be the only contributor to the accumulated net energy at the end of the measurement, which serves as a benchmark for comparison with the accumulated net energy at higher noise levels.

The period-1 rotation of the pendulum system ceases to be stable when C_1 is increased up to 0.04. Hence, control assistance is necessary when C_1 is set to be within the range of $(0.04, 1]$ in order to maintain the rotational state of the pendulum. In the next case, the sample of the time history of the pendulum system when it is subjected to stochastic excitation in a moderate scale ($C_1 = 0.3$) is illustrated in Fig. 6a. The time interval that the solenoid is switched on-and-off is varied, in this case, within the range of $[0.411, 0.617]$ s. Period-1 rotation could still be observed most of the time, as the occurrence of the moments when the vertical support excitation is less destructive. Consequently, less control effort is required in this case with only four instances of the control voltage input observed in this interval of the experimental data. FFT spectrum of the vertical support excitation in Fig. 6b reveals that the spectrum is no longer discrete, and it is stochastic in nature. The amplitude of the vertical excitation at the fundamental frequency becomes one-fourth of its periodic counterpart. The energy is slightly spread in the vicinity of the fundamental frequency as a consequence of slight variation in the on-and-off time interval. The shape of the spectrum, on the other hand, is somewhat similar to that of the Pierson-Moskowitz wave spectrum with a narrower and sharper peak, as illustrated by the smoothened curve (line 2). The angular velocity at which the pendulum rotates, fluctuates within the range of $[4.8, 19.4]$ rad/s as depicted in Fig. 6c. It is wider than its periodic counterpart. The occasional randomness of the excitation causes the pendulum rotation to lose angular velocity at some instances, which is then rectified by the control action, and hence the lower limit of angular velocity range is extended when stochasticity is introduced to the excitation.

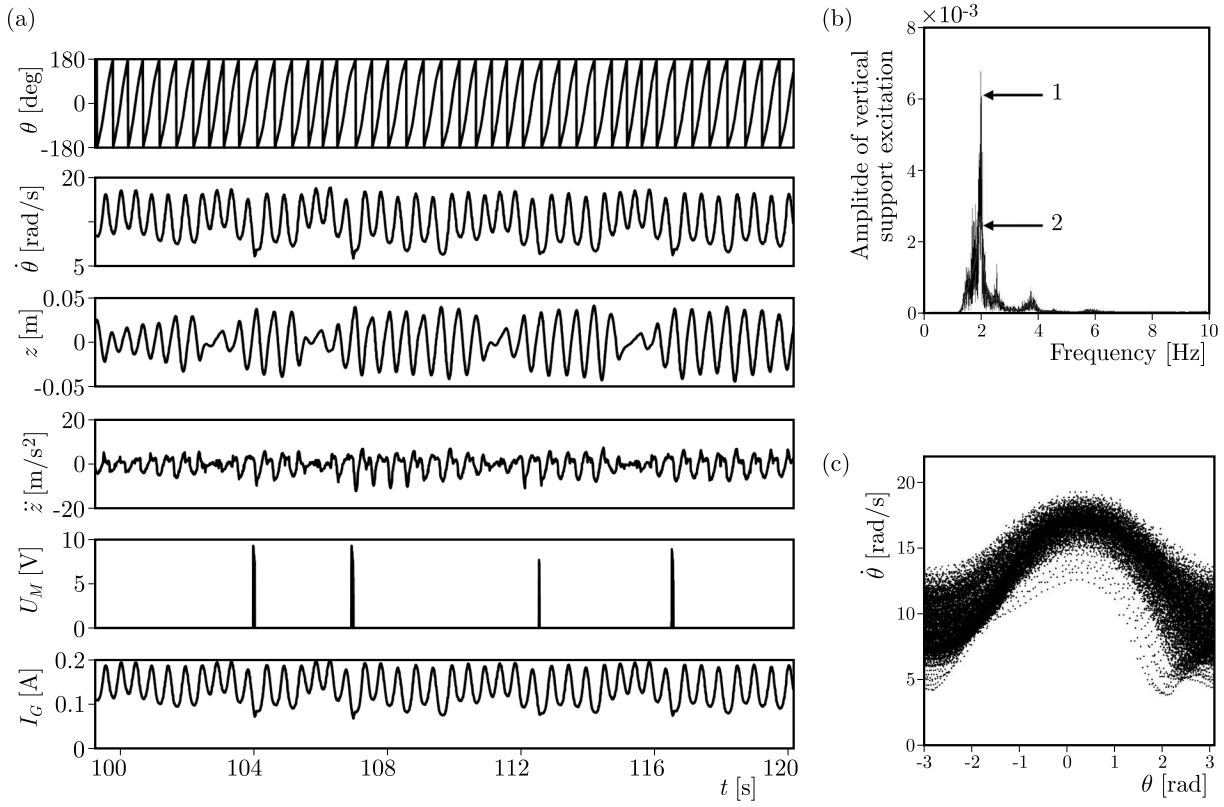

Fig. 6. (a) Time response of the pendulum system for $C_1 = 0.3$; (b) FFT spectrum for vertical support excitation generated using experimental results; (c) phase portrait of the pendulum axis

The sample time history of the pendulum system when $C_1 = 1$ is illustratedin Fig. 7a. In this case, the full scale of the Pierson-Moskowitz spectrum is used, and the time interval that the solenoid is switched on-and-off varies within the range of $[0.143, 0.830]$ s. It can be observed from the vertical axis data that the vertical support excitation is irregular at higher level of noise, which causes the pendulum trajectory to be intermittently distracted from its rotation attractor. This necessitates frequent control actions to assist the pendulum in regaining angular momentum and synchronizing again with the vertical support excitation. Accordingly, more control efforts are required at a higher level of noise, which is seen in the fifth row of Fig. 7a with 15 instances of the control voltage input observed in this interval of the experimental data. The contents of irregularities can be assessed via the FFT spectrum of the vertical support excitation in Fig. 7b. The smoothened spectrum (line 2) depicts a curve, and the shape of the spectrum is similar to that displayed in Fig. 3a. The spectrum peaks at the fundamental frequency, and the amplitude of the vertical support excitation at the fundamental frequency is lesser than in the previous cases. This is expected as the energy of the vertical excitation has been spread over a wider frequency range due to the maximum difference of 0.687 s in varying the time interval. The vertical support excitation does not possess enough energy in the vicinity of the fundamental frequency to sustain the pendulum rotation. This prompts the pendulum to lose its angular velocity and almost stall at some point in time before the controller is alerted to react to sudden disturbances. This is seen in the phase portrait of the pendulum axis, where the fluctuation range of angular velocity is widened to $[3.6, 19.8]$ rad/s.

$$E_{accumulated} = \eta K_G \int_{t_1}^{t_2} I_G \dot{\theta}\, dt - K_M \int_{t_1}^{t_2} I_M \dot{\theta}\, dt \tag{5.1}$$

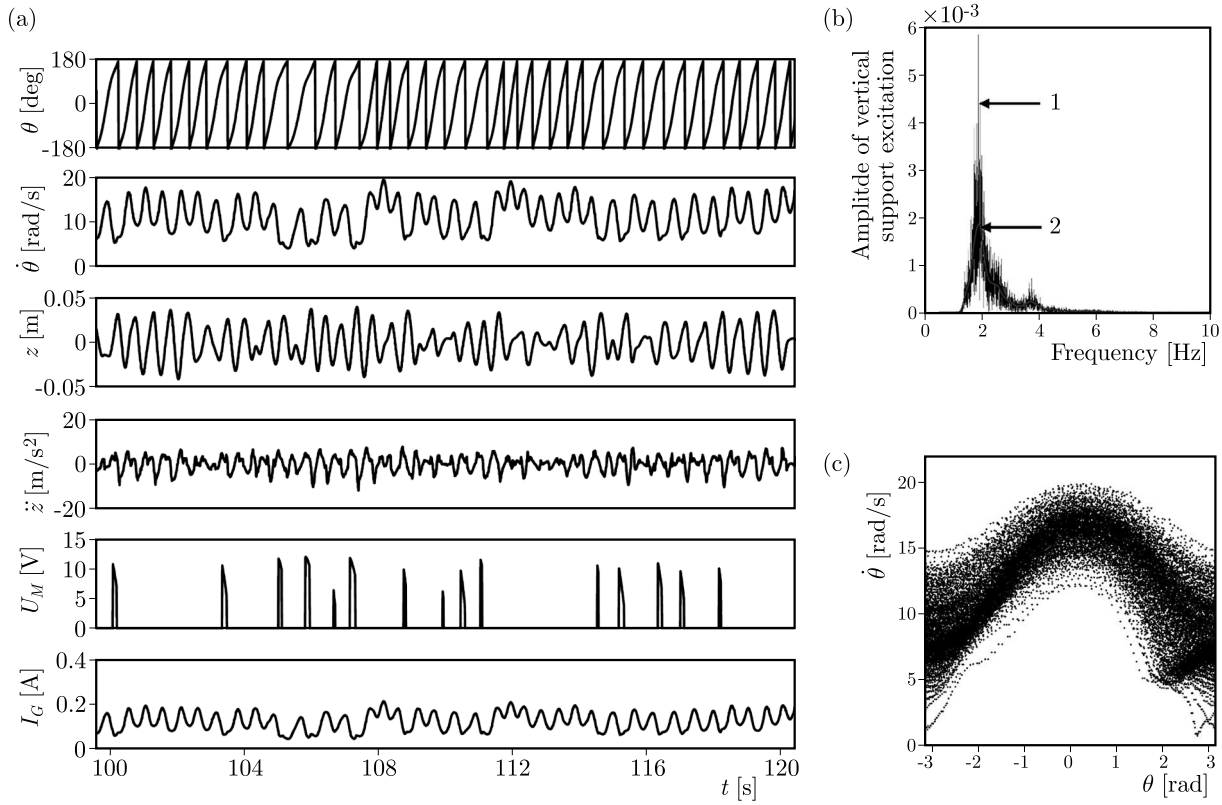

Fig. 7. (a) Time response of the pendulum system for $C_1 = 1$; (b) FFT spectrum for vertical support excitation generated using experimental results; (c) phase portrait of the pendulum axis

Energy generation is measured via current measurement from the generator, and the accumulated net energy is computed using Eq. (5.1) in real time during the course of the experiment in all the above cases. In Eq. (5.1), t_1 is the time when computation of the accumulated net energy begins and t_2 is the time when computation of the accumulated net energy ends. Figure 8 illustrates sample time histories of the accumulated net energy for the above three cases computed over a period of $t_2 - t_1 = 300$ s. In the case when the noise is disabled ($C_1 = 0$), pendulum rotation is sustainable without interference from the controller. Hence, the power generated from the DC generator is the sole contributor to computation of the accumulated net energy, and it can be seen from Fig. 8 that the accumulated net energy for $C_1 = 0$ increases steadily as the experiment progresses. The average accumulated net energy at the end of 300 s, obtained using 10 sets of data, is 24.51 J for $C_1 = 0$. On the other hand, in the cases when noise is added to the vertical excitation, control effort is required to sustain the pendulum rotation for maximizing the energy output from the generator. Therefore, energy is invested for exerting the control effort by means of actuation of the DC motor and this is taken into consideration while computing the accumulated net energy. For the case when a moderate level of noise is introduced to the excitation ($C_1 = 0.3$), occasional control torque is required to maintain the pendulum rotation and some energy is invested to achieve this purpose. The average accumulated net energy at the end of 300 s is 14.01 J for $C_1 = 0.3$, which is 57.16% of its periodic counterpart. For the case when the full scale of Pierson-Moskowitz spectrum is introduced to the excitation ($C_1 = 1$), the accumulated net energy is observed to be the least. Its average accumulated net energy at the end of 300 s is calculated as 4.67 J, which is 19.05% of the case when $C_1 = 0$. This is expected as more control input is necessary to prevent the pendulum motion from losing angular velocity when the pendulum is frequently subjected to the destructive vertical excitation.

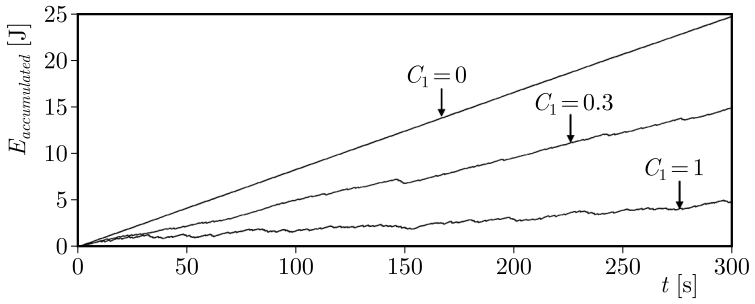

Fig. 8. Comparison of time histories of accumulated net energy for $C_1 = 0$, $C_1 = 0.3$ and $C_1 = 1$

6. Conclusion

An experimental pendulum system, which exerts a non-linear vertical excitation on a pendulum via a RLC-circuit powered solenoid is used to conduct investigations on pendulum rotation subjected to a stochastic excitation. The pendulum system, which was previously reported in the open literature, is enhanced with a control system by adding a rotational actuator and some necessary transducers. In addition, a generator is mounted in parallel to the pendulum axis for extracting energy out of rotating motion of the pendulum.

The stochastic excitation of the pendulum system is accomplished by a variable time interval for switching the RLC-circuit on and off according to a random distribution. In particular, the Pierson-Moskowitz wave spectrum is selected as the random distribution, and the generation of the random time interval is implemented in the experiment using an inverse transform technique. On the other hand, a bang-bang control algorithm is tailored to assist rotational motion of the pendulum as it is subjected to the random excitation. The main inputs of the controller are

the displacement and velocity of the angular axis and the acceleration of the vertical axis. The output is the command signal to the rotational actuator.

Using the proposed method of stochastic excitation and control scheme, the experimental results are illustrated for various levels of noise introduced to the vertical support excitation. The observations demonstrate the viability of the pendulum system in emulating a random excitation, which is similar to that of the sea wave excitation in experimental investigations of a vertical pendulum. The enhanced version of the experiment apparatus takes advantage of the rotational actuator and generator to respectively assist the pendulum motion and benefit from motion itself when it is excited vertically. In addition, the proposed control scheme can effectively retain the rotational state of the pendulum for all the above cases without suffering an energy deficit. The energy cost of the control increases with the level of noise introduced to the vertical excitation.

References

1. Alevras P., Yurchenko D., 2014, Stochastic rotational response of a parametric pendulum coupled with an SDOF system, *Probabilistic Engineering Mechanics*, **37**, 124-131
2. Alevras P., Yurchenko D., Naess A., 2014, Stochastic synchronization of rotating parametric pendulums, *Meccanica*, **49**, 8, 1945-1954
3. Blackburn J.A., 2006, Noise activated transitions among periodic states of a pendulum with a vertically oscillating pivot, mediated by a chaotic attractor, *Proceedings of the Royal Society A: Mathematical, Physical and Engineering Science*, **462**, 2067, 1043-1052
4. Blackburn J.A., Grønbech-Jensen N., Smith H.J.T., 1995, Stochastic noise and chaotic transients, *Physical Review Letters*, **74**, 6, 908
5. Brzeski P., Perlikowski P., Yanchuk S., Kapitaniak T., 2012, The dynamics of the pendulum suspended on the forced Duffing oscillator, *Journal of Sound and Vibration*, **331**, 24, 5347-5357
6. Dadone P., Lacarbonara W., Nayfeh A.H., Vanlandingham H.F., 2003, Payload pendulation reduction using a variable-geometry-truss architecture with LQR and fuzzy controls, *Journal of Vibration and Control*, **9**, 805-837
7. De Paula A.S., Savi M.A., Wiercigroch M., Pavlovskaia E., 2012, Bifurcation control of a parametric pendulum, *International Journal of Bifurcation and Chaos*, **22**, 1250111
8. Devroye L., 1986, *Non-uniform Random Variate Generation*, Springer-Verlag, New York
9. Horton B.W., Wiercigroch M., 2008, Effects of heave excitation on rotations of a pendulum for wave energy extraction, *IUTAM Symposium on Fluid-Structure Interaction in Ocean Engineering*, 117-128
10. Kecik K., Warminski J., 2011, Dynamics of an autoparametric pendulum-like system with a nonlinear semiactive suspension, *Mathematical Problems in Engineering*
11. Litak G., Borowiec M., Wiercigroch M., 2008, Phase locking and rotational motion of a parametric pendulum in noisy and chaotic conditions, *Dynamical Systems*, **23**, 3, 259-265
12. Mendrela E.A., Pudlowski Z.J., 1992, Transients and dynamics in a linear reluctance self-oscillating motor, *IEEE Transactions on Energy Conversion*, **7**, 1, 183-191
13. Najdecka A., 2013, Rotating dynamics of pendula systems for energy harvesting from ambient vibrations, Ph.D. Thesis, University of Aberdeen, Scotland
14. Pierson W.J., Moskowitz L., 1964, A proposed spectral form for fully developed wind seas based on the similarity theory of SA Kitaigorodskii, *Journal of Geophysical Research*, **69**, 24, 5181-5190
15. Teh S.-H., Chan K.-H., Woo K.-C., Demrdash H., 2015, Rotating a pendulum with an electromechanical excitation, *International Journal of Non-Linear Mechanics*, **70**, 73-83

16. Vaziri V., Najdecka A., Wiercigroch M., 2014, Experimental control for initiating and maintaining rotation of parametric pendulum, *The European Physical Journal Special Topics*, **223**, 795-812

17. Warminski J., Kecik K., 2006, Autoparametric vibrations of a nonlinear system with pendulum, *Mathematical Problems in Engineering*

18. Warminski J., Kecik K., 2009, Instabilities in the main parametric resonance area of a mechanical system with a pendulum, *Journal of Sound and Vibration*, **322**, 3, 612-628

19. Yukoi Y., Hikihara T., 2011a, Start control of parametric pendulum into periodic rotation, *Transactions of the Institute of Systems, Control and Information Engineers*, **24**, 54-60

20. Yukoi Y., Hikihara T., 2011b, Tolerance of start-up control of rotation in parametric pendulum by delayed feedback, *Physics Letters A*, **375**, 1779-1783

21. Yurchenko D., Alevras P., 2013, Stochastic dynamics of a parametrically base excited rotating pendulum, *Procedia IUTAM*, **6**, 160-168

22. Yurchenko D., Naess A., Alevras P., 2013, Pendulum's rotational motion governed by a stochastic Mathieu equation, *Probabilistic Engineering Mechanics*, **31**, 12-18

Manuscript received March 14, 2015; accepted for print October 26, 2015

JOURNAL OF THEORETICAL AND APPLIED MECHANICS
54, 3, pp. 731-742, Warsaw 2016
DOI: 10.15632/jtam-pl.54.3.731

FINITE STRAIN FORMULATION OF ELASTO-PLASTICITY WITHOUT YIELD SURFACE: THEORY, PARAMETER IDENTIFICATION AND APPLICATIONS

Cyprian Suchocki, Paweł Skoczylas
Warsaw University of Technology, Department of Mechanics and Armament Technology, Warsaw, Poland
e-mail: c.suchocki@imik.wip.pw.edu.pl

In this study, a finite strain formulation of elasto-plasticity without the yield surface is analyzed. It is found that the presented model allows for a good description of the elasto-plastic response for many metallic materials. Furthermore, it is noted that the model involving a limited number of material parameters is able to capture such effects as indefinite elastic limit, strain hardening, strain softening and the Bauschinger effect. An algorithm for the evaluation of constants is described and the determined values are given for NC high carbon tool steel, copper, brass, Inconel alloy, tungsten heavy alloy and aluminum.

Keywords: constitutive equation, plasticity, metals, material constants

1. Introduction

In continuum mechanics, two main concepts of the plasticity theory can be distinguished, i.e. flow theories and theories of plasticity without the yield surface, including endochronic plasticity. The origins of constitutive theories based on the flow rules date back to the mid-19th century. The fundamentals of plasticity theories not employing the yield surface were formulated much later (e.g. Ilyushin, 1963; Pipkin and Rivlin, 1965).

The first steps associated with replacing the flow rule and yield criterion-based formulation of elasto-plasticity with a new one are claimed to Ilyushin (1963) who first introduced the concept of arc length in the strain space. This approach was later extended by Pipkin and Rivlin (1965) who developed a novel, general theory of plasticity for the case of finite strains and rotations, however, without proposing a specific form of the constitutive equation.

The arc length calculated in nine-dimensional finite strain space is the basic concept for the new formulation of elasto-plasticity. This scalar value is utilized to build a functional of strain history analogous to the history functional used in the theory of viscoelasticity. Pipkin and Rivlin (1965) considered the most general form of the strain history functional, which in practice can be assumed in the form of a hereditary integral, where, instead of time, the arc length in the strain space is assumed as the variable of integration. For a constitutive theory constructed in such a manner, the arc length plays the role of an intrinsic time analogously to the time in the theory of viscoelasticity.

Pipkin and Rivlin (1965) postulated that the arc length should be calculated utilizing a Pythagorean metric. A different approach was introduced by Valanis (1971a,b) who proposed using a non-Pythagorean metric for calculation of the arc length in the infinitesimal strain space and additional multiplication by a scaling function. The plasticity theories which employ a scaling function in their definition of the intrinsic time are called endochronic (cf. Valanis, 1971b). Such concepts were strongly criticized (e.g. Rivlin, 1981) as nonphysical. Some of the imperfections of the original endochronic theory were eliminated in a later constitutive model

(cf. Valanis, 1980). However, this was achieved at the price of splitting the strain tensor into elastic and plastic components and introducing a yield criterion.

A number of models exist which transfer some concepts of the endochronic formulation to the flow theory. In particular, the flow rule for kinematic hardening may utilize a hereditary integral to govern the evolution of the back stress (e.g. Backhaus, 1976). This framework was further extended to take into account such effects as the memory of maximal prestrain and the amplitude-dependent hardening in the case of cyclic loadings (cf. Mróz and Rodzik, 1996). The effective infinitesimal plastic strain is used as the intrinsic time in models of this type.

In the present work, a finite strain formulation of plasticity without the yield surface, previously introduced by Suchocki (2015), is analyzed upon its ability to capture the inelastic response of metals. In order to clearly lay out basic theory assumptions, the infinitesimal strain formulation is described first. Subsequently, the novel finite strain generalization is presented and examined. It is found that the proposed constitutive model, which involves a very limited number of material parameters, is not only able to accurately fit the stress-strain data but also to predict such behavior as indefinite elastic limit, strain hardening, strain softening and the Bauschinger effect. A numerical algorithm used for the evaluation of the material constants is described. The model parameters are determined for a variety of metallic materials. Finally, a parameric study is conducted.

2. Small strain formulation

Below, the basic notions of rate-independent plasticity are discussed in the case of infinitesimal deformations, cf. Rivlin (1981). The following assumptions have been adopted:

- Only isothermal deformation processes are considered.
- Isotropic materials with elasto-plastic properties are analyzed.
- The volumetric response is purely elastic (Fig. 1a).
- The total shear stress is assumed as a sum of the elastic stress and N rate-independent stress-like internal state variables (Fig. 1b).
- The internal state variables depend on shear deformation only and are governed by differential evolution equations.

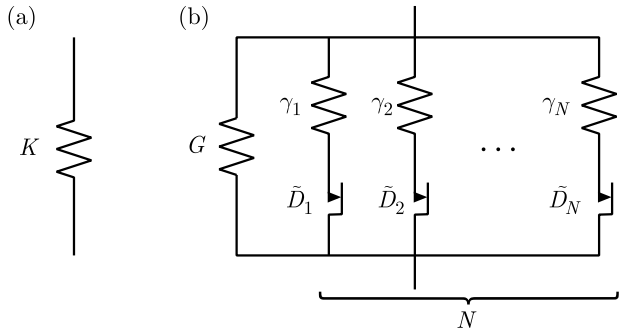

Fig. 1. Mechanical scheme of the constitutive model; (a) volumetric response, (b) shear response

The total Cauchy stress tensor $\boldsymbol{\sigma}$ is a sum of the volumetric stress tensor $p\mathbf{1}$ and the stress deviator $\mathbf{s}$, i.e.

$$\boldsymbol{\sigma} = p\mathbf{1} + \mathbf{s} \qquad p = K\epsilon \qquad \mathbf{s} = \mathbf{s}_0 + \sum_{k=1}^{N} \widetilde{\mathbf{h}}_k \qquad \mathbf{s}_0 = 2G\mathbf{e} \tag{2.1}$$

where

$$\epsilon = \operatorname{tr}\boldsymbol{\varepsilon} \qquad \mathbf{e} = \boldsymbol{\varepsilon} - \frac{1}{3}(\operatorname{tr}\boldsymbol{\varepsilon})\mathbf{1} \tag{2.2}$$

whereas $\widetilde{\mathbf{h}}_k$ $(k = 1, 2, \ldots, N)$ are tensorial internal state variables while K and G are the bulk and shear moduli, respectively. The internal state variable evolution equation is a modification of the differential equation following from the Maxwell mechanistic model, i.e.

$$\dot{\widetilde{\mathbf{h}}}_k + \frac{1}{\widetilde{D}_k M(|\dot{\mathbf{e}}|)}\widetilde{\mathbf{h}}_k = \gamma_k \dot{\mathbf{s}}_0 \qquad M(|\dot{\mathbf{e}}|) = (\operatorname{tr}\dot{\mathbf{e}}^2)^{-\frac{1}{2}} \qquad k = 1, 2, \ldots, N \tag{2.3}$$

where γ_k is a dimensionless parameter and the product $\widetilde{D}_k M(|\dot{\mathbf{e}}|)$ is a rate-dependent relaxation time. The particular choice of $M(|\dot{\mathbf{e}}|)$ given by $(2.3)_2$ allows one to eliminate time from the evolution equation. After inserting Eqs $(2.1)_4$ and $(2.3)_2$ into Eq. $(2.3)_1$ and multiplying it by a time differential, an incremental equation is obtained

$$\mathrm{d}\widetilde{\mathbf{h}}_k + \frac{\sqrt{\operatorname{tr}\mathrm{d}\mathbf{e}^2}}{\widetilde{D}_k}\widetilde{\mathbf{h}}_k = 2\gamma_k G\,\mathrm{d}\mathbf{e} \qquad k = 1, 2, \ldots, N \tag{2.4}$$

which states that the evolution of $\widetilde{\mathbf{h}}_k$ $(k = 1, 2, \ldots, N)$ depends solely on the deformation path in the strain space and is rate-independent.

An intrinsic time ζ is introduced, cf. Valanis (1971a,b), i.e.

$$\dot{\zeta} = \frac{1}{M(|\dot{\mathbf{e}}|)} \qquad \zeta(\tau) = \int_{-\infty}^{\tau} \frac{\mathrm{d}\tau'}{M(\tau')} \qquad \zeta(t) = z \tag{2.5}$$

After substituting Eq. $(2.3)_2$ into Eq. $(2.5)_2$

$$\zeta(\tau) = \int_{-\infty}^{\tau} \sqrt{\mathrm{d}\mathbf{e}(\tau') \cdot \mathrm{d}\mathbf{e}(\tau')} \tag{2.6}$$

It can be seen from (2.6) that the intrinsic time has an interpretation of the arc length in the deviatoric strain space. Integration of Eq. $(2.3)_1$ yields

$$\widetilde{\mathbf{h}}_k(t) = \int_0^{z(t)} \gamma_k e^{-\frac{z-\zeta}{\widetilde{D}_k}} \frac{\partial \mathbf{s}_0(\zeta)}{\partial \zeta}\,\mathrm{d}\zeta \qquad k = 1, 2, \ldots, N \tag{2.7}$$

which is reminiscent of a similar equation present in both linear and nonlinear viscoelasticity.

3. Finite strain formulation

All the basic assumptions listed in the previous Section apply to the finite strain model aswell. The total stress $\mathbf{S}$ is given as a sum of the volumetric stress $\mathbf{S}_0^{vol}$, elastic isochoric stress $\mathbf{S}_0^{iso}$ and the stress-like tensorial state variables $\widetilde{\mathbf{H}}_k$ $(k = 1, 2, \ldots, N)$, i.e.

$$\mathbf{S} = \mathbf{S}_0^{vol} + \mathbf{S}_0^{iso} + \sum_{k=1}^{N} \widetilde{\mathbf{H}}_k \qquad \mathbf{S}_0^{vol} = J\frac{\partial U}{\partial J}\mathbf{C}^{-1} \qquad \mathbf{S}_0^{iso} = 2J^{-\frac{2}{3}}\Big[\frac{\partial \overline{W}}{\partial \overline{\mathbf{C}}}\Big] \tag{3.1}$$

where, $\mathbf{C}$ and $\overline{\mathbf{C}}$ are the total and isochoric right Cauchy-Green (C-G) tensors, respectively, $J = \det\mathbf{F}$ is the determinant of the deformation gradient tensor $\mathbf{F}$, whereas $U = U(J)$ and

$\overline{W} = \overline{W}(\bar{I}_1, \bar{I}_2)$ are the elastic stored energy functions with $\bar{I}_1$ and $\bar{I}_2$ being scalar invariants of $\overline{\mathbf{C}}$ while $\mathrm{DEV}\,[\bullet] = [\bullet] - \frac{1}{3}([\bullet] \cdot \overline{\mathbf{C}})\overline{\mathbf{C}}^{-1}$. The evolution of internal state variables is governed by differential equations

$$\dot{\widetilde{\mathbf{H}}}_k + \frac{1}{\widetilde{D}_k M(|\dot{\overline{\mathbf{C}}}|)} \widetilde{\mathbf{H}}_k = \gamma_k \dot{\mathbf{S}}_0^{iso} \qquad k = 1, 2, \ldots, N \tag{3.2}$$

with

$$M(|\dot{\overline{\mathbf{C}}}|) = \bar{J}_2^{-\frac{1}{2}} \qquad \bar{J}_2 = \mathrm{tr}\,\dot{\overline{\mathbf{C}}}^2 \tag{3.3}$$

This specific choice of $M(|\dot{\overline{\mathbf{C}}}|)$ ensures that the evolution of $\widetilde{\mathbf{H}}_k$ $(k = 1, 2, \ldots, N)$ is rate-independent. Integration of (3.2) yields

$$\widetilde{\mathbf{H}}_k(t) = \int_0^{z(t)} \gamma_k \mathrm{e}^{-\frac{z-\zeta}{\widetilde{D}_k}} \frac{\partial \mathbf{S}_0^{iso}(\zeta)}{\partial \zeta}\, \mathrm{d}\zeta \qquad k = 1, 2, \ldots, N \tag{3.4}$$

where the following equalities are used

$$\dot{\zeta} = \frac{1}{M(|\dot{\overline{\mathbf{C}}}|)} \qquad \zeta(\tau) = \int_{-\infty}^{\tau} \sqrt{\mathrm{d}\overline{\mathbf{C}}(\tau') \cdot \mathrm{d}\overline{\mathbf{C}}(\tau')} \qquad \zeta(t) = z \tag{3.5}$$

Equation (3.4) is a special case of the general, functional stress-strain relation formulated by Pipkin and Rivlin (1965), and the intrinsic time introduced in Eqs (3.5) is a modification of the fictitious time measure proposed therin.

4. One-dimensional tension-compression

A uniaxial tension along the X_1-direction (Fig. 2b) is defined by the following set of equations

$$x_1 = \lambda_1 X_1 \qquad x_2 = \lambda X_2 \qquad x_3 = \lambda X_3 \tag{4.1}$$

where the principal stretches $\lambda_1 > 1$ and $\lambda < 1$ for tension, whereas $\lambda_1 < 1$ and $\lambda > 1$ for compression processes. Applying the boundary condition of the stress-free lateral surface, the scalar equations can be written as follows

$$S_{11} = S_{0(11)}^{vol} + S_{0(11)}^{iso} + \sum_{k=1}^{N} \widetilde{H}_{k(11)} \qquad 0 = S_{0(22)}^{vol} + S_{0(22)}^{iso} + \sum_{k=1}^{N} \widetilde{H}_{k(22)} \tag{4.2}$$

Is is assumed that $\overline{W}(\overline{\mathbf{C}}) = \overline{W}(\bar{I}_1)$, which yields

$$\mathbf{S}_0^{vol} = Jp\mathbf{C}^{-1} \qquad p = \frac{\partial U}{\partial J} \qquad \mathbf{S}_0^{iso} = 2J^{-\frac{2}{3}} \frac{\partial \overline{W}}{\partial \bar{I}_1}\Big(\mathbf{1} - \frac{1}{3} I_1 \mathbf{C}^{-1}\Big) \tag{4.3}$$

In the considered case $I_1 = \lambda_1^2 + 2\lambda^2$, which leads to the following formulas for the isochoric elastic stress components

$$S_{0(11)}^{iso} = \frac{4}{3} J^{-\frac{2}{3}} \frac{\partial \overline{W}}{\partial \bar{I}_1}\Big[1 - \Big(\frac{\lambda}{\lambda_1}\Big)^2\Big] \qquad S_{0(22)}^{iso} = -\frac{1}{2}\Big(\frac{\lambda_1}{\lambda}\Big)^2 S_{0(11)}^{iso} \tag{4.4}$$

By utilizing Eq. $(4.3)_1$ in Eqs (4.2), one obtains

$$S_{11} = Jp\frac{1}{\lambda_1^2} + S^{iso}_{0(11)} + \sum_{k=1}^{N} \widetilde{H}_{k(11)} \qquad 0 = Jp\frac{1}{\lambda^2} + S^{iso}_{0(22)} + \sum_{k=1}^{N} \widetilde{H}_{k(22)} \tag{4.5}$$

After eliminating the Jp factor, and using $(4.4)_2$, the following form of the process equation is found

$$S_{11} = \frac{3}{2}S^{iso}_{0(11)} + \sum_{k=1}^{N}\Big[\widetilde{H}_{k(11)} - \Big(\frac{\lambda}{\lambda_1}\Big)^2 \widetilde{H}_{k(22)}\Big] \tag{4.6}$$

In this study, two specific forms of $\overline{W}$ are considered, i.e. neo-Hooke and the one proposed by Knowles

$$\overline{W}(\bar{I}_1) = \frac{\mu}{2}(\bar{I}_1 - 3) \qquad \overline{W}(\bar{I}_1) = \frac{\mu}{2b}\Big\{\Big[1 + \frac{b}{\kappa}(\bar{I}_1 - 3)\Big]^{\kappa} - 1\Big\} \tag{4.7}$$

with μ, b and κ being the elasticity constants. After inserting $(4.7)_1$ into $(4.4)_1$, the following formula is found

$$S^{iso}_{0(11)} = \frac{2}{3}J^{-\frac{2}{3}}\mu\Big[1 - \Big(\frac{\lambda}{\lambda_1}\Big)^2\Big] \tag{4.8}$$

whereas substituting $(4.7)_2$ into $(4.4)_1$ yields

$$S^{iso}_{0(11)} = \frac{2}{3}J^{-\frac{2}{3}}\mu\Big[1 + \frac{b}{\kappa}(\bar{I}_1 - 3)\Big]^{\kappa-1}\Big[1 - \Big(\frac{\lambda}{\lambda_1}\Big)^2\Big] \tag{4.9}$$

In the case of material incompressibility $J = 1$ and $\lambda = \lambda_1^{-\frac{1}{2}}$, whereas $\bar{I}_1 = I_1 = \lambda_1 + 2\lambda_1^{-\frac{1}{2}}$. Thus, Eqs (4.8) and (4.9) take respectively forms

$$S^{iso}_{0(11)} = \frac{2}{3}\mu\Big(1 - \frac{1}{\lambda_1^3}\Big) \qquad S^{iso}_{0(11)} = \frac{2}{3}\mu\Big[1 + \frac{b}{\kappa}(I_1 - 3)\Big]^{\kappa-1}\Big(1 - \frac{1}{\lambda_1^3}\Big) \tag{4.10}$$

By applying the incompressibility condition to Eq. (4.6), the one-dimensional process equation is found, i.e.

$$S_{11} = \frac{3}{2}S^{iso}_{0(11)} + \sum_{k=1}^{N}\Big(\widetilde{H}_{k(11)} - \widetilde{H}_{k(22)}\frac{1}{\lambda_1^3}\Big) \tag{4.11}$$

whereas the engineering and Cuachy stresses are calculated according to the formulas

$$T_{11} = \lambda_1 S_{11} \qquad \sigma_{11} = \lambda_1 T_{11} \tag{4.12}$$

Equations (4.10)-(4.12) along with Eq. $(4.4)_2$ and two scalar equations following from Eq. (3.2) form up a system of nonlinear algebraic and differential equations which can be solved numerically. It is assumed that the excitation is kinematic with a constant strain rate T, thus, at the time increment $n+1$

$$t_{n+1} = t_n + \Delta t \qquad \lambda_1(t_{n+1}) = 1 + Tt_{n+1}$$

In the case of incompressibility $\bar{J}_2 = J_2 = \operatorname{tr}\dot{\mathbf{C}}$. Furthermore, an auxiliary quantity is defined as

$$\widetilde{J}(t_{n+1}) = J_2(t_{n+1})\Delta t^2$$

Material parameter optimization algorithm

Input: $\mathbf{p}^0$, $(\widetilde{T}_{11})_j$, w_j $(j=1,2,\ldots,K)$, N, $\widetilde{T}$, i_{max}, $i=1$

1. Calculate the inital value of the weighted error function

$$\mathcal{F}^0(\mathbf{p}^0)=\sum_{j=1}^{K} w_j\left[(T_{11}(\mathbf{p}^0))_j-(\widetilde{T}_{11})_j\right]^2$$

2. Assemble the initial matrix of parameter values

$$\mathbf{M}^0_{5\times(1+2N)}=\begin{bmatrix}\mu_1 & \gamma_{11} & \cdots & \gamma_{N1} & \widetilde{D}_{11} & \cdots & \widetilde{D}_{N1}\\ \mu_2 & \gamma_{12} & \cdots & \gamma_{N2} & \widetilde{D}_{12} & \cdots & \widetilde{D}_{N2}\\ \vdots & \vdots & \vdots & \vdots & \vdots & \vdots & \vdots\\ \mu_5 & \gamma_{15} & \cdots & \gamma_{N5} & \widetilde{D}_{15} & \cdots & \widetilde{D}_{N5}\end{bmatrix}$$

3. Find a parameter combination minimizing the error function

$$\mathbf{p}^i=\left[\mu^{opt},\gamma_1^{opt},\ldots,\gamma_N^{opt},\widetilde{D}_1^{opt},\ldots,\widetilde{D}_N^{opt}\right]^{\mathrm{T}}$$

4. Check the stop criterion, i.e.

$$\left|\frac{\mathcal{F}^i(\mathbf{p}^i)-\mathcal{F}^{i-1}(\mathbf{p}^{i-1})}{\mathcal{F}^{i-1}(\mathbf{p}^{i-1})}\right|<\widetilde{T}$$

5. Assemble the matrix of parameter values for the next iteration

   (a) Calculate parameter value increments $(k=1,2,\ldots,N)$

$$\Delta\mathbf{p}=\left[\Delta\mu,\Delta\gamma_1,\ldots,\Delta\gamma_N,\Delta\widetilde{D}_1,\ldots,\Delta\widetilde{D}_N\right]^{\mathrm{T}}$$

$$\Delta\mu=\frac{|\mu^{opt}|}{5i}\qquad \Delta\gamma_k=\frac{|\gamma_k^{opt}|}{5i}\qquad \Delta\widetilde{D}_k=\frac{|\widetilde{D}_k^{opt}|}{5i}$$

   (b) Compute $\mathbf{M}^i_{5\times(1+2N)}$ components $(k=1,2,\ldots,5,\ l=1,2,\ldots,1+2N)$

$$\left[\mathbf{M}^i_{5\times(1+2N)}\right]_{kl}=M^i_{kl}=p^i_l+\frac{k-3}{2}\Delta p_l$$

6. Go to step 3 if $i<i_{max}$; otherwise display optimal material parameter values

which is determined by the following formula

$$\widetilde{J}(t_{n+1})=2(T\Delta t)^2\Big\{\frac{2}{3}\Big[\frac{1}{3}\Big(\lambda_1^4(t_{n+1})+\frac{2}{\lambda_1^2(t_{n+1})}\Big)-2\Big]\Big(\lambda_1^3(t_{n+1})-\frac{1}{\lambda_1^3(t_{n+1})}\Big)^2 + 2\lambda_1^2(t_{n+1})+\frac{1}{\lambda_1^4(t_{n+1})}\Big\}$$

According to Eqs $(4.10)_1$ and $(4.4)_2$, the isochoric elastic stresses are given as

$$S^{iso}_{0(11)}(t_{n+1})=\frac{2}{3}\mu\Big(1-\frac{1}{\lambda_1^3(t_{n+1})}\Big)\qquad S^{iso}_{0(22)}(t_{n+1})=-\frac{1}{2}\lambda_1^3(t_{n+1})S^{iso}_{0(11)}(t_{n+1})$$

The total second P-K stress is calculated using Eq. (4.11), assuming $N = 1$, i.e.

$$S_{11}(t_{n+1}) = \frac{3}{2} S^{iso}_{0(11)}(t_{n+1}) + \widetilde{H}_{1(11)}(t_{n+1}) - \frac{1}{\lambda_1^3(t_{n+1})} \widetilde{H}_{1(22)}(t_{n+1})$$

whereas the internal state variable components are calculated from the following recurrence-update formulas

$$\widetilde{H}_{1(11)}(t_{n+1}) = \frac{\Big(1 - \frac{1}{2\widetilde{D}_1 \widetilde{J}^{-\frac{1}{2}}(t_{n+1})}\Big)\widetilde{H}_{1(11)}(t_n) + \gamma_1 \Big(S^{iso}_{0(11)}(t_{n+1}) - S^{iso}_{0(11)}(t_n)\Big)}{1 + \frac{1}{2\widetilde{D}_1 \widetilde{J}^{-\frac{1}{2}}(t_{n+1})}}$$

$$\widetilde{H}_{1(22)}(t_{n+1}) = \frac{\Big(1 - \frac{1}{2\widetilde{D}_1 \widetilde{J}^{-\frac{1}{2}}(t_{n+1})}\Big)\widetilde{H}_{1(22)}(t_n) + \gamma_1 \Big(S^{iso}_{0(22)}(t_{n+1}) - S^{iso}_{0(22)}(t_n)\Big)}{\Big(1 + \frac{1}{2\widetilde{D}_1 \widetilde{J}^{-\frac{1}{2}}(t_{n+1})}\Big)}$$

which have been developed utilizing the central difference method.

The given above set of discretized process equations in the form derived for an incompressible material is utilized within the parameter evaluation algorithm for computation of theoretical stress values. The assumption of material incompressibility has been adopted for the sake of simplicity. The relative error in estimation of the stretch ratio in the lateral direction that results from this assumption does not exceed 2% for the considered class of materials.

5. Experimetal setup

A number of experiments have been performed in order to obtain the data which allowed one to asses the model's capability of capturing the mechanical response of metals. The Instron 1115 material testing machine was used for the experiments (Fig. 2a).

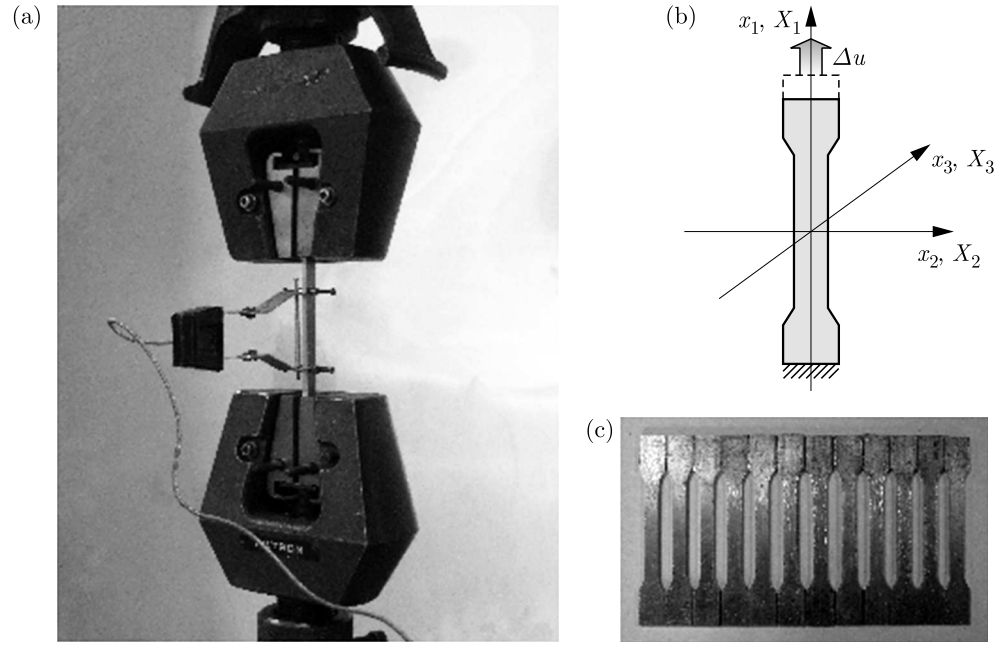

Fig. 2. (a) Experimental set-up. (b) Deformation process and coordinate systems. (c) Dogbone specimens

The conducted tests included one-dimensional tension (Fig. 2b) of copper, Inconel No. 1 (supersaturated), Inconel No. 2 (supersaturated and aged), brass, NC tool steel, aluminum and

tungsten heavy alloy (THA). In each case, unloading was performed shortly before the failure. The specimens (Fig. 2c) were machined according to the Polish standard PN-91 H-04310. Each tension test was repeated for at least three times in order to make sure that the registered stress-strain curves were reproducible. The specimens were tested at room temperature of 20°C.

6. Curve fitting

A pattern search algorithm has been used for the evaluation of the model parameters. It is a modification of the scheme proposed by Zalewski (2009). In each iteration, a matrix $\mathbf{M}^{i}_{5\times(1+2N)}$ containing several sets of material constants is assembled. Every parameter set is subsequently used to compute theoretical stress values. A combination of constant values $\mathbf{p}^{i+1}$, which results in the best approximation of the stress-stretch curve, is allowed to proceed to the next iteration $i+1$. The performed calculations have been listed in an outline, which assumed making use of neo-Hooke stored-energy function. The curve fitting results are presented in Figs. 3 and 4, whereas the evaluated values of the material parameters are gathered in Table 1.

Table 1. Determined values of material parameters

Material	μ [MPa]	b [–]	κ [–]	γ_1 [–]	$\widetilde{D}_1$ [–]
copper	367.33	22.41	0.68	132.80	0.0053
Inconel No. 1	1114.68	-	-	83.43	0.0034
Inconel No. 2	1152.58	-	-	74.12	0.013
brass	681.68	-	-	35.67	0.013
steel NC 6	1065.19	-	-	47.06	0.0081
aluminum	546.70	-	-	30.72	0.0098
THA	1226.94	-	-	88.48	0.0060

In each case, a single internal state variable has been assumed. In the case of copper, the version of the constitutive equation employing the Knowles stored-energy function has been used in order to reproduce the strain-softening phenomenon (Fig. 3a). For all the remaining metals, the neo-Hooke function has been utilized.

An excellent agreement between the theoretical and experimental curves has been achieved for THA (Fig. 4a). In some cases, fitting monotonic stress-stretch data leads to obtaining a better approximation as it can be seen in the case of brass (Fig. 4b).

7. Parametric studies

Several simulations have been carried out in order to asses the model behavior, its sensitivity and the influence of the experimental data used for material parameter evaluation.

In Fig. 5a, the results of loading-unloading simulations are presented which have been performed for five different values of the maximum stretch. The material parameter set has been evaluated from the brass monotonic loading data (model 1). In Fig. 5b, the results of performing the same simulations are shown where the set of constants has been determined from the brass hysteresis data (model 2). In Fig. 5c, the hysteresis loops obtained for the two different material parameter sets are compared. It can be seen that utilizing the monotonic loading data for the determination of material constants instead of using the hysteresis data, does not produce any negative consequences. What is more, an excellent approximation is achieved in the initial part of the stress-stretch curve (Fig. 4b). In Fig. 5d, the result of one-dimensional, cyclic loading-unloading simulation is shown (model 1).

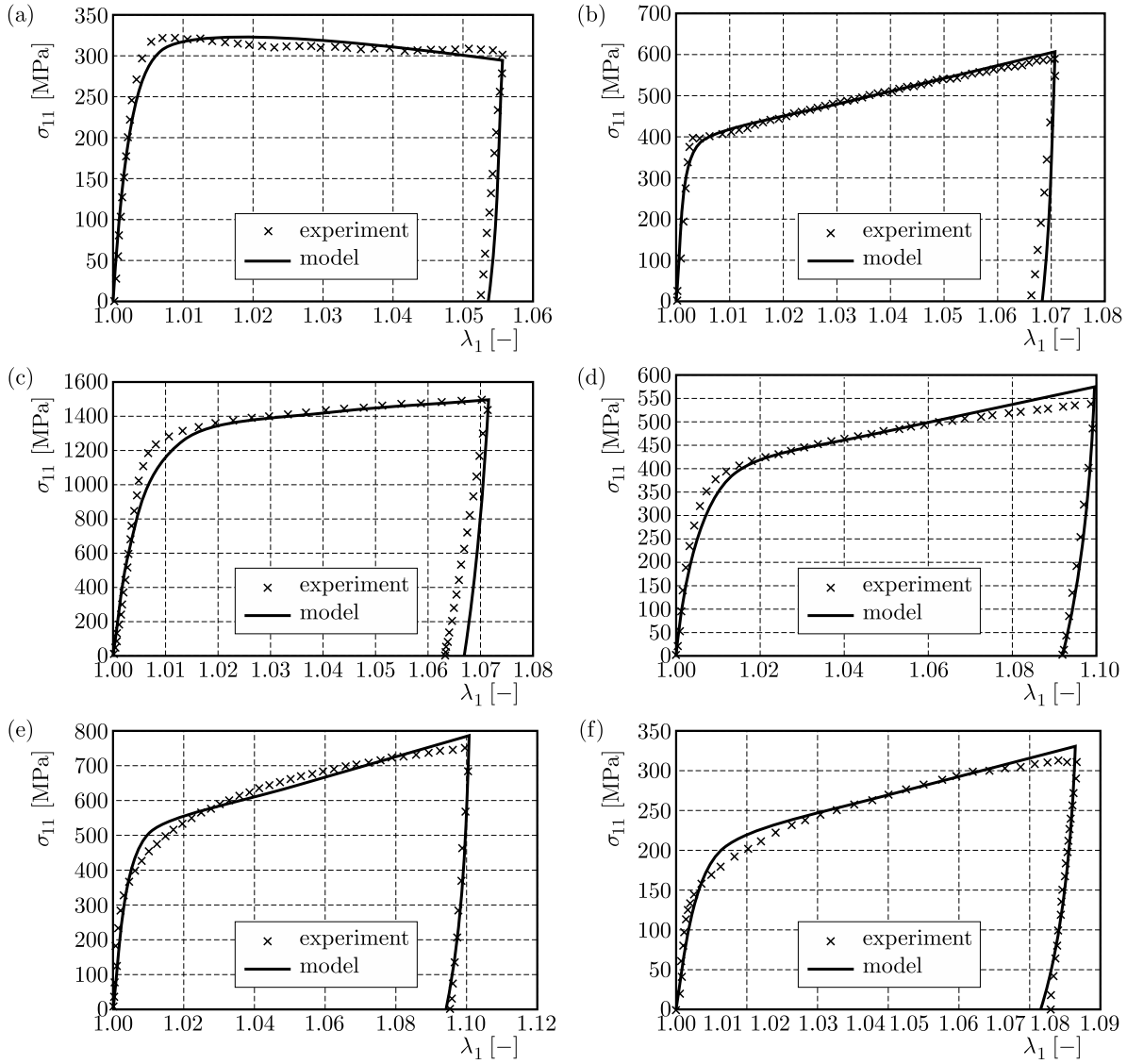

Fig. 3. Fitting of constitutive model predictions to experimental data: (a) copper, (b) Inconel No. 1, (c) Inconel No. 2, (d) brass, (e) NC steel, (f) aluminum

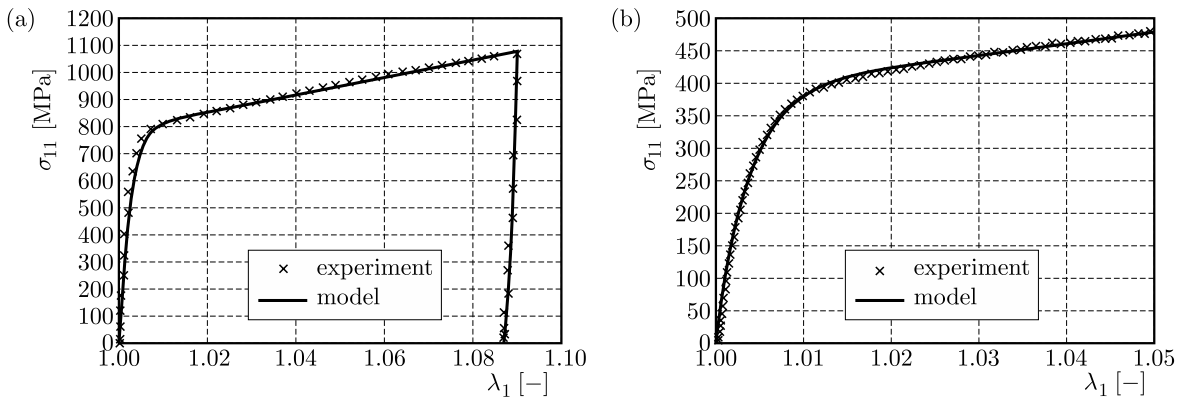

Fig. 4. Curve fitting results: (a) THA hysteresis data, (b) brass monotonic tension data

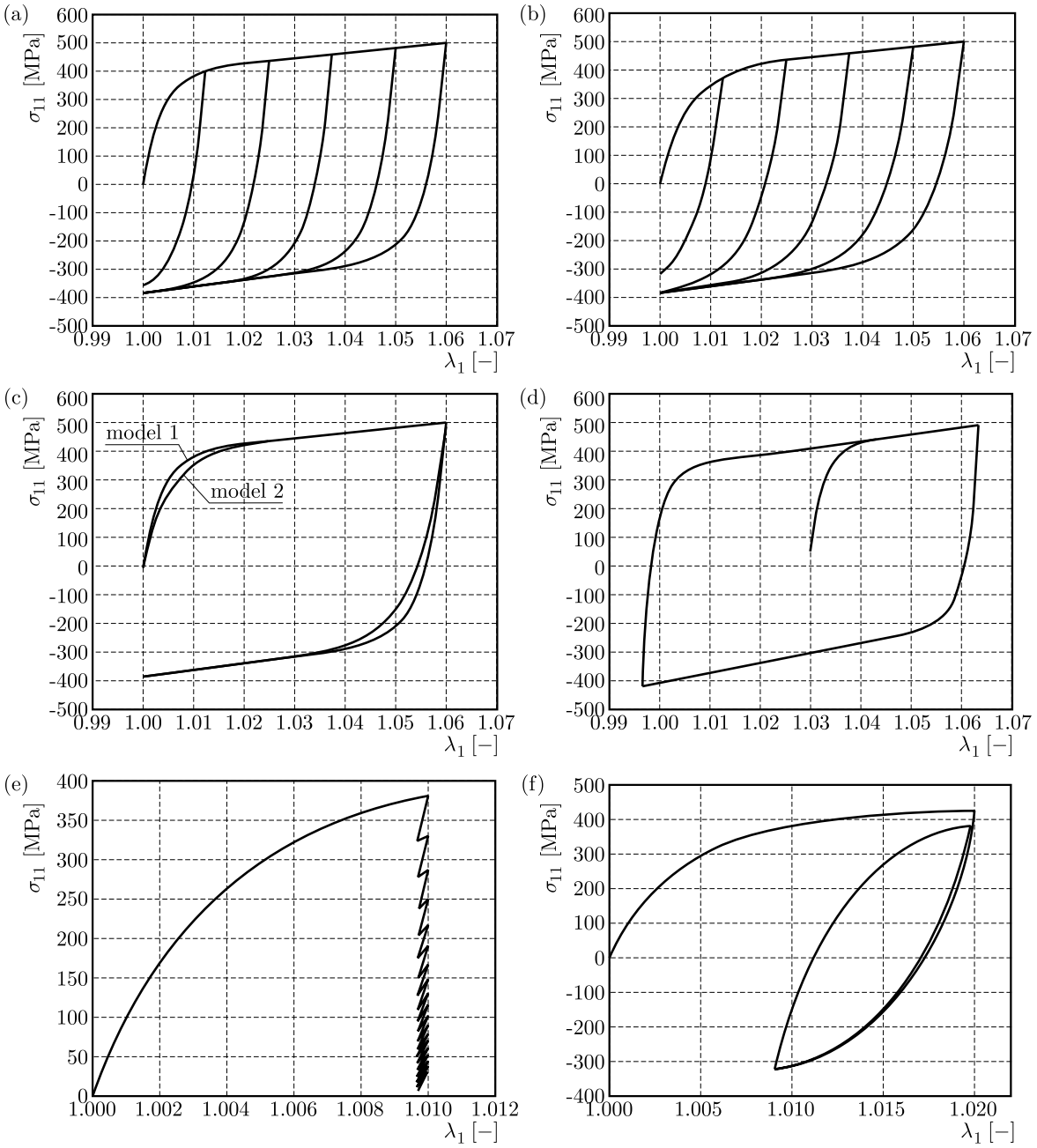

Fig. 5. Results for the brass deformation process simulation; (a) loading-unloading simulations for model 1, (b) loading-unloading simulations for model 2, (c) comparison of simulation results, (d) hysteresis loop for brass, (e) cyclic unloading-loading with small stretch amplitude, (f) cyclic unloading-loading with large stretch amplitude

The response to cyclic loading-unloading stretch histories with a prestrain has been investigated (model 1). The stretch was monotonically increased to $\lambda_1^{max} = 1.01$. Subsequently, unloading was performed to $\lambda_1^{min} = 1.0097$ which was followed by loading until $\lambda_1^{\max}$ [–] was reached again. The unloading-loading cycle was repeated for 40 times. It can be seen in Fig. 5e that the unloading slope is larger than in the case of the following reloading, so that the hysteresis loop does not form and a stress decrease is observed. This defect is known for the group of endochronic models and was discussed by Rivlin (1981). The same simulation was repeated for a larger stretch amplitude, i.e. $\lambda_1^{min} = 1.009$ and $\lambda_1^{max} = 1.02$ which resulted in formation of a stress-stretch loop (Fig. 5f). It is concluded that for cyclic loadings with a prestrain, the model's applicability is limited to the case of large stress/stretch amplitudes.

In Fig. 6 the results of two loading-unloading simulations, i.e. in tension and in compression, are plotted. The material constant values determined for brass (model 1) are utilized. It can be seen that the material responses in tension and compression are almost the same. What is more, the Bauschinger effect can be observed.

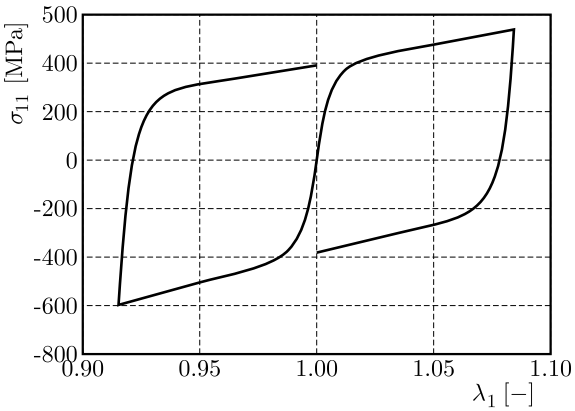

Fig. 6. Simulation of the Bauschinger effect in brass for tension and compression

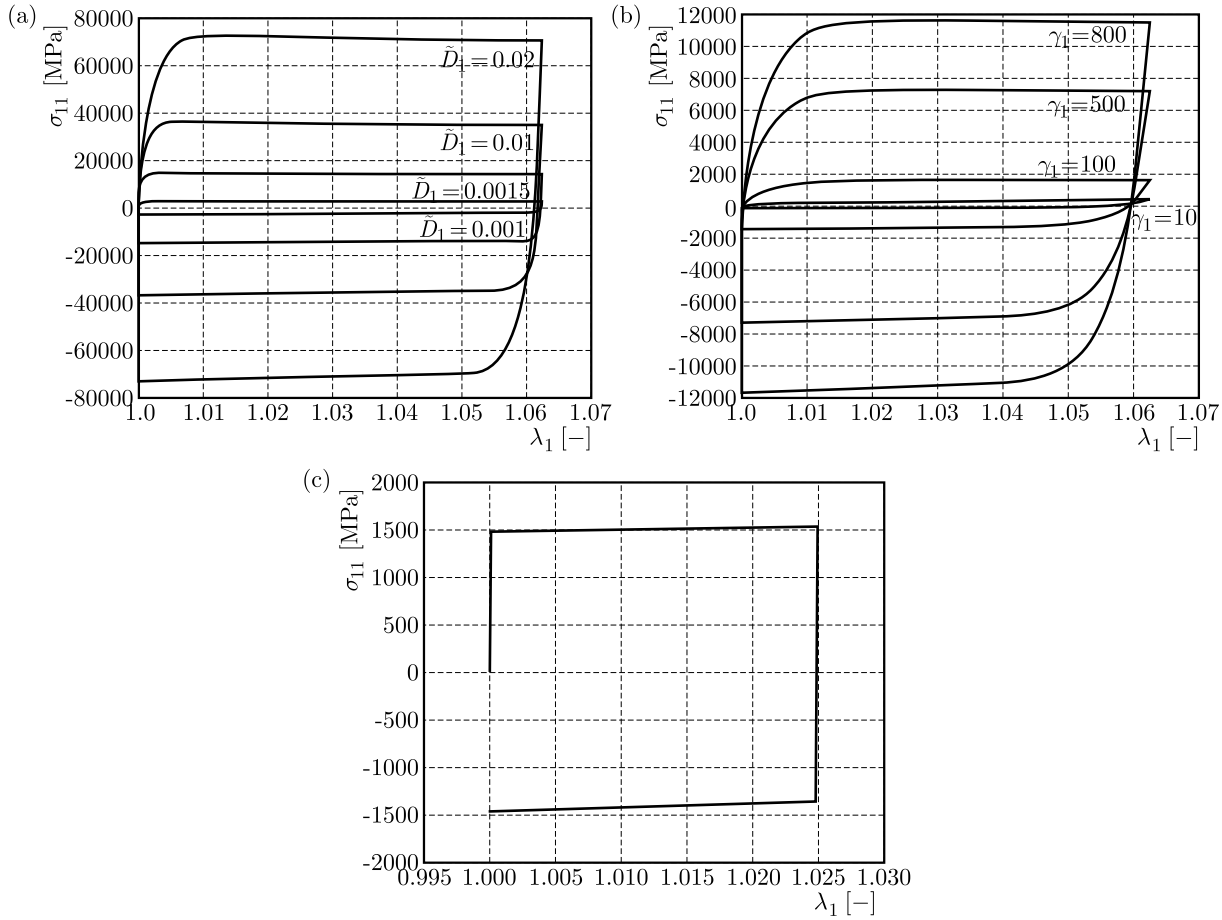

Fig. 7. Parametric study results; (a) hysteresis loops for different values of parameter $\widetilde{D}_1$, (b) hysteresis loops for different values of the coefficient γ_1, (c) the case of a rigid-perfectly plastic solid

The influence of the constant values has been investigated. In Fig. 7a, the uniaxial loading--unloading stress-stretch curves obtained for different values of the parameter $\widetilde{D}_1$ are shown. In Fig. 7b, the uniaxial loading-unloading curves generated for different values of the coefficient γ_1

are plotted. Some adjustments of the $\widetilde{D}_1$ value allow one to obtain the response of a rigid--perfectly plastic solid (Fig. 7c).

8. Conclusions

In this study, a finite strain formulation of plasticity without a yield surface has been presented and analyzed. The material parameter values are identified for a number of metallic materials. A good agreement between the theoretical predictions and the experimental data is achieved. It is found that the presented model can capture such behavior as indefinite elastic limit, strain hardening, strain softening and the Bauschinger effect. The model limitations are discussed as well. The algorithm for material constant evaluation has been presented and a parametric study conducted.

Acknowledgement
This work was supported by project INNOTECH-K2/IN2/27/182101/NCBR/13.

References

1. Backhaus G., 1976, Fließspannungen und Fließbedingung bei zyklischen Verformungen, *ZAMM*, **56**, 8, 337-348
2. Ilyushin A.A., 1963, *Plasticity, Foundations of the General Mathematical Theory* (in Russian), Academy of Sciences of the USSR, Moscow
3. Mróz Z., Rodzik P., 1996, On multisurface and integral description of anisotropic hardening evolution in metals, *European Journal of Mechanics – A/Solids*, **15**, 1, 1-28
4. Pipkin A.C., Rivlin R.S., 1965, Mechanics of rate-independent materials, *ZAMP*, **16**, 313-327
5. Rivlin R.S., 1981, Some comments on the endochronic theory of plasticity, *International Journal of Solids and Structures*, **17**, 231-248
6. Suchocki C., 2015, An internal-state-variable based viscoelastic-plastic model for polymers, *Journal of Theoretical and Applied Mechanics*, **53**, 593-604
7. Valanis K.C., 1971a, A theory of viscoplasticity without a yield surface, Part I: General theory, *Archives of Mechanics*, **23**, 517-534
8. Valanis K.C., 1971b, A theory of viscoplasticity without a yield surface, Part II: Application to mechanical behavior of metals, *Archives of Mechanics*, **23**, 535-551
9. Valanis K.C., 1980, Fundamental consequences of a new intrinsic time measure, plasticity as a limit of the endochronic theory, *Archives of Mechanics*, **32**, 171-191
10. Zalewski R., 2009, Numerical method of Chaboche's model parameters identification basing on special granular structures experimental data, *Modelling in Engineering*, **38**, 2, 309-319, (in Polish)

Manuscript received July 22, 2015; accepted for print October 28, 2015

JOURNAL OF THEORETICAL AND APPLIED MECHANICS
54, 3, pp. 743-755, Warsaw 2016
DOI: 10.15632/jtam-pl.54.3.743

GREEN'S FUNCTION FOR A MULTIFIELD MATERIAL WITH A HEAT SOURCE

Bogdan Rogowski

Lodz University of Technology, Department of Mechanics of Materials, Łódź, Poland
e-mail: bogdan.rogowski@p.lodz.pl

Green's functions for a multifield material subjected to a point heat source are presented in an explicit analytical form. The study concerns the steady-state thermal loading infinite region, half-space region and two-constituent magneto-electro-thermo-elastic material region. The new mono-harmonic potential functions, obtained by the author, are used in the analysis. The elastic displacement, electric potential, magnetic potential and induced by those coupled multifield physical quantities, caused by internal or external heat sources, are limited and presented in a very useful form, exactly and explicitly.

Keywords: Green's functions, point heat source, multifield material, magneto-electro-thermo-elastic fundamental solution, multifield composites, exact solution

1. Introduction

The basic solutions, related among others to multifield materials, are Green's functions, which were first proposed by George Green in 1828. There are two different analysis processes for solutions in scientific literature. One has focused on the displacement, electric potential and magnetic potential, constructing equilibrium equations. The second has emphasized equilibrium equations of stresses, electric displacements and magnetic inductions as well as compatibility equations for strains. There is Stroh's formalism (Stroh, 1958) and Lekhnitskii's approach (Lekhnitskii, 1963), for example. On the other hand, there are three commonly used methods in analyzing boundary effects: the theoretical solution, numerical solution and the experiment. But, appropriate Green's functions for a thermoelastic half-space is a specific task. This is due to the fact that the fundamental solution for the displacements is not limited at infinity, which is inconsistent with the mechanical sense. For example, Hou *et al.* (2008) derived a solution with a logarithmic singularity in the generalized displacement fields. Thus, the consideration of static equilibrium of the thermoelastic half-space, a quarter of the space, an octant, a wedge, and a half-wedge under the action of a unit point (as well as distributed) of the internal heat source and boundary temperature or heat flux is a special and important task. The importance is dictated by the fact that the computational scheme of many structural elements is reduced to those volume material regions.

In the context of multifield materials, the solutions depend on a large number of material parameters. For magneto-electro-thermo-elastic materials, it is twenty one, making any solution other than explicit analytical one impractical. The exact formulae, in terms of elementary functions for multifield materials, are presented in this study. The generalized displacements have been obtained with an accuracy up to arbitrary constants, which do not affect the value of stresses. This is the major motivation of the study presented in this paper. Although it sounds theoretically more reasonable, experiment based verification is still desired. It is mentioned here that mono-harmonic potential functions can be found in Chen *et al.* (2004), but some simpler results, obtained by the author of this paper, are presented for the reader's convenience.

The exact solutions related to crack and contact problems of multifield materials were recently presented by Rogowski (2012-2015) for instance.

2. The thermoelastic fundamental solution for magneto-electro-thermo-elastic multifield materials

2.1. The fundamental equations for a magneto-electro-thermo-elastic medium

We consider an axisymmetric problem. Assume that the field variables are functions of r and z in the cylindrical coordinate system (r, θ, z). Constitutive equations for a piezoelectric, piezomagnetic, electromagnetic and thermoelastic material polarized in the positive z-direction subjected to mechanical, thermal, magnetical and electrical fields can be written, in matrix representation, as

$$\begin{Bmatrix}\sigma_r\\ \sigma_\theta\\ \sigma_z\\ \sigma_{rz}\end{Bmatrix} = \begin{bmatrix}c_{11} & c_{12} & c_{13} & 0\\ c_{12} & c_{11} & c_{13} & 0\\ c_{13} & c_{13} & c_{33} & 0\\ 0 & 0 & 0 & c_{44}\end{bmatrix}\begin{Bmatrix}u_{r,r}-\alpha_r T\\ u_r/r-\alpha_r T\\ u_{z,z}-\alpha_z T\\ u_{r,z}+u_{z,r}\end{Bmatrix} + \begin{bmatrix}0 & e_{31}\\ 0 & e_{31}\\ 0 & e_{33}\\ e_{15} & 0\end{bmatrix}\begin{Bmatrix}\phi_{,r}\\ \phi_{,z}\end{Bmatrix} + \begin{bmatrix}0 & q_{31}\\ 0 & q_{31}\\ 0 & q_{33}\\ q_{15} & 0\end{bmatrix}\begin{Bmatrix}\psi_{,r}\\ \psi_{,z}\end{Bmatrix}$$

$$\begin{Bmatrix}D_r\\ D_z\end{Bmatrix} = \begin{bmatrix}0 & 0 & 0 & e_{15}\\ e_{31} & e_{31} & e_{33} & 0\end{bmatrix}\begin{Bmatrix}u_{r,r}+\alpha_r T\\ u_r/r+\alpha_r T\\ u_{z,z}+\alpha_z T\\ u_{r,z}+u_{z,r}\end{Bmatrix} - \begin{bmatrix}\varepsilon_{11} & 0\\ 0 & \varepsilon_{33}\end{bmatrix}\begin{Bmatrix}\phi_{,r}\\ \phi_{,z}\end{Bmatrix} - \begin{bmatrix}d_{11} & 0\\ 0 & d_{33}\end{bmatrix}\begin{Bmatrix}\psi_{,r}\\ \psi_{,z}\end{Bmatrix} \tag{2.1}$$

$$\begin{Bmatrix}B_r\\ B_z\end{Bmatrix} = \begin{bmatrix}0 & 0 & 0 & q_{15}\\ q_{31} & q_{31} & q_{33} & 0\end{bmatrix}\begin{Bmatrix}u_{r,r}+\alpha_r T\\ u_r/r+\alpha_r T\\ u_{z,z}+\alpha_z T\\ u_{r,z}+u_{z,r}\end{Bmatrix} - \begin{bmatrix}d_{11} & 0\\ 0 & d_{33}\end{bmatrix}\begin{Bmatrix}\phi_{,r}\\ \phi_{,z}\end{Bmatrix} - \begin{bmatrix}\mu_{11} & 0\\ 0 & \mu_{33}\end{bmatrix}\begin{Bmatrix}\psi_{,r}\\ \psi_{,z}\end{Bmatrix}$$

where σ_{ij}, D_i, B_i are mechanical stresses, electric displacements and magnetic inductions, respectively; T is a temperature change; c_{11}, c_{12}, c_{13}, c_{33}, c_{44} denote elastic stiffness; ε_{11}, ε_{33}, and μ_{11}, μ_{33} denote dielectric permittivities and magnetic permeabilities, respectively; e_{kl}, q_{kl} and d_{ll} are piezoelectric, piezomagnetic and magnetoelectric coefficients, respectively, and u_r, u_z are mechanical displacements, while ϕ and ψ are electric and magnetic potentials, respectively; α_r and α_z are thermal expansion coefficients. The subscripts following a comma denote partial differentation with respect to the indicated variables. We mention that various uncoupled cases can be reduced by setting the appropriate coupling coefficients to zero.

The equilibrium equations and the Maxwell equations, in the absence of body forces, electric and magnetic charge densities are given by

$$\begin{aligned}&\frac{\partial\sigma_r}{\partial r}+\frac{\partial\sigma_{rz}}{\partial z}+\frac{\sigma_r-\sigma_\theta}{r}=0 \qquad && \frac{\partial\sigma_{rz}}{\partial r}+\frac{\partial\sigma_z}{\partial z}+\frac{\sigma_{rz}}{r}=0\\ &\frac{\partial D_r}{\partial r}+\frac{\partial D_z}{\partial z}+\frac{D_r}{r}=0 && \frac{\partial B_r}{\partial r}+\frac{\partial B_z}{\partial z}+\frac{B_r}{r}=0\end{aligned} \tag{2.2}$$

The temperature field in the medium without heat generation in a steady-state is governed by the following equation

$$\lambda_r\Big(\frac{\partial^2 T}{\partial r^2}+\frac{1}{r}\frac{\partial T}{\partial r}\Big)+\lambda_z\frac{\partial^2 T}{\partial z^2}=0 \tag{2.3}$$

where λ_r, λ_z are coefficients of thermal conductivity. Substituting constitutive equations (2.1) into equilibrium equations (2.2) yields the basic governing equilibrium equations for the displa-

cements u_r and u_z, electric potential ϕ and magnetic potential ψ as follows

$$\begin{aligned}
&c_{11}B_1u_r + c_{44}D^2u_r + (c_{13}+c_{44})D\frac{\partial u_z}{\partial r} + (e_{15}+e_{31})D\frac{\partial \phi}{\partial r} + (q_{15}+q_{31})D\frac{\partial \psi}{\partial r} - \beta_1\frac{\partial T}{\partial r} = 0\\
&c_{44}B_0u_z + c_{33}D^2u_z + (c_{13}+c_{44})D\frac{\partial[ru_r]}{r\partial r} + (e_{15}B_0 + e_{33}D^2)\phi\\
&\quad + (q_{15}B_0 + q_{33}D^2)\psi - \beta_3 DT = 0\\
&(e_{15}+e_{31})D\frac{\partial[ru_r]}{r\partial r} + (e_{15}B_0 + e_{33}D^2)u_z - (\varepsilon_{11}B_0 + e_{33}D^2)\phi\\
&\quad - (d_{11}B_0 + d_{33}D^2)\psi + p_3 DT = 0\\
&(q_{15}+q_{31})D\frac{\partial[ru_r]}{r\partial r} + (q_{15}B_0 + q_{33}D^2)u_z - (d_{11}B_0 + d_{33}D^2)\phi\\
&\quad - (\mu_{11}B_0 + \mu_{33}D^2)\psi + \gamma_3 DT = 0
\end{aligned} \tag{2.4}$$

where the following differential operators have been introduced

$$B_k = \frac{\partial^2}{\partial r^2} + \frac{1}{r}\frac{\partial}{\partial r} - \frac{k}{r^2} \qquad k = 0, 1 \qquad D = \frac{\partial}{\partial z} \qquad D^2 = \frac{\partial^2}{\partial z^2} \tag{2.5}$$

In addition, β_i are the thermal moduli and p_3, γ_3 are pyroelectric and pyromagnetic constants, respectively, defined by

$$\begin{aligned}
&\beta_1 = (c_{11}+c_{12})\alpha_r + c_{13}\alpha_z \qquad &&\beta_3 = 2c_{13}\alpha_r + c_{33}\alpha_z\\
&p_3 = 2e_{31}\alpha_r + e_{33}\alpha_z \qquad &&\gamma_3 = 2q_{31}\alpha_r + q_{33}\alpha_z
\end{aligned} \tag{2.6}$$

Equations (2.1) to (2.3) contain 13 equations and 13 unknowns. The 13 unknowns are: two elastic displacements, fourth stresses, two electric displacements and two magnetic inductions, one electric and one magnetic potential and temperature change of the body. Therefore, the 13 unknowns can be determined by solving the 13 equations (2.1) to (2.3).

The governing equations are generalized equilibrium equations (2.4) and heat conduction equation (2.3), which induces five unknowns. These are: two displacements, one electric and one magnetic potential and temperature change of the body.

The transversely isotropic multifield material is characterized by 17 material constants. If the effect of temperature change is taken into account then also four thermal constants appear in the analysis.

Based on the method named the Schmidt method (Morse and Feshbach, 1953) the general solution to the governing equations are obtained by the generalized Almansi theorem.

Then equations (2.4) can be further simplified to

$$\begin{aligned}
&u_r(r,z) = \sum_{i=0}^{4}\alpha_{1i}\lambda_i\frac{\partial\varphi_i}{\partial r} \qquad &&u_z(r,z) = \sum_{i=0}^{4}\frac{1}{\lambda_i}\frac{\partial\varphi_i}{\partial z}\\
&\phi(r,z) = -\sum_{i=0}^{4}\frac{\alpha_{3i}}{\lambda_i}\frac{\partial\varphi_i}{\partial z} \qquad &&\psi(r,z) = -\sum_{i=0}^{4}\frac{\alpha_{4i}}{\lambda_i}\frac{\partial\varphi_i}{\partial z}\\
&T(r,z) = \frac{\alpha_{00}}{\lambda_0^2}\frac{\partial^2\varphi_0}{\partial z^2}
\end{aligned} \tag{2.7}$$

where

$$\begin{aligned}
&a_{1i} = \frac{a_1\lambda_i^6 + b_1\lambda_i^4 + c_1\lambda_i^2 + d_1}{a_2\lambda_i^6 + b_2\lambda_i^4 + c_2\lambda_i^2 + d_2}\frac{1}{\lambda_i^2} \qquad &&a_{3i} = \frac{a_3\lambda_i^6 + b_3\lambda_i^4 + c_3\lambda_i^2 + d_3}{a_2\lambda_i^6 + b_2\lambda_i^4 + c_2\lambda_i^2 + d_2}\\
&a_{4i} = \frac{a_4\lambda_i^6 + b_4\lambda_i^4 + c_4\lambda_i^2 + d_4}{a_2\lambda_i^6 + b_2\lambda_i^4 + c_2\lambda_i^2 + d_2} \qquad &&a_{00} = \frac{a\lambda_0^8 + b\lambda_0^6 + c\lambda_0^4 + d\lambda_0^2 + e}{a_2\lambda_0^6 + b_2\lambda_0^4 + c_2\lambda_0^2 + d_2}
\end{aligned} \tag{2.8}$$

where $\lambda_0^2 = \lambda_r/\lambda_z$ and λ_i^2 are the roots of the following characteristic algebraic equation

$$a\lambda^8 + b\lambda^6 + c\lambda^4 + d\lambda^2 + e = 0 \tag{2.9}$$

whose parameters a, b, c, d and e and roots (eigenvalues) λ_i^2 $(i = 1, 2, 3, 4)$ are given in Appendix A.

The mono-harmonic functions satisfy the equations

$$\Big(\Delta + \frac{1}{\lambda_i^2}\frac{\partial^2}{\partial z^2}\Big)\varphi_i(r, z) = 0 \qquad i = 0, 1, 2, 3, 4 \tag{2.10}$$

The parameters a_1, b_1, c_1, d_1, b_2, c_2, d_2 and coefficients a_{3i} and a_{4i}, which are defined by the coefficient a_{1i}, are listed in Appendix A for the reader's convenience.

The stresses are

$$\begin{aligned}
\sigma_r &= -\sum_{i=0}^{4}\frac{\alpha_{5i}}{\lambda_i}\frac{\partial^2\varphi_i}{\partial z^2} - (c_{11} - c_{12})\frac{u_r}{r} - \beta_1 T \\
\sigma_\theta &= -\sum_{i=0}^{4}\frac{\alpha_{5i}}{\lambda_i}\frac{\partial^2\varphi_i}{\partial z^2} - (c_{11} - c_{12})\frac{\partial u_r}{\partial r} - \beta_1 T \\
\sigma_z &= \sum_{i=0}^{4}\frac{\alpha_{5i}}{\lambda_i^3}\frac{\partial^2\varphi_i}{\partial z^2} + \lambda_0^{-2}\beta_1 T \qquad \sigma_{zr} = \sum_{i=0}^{4}\frac{\alpha_{5i}}{\lambda_i}\frac{\partial^2\varphi_i}{\partial r\partial z} + \lambda_0^{-2}\beta_1 a_{00}\frac{\partial^2\varphi_0}{\partial r\partial z}
\end{aligned} \tag{2.11}$$

where

$$a_{5i} = c_{11}a_{1i} - c_{13} + e_{31}a_{3i} + q_{31}a_{4i} \tag{2.12}$$

The components of the electric field vector E_r and E_z are

$$E_r = -\frac{\partial\phi}{\partial r} = \sum_{i=0}^{4}\frac{\alpha_{3i}}{\lambda_i}\frac{\partial^2\varphi_i}{\partial r\partial z} \qquad E_z = -\frac{\partial\phi}{\partial z} = \sum_{i=0}^{4}\frac{\alpha_{3i}}{\lambda_i}\frac{\partial^2\varphi_i}{\partial z^2} \tag{2.13}$$

The electric displacements are

$$\begin{aligned}
D_r &= e_{15}\Big(\frac{\partial u_r}{\partial z} + \frac{\partial u_z}{\partial r}\Big) + \varepsilon_{11}E_r + d_{11}H_r = \sum_{i=0}^{4}a_{6i}\lambda_i\frac{\partial^2\varphi_i}{\partial r\partial z} \\
D_z &= e_{31}\Big(\frac{\partial u_r}{\partial r} + \frac{u_r}{r}\Big) + e_{33}\frac{\partial u_z}{\partial z} + \varepsilon_{33}E_z + d_{33}H_z + \beta_3 T = \sum_{i=0}^{4}\frac{a_{6i}}{\lambda_i}\frac{\partial^2\varphi_i}{\partial z^2}
\end{aligned} \tag{2.14}$$

where

$$a_{6i} = e_{15}a_{1i} + \frac{e_{15} + \varepsilon_{11}a_{3i} + d_{11}a_{4i}}{\lambda_i^2} \tag{2.15}$$

The components of the magnetic field vector H_r and H_z are

$$H_r = -\frac{\partial\psi}{\partial r} = \sum_{i=0}^{4}\frac{\alpha_{4i}}{\lambda_i}\frac{\partial^2\varphi_i}{\partial r\partial z} \qquad H_z = -\frac{\partial\psi}{\partial z} = \sum_{i=0}^{4}\frac{\alpha_{4i}}{\lambda_i}\frac{\partial^2\varphi_i}{\partial z^2} \tag{2.16}$$

The magnetic inductions are

$$\begin{aligned}
B_r &= q_{15}\Big(\frac{\partial u_r}{\partial z} + \frac{\partial u_z}{\partial r}\Big) + \mu_{11}H_r + d_{11}E_r = \sum_{i=0}^{4}a_{7i}\lambda_i\frac{\partial^2\varphi_i}{\partial r\partial z} \\
B_z &= q_{31}\Big(\frac{\partial u_r}{\partial r} + \frac{u_r}{r}\Big) + q_{33}\frac{\partial u_z}{\partial z} + \mu_{33}H_z + d_{33}E_z + \gamma_3 T = \sum_{i=0}^{4}\frac{a_{7i}}{\lambda_i}\frac{\partial^2\varphi_i}{\partial z^2}
\end{aligned} \tag{2.17}$$

where

$$a_{7i} = q_{15}a_{1i} + \frac{q_{15} + \mu_{11}a_{4i} + d_{11}a_{3i}}{\lambda_i^2} \tag{2.18}$$

3. Thermal problems for multifield materials

Consider the problem of a point heat source placed within the multifield material. Introduce the following mono-harmonic functions, which are even functions with respect to the z-coordinate

$$\begin{aligned}&\varphi_i(r,z_i)=A_i\Big[z_i\,\mathrm{arcsin\,}h\Big(\frac{z_i}{r}\Big)-R_i\Big] \qquad z_i=\lambda_i z \qquad R_i=\sqrt{r^2+z_i^2}\\ &i=0,1,2,3,4\end{aligned} \tag{3.1}$$

where A_i are constants to be determined.

The derivatives φ_i are as follows

$$\begin{aligned}&\frac{\partial\varphi_i}{\partial r}=-\frac{R_i}{r} \qquad \frac{\partial\varphi_i}{\partial z_i}=\mathrm{arcsin\,}h\Big(\frac{z_i}{r}\Big) \qquad \frac{\partial^2\varphi_i}{\partial r\partial z_i}=-\frac{z_i}{rR_i}\\ &\frac{\partial^2\varphi_i}{\partial z_i^2}=\frac{1}{R_i} \qquad \frac{\partial^2\varphi_i}{\partial r^2}=\frac{z_i^2}{r^2R_i} \qquad \frac{\partial^2\varphi_i}{\partial r^2}+\frac{1}{r}\frac{\partial\varphi_i}{\partial r}+\frac{\partial^2\varphi_i}{\partial z_i^2}=0\end{aligned} \tag{3.2}$$

The physical multifields are as follows

$$\begin{aligned}&u_r=-\sum A_ia_{1i}\lambda_i\frac{R_i}{r} \qquad (u_z,\phi,\psi)=\sum A_i(1,-a_{3i},-a_{4i})\,\mathrm{arcsin\,}h\Big(\frac{z_i}{r}\Big)\\ &T=A_0a_{00}\frac{1}{R_0} \qquad \frac{\partial T}{\partial z}=-A_0a_{00}\frac{\lambda_0^2z}{R_0^3} \qquad \frac{\partial T}{\partial r}=-A_0a_{00}\frac{r}{R_0^3}\\ &\sigma_r=-\sum A_ia_{5i}\lambda_i\frac{1}{R_i}+(c_{11}-c_{12})\sum A_ia_{1i}\lambda_i\frac{R_i}{r^2}-\beta_1T\\ &\sigma_\theta=-\sum A_ia_{5i}\lambda_i\frac{1}{R_i}-(c_{11}-c_{12})\sum A_ia_{1i}\lambda_i\Big(\frac{R_i}{r^2}-\frac{1}{R_i}\Big)-\beta_1T\\ &\sigma_z=\sum A_i\frac{a_{5i}}{\lambda_i}\frac{1}{R_i}+\frac{\beta_1}{\lambda_0^2}T \qquad \sigma_{zr}=-\sum A_ia_{5i}\frac{z_i}{rR_i}-\frac{\beta_1}{\lambda_0}\frac{z}{r}T\\ &E_r=-\sum A_ia_{3i}\frac{z_i}{rR_i} \qquad E_z=\sum A_ia_{3i}\lambda_i\frac{1}{R_i}\\ &H_r=-\sum A_ia_{4i}\frac{z_i}{rR_i} \qquad H_z=\sum A_ia_{4i}\lambda_i\frac{1}{R_i}\\ &D_r=\sum A_ia_{6i}\lambda_i^2\frac{z_i}{rR_i} \qquad D_z=\sum A_ia_{6i}\lambda_i\frac{1}{R_i}\\ &B_r=\sum A_ia_{7i}\lambda_i^2\frac{z_i}{rR_i} \qquad B_z=\sum A_ia_{7i}\lambda_i\frac{1}{R_i}\end{aligned} \tag{3.3}$$

where the following abbreviation notation is used $\sum=\sum_{i=0}^{4}$.

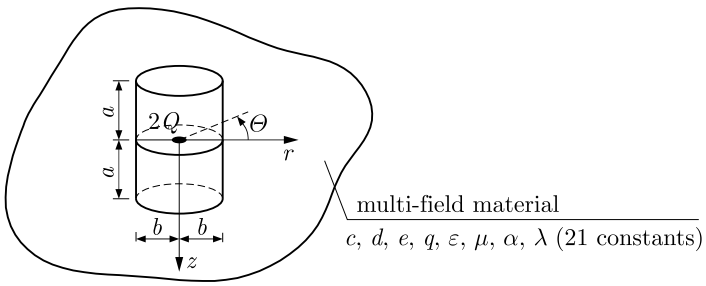

Fig. 1. A point heat source $2Q$ in an infinite multifield material

When we use the physical consideration that the total heat flux transmitted through a cylinder $0\leqslant z\leqslant a$, $r\leqslant b$ must be equal to a point heat source Q (see Fig. 1), the following equation can be written

$$-2\pi\lambda_z \int_0^b \frac{\partial T}{\partial z}(r,a) r\, dr - 2\pi\lambda_r \int_0^a \frac{\partial T}{\partial r}(b,z)\, dz = Q \tag{3.4}$$

The substitution of Eq$(3.3)_{4,5}$ and integrations yields

$$\begin{aligned}\frac{Q}{2\pi} &= \lambda_z\lambda_0^2 a a_{00} A_0 \int_0^b \frac{r}{\sqrt{(r^2+\lambda_0^2 a^2)^3}}\, dr + \lambda_r b^2 a_{00} A_0 \int_0^a \frac{1}{\sqrt{(b^2+\lambda_0^2 z^2)^3}}\, dz \\ &= \lambda_r a a_{00} A_0 \Big(-\frac{1}{\sqrt{r^2+\lambda_0^2 a^2}}\Big)\Big|_0^b - \lambda_r a_{00} A_0 \Big(1 - \frac{z}{\sqrt{b^2+\lambda_0^2 z^2}}\Big)\Big|_0^a \\ &= \lambda_r a_{00} A_0 \Big(-\frac{a}{\sqrt{b^2+\lambda_0^2 a^2}} + \frac{1}{\lambda_0} + \frac{a}{\sqrt{b^2+\lambda_0^2 a^2}}\Big) = a_{00} A_0 \sqrt{\lambda_r\lambda_z}\end{aligned} \tag{3.5}$$

that is

$$A_0 = \frac{Q}{2\pi a_{00}\sqrt{\lambda_r\lambda_z}} \tag{3.6}$$

Note that in an infinite medium with the point heat source $2Q$, the constant A_0 assumes the same value. The temperature and heat fluxes are

$$T = \frac{Q}{2\pi\sqrt{\lambda_r\lambda_z}}\frac{1}{R_0} \qquad \lambda_z\frac{\partial T}{\partial z} = -\frac{Q}{2\pi}\frac{\lambda_0 z}{R_0^3} \qquad \lambda_r\frac{\partial T}{\partial r} = -\frac{Q}{2\pi}\frac{\lambda_0 r}{R_0^3} \tag{3.7}$$

Of course

$$\lambda_r\Big(\frac{\partial^2 T}{\partial r^2} + \frac{1}{r}\frac{\partial T}{\partial r}\Big) + \lambda_z\frac{\partial^2 T}{\partial z^2} = 0 \tag{3.8}$$

3.1. The half-space problem

The boundary conditions and the corresponding equations for A_i are

$$\begin{aligned}&\text{(a)} \quad \sigma_{zr}(r,0) = 0 \qquad \text{is identically satisfied} \\ &\text{(b)} \quad \sigma_z(r,0) = 0 \qquad \sum_{i=1}^4 A_i\frac{a_{5i}}{\lambda_i} + \frac{Q}{2\pi\lambda_z a_{00}}\Big(\frac{\beta_1 a_{00}}{\lambda_0} + a_{50}\Big)\frac{1}{\lambda_0^2} = 0 \\ &\text{(c)} \quad D_z(r,0) = 0 \qquad \sum_{i=1}^4 A_i a_{6i}\lambda_i + \frac{Q}{2\pi\lambda_z a_{00}} a_{60} = 0 \\ &\text{(d)} \quad B_z(r,0) = 0 \qquad \sum_{i=1}^4 A_i a_{7i}\lambda_i + \frac{Q}{2\pi\lambda_z a_{00}} a_{70} = 0 \\ &\text{(e)} \quad u_r \ \text{ is finite at } \ r = 0 \qquad \sum_{i=1}^4 A_i a_{1i}\lambda_i^2 + \frac{Q}{2\pi\lambda_z a_{00}} a_{10}\lambda_0 = 0\end{aligned} \tag{3.9}$$

Thus, the coupled field in a semi-infinite transversely isotropic multifield material is determined by solution (3.3) and the following constants $A_i\lambda_i$

$$\begin{bmatrix} A_1\lambda_1 \\ A_2\lambda_2 \\ A_3\lambda_3 \\ A_4\lambda_4 \end{bmatrix} = -\frac{Q}{2\pi\lambda_z a_{00}} \begin{bmatrix} \frac{a_{51}}{\lambda_1^2} & \frac{a_{52}}{\lambda_2^2} & \frac{a_{53}}{\lambda_3^2} & \frac{a_{54}}{\lambda_4^2} \\ a_{61} & a_{62} & a_{63} & a_{64} \\ a_{71} & a_{72} & a_{73} & a_{74} \\ a_{11}\lambda_1 & a_{12}\lambda_2 & a_{13}\lambda_3 & a_{14}\lambda_4 \end{bmatrix}^{-1} \begin{bmatrix} \frac{1}{\lambda_0^2}\Big(\frac{\beta_1 a_{00}}{\lambda_0} + a_{50}\Big) \\ a_{60} \\ a_{70} \\ a_{10}\lambda_0 \end{bmatrix} \tag{3.10}$$

Generally, the permittivity and permeability of air or vacuum is about 680 and 475 times smaller, respectively, than that of commercial multifield materials. In reality, D_z and B_z do not transmit through the free boundary of half-space as assumed in conditions (c) and (d) of equations (3.9). It can be seen from equations (3.10) and (3.3) that Green's functions for point heat sources applied on the boundary of the half-space are expressed exactly and explicitly in terms of elementary functions. This will be greatly beneficial to the succeeding analysis of thermoelastic problems of magneto-electro-thermo-elastic materials. Note that the total heat flux transmitted through the free boundary $z = 0$ is

$$Q + 2\pi\lambda_z \int_0^\infty \frac{\partial T}{\partial z} r \, dr = Q + Q\frac{\lambda_0 z}{R_0}\Big|_0^\infty = Q - Q = 0 \tag{3.11}$$

This is a confirmation of the correctness of the obtained result. Note again that

$$\begin{aligned} &a_{5i} = c_{11}a_{1i} - c_{13} + e_{31}a_{3i} + q_{31}a_{4i} \qquad a_{6i} = e_{15}a_{1i} + \frac{e_{15} + \varepsilon_{11}a_{3i} + d_{11}a_{4i}}{\lambda_i^2} \\ &a_{7i} = q_{15}a_{1i} + \frac{q_{15} + \mu_{11}a_{4i} + d_{11}a_{3i}}{\lambda_i^2} \end{aligned} \tag{3.12}$$

and a_{1i}, a_{3i}, a_{4i} are defined by equations (3.15), see also very coupled but alternative equations (A2) and (A3) in Appendix A and equations (3.22) in special cases.

3.2. An infinite body containing a point heat source $2Q$

If

$$\sum_{i=0}^{4} A_i a_{1i}\lambda_i^2 = 0 \qquad \text{and} \qquad \sum_{i=0}^{4} A_i(1, -a_{3i}, -a_{4i}) = 0 \tag{3.13}$$

then the generalized displacements u_r, u_z, ϕ and ψ caused by the internal heat source $2Q$ are limited, but they cannot be calculated in the neighborhood of the z-axis, that is when $r \to 0$. The displacements which are obtained with an accuracy up to an arbitrary constant do not affect the value of stresses. Arbitrary constants can be treated as linear displacements of the medium as a rigid body in the axial direction without rotation.

The solution to algebraic system of equations (3.13) is

$$\begin{bmatrix} A_1 \\ A_2 \\ A_3 \\ A_4 \end{bmatrix} = -\frac{Q}{2\pi a_{00}\sqrt{\lambda_r\lambda_z}} \begin{bmatrix} 1 & 1 & 1 & 1 \\ a_{31} & a_{32} & a_{33} & a_{34} \\ a_{41} & a_{42} & a_{43} & a_{44} \\ a_{11}\lambda_1^2 & a_{12}\lambda_2^2 & a_{13}\lambda_3^2 & a_{14}\lambda_4^2 \end{bmatrix}^{-1} \begin{bmatrix} 1 \\ a_{30} \\ a_{40} \\ a_{10}\lambda_0^2 \end{bmatrix} \tag{3.14}$$

where the coefficients a_{1i}, a_{3i}, a_{4i} for $i = 0, 1, 2, 3, 4$ are as follows

$$\begin{Bmatrix} a_{1i} \\ a_{3i} \\ a_{4i} \end{Bmatrix} = \begin{bmatrix} (e_{31} + e_{15})\lambda_i^2 & \varepsilon_{11} - \varepsilon_{33}\lambda_i^2 & d_{11} - d_{33}\lambda_i^2 \\ (q_{31} + q_{15})\lambda_i^2 & d_{11} - d_{33}\lambda_i^2 & \mu_{11} - \mu_{33}\lambda_i^2 \\ c_{11} + c_{13}\lambda_i^2 & e_{31} + e_{33}\lambda_i^2 & q_{31} + q_{33}\lambda_i^2 \end{bmatrix}^{-1} \begin{Bmatrix} e_{33}\lambda_i^2 - e_{15} + p_3 a_{00}\lambda_i\delta_{i0} \\ q_{33}\lambda_i^2 - q_{15} + \gamma_3 a_{00}\lambda_i\delta_{i0} \\ c_{33}\lambda_i^2 + c_{13} - (\beta_3 + \beta_1\lambda_i^{-2})a_{00}\lambda_i\delta_{i0} \end{Bmatrix} \tag{3.15}$$

This is an alternative and simpler form of parameters defined by equations (A2) and (A3).

Note that the units of the elements of the last matrix are for typical multifield materials

$$\begin{aligned} &[e] = \mathrm{C/m^2} \qquad [p_3] = 10^{-6}\mathrm{C/(m^2K)} \qquad [a_{00}] = 10^6\mathrm{K} \qquad [p_3 a_{00}] = \mathrm{C/m^2} \\ &[q] = 10^2\mathrm{N/(Am)} \qquad [\gamma_3] = 10^{-4}\mathrm{N/(AmK)} \qquad [\gamma_3 a_{00}] = 10^2\mathrm{N/(Am)} \\ &[c] = 10^{10}\mathrm{N/m^2} \qquad [\beta_1, \beta_3] = 10^4\mathrm{N/(m^2K)} \qquad [(\beta_1, \beta_3)a_{00}] = 10^{10}\mathrm{N/m^2} \end{aligned} \tag{3.16}$$

with the multiplier $\in \langle 1, 10\rangle$.

This states that the constituents of the sums are of the same order in each row of the last matrix in (3.15).

Green's functions for the internal heat source applied in multifield materials are determined by equations (3.3), (3.14) and (3.15). All physical components of multifield materials are expressed in forms of elementary functions. It is very simple and straightforward to give numerical results. The results may help the understanding of behaviour of "smart" devices and "intelligent" structures made by multifield materials.

3.3. Single phase materials and multifield composite materials

Multifield composite materials usually comprise alternating piezoelectric and piezomagnetic materials. If the material is piezoelectric then we define the matrix

$$\mathbf{C}_E = \begin{bmatrix} (e_{31}+e_{15})\lambda_i^2 & \varepsilon_{11}-\varepsilon_{33}\lambda_i^2 & 0 \\ 0 & 0 & -\infty \\ c_{11}+c_{13}\lambda_i^2 & e_{31}+e_{33}\lambda_i^2 & 0 \end{bmatrix} \tag{3.17}$$

and its inverse matrix

$$\mathbf{C}_E^{-1} = \frac{1}{\Delta_E}\begin{bmatrix} e_{31}+e_{33}\lambda_i^2 & 0 & -(\varepsilon_{11}-\varepsilon_{33}\lambda_i^2) \\ -(c_{11}+c_{13}\lambda_i^2) & 0 & (e_{31}+e_{15})\lambda_i^2 \\ 0 & 0 & 0 \end{bmatrix} \tag{3.18}$$

$$\Delta_E = (e_{31}+e_{15})\lambda_i^2(e_{31}+e_{33}\lambda_i^2) - (c_{11}+c_{13}\lambda_i^2)(\varepsilon_{11}-\varepsilon_{33}\lambda_i^2)$$

Of course

$$\mathbf{C}_E\mathbf{C}_E^{-1} = \begin{bmatrix} 1 & 0 & 0 \\ 0 & 1 & 0 \\ 0 & 0 & 1 \end{bmatrix} \tag{3.19}$$

For piezomagnetic material, it is

$$\mathbf{C}_H = \begin{bmatrix} 0 & -\infty & 0 \\ (q_{31}+q_{15})\lambda_i^2 & 0 & \mu_{11}-\mu_{33}\lambda_i^2 \\ c_{11}+c_{13}\lambda_i^2 & 0 & q_{31}+q_{33}\lambda_i^2 \end{bmatrix} \tag{3.20}$$

Then we obtain

$$\mathbf{C}_H^{-1} = \frac{1}{\Delta_H}\begin{bmatrix} 0 & q_{31}+q_{33}\lambda_i^2 & -(\mu_{11}-\mu_{33}\lambda_i^2) \\ 0 & 0 & 0 \\ 0 & -(c_{11}+c_{13}\lambda_i^2) & (q_{31}+q_{15})\lambda_i^2 \end{bmatrix} \tag{3.21}$$

$$\Delta_H = (q_{31}+q_{15})\lambda_i^2(q_{31}+q_{33}\lambda_i^2) - (c_{11}+c_{13}\lambda_i^2)(\mu_{11}-\mu_{33}\lambda_i^2)$$

where $\mathbf{C}_H\mathbf{C}_H^{-1} = \mathbf{I}$; $\mathbf{I}$ is the square unit matrix.

Thus

$$\begin{Bmatrix} a_{1i} \\ a_{3i} \end{Bmatrix}^E = \frac{1}{\Delta_E}\begin{bmatrix} e_{31}+e_{33}\lambda_i^2 & -(\varepsilon_{11}-\varepsilon_{33}\lambda_i^2) \\ -(c_{11}+c_{13}\lambda_i^2) & (e_{31}+e_{15})\lambda_i^2 \end{bmatrix}\begin{Bmatrix} e_{33}\lambda_i^2 - e_{15} + p_3 a_{00}\lambda_i\delta_{i0} \\ c_{33}\lambda_i^2 + c_{13} - (\beta_3+\beta_1\lambda_i^{-2})a_{00}\lambda_i\delta_{i0} \end{Bmatrix}$$

$$\begin{Bmatrix} a_{1i} \\ a_{4i} \end{Bmatrix}^H = \frac{1}{\Delta_H}\begin{bmatrix} q_{31}+q_{33}\lambda_i^2 & -(\mu_{11}-\mu_{33}\lambda_i^2) \\ -(c_{11}+c_{13}\lambda_i^2) & (q_{31}+q_{15})\lambda_i^2 \end{bmatrix}\begin{Bmatrix} q_{33}\lambda_i^2 - q_{15} + \gamma_3 a_{00}\lambda_i\delta_{i0} \\ c_{33}\lambda_i^2 + c_{13} - (\beta_3+\beta_1\lambda_i^{-2})a_{00}\lambda_i\delta_{i0} \end{Bmatrix} \tag{3.22}$$

respectively for the piezoelectric and piezomagnetic thermoelastic materials.

Note that for the piezoelectric material is $a_{4i} = 0$, but a_{3i} defines a_{7i}, that is also B_z by the electromagnetic constant d_{11}. Similarly is for the piezomagnetic material where $a_{3i} = 0$, but a_{4i} defines a_{6i}, that is also D_z as a consequence of the electromagnetic effect (see equations (3.12)).

Fore the two-phase multifield material, the constant A_0 will be

$$A_0 = \frac{Q}{\pi\left(a_{00}\sqrt{\lambda_r\lambda_z} + a'_{00}\sqrt{\lambda'_r\lambda'_z}\right)} \tag{3.23}$$

where the material parameter of the second material is denoted by prime.

The inverse matrices are obtained as arithmetically average values in this case. Since the plane $z = 0$ is a plane of symmetry ($\sigma_{zr} = 0$, $H_r = 0$, $E_r = 0$, $u_z = 0$, $\phi = 0$ and $\psi = 0$ on this plane), the solutions may be used for the two-phase multifield composite material.

3.4. Solution for a purely thermoelastic material

For a transversely isotropic thermoelastic medium, the temperature field is the same as that obtained in Section 3 and described by equations (3.7). The thermoelastic solution for the purely elastic problem can be easily derived from that of the piezoelectric material (on assumption that $\varepsilon_{11} - \varepsilon_{33}\lambda_i^2 \to \infty$ and $e_{31} = e_{33} = e_{15} = 0$) or the piezomagnetic material (by assuming $\mu_{11} - \mu_{33}\lambda_i^2 \to \infty$ and $q_{31} = q_{33} = q_{15} = 0$). Both formulae (3.22) give the same result

$$a_{1i} = \frac{c_{33}\lambda_i^2 + c_{13} - (\beta_3 + \beta_1\lambda_i^{-2})a_{00}\lambda_i\delta_{i0}}{c_{11} + c_{13}\lambda_i^2} \qquad i = 0, 1, 2 \tag{3.24}$$

and equations (2.12) and (2.8) yield

$$a_{5i} = c_{11}a_{1i} - c_{13} \qquad a_{00} = \frac{c_{44}c_{33}(\lambda_0^2 - \lambda_1^2)(\lambda_0^2 - \lambda_2^2)}{\beta_1(c_{33}\lambda_0^2 - c_{44}) - \beta_3\lambda_0^2(c_{13} + c_{44})} \tag{3.25}$$

The remaining material parameters a_{3i}, a_{4i}, a_{6i} and a_{7i} vanish.

The constants A_1 and A_2 are obtained as follows

$$\begin{aligned} A_1 &= -\frac{Q\lambda_1}{2\pi\lambda_r a_{00}} \frac{\left(\frac{\beta_1 a_{00}}{\lambda_0} + a_{50}\right)a_{12}\lambda_2^3 - a_{10}a_{52}\lambda_0^3}{a_{51}a_{12}\lambda_2^3 - a_{52}a_{11}\lambda_1^3} \\ A_2 &= \frac{Q\lambda_2}{2\pi\lambda_r a_{00}} \frac{\left(\frac{\beta_1 a_{00}}{\lambda_0} + a_{50}\right)a_{11}\lambda_1^3 - a_{10}a_{51}\lambda_0^3}{a_{51}a_{12}\lambda_2^3 - a_{52}a_{11}\lambda_1^3} \end{aligned} \tag{3.26}$$

for the half-space problem and

$$A_1 = -\frac{Q}{2\pi a_{00}\sqrt{\lambda_r\lambda_z}} \frac{a_{12}\lambda_2^2 - a_{10}\lambda_0^2}{a_{12}\lambda_2^2 - a_{11}\lambda_1^2} \qquad A_2 = \frac{Q}{2\pi a_{00}\sqrt{\lambda_r\lambda_z}} \frac{a_{11}\lambda_1^2 - a_{10}\lambda_0^2}{a_{12}\lambda_2^2 - a_{11}\lambda_1^2} \tag{3.27}$$

for an infinite body.

The parameters λ_1 and λ_2 are the roots of the following equation

$$c_{33}c_{44}\lambda^4 - [c_{11}c_{33} - c_{13}(c_{13} + 2c_{44})]\lambda^2 + c_{11}c_{44} = 0 \tag{3.28}$$

These parameters are the eigenvalues of the transversely isotropic material.

By defining

$$\begin{aligned} \alpha &= \sqrt{\frac{c_{11}c_{33} - c_{13}(2c_{44} + c_{13}) + 2c_{44}\sqrt{c_{11}c_{33}}}{c_{33}c_{44}}} \\ \beta &= \sqrt{\frac{c_{11}c_{33} - c_{13}(2c_{44} + c_{13}) - 2c_{44}\sqrt{c_{11}c_{33}}}{c_{33}c_{44}}} \end{aligned} \tag{3.29}$$

the eigenvalues λ_1 and λ_2 can be written as

$$\lambda_1 = \frac{1}{2}(\alpha + \beta) \qquad \lambda_2 = \frac{1}{2}(\alpha - \beta) \tag{3.30}$$

It is noted that λ_1 and λ_2 can be either two positive real numbers or complex conjugate with a positive real part. In other words, $\alpha = \lambda_1 + \lambda_2$ and it is always real. The results are valid even for the degenerate case of $\beta = \lambda_1 - \lambda_2 = 0$, including the isotropic material where $\lambda_1 = \lambda_2 = 1$. In this case, the limiting calculations with the use of de l'Hospital's rule give the solution.

4. Conclusions

- In comparison with the traditional methods applied to the solution of boundary value problems of thermoelasticity, in the proposed method, there is no need to solve boundary value problems of heat conduction for preliminary determination of the temperature field (the first stage of solving the problem) and then to solve the equations of thermoelasticity (the second stage of solving the problem).
- Green's functions for the half-space, infinite space made by multifield materials are obtained in an exact analytical form; the solutions are regular.
- For the temperature and heat flux applied along the circumference on an arbitrary plane, the thermal loading conditions may be written by means of the Dirac delta function. Then integration and/or superposition of Green's functions gives the multi-field result.

Appendix A. The material coefficients for mulifield materials

A1. The material parameters in characteristic equation (2.9) are as follows

$$a = c_{44}[\mu_{33}e_{33}^2 + \varepsilon_{33}q_{33}^2 + c_{33}\mu_{33}\varepsilon_{33} - d_{33}(c_{33}d_{33} + 2e_{33}q_{33})]$$

$$\begin{aligned} b = {} & \mu_{33}\{(e_{31}+e_{15})[2c_{13}e_{33} - c_{33}(e_{31}+e_{15})] + 2c_{44}e_{33}e_{31} - c_{11}e_{33}^2 - c_{33}c_{44}\varepsilon_{11}\} \\ & + \varepsilon_{33}\{(q_{31}+q_{15})[2c_{13}q_{33} - c_{33}(q_{31}+q_{15})] + 2c_{44}q_{33}q_{31} - c_{11}q_{33}^2 - c_{33}c_{44}\mu_{11}\} \\ & - \mu_{33}\varepsilon_{33}\widetilde{c}^2 - (e_{31}+e_{15})^2 q_{33}^2 - (q_{31}+q_{15})^2 e_{33}^2 - c_{44}\mu_{11}e_{33}^2 - c_{44}\varepsilon_{11}q_{33}^2 \\ & + 2e_{33}q_{33}(q_{31}+q_{15})(e_{31}+e_{15}) + d_{33}^2\widetilde{c}^2 + 2c_{33}d_{33}(e_{31}+e_{15})(q_{31}+q_{15}) \\ & + 2c_{44}c_{33}d_{11}d_{33} + 2e_{33}q_{33}(c_{44}d_{11} + c_{11}d_{33}) - 2d_{33}(c_{13}+c_{44})[e_{33}(q_{31}+q_{15}) \\ & + q_{33}(e_{31}+e_{15})] \end{aligned}$$

$$\begin{aligned} c = {} & \mu_{33}\{2e_{15}[c_{11}e_{33} - c_{13}(e_{31}+e_{15})] + c_{44}e_{31}^2 + \varepsilon_{11}\widetilde{c}^2\} \\ & + \varepsilon_{33}\{2q_{15}[c_{11}q_{33} - c_{13}(q_{31}+q_{15})] + c_{44}q_{31}^2 + \mu_{11}\widetilde{c}^2\} \\ & + c_{33}c_{44}\mu_{11}\varepsilon_{11} + c_{11}c_{44}\mu_{33}\varepsilon_{33} + 2(c_{13}+c_{44})(q_{31}+q_{15})(d_{11}e_{33} + d_{33}e_{15} - q_{33}\varepsilon_{11}) \\ & + 2(c_{13}+c_{44})(e_{31}+e_{15})(d_{11}q_{33} + d_{33}q_{15} - e_{33}\mu_{11}) \\ & + (q_{31}+q_{15})^2(c_{33}\varepsilon_{11} + 2e_{33}e_{15}) + (e_{31}+e_{15})^2(c_{33}\mu_{11} + 2q_{33}q_{15}) \\ & - 2(q_{31}+q_{15})(e_{31}+e_{15})(e_{33}q_{15} + q_{33}e_{15} + c_{33}d_{11} + c_{44}d_{33}) \\ & - 2c_{11}d_{33}(e_{33}q_{15} + q_{33}e_{15}) - 2c_{44}d_{11}(q_{33}e_{15} + e_{33}q_{15}) \\ & - 2c_{11}d_{11}q_{33}e_{33} - 2c_{44}d_{33}q_{15}e_{15} + 2c_{44}q_{15}q_{33}\varepsilon_{11} \\ & + 2c_{44}e_{15}e_{33}\mu_{11} + c_{11}q_{33}^2\varepsilon_{11} + c_{11}e_{33}^2\mu_{11} - 2\widetilde{c}^2 d_{33}d_{11} - c_{11}c_{44}d_{33}^2 - c_{44}c_{33}d_{11}^2 \end{aligned}$$

$$d = -c_{11}\mu_{33}(c_{44}\varepsilon_{11} + e_{15}^2) - c_{11}\varepsilon_{33}(c_{44}\mu_{11} + q_{15}^2) - c_{44}(e_{31}^2\mu_{11} + q_{31}^2\varepsilon_{11}) - e_{31}^2q_{15}^2 - q_{31}^2e_{15}^2$$
$$- \mu_{11}\varepsilon_{11}\widetilde{c}^2 + d_{11}\widetilde{c}^2 + 2c_{11}c_{44}d_{11}d_{33} + 2c_{13}q_{15}q_{31}\varepsilon_{11} + 2c_{13}e_{15}e_{31}\mu_{11} - 2c_{11}q_{15}q_{33}\varepsilon_{11}$$
$$- 2c_{11}e_{15}e_{33}\mu_{11} + 2c_{13}q_{15}^2\varepsilon_{11} + 2c_{13}e_{15}^2\mu_{11} + 2e_{31}e_{15}q_{31}q_{15} + 2c_{11}e_{15}q_{15}d_{33}$$
$$+ d_{11}[-2c_{13}e_{15}(q_{15} + q_{31}) - 2c_{13}q_{15}(e_{15} + e_{31})] + d_{11}[2c_{11}(e_{15}q_{33} + q_{15}e_{33}) + 2c_{44}e_{31}q_{31}]$$

$$e = c_{11}[\mu_{11}e_{15}^2 + \varepsilon_{11}q_{15}^2 + c_{44}\varepsilon_{11}\mu_{11} - d_{11}(c_{44}d_{11} + 2e_{15}q_{15})]$$

$$\widetilde{c}^2 = c_{11}c_{33} - c_{13}(c_{13} + 2c_{44})$$

A2. The parameters a_1, b_1, c_1, d_1, and a_2, b_2, c_2, d_2 in Eq. (2.8) are

$$a_1 = \beta_1[c_{33}(\varepsilon_{33}\mu_{33} - d_{33}^2) + \mu_{33}e_{33}^2 + \varepsilon_{33}q_{33}^2 - 2e_{33}d_{33}q_{33}] + \beta_3[-(c_{13} + c_{44})(\varepsilon_{33}\mu_{33} - d_{33}^2)$$
$$- (e_{31} + e_{15})(\mu_{33}e_{33} - d_{33}q_{33}) - (q_{31} + q_{15})(q_{33}\varepsilon_{33} - d_{33}e_{33})]$$
$$+ \gamma_3[-(c_{13} + c_{44})(d_{33}e_{33} - q_{33}\varepsilon_{33}) + (e_{31} + e_{15})(d_{33}c_{33} + q_{33}e_{33})$$
$$- (q_{31} + q_{15})(c_{33}\varepsilon_{33} + e_{33}^2)] + p_3[-(c_{13} + c_{44})(d_{33}q_{33} - e_{33}\mu_{33})$$
$$+ (q_{31} + q_{15})(d_{33}c_{33} + q_{33}e_{33}) - (e_{31} + e_{15})(c_{33}\mu_{33} + q_{33}^2)]$$

$$b_1 = \beta_1[c_{33}(2d_{11}d_{33} - \varepsilon_{33}\mu_{11} - \mu_{33}\varepsilon_{11}) + c_{44}(d_{33}^2 - \varepsilon_{33}\mu_{33}) - \varepsilon_{11}q_{33}^2 - \mu_{11}e_{33}^2$$
$$+ 2d_{33}(e_{33}q_{15} + q_{33}e_{15}) + 2d_{11}e_{33}q_{33} - 2q_{15}q_{33}\varepsilon_{33} - 2e_{15}e_{33}\mu_{33}]$$
$$+ \beta_3[-(c_{13} + c_{44})(2d_{11}d_{33} - \varepsilon_{33}\mu_{11} - \mu_{33}\varepsilon_{11})$$
$$+ (q_{13} + q_{15})(q_{15}\varepsilon_{33} + q_{33}\varepsilon_{15} - d_{11}e_{33} - d_{33}e_{15})$$
$$+ (e_{31} + e_{15})(e_{15}\mu_{33} + e_{33}\mu_{11} - d_{11}q_{33} - d_{11}q_{15})]$$
$$+ \gamma_3[(c_{13} + c_{44})(d_{11}e_{33} + d_{33}e_{15} - q_{15}\varepsilon_{33} - q_{33}\varepsilon_{11})$$
$$- (e_{31} + e_{15})(c_{44}d_{33} + c_{33}d_{11} + q_{15}e_{33} + e_{15}q_{33}) + (q_{31} + q_{15})(c_{44}\varepsilon_{33} + c_{33}\varepsilon_{11} + 2e_{15}e_{33})]$$
$$+ p_3[(c_{13} + c_{44})(d_{11}q_{33} + d_{33}q_{15} - e_{15}\mu_{33} - e_{33}\mu_{11})$$
$$- (q_{31} + q_{15})(c_{44}d_{33} + c_{33}d_{11} + q_{15}e_{33} + e_{15}q_{33}) + (e_{31} + e_{15})(c_{44}\mu_{33} + c_{33}\mu_{11} + 2q_{15}q_{33})]$$

$$c_1 = \beta_1[c_{44}(\varepsilon_{11}\mu_{33} + \varepsilon_{33}\mu_{11} - 2d_{11}d_{33}) + c_{33}(\varepsilon_{11}\mu_{11} - d_{11}^2) + \varepsilon_{33}q_{15}^2 + \mu_{33}e_{15}^2$$
$$- 2d_{11}(e_{15}q_{33} + q_{15}e_{33}) + 2q_{15}q_{33}\varepsilon_{11} + 2\mu_{11}e_{15}e_{33}]$$
$$+ \beta_3[(c_{13} + c_{44})(d_{11}^2 - \varepsilon_{11}\mu_{11}) - (e_{31} + e_{15})(\mu_{11}e_{15} - d_{11}q_{15})$$
$$- (q_{31} + q_{15})(\varepsilon_{11}q_{15} - d_{11}e_{15})] + \gamma_3[(c_{13} + c_{44})(q_{15}\varepsilon_{11} - e_{15}d_{11})$$
$$+ (e_{31} + e_{15})(d_{11}c_{44} + q_{15}e_{15}) - (q_{31} + q_{15})(c_{44}\varepsilon_{11} + e_{15}^2)]$$
$$+ p_3[(c_{13} + c_{44})(e_{15}\mu_{11} - q_{15}d_{11})$$
$$+ (q_{31} + q_{15})(d_{11}c_{44} + q_{15}e_{15}) - (e_{31} + e_{15})(c_{44}\mu_{11} + q_{15}^2)]$$

$$d_1 = -\beta_1[c_{44}(\varepsilon_{11}\mu_{11} - d_{11}^2) + \mu_{11}e_{15}^2 + \varepsilon_{11}q_{15}^2 - 2e_{15}q_{15}d_{11}]$$

$$a_2 = c_{44}[\beta_3(\varepsilon_{33}\mu_{33} - d_{33}^2) + \gamma_3(d_{33}e_{33} + q_{33}\varepsilon_{33}) + p_3(d_{33}q_{33} - e_{33}\mu_{33})]$$

$$b_2 = \beta_1[(c_{13} + c_{44})(\varepsilon_{33}\mu_{33} - d_{33}^2) - (e_{31} + e_{15})(d_{33}q_{33} - \mu_{33}e_{33})$$
$$- (q_{31} + q_{15})(d_{33}e_{33} - \varepsilon_{33}q_{33})] - \beta_3[c_{11}(\varepsilon_{33}\mu_{33} + d_{33}^2)$$
$$+ c_{44}(\mu_{11}\varepsilon_{33} + \mu_{33}\varepsilon_{11}) - 2(q_{31} + q_{15})(e_{31} + e_{15})d_{33} + (q_{31} + q_{15})^2\varepsilon_{33} + (e_{31} + e_{15})^2\mu_{33}]$$
$$- \gamma_3[c_{11}(d_{33}e_{33} - q_{33}\varepsilon_{33}) + c_{44}(d_{11}e_{33} + d_{33}e_{15} - q_{15}\varepsilon_{33} - q_{33}\varepsilon_{11})$$
$$- (c_{13} + c_{44})d_{33}(e_{31} + e_{15}) - q_{33}(e_{31} + e_{15})^2 + \varepsilon_{33}(q_{31} + q_{15})(c_{13} + c_{44})$$
$$+ e_{33}(q_{31} + q_{15})(e_{31} + e_{15})] - p_3[c_{11}(d_{33}q_{33} - e_{33}\mu_{33})$$
$$+ c_{44}(d_{11}q_{33} + d_{33}q_{15} - e_{15}\mu_{33} - e_{33}\mu_{11}) - (c_{13} + c_{44})d_{33}(q_{31} + q_{15})$$
$$- e_{33}(q_{31} + q_{15})^2 + \mu_{33}(e_{31} + e_{15})(c_{13} + c_{44}) + q_{33}(q_{31} + q_{15})(e_{31} + e_{15})]$$

$$
\begin{aligned}
c_2 = \beta_1[&-(c_{13}+c_{44})(\varepsilon_{11}\mu_{33}+\varepsilon_{33}\mu_{11})+(e_{31}+e_{15})(d_{11}q_{33}+d_{33}q_{15})\\
&+(q_{31}+q_{15})(d_{11}e_{33}+d_{33}e_{15})-(q_{31}+q_{15})(q_{15}\varepsilon_{33}+q_{33}\varepsilon_{11})\\
&-(e_{31}+e_{15})(e_{15}\mu_{33}+e_{33}\mu_{11})+2(c_{13}+c_{44})d_{11}d_{33}]+\beta_3[c_{44}(\varepsilon_{11}\mu_{11}+d_{11}^2)\\
&+c_{11}(\mu_{11}\varepsilon_{33}+\mu_{33}\varepsilon_{11})+\mu_{11}(e_{31}+e_{15})^2+\varepsilon_{11}(q_{31}+q_{15})^2-2(e_{31}+e_{15})(q_{31}+q_{15})d_{11}]\\
&-\gamma_3[c_{44}(q_{15}\varepsilon_{11}-e_{15}d_{11})+(e_{31}+e_{15})((c_{13}+c_{44})d_{11}+(e_{31}+e_{15})q_{15})\\
&-(q_{31}+q_{15})((c_{13}+c_{44})\varepsilon_{11}+(e_{31}+e_{15})e_{15})-c_{11}(d_{11}e_{33}+e_{15}d_{33}-\varepsilon_{11}q_{33}-\varepsilon_{33}q_{15})]\\
&-p_3[c_{44}(e_{15}\mu_{11}-q_{15}d_{11})+(q_{31}+q_{15})((c_{13}+c_{44})d_{11}+(q_{31}+q_{15})e_{15})\\
&-(e_{31}+e_{15})((c_{13}+c_{44})\mu_{11}+(q_{31}+q_{15})q_{15})-c_{11}(d_{11}q_{33}+q_{15}d_{33}-\mu_{11}e_{33}-\mu_{33}e_{15})]
\end{aligned}
$$

$$
\begin{aligned}
d_2 = \beta_1[&(c_{13}+c_{44})\varepsilon_{11}\mu_{11}-(e_{31}+e_{15})d_{11}q_{15}-(q_{31}+q_{15})d_{11}e_{15}+(q_{31}+q_{15})q_{15}\varepsilon_{11}\\
&+(e_{31}+e_{15})\mu_{11}e_{15}-(c_{13}+c_{44})d_{11}^2]-\beta_3[c_{11}(\varepsilon_{11}\mu_{11}-d_{11}^2)]-\gamma_3[c_{11}(e_{15}d_{11}-q_{15}\varepsilon_{11})]\\
&-p_3[c_{11}(q_{15}d_{11}-e_{15}\mu_{11})]
\end{aligned}
$$

A3. The parameters a_{3i} and a_{4i} in Eq. (2.8) are defined by the parameter a_{1i} as follows

$$
\begin{aligned}
a_{3i} = &\Big\{\{\beta_1[(e_{31}+e_{15})(q_{33}\lambda_i^2-q_{15})-(c_{13}+c_{44})(d_{11}-d_{33}\lambda_i^2)]\\
&+\beta_3[(e_{31}+e_{15})(q_{31}+q_{15})\lambda_i+(c_{44}\lambda_i^2-c_{11})(d_{11}-d_{33}\lambda_i^2)]\\
&+p_3[\lambda_i(c_{13}+c_{44})(q_{31}+q_{15})+(c_{44}\lambda_i^2-c_{11})(q_{33}\lambda_i^2-q_{15})]\}a_{1i}\lambda_i\\
&+\beta_1[(c_{33}\lambda_i^2-c_{44})(d_{11}-d_{33}\lambda_i^2)-(q_{33}\lambda_i^2-q_{15})(e_{33}\lambda_i^2-e_{15})]\\
&+\beta_3\lambda_i[(c_{13}+c_{44})(d_{11}-d_{33}\lambda_i^2)-(q_{31}+q_{15})(e_{33}\lambda_i^2-e_{15})]\\
&+p_3\lambda_i[(c_{13}+c_{44})(q_{33}\lambda_i^2-q_{15})-(q_{31}+q_{15})(c_{33}\lambda_i^2-c_{44})]\Big\}\\
&\cdot\{p_3\lambda_i[(e_{31}+e_{15})(q_{33}\lambda_i^2-q_{15})-(q_{31}+q_{15})(e_{33}\lambda_i^2-e_{15})]\\
&+\beta_1[(e_{33}\lambda_i^2-e_{15})(d_{11}-d_{33}\lambda_i^2)-(q_{33}\lambda_i^2-q_{15})(\varepsilon_{11}-\varepsilon_{33}\lambda_i^2)]\\
&+\beta_3\lambda_i[(e_{31}+e_{15})(d_{11}-d_{33}\lambda_i^2)-(q_{31}+q_{15})(\varepsilon_{11}-\varepsilon_{33}\lambda_i^2)]\}^{-1}
\end{aligned}
$$

$$
\begin{aligned}
a_{4i} = -&\Big\{\{\beta_1[(e_{31}+e_{15})(e_{33}\lambda_i^2-e_{15})-(c_{13}+c_{44})(\varepsilon_{11}-\varepsilon_{33}\lambda_i^2)]\\
&+\beta_3[(e_{31}+e_{15})^2\lambda_i+(c_{44}\lambda_i^2-c_{11})(\varepsilon_{11}-\varepsilon_{33}\lambda_i^2)]\\
&+p_3[\lambda_i(c_{13}+c_{44})(e_{31}+e_{15})+(c_{44}\lambda_i^2-c_{11})(e_{33}\lambda_i^2-e_{15})]\}a_{1i}\lambda_i\\
&+\beta_1[(c_{33}\lambda_i^2-c_{44})(\varepsilon_{11}-\varepsilon_{33}\lambda_i^2)-(e_{33}\lambda_i^2-e_{15})^2]\\
&+\beta_3\lambda_i[(c_{13}+c_{44})(\varepsilon_{11}-\varepsilon_{33}\lambda_i^2)-(e_{31}+e_{15})(e_{33}\lambda_i^2-e_{15})]\\
&+p_3\lambda_i[(c_{13}+c_{44})(e_{33}\lambda_i^2-e_{15})-(e_{31}+e_{15})(c_{33}\lambda_i^2-c_{44})]\Big\}\\
&\cdot\{p_3\lambda_i[(e_{31}+e_{15})(q_{33}\lambda_i^2-q_{15})-(q_{31}+q_{15})(e_{33}\lambda_i^2-e_{15})]\\
&+\beta_1[(e_{33}\lambda_i^2-e_{15})(d_{11}-d_{33}\lambda_i^2)-(q_{33}\lambda_i^2-q_{15})(\varepsilon_{11}-\varepsilon_{33}\lambda_i^2)]\\
&+\beta_3\lambda_i[(e_{31}+e_{15})(d_{11}-d_{33}\lambda_i^2)-(q_{31}+q_{15})(\varepsilon_{11}-\varepsilon_{33}\lambda_i^2)]\}^{-1}
\end{aligned}
$$

A4. The roots of characteristic equation (2.9) are presented by the formulae (eigenvalues of multifield materials)

$$
\lambda_1^2 = -\frac{b}{4a}-\frac{1}{2}\sqrt{R_5+R_6}-\frac{1}{2}\sqrt{2R_5-R_6+\frac{1}{4}\frac{R_7}{\sqrt{R_5+R_6}}}
$$

$$
\lambda_2^2 = -\frac{b}{4a}-\frac{1}{2}\sqrt{R_5+R_6}+\frac{1}{2}\sqrt{2R_5-R_6+\frac{1}{4}\frac{R_7}{\sqrt{R_5+R_6}}}
$$

$$\lambda_3^2 = -\frac{b}{4a} + \frac{1}{2}\sqrt{R_5 + R_6} - \frac{1}{2}\sqrt{2R_5 - R_6 - \frac{1}{4}\frac{R_7}{\sqrt{R_5 + R_6}}}$$

$$\lambda_4^2 = -\frac{b}{4a} + \frac{1}{2}\sqrt{R_5 + R_6} + \frac{1}{2}\sqrt{2R_5 - R_6 - \frac{1}{4}\frac{R_7}{\sqrt{R_5 + R_6}}}$$

where

$$R_1 = 2c^3 - 9bcd + 27ad^2 + 27b^2e - 72ace \qquad R_2 = c^2 - 3bd + 12ae$$

$$R_3 = \sqrt{R_1^2 - 4R_2^3} \qquad R_4 = \sqrt[3]{\frac{1}{2}(R_1 + R_3)}$$

$$R_5 = \frac{b^2}{4a^2} - \frac{2c}{3a} \qquad R_6 = \frac{R_2}{3aR_4} + \frac{R_4}{3a} \qquad R_7 = \frac{b^3}{a^3} - \frac{4bc}{a^2} + \frac{8d}{a}$$

References

1. Chen W.Q., Lee K.Y., Ding H.J., 2004, General solution for transversely isotropic magneto-electro-thermo-elasticity and the potential theory method, *International Journal of Engineering Science*, **42**, 1361-1379
2. Hou P.F., Leung A.Y.T., Ding H.J., 2008, A point heat source on the surface of a semi-infinite transversely isotropic electro-magneto-thermo-elastic material, *International Journal of Engineering Science*, **46**, 273-285
3. Lekhnitskii S., 1963, *Theory of Elasticity in an Anisotropic Elastic Body*, Holden-Day Inc., San Francisco
4. Morse P.M., Feshbach H., 1953, *Methods of Theoretical Physics*, McGraw Hill, New York
5. Rogowski B., 2012, A concave indenter on a piezo-electro-magneto-elastic substrate or a layer elastically supported, *The Journal of Strain Analysis for Engineering Design*, **47**, 6, 362-378
6. Rogowski B., 2013, Anti-plane crack emanating from the interface in a bounded smart PEMO-elastic structure, *International Journal of. Applied Mechanics and Engineering*, **18**, 4, 1165-1199
7. Rogowski B., 2014, The analysis of mode I conducting crack under general applied loads in piezoelectromagnetoelastic layer, *International Journal of Engineering Science*, **75**, 11-30
8. Rogowski B., 2015, The transient analysis of conducting crack in magneto-electro-elastic half-space under anti-plane mechanical and in-plane electric and magnetic impact, *Archive of Applied Mechanics*, **85**, 29-50
9. Stroh A.H., 1958, Dislocations and cracks in anisotropic elasticity, *Philosophical Magazine*, **3**, 625-646

Manuscript received May 12, 2015; accepted for print November 8, 2015

JOURNAL OF THEORETICAL AND APPLIED MECHANICS
54, 3, pp. 757-768, Warsaw 2016
DOI: 10.15632/jtam-pl.54.3.757

THE DEVELOPMENT OF MECHATRONIC ACTIVE CONTROL SYSTEM OF TOOL SPATIAL POSITION IN PARALLEL KINEMATICS MACHINE TOOL

Vasil B. Strutinsky, Anatoliy S. Demyanenko
National Technical University of Ukraine "KPI", Faculty of Mechanical Engineering, Kyiv, Ukraine
e-mail: kvm_mmi@mail.ru; a.s.demyanenko@gmail.com

The method and the mechatronic system of active control of the dynamic spatial positioning of the executive body of a parallel kinematics machine tool are proposed. By means of geometric modeling, the basic analytical relations that characterize the interconnection between the rods of the mechatronic control system and the power rods of the parallel kinematics machine tool are calculated. The analytical dependencies that characterize errors of the spatial position of the executive body of the parallel kinematics machine tool are set out. The prototype of the mechatronic system of active control of the dynamic spatial position of the executive body of the parallel kinematics machine tool has been manufactured and its presetting and viability checking made. The special equipment to control the exact position of the tool of the parallel kinematics machine tool when it comes to the position is proposed.

Keywords: parallel kinematics machine tool, accuracy, mechatronics, calibration

1. Introduction

Parallel kinematics machine tools are progressive manufacturing equipment. The main advantages of parallel kinematic machine tools are low material and energy intensity (Weck and Staimer, 2000). But as a result, there is a decrease in stiffness of the machine tool bearing system and, therefore, low accuracy and poor dynamic characteristics of engines (Strutinsky, 2012). Briot and Bonev (2007) stated theoretically that parallel robots are more accurate than serial ones, but in practice small errors in the drive system of 6 rods can cause the significant errors in the executive body location and its movement trajectory. Therefore, one of the efforts to increase the accuracy of parallel kinematics machine tools and robots can be their structural improvement. Nowadays, there are a significant number of investigations that are dedicated to the structural improvement of parallel kinematics machine tools (Dindorf and Laski, 2010; Guan, 2012; Huang, 2010).

Though there is a lot of designs of parallel kinematics machine tools and robots, the actual problem is still to achieve their high parameters of the kinematic and, especially, dynamic accuracy (Pandilov and Dukovski, 2012). The problem of the position accuracy of planar kinematically redundant parallel robots was considered in details in (Kotlarski *et al.*, 2012). It was proposed to use the optimization of the redundant actuator position in a discrete manner. The authors used several exemplarily chosen trajectories on which they showed the improvement in terms of the accuracy of that planar kinematically redundant parallel mechanism. To some extent, those methods can be extrapolated to the spatial parallel kinematics mechanism.

On the other hand, the improved accuracy of spatial parallel kinematics machine tools is usually held by means of periodical calibration (Ibaraki *et al.*, 2004; Joubair *et al.*, 2014; Wu *et al.*, 2014). The perspective concept of calibrating the parallel kinematics machine using an exteroceptive sensor-camera, which is measuring the end-effector position was discussed by Andreff and Martinet (2009). The methodology offered by the authors was based on using an inverted

camera projection model which reduced the number of kinematic parameters to identify. There is another interesting research work (Szatmári, 2007), in which the author made the accuracy test of a hexapod-type machine tool by means of the laser interferometer which was used to take bidirectional repeated measurements along X and Y axes. The results showed that the accuracy of motion of the hexapod mechanism was rather poor, but the repeatability of the measurements was very accurate. So, as the errors have a systematic character, the promising way to improve the accuracy of parallel kinematics machine tools and robots is to correct these errors through the controller, on the CNC level.

All these developments do not provide full improvement of the accuracy of parallel kinematics machine tools especially during processing of a workpiece. But they show a promising direction to increase the accuracy of parallel kinematics machine tools, which is the introduction of a closed loop measuring system providing the possibility of correcting control signals for actuators and, accordingly, improving the accuracy of such machines during processing.

The main objective of this work is to develop a method to improve the accuracy of parallel kinematics machine tools through implementation of an active control system of the dynamic spatial position of its platform on which the tool is mounted. In order to achieve this goal, analytical dependencies that determine the regularity of work of the active control system of the dynamic spatial position of the tool will be discussed. The dependencies between lengths of the rods of the proposed measuring mechanism and the parallel kinematics machine tool rods as well as analytical dependencies relating small displacements of the executive body and lengths of the rods will be set. The prototype of the proposed system is described. It is shown that an additional calibration error in the output tool position of the executive body of the parallel kinematics machine tool should be taken into account. Therefore, the construction of special equipment to track these errors periodically is offered.

2. The method and the mechatronic system for active control of dynamic spatial positioning of the tool in a parallel kinematics machine tool

The parallel kinematics machine tool is based on the mechanism of a hexapod type and has six rods of variable lengths $L_1, \ldots, L_6$, which are connected with the mobile executive body PL, where tool I which is designed to handle the contoured surface of the workpiece D is mounted (Fig. 1).

The machine tool has a base with two power belts H1 and H2. The hinged support rods of variable length are mounted on this base.

The tool moves along a complex trajectory, thus changing its transverse angular position in the process of machining of the workpiece. Changing the spatial position of the executive body is achieved by changing the length of the rods of the machine tool. The terms of the executive body in space are determined by its translational displacement of some point (pole) and transverse angular position of the executive body relative to the pole.

Assume some center point p of the tool as a pole. Therefore, the law of the tool movement will be described by the trajectory of the pole and current Euler angles that define the angular position of the tool at each point of the trajectory. The Euler-Krylov angles ψ, θ, φ which define the rotation angles of the executive body relative to axes Ox, Oy and Oz are assumed (see Fig. 1). The position of the tool will be defined as a vector which has six components. Three of them are linear coordinates (set of linear movements x, y, z) of the tool, and three rotational (angular values ψ, θ, φ). Accordingly, the position of each point U of the executive body is characterized by the relevant vector which has been defined in space of 6 dimensions.

Using the injected vector has a certain inconvenience caused by heterogeneity of its components. Therefore, it is proposed to use a modified vector, which differs by angular values brought

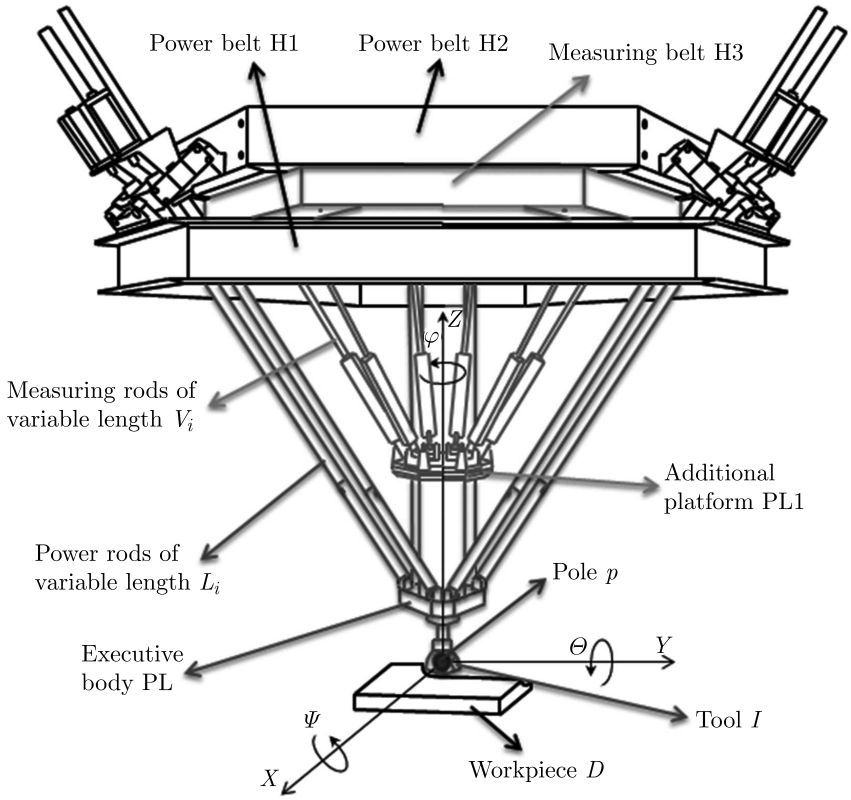

Fig. 1. The scheme of the parallel kinematics machine tool with a mechatronic system of active control of dynamic spatial positioning of the tool

in line. Taking this into count, the parameter vector that defines the position of the point U can be written as

$$\mathbf{X}_U = [x, y, z, m_\psi\psi, m_\theta\theta, m_\varphi\varphi]^{\mathrm{T}} \tag{2.1}$$

where m_ψ, m_θ, m_φ are scale factors with the coordinates dimension.

In general, the vector that defines the position of the point U, can be written as

$$\mathbf{X} = [x_i] \qquad i = 1, 2, \ldots, 6 \tag{2.2}$$

where x_i is the corresponding component of the vector.

In the process of programming of the law of motion for a parallel kinematics machine tool, the changes in the time t component of the vector $\mathbf{X}$ are set as

$$\mathbf{X}_1 = [x_i(t)] \tag{2.3}$$

As a result of solution of the inverse problem, the kinematics vector of l-coordinates is calculated.

The resulting vector of l-coordinates is presented in the form

$$\mathbf{L} = [l_j] \qquad j = 1, 2, \ldots, 6 \tag{2.4}$$

The vector components given as functions of time are

$$l_i = l_i(t) \tag{2.5}$$

Necessary laws for l-coordinates changes are implemented by the drives. As a result of changes of lengths of the rods, the executive body of the machine tool is positioned in the appropriate position, which is characterized by the vector $\mathbf{X}$.

The accuracy of the executive body setting in the required position is determined by the vector of errors

$$\boldsymbol{\delta} x_i = \mathbf{X}_0 - \mathbf{X}_U \tag{2.6}$$

where $\mathbf{X}_0$ is a vector describing the desired position that has been set in the CNC system and $\mathbf{X}_U$ is the vector describing the actual position of the executive body of the parallel kinematics machine tool.

The vector $\boldsymbol{\delta} x_i$ depends on numerous random factors. Defining of the vector of errors as a function of time is a task of the mechatronic system of active control of dynamic spatial positioning of the executive body of the parallel kinematics machine tool.

The developed method and the mechatronic system of active control of dynamic spatial positioning of the tool is based on making use of an additional parallel kinematics mechanism which has six measuring rods of variable length $V_1, \ldots, V_6$, connecting with the executive body with power belt H3 which is rigidly connected with power belts H1 and H2. The measuring rods have sensors that record changes in lengths of the rods. If one changes the x-coordinate according to relationship (2.3), the length of the rods is changing and, therefore, the vector

$$\mathbf{V} = [v_j] \qquad j = 1, 2, \ldots, 6 \tag{2.7}$$

According to these values, the executive body positioning error is defined by formula (2.6).

3. Basic analytical dependencies characterizing the consistent pattern of the active control system

The l-coordinates vector is functionally dependent on the vector of input parameters $\mathbf{X}_i$. This dependence is nonlinear and, in general, can be written as

$$\mathbf{L} = \mathbf{F}(\mathbf{X}) \tag{3.1}$$

where $\mathbf{F}(\mathbf{X})$ is a vector whose components in general can describe the dependences for the l-coordinates of the components of the vector of input parameters and time

$$\mathbf{F}(\mathbf{x}) = [l_j([x_i], t)] \qquad j = 1, 2, \ldots, 6 \tag{3.2}$$

$\mathbf{V}$ is the vector of coordinates and also depends on the vector of input parameters x_i according to the equation

$$\mathbf{V} = \mathbf{F}_1(\mathbf{X}) \tag{3.3}$$

where $\mathbf{F}_1(\mathbf{x}) = [v_j([x_i], t)]$, $j = 1, 2, \ldots, 6$.

By combining dependencies (3.2) and (3.3), we can get a relationship between the l-coordinates and v-coordinates of our machine tool in the form

$$\mathbf{V} = \boldsymbol{\Phi}(\mathbf{L}) \tag{3.4}$$

Dependency (3.4) can be applied only to a specific law of the executive body movement set in form (2.4).

To study the patterns of communication of the v-coordinates and l-coordinates, the inherent law of the executive body movement corresponding to the processing of a convex surface of an ellipsoid type is chosen (Fig. 2).

The tool moves along a curved trajectory when processing the convex surface (Fig. 3). Let us assume the shape of the selected area as a trajectory of an arc of a circle with radius

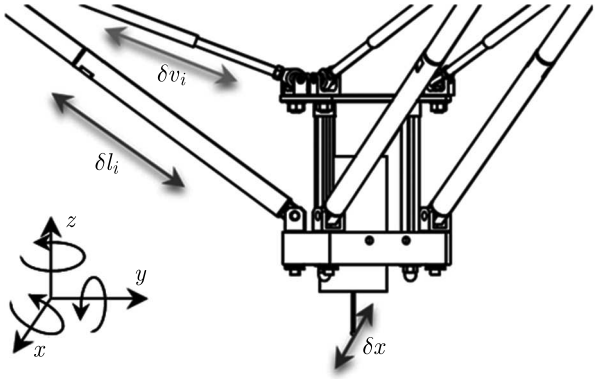

Fig. 2. Relationship between infinitesimal changes of x-coordinate, l- and v-coordinates

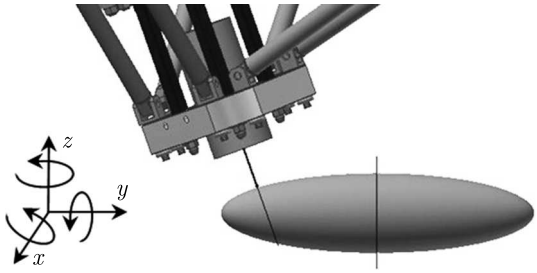

Fig. 3. The scheme of configuration changes of the parallel kinematics machine tool when processing a convex surface of an ellipsoid type

$R(x = 0, \theta = 0, \varphi = 0)$. By means of geometric modeling in Autodesk Inventor, length of each rod of the machine tool for the fixed values of the rotation angle ψ is defined

$$\boldsymbol{\psi} = \begin{bmatrix} -20 \\ -15 \\ -10 \\ -5 \\ 0 \\ 5 \\ 10 \\ 15 \\ 20 \end{bmatrix} \quad \mathbf{L}_1 = \begin{bmatrix} 1159.303 \\ 1144.890 \\ 1132.842 \\ 1123.325 \\ 1116.476 \\ 1112.392 \\ 1111.135 \\ 1112.724 \\ 1117.134 \end{bmatrix} \quad \mathbf{V}_1 = \begin{bmatrix} 790.070 \\ 746.319 \\ 707.831 \\ 675.820 \\ 649.946 \\ 635.945 \\ 629.925 \\ 633.758 \\ 647.239 \end{bmatrix} \cdots$$

$$\mathbf{L}_6 = \begin{bmatrix} 1175.619 \\ 1157.885 \\ 1141.988 \\ 1128.125 \\ 1116.476 \\ 1107.196 \\ 1100.416 \\ 1096.231 \\ 1094.703 \end{bmatrix} \quad \mathbf{V}_6 = \begin{bmatrix} 784.250 \\ 742.082 \\ 705.212 \\ 674.808 \\ 649.946 \\ 637.841 \\ 632.962 \\ 637.633 \\ 651.613 \end{bmatrix}$$

The resulting point values of the rods lengths are smoothed by cubic splines (Fig. 4).

Analyzing the graphs, we can see that the laws for the rods lengths of the machine tool and for the measuring rods are similar.

During the researches, the correlation between the power rods length of the machine tool and the measuring rods of the additional mechatronic mechanism was defined (Fig. 5). This relation-

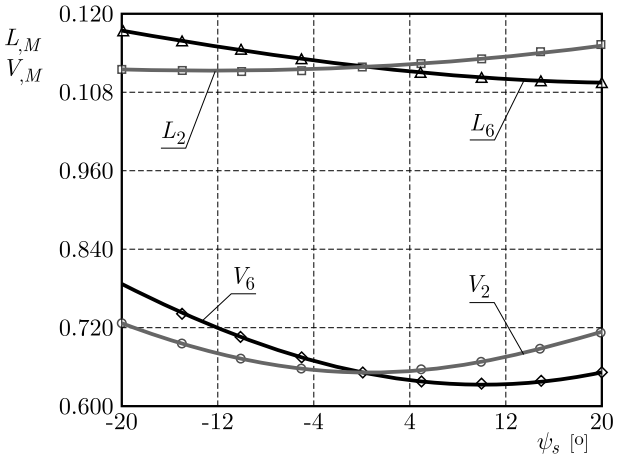

Fig. 4. The dependence between length of the rod and the angular distance while moving the tool along a convex surface such as an ellipsoid with radius of curvature $R = 200\,\text{mm}$

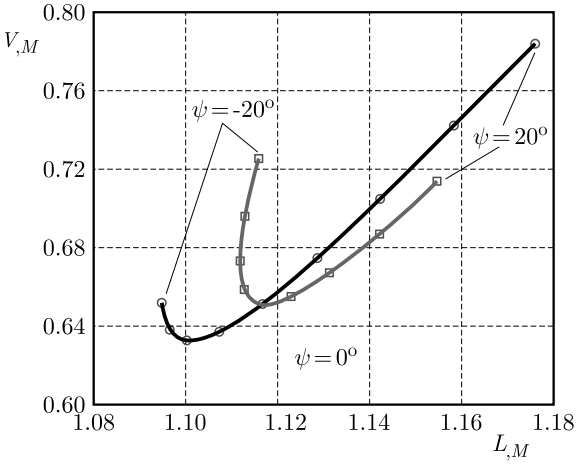

Fig. 5. The relationship between length of the rods of an additional mechanism and length ov the rods of the parallel kinematics machine tool

ship can be described by ambiguous dependencies with extremes. The presence of complex and ambiguous relationships of parameters requires a specific approach to determine the functional dependence for v-coordinates of l-coordinates. It is proposed to find these dependencies based on small increments of coordinates as shown below.

Let us define the relationship between infinitesimal changes of x-coordinates and l-coordinates. Each component of the vector $\mathbf{L}$ is a coordinate of a function type of 6 variables which are the x-coordinates. Using differentiation functions of several variables, we can find the vector of differentials of the l-coordinates

$$[dl_j] = \sum_{i=1}^{6} \frac{\partial l_j}{\partial x_i} dx_i \qquad j = 1, 2, \ldots, 6 \tag{3.5}$$

where dl_j is a differential of the j-th l-coordinate.

All values that are dependent allow direct calculation. As a result, the partial derivatives $\partial l_j / \partial x_i$ are found.

Now we can write down equation (3.5) in a matrix-vector form

$$d\mathbf{L} = \mathbf{M}\, d\mathbf{X} \tag{3.6}$$

where the matrix $\mathbf{M}$ has relevant partial derivatives of the l-coordinate of the x-coordinates

$$\mathbf{M} = \begin{bmatrix} m_{11} & \cdots & m_{16} \\ m_{21} & \cdots & m_{26} \\ \vdots & \vdots & \vdots \\ m_{61} & \cdots & m_{66} \end{bmatrix} \qquad m_{ji} = \frac{\partial l_j}{\partial x_i} \tag{3.7}$$

If during solving all the input parameters are specified as functions of time t, then the components of the matrix can be found as differentials of a complex function

$$m_{ji} = \frac{\partial l_j}{\partial t}\frac{\partial t}{\partial x_i} = \frac{\partial l_j}{\partial t} \backslash \frac{\partial x_i}{\partial t} \tag{3.8}$$

During computing, it is possible that singularities may occur due to the advent of the component matrix $m_{ji} = 0$ or $m_{ji} = \infty$. One reason for this phenomenon may be the condition

$$\frac{\partial x_i}{\partial t} = \begin{cases} 0 \\ \infty \end{cases} \qquad \vee \qquad \frac{\partial l_i}{\partial t} = \begin{cases} 0 \\ \infty \end{cases} \tag{3.9}$$

These particular cases should be analyzed in the solution process of the direct kinematics problem.

Similarly, the dependence of the v-coordinates changes in the x-coordinate is determined

$$d\mathbf{V} = \mathbf{Q}\, d\mathbf{X} \tag{3.10}$$

where the matrix $\mathbf{Q}$ has components of relevant partial derivatives of the v-coordinates for the x-coordinates

$$\mathbf{Q} = \begin{bmatrix} q_{11} & \cdots & q_{16} \\ q_{21} & \cdots & q_{26} \\ \vdots & \vdots & \vdots \\ q_{61} & \cdots & q_{66} \end{bmatrix} \qquad q_{ji} = \frac{\partial v_j}{\partial x_i} \tag{3.11}$$

During the first phase of research, we confine ourselves to the case of the absence of infinite values of the matrices $\mathbf{M}$ and $\mathbf{Q}$.

For the average position of the executive body ($\psi = 0°$), the components of matrix $\mathbf{M}$ and $\mathbf{Q}$ are calculated. For example, for the matrix $\mathbf{M}$ at this point, we have

$$\mathbf{M} = \begin{bmatrix} -3.761 & -2.096 & 24.750 & 4.889 & 2.849 & 1.941 \\ -1.584 & -0.883 & 10.424 & 2.059 & 1.200 & 0.818 \\ 1.375 & 0.766 & -9.047 & -1.787 & -1.041 & -0.710 \\ 1.877 & 1.046 & -12.355 & -2.441 & -1.422 & -0.969 \\ 1.957 & 1.090 & -12.880 & -2.544 & -1.482 & -1.010 \\ -2.369 & -1.320 & 15.591 & 3.080 & 1.795 & 1.223 \end{bmatrix} \tag{3.12}$$

Resulting matrix (3.12) is singular. Its determinant is zero and rank is one. This also applies to the matrix $\mathbf{Q}$.

Let us solve the equation that relates the differential of the x-coordinates and the l-coordinates. To do this, we define the differential of each x-coordinate as a function of 6 variables of the l-coordinates

$$[dx_i] = \sum_{j=1}^{6} \frac{\partial x_i}{\partial l_j} dl_j \tag{3.13}$$

Note that

$$\frac{\partial x_i}{\partial l_j} = \frac{\partial x_i}{\partial t} \backslash \frac{\partial l_j}{\partial t} = \frac{1}{\frac{\partial l_j}{\partial t} \backslash \frac{\partial x_i}{\partial t}} = \frac{1}{m_{ji}} = \frac{\partial l_j}{\partial t} \frac{\partial t}{\partial x_i} = \frac{\partial l_j}{\partial t} \backslash \frac{\partial x_i}{\partial t} \tag{3.14}$$

Hence, the ratios are defined by means of components of the matrix **M**, and it is an inverse to them. Herewith

$$d\mathbf{X} = \mathbf{N}\, d\mathbf{L} \tag{3.15}$$

where **N** is a transpose matrix whose components are the components of the inverse matrix **M**. Thus the differential of the x-coordinates can be expressed by differentials of the l-coordinates by the formulas

$$dx_i = \sum_{j=1}^{6} n_{ji} dl_j \tag{3.16}$$

where $n_{ji} = 1/m_{ji}$.

Similarly, a link of the x-coordinates and the v-coordinates can be found out

$$d\mathbf{X} = \mathbf{P}\, d\mathbf{V} \tag{3.17}$$

In a index form

$$dx_i = \sum_{j=1}^{6} p_{ji} dv_j \tag{3.18}$$

where the components of the matrix **P** are defined as $p_{ji} = 1/g_{ji}$.

Combining matrix vector eautions (3.15) and (3.17), we can define

$$\mathbf{N}\, d\mathbf{L} = \mathbf{P}\, d\mathbf{V} \tag{3.19}$$

In the index form

$$\sum_{j=1}^{6} n_{ji} dl_j = \sum_{j=1}^{6} p_{ji} dv_j \tag{3.20}$$

Formula (3.20) establishes a synonymous dependence of the l-coordinate and the v-coordinates.

Moving from the differentials dx_i and dl_j to the end increments of the corresponding values, we get

$$\delta x_i^l = \sum_{j=1}^{6} n_{ji} \delta l_j \tag{3.21}$$

The elements of **P** and **N** matrix establish a connection of two groups of changes of the physical coordinates. They allow us to establish a relationship for coordinate changes.

Equation (3.21) determines changes in the spatial position of the machine tool according to the l-coordinates changes.

Similarly, the x-coordinate by changes in the v-coordinates can be determined

$$dx_i^v = \sum_{j=1}^{6} p_{ji} dv_j \tag{3.22}$$

Equation (3.22) establishes the repositioning changes of the tool after measuring the v-coordinates. The spatial position errors of the tool can be find as the difference of the vectors

$$[\Delta_i] = [\delta x_i^l] - [\delta x_i^v] \tag{3.23}$$

The errors are calculated in a fixed position around the executive body, which is defined by the vector $\mathbf{X}_0$ and its corresponding vectors $\mathbf{L}_0$ and $\mathbf{V}_0$.

The vectors $\mathbf{L}_0$ and $\mathbf{V}_0$ depend on the x-coordinate and are set by formulas (3.1) and (3.4). Thus, there is an error in the output tool position which is defined by formula (2.6). To improve the accuracy of the calculation of changes in the spatial position of the tool by formula (3.33), it is proposed to conduct periodic adjustment of this dependency by experimental measurements of the exact position of the tool. To do this, the measurements of the exact position of the tool are done in a number of points $k = 1, 2, \ldots, K$. The actual position errors of the tool are identified by formula (2.6). The resulting array of errors

$$[\delta x_i^k] \qquad i = 1, 2, \ldots, 6 \qquad k = 1, 2, \ldots, K \tag{3.24}$$

is smoothed within the workspace which enables obtaining continuous values of the vector of errors $[\delta x_i^k]$. The actual spatial position errors are modified by equation (3.33) and are

$$[\Delta_i] = [\delta x_i^l] - [\delta x_i^v] - [\delta x_i^c] \tag{3.25}$$

4. Structural implementation of the mechatronic active control system

The improved accuracy and stability of the parallel kinematics machine is achieved by correction of control laws, which is realized directly in the CNC system. To achieve this goal, the measurements of the actual spatial position of the tool is made. The measurements are made by the mechatronic system of active control of dynamic spatial positioning of the tool. Its constructive implementation corresponds to the scheme shown in Fig. 1.

The system of active control has been implemented as a prototype. The executive body of the machine P moves in space by six rods of variable length Li and six measuring rods Vi (Fig. 6).

Fig. 6. Structural implementation of the mechatronic system of active control of dynamic spatial positioning of the tool of the parallel kinematics machine

To implement the active control of spatial positioning of the tool, an additional mechatronic mechanism with six measuring rods V has been made. The basis of the measuring rod is linear

potentiometric displacement sensor PC-M-200. The voltage obtained from the sensor are handled by the analog-to-digital converter (ADC) M-DAQ14 which sends the obtained data to a personal computer for further analysis and processing. To convert an analog signal into a discrete one and display it on a virtual oscilloscope in LabView environment has been developed. Block Diagram and the User Interface of developed VI are shown in Figs. 7a and 7b, respectively.

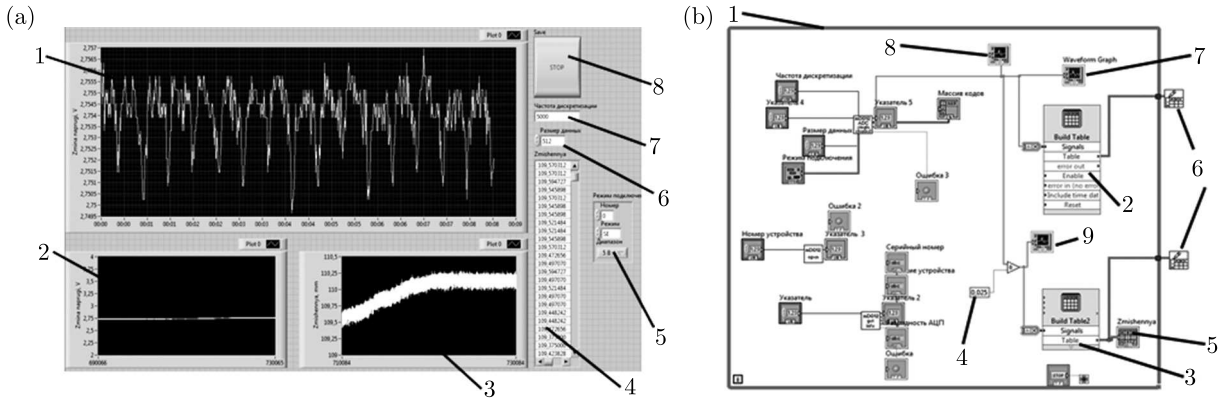

Fig. 7. The developed LabView VI: (a) user interface; (b) Block Diagram to display and record the data from ADC during measurements with the linear displacement sensor

In Waveform Graph 1 (Fig. 7a) voltage changes in the received signal at the time interval 0.08 s is displayed. Based on these values, we can control the level of noise and the accuracy of the measurements. The boxes of Waveform Chart 2, 3 present the voltage value received from the sensor and the linear displacement throughout the spectrum of measurements, respectively. Element 4 displays numerical values of the elongation of the sensor. In box 5, we can adjust the measuring range: ±1.25 V, ±2.5 V, ±5 V and ±10 V and set the mode for measurement and ADC channels from which the voltage value is received. The range of the data processed by ADC is set box 6. The frequency of analog signal 7 can be set in the range up to 20000 Hz. Pressing «Stop» 8 completes the program display and record the data in the .xls or .txt format.

The cycle «While-Loop»1 which provides the collection of data from the converter until «Stop»is clicked in the block diagram (Fig. 7b). Functions «Build table» 2, 3 form a table of values of the amplitude based on the received signal. Two tables are formed as a result: the input voltage V and the converted to millimeters data by means of using the pre-calculated numerical constants 4. The value of elongation of the sensor rod is given in element 5. To record the data, routines Write to Spreadsheet File.vi 6 is used. The real time display of the signal from the sensor is implemented in Waveform Graph, Windows 7, that provides visual control of the signal noise. The Waveform Chart 8 and Waveform Chart 9, display the voltage value and the corresponding elongation of the sensor rod.

The periodical calibration of the system to control the exact position of the executive body of the machine when its output is clearly fixed in the position within the workspace.

To set a fixed position, special devices (gauges) have been developed. These devices are a system of spheres that are located in well-defined positions within the workspace of the machine tool. The spheres are made of ceramic which has minimal thermal deformations. The spheres are placed in the holes of similar modules at the vertices of squares of the parts 100 ± 0.002 mm (Fig. 8)

By means of these modules we can form flat or spatial structures of different configurations. Each module consists of base 1 in which precision spheres 2 with a diameter 35 ± 0.001 mm are set. These spheres are fixed in the base with clamps 3. To determine the precision parameters of the machine tool with rectilinear motion and grooves 4 in the base are provided.

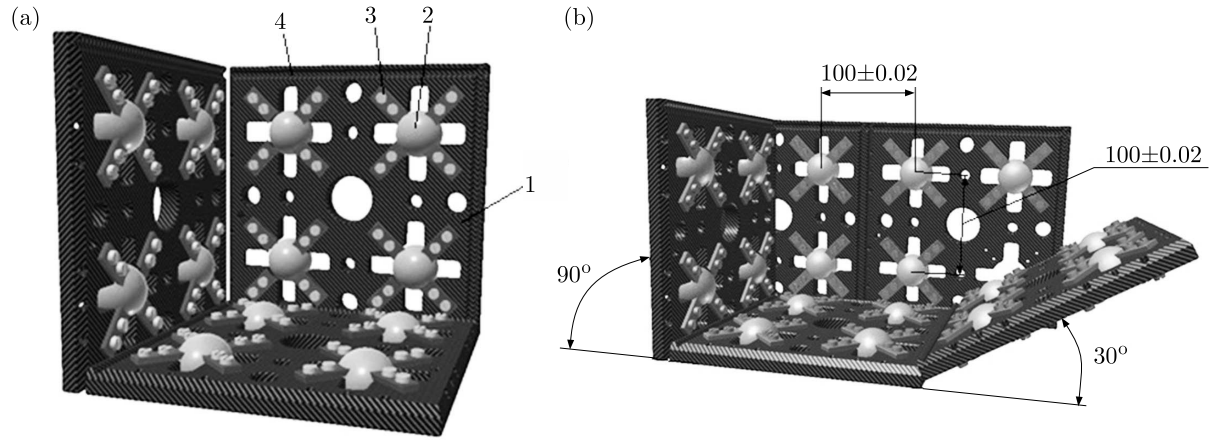

Fig. 8. Special equipment which consists of modules of the same type to determine the accuracy of the executive body output in positions: (a) disposition of modules in the cube form, (b) spatial disposition of modules

The developed equipment is set on the table of the parallel kinematics machine tool. To perform the calibration operation, the meter with a contact probe is set in the spindle. During the calibration, the output position of the executive body of the machine tool is determined which corresponds to spatial arrangement of the spheres of the developed equipment in the appropriate configuration.

5. Conclusions

In this paper, the method and the mechatronic system of active control of the dynamic spatial positioning of the executive body of the parallel kinematics machine tool which is implemented as an additional parallel kinematic mechanism with six measuring rods. The basic analytical relationships that determine the regularity of work of the active control system of the dynamic spatial positioning of the tool are proposed and additionally equated by means of geometric modeling. It is shown that the laws for the machine tool and the additional measuring mechanism yield similar changes of rods lengths. The proposed analytical method of connecting small movements of the executive body and changes in the rods length give us the opportunity to determine analytical formulas that characterize the spatial position error of the executive body of the parallel kinematics machine tool when the output is in a fixed position.

The structural implementation of the mechatronic system of active control of the dynamic spatial positioning of the executive body of the parallel kinematics machine tool is proposed and manufactured as a prototype. Its preliminary setup and test efficiency are held. It is noted that the resulting array of spatial position errors that can be found on the base of the proposed analytical equations contains the additional error in the output tool position which should be taken into account. It can be done by means of conducting periodic adjustment of theses formulas by experimental measurements of the exact position of the tool. Thereby, the construction of special equipment to determine the exact position of the executive body of the parallel kinematics machine tool and its calibration is proposed.

References

1. Andreff N., Martinet P., 2009, Vision-based self-calibration and control of parallel kinematic mechanisms without proprioceptive sensing, *Intelligent Service Robotics*, **2**, 71-80
2. Briot S., Bonev I.A., 2007, Are parallel robots more accurate than serial robots, *Transactions of the Canadian Society for Mechanical Engineering*, **31**, 445-455

3. Dindorf R., Laski P., 2010, Design and experimental test of a pneumatic parallel manipulator tripod type 3UPRR, *Acta Mechanica et Automatica*, **4**, 9-13

4. Guan L., 2012, *Design, Analysis, and Prototyping of A 3xPPRS Parallel Kinematic Mechanism for Meso-Milling*, Department of Mechanical and Industrial Engineering University of Toronto

5. Huang H., 2010, A 6-DOF adaptive parallel manipulator with large tilting capacity, *Robotics and Computer-Integrated Manufacturing*, **28**, 275-283

6. Ibaraki S., Yokawa T., Yoshiaki K., Masao N., 2004, A study on the improvement of motion accuracy of hexapod-type parallel mechanism machine tools (2nd Report) – A calibration method to evaluate positioning errors on the global coordinate system, *Journal of the Japan Society for Precision Engineering*, **40**, 557-561

7. Joubair A., Slamani M., Bonev I., 2014, Kinematic calibration of a five-bar planar parallel robot using all working modes, *Robotics and Computer-Integrated Manufacturing*, **29**, 15-25

8. Kotlarski J., Heimann B., Ortmaier T., 2012, Improving the pose accuracy of planar parallel robots using mechanisms of variable geometry, *Advances in Robot Manipulators*, 381-400

9. Pandilov Z., Dukovski V., 2012, Parallel kinematics machine tools: overview – from history to the future, *Annals of Faculty Engineering Hunedoara, International Journal of Engineering*, **10**, 111-124

10. Strutinsky S.V., 2012, Skhemna realizatsiya prostorovoyi systemy pryvodiv dlya manipulyuvannya obyektamy mashynobuduvannya (in Ukrainian), *Naukovyy Zhurnal "Tekhnolohichni kompleksy"*, **2**, 97-103

11. Szatmári S., 2007, Kinematic calibration of parallel kinematic machines on the example of the hexapod of simple design, Dissertation zur Erlangung des akademischen Grades Doktoringenieur, 146 p.

12. Weck M., Staimer D., 2000, On the accuracy of parallel machine tools: design, compensation and calibration, *2nd Chemnitz Parallel Kinematics Seminar*, 73-83

13. Wu J.-F., Zhang R., Wang R., Yao Y., 2014, A systematic optimization approach for the calibration of parallel kinematics machine tools by a laser tracker, *International Journal of Machine Tools and Manufacture*, **86**, 1-11

Manuscript received July 16, 2015; accepted for print November 10, 2015

JOURNAL OF THEORETICAL AND APPLIED MECHANICS
54, 3, pp. 769-781, Warsaw 2016
DOI: 10.15632/jtam-pl.54.3.769

A MICROMECHANICAL APPROACH TO NUMERICAL MODELING OF YIELDING OF OPEN-CELL POROUS STRUCTURES UNDER COMPRESSIVE LOADS

Reza Hedayati

Amirkabir University of Technology (Tehran Polytechnic), Department of Mechanical Engineering, Hafez Ave, Tehran, Iran

Delft University of Technology (TU Delft), Department of Biomechanical Engineering, Delft, The Netherlands

e-mail: rezahedayati@gmail.com; r.hedayati@tudelft.nl; rezahedayati@aut.ac.ir

Mojtaba Sadighi

Amirkabir University of Technology (Tehran Polytechnic), Department of Mechanical Engineering, Hafez Ave, Tehran

Today, interconnected open-cell porous structures made of titanium and its alloys are replacing the prevalent solid metals used in bone substitute implants. The advent of additive manufacturing techniques has enabled manufacturing of open-cell structures with arbitrary micro-structural geometry. In this paper, rhombic dodecahedron structures manufactured using SLM technique and tested by Amin Yavari *et al.* (2014) are investigated numerically using ANSYS and LS-DYNA finite element codes for the modeling of the elastic and post-yielding behavior of the lattice structure, respectively. Implementing a micro-mechanical approach to the numerical modeling of the yielding behavior of open-cell porous materials is the main contribution of this work.One of the advantages of micro-mechanical modeling of an open-cell structure is that, in contrast to the macro-mechanical finite element modeling, it is not necessary to obtain several material constants for different foam material models through heavy experimental tests. The results of the study showed that considering the irregularity in defining the cross-sections of the struts decreases both the yielding stress and densification strain of the numerical structure to the values obtained from the experimental tests. Moreover, the stress-strain curve of the irregular structure was much smoother in two points of yielding and densification, which is also observable in experimental plots. Considering the irregularity in the structure also decreased the elastic modulus of the lattice structure by about 20-30%. The post-densification modulus was more influenced by irregularity as it was decreased by more than 50%. In summary, it was demonstrated that using beam elements with variable cross-sections for constructing open-cell biomaterials could result in numerical results sufficiently close to the experimental data.

Keywords: rhombic dodecahedron, additive manufacturing, micro-structure, porous biomaterials, implant, finite element

1. Introduction

For many decades, pure Ti and its alloys have been widely used for the manufacturing of metal implants because of their exceptionally good corrosion resistance and excellent biocompatibility. Although the durability of Ti-based biomaterials is quite good, some implants still fail as a result of instability and aseptic loosening. The first cause of aseptic loosening is the huge difference between the stiffness of cortical bone and the metallic biomaterial, which unloads the natural bone and leads to its absorption after a while (a phenomenon known as stress shielding). Introduction of porosity into bulk metals significantly decreases their stiffness to values close to those of the bone which is very advantageous in avoiding stress shielding. The second reason of implant loosening is weak interfacial bond between the implant surface and the living tissue (Campoli

et al., 2013). The presence of ample spaces inside porous biomaterials allows for extensive body fluid transport through the porous scaffold matrix which triggers bone ingrowth (Head *et al.*, 1995; Lu *et al.*, 1999; Ryan *et al.*, 2006).

Several manufacturing techniques are used for production of porous metals (Ryan *et al.*, 2006) including the space holder technology (Kwok *et al.*, 2008) and additive manufacturing (AM) techniques (Heinl *et al.*, 2008). The main advantage of additive manufacturing techniques as compared to other traditional manufacturing techniques is their ability to manufacture interconnected porous biomaterials with pre-determined unit cell types. Selective laser melting (SLM) (Mullen *et al.*, 2009) and selective electron beam melting (SEBM) (Heinl *et al.*, 2008) are among the AM methods that are used for production of porous metallic biomaterials (Campoli *et al.*, 2013).

There is not a large class of unit cells which after being packed together can create tessellated structures. Cube (Gibson and Ashby, 1997; Luxner *et al.*, 2009; Parthasarathy *et al.*, 2010), truncated cube (Hedayati *et al.*, 2016d), rhombic dodecahedron (Babaee *et al.*, 2012; Borlefis, 2012; Campoli *et al.*, 2013; Hedayati *et al.*, 2016a; Shulmeister *et al.*, 1998), truncated cuboctahedron (Hedayati *et al.*, 2016c), tetrakaidecahedrons (Warren and Kraynik, 1997; Zheng *et al.*, 2014), rhombicuboctahedron (Hedayati *et al.*, 2016e), 3D-Kagome (Ptochos and Labeas, 2012a,b), Pyramidal (Ptochos and Labeas, 2012a), diamond (Ahmadi *et al.*, 2014; Campoli *et al.*, 2013; Hedayati *et al.*, 2016b), truncated octahedron, and Weaire-Phelan (Bitsche *et al.*, 2005; Buffel *et al.*, 2014; Kraynik and Reinelt, 1996) are the main morphologies which have been more extensively studied. The two latter morphologies have also been proposed as the closest morphologies for foams manufactured using traditional foam manufacturing techniques. The rhombic dodecahedron structure has been shown to be a proper unit cell geometry for being used in bone substitute implants. Analytical relationships for elastic properties of this type of structure can be found in (Babaee *et al.*, 2012) and its complete experimental stress-strain curve data can be found in (Amin Yavari *et al.*, 2013).

Although increased porosity and pore size are obviously preferential for new bone growth in Ti implant (Bram *et al.*, 2000; Karageorgiou and Kaplan, 2005), it should be kept in mind that another consequence of the porosity and pore size increase is the reduction of the implant mechanical properties. This reduction is preferential in elastic modulus but undesirable for fatigue durability and yield strength. Thus depending on the intended application, a balance between different mechanical properties and biological performance should be found (Chen *et al.*, 2009).

Analytical, experimental, and numerical methods have been used by different authors for investigating the behavior of 3D open-cell porous structures in static loadings. Analytical relationships look very helpful in predicting the elastic modulus and yield stress of porous structures. Analytical relationships give the user the elastic properties of a specific porous material with particular micro-geometry, pore size, or relative density. However, analytical relationships cannot be easily derived for the post yielding behavior of these structures because after yielding, many complex deformation regimes, such as buckling, plasticity, and contact between adjacent cells are activated simultaneously. For the post-yielding regime, experimental and numerical techniques show to be helpful. Using numerical techniques, such as finite element, is less costly and time-consuming than experimental procedures and also provides the researcher with ability to reconstruct any morphology, strut size, or sample size.

While the macro-mechanical finite element method has been extensively used in prediction of behavior of open-cell porous structures for almost two last decades, the micro-mechanical approach has not been used sufficiently in previous studies. The authors could not find any previous study regarding the numerical modeling of post-yielding behavior of open-cell porous structures by using finite element models made of beam elements. The micro-mechanical modeling approach enables the researchers to observe the mechanisms occurring in the micro-structural scale and helps them find out what main deformation mechanisms are dominating.

Porous structures (including open-cell structures), when crushed under compression, usually show a three-stage stress-strain curve. In the first stage, similar to most engineering materials, these materials show an elastic linear part. The second stage starts when some parts of cell edges in the open-cell porous structure (or "cell walls" in a closed-cell porous structure) are yielded, and the stress-strain curve becomes non-linear. Since after being yielded, the cell edges are free to move because of the voids in their periphery, the displacement of the sample accumulates greatly(usually for more than 50-60%) by keeping the applied load constant or by increasing it very slightly. This stage is known as the plateau stage and the (almost constant) stress in this stage is called the plateau stress. When the sample is crushed enough and the neighbor cell edges come into contact with each other, the third stage (densification stage) is started. Since the cell edges are not as free as in the second stage, the load again starts to increase (nonlinearly). The stress and strain at the beginning of the densification stage are called the densification stress and strain, respectively. An appropriate micro-mechanical finite element model for open-cell foams must be capable of predicting all the noted values with acceptable accuracy.

In this paper, the pre- and post-yielding regimes of porous structures manufactured and experimentally tested by Amin Yavari *et al.* (2013) will be investigated numerically using ANSYS and LS-DYNA finite element packages. In their work, rhombic dodecahedron interconnected cells were created using SLM method. The manufacturing technique was not perfect and there were some imperfections in the micro-structure of the porous structures (Fig. 1). In particular, it was noted that some struts were significantly weaker than others (Amin Yavari *et al.*, 2013). In this paper, the procedure of developing a finite element model for simulating the yielding behavior of the rhombic dodecahedron structure is presented. The effect of considering the irregularity in the cross-section area of the struts, as a way of introducing the presence of imperfections in the actual manufactured samples, on the obtained mechanical properties will also be investigated.

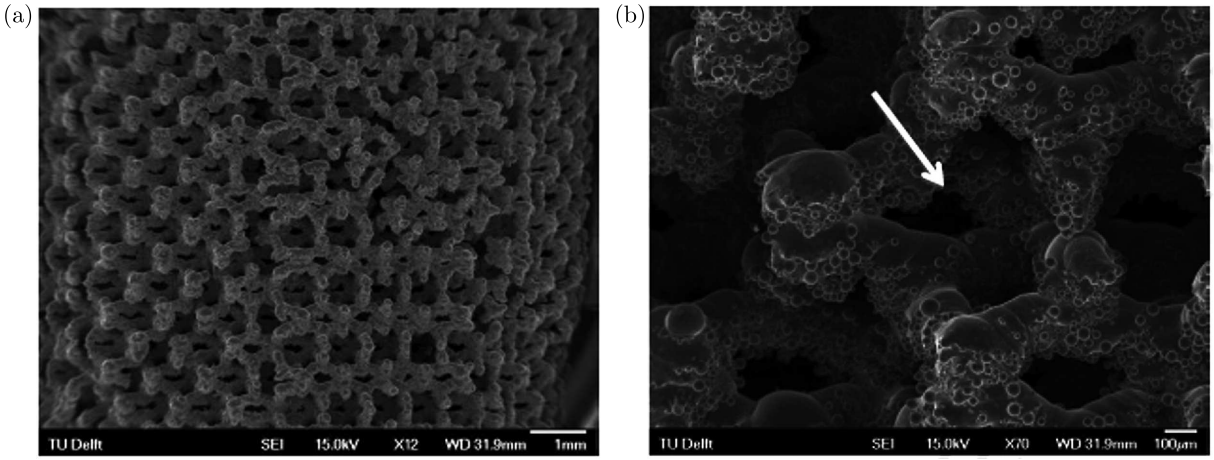

Fig. 1. Micro images of the additively manufactured porous structures (Amin Yavari *et al.*, 2013)

2. Materials and methods

2.1. Numerical modeling

2.1.1. Creation of a lattice structure

If a single unit cell with all of its struts is going to be repeated in the three main directions of space to make a lattice structure, some edges of the neighbor unit cells overlap each other. The overlapping of common edges of the adjacent cells can stiffen the structure in an artificial way leading to incorrect results. To overcome this problem, after creating a unit cell (e.g. cell ABCDEF in Fig. 2), it is checked if it has any edge overlapped on already created edges of

its adjacent cells. For example in Fig. 2, the newly created edge EF overlies on the previously created edge 23 and edge AF overlies on edge 27. After recognizing the overlapped struts, the edges and nodes attached to each end of the older strut are recognized and their relevant numbers are saved into an array (edges 12, 34, 87 and nodes 8, 1 and 4). The older overlapped beam edges (edges 23 and 27) as well as the edges connected to them (edges 12, 34, and 87) are then removed (Fig. 2b). In the next step, the remaining nodes of the removed struts (nodes 1, 4, and 8) are connected to the corresponding nodes of the remaining overlapped strut (edges EF and AF) by creating new edge lines (edges 1f, 4E, and A8) (Fig. 2c). While this procedure is robust, it takes a long time for being completed, especially for large 3D structures.

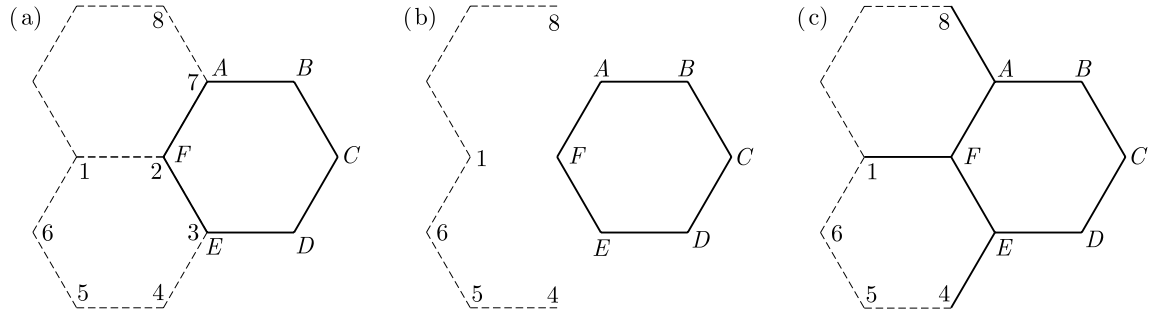

Fig. 2. The procedure of eliminating the overlapping of beam elements

2.1.2. Modeling the irregularities

For modelling the elastic behaviour of the specimens, implicit finite element method was used. Four specimens with pore sizes, strut sizes, and porosities listed in Table 1 were simulated. The specimens had relative densities in the range of 68-84%, strut diameters between 140 μm and 251 μm, and pore sizes between 486 μm and 608 μm (Table 1). Relative density is defined as the ratio of density of the porous structure to density of the bulk material it is made of. The cross-section of the struts had circular cross-sections. The 3D lattice structure of each case was created using Timoshenko beam elements that take into account the shear deformation and rotational inertia effects. Two rigid grips were also modelled and placed under and above the porous structure (Fig. 3).

Table 1. Geometrical specifications of four different samples investigated (Amin Yavari *et al.*, 2013)

	Sample 1 Ti 120-500	Sample 2 Ti 170-450	Sample 3 Ti 170-500	Sample 4 Ti 230-500
Dimensions ($D \times L$) [mm×mm]	10×15	10×15	10×15	10×15
Pore size [μm]± SD	560 ± 173	486 ± 162	608 ± 182	560 ± 186
Strut size [μm]± SD	140 ± 38	216 ± 64	218 ± 62	251 ± 76
Porosity [%]	84.22	71.2	77.68	68.45

Variations in diameters of the additively manufactured struts were applied to the FE models by discretising the struts by beam elements with different diameters. The diameters of each of the beam elements were taken from a Gaussian distribution function in ANSYS. For the mean and standard deviation of the Gaussian distribution, those of the diameters of the struts of the experimental tests were implemented. Generally, increasing the number of elements along a strut decreases its mechanical properties which leads to a decrease in the overall structure elastic modulus. Especially, it was seen that using more than two beam elements per each strut may lead to instabilities in the yielding analyses. It is because increasing the number of beam

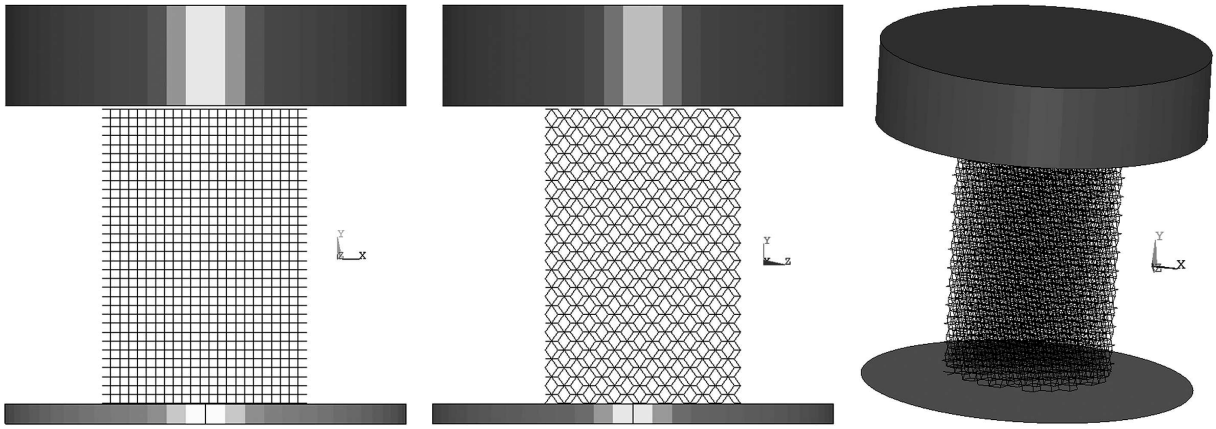

Front view Side view 3D view

Fig. 3. Finite element model of rhombic dodecahedron lattice structure

elements per strut increases the number of struts with very small cross-sections which will lead to failure of a large group of struts (catastrophic failure). A simple probability calculation can show that the number of weak struts in a three-element-per-strut structure is much higher than a one-element-per-strut structure. To explain this better, consider as an example struts having diameter lower than d_{cr} in a FE lattice structure as weak struts and assume that they constitute 10% of the FE structure having one element per strut (see Fig. 1b) and 90% of the struts of this structure are strong. Now the structure with three elements per strut has only $0.9^3 = 72\%$ strong elements because each strut can be considered strong only if all of its elements have diameters larger than d_{cr}. Therefore, the number of weak struts in the three-element-per-struts structure is almost triple of that in the one-element-per-strut structure, which can lead to catastrophic failure of the lattice structure much easier. The considerations taken into account in the Gaussian distribution of our numerical modelling might not also be true in the structures created using the additive manufacturing techniques. For example, it has been seen that in actual SLM-made structures, the majority of weak struts only have one very small cross-section among them (Fig. 1b), while in our numerical modelling, the struts can have more than one weak element. In fact, if it is necessary to use more than one element per strut, more data than just the standard deviation of strut diameter needs to be known.

Another problem that can arise from using more than one element per strut is that most of the beam theories are valid for length/diameter ratios larger than four. For the porous structures considered in this study (Table 1) and in most similar studies, if the number of elements per strut becomes larger than one, then the length/diameter ratio of each beam element becomes smaller than two, which can lead to inaccuracies in obtained stress values for given displacements. Therefore, in all the models created in this study, only one beam element was used to represent each strut. However, diameters of different struts of the FE model were considered to be different. For the FE structure, 21 different strut diameters (ranging between the minimum and maximum diameter values obtained by optical observations) were considered.

2.1.3. Material model

For modeling the behavior of the lattice structure in post-yielding regime, an explicit finite element code LS-DYNA was implemented. A plastic kinematic material model (with constants given in Table 2) was used for modeling the mechanical behavior of the metal. In this material model, the material behavior is assumed to be bilinear. Automatic-node-to-surface contact algorithm was used for modeling the interaction between the structure and the grips, and automatic single surface contact algorithm was used for modeling the interactions between neighbor struts.

The struts were free to move in the direction parallel to the grip faces. The density of 4420 kg/m^3 (Ti6Al4V) was used for the explicit analysis. The lower grip was fixed and the upper grip was moved downward with a constant velocity of 3 mm/min.

Table 2. Mechanical properties of Ti6Al4V

Property	Value
Elastic modulus	113.8 GPa
Poisson's ratio	0.342
Tangent modulus	1.25 GPa
Yield stress	1000 MPa
Ultimate tensile strength	1200 MPa

3. Results

The sequential deformation of the lattice structures having regular and irregular strut cross--section areas are shown in Figs. 4 and 5, respectively. The 45° failure pattern can be observed in both structures, but more obvious in the regular one (Fig. 4). The failure pattern looks like

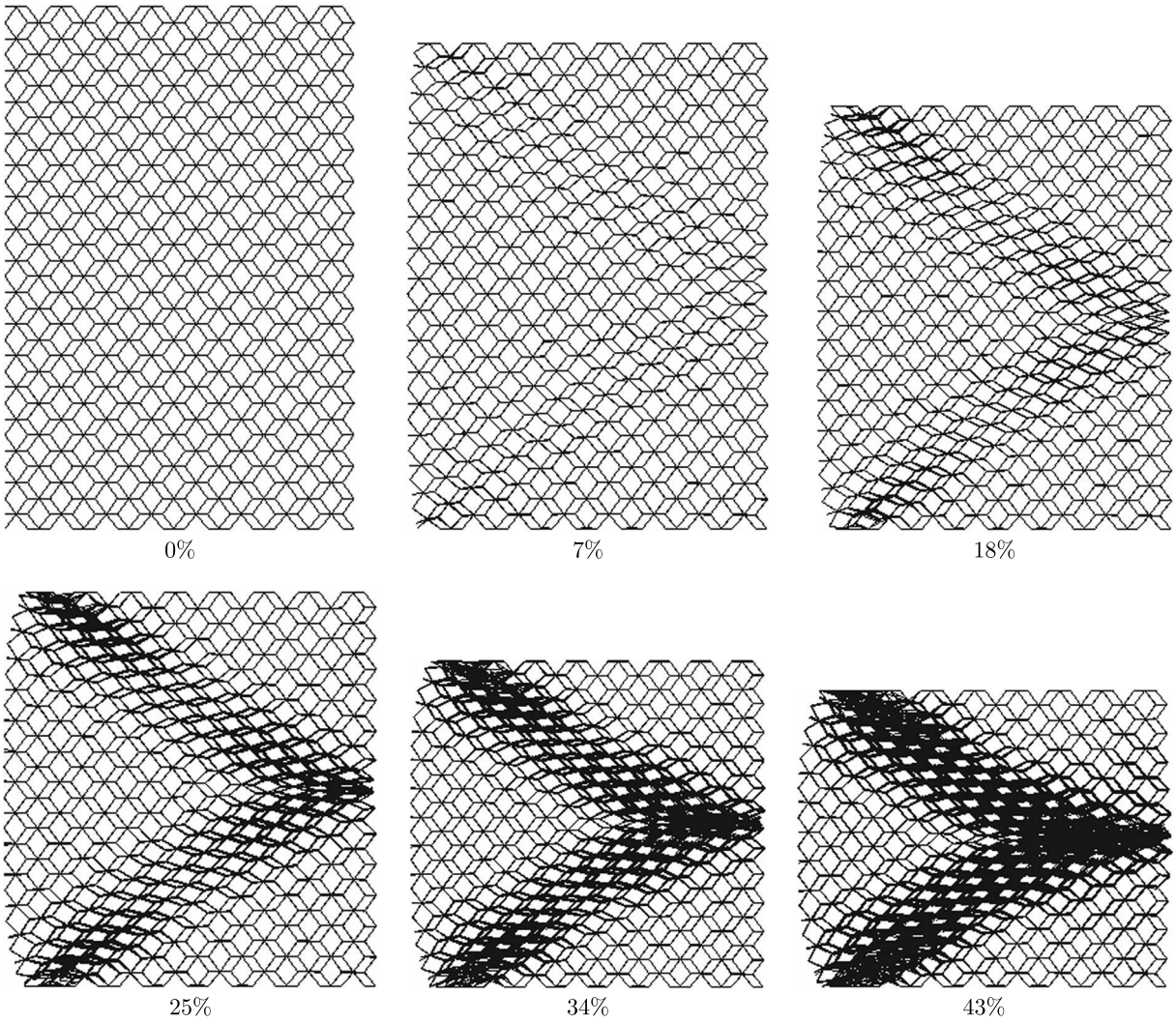

Fig. 4. Deformation of the regular structure at different compressive strains

a sideways V in the regular structure, while it is more similar to sideways X in the irregular structure (Fig. 5). The main deformation mechanisms in the four lattice structures (Table 1) were observed to be first the elastic bending of the struts and then the local plasticity. Local buckling did not occur in the struts. This could be expected because no strut in the initial configuration of this structure was parallel to the direction of loading. The fact that the local yielding occurs far before buckling was also analytically shown for the diamond structure by Ahmadi *et al.* (2014).

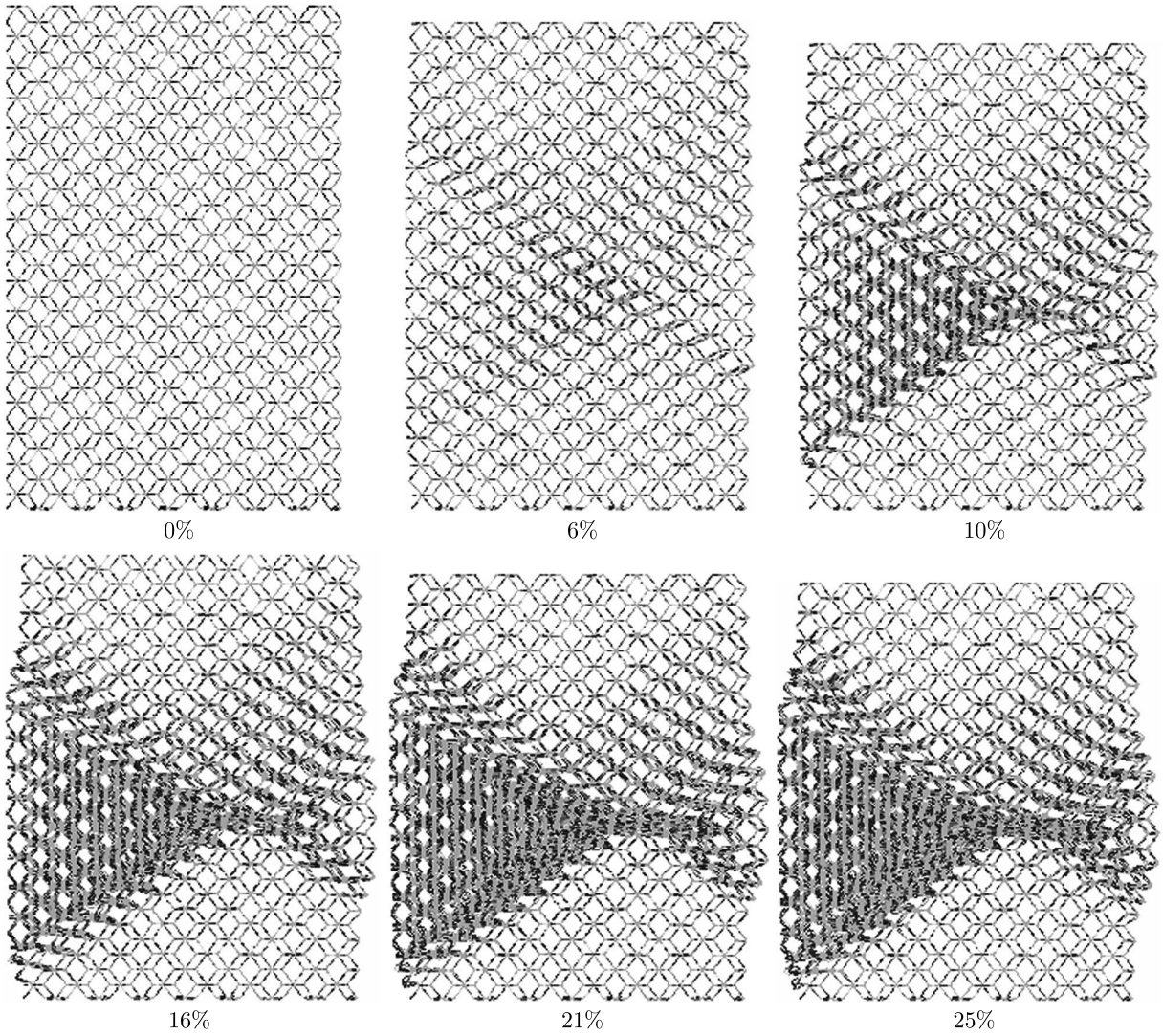

Fig. 5. Deformation of the irregular structure at different compressive strains

The stress-strain curves of the regular and irregular FE models of test sample 1 (Ti 120-500) are plotted and compared to each other in Fig. 6. Introduction of irregularity in the cross-section of the struts decreased both the yielding stress and densification strain. Both the values obtained from the irregular FE structure were closer to the experimental results (Table 3). Moreover, the stress-strain curve of the irregular structure was much smoother in the two points of yielding and densification (Fig. 6) which was in accordance to the observations in the stress-strain plots obtained from the experimental tests. Considering irregularity in the structure also decreased the elastic modulus by about 30% (Fig. 6). The post-densification modulus was more influenced by considering the irregularities and was decreased by more than 50% (Fig. 6).

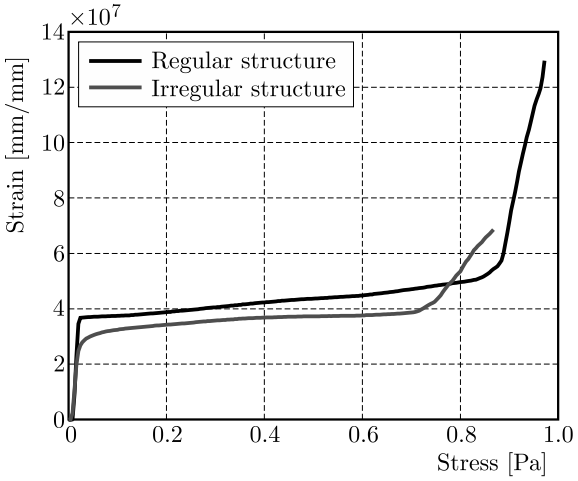

Fig. 6. Comparison of the stress-strain curves of the regular and irregular structures

Table 3. Comparison of plateau stress and densification strain of the numerical model and experimental tests of the four considered porous structures

	Sample 1 Ti 120-500	Sample 2 Ti 170-450	Sample 3 Ti 170-500	Sample 4 Ti 230-500
ε_d (FEM)	0.71	0.75	0.76	0.65
ε_d (Experiment)	0.61	0.76	0.70	0.56
σ_p (FEM)	20 MPa	85 MPa	48 MPa	110 MPa
σ_p (Experiment)	15.8 MPa	67.8 MPa	34.8 MPa	91.8 MPa

The elastic moduli obtained from theory (Babaee *et al.*, 2012), our FEM code, and experimental tests (Amin Yavari *et al.*, 2013) are compared in Fig. 7. As it can be seen, the numerical values are lower than the theoretical values due to the fact that variations in the cross-section areas have been considered in the FE model. However, the numerical elastic modulus is higher than that in the experimental tests, since the irregularities of diameter along each strut length has not been considered.

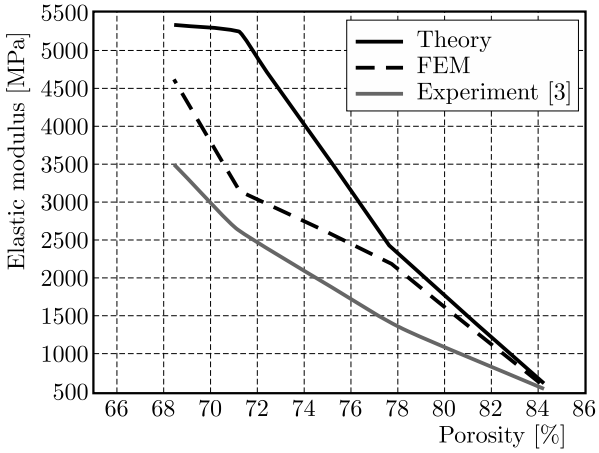

Fig. 7. Comparison of elastic moduli obtained from theory, our FEM code and experimental tests (Amin Yavari *et al.*, 2013)

Using the obtained stress-strain curves (Fig. 8) from explicit simulations of the four cases (Table 1), the following values were calculated: elastic modulus E, strain at the beginning of the plateau region ε_p, densification strain ε_D, plateau stress σ_p, and the plateau end stress σ_D.

As obvious in Fig. 9 and Table 3, the experimental and numerical results were relatively in good accordance. Both the plateau stress and densification strain of the FEM solution were larger than the experimental values (Fig. 9). This can be attributed to the lower amount of damage considered in the FE models procedure compared to the real irregularities present in the manufactured samples, as the irregularities along the strut length had not been considered in the FE models.

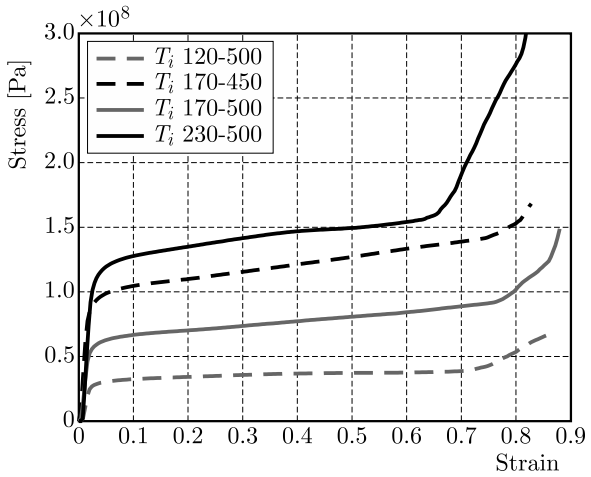

Fig. 8. Stress-strain curves for the four irregular samples

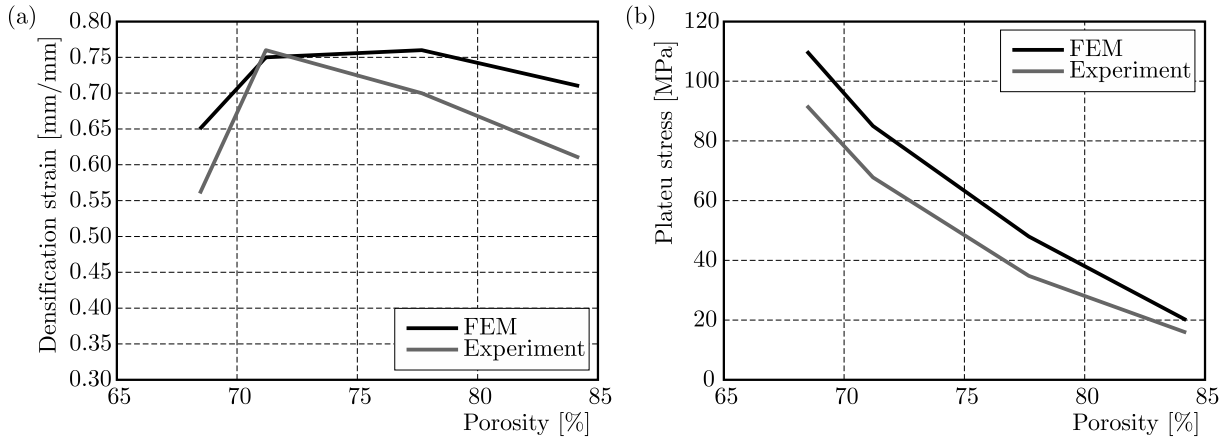

Fig. 9. Variation of (a) densification strain, and (b) plateau stress with respect to porosity

Both the numerical and experimental results show a decrease in the plateau stress by increasing the porosity (Fig. 9b). However, by increasing the porosity, the densification strain of the structure is initially increased and then decreases. This behaviour is observed in both the numerical and experimental curves (Fig. 9a). The maximum densification strain occurs for the relative density of about 70% (Fig. 9a).

4. Discussions

4.1. Computational time

In this study, the yielding behavior of open-cell foams was modeled using an explicit finite element code. In explicit finite element simulations, the structure is deformed through numerous time steps with very short durations. The time step is determined through the relationship

$\Delta t = l/c$, where l is the smallest element dimension throughout the entire model and c is the speed of sound in the material. For yielding simulation, the calculated time step Δt is usually very small (less than a microsecond). On the other hand, the yielding procedure is a quasi-static phenomenon which can take several minutes to be completed. This is why solving the yielding deformation using the explicit finite element method can lead to computational times larger than several days. The mass scaling was shown to be a very effective way of decreasing the solution time without having a significant effect on the obtained mechanical properties.

4.2. Effect of irregularities

45° deformation bands existed for both the regular and irregular lattice structures in post-yielding regime (Figs. 4 and 5, see also (Silva and Gibson, 1997; Alkhader and Vural, 2008; Demiray *et al.*, 2009). By applying the irregularity in cross-section areas of the struts, this 45° deformation bands became vaguer (Fig. 5). This is because in the irregular structure, the struts start to fail sooner than they would fail in the regular structure. When the initial struts start to fail and, as a result, they are removed from the analysis, the load applied to their neighbor struts start to increase, and that makes the failure pattern grow around the initially failed struts as nucleuses. The results obtained from static and yielding simulations demonstrated that considering the irregularities has a significant effect on the response of the structure. In all the cases, considering the irregularities weakened the structure. Applying the irregularity in different cases decreased the plateau stress by 30-50% and the elastic modulus by 10-20%. A similar decrease in the elastic modulus was reported by Campoli *et al.* (2013).

4.3. Advantages of micro-mechanical modeling

Several material models have been proposed in different studies for modeling the post-yielding behavior of foams in macro-mechanical analyses. For example, in LS-DYNA package, the material models MAT_LOW_DENSITY_FOAM, MAT_CRUSHABLE_FOAM, MAT_MODIFIED_CRUSHABLE_FOAM, MAT_SOIL_AND_FOAM, MAT_BLATZ-KO_FOAM, MAT_FU_CHANG, MAT_PITZER_CRUSHABLE_FOAM, MAT_DESHPANDE_FLECK_FOAM, etc. are available for the modeling the behavior of the foam. Each of the above-mentioned material models require several material constants to be determined through mechanical tests before being applicable in finite element simulations. For each foam type, the complex and time-consuming procedure of experimental tests for finding the constants must be repeated.

The micro-mechanical modeling of an open-cell foam has the advantage that the material constants of the foam structure do not have to be found through mechanical tests. In fact, in micro-mechanical models, the necessary material properties are those of the bulk material from which the foam is made of such as elastic modulus E_s, Poisson's ratio ν_s, tangent modulus T_s, and yield stress σ_{y_s}.

5. Conclusions

In this paper, structures manufactured using the SLM technique and tested by Amin Yavari *et al.* (2013) were numerically modeled using ANSYS and LS-DYNA finite element codes for investigating the elastic and post-yielding behavior of the lattice structure, respectively. Implementing a micro-mechanical approach to the numerical modeling of the yielding behavior of open-cell porous materials is the main contribution of this work. One of the advantages of the micro-mechanical modeling of an open-cell structure is that, in contrast to the macro-mechanical finite element modeling, it is not necessary to obtain several material constants for different foam

material models through heavy experimental tests. Regular and irregular lattice structures were created. After crushing the FE structure under compression, 45° failure patterns were observed in both the regular and irregular structures, but more obvious in the regular structure. The failure patterns in the regular and irregular structures looked like sideways V and X signs, respectively. The results also showed that considering the irregularity in the cross-section area of different struts in the rhombic dodecahedron lattice structure decreases both the yielding stress and densification strain to values close to the experimental data. Moreover, compared to the regular FE structure, the stress-strain curve of the irregular FE structure was much smoother in the two points of yielding and densification, which was also observable in many experimental plots. Considering the irregularity in the structure also decreased the elastic modulus of the lattice structure by about 20-30%. The post-densification modulus was more influenced by irregularity as it was decreased by more than 50%. In summary, it is demonstrated that using beam elements with variable cross-sections for constructing open-cell porous biomaterials can give numerical results sufficiently close to the experimental data.

References

1. Ahmadi S., Campoli G., Amin Yavari S., Sajadi B., Wauthlé R., Schrooten J., Weinans H., Zadpoor A.A., 2014, Mechanical behavior of regular open-cell porous biomaterials made of diamond lattice unit cells, *Journal of the Mechanical Behavior of Biomedical Materials*, **34**, 106-115
2. Alkhader M., Vural M., 2008, Mechanical response of cellular solids: role of cellular topology and microstructural irregularity, *International Journal of Engineering Science*, **46**, 10, 1035-1051 sufficiently
3. Amin Yavari S., Wauthlé R., Van der Stok J., Riemslag A., Janssen M., Mulier M., Kruth J.-P., Schrooten J., Weinans H., Zadpoor A.A., 2013, Fatigue behavior of porous biomaterials manufactured using selective laser melting, *Materials Science and Engineering: C*, **33**, 8, 4849-4858
4. Babaee S., Jahromi B.H., Ajdari A., Nayeb-Hashemi H., Vaziri A., 2012, Mechanical properties of open-cell rhombic dodecahedron cellular structures, *Acta Materialia*, **60**, 6, 2873-2885
5. Bitsche R., Daxner T., Böhm H.J., 2005, *Space-Filling Polyhedra as Mechanical Models for Solidified Dry Foams*, Technische Universität Wien
6. Borleffs M., 2012, *Finite Element Modeling to Predict Bulk Mechanical Properties of 3D Printed Metal Foams*, TU Delft, Delft University of Technology
7. Bram M., Stiller C., Buchkremer H.P., Stöver D., Baur H., 2000, High-porosity titanium, stainless steel, and superalloy parts, *Advanced Engineering Materials*, **2**, 4, 196-199
8. Buffel B., Desplentere F., Bracke K., Verpoest I., 2014, Modelling open cell-foams based on the Weaire-Phelan unit cell with a minimal surface energy approach *International Journal of Solids and Structures*, **51**, 19, 3461-3470
9. Campoli G., Borleffs M., Amin Yavari S., Wauthle R., Weinans H., Zadpoor A.A., 2013, Mechanical properties of open-cell metallic biomaterials manufactured using additive manufacturing, *Materials and Design*, **49**, 957-965
10. Chen L.-J., Ting L., Li Y.-M., Hao H., Hu Y.-H., 2009, Porous titanium implants fabricated by metal injection molding, *Transactions of Nonferrous Metals Society of China*, **19**, 5, 1174-1179
11. Demiray S., Becker W., Hohe J., 2009, Investigation of the fatigue behavior of open cell foams by a micromechanical 3-D model, *Materials Science and Engineering: A*, **504**, 1, 141-149
12. Gibson L.J., Ashby M.F., 1997, *Cellular Solids: Structure and Properties*, Cambridge University Press

13. Head W.C., Bauk D.J., Emerson R.H. Jr, 1995, Titanium as the material of choice for cementless femoral components in total hip arthroplasty, *Clinical Orthopaedics and Related Research*, **311**, 85-90

14. Hedayati R., Hosseini-Toudeshky H., Sadighi M., Mohammadi-Aghdam M., Zadpoor A.A., 2016a, Computational prediction of the fatigue behavior of additively manufactured porous metallic biomaterials, *International Journal of Fatigue*, **84**, 67-79

15. Hedayati R., Sadighi M., Mohammadi-Aghdam M., Zadpoor A.A., 2016b, Effect of mass multiple counting on the elastic properties of open-cell regular porous biomaterials, *Materials and Design*, **89**, 9-20

16. Hedayati R., Sadighi M., Mohammadi-Aghdam M., Zadpoor A.A., 2016c, Mechanical behavior of additively manufactured porous biomaterials made from truncated cuboctahedron unit cells, *International Journal of Mechanical Sciences*, **106**, 19-38

17. Hedayati R., Sadighi M., Mohammadi-Aghdam M., Zadpoor A.A., 2016d, Mechanical properties of regular porous biomaterials made from truncated cube repeating unit cells: analytical solutions and computational models, *Materials Science and Engineering: C*, **60**, 163-183

18. Hedayati R., Sadighi M., Mohammadi-Aghdam M., Zadpoor A.A., 2016e, Mechanics of additively manufactured porous biomaterials based on the rhombicuboctahedron unit cell, *Journal of the Mechanical Behavior of Biomedical Materials*, **53**, 272-294

19. Heinl P., Müller L., Körner C., Singer R.F., Müller F.A., 2008, Cellular Ti-6Al-4V structures with interconnected macro porosity for bone implants fabricated by selective electron beam melting, *Acta Biomaterialia*, **4**, 5, 1536-1544

20. Karageorgiou V., Kaplan D., 2005, Porosity of 3D biomaterial scaffolds and osteogenesis, *Biomaterials*, **26**, 27, 5474-5491

21. Kraynik A.M., Reinelt D.A., 1996, Linear elastic behavior of dry soap foams, *Journal of Colloid and interface Science*, **181**, 2, 511-520

22. Kwok P.J., Oppenheimer S.M., Dunand D.C., 2008, Porous titanium by electro-chemical dissolution of steel space-holders, *Advanced Engineering Materials*, **10**, 9, 820-825

23. Lu J., Flautre B., Anselme K., Hardouin P., Gallur A., Descamps M., Thierry B., 1999, Role of interconnections in porous bioceramics on bone recolonization in vitro and in vivo, *Journal of Materials Science: Materials in Medicine*, **10**, 2, 111-120

24. Luxner M.H., Woesz A., Stampfl J., Fratzl P., Pettermann H.E., 2009, A finite element study on the effects of disorder in cellular structures, *Acta Biomaterialia*, **5**, 1, 381-390

25. Mullen L., Stamp R.C., Brooks W.K., Jones E., Sutcliffe C.J., 2009, Selective laser melting: a regular unit cell approach for the manufacture of porous, titanium, bone in-growth constructs, suitable for orthopedic applications, *Journal of Biomedical Materials Research, Part B: Applied Biomaterials*, **89**, 2, 325-334

26. Parthasarathy J., Starly B., Raman S., Christensen A., 2010, Mechanical evaluation of porous titanium (Ti6Al4V) structures with electron beam melting (EBM), *Journal of the Mechanical Behavior of Biomedical Materials*, **3**, 3, 249-259

27. Ptochos E., Labeas G., 2012a, Elastic modulus and Poisson's ratio determination of microlattice cellular structures by analytical, numerical and homogenisation methods, *Journal of Sandwich Structures and Materials*, p. 1099636212444285

28. Ptochos E., Labeas G., 2012b, Shear modulus determination of cuboid metallic open-lattice cellular structures by analytical, numerical and homogenisation methods, *Strain*, **48**, 5, 415-429

29. Ryan G., Pandit A., Apatsidis D.P., 2006, Fabrication methods of porous metals for use in orthopaedic applications, *Biomaterials*, **27**, 13, 2651-2670

30. Shulmeister V., Van der Burg M., Van der Giessen E., Marissen R., 1988, A numerical study of large deformations of low-density elastomeric open-cell foams, *Mechanics of Materials*, **30**, 2, 125-140

31. Silva M.J., Gibson L.J., 1997, The effects of non-periodic microstructure and defects on the compressive strength of two-dimensional cellular solids, *International Journal of Mechanical Sciences*, **39**, 5, 549-563

32. Warren W., Kraynik A., 1997, Linear elastic behavior of a low-density Kelvin foam with open cells, *Journal of Applied Mechanics*, **64**, 4, 787-794

33. Zheng X., Lee H., Weisgraber T.H., Shusteff M., DeOtte J., Duoss E.B., Kuntz J.D., Biener M.M., Ge Q., Jackson J.A., 2014, Ultralight, ultrastiff mechanical metamaterials, *Science*, **344**, 6190, 1373-1377

Manuscript received October 29, 2014; accepted for print November 23, 2015

JOURNAL OF THEORETICAL AND APPLIED MECHANICS
54, 3, pp. 783-794, Warsaw 2016
DOI: 10.15632/jtam-pl.54.3.783

TIME-INDEPENDENT STOCHASTIC DESIGN SENSITIVITY ANALYSIS OF STRUCTURAL SYSTEMS WITH SECOND-ORDER ACCURACY

Hanna Weber
West Pomeranian University of Technology in Szczecin, Faculty of Civil Engineering and Architecture, Poland
e-mail: weber@zut.edu.pl

In the paper, the static sensitivity of complex structures with respect to random design parameters is presented. Using the adjoint system method, based on the mean-point second-order perturbation method, the first two probabilistic moments of time-independent sensitivity are formulated with means and cross-covariances of random design parameters as the input data. It enables one to obtain the second-order accuracy of the solution. The presented formulations are illustrated by a number of numerical examples. The influence of finite element mesh density for the obtained results is discussed using the analysis of the spatial bar dome.

Keyword: design sensitivity, statics, random parameter, finite element

1. Introduction

Since the beginning of mankind, humans have had aspirations to overcome their weaknesses and limitations. It is the element of our nature, which became the basis of development in all fields of life. In the civil engineering there are amazing objects that crossed existing barriers of height, span and slenderness. These types of structures can not be computed by analytical methods because of complexity of the system. Hence, the Finite Element Method (FEM) has become the basis of contemporary structure analysis (Bathe, 1982; Zienkiewicz and Taylor, 1991; Kincayd and Cheney, 2002). It is an approximate method which allows one to obtain highly precise results with a properly dense FEM mesh.

A significant element of correct design is to model an object to reflect reality as closely as possible while taking into account many factors including connections, materials, external loads, etc. (see Leet *et al.*, 2010). Engineers' aim is to create programs for optimal design of new or strengthen the existing structures. It involves findings the best solutions bearing in mind many different aspects such as the maximum load, allowable displacement, cost, time and possibility of execution, etc. (Niczyj, 2003; Choi and Kim, 2010). A very important case is to find an answer to the question of how the changing of design parameters affects the structural response. It is a subject of study of sensitivity analysis that can be found in (Haug *et al.*, 1986; Mroz and Haftka, 1986; Hien and Kleiber, 1989; Drewko and Hien, 2005; Ding *et al.*, 2012; Mroz and Bojczuk, 2012; Choi and Kim, 2013). This type of computations by using deterministic variables has been extensively discussed in the literature. However, it has been proved that in systems with many degrees of freedom (MDOF), even small uncertainties in structural parameters or external loads may have a significant impact on the work and load capacity of the system. The stochastic analysis (Adomian, 1983; Hisada and Nakagiri, 1981; Spanos and Ghanem, 1989; Ghanem and Spanos, 1991; Kleiber and Hien, 1992; Li and Chen, 2009) includes randomness in the described factors, and for complex systems it needs to be considered by numerical methods because analytical solutions are in many cases impossible.

There are three main trends in the analysis with random variables: perturbation approach (Greene *et al.*, 2011; Liu *et al.*, 2013), Monte Carlo simulation (Fishman, 1995; Rubinstein

and Kroese, 2008), and Neumann's expansion (Liu *et al.*, 1986). The goal of this paper is a numerical nonstatistical analysis of statics and time-independent sensitivity for MDOF systems by random parameters. Starting from the stochastic version of the equilibrium equation, using the mean-point second-order perturbation method, the equations for the first two probabilistic moments of the sensitivity gradients with respect to the design parameters are derived, where the means and cross-covariances of random variables are treated as the input data. Thereby, not only the deterministic values of static response sensitivity are obtained but also the accuracy of the received results as expected values and cross-covariances. These formulations are illustrated by numerical examples.

2. Formulation of the stochastic sensitivity for statics in the finite element context

The objective of structural sensitivity analysis is to consider the impact of design variable changes on the system response. In this paper, the design variable vector is denoted by $\mathbf{b} = \{b_a\}$, $a = 1, 2, \ldots, A$. It can be cross-sectional areas of structural elements, thickness of a shell or plate, mass density, Young's modulus etc., while displacements, stresses or natural frequencies in main nodes can be treated as structural response measures.

The result of deterministic computation is only one variable at a given point, while the stochastic analysis determines also the accuracy of the obtained value. During the second process, the system is described by random variables. The time-independent random variable vector is assumed in the form $\mathbf{h} = \{h_r\}$, $r = 1, 2, \ldots, \widehat{r}$ and defined by means $\overline{h}_r = \mathrm{E}[h_r]$ and cross--covariances $\mathrm{Cov}\,(h_r, h_s)$, $r, s = 1, 2, \ldots, \widehat{r}$. From the definition, given by Kleiber and Hien (1992), the first probabilistic moment of the random variable is expressed by

$$\mathrm{E}[h_r] = \int_{-\infty}^{+\infty} h_r p(h_r)\, dh_r \tag{2.1}$$

and the second

$$\mathrm{Cov}\,(h_r, h_s) = \mathrm{E}[(h_r - \overline{h}_r)(h_s - \overline{h}_s)] = \alpha_r \alpha_s \overline{h}_r \overline{h}_s \mu(h_r, h_s) \tag{2.2}$$

where

$$\mu(h_r, h_s) = \int_{-\infty}^{+\infty}\int_{-\infty}^{+\infty} h_r h_s p(h_r, h_s) dh_r dh_s \tag{2.3}$$

and

$$\alpha_r = \frac{\sqrt{\mathrm{Var}\,(h_r)}}{\overline{h}_r} = \frac{\sigma(h_r)}{\overline{h}_r} \tag{2.4}$$

In Equations (2.1)-(2.4) $p(h_r)$, $p(h_r, h_s)$, $\mu(h_r, h_s)$, $\mathrm{Var}\,(h_r)$, $\sigma(h_r)$ and α denote the probability density function, joint probability density function, adopted function of correlation, variance, standard deviation and the coefficient of variation, respectively.

In this paper from this moment forth, the summation notation is included. In the following equations, two repeated indices imply the sum, which results in greater transparency of presentation. Let us consider a linear elastic complex structure with N degrees of freedom. The static response of the system can be formulated then by the functional (Kleiber and Hien, 1992)

$$\phi = G[q_\alpha(b_a, h_r), b_a] \qquad \alpha = 1, 2, \ldots, N \tag{2.5}$$

where q_α is determined as the time-independent vector of generalized coordinates. In the stochastic analysis of systems with multi degrees of freedom (MDOF), the stiffness matrix $K_{\alpha\beta}$ and the nodal load vector Q_α are explicit functions of both the design parameter and the random variable vector. In the static case, the considered system is time-independent, therefore damping and mass effects are omitted during computations. Consequently, the equilibrium equation is written in the stochastic form as

$$K_{\alpha\beta}(b_a, h_r)q_\beta(b_a, h_r) = Q_\alpha(b_a, h_r) \qquad \alpha, \beta = 1, 2, \ldots, N \tag{2.6}$$

A solution to Eq. (2.6) with respect to q_β (Eq. (2.7)) proves that the nodal displacement vector is an implicit function of b_a and h_r

$$q_\beta(b_a, h_r) = K^{-1}_{\alpha\beta}(b_a, h_r)Q_\alpha(b_a, h_r) \tag{2.7}$$

To evaluate the probabilistic distribution of the static structural response with respect to the design parameters, we tend to obtain an absolute partial derivative of the functional ϕ with respect to the design variable, i.e. $d\phi/db_a$. Assuming that the stiffness matrix and the nodal load vector are twice continuously differentiable with respect to b_a, the chain rule of differentiation gives

$$\frac{d\phi}{db_a} = \frac{\partial G}{\partial b_a} + \frac{\partial G}{\partial q_\alpha}\frac{dq_\alpha}{db_a} \qquad \alpha = 1, 2, \ldots, N \qquad a = 1, 2, \ldots, A \tag{2.8}$$

According to Eq. (2.5), G is an explicit function of b_a and q_α, therefore, the partial derivatives $\partial G/\partial b_a$ and $\partial G/\partial q_\alpha$ are known. The goal of the procedure is to find the absolute partial derivative of the general coordinate vector with respect to the design variable, i.e. dq_α/db_a. To formulate the static sensitivity problem, the so-called adjoint system method is used (Kleiber and Hien, 1992; Choi and Kim, 2010). The adjoint equation system is adopted in the form

$$K_{\alpha\beta}\lambda_\beta = \frac{\partial G}{\partial q_\alpha} \qquad \alpha, \beta = 1, 2, \ldots, N \tag{2.9}$$

Seeing that the stiffness matrix $K_{\alpha\beta}$ and the vector $\partial G/\partial q_\alpha$ are functions of the design and random variable, the solution to Eq. (2.9) with respect to λ_β written as

$$\lambda_\beta(b_a, h_r) = K^{-1}_{\alpha\beta}(b_a, h_r)\frac{\partial G}{\partial q_\alpha}(b_a, h_r) \tag{2.10}$$

demonstrates that the adjoint variable vector is an implicit function of b_a and h_r and it is expressed as $\lambda = \{\lambda_\alpha(b_a, h_r)\}$, $\alpha = 1, 2, \ldots, N$. Differentiating Eq. (2.6) with respect to the design variable and then solving it to obtain the vector dq_α/db_a and putting it into Eq. (2.8) leads to

$$\frac{d\phi}{db_a} = \frac{\partial G}{\partial b_a} + K^{-1}_{\alpha\beta}\frac{\partial G}{\partial q_\alpha}\Big(\frac{\partial Q_\alpha}{\partial b_a} - \frac{\partial K_{\alpha\beta}}{\partial b_a}q_\beta\Big) \tag{2.11}$$

Substituting Eq. (2.10) into Eq. (2.11) we receive the equation for design sensitivity of the system (Kleiber and Hien, 1992)

$$\frac{d\phi}{db_a} = \frac{\partial G}{\partial b_a} + \lambda_\alpha\Big(\frac{\partial Q_\alpha}{\partial b_a} - \frac{\partial K_{\alpha\beta}}{\partial b_a}q_\beta\Big) \tag{2.12}$$

It should be noted that all terms in Eq. (2.12) are simultaneously functions of the design parameter and the random variable vectors. Now, all elements from Eqs. (2.6) and (2.9) are expanded in power series around the means $\overline{h}_r$, in accordance with the following equation

$$(\cdot) = (\cdot)(\overline{\mathbf{h}}) + \Big[\frac{\partial(\cdot)}{\partial h_r}\delta h_r + \frac{1}{2}\frac{\partial^2(\cdot)}{\partial h_r \partial h_s}\delta h_r \delta h_s\Big]_{\mathbf{h}=\overline{\mathbf{h}}} \qquad r, s = 1, 2, \ldots, \widehat{r} \tag{2.13}$$

where δh_r denotes the first variations h_r about the means $\overline{h}_r$, and for any small parameter ϵ it can be written as (Hien, 2003)

$$\delta h_r = \epsilon(h_r - \overline{h}_r) \tag{2.14}$$

while $\delta h_r \delta h_s$ is called the second mixed variation of h_r and h_s about their means $\overline{h}_r$ and $\overline{h}_s$

$$\delta h_r \delta h_s = \epsilon^2 (h_r - \overline{h}_r)(h_s - \overline{h}_s) \tag{2.15}$$

All the functions of the random variable are expanded in Taylor series up to the second order and substituted to Eqs. (2.6) and (2.9). After rearranging the equations and comparing terms with the same order of ϵ, we receive the primary and adjoint systems of equations (compare, Kleiber and Hien, 1992):
— one pair of systems of N equations of the zeroth-order

$$K_{\alpha\beta} q_\beta = Q_\alpha \qquad K_{\alpha\beta}\lambda_\beta = \frac{\partial G}{\partial q_\alpha} \tag{2.16}$$

— $\widehat{r}$ pairs of systems of N equations of the first-order

$$K_{\alpha\beta}\frac{dq_\beta}{dh_r} = \frac{\partial Q_\alpha}{\partial h_r} - \frac{\partial K_{\alpha\beta}}{\partial h_r} q_\beta \qquad K_{\alpha\beta}\frac{d\lambda_\beta}{dh_r} = \frac{\partial^2 G}{\partial h_r \partial q_\alpha} - \frac{\partial K_{\alpha\beta}}{\partial h_r}\lambda_\beta \tag{2.17}$$

— one pair of systems of N equations of the second-order

$$\begin{aligned} K_{\alpha\beta}\frac{d^2 q_\beta}{dh_r dh_s}\Big|_{\mathbf{h}=\overline{\mathbf{h}}} \operatorname{Cov}(h_r, h_s) &= \Big[\frac{\partial^2 Q_\alpha}{\partial h_r \partial h_s} - \frac{\partial^2 K_{\alpha\beta}}{\partial h_r \partial h_s} q_\beta - 2\frac{\partial K_{\alpha\beta}}{\partial h_r}\frac{dq_\beta}{dh_s}\Big]_{\mathbf{h}=\overline{\mathbf{h}}} \operatorname{Cov}(h_r, h_s) \\ K_{\alpha\beta}\frac{d^2 \lambda_\beta}{dh_r dh_s}\Big|_{\mathbf{h}=\overline{\mathbf{h}}} \operatorname{Cov}(h_r, h_s) &= \Big[\frac{\partial^3 G}{\partial h_r \partial h_s \partial q_\alpha} - \frac{\partial^2 K_{\alpha\beta}}{\partial h_r \partial h_s}\lambda_\beta - 2\frac{\partial K_{\alpha\beta}}{\partial h_r}\frac{d\lambda_\beta}{dh_s}\Big]_{\mathbf{h}=\overline{\mathbf{h}}} \operatorname{Cov}(h_r, h_s) \end{aligned} \tag{2.18}$$

From the definition (Kleiber and Hien, 1992), the first probabilistic moment for the sensitivity gradient is given by

$$\mathrm{E}\Big[\frac{d\phi}{db_a}\Big] = \underbrace{\int_{-\infty}^{+\infty}\int_{-\infty}^{+\infty}\dots\int_{-\infty}^{+\infty}}_{A-\text{fold}} \frac{d\phi}{db_a} p_A(b_1, b_2, \dots, b_A)\, db_1\, db_2 \cdots db_A \tag{2.19}$$

while the second probabilistic moment is expressed analogically as

$$\operatorname{Cov}\Big(\frac{d\phi}{db_a}, \frac{d\phi}{db_b}\Big) = \mathrm{E}\Big[\Big(\frac{d\phi}{db_a} - \mathrm{E}\Big[\frac{d\phi}{db_a}\Big]\Big)\Big(\frac{d\phi}{db_b} - \mathrm{E}\Big[\frac{d\phi}{db_b}\Big]\Big)\Big] \tag{2.20}$$

The mean value of Eq. (2.12) may be written as

$$\mathrm{E}\Big[\frac{d\phi}{db_a}\Big] = \mathrm{E}\Big[\frac{\partial G}{\partial b_a}\Big] + \mathrm{E}\Big[\lambda_\alpha \frac{\partial Q_\alpha}{\partial b_a}\Big] - \mathrm{E}\Big[\lambda_\alpha \frac{\partial K_{\alpha\beta}}{\partial b_a} q_\beta\Big] \tag{2.21}$$

Substituting Eq. (2.12) into Eq. (2.21) gives an expression for the second probabilistic moment of the design sensitivity gradient in the form

$$\begin{aligned} \operatorname{Cov}\Big(\frac{d\phi}{db_a}, \frac{d\phi}{db_b}\Big) = \mathrm{E}\Big[\Big(\frac{\partial G}{\partial b_a} + \lambda_\alpha\Big(\frac{\partial Q_\alpha}{\partial b_a} - \frac{\partial K_{\alpha\beta}}{\partial b_a} q_\beta\Big) - \mathrm{E}\Big[\frac{d\phi}{db_a}\Big]\Big) \\ \cdot \Big(\frac{\partial G}{\partial b_b} + \lambda_\gamma\Big(\frac{\partial Q_\gamma}{\partial b_b} - \frac{\partial K_{\gamma\delta}}{\partial b_b} q_\delta\Big) - \mathrm{E}\Big[\frac{d\phi}{db_b}\Big]\Big)\Big] \end{aligned} \tag{2.22}$$

All functions of the random variables from Eqs. (2.21) and (2.22) are expanded in Taylor series in accordance with Eq. (2.13) and are premultiplied. Excluding members in orders higher than the second and averaging the other terms, leads to an expression of the mean values of the design sensitivity gradient, cf. Hien and Kleiber (1991), Kleiber and Hien (1992)

$$\begin{aligned}\mathrm{E}\Big[\frac{d\phi}{db_a}\Big] = \Big[&\frac{\partial G}{\partial b_a} + \lambda_\alpha \mathcal{A}_{\alpha a} \\ &+ \frac{1}{2}\Big(\frac{\partial^3 G}{\partial h_r \partial h_s \partial b_a} + \frac{d^2\lambda_\alpha}{dh_r dh_s}\mathcal{A}_{\alpha a} + 2\frac{d\lambda_\alpha}{dh_r}\mathcal{B}_{\alpha sa} + \lambda_\alpha \mathcal{C}_{\alpha rsa}\Big)\,\mathrm{Cov}\,(h_r, h_s)\Big]_{\mathbf{h}=\overline{\mathbf{h}}}\end{aligned} \tag{2.23}$$

where, for clarity purposes, the following equations are used

$$\begin{aligned}\mathcal{A}_{\alpha a} &= \frac{\partial Q_\alpha}{\partial b_a} - \frac{\partial K_{\alpha\beta}}{\partial b_a} q_\beta \\ \mathcal{B}_{\alpha ra} &= \frac{\partial^2 Q_\alpha}{\partial h_r \partial b_a} - \frac{\partial^2 K_{\alpha\beta}}{\partial h_r \partial b_a} q_\beta - \frac{\partial K_{\alpha\beta}}{\partial b_a}\frac{dq_\beta}{dh_r} \\ \mathcal{C}_{\alpha rsa} &= \frac{\partial^3 Q_\alpha}{\partial h_r \partial h_s \partial b_a} - \frac{\partial^3 K_{\alpha\beta}}{\partial h_r \partial h_s \partial b_a} q_\beta - 2\frac{\partial^2 K_{\alpha\beta}}{\partial h_r \partial b_a}\frac{dq_\beta}{dh_s} - \frac{\partial K_{\alpha\beta}}{\partial b_a}\frac{d^2 q_\beta}{dh_r dh_s}\end{aligned} \tag{2.24}$$

The cross-covariances at $d\phi/db_a$ and $d\phi/db_b$ are

$$\begin{aligned}\mathrm{Cov}\Big(\frac{d\phi}{db_a}, \frac{d\phi}{db_b}\Big) = \Big[&\Big(\frac{\partial^2 G}{\partial h_r \partial b_a}\frac{\partial^2 G}{\partial h_s \partial b_b} + (\mathcal{A}_{\beta b}\mathcal{B}_{\alpha as} + \mathcal{A}_{\alpha a}\mathcal{B}_{\beta bs})\lambda_\alpha \frac{d\lambda_\beta}{dh_r} \\ &- \Big(\frac{\partial G}{\partial b_a}\mathcal{C}_{\beta rsb} + \frac{\partial^2 G}{\partial h_r \partial b_a}\mathcal{B}_{\beta rb} + \frac{\partial^3 G}{\partial h_r \partial h_s \partial b_a}\mathcal{A}_{\beta b}\Big)\lambda_\beta \\ &- \Big(\frac{\partial G}{\partial b_b}\mathcal{C}_{\alpha rsa} + \frac{\partial^2 G}{\partial h_r \partial b_b}\mathcal{B}_{\alpha ra} + \frac{\partial^3 G}{\partial h_r \partial h_s \partial b_b}\mathcal{A}_{\alpha a}\Big)\lambda_\alpha \\ &- \Big(2\frac{\partial G}{\partial b_a}\mathcal{B}_{\alpha sb} + \frac{\partial^2 G}{\partial h_s \partial b_a}\mathcal{A}_{\alpha b} + 2\frac{\partial G}{\partial b_b}\mathcal{B}_{\alpha ra} + \frac{\partial^2 G}{\partial h_s \partial b_b}\mathcal{A}_{\alpha a}\Big)\frac{\lambda_\alpha}{dh_r} \\ &- \Big(\frac{\partial G}{\partial b_b}\mathcal{A}_{\alpha a} + \frac{\partial G}{\partial b_a}\mathcal{A}_{\alpha b}\Big)\frac{d^2\lambda_\alpha}{dh_r dh_s} + \lambda_\alpha\lambda_\beta\mathcal{B}_{\alpha ar}\mathcal{B}_{\beta bs} + \mathcal{A}_{\alpha a}\mathcal{A}_{\beta b}\frac{d\lambda_\alpha}{dh_r}\frac{d\lambda_\beta}{dh_s}\Big)\,\mathrm{Cov}\,(h_r, h_s) \\ &- \frac{1}{4}\Big(\frac{\partial^3 G}{\partial h_t \partial h_u \partial b_b} + 2\frac{d\lambda_\beta}{dh_t}\mathcal{B}_{\beta ub} + \mathcal{A}_{\beta b}\frac{d^2\lambda_\beta}{dh_t dh_u} + \lambda_\beta \mathcal{C}_{\beta tub}\Big) \\ &\cdot \Big(\frac{\partial^3 G}{\partial h_r \partial h_s \partial b_a} + \frac{d^2\lambda_\alpha}{dh_r dh_s}\mathcal{A}_{\alpha a} + 2\frac{d\lambda_\alpha}{dh_r}\mathcal{B}_{\alpha sa} + \lambda_\alpha \mathcal{C}_{\alpha rsa}\Big)\,\mathrm{Cov}\,(h_r, h_s)\,\mathrm{Cov}\,(h_t, h_u)\Big]_{\mathbf{h}=\overline{\mathbf{h}}}\end{aligned} \tag{2.25}$$

with $r, s, t, u = 1, 2, \ldots, \widehat{r}$. Interestingly, Eq. (2.25) is obtained by including terms up to the second order, not only to the first like in Hien and Kleiber (1991), Kleiber and Hien (1992). The procedure of obtaining and averaging particular members of the first two probabilistic moments of the static design sensitivity can be found in detail in Weber (2014), while this paper is confined to present only the final version of these equations.

The equation for covariances at $d\phi/db_a$ and $d\phi/db_b$ in Weber (2014) is obtained by using the expressions for $E[d\phi/db_a]$ and $E[d\phi/db_b]$ as the final products. To derive Eq. (2.25), the members $E[d\phi/db_a]$ and $E[d\phi/db_b]$ are determined by Eq. (2.23) and substituted into Eq. (2.22). After ordering particular members, a more concise expression for the second probabilistic moment of the static design sensitivity than that presented by Weber (2014) is received.

3. Numerical examples – results and discussion

Deterministic and stochastic computations are executed by the finite element code POLSAP (see, Hien and Kleiber, 1990), properly adapted for this type of analysis. At the beginning of

numerical illustrations, let us consider a three-bar truss system. The analytical equations of nodal displacements and their sensitivities with respect to cross-sectional areas of the elements, were derived for the model by Choi and Kim (2010). The goal of this example is to obtain not only the deterministic displacements of nodes, but also their expected values and standard deviations by POLSAP and compare them with the results given by equations formulated by Choi and Kim (2010).

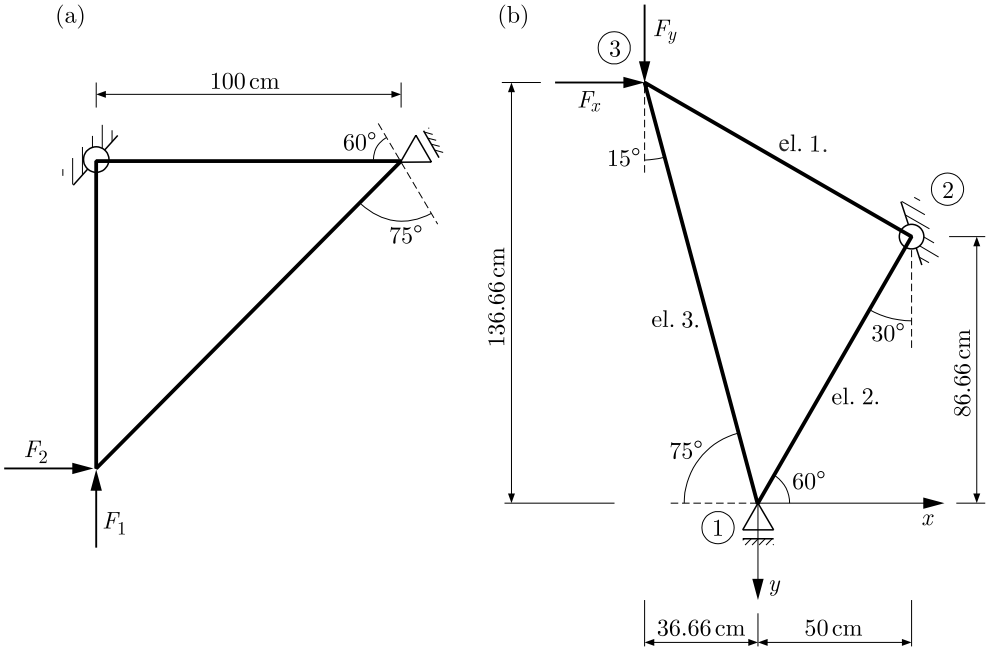

Fig. 1. Three-bar truss system (a) presented in Choi and Kim (2010), (b) adopted in numerical computation

To simplify the numerical model, the Choi and Kim system (2010) (see Fig. 1a) is rotated as shown in Fig. 1b, and nodal loads are reduced to vertical and horizontal forces $F_x = 18.33\,\text{kN}$ and $F_y = 68.30\,\text{kN}$ that correspond to forces $F_1 = F_2 = 50\,\text{kN}$. All results shown in Tables 1 and 2 are given for the adopted global coordinate system xy presented in Fig. 1b. Therefore, to compare the displacements and sensitivities, the values received by equations from literature have to be transformed by using trigonometric functions with an angle of 30 degrees.

The input data of the material and elements are adopted for simplification as: Young's modulus $E = 200\,\text{GPa}$ and cross-sectional areas of specific bars $A_1 = A_2 = A_3 = 5\,\text{cm}^2$. One bar is assumed as one truss element in the numerical model. The cross-sectional areas of particular elements are adopted as random design variables with the means $E[A_r] = 5\ \text{cm}^2$, and correlation function defined by the equation, cf. Kleiber and Hien (1992)

$$\mu(A_r, A_s) = \exp\Big(\frac{-|x_r - x_s|}{\lambda}\Big)\exp\Big(\frac{-|y_r - y_s|}{\lambda}\Big) \tag{3.1}$$

where x_r, x_s and y_r, y_s designates the x- and y-coordinates of the mid-points of the next two elements in the model, respectively. The symbol λ denotes the decay factor depending on the unit system used in numerical analysis. Its value is selected in order to receive no diagonal and non-zero covariance matrix of the random variables. For this example, $\lambda = 300$ and the coefficient of variation $\alpha = 0.1$ are adopted as the input data. In the second moment perturbation method, the random variables must fulfill the condition about small fluctuation and continuity at $\overline{h}_r$, therefore, the selection of α-coefficient is a very important part of numerical computations, cf. Weber (2014).

The correlation function shows a dependence between the random variables. The bigger the distance from one element to another, the smaller impact between them is observed. For the members situated at a considerable distance from each other, the described dependence tends to zero. Using Eq. (3.1), we obtain results equal to 1 on the main diagonal, and the values in the range from 0 to 1 for other elements. Additionally, the bigger the difference between the coordinates, the smaller results of the coefficient in the matrix, which satisfies the assumptions for the correlation function.

The deterministic and expected values of displacements obtained by POLSAP are similar to those given by Choi and Kim (2010) (see Table 1). The maximum difference between analytical and deterministic results is about 0.3%, while that between deterministic and stochastic is 0.85%.

Table 1. Non-zero nodal static displacements for the three-bar truss system, [cm]

Node number	Coordinate	Analytical values	POLSAP	
			Deterministic displacements	Expected values
1	x	0.073205	0.073416	0.073905
3	x	−0.084108	−0.084146	−0.084863
3	y	0.145680	0.145868	0.147066

The functional of the structural response defined by Eq. (2.5) is accepted in numerical analysis in the form

$$\phi = \frac{|q_\alpha|}{q_{all}} - 1 < 0 \tag{3.2}$$

where q_α, q_{all} are the actual and allowable displacements in a selected node. To compare the sensitivity results obtained from Choi and Kim (2010) and POLSAP, $q_{all} = 1.0\,\text{cm}$ is assumed for every node, otherwise the values given by the equations from literature should be divided by the accepted q_{all}.

In Table 2, displacement design sensitivities for selected nodes are presented. The maximum difference between analytical and deterministic values is 0.43%. The deterministic and stochastic results of static sensitivity vary in the range of 2.5-3.0%. The standard deviation is 19.4% of expected values.

Table 2. Displacement design sensitivity - bar cross-sectional areas as random design variables, [1/cm^2]

Node number	Displa-cement direction	Obtained values based on Choi and Kim (2010)	POLSAP		
			Deterministic values	Expected values	Standard deviations
cross-sectional area of el. no. 2 as design variable					
1	x	−1.46410E-2	−1.46831E-2	−1.50737E-2	2.92693E-3
3	y	−4.64102E-3	−4.66079E-3	−4.77790E-3	9.27750E-4
cross-sectional area of el. no. 3 as design variable					
3	x	−1.41421E-2	−1.41423E-2	−1.45617E-2	2.82752E-3
3	y	−2.44949E-2	−2.45133E-2	−2.52209E-2	4.89726E-3

The second numerical example is a spatial dome presented in Fig. 2 (compare Weber and Hien, 2010; Weber, 2014). The geometrical dimensions included in the analysis are: base diameter 1000 cm and height 500 cm. Each bar in the structure is modelled as a one beam element with the following characteristics: Young's modulus $E = 200\,\text{GPa}$, mass density $7.85\,\text{KNs}^2/\text{m}^4$, Poisson's ratio $\nu = 0.3$ and cross-section area $A = 20\,\text{cm}^2$. Nodes 1, 3, 5, 7 and 9 are supported by pins.

For the static and sensitivity analysis, only one vertical force is taken into account $F_z = 1000\,\text{kN}$. For clarity purposes, the dead weight of the structure is omitted during computations. As it is well known, this type of bar structures loaded only in nodes is usually modelled as a truss system. However, the goal of this presentation is to show the influence of complexity of the finite element mesh on static sensitivity results. Therefore, in this system, the rigid connections between bars are assumed. A comparison of the results obtained for the truss and beam model of this structure can be found in Weber (2014).

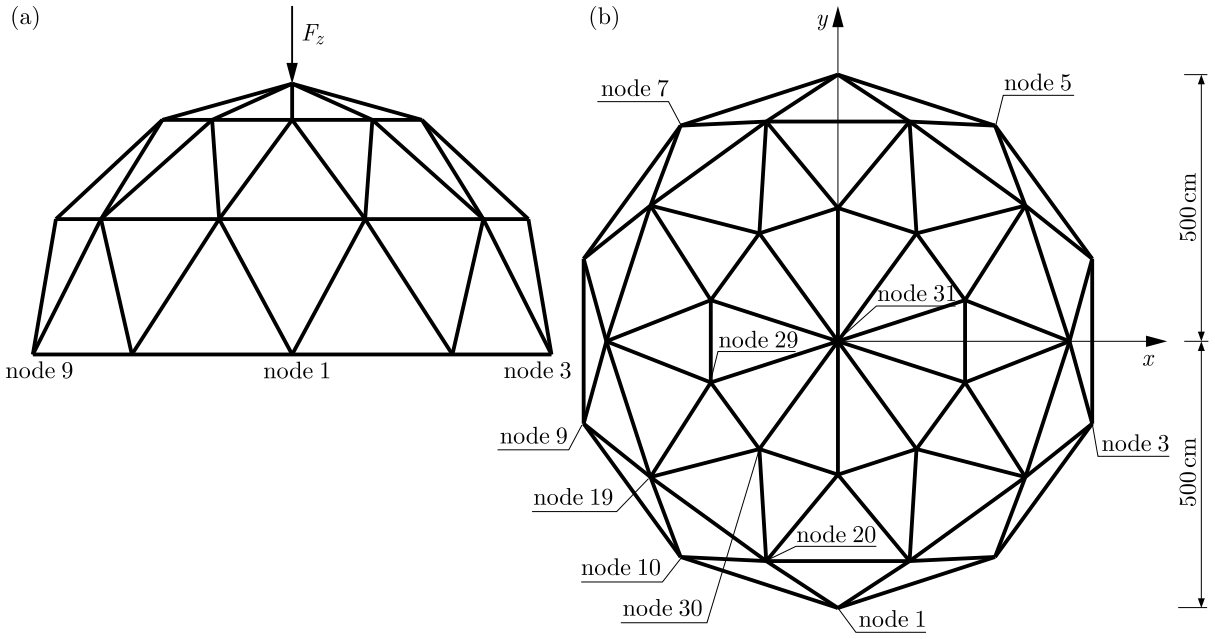

Fig. 2. Spatial dome (a) front, (b) bird eye – view

In static and sensitivity computations, the cross-sectional areas of elements are adopted as random design variables with the mean values $\overline{A} = 20\,\text{cm}^2$. The correlation function and functional response of the system are assumed as in Eqs. (3.1) and (3.2). The decay factor $\lambda = 200$ and the coefficient of variation $\alpha = 0.1$ are used in numerical computations.

The largest vertical deflection occurs at the top of the dome, which is predictable because of the point of force application. The deterministic and expected values of the nodal displacements in different directions vary by about 1%, which is acceptable.

The considered system is symmetric in terms of geometry, supported conditions and external load. Numerical computations give the same results in corresponding nodes, which confirms that the model input to the program is correct. However, for clarity purposes, Table 3 presents the values of displacements only for selected nodes.

Table 3. Selected nodal static displacements for the spatial dome, [cm]

Node number	Coordinate	Deterministic displacements	Expected values	Difference [%]
31	z	−2.049777	−2.070121	0.99
29	x	−0.260314	−0.262972	1.02
30	x	−0.162236	−0.163888	1.02
20	y	−0.144629	−0.145915	0.89
19	y	−0.100229	−0.101091	0.86

Both deterministic and stochastic analysis of static sensitivity study the vulnerability of various node displacements with respect to cross-sectional areas of different elements. The value

of q_{all} is chosen separately for every node and movement direction, according to Eq. (3.2). The most significant results of static displacement sensitivity for selected nodes, with the cross-sectional areas of elements as the random design variables, are given in Table 4. The differences between deterministic and expected values are about 2.5-3%, while the standard deviations are equal to 20% of expected values. In both examples, all computations have been conducted in centimeters and kilonewtons as basic units.

Table 4. Displacement design sensitivity – bar cross-sectional areas as random design variables, $[1/\text{cm}^2]$

Node number	Displ. direct.	q_{all} [cm]	Design el. number	Deterministic values	Expected values	Standard deviations
31	z	2.5	72	−1.94449E-3	−2.00421E-3	3.88446E-4
10	z	1.0	29	−2.18042E-3	−2.23223E-3	3.78821E-4
29	x	1.0	71	9.89193E-3	1.01891E-2	1.97174E-3
30	x	1.0	72	6.14086E-3	6.32574E-3	1.22490E-3
20	y	1.0	32	−3.17786E-3	−3.25960E-3	5.7216E-4
19	y	1.0	40	−3.59847E-3	−3.69325E-3	6.59437E-4

Considering various examples of the static displacement sensitivity allows one to spot a pattern. In most instances, a point displacement is the most sensitive with respect to, e.g., the cross-sectional areas of elements in the immediate vicinity of the considered point. However, in some cases there are certain derogations of the pattern when a displacement of a node turns out to be the most sensitive with respect to the cross-section of an element not lying directly by the examined node. Then sensitivity analysis allows one to find the key element of the considered displacement. This computation changes our view of the importance of individual structural members in the system and thereby should have a significant role in modern design.

To show the influence of finite element mesh complexity on the results of stochastic static sensitivity, the second model of the spatial dome is created, where one bar is divided into four beam elements, cf. Fig. 3. It yields a system consisting of 320 members. Thereby, we can determine not only which element but also which part of it generates the displacement at a specific point the most sensitive with respect to the cross-section area. This may be useful while examining the model in terms of the predicted path of failure or structure strengthening.

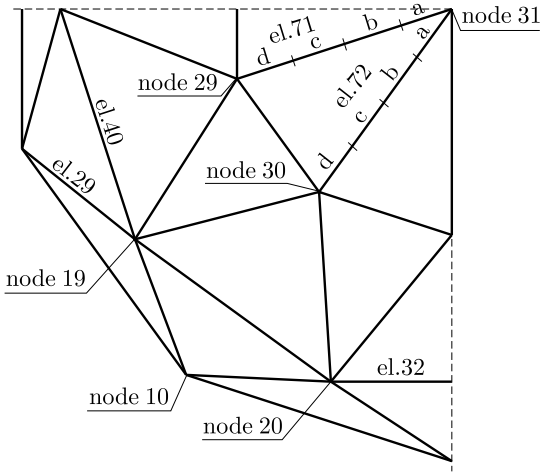

Fig. 3. Selected element number

The comparison of results received for the first and second numerical models are summarized in Table 5. It is clear that the sensitivity values obtained for the 320 element scheme is about

four times less than for the 80 element one. It seems to be natural, because we examine the sensitivity with respect to the cross-sectional areas of the elements four times shorter than at the beginning. Careful analysis presented by Weber (2014) gives the following dependence: the higher the number of finite elements in the mesh, the smaller impact of changes in cross-section areas of elements on the nodal displacements.

Table 5. Displacement design sensitivity - bar cross-sectional areas as random design variables, $[1/\text{cm}^2]$

Node number	Displ. direct.	q_{all} [cm]	Design el. number	Deterministic values	Expected values	Standard deviations
31	z	2.5	72a	−5.18116E-4	−5.34095E-4	1.04516E-4
			72b	−4.71989E-4	−4.86661E-4	9.51452E-5
			72c	−4.62112E-4	−4.76374E-4	9.25389E-5
			72d	−4.88431E-4	−5.03158E-4	9.66361E-5
29	x	1.0	71a	2.41918E-3	2.49298E-3	4.87353E-4
			71b	2.50572E-3	2.58152E-3	5.02619E-4
			71c	2.51620E-3	2.59250E-3	5.05291E-4
			71d	2.45059E-3	2.52538E-3	4.94002E-4

4. Concluding remarks

In the stochastic static sensitivity analysis by using the second order perturbation method, the same member, for example the cross-section area of an element, is both the design and random variable. It is significant in terms of the cost of numerical computations. It allows us to obtain complex results in the form of deterministic and expected values, and standard deviations. On the basis of the presented formulation, using the first two perturbation moments of random variables as the input data, we obtain the means and cross-covariances of the static design sensitivity with the second order accuracy. We receive results with the same precision as those in the Monte Carlo simulation, but by considering an $\widehat{r}$ order system of equations no $\widehat{r}^3$.

It is known that even small uncertainties in design parameters may have a large influence on results of displacements and internal forces, therefore this type of analysis seems to be very important in the design. Sensitivity analysis sometimes can provide a completely new insight into the work of a structure and the meaning of particular members in the considered system. It allows one to find the most sensitive point that determines the stability of the entire system.

In this paper, only design sensitivity with random parameters for the static case is presented. It seems that dynamic computations need to be an integral part of analysis of complex structures. Only by using both static and dynamic stochastic design sensitivity, we can determine the optimal solution for a system while taking into account all relevant aspects. Therefore, the dynamic sensitivity by deterministic and random parameters will be the subject of further work.

Acknowledgments

I would like to express my gratitude to promoter of my doctoral dissertation Professor Tran Duong Hien, for providing a computer programme for this research.

References

1. Adomian G., 1983, *Stochastic Systems*, Academic Press
2. Bathe K.-J., 1982, *Finite Element Procedures in Engineering Analysis*, Prentice-Hall

3. Choi K.K., Kim N.-H., 2010, *Structural Sensitivity Analysis and Optimization*, Springer
4. Ding J., Pan Z., Chen L., 2012, Parameter identification of multibody systems based on second order sensitivity analysis, *International Journal of Non-Linear Mechanics*, **47**, 1105-1110
5. Drewko J., Hien T.D., 2005, First- and second-order sensitivities of beams with respect to cross-sectional cracks, *Archive of Applied Mechanics*, **74**, 309-324
6. Fishman G.S., 1995, *Monte Carlo: Concept, Algoritms and Aplications*, Springer
7. Ghanem R.G., Spanos P.D., 1991, *Stochastic Finite Elements: A Spectral Approach*, Springer
8. Greene M.S., Liu Y., Chen W., Liu W.K., 2011, Computational uncertainty analysis in multiresolution materials via stochastic constitutive theory, *Computer Methods in Applied Mechanics and Engineering*, **200**, 309-325
9. Haug E.J., Choi K.K., Komkov V., 1986, *Design Sensitivity Analysis of Structural Systems*, Academic Press
10. Hien T.D., 2003, *Numerical Analysis of Stochastic Systems*, Wyd. PS
11. Hien T.D., Kleiber M., 1989, Computational aspects in structural design sensitivity analysis for statics and dynamics, *Computers and Structures*, **33**, 939-950
12. Hien T.D., Kleiber M., 1990, *POLSAP — A Finite Element Code for Deterministic and Stochastic Analyses of Large 3D Structures*, IPPT PAN
13. Hien T.D., Kleiber M., 1991, Stochastic structural design sensitivity of static response, *Computers and Structures*, **38**, 5/6, 659-667
14. Hisada T., Nakagiri S., 1981, Stochastic finite element method for structural safety and relability, *Proceedings of 3rd International Conference on Structural Safety and Reliability*, 395-402
15. Kincayd D., Cheney W., 2002, *Numerical Analysis. Mathematic of Scientific Computing*, 3rd ed., Wadsworth Group
16. Kleiber M., Hien T.D., 1992, *The Stochastic Finite Element Method*, Willey
17. Leet K.M., Uang Ch.-M., GilbertA.M., 2010, *Fundamentals of Structural Analysis*, 4th ed., Mc Graw-Hill
18. Li J., Chen J., 2009, *Stochastic Dynamics of Structures*, Wiley
19. Liu W.K., Belytschko T., Mani A., 1986, Random field finite elements, *International Journal for Numerical Methods in Engineering*, **23**, 1831-1845
20. Liu Y., Greene M.S., Chen W., Dikin A.D., Liu W.K., 2013, Computational microstructure characterization and reconstruction for stochastic multiscale material design, *Computer-Aided Design*, 65-76
21. Mroz Z., Bojczuk D., 2012, Shape and topology sensitivity analysis and its application to structural design, *Archive of Applied Mechanics*, **82**, 1541-1555
22. Mroz Z., Haftka R.T., 1986, First- and second-order sensitivity analysis of linear and nonlinear systems, *AIAA Journal*, **24**, 1187-1192
23. Niczyj J., 2003, *Multi-Criteria Optimization of Reliability and Estimation of the Technical State of Bar Structures Using Fuzzy Sets Theory* (in Polish), Wyd. PS
24. Rubinstein R.Y., Kroese D. P., 2008, *Simulation and the Monte Carlo Method*, 2nd ed., Willey
25. Spanos P.D., Ghanem R.G., 1989, Stochastic finite element expansion for random media, *Journal of Engineering Mechanics*, **115**, 5, 1035-1053
26. Weber H., Hien T.D., 2010, Elimination of beat effects in structures by added lumped mass, *Pomiary Automatyka Kontrola*, **56**, 617-619

27. Weber H., 2014, Numerical analysis of static and dynamic sensitivity of complex structural systems with random parameters, Ph.D Thesis, West Pomeranian University of Technology Szczecin

28. Zienkiewicz O.C., Taylor R.M., 1991, *The Finite Element Method*, McGraw-Hill

Manuscript received May 18, 2015; accepted for print November 24, 2015

JOURNAL OF THEORETICAL AND APPLIED MECHANICS
54, 3, pp. 795-810, Warsaw 2016
DOI: 10.15632/jtam-pl.54.3.795

AN EXPERIMENTAL AND NUMERICAL STUDY OF SUPERCAVITATING FLOWS AROUND AXISYMMETRIC CAVITATORS

S. Morteza Javadpour, Said Farahat
University of Sistan and Baluchestan, Department of Mechanical Engineering, Zahedan, Iran
e-mail: javadpour_m@yahoo.com; farahat@hamoon.usb.ac.ir

Hossein Ajam
Ferdowsi University of Mashhad, Department of Mechanical Engineering, Mashhad, Iran; e-mail: h.ajam@um.ac.ir

Mahmoud Salari
Imam Hossein University, Department of Mechanical Engineering, Tehran, Iran; e-mail: msalari@ihu.ac.ir

Alireza Hossein Nezhad
University of Sistan and Baluchestan, Department of Mechanical Engineering, Zahedan, Iran
e-mail: nezhadd@hamoon.usb.ac.ir

It has been shown that developing a supercavitating flow around under-water projectiles has a significant effect on their drag reduction. As such, it has been a subject of growing attention in the recent decades. In this paper, a numerical and experimental study of supercavitating flows around axisymmetric cavitators is presented. The experiments are conducted in a semi-open loop water tunnel. According to the Reynolds-Averaged Navier-Stokes equations and mass transfer model, a three-component cavitation model is proposed to simulate the cavitating flow. The corresponding governing equations are solved using the finite element method and the mixture Rayleigh-Plesset model. The main objective of this research is to study the effects of some important parameters of these flows such as the cavitation number, Reynolds number and conic angle of the cavitators on the drag coefficient as well as the dimensions of cavities developed around the submerged bodies. A comparison of the numerical and experimental results shows that the numerical method is able to predict accurately the shape parameters of the natural cavitation phenomena such as cavity length, cavity diameter and cavity shape. The results also indicate that the cavitation number declines from 0.32 to 0.25 leading to a 28 percent decrease in the drag coefficient for a 30° cone cavitator. By increasing the Reynolds number, the cavity length is extended up to 322% for a 60° cone cavitator.

Keywords: natural cavitation, mass transfer, water tunnel, finite element method, drag coefficient, axisymmetric cavitators

1. Introduction

Cavitation is the formation of vapor bubbles within a liquid when the liquid pressure falls less than the saturated vapor pressure while the fluid temperature remains lower than the boiling temperature at ambient conditions. Cavitation phenomena are observed in many hydrodynamic mechanical devices such as pumps, turbines, nozzles and marine propellers, which can significantly influence the performance of these devices. Cavitation may cause negative effects like structural damages, noise production and power losses in plants, or generates positive effects such as drag reduction of underwater moving bodies. However, for military purposes such as torpedoes, it is necessary to generate partially- or fully super-cavitating regime to reduce viscous drag intentionally.

The cavitation phenomenon is divided into three stages. The initial form of cavitation is the bubble stage which has destructive impacts on mechanical systems. Partial cavitation is another

stage in which the cavity region covers some parts of the body. The last stage is supercavitation in which size of the produced cavity exceeds the characteristic length of the body. When supercavitation occurs, the drag of the bodies surrounded by the cavity is reduced significantly. This is due to reduction in the skin friction drag which depends on viscosity of the near-wall fluid flow, where the vaporous pocket of supercavity surrounds the moving underwater body. Supercavitation can also be divided into natural and ventilated cases. The natural supercavitation occurs when free stream velocity rises above a certain limit ($U > 45\,\mathrm{m/s}$ at sea level, which increases with submersion depth, or p_∞ of the body. This phenomenon can also be achieved by decreasing the ambient pressure p_∞, which is only feasible in cavitation tunnels.

The static hydrodynamic forces and the cavity shape associated with cavitators were modeled by many researchers in the last decades (Logvinovich, 1969, 1980; Kuklinski *et al.*, 2001; Vasin and Paryshev, 2001; Wang *et al.*, 2005; Chen *et al.*, 2006; Chen and Lu, 2008; Deng *et al.*, 2004).

In the recent years, most of the studies related to supercavitating flows have been carried out numerically. Choi and Ruzzene (2006) explained stability conditions of a supercavitating vehicle using the finite element method (FEM). Hu and Gao (2010) used the cavitation model of Fluent software to simulate two-phase cavitating flows that contain water and vapor on axisymmetric bodies with disk cavitators. They showed that the vapor volume fraction and threshold phase-change pressure within the cavity under the same cavitation number gradually ascends as the Reynolds number increases. Huang *et al.* (2010) predicted the effects of cavitation over a NACA66 hydrofoil. They combined state equations of the cavitation model with a linear viscous turbulent method of mixed fluids in the Fluent software to simulate a steady cavitating flow. Since most cavitating flows are implemented at high Reynolds numbers and under unsteady conditions, a suitable turbulence model is required to provide an accurate estimate of cavitation. A variety of approaches, such as standard or modified two-equation turbulence models ($k-\varepsilon, k-\omega$), have been used to investigate the effects of turbulence on cavitating flows (Wu *et al.*, 2005; Liu *et al.*, 2009, Huang and Wang, 2011; Phoemsapthawee *et al.*, 2012). Large eddy simulation (LES) is another approach used in numerical cavitation modeling recently (Wang and Ostoja-Starzewski, 2007; Huuva, 2008; Liu *et al.*, 2010; Lu *et al.*, 2010). Nouri *et al.* (2008) used a modified version of the $k-\varepsilon$ turbulence model to simulate unsteady behavior of the cavity shedding and the re-entrant flow field. Park and Rhee (2012) studied the standard $k-\varepsilon$ and realizable $k-\varepsilon$ turbulence models by selecting Singhal's cavitation model at a cavitation number of 0.3. They observed that the standard $k-\varepsilon$ model was more efficient in capturing the re-entrant jet than the realizable $k-\varepsilon$ model.

In the past decade, several researchers have experimentally investigated supercavitating flows around the bodies. Most of these studies focused on the shape of generated cavitation, velocity and pressure distributions of the flow field as well as control and stability of supercavitating vehicles. Lindau *et al.* (2002) studied a supercavitating flow around a flat disk cavitator. Beside general cavitating flows, many studies on supercavitating flows have been undertaken using experimental and numerical methods. Experimental methods mainly rely on pressure measurements and image processing technology. Lee *et al.* (2008) studied ventilated supercavitation for a vehicle pitching up and down in the supercavity closed region. Hrubes (2001) studied a supercavitating flow in underwater projectiles using image production and processing to examine flight behavior, stability mechanism, cavity shape and in-barrel launch characteristics. Recently, Li *et al.* (2008) studied the cavitating flow by the flow visualization technique using a high-speed camera. They also measured details of the velocity field by the particle image velocimetry (PIV) to validate the computational models. The shape properties of natural and ventilated supercavitation on a series of projectile were investigated experimentally by Zhang *et al.* (2007). Wu and Chahine (2007) studied supercavitation on the back of a simulated projectile and measured the properties of the fluid inside the supercavity. Hua *et al.* (2004) conducted an experimental study on a cavitation tunnel with four axisymmetric bodies at different attack angles. Feng *et*

al. (2002) studied behavior of a supercavitating and cavitating flow around a conical body of evolution with and without ventilation at several attack angles. Zhang *et al.* (2007) performed a series of projectile and closed-loop water-tunnel experiments to study shape properties of natural and ventilated supercavitation. Saranjam (2013) did an experimental and numerical study of cavitation on an underwater moving object based on unsteady effects and dynamic behavior of the body.

Most experimental studies on supercavitation have been performed in a closed-loop water tunnel with only a few investigations examining the supercavitation flow in an open circuit water tunnel. Also, many experimental studies have been performed to obtain detailed information on the cavity shape (Fang *et al.*, 2002; Saranjam, 2013, Ji and Luo, 2010; Ahn *et al.*, 2010; Zou *et al.*, 2010). In this study, important supercavitation parameters including the shape of cavity, formation and the drag coefficient of the cavitator are investigated experimentally in a semi-open water tunnel complemented by a numerical analysis with the CFX software.

The paper is organized as follows: first a description of the physical problem followed by an experimental and numerical analysis is presented. Then, the experimental and computational results are presented and discussed. Finally, a summary of the results is given and the related conclusions are drawn.

2. Exprimental set-up

The experiments were conducted in a water tunnel located at the Marine Research Center of Iran. The tunnel is a semi-open loop water tunnel with a maximum velocity of 40 m/s. The water tunnel is equipped with a computerized control system, a high frequency data acquisitioning system, DAS, and a high-speed camera. A schematic view of the components of the water tunnel is shown in Fig. 1. The body of the model includes cone and cylindrical parts.

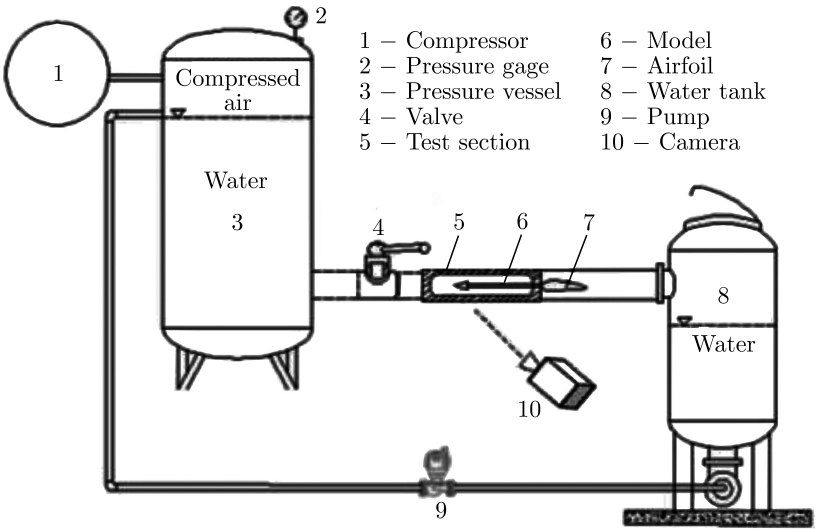

Fig. 1. A schematic view of the water tunnel. The figure is not to scale

The cavitating flow generated around the symmetric cone was investigated based on the experimental observations carried out in a water tunnel. Figure 2a shows the test section, where the cone cavitator is also placed. The test section has a cylindrical form with diameter of D and a length of $5D$ (Fig. 2b). The side walls of the test section are made of plexiglas with a highly smoothed surface. At the outlet of the test section, atmospheric pressure conditions occur and the fluid flow is discharged into an open surface storage tank. This water tunnel also includes a vertical cylindrical tank as the main water tank which is initially filled with pure water up

to a certain level and then the remaining volume is charged with pressurized air. Depending on the requested speed, the pressure of the air within the tank is varied. The model is attached to an electronically-load cell mounted outside the test section. The model with the cone cavitator is shown in Fig. 3. The base diameter of the cone cavitator is 10 mm and the cone angles for the noses are 30°, 45° and 60°. The cone length of y_0 is calculated according to the cone angle. The Reynolds number (Re) based on the diameter of the test section changes from 1120000 to 1480000 relative to the stream velocity within the test section.

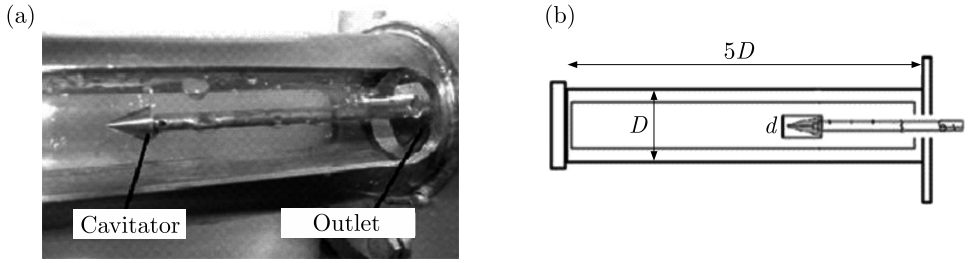

Fig. 2. (a) Test section of the water tunnel. (b) Dimensions of the test section

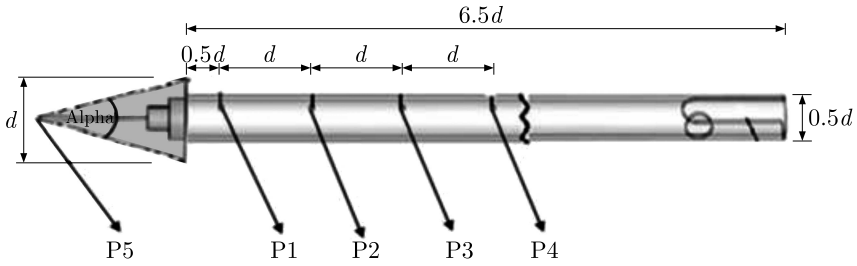

Fig. 3. A schematic view of the model and the position of pressure measurement cavities

The water tunnel was also equipped with some electronic pressure sensors to measure pressures in the flow. Five pressure sensors were used to gauge the pressure on the surface of the cylindrical part of the model (Fig. 3) behind the cone cavitator. Two pressure sensors were also placed inside the test section (P6) and the water tank (P7). The accuracy of sensors was ±0.01 bar. The output analog signals of the sensors were converted into digital signals via an A/D card, and the digital results were finally recorded online. It should be noted that the frequency of data recording was 1000 Hz for all of the sensors in the experiments. The cavitation profile formed around the cavitator was captured by a high-speed camera with a frame rate of 600 fps.

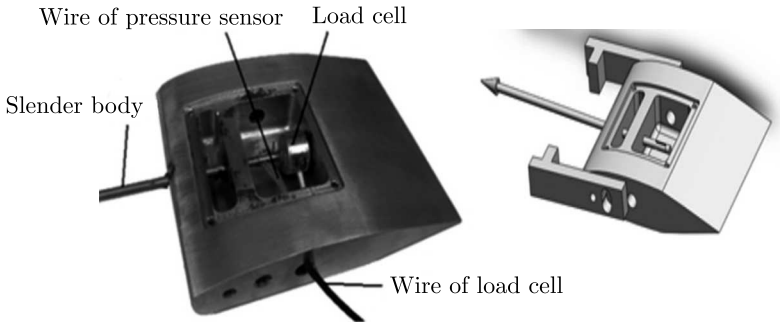

Fig. 4. Load cell mounted within the airfoil

To measure the drag force, an electronically-load cell of 49 N was mounted within a standard airfoil at the outlet of the test section (Fig. 4). Also, as shown in Fig. 4, the connecting wires of

the load cell and the pressure sensor were driven out of the water tunnel test section via that airfoil.

To validate the experimental results of this study, the results of the cavitating flow around a flat disk were compared with the results of Franc and Michel (2004). In Fig. 5, the results of the present study for dimensionless cavity length (Lc/d) with respect to the cavitation number of the flow are compared with the experimental data of Franc and Michel. As can be seen, the results are in good agreement with their experimental data.According to Eq. (2.1), the theoretical value of the blockage cavitation number is about 0.211, whereas the minimum value of the cavitation number at the maximum velocity of the present tests is about 0.25. Since $\sigma_{blockage} < 0.25$, the effect of blockage on the measured drag coefficient and cavity shape is expected to be negligible

$$\sigma_{blockage} = \frac{S_u^2}{S_d^2} - 1 \tag{2.1}$$

where S_u and S_d are the cross-sectional areas of the upstream and downstream regions of the liquid flow, respectively.

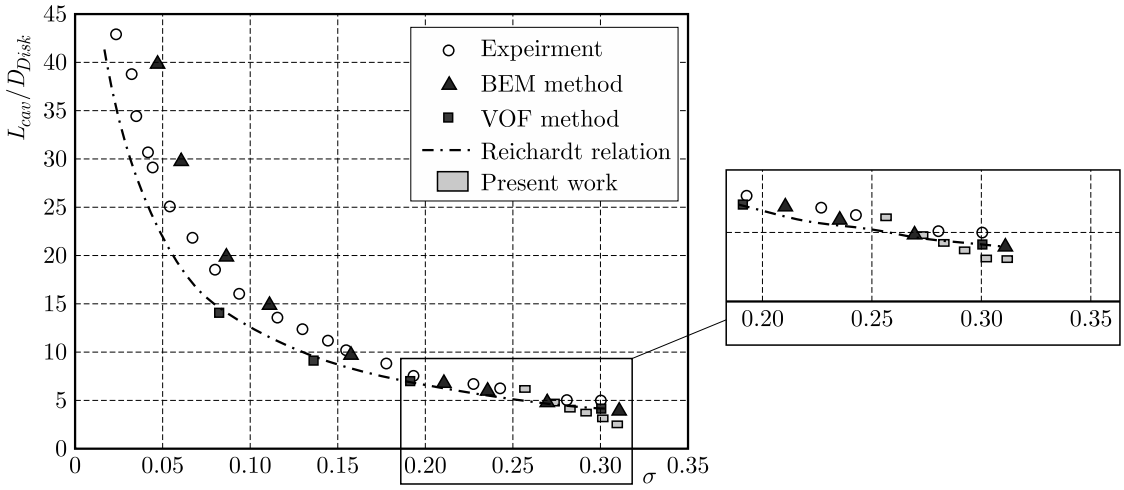

Fig. 5. Comparison of the present experimental results with the results of Franc and Michel (2004)

One of the fundamental dimensionless parameters for natural supercavities is the Froude number, $\mathrm{Fr} = U_\infty/\sqrt{gD}$. In these tests, the Froude number varies from 44.7 to 59 with the cavitation number ranging between 0.25 and 0.36. Semenenko (2001), citing Logvinovitch (1973), states that the effect of gravity can be significant if $\sigma_v \mathrm{Fr} < 2$. Thus, at the present application, there is no need to incorporate the gravity effects.

3. Mathematical models

3.1. Governing equations

In this study, a mixture-type multiphase-flow model based on the isotropic hypothesis for the fluid along with the Reynolds averaged Navier-Stokes (RANS) equations are employed. The mass and momentum conservation equations are solved numerically to obtain the velocity and pressure fields. The mass, momentum, and volume fraction equations can be written as

$$\begin{aligned}
&\frac{\partial \rho_m}{\partial t} + \frac{\partial}{\partial x_i}(\rho_m u_i) = 0 \\
&\frac{\partial}{\partial t}(\rho_m u_i) + \frac{\partial}{\partial x_j}(\rho_m u_i u_j) = -\frac{\partial P}{\partial x_i} + \frac{\partial}{\partial x_j}\Big[\mu_m\Big(\frac{\partial u_i}{\partial x_j} + \frac{\partial u_j}{\partial x_i}\Big)\Big] + \frac{\partial}{\partial x_j}(\tau_{tij}) \\
&\frac{\partial}{\partial t}(\rho_v \alpha_v) + \frac{\partial}{\partial x_i}(\rho_v \alpha_v u_i) = m^- - m^+
\end{aligned} \tag{3.1}$$

where α_v is the vapor volume fraction, ρ_v is vapor density, ρ_l is liquid density and m^-, m^+ are mass transfer rates related to evaporation and condensation in cavitation, respectively. The density and dynamic viscosity of the mixture is calculated as

$$\rho_m = \alpha_v \rho_v + (1 - \alpha_v)\rho_l \qquad \mu_m = \alpha_v \mu_v + (1 - \alpha_v)\mu_l \tag{3.2}$$

The non-dimensional parameters of interest in this study, including the cavitation number, drag coefficient and the Reynolds number, are defined as

$$\sigma_v = \frac{P - P_v}{\frac{1}{2}\rho_l U_\infty^2} \qquad C_d = \frac{F_d}{\frac{1}{2}\rho_l U_\infty^2 A} \qquad \mathrm{Re} = \frac{\rho_l U_\infty D}{\mu_l} \tag{3.3}$$

where P_v, F_d and A are the vapor pressure, drag force and area of test section, respectively.

3.2. Turbulence model

The Reynolds stress can be modeled through the Boussinesq hypothesis according to the following equation

$$\tau_{tij} = \mu_t\Big(\frac{\partial u_i}{\partial x_j} + \frac{\partial u_j}{\partial x_i}\Big) - \frac{2}{3}\Big(\rho k + \mu_t \frac{\partial u_k}{\partial x_k}\Big)\delta_{ij} \tag{3.4}$$

The standard $k-\varepsilon$ turbulence model,which is based on the Boussinesq hypothesis with transport equations for the turbulent kinetic energy k and its dissipation rate ε is adopted for the turbulence closure. The turbulent viscosity μ_t, is computed by combining k and ε as $\mu_t = (\rho_m C_\mu k^2)/\varepsilon$, and the turbulence kinetic energy and its rate of dissipation are obtained from the transport equations as follows

$$\begin{aligned}
&\frac{\partial(\rho_m k)}{\partial t} + \frac{\partial(\rho_m u_j k)}{\partial x_j} = \frac{\partial}{\partial x_j}\Big[\Big(\mu + \frac{\mu_t}{\sigma_k}\Big)\frac{\partial k}{\partial x_j}\Big] + G_k + G_b - \rho\varepsilon - Y_M \\
&\frac{\partial(\rho_m \varepsilon)}{\partial t} + \frac{\partial(\rho_m u_j)}{\partial x_j} = \frac{\partial}{\partial x_j}\Big[\Big(\mu + \frac{\mu_t}{\sigma_\varepsilon}\Big)\frac{\partial \varepsilon}{\partial x_j}\Big] + C_{\varepsilon 1}\frac{\varepsilon}{k}(G_k + C_{3\varepsilon}G_b) - C_{\varepsilon 2}\rho\frac{\varepsilon^2}{k}
\end{aligned} \tag{3.5}$$

where C_μ is an empirical constant (0.09). Here, the model constants $C_{\varepsilon 1}$, $C_{\varepsilon 2}$, σ_k and σ_ε are 1.44, 1.92, 1.0 and 1.3, respectively. The turbulent viscosity is used to calculate the Reynolds stresses to close the momentum equations. To model the flow close to the wall, a scalable wall-function approach has been adopted. The finite volume method is employed to discretize the integral-differential equations. The second-order upwind scheme is applied to discretize the turbulent transportation equations.

3.3. Cavitation model

To model the cavitating flows, the two phases of liquid and vapor as well as the phase transition mechanism between them need to be specified. In this study, a "two-phase mixture" approach is introduced by the local vapor volume, which has the spatial and temporal variation of the vapor function, as described by the transport equation together with the source terms for the mass transfer rate between the two phases. Numerical models of cavitation differ in terms of

the mass transfer term $\dot{m}$. The most common semi analytical models are the Singhal cavitation model (2002), Merkle model (1998), Schnerr and Sauer model (2001) and Kunz model (1999). In the present study, the cavitation model developed by Singhal *et al.* (2002) is used. The source terms included in the transport equation define vapor generation (liquid evaporation) and vapor condensation respectively. The source terms are functions of local flow conditions (static pressure and velocity) and fluid properties (liquid and vapor phase densities, saturation pressure and liquid vapor surface tension). The source terms are derived from the Rayleigh-Plesset equation, where high-order terms and viscosity terms can be found according to Singhal *et al.* (2002)

$$\dot{m}^- = C_{evap}\frac{V_{ch}}{\sigma}\rho_l\rho_v\sqrt{\frac{2}{3}\frac{p_v - p}{\rho_l}}\frac{\rho_l\alpha_l}{\rho_m} \qquad \dot{m}^+ = C_{cond}\frac{V_{ch}}{\sigma}\rho_l\rho_v\sqrt{\frac{2}{3}\frac{p - p_v}{\rho_l}}\frac{\rho_v\alpha_v}{\rho_m} \tag{3.6}$$

where $C_{evap} = 0.02$, $C_{cond} = 0.01$ and $V_{ch} = \sqrt{k}$, p_v, σ and k denote the saturated pressure of liquid, surface tension and turbulence energy, respectively.

4. Numerical method

Numerical simulation (Ansys CFX 14) can be used to detect cavitation in the cavitation flow around the cone cavitator. It is important to note that ANSYS CFX uses the CV-FEM (control volume-finite element) method, with the latter having superior performance with the hexahedral mesh than with the tetrahedral one, which tends to degrade the computing efficiency.

Given the application of the CV-FEM method in ANSYS CFX 14, the linearized momentum and mass equations are solved simultaneously with an algebraic multi-grid method based on the additive correction multi-grid strategy. The implementation of this strategy in ANSYS CFX has been found to offer a robust and efficient prediction of the cavitation in pumps (Athavale *et al.*, 2002; Pouffary *et al.*, 2003). The high resolution scheme is adopted in space discretization to solve the differential equation as it has the second-order space accuracy.

5. Computational domain and boundary condition

The domain of the problem and boundary conditions are shown in Fig. 6.

The boundary conditions in the water tunnel are as follows:

- At the inlet, the velocity components, volume fractions, turbulence intensity and the length scale are specified.
- At the outlet, the pressure, volume fractions, turbulence intensity and the length scale are specified.
- The wall of the water tunnel and cavitator is assumed to be in no slip conditions.

The computational domain is $33d$ in length and $5d$ in diameter. To show the grid independency of the results, grids similar to that of Fig. 7 are used. Then, length and diameter cavity fractions are calculated and plotted in Fig. 8 at four different nodes ($N = 120\,000$, $N = 340\,000$, $N = 530\,000$ and $N = 720\,000$ nodes). It is observed that changes between the last two grids are small, so the grid with $N = 530\,000$ nodes is chosen for the present study.In the total domain, the structural grid with 530 000 nodes is formed. Figure 9 shows a 2D view of the mesh near the cavitator. Since the interaction between the near-wall flow and cavity should be taken into consideration, the near-wall mesh of the test body is well refined to ensure non-dimensional normal distance from the wall. The value of y^+ at the wall surface of the cavitator is smaller than 100 (Fig. 9).

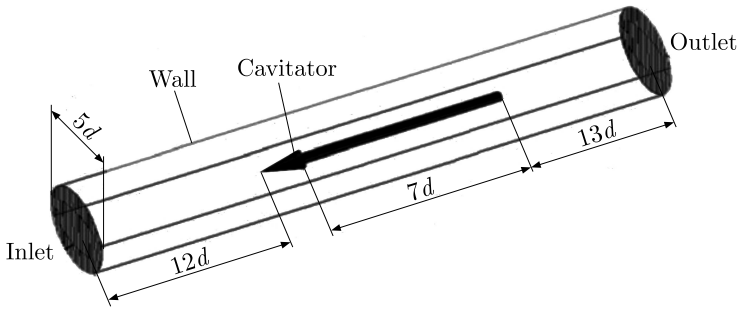

Fig. 6. Boundary condition and domain extent. The figure is not to scale

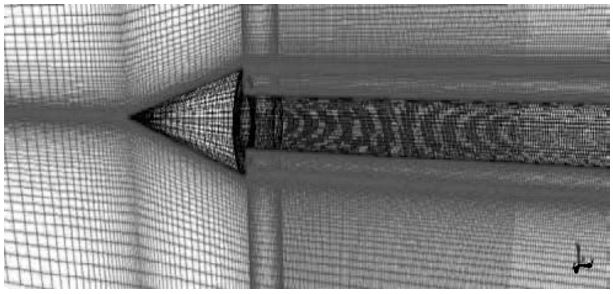

Fig. 7. The structure grid near the body

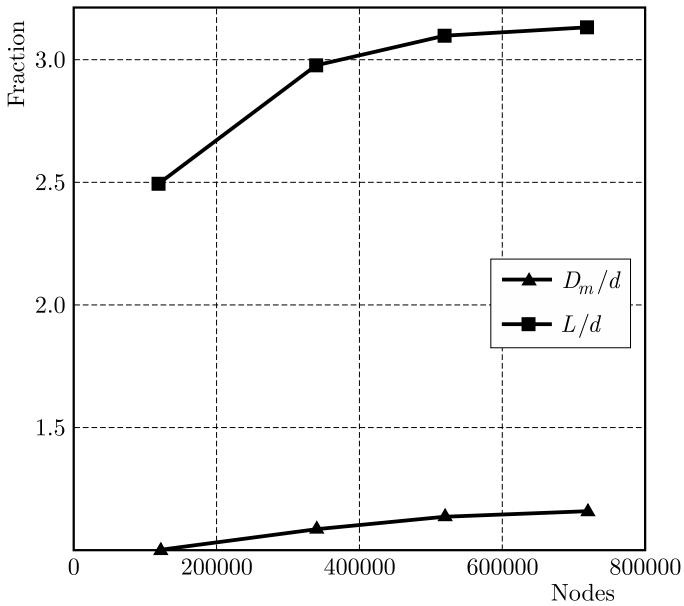

Fig. 8. Variations in length and diameter of cavity fractions at four different nodes

6. Results and discussion

6.1. Drag coefficient

In this Section, the drag force and drag coefficient are investigated for different cavitators. Figure 10 shows the drag force of the cavitator for $112 \cdot 10^4 < \mathrm{Re} < 148 \cdot 10^4$. It is observed that the drag force rises at a certain slope when velocity is increased. Generally, the drag is divided into pressure drag and viscous drag. The pressure remains constant in the cavity, but by decreasing the flow velocity, the pressure rises in the tip of the cavitator. Thus, as the flow velocity decreases, the friction drag drops and the pressure drag rises. This leads to overall

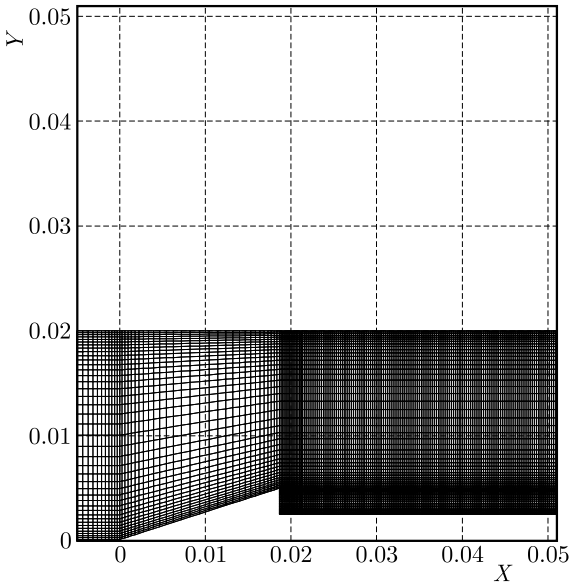

Fig. 9. Mesh near the cavitator

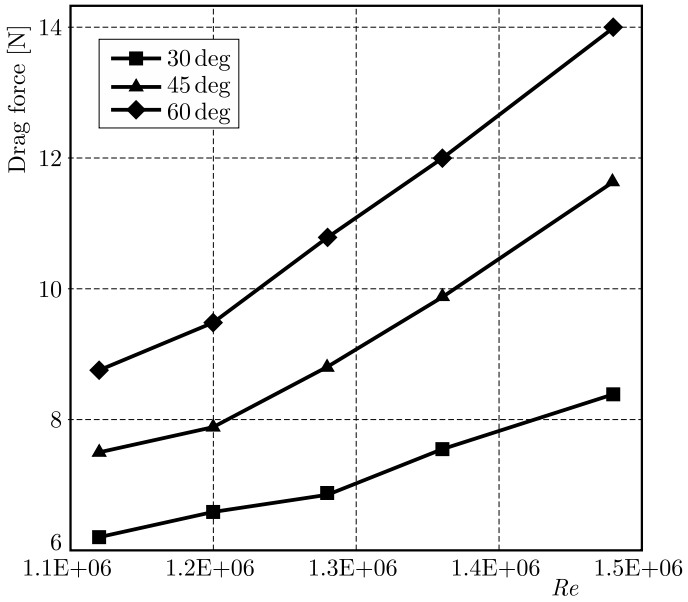

Fig. 10. Variation of the drag force found experimentally with the Reynolds number

reduction of the total drag. Finally, the drag coefficient goes up because variation in the square of velocity is greater than the total drag reduction (Eq. $(3.3)_2$).

Figures 11a and 11b indicate the experimental and numerical drag coefficients versus the cavitation and Reynolds numbers for various cavitator angles. A detailed comparison between the numerical results and available experimental data shows their good agreement for various angles of the cavitator. The results suggestthat the drag coefficient declines when the Reynolds number is increased. Figure 11b shows that at a constant Reynolds number, the drag coefficient increases proportionally to a rise in the cavitator angle. Equation $(3.3)_1$ illustrates the relation between flow velocity and the cavitation number. In the range of Reynolds numbers tested, the cavitation number variation is reduced with an increase in the cavitator angle (Fig. 11b). For $112 \cdot 10^4 < \mathrm{Re} < 148 \cdot 10^4$, by increasing the angle of the cavitator, changes in the cavitation number are lessened, and the slope of the drag coefficient versus the Reynolds number is reduced. In other

words, by increasing the angle of the cavitator, similar changes occur in the square velocity and the drag force (Eq. $(3.3)_2$). Also, changes in the drag coefficient and cavitation number are similar for different cavitator types. For example, in a 60° cone cavitator, the cavitation number variation is as small as the drag coefficient variations.

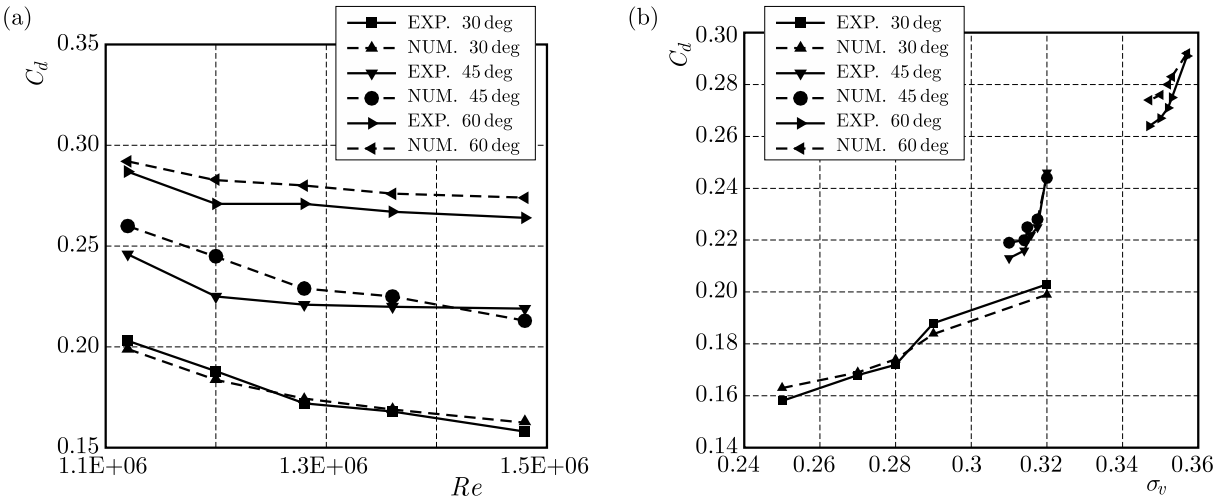

Fig. 11. Variation of the drag coefficient with the Reynolds number (a) and with the cavitation number (b)

6.2. Cavity shape

Figure 12 shows the effect of velocity variations on the cavity shape in the 30° cone cavitator. The results indicate that the effect of velocity on the length of cavity is not significant. In Fig. 13, the shape of cavity for different cavitators at the velocity of 37 m/s is displayed. The angle of the cavitator can affect the shape and type of cavitation.

Figure 16 shows contours of the volume fraction and streamlines around the 30° cone cavitator. Figures 15 and 16 show contours of the pressure coefficient and turbulent eddy viscosity of the fully developed cavitating flow around the 45° cone cavitator with the cavitation number of 0.33. A comparison of Figs. 15 and 16 shows that the turbulent eddy viscosity is larger where the cavity is closed as a result of the re-entrant jet. Also, it is observed that the cavity pressure remains constant and where the cavity is closed, the pressure value peaks and then drops gradually. Thus, using this phenomenon, the length of cavity is estimated. For instance, when the flow velocity is 32 m/s, the cavity length of the 30° cavitator will be 30.9 mm (Fig. 17).

The shape of the simulated cavity is compared with the one shown for the 30° cone cavitator in Fig. 18. As can be seen, there is a good qualitative agreement between the experimental and numerical results obtained using CFX.

The experimental and numerical results indicate that with an increase in the Reynolds number, the maximum diameter of cavity rises to reach a nearly constant value. According to Fig. 19a, the relationship between flow velocity and natural cavitation numbers is weakened as the angle of the cavitator decreases. Moreover, the curve slope decreases as the Reynolds number rises. For lower angles, the results reveal that the maximum diameter of cavity remains constant as the cavitation number increases (Fig. 19b). For example, for 45° and 60° cavitators, the variation in the maximal diameter of cavity is negligible because the cavitation number variation is insignificant.

Figures 20a and 20b indicate the non-dimentionalized supercavity length for 30°, 45° and 60° cone cavitators for which a comparison of the numerical and experimental results have been made. Figure 20a shows that the increased Reynolds number enlarges the cavity length at a

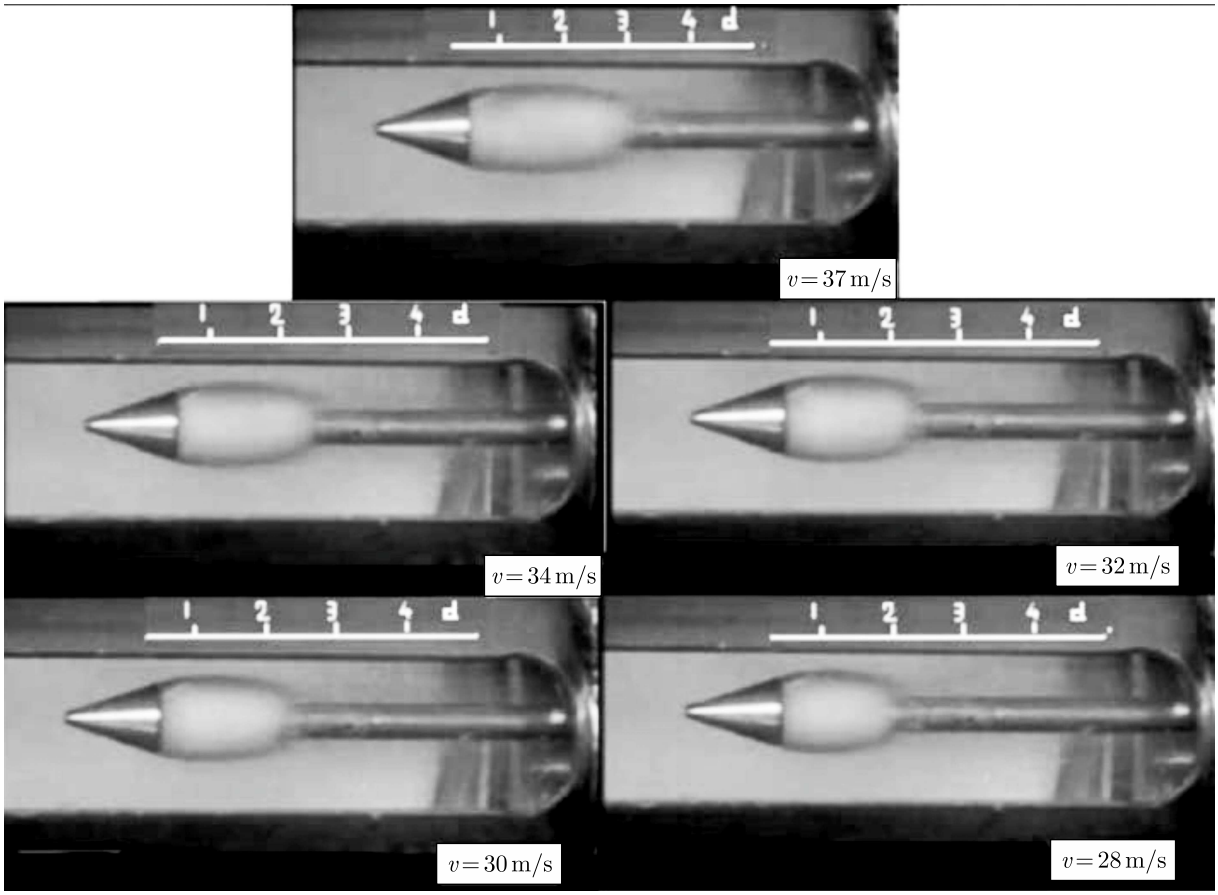

Fig. 12. Experimental results related to formation, evaporation, and condensation of supercavitation around the 30° cone cavitator in the water tunnel under different velocities

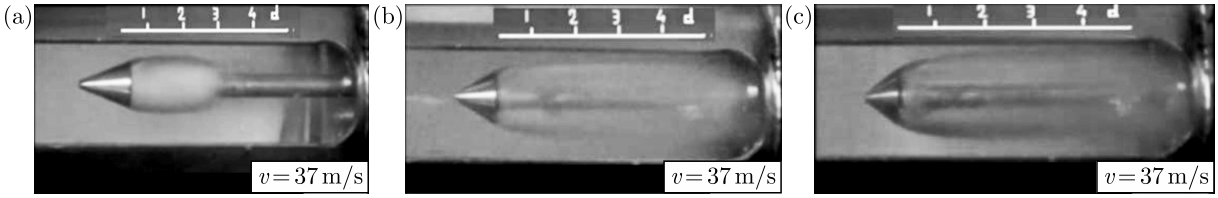

Fig. 13. Experimental results related to formation, evaporation and condensation cavity at different cavitators in the water tunnel at a velocity of 37 m/s; (a) 30° cone cavitator, (b) 45° cone cavitator, (c) 60° cone cavitator

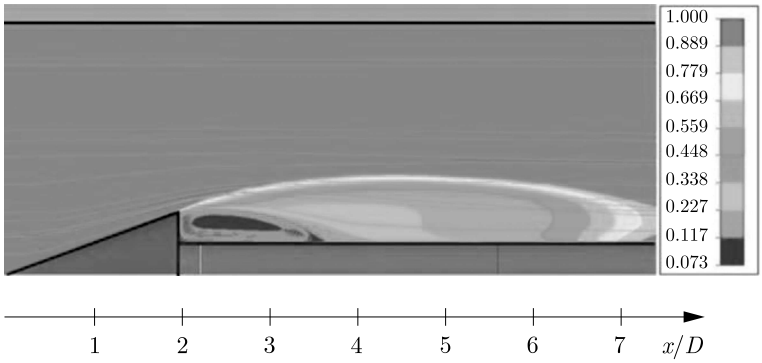

Fig. 14. Streamlines and water volume fraction contours around the 30° cone cavitator at the velocity of 37 m/s

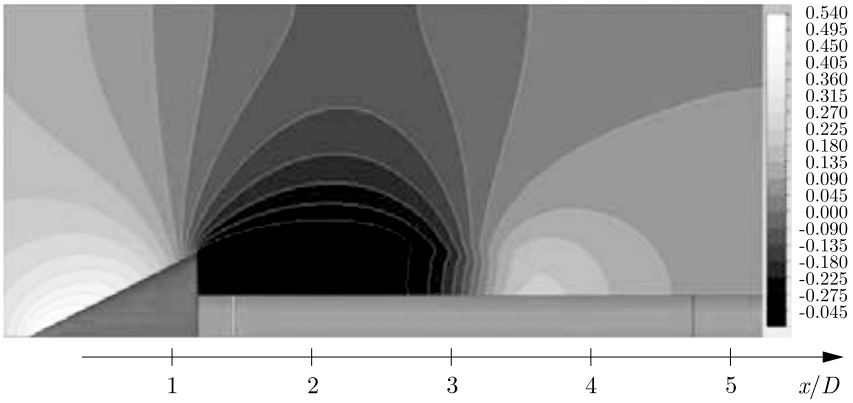

Fig. 15. Pressure coefficient contours around the 45° cone cavitator

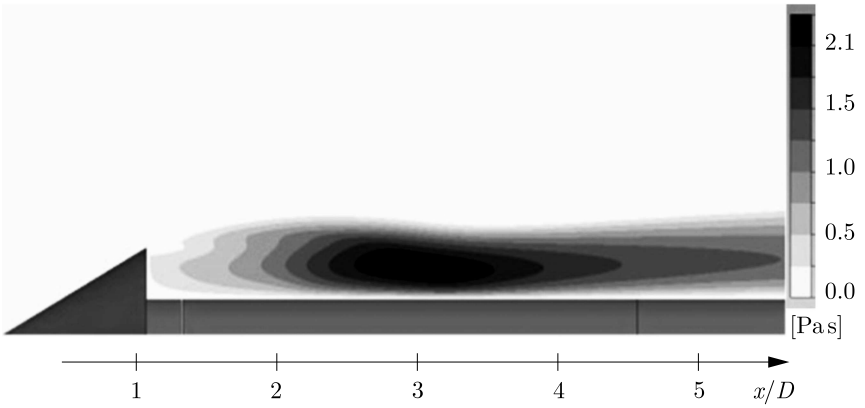

Fig. 16. Turbulent eddy viscosity contours around the 45° cone cavitator

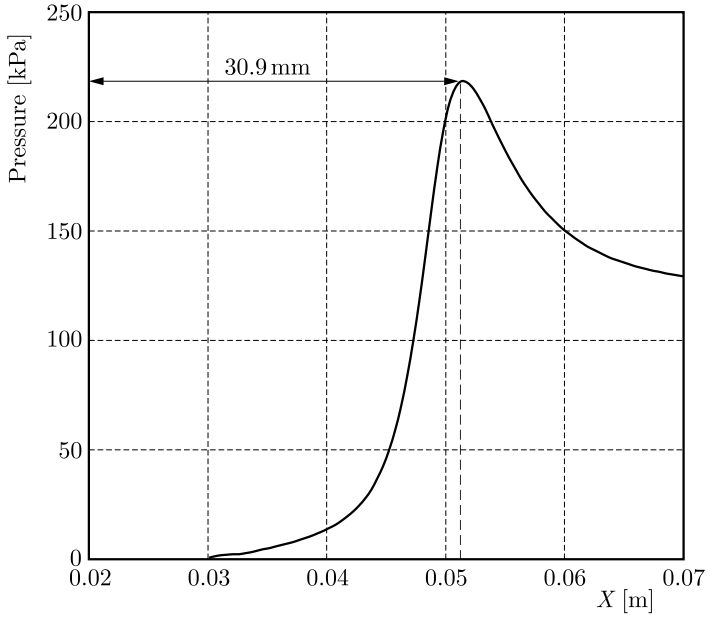

Fig. 17. Cavity length of the 30° cone cavitatorat $v = 32\,\mathrm{m/s}$

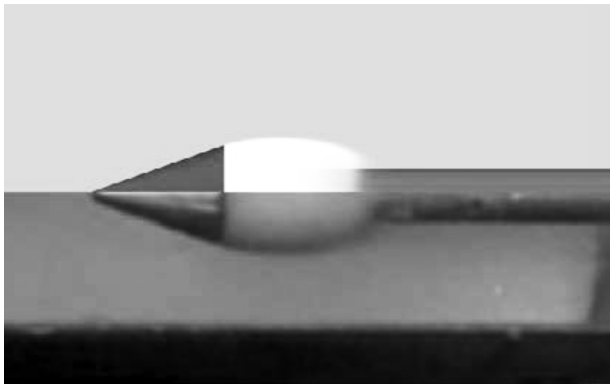

Fig. 18. The shape of the natural cavity from experiments and simulations at $v = 28\,\mathrm{m/s}$ for the 30° conecavitator

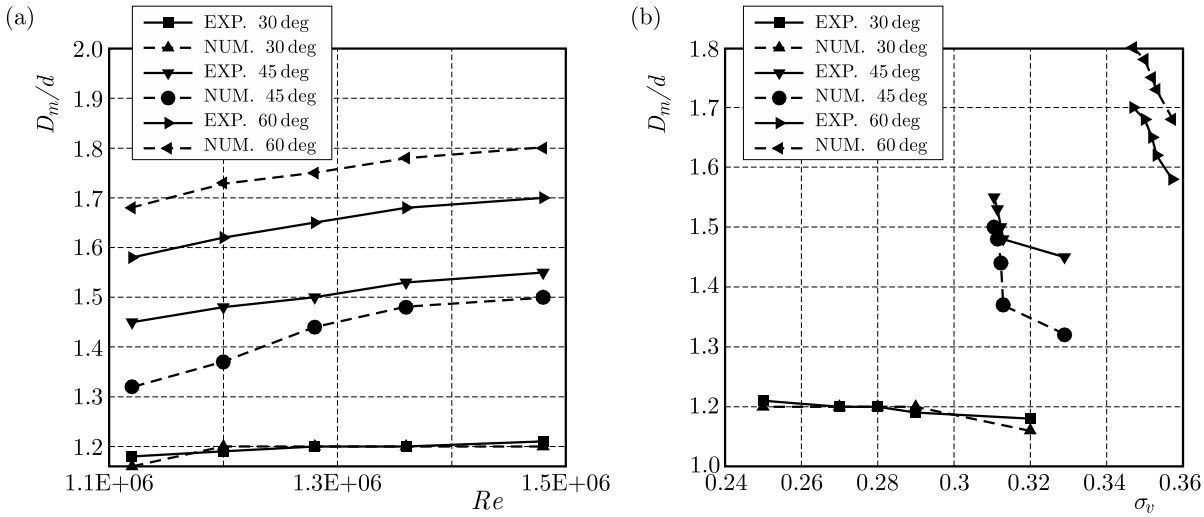

Fig. 19. Variation of the maximum cavity diameter (a) with the Reynolds number and (b) with the cavitation number for various types of cavitators

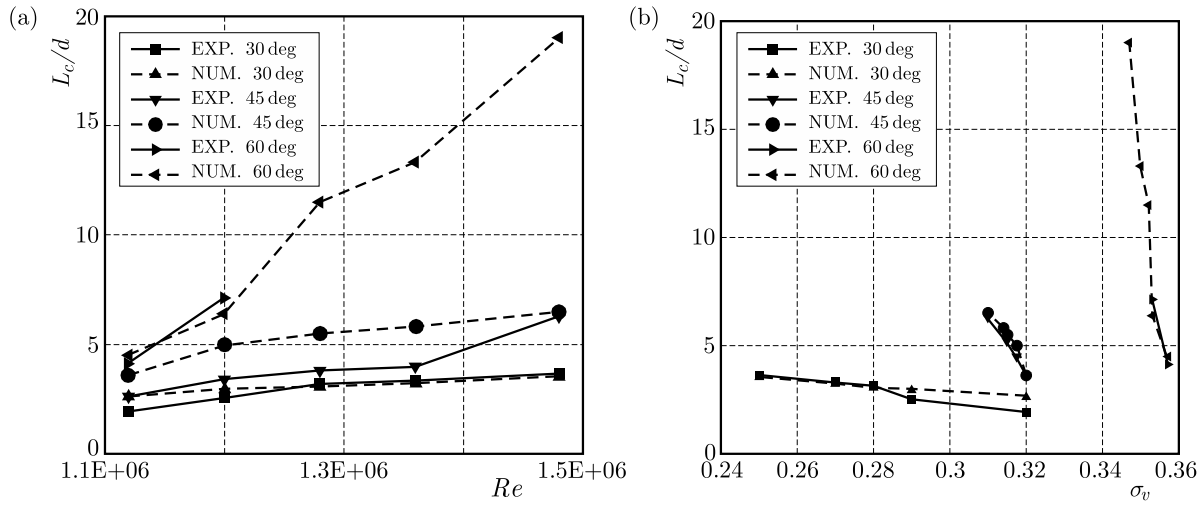

Fig. 20. Cavity lengths variation (a) with the Reynolds number and (b) with the cavitation number for various types of cavitator

constant slope.The length of the supercavity increases exponentially when the cavitation number decreases (Fig. 20b). Also, by increasing the angle of the cavitator, the cavity length variation is augmented. The results indicate that the cavity length is associated with the cavitation number and flow velocity along with a number of other parameters like geometry of the cavitator. Note that the cavitator length for higher angles rises significantly with an increase in the Reynolds number. A comparison of the numerical and experimental results confirms the acceptable level of accuracy.

7. Conclusion

In this paper, the cavitating flow around some cone cavitators is studied both numerically and experimentally. The experimental tests are carried out in a semi-open loop water tunnel. The effects of the cone angle of cavitators, magnitude of the free stream velocity and the cavitation number on the shape of the formed cavity and their drag coefficients are investigated.

To sum up, the following conclusions can be drawn:

- A good agreement is found between the numerical and experimental results, indicating that the proposed method is capable of predicting the cavitating flow to calculate both the cavity shape and its length.
- The cavity length is directly proportional to the cone angle of the cavitator. Thus, a way to increase the cavity length is to increase the cone angles of the cavitators.
- The drag coefficient of bodies drops as the cavitation number decreases. The drag coefficient variation is similar to cavitation number variation. If the Reynolds number remains constant, a decrease in the cone angle of the cavitator reduces the drag coefficient down to approximately 40%. Also, by increasing the cavitation number from 0.25 to 0.32, the drag coefficient is increased by 28% for the cavitator of 30° cone angle.
- The maximum diameter of the cavity shape and its length decrease as the cavitation number increases. For a cavitator with a 60° cone angle, the reduction of the maximum diameter and length of the cavity is 1.2 and 6.3 times greater than in the 30° cone cavitator respectively.
- For a free-stream velocity of $v = 28\,\mathrm{m/s}$, the difference of cavity length for the three cavitators is almost negligible (2.2 cm), but with an increase in the flow velocity, the displacement of cavity length for the three cavitators is increased. The cavity diameter is reduced as the flow velocity declines at a constant rate for the three cavitators. Also, by increasing the Reynolds number from $112 \cdot 10^4$ to $148 \cdot 10^4$, the cavity length increases by about 95 to 375% for the 60° cone cavitator.

References

1. Ahn B., Ahn C., Lee C., Kim T., 2010, Experimental and numerical studies on supercavitating flow of axisymmetric cavitators, *International Journal of Naval Architecture and Ocean Engineering*, **2**, 39-44
2. Athavale M.M, Li H.Y., Jiang Y., Singal A.K., 2002, Application of the full cavitation model to pumps and Inducers, *International Journal of Rotating Machinery*, **8**, 45-56
3. Chen Y., Lu C.-J., 2008, A homogenous-equilibrium model based numerical code for cavitation flows and evaluation by computation cases, *Journal of Hydrodynamics*, **20**, 2, 186-194
4. Chen Y., Lu C.-J., Wu L., 2006, Modelling and computation of unsteady turbulent cavitation flow, *Journal of Hydrodynamics, Ser. B*, **18**, 5, 559-566

5. Choi J.Y., Ruzzene M., 2006. Stability analysis of supercavitating underwater vehicles with adaptive cavitator, *International Journal of Mechanical Sciences*, **48**, 1360-1370

6. Deng F., Zhang Y., Chen W., Yuan X., Dang J., 2004, Experimental investigation on the incipiency and the shape of supercavity for slender bodies with different headforms, *Journal of Northwestern Polytechnical University*, **22**, 3, 269273

7. Fong X.-M., Lu C.-J., Hu T.-Q., 2002, Experimental research on a supercavitating slender body of revolution with ventilation, *Journal of Hydrodynamics, Ser. B*, **2**, 17-23

8. Franc J.P., Michel J.M., 2004, *Fundamentals of Cavitation*, Section 6, Kluwer Academic Publisher, Netherlands

9. Hrubes J.D., 2001, High-speed imaging of supercavitating underwater projectiles, *Experiments in Fluids*, **30**, 57-64

10. Huang B., Wang G., 2011, Partially averaged Navier-Stokes method for time-dependent turbulent cavitating flows, *Journal of Hydrodynamics*, **23**, 1, 26-33

11. Huang S., He M., Wang C., Chang X., 2010, Simulation of cavitating flow around a 2-D hydrofoil, *Journal of Marine Science and Application*, **9**, 63-68

12. Hu X., Gao Y., 2010, Investigation of the disk cavitator cavitating flow characteristics under relatively high cavitation number, *Applied Mechanics and Materials*, **29-32**, 2555-2562

13. Huuva T., 2008, Large eddy simulation of cavitating and non-cavitating flow, PhD thesis, Chalmers University of Technology, Sweden

14. Ji B., Luo X., 2010, Numerical investigation of the ventilated cavitating flow around an underwater wehicle based on a three-component caviation model, *Journal of Hydrodynamics*, **22**, 6, 753-759

15. Kuklinski R., Henoch C., Castano J., 2001, Experimental study of ventilated cavities on dynamic test model, *4th International Symposium on Cavitation*, California, USA

16. Kunz R.F., Boger D.A., Chyczewski T.S., Stinebring D.R., Gibeling H.J., Govindan T.R., 1999. Multi-phase CFD analysis of natural and ventilated cavitation about submerged bodies, *ASME Paper FEDSM*, 99-7364

17. Launder B.E., Spalding D.B., 1972, *Lectures in Mathematical Models of Turbulence*, Academic Press, London, UK

18. Lee Q.-T., Xue L.-P., He Y.-S., 2008, Experimental study of ventilated supercavities with a dynamic pitching model, *Journal of Hydrodynamics*, **20**, 4, 456-460

19. Li X., Wang G., Zhang M., Shyy W., 2008, Structures of supercavitating multiphase flows, *Journal Thermal Science*, **47**, 1263-1275

20. Lin H., Lin Q., Hu T., 2004, An experimental study on fluctuating hydrodynamic loads on cavitating axisymmetric slender bodies, *Journal of Hydrodynamics, Ser. A*, **19**, 6, 794-800

21. Lindau J.W., Kunz R.F., Boger D.A., Stinebring D.R., Gibeling H.J., 2002, High Reynolds number, unsteady, multiphase CFD modeling of cavitating flows, *Journal of Fluids Engineering, Transactions of ASME*, **124**, 3, 607-616

22. Liu D., Hong F., Lu F., 2010, The numerical and experimental research on unsteady cloud cavitating flow of 3D elliptical hydrofoil, *Journal of Hydrodynamics*, **22**, 5, 759-763

23. Liu D., Liu S., Wu Y., Xu H., 2009, LES numerical simulation of cavitation bubble shedding on ALE 25 and ALE 15 hydrofoils, *Journal of Hydrodynamics*, **21**, 6, 807-813

24. Logvinovich G.V., 1969, *Hydrodynamics of Flows with Free Boundaries*, Kiev, USSR, Naukova Dumka

25. Logvinovich G.V., 1980, Some problems in planing surfaces (in Russian), *Trudy Tsagi*, **2052**, Moscow, Russia, Central Aero and Hydrodynamics Institute

26. Lu N., Bensow R.E., Bark G., 2010, LES of unsteady cavitation on the delft twisted foil, *Journal of Hydrodynamics, Ser. B*, **22**, 5, 784-791

27. Merkle C.L., Feng J., Buelow P.E.O., 1998, Computational modeling of the dynamics of sheet cavitation, *Proceeding of the 3rd International Symposium on Cavitation (CAV98)*, Grenoble, France

28. Nouri N.M., Shienejad A., Eslamdoost A., 2008, Multi phase computational fluid dynamics modeling of cavitating flows over axisymmetric head-forms, *IUST International Journal of Engineering Science*, **19**, 1/5, 71-81

29. Park S., Rhee S.H., 2012, Computational analysis of turbulent supercavitating flow around a twodimensional wedge-shaped cavitator geometry, *Computers and Fluids*, **70**, 73-85

30. Phoemsapthawee S., Leroux J., Kerampran S., Laurens J., 2012, Implementation of a transpiration velocity based cavitation model within a RANS solver, *European Journal of Mechanics B/Fluids*, **32**, 45-51

31. Pouffary B., Fortes-Patella R., Reboud J.L., 2003, Numerical simulation of cavitating flow around a 2D hydrofoil: a barotropic approach, *Fith International Symposium on Cavitation*, Osaka, Japan

32. Saranjam B., 2013, Experimental and numerical investigation of an unsteady supercavitating moving body, *Ocean Engineering*, **59**, 9-14

33. Schnerr G., Sauer J., 2001, Physical and numerical modeling of unsteady cavitation dynamics, *4th International Conference on Multiphase Flows*, New Orleans, USA

34. Semenenko V.N., 2001, Dynamic processes of supercavitation and computer simulation, *RTO AVT Lecture Series on Supercavitatingows at VKI*

35. Singhal A.K., Athavale M.M., Li H., Jiang Y., 2002, Mathematical basis and validation of the full cavitation model, *Journal of Fluids Enginnering*, **124**, 617-624

36. Vasin A.D., Paryshev E.V., 2001, Immersion of a cylinder in a fluid through a cylindrical free surface, *Journal of Fluid Dynamics*, **36**, 2, 168-177

37. Wang G., Ostoja-Starzewski M., 2007, Large eddy simulation of a sheet/cloud cavitation on a NACA 0015 hydrofoil, *Applied Mathematical Modelling*, **31**, 3, 417-447

38. Wang H., Zhang J., Wei Y., Yu K., Jia L., 2005, Study on relations between cavity form and typical cavitator parameters, *Journal of Hydrodynamics, Ser. A*, **20**, 2, 251-257

39. Wu J., Wang G., Shyy W., 2005, Time-dependent turbulent cavitating flow computation with interfacial transport and filter-based models, *International Journal for Numerical Methods in Fluids*, **49**, 739-746

40. Wu X., Chahine G.L., 2007, Characterization of the content of the cavity behind a high-speed supercavitating body, *Journal of Fluids Enginnering*, **45**, 129-136

41. Zhang X.-W., Wei Y.-J., Zhang J.-Z., Chen Y., Yu K.-P., 2007, Experimental research on the shape characters of natural and ventilated supercavitation, *Journal of Hydrodynamics, Ser. B*, **19**, 5, 564-571

42. Zou W., Yu K., Wan X., 2010, Research on the gas-leakage rate of unsteady ventilated supercavity, *Journal of Hydrodynamics*, **22**, 5, 778-783

Manuscript received June 4, 2015; accepted for print November 26, 2015

JOURNAL OF THEORETICAL AND APPLIED MECHANICS
54, 3, pp. 811-825, Warsaw 2016
DOI: 10.15632/jtam-pl.54.3.811

NUMERICAL INVESTIGATION OF POOL NUCLEATE BOILING IN NANOFLUID WITH LATTICE BOLTZMANN METHOD

Afsaneh Rostamzadeh, Khosrow Jafarpur, Ebrahim Goshtsbi Rad
School of Mechanical Engineering, Shiraz University, Shiraz, Iran
e-mail: af_rostamzadeh@yahoo.com; kjafarme@shirazu.ac.ir; goshtasb@shirazu.ac.ir

Due to significant improvement of thermal performance and other properties of nanofluids, this group of liquids is in high demand. According to the literature, the effect of nanoparticles on boiling heat transfer enhancement or degradation is not the same among different investigations. In the present article, the pseudo-potential multiphase lattice Boltzmann method is used to simulate nucleate pool boiling with two different fluids: a pure liquid and a nanofluid. The current results indicate that the contact angle is the same for both the fluid and nanofluid when the vapor bubble detachment occurs. Also, bubble departure diameter is greater in the base liquid while bubble release frequency is higher in the nanofluid. In brief, the present results demonstrate that using a nanofluid instead of its base fluid will increase the boiling heat transfer coefficient.

Keywords: pool boiling, nanofluid, lattice Boltzmann method, heat transfer

1. Introduction

Boiling and two phase flow phenomena are observed in many industrial processes and applications, such as refrigeration, air-conditioning, energy conversion systems, heat exchange systems, thermochemical processes, cooling of high-power electronic components, cooling of nuclear reactors, food, as well as space applications (Barber *et al.*, 2011). Enhancement of boiling heat transfer may improve energy efficiency and achieves significant reduction of energy consumption. In other words, for industrial boiling systems, the enhancement of boiling heat transfer may cause an enormous increase in the power level of boilers without any increase in size or operating temperature. For this purpose, many researchers used nanofluids to enhance boiling heat transfer and convective boiling performance (Ahn *et al.*, 2010; Cheng, 2009; Cheng *et al.*, 2008; Das *et al.*, 2003; Kim, 2007; Kwark *et al.*, 2010; Lee and Mudawar, 2007; Taylor and Phelan, 2009; Wang and Mujumdar, 2007; You *et al.*, 2003). Nanofluids are practical liquid suspensions containing particles that are smaller than 100 nm. With some enhanced properties, they have wide potential applications for intensifying heat transfer and energy efficiency in a variety of systems (Huminic and Huminic, 2011; Kole and Dey, 2012; Park *et al.*, 2009; Zeinali Heris, 2011). However, the study of nanofluid two-phase flow and thermal physics is still in the initial stages. Considering the lack of theoretical knowledge of the underlying mechanism of boiling heat transfer with and without nanoparticles, further investigations in this field of research are exceedingly in demand. Basically, this phenomenon is very complicated because of nonlinearity of the boiling process. Besides, in some numerical models such as Level Set and Volume of fluid (VOF) methods (Hirt and Nichols, 1981; Osher and Sethian, 1988), the interface tracking process increases the complexity of the problem and the computational costs.

As an effective numerical approach, the Lattice Boltzmann Method (LBM) has been successfully applied to simulate fluid flow and transport phenomena. Unlike conventional CFD methods, the LBM is based on microscopic models and mesoscopic kinetic equations. The main advantages of LBM are the simplicity of programming and the parallelism of the algorithm. Therefore,

this method is an appropriate technique for modeling single component hydrodynamics, multiphase and multicomponent flows (Sukop and Thorne, 2007). Researchers have developed LBM to find a precise model for multiphase flows, such as the color function model (Rothman and Keller, 1988), the interaction potential model (Shan and Chen, 1993) and the free energy model (Swift *et al.*, 1996). Their new models have been successful to some extent. To model multiphase problems, there are some defects in traditional CFD methods. For example, the difficulty in the implementation of interface tracking between immiscible phases, but the LBM is capable of incorporating these interactions without tracking. In addition to this important property, no assumptions or empirical correlations are used in the LBM method. Moreover, the lattice Boltzmann studies for nucleate boiling have been performed by some researchers as well. They have investigated the vapor bubble behavior and claimed that their numerical results could be considered as a basic work or reference for application of boiling performances (Cheng *et al.*, 2010; Dong *et al.*, 2010; Hazi and Markus, 2009; Inamuro *et al.*, 2004; Jain and Tentner, 2009; Liu *et al.*, 2010; Sun *et al.*, 2013; Yang *et al.*, 2001; Zhang and Chen, 2003; Zheng *et al.*, 2006).

Although, a significant number of researches exist on the pool boiling of nanofluids focused on heat transfer performance including the critical heat flux and heat transfer coefficient, the investigations of the nanoparticle influence on the bubble dynamics are quite limited. Also these studies do not fully explain the mechanism responsible for the augmentation or deterioration of the heat transfer coefficient in nanofluids, and some of them are inconsistent as well. However, most of the previous works have described the surface modification or the interaction between the nanoparticles and liquid vapor interface (Phan *et al.*, 2010; Vafaei and Wen, 2010). Vafaei and Wen (2010) examined dynamics of a gas bubble in a nanofluid made of gold nanoparticles. The bubble was not formed by boiling but gas was injected in the liquid with a nozzle. They demonstrated that the nanoparticles significantly affect the bubble growth. The bubble growth during boiling has been studied using a pure liquid on nano coated surfaces; this was the work done by Phan *et al.* (2010). Effect of surface wettability was investigated for several surfaces with various nano-coatings. It was found that a higher surface wettability increases the bubble departure radius and decreases the bubble release frequency. Therefore, in this study, the multiphase (liquid and vapor phases) lattice Boltzmann method based on a pseudo-potential model is applied to simulate pool-boiling nanofluids. Moreover, the current work examines dynamic growth of vapor bubbles in a nanofluid as well as the governing thermal effects. The effective parameters such as growth time, waiting time, bubble release frequency and bubble detachment diameter, which govern the heat transfer from the heater surfaces to the boiling fluids are obtained and compared for both pure liquids and nanofluids. Besides, the heat transfer performance for nanofluids relative to base fluids is studied as well.

2. Model description

2.1. Dynamic and thermal Lattice Boltzmann model

The density distribution function and the temperature distribution function are needed to simulate the phase change process in the LBM method. In the case that forces and potentials act on the particles, there are some methods to incorporate the force term in the LBM model (Shan and Chen, 1993; Guo *et al.*, 2002; Buick and Greated, 2000). Kupershtokh (2004) showed that the Exact Difference Method (EDM) has better accuracy compared with other methods. Therefore, the evolution equation of the density distribution function is written as follows (Kupershtokh, 2004)

$$f_i(\mathbf{x}+\mathbf{e}_i\Delta t, t+\Delta t) - f_i(\mathbf{x},t) = -\frac{1}{\tau}[f_i(\mathbf{x},t) - f_i^{eq}(\mathbf{x},t)] + \Delta f_i(\mathbf{x},t) \tag{2.1}$$

where $f_i(\mathbf{x},t)$ is the particle distribution function, $\mathbf{e}_i$ is the lattice velocity vector; τ is the velocity relaxation time, Δt is the time step, $\Delta f_i(\mathbf{x},t)$ is the force term. The equilibrium distribution function is taken as

$$f_i^{eq} = \omega_i \rho \Big[1 + 3\frac{\mathbf{e}_i\mathbf{u}}{c^2} + \frac{9}{2}\frac{(\mathbf{e}_i\mathbf{u})^2}{c^4} - \frac{3}{2}\frac{\mathbf{u}^2}{c^2}\Big] \tag{2.2}$$

In Eq. (2.2), $c = \Delta x/\Delta t$ is the lattice speed (Δx is the lattice spacing) and ω_i are the weight coefficients. For D_2Q_9 scheme, the weighting coefficients ω_i are given by $\omega_0 = 4/9$, $\omega_{1-4} = 1/9$ and $\omega_{5-8} = 1/36$. The discrete lattice velocity vector $\mathbf{e}_i$ is given as

$$\mathbf{e}_i = \begin{cases} (0,0) & i = 0 \\ (\pm 1, 0)c, (0, \pm 1)c & i = 1, \ldots, 4 \\ (\pm 1, \pm 1)c & i = 5, \ldots, 8 \end{cases} \tag{2.3}$$

The force term in EDM is calculated from

$$\Delta f_i(\mathbf{x},t) = f_i^{eq}(\rho, \mathbf{u} + \Delta u) - f_i^{eq}(\rho, \mathbf{u}) \tag{2.4}$$

where $\Delta\mathbf{u} = (\Delta t/\rho)\mathbf{F}$ is the velocity change due to the force term. The density and velocity of the fluid are given by

$$\rho(\mathbf{x},t) = \sum_i f_i(\mathbf{x},t) \qquad \rho(\mathbf{x},t)\mathbf{u}(\mathbf{x},t) = \sum_i f_i(\mathbf{x},t)\mathbf{e}_i \tag{2.5}$$

The evolution equation of the temperature distribution function is

$$g_i(\mathbf{x} + \mathbf{e}_i\Delta t, t + \Delta t) - g_i(\mathbf{x},t) = -\frac{1}{\tau_\theta}[g_i(\mathbf{x},t) - g_i^{eq}(\mathbf{x},t)] + \omega_i \phi \Delta t \tag{2.6}$$

In Eq. (2.6), τ_0 is the relaxation time; ϕ is the source term which is responsible for the phase change derived by Gong and Cheng (2012). Then, the equation for the phase change is as follows

$$\phi = T\Big[1 - \frac{1}{\rho c_v}\Big(\frac{\partial p}{\partial T}\Big)_\rho\Big]\nabla \cdot \mathbf{U} \tag{2.7}$$

g_i^{eq} is the equilibrium distribution function for temperature given by

$$g_i^{eq} = \omega_i T\Big[1 + 3\frac{\mathbf{e}_i\mathbf{U}}{c^2} + \frac{9}{2}\frac{(\mathbf{e}_i\mathbf{U})^2}{c^4} - \frac{3}{2}\frac{\mathbf{U}^2}{c^2}\Big] \tag{2.8}$$

When any force exists in the system, the real fluid velocity is modified by $\rho\mathbf{U} = \sum_i \mathbf{e}_i f_i + \mathbf{F}\Delta t/2$.

Also, the temperature is obtained as follows

$$T(\mathbf{x},t) = \sum_i g_i(\mathbf{x},t) \tag{2.9}$$

Moreover, the thermal diffusivity and kinematic viscosity are calculated from

$$\alpha = c^2\Big(\tau_\theta - \frac{1}{2}\Big)\frac{\Delta t}{3} \qquad \nu = c^2\Big(\tau - \frac{1}{2}\Big)\frac{\Delta t}{3} \tag{2.10}$$

In the current work, $\mathbf{F}$ represents multiphase flow and is a resultant vector of interparticle interaction forces. It contains forces responsible for phase separation, gravity and interaction between the solid surface and the fluid.

2.1.1. Multiphase lattice Boltzmann model

In this investigation, the pseudo-potential proposed by Shan and Chen (1993) is used. The separation of different phases microscopically is due to interaction between the molecules of a fluid (Shan and Doolen, 1995). The interparticle interaction force can be expressed as (Yuan and Schaefer, 2006)

$$\mathbf{F}_{int}(\mathbf{x},t) = -c_0 g\psi(\mathbf{x},t)\nabla\psi(\mathbf{x},t) \tag{2.11}$$

where c_0 is a constant depending on the lattice structure, and for the D_2Q_9 model it is equal to 6.0. The coefficient for the strength of the interparticle force is g, with $g > 0$ representing a repulsive force between the particles and $g < 0$ an attractive force. $\psi(\mathbf{x})$ is called "effective mass" which is defined as a function of $\mathbf{x}$ through its dependency on the local density, and is specified by the equation of state with the following equation for present simulation

$$\psi(\rho) = \sqrt{\frac{2(p-\rho/3)}{c_0 g}} \tag{2.12}$$

The modified expression for the interparticle interaction force proposed by Gong and Cheng (2012) is used to improve the accuracy of the multiphase model

$$\mathbf{F}_{int}(\mathbf{x}) = -\beta c_0\psi(\mathbf{x})g\nabla\psi(\mathbf{x}) - \frac{1-\beta}{2}c_0 g\nabla\psi^2(\mathbf{x}) \tag{2.13}$$

where β is the weighting factor (for Peng-Robinson equation of state, $\beta = 1.16$).

For numerical evaluation of the gradient term $\nabla\psi$ in a D_2Q_9 lattice, both nearest and next-nearest sites have been used, which gives a six-point scheme for two dimensions, i.e.

$$\begin{aligned}
\frac{\partial\psi(i,j)}{\partial x} &= c_1[\psi(i+1,j) - \psi(i-1,j)] \\
&\quad + c_2[\psi(i+1,j+1) - \psi(i-1,j+1) + \psi(i+1,j-1) - \psi(i-1,j-1)] \\
\frac{\partial\psi(i,j)}{\partial y} &= c_1[\psi(i,j+1) - \psi(i,j-1)] \\
&\quad + c_2[\psi(i+1,j+1) - \psi(i+1,j-1) + \psi(i-1,j+1) - \psi(i-1,j-1)]
\end{aligned} \tag{2.14}$$

c_1 and c_2 are weighting coefficients for the nearest and next nearest sites, respectively. In this article, $c_1 = 4c_2 = 1/3$ proposed by Yuan and Schaefer (2006) have been used.

In addition to the interparticle forces, if the problem includes a solid wall boundary, it is essential to consider the forces between the fluid particles and surfaces. This interaction force can also model the wettability of the surface with the fluid, defined as

$$F_{ads}(\mathbf{x}) = -G_{ads}\psi(\mathbf{x})\sum_i \omega_i s(\mathbf{x}+\mathbf{e}_i\Delta t)\mathbf{e}_i \tag{2.15}$$

The adsorption coefficient parameter G_{ads} (in Eq. (2.15)) controls the strength of the force between the wall and fluid; s is the switch that takes a value of one if the site at $\mathbf{x}+\mathbf{e}_i\Delta t$ is a solid and is zero otherwise.

On the other hand, the gravity force is given by

$$F_{gravity}(\mathbf{x}) = \mathbf{G}[\rho(\mathbf{x}) - \rho_{ave}] \tag{2.16}$$

where $\mathbf{G}$ is the acceleration of gravity and ρ_{ave} the average density of the whole computation domain at each time step.

2.1.2. Equation of state (EOS)

According to the definition of the equation of state (EOS), if there is no interaction force, the fluid will behave like an ideal gas, however, by selecting a more realistic EOS, a better performance will be obtained from the LBE simulation. Yuan and Schaefer (2006) discussed a non-ideal EOS. Referring to those results, the Peng-Robinson EOS is more accurate for real gases. So, in this study, P-R EOS has been chosen; the constants of this equation have been set as $a = 2/49$, $b = 2/21$ and $R = 1$

$$p = \frac{\rho RT}{1 - b\rho} - \frac{a\rho^2 \varepsilon(T)}{1 + 2b\rho - b^2\rho^2} \qquad a = 0.45724\frac{R^2 T_c^2}{P_c} \qquad b = 0.0779\frac{RT_c}{P_c} \tag{2.17}$$

where

$$\varepsilon(T) = \left[1 + (0.37464 + 1.54226\omega - 0.26992\omega^2)\left(1 - \sqrt{\frac{T}{T_c}}\right)\right]^2$$

with ω as the acentric factor.

At the critical point, $\partial P_c/\partial\rho_c = 0$ and $\partial^2 P_c/\partial\rho_c^2 = 0$ should be satisfied (and therefore $T_c = 0.0729$ and $P_c = 0.0595$). In the current investigation, dimensionless variables such as T/T_c, ρ/ρ_c and all other variables are chosen based on the lattice unit. As it was previously presented (Liu and Cheng, 2013), the liquid-vapor interface is defined as the location where the density is at $\rho_i = (\rho_l + \rho_v)/2$.

2.2. Nanofluid properties

The properties of nanofluids may be defined in terms of φ (volume fraction of nanoparticles), thermo-physical properties of nanoparticles and pure liquid.

The effective dynamic viscosity of the nanofluid μ_{nf} in the present work has been calculated based on the model given by Brinkman (Brinkman, 1952)

$$\mu_{nf} = \frac{\mu_f}{(1 - \varphi)^{2.5}} \tag{2.18}$$

where μ_f, φ are viscosity of fluid and volume fraction of the particles, respectively.

Also, the effective density of the nanofluid is obtained from

$$\rho_{nf} = (1 - \varphi)\rho_f + \varphi\rho_p \tag{2.19}$$

In Eq. (2.19), ρ_{nf}, ρ_f and ρ_p are the density of the nanofluids, base fluid and nanoparticles, respectively.

For the specific heat capacity of the nanofluid Cp_{nf} at constant pressure, the following expression is used

$$\rho_{nf} Cp_{nf} = (1 - \varphi)\rho_f Cp_f + \varphi\rho_p Cp_p \tag{2.20}$$

Cp_f and Cp_p in Eq. (2.20, are the specific heat capacities at constant pressure for the base fluid and nanoparticles, respectively.

The thermal conductivity of nanofluid knf is determined by (Hamilton and Crosser, 1962)

$$\frac{k_{nf}}{k_f} = \frac{k_p + 2k_f - 2\varphi(k_f - k_p)}{k_p + 2k_f + \varphi(k_f - k_p)} \tag{2.21}$$

where k_f is thermal conductivity of water and k_p is thermal conductivity of nanoparticles.

3. Results and discussion

3.1. Coexistence curve and surface tension

First, simulation has been done for a single component multiphase flow to assess validity of the proposed model. A 150×150 lattice structure and periodic boundary condition were chosen for all directions. A bubble (droplet) with radius of 5 lattice nodes was placed in the center. Simulation proceeded until equilibrium was reached. Densities of the vapor and liquid are shown in Fig. 1. Analytical solution given by the Maxwell construction is also displayed. It is clear that the liquid and vapor branches of the coexistence curve are reproduced quite well. T_r and ρ_r represent the reduced temperature and reduced density, respectively, which were defined the same as the dimensionless temperature and density.

In addition, if the initial density is set to be randomly distributed around the critical density, phase separation will occur for temperatures below the critical value. After 40000 time steps, the steady state is reached and the phase separation ultimately leads to a single droplet in the vapor phase or vice versa.

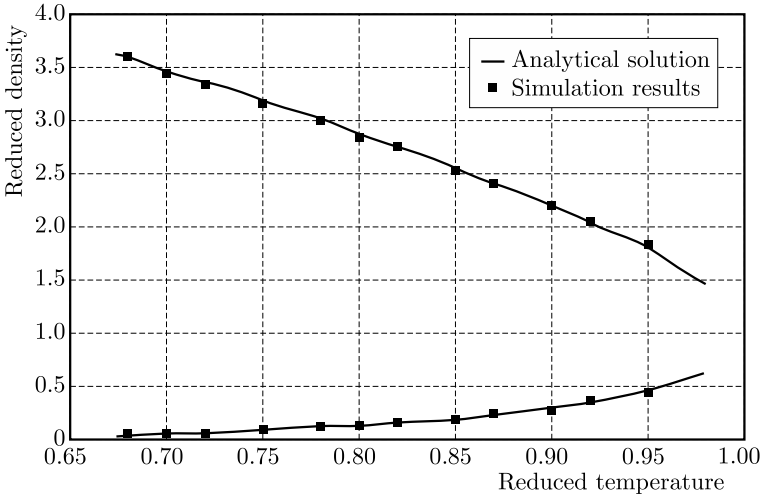

Fig. 1. Coexistence curve

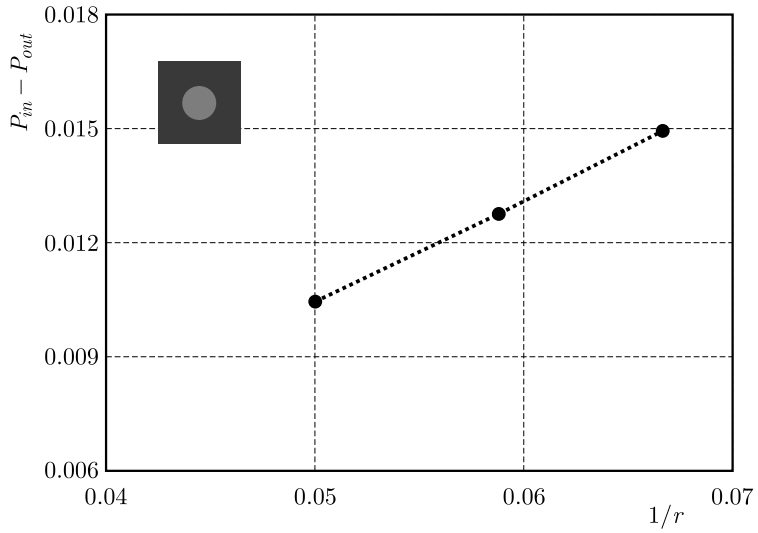

Fig. 2. Comparison of the simulation results with the Laplace equation

Also, the surface tension coefficient for the P-R equation of state at different temperatures is calculated by measuring the density and finding the pressure difference inside and outside the

bubble (droplet) using the EOS. The results shown in Fig. 2 indicate a linear dependence of the inverse radius on the pressure difference for the liquid. According to the Laplace law, for the 2D bubble (droplet) one can estimate the surface tension given as follows: $\Delta p = \sigma/R$.

3.2. Bubble growth and departure in pool boiling for pure liquid

To simulate bubble growth and its departure from the heated horizontal thermal surface in pool boiling, a rectangular domain with periodic lateral directions is used. A non-slip solid wall with constant temperature is employed at the bottom of the domain. Constant temperature and constant pressure (corresponding to the saturated pressure of T_{bulk}) are specified at the top boundary. A 150×450 lattice structure is generated for computation purposes. By applying different mesh sizes, the bubble departure and bubble growth are independent of the mesh size. Initially, the computational domain has been occupied by the liquid phase at the temperature $T_{bulk} = 0.82T_c$, and the temperature T_w has been specified as $0.88T_c$ at the wall boundary.

A spherical bubble with a radius of three lattice units has been initially located at coordinates $(75, 0)$. The present numerical model requires some setting in the parameters before the start of bubble growth, e.g. dimensionless gravity to be set as $G = +0.00002$ in the y direction. Also, by varying the parameter G_{ads}, which specifies the strength of the contribution force between the fluid particle and surfaces, the complete range of contact angles can be obtained. For example, $G_{ads} = -0.1$ corresponds to 90° contact angle. The nondimensional time step has been created by length and velocity scales as follows

$$l_0 = \sqrt{\frac{\sigma}{G(\rho_L - \rho_V)}} \qquad \mathbf{U}_0 = \sqrt{Gl_0} \qquad t^* = \frac{tU_0}{l_0} \tag{3.1}$$

where σ is the surface tension.

Profiles of vapor bubble growth and departure from a heated wall are shown in Fig. 3. The growth and departure of the vapor bubble from the solid heating surface are dynamic processes for which the momentum and energy exchanges between the growing bubble and the surrounding liquid must be considered. At the first stage, the growth of the bubble requires a certain amount of energy from the heating surface to vaporize the surrounding liquid. In the next stage, the bubble departure is determined by the net forces acting on the bubble during its growth. Buoyancy has often played a major role between the forces that act on the bubble such as surface tension and dynamic forces.

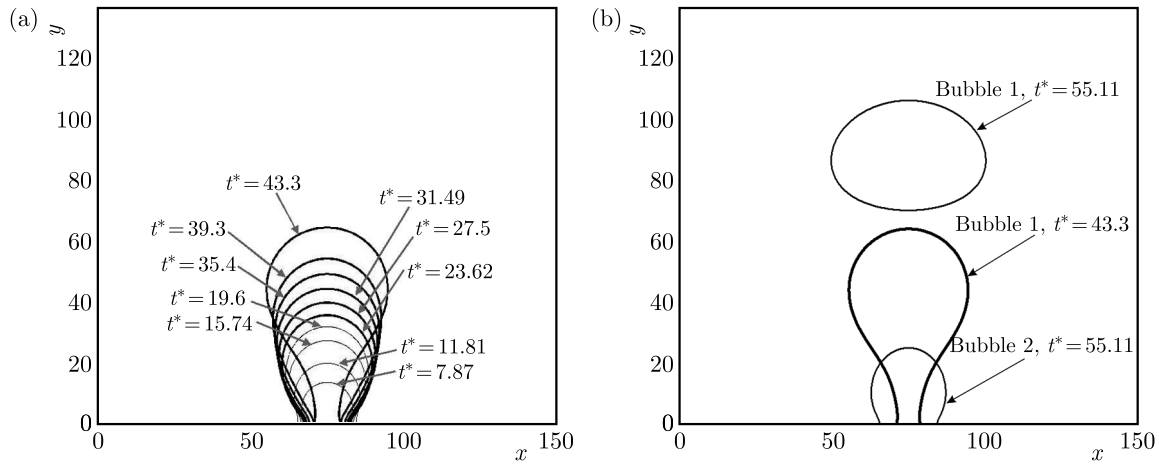

Fig. 3. Bubble (a) expanding and (b) departure process

In Fig. 4, vapor bubble streamlines and interfaces are shown before and after its detachment. The dynamic behavior of the bubble is growth, departure and rise due to the action of buoyancy. These are clearly shown in Figs. 3 and 4. It is noted that the induced velocity causes transformation of the natural convection process into localized forced convection and increases heat transfer by moving the cold fluid towards the superheated wall. It is found that the simulation results of the bubble dynamics and growth pattern shown in Figs. 3 and 4 are similar to the results of the available experimental data of Mukherjee and Dhir (2004).

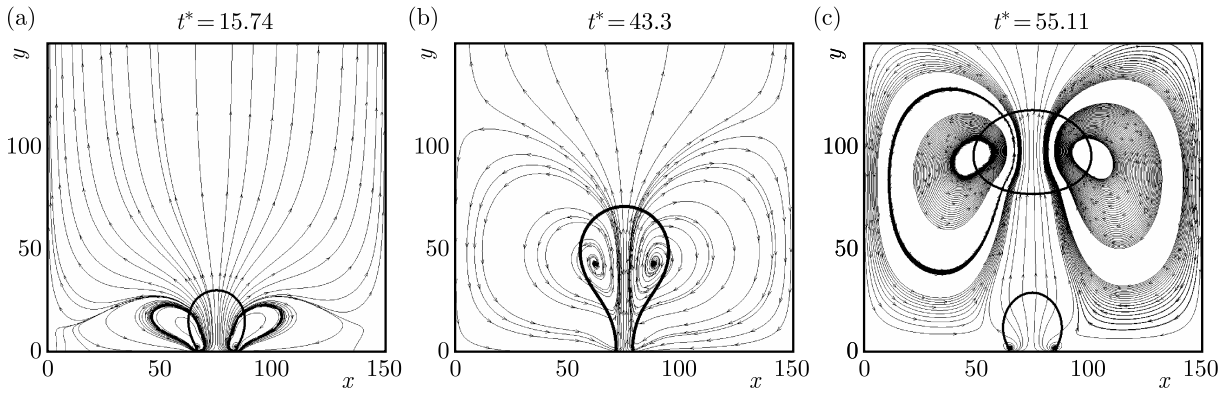

Fig. 4. Flow fields at various time (a) $t^* = 15.74$, (b) $t^* = 43.3$, (c) $t^* = 55.11$

In the early stage, the growth of the vapor bubble is influenced by the over-pressure force and controlled by the inertia as shown in Fig. 4a at $t^* = 15.74$. Following this, the growth proceeds until the buoyancy force overcomes the adhesion forces, which is shown in Fig. 4b and finally the bubble departs (Fig. 4c).

Figure 5 indicates the relationship between the detachment diameters and the gravity acceleration. The equivalent diameter for the growing bubble has been calculated according to a hypothetical sphere with the same volume as the original bubble shape. The bubble departure diameter is proportional to the inverse of the square root of the gravity acceleration. These calculated results are in good agreement with other correlations previously presented by Fritz (1935) and Phan *et al.* (2010). Their analytical analyses showed that the bubble departure diameter is proportional to $G^{-0.5}$ while the current LBM outcomes predict the variation of bubble departure diameter to be proportional to $G^{-0.51}$.

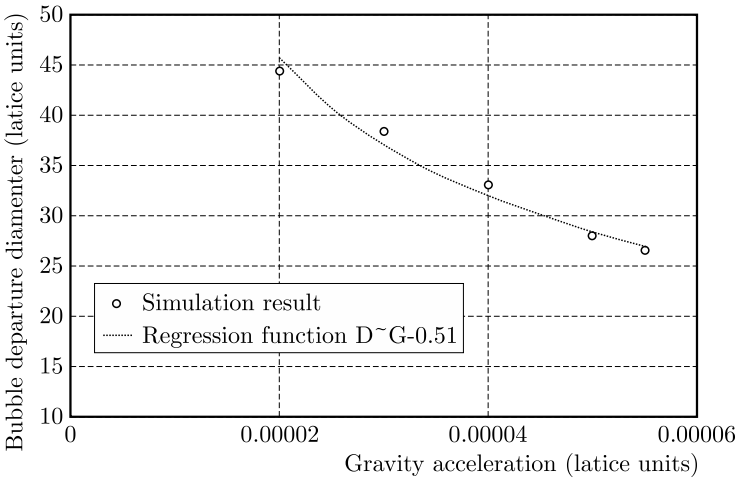

Fig. 5. Change in the bubble departure vs. gravity acceleration

3.3. Dynamic growth of a bubble in a nanofluid

In the investigation of two-phase flow and boiling phenomena of nanofluids, aluminum oxide nanoparticles are chosen because of their well-recorded thermal properties and widespread use in such types of research. In this study, the nanofluid is assumed as one-component. On the assumption of no slip and thermal equilibrium between the base fluid and nanoparticles, the properties of nanofluids can be defined in terms of the ratio of the solid volume fraction of the particles in a pure fluid φ. So, thermo-physical properties of the nanofluid such as thermal conductivity, viscosity, liquid density and specific heat capacity are calculated based on equations described in Section 2.2. Moreover, it is assumed that the nanoparticles do not have an important role in the interparticle forces, consequently, the EOS for nanofluid can be considered equal to that of the pure liquid (Kim *et al.*, 2006; Kim *et al.*, 2007).

In the present work, the base fluid is water and 1% volume fraction of nanoparticles is added to the base fluid in order to investigate the effect of the bubble growth dynamics and heat transfer. Thermo-physical properties of the selected nanoparticles and water at 20°C are reported in Table 1.

Table 1. Thermo-physical properties of water and nanoparticles

	ρ [kg/m^3]	C_p [J/(kg K)]	k [W/(m K)]	$\alpha \cdot 10^7$ [m^2/s]
Water (Bejan, 2013)	997.1	4179	0.613	1.47
Al_2O_3 (Abu-Nada, 2009)	3890	775	31.8	105

3.4. Bubble release frequency

When a bubble starts to grow on a heating surface, a specific amount of time (growing time t_g) is required until the bubble departs from the surface. On the other hand, a time interval, called the waiting period t_w is the duration between the release of one bubble to the nucleation of the next at a given nucleation site. Accordingly, the bubble frequency is defined as $f = 1/(t_g + t_w)$.

The present numerical results show that growing time and waiting period for nanofluids are shorter than in their base pure liquids. For example, the times for bubble dynamics in nanofluids are $t^* = 11.81102$, 27.55906, and 43.66929, respectively, and the flow patterns are similar to the bubble dynamics in the liquid phase as shown in Fig. 4. It is obvious that these time values are much lower than in pure liquids, which leads to an increase in the bubble release frequency of the nanofluid. Reduction of these times for the nanofluids relative to the base liquids for different time steps at the growing process is 25, 36, and 21%, respectively. Also, at this condition the bubble release frequency for the nanofluid is 27% higher than for the base liquid.

Figure 6 depicts a comparison between numerical results of the time variation of bubble diameter for the pure liquid and nanofluid with 1% volume fraction of aluminum oxide nanoparticles. It appears that using the nanofluid makes the process of bubble growth and departure faster than in the base fluid. As the time passes, the variation in diameter between the nanofluid and the base fluid increases. Also the detachment diameter for the nanofluid is smaller than in the base liquid, which is consistent with the increase in the bubble release frequency. This phenomenon has been observed for all gravity accelerations investigated in this work.

The growth time of a vapor bubble for the nanofluid and the pure liquid is shown in Fig. 7. Differences in the growth time between the nanofluid and the base fluid decrease with the increasing acceleration of gravity. In fact, buoyancy is the force that overcomes surface tension at the bubble base and pulls the bubble from the surface. Moreover, the change of bubble departure with gravity acceleration for the nanofluid is similar to that of the base fluid as shown in Fig.5. However, it should be noted that the bubble radius at the time of detachment is decreased for the nanofluid in comparison to the pure fluid for all gravity accelerations. Reduction of the

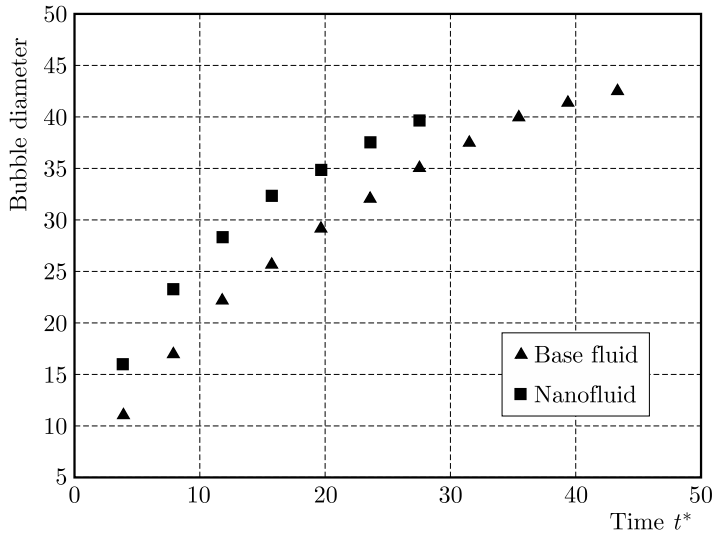

Fig. 6. Bubble diameter variation for the nanofluid and base liquid

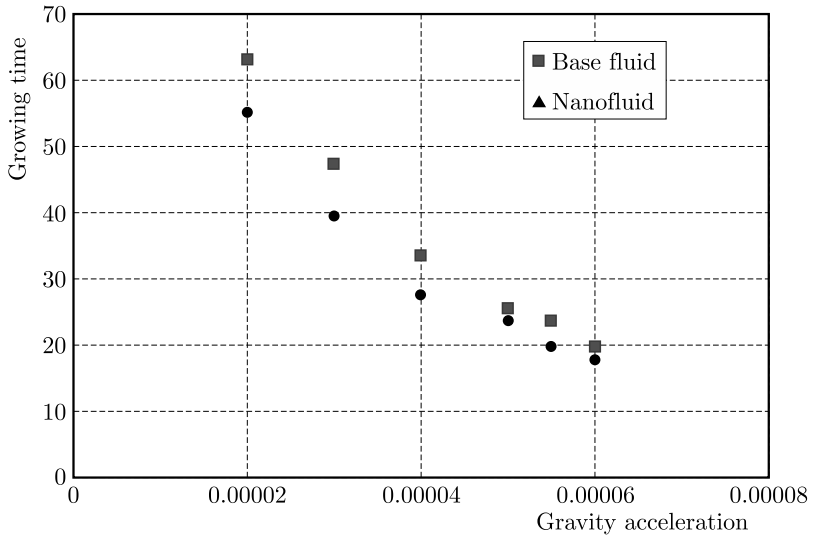

Fig. 7. Plot of growing time versus gravity acceleration for the nanofluid and base fluid (water)

departure diameter for the bubble with the gravity acceleration for the nanofluid is slightly higher than that for the base liquid.

In the current investigation, problems that possibly occur in experimental works such as particle deposition do not exist. In other words, on this assumption, the bubble dynamics is independent of the heating surface or at least this factor does not have an effective role. Indeed, the deposition of particles on the heating surface could change surface roughness. This could lead to an increase in the number of nucleation sites or, conversely, it could reduce thermal conductivity that provides a barrier to heat transfer and decreases bubble generation. Thus, this explanation can be one of the reasons for inconsistency in the previous researches. The contact angles of the detaching vapor bubble for the nanofluid and base fluid with the same G_{ads} and acceleration of gravity, are similar (see Fig. 3).

It is possible to estimate the power absorbed by a bubble during its growth. The power required to grow a bubble by evaporation for both the nanofluid and the base fluid is obtained from the following equation

$$p(t) = \rho_v h_{lv} \frac{dV}{dt} = m^{\circ} h_{lv} \tag{3.2}$$

According to thermodynamic relations, the specific latent heat (h_{lv}) is derived by Gong and Cheng (2013) for any equation of state. The vaporization power calculated for nanofluids and water is shown in Fig. 8. From this figure, it is obvious that the power is increasing as the bubble grows for both the base fluid and nanofluid. At the beginning, the growing power for the nanofluid is greater than that of the base fluid. However, after a while, the bubble in the base fluid increases in volume, therefore the evaporation heat flux will be increased and, finally. the power heat fluxes for both the base fluid as well as the nanofluid become approximately equal. On the other hand, because the bubble release frequency for the nanofluid is greater than of the base fluid, eventually the nanofluid will absorb more power than the base fluid.

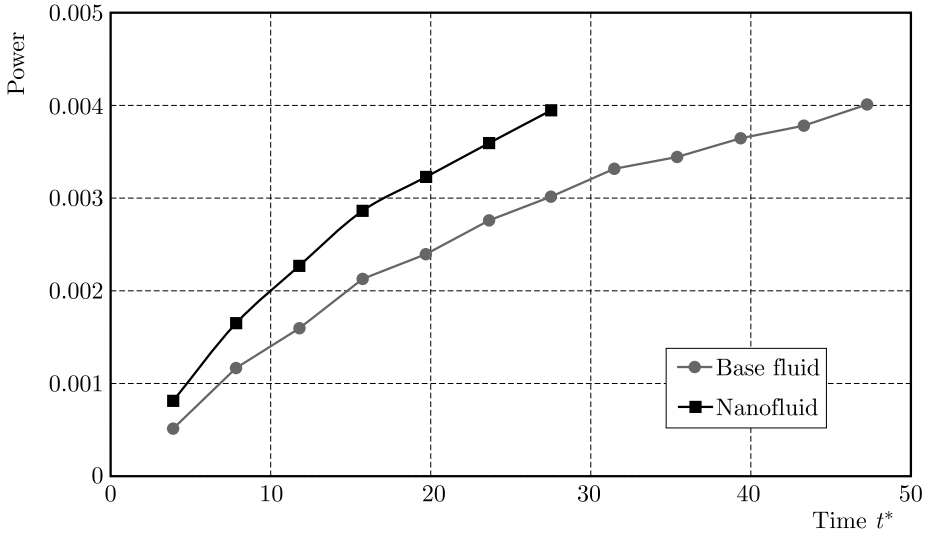

Fig. 8. Power required for vaporization

In the present work, the heat transfer coefficients during nucleate pool boiling have been investigated as well. The heat transfer coefficient associated with the boiling process is computed from the following equation

$$h_{avg} = \frac{1}{A}\int\limits_{A} \frac{q}{\Delta T}\, dA \qquad q = k_{eff}\left.\frac{\partial T}{\partial y}\right|_{w} \tag{3.3}$$

where k_{eff} is thermal conductivity of the nanofluid. The heat transfer coefficient could be averaged over the area and time. Time averaging is calculated during one cycle, from the initial stage to bubble detachment.

The heat transfer coefficient enhancement compared to the base fluid is displayed in Fig. 9. By increasing the temperature difference, the increment in the heat transfer coefficient tends to be larger, although a slight increase in the heat transfer coefficient with temperature difference has been observed. The maximum enhancement of the heat transfer coefficient is 18%. The main reason for the increase of the heat transfer coefficient is the modification of thermo-physical properties of the nanofluid. For example, these properties such as thermal conductivity and thermal diffusivity of the nanofluid are improved and enhanced in comparison to the base fluid. From these results, the heat transfer in microlayer vaporization is greater and leads to an increase in the growth of the vapor bubble. In this work, the nanofluid is considered homogeneous, therefore, in the microlayer aggregation of nanoparticles does not occur relative to other regions, and thermo-physical properties in all regions are identically developed. Furthermore, in the previous experimental researches, it has been shown that the suspended nanoparticles in the base liquid decrease the radius of the bubble and, therefore, more active sites on the heating

surface occur. Consequently, the boiling heat transfer coefficient increases, which is consistent with the present results (Raveshi *et al.*, 2013; Kim and Kim, 2009; Yang and Liu, 2011).

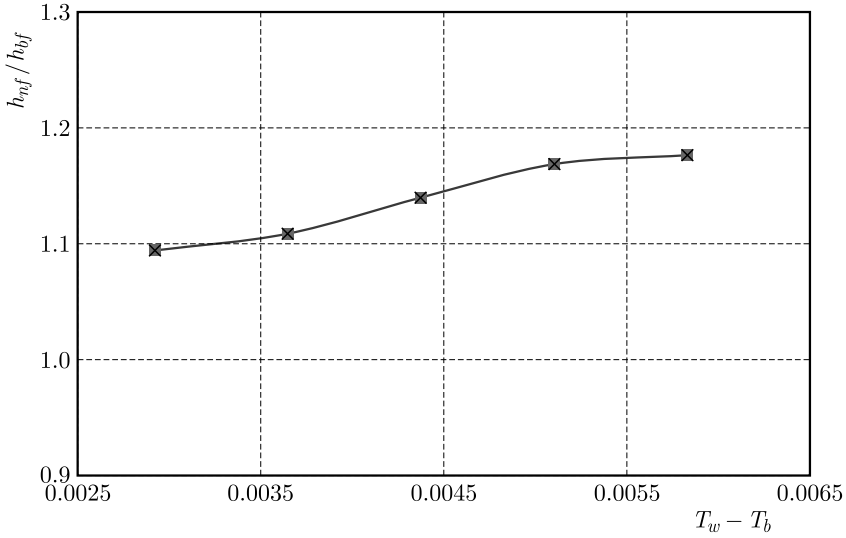

Fig. 9. Enhancement of the heat transfer coefficient versus ΔT

4. Conclusion

In this research, based on the pseudo-potential multiphase lattice Boltzmann method as well as the modified LBM thermal model, the bubble growth and departure from a horizontal heated surface are investigated for a pure liquid and a nanofluid. The comparison of the present results with those of analytical studies reveals that the current numerical results are in good agreement with the analytical solution.

To answer the question of whether nanofluids can cause the enhancement of pool boiling heat transfer performance or not bubble growth, the diameter of departure, contact angle and bubble release frequency of nanofluid are examined in the present work. By comparing the results of nucleate pool boiling for a 1% volume fraction nanofluid and those for the base fluid, the following results are observed. The bubble diameter at detachment is smaller for the nanofluid in comparison to its base liquid. Also, the power heat flux absorbed by the vapor bubble in the nanofluid is greater than in the pure liquid. Moreover, the bubble release frequency is higher for the nanofluid. In addition, the contact angle has been found to be similar for both fluids. Considering the above results, it is concluded that all three phenomena, smaller growing and waiting time, improved thermo-physical properties and smaller bubble departure diameter in the nanofluid, enhance the heat transfer coefficient.

References

1. Abu-Nada E., 2009, Effects of variable viscosity and thermal conductivity of Al_2O_3-water nanofluid on heat transfer enhancement in natural convection, *International Journal of Heat and Fluid Flow*, **30**, 4, 679-90

2. Ahn H.S. , Kim H., Jo H., Kang S., Chang W., Kim M.H., 2010, Experimental study of critical heat flux enhancement during forced convective flow boiling of nanofluid on a short heated surface, *International Journal of Multiphase Flow*, **36**, 5, 375-84

3. Barber J., Brutin D., Tadrist L., 2011, A review on boiling heat transfer enhancement with nanofluids, *Nanoscale Research Letters*, **6**, 1, 1-16

4. Bejan A., 2013, *Convection Heat Transfer*, John Wiley & Sons
5. Brinkman H., 1952, The viscosity of concentrated suspensions and solutions, *The Journal of Chemical Physics*, **20**, 4, 571
6. Buick J., Greated C., 2000, Gravity in a lattice Boltzmann model, *Physical Review E*, **61**, 5, 5307
7. Cheng L., 2009, Nanofluid heat transfer technologies, *Recent Patents on Engineering*, **3**, 1, 1-7
8. Cheng L., Bandarra F., Enio P., Thome J.R., 2008, Nanofluid two-phase flow and thermal physics: a new research frontier of nanotechnology and its challenges, *Journal of Nanoscience and Nanotechnology*, **8**, 7, 3315-3332
9. Cheng M., Hua J., Lou J., 2010, Simulation of bubble-bubble interaction using a lattice Boltzmann method, *Computers and Fluids*, **39**, 2, 260-70
10. Das S. K., Putra N., Roetzel W., 2003, Pool boiling characteristics of nano-fluids, *International Journal of Heat and Mass Transfer*, **46**, 5, 851-862
11. Dong Z., Li W., Song Y., 2010, A numerical investigation of bubble growth on and departure from a superheated wall by lattice Boltzmann method, *International Journal of Heat and Mass Transfer*, **53**, 21, 4908-4916
12. Fritz W., 1935, Maximum volume of vapor bubbles, *Physik Zeitschr*, **36**, 11, 379-84
13. Gong S., Cheng P., 2012, A lattice Boltzmann method for simulation of liquid-vapor phase--change heat transfer, *International Journal of Heat and Mass Transfer*, **55**, 17, 4923-7
14. Gong S., Cheng P., 2013, Lattice Boltzmann simulation of periodic bubble nucleation, growth and departure from a heated surface in pool boiling, *International Journal of Heat and Mass Transfer*, **64**, 122-132
15. Guo Z., Zheng C., Shi B., 2002, Discrete lattice effects on the forcing term in the lattice Boltzmann method, *Physical Review E*, **65**, 4, 046308
16. Hamilton R., Crosser O., 1962, Thermal conductivity of heterogeneous two-component systems, *Industrial and Engineering Chemistry Fundamentals*, **1**, 3, 187-191
17. Hazi G., Markus A., 2009, On the bubble departure diameter and release frequency based on numerical simulation results, *International Journal of Heat and Mass Transfer*, **52**, 5, 1472-1480
18. Hirt C.W., Nichols B.D., 1981, Volume of fluid (VOF) method for the dynamics of free boundaries, *Journal of Computational Physics*, **39**, 1, 201-225
19. Huminic G., Huminic A., 2011, Heat transfer characteristics of a two-phase closed thermosyphons using nanofluids, *Experimental Thermal and Fluid Science*, **35**, 3, 550-557
20. Inamuro T., Ogata T., Ogino F., 2004, Numerical simulation of bubble flows by the lattice Boltzmann method, *Future Generation Computer Systems*, **20**, 6, 959-964
21. Jain P.K., Tentner A., 2009, A lattice Boltzmann framework to simulate boiling water reactor core hydrodynamics, *Computers and Mathematics with Applications*, **58**, 5, 975-986
22. Kim H., Kim M., 2009, Experimental study of the characteristics and mechanism of pool boiling CHF enhancement using nanofluids, *Heat and Mass Transfer*, **45**, 7, 991-998
23. Kim S., Bang I. C., Buongiorno J., Hu L., 2006, Effects of nanoparticle deposition on surface wettability influencing boiling heat transfer in nanofluids, *Applied Physics Letters*, **89**, 15, 153107
24. Kim S., Bang I.C., Buongiorno J., Hu L., 2007, Surface wettability change during pool boiling of nanofluids and its effect on critical heat flux, *International Journal of Heat and Mass Transfer*, **50**, 19, 4105-4116
25. Kim S.J., 2007, *Pool Boiling Heat Transfer Characteristics of Nanofluids*, Massachusetts Institute of Technology

26. Kole M., Dey T., 2012, Investigations on the pool boiling heat transfer and critical heat flux of ZnO-ethylene glycol nanofluids, *Applied Thermal Engineering*, **37**, 112-119

27. Kupershtokh A., 2004, New method of incorporating a body force term into the lattice Boltzmann equation, *Proceedings of 5th International EHD Workshop*, University of Poitiers, Poitiers, France

28. Kwark S.M., Kumar R., Moreno G., Yoo J., You S.M., 2010, Pool boiling characteristics of low concentration nanofluids, *International Journal of Heat and Mass Transfer*, **53**, 5, 972-981

29. Lee J., Mudawar I., 2007, Assessment of the effectiveness of nanofluids for single-phase and two-phase heat transfer in micro-channels, *International Journal of Heat and Mass Transfer*, **50**, 3, 452-463

30. Liu X., Cheng P., 2013, Lattice Boltzmann simulation of steady laminar film condensation on a vertical hydrophilic subcooled flat plate, *International Journal of Heat and Mass Transfer*, **62**, 507-514

31. Liu M., Yu Z., Wang T., Wang J., Fan L.-S., 2010, A modified pseudopotential for a lattice Boltzmann simulation of bubbly flow, *Chemical Engineering Science*, **65**, 20, 5615-5623

32. Mukherjee A., Dhir V., 2004, Study of lateral merger of vapor bubbles during nucleate pool boiling, *Journal of Heat Transfer*, **126**, 6, 1023-1039

33. Osher S., Sethian J.A., 1988, Fronts propagating with curvature-dependent speed: algorithms based on Hamilton-Jacobi formulations, *Journal of Computational Physics*, **79**, 1, 12-49

34. Park K.-J., Jung D., Shim S.E., 2009, Nucleate boiling heat transfer in aqueous solutions with carbon nanotubes up to critical heat fluxes, *International Journal of Multiphase Flow*, **35**, 6, 525-532

35. Phan H.T., Caney N., Marty P., Colasson S., Gavillet J., 2010, Surface coating with nanofluids: the effects on pool boiling heat transfer, *Nanoscale and Microscale Thermophysical Engineering*, **14**, 4, 229-244

36. Phan H.T., Caney N., Marty P., Colasson S., Gavillet J., 2010, A model to predict the effect of contact angle on the bubble departure diameter during heterogeneous boiling, *International Communications in Heat and Mass Transfer*, **37**, 8, 964-969

37. Raveshi M.R., Keshavarz A., Mojarrad M.S., Amiri S., 2013, Experimental investigation of pool boiling heat transfer enhancement of alumina-water-ethylene glycol nanofluids, *Experimental Thermal and Fluid Science*, **44**, 805-814

38. Rothman D.H., Keller J.M., 1988, Immiscible cellular-automaton fluids, *Journal of Statistical Physics*, **52**, 3/4, 1119-1127

39. Shan X., Chen H., 1993, Lattice Boltzmann model for simulating flows with multiple phases and components, *Physical Review E*, **47**, 3, 1815

40. Shan X., Doolen G., 1995, Multicomponent lattice-Boltzmann model with interparticle interaction, *Journal of Statistical Physics*, **81**, 1/2, 379-393

41. Sukop M.C., Thorne D.T., 2007, *Lattice Boltzmann Modeling: an Introduction for Geoscientists and Engineers*, Springer

42. Sun T., Li W., Yang S., 2013, Numerical simulation of bubble growth and departure during flow boiling period by lattice Boltzmann method, *International Journal of Heat and Fluid Flow*, **44**, 120-129

43. Swift M.R., Orlandini E., Osborn W., Yeomans J., 1996, Lattice Boltzmann simulations of liquid-gas and binary fluid systems, *Physical Review E*, **54**, 5, 5041

44. Taylor R.A., Phelan P.E., 2009, Pool boiling of nanofluids: comprehensive review of existing data and limited new data, *International Journal of Heat and Mass Transfer*, **52**, 23, 5339-5347

45. Vafaei S., Wen D., 2010, Effect of gold nanoparticles on the dynamics of gas bubbles, *Langmuir*, **26**, 10, 6902-6907

46. Wang X.-Q., Mujumdar A.S., 2007, Heat transfer characteristics of nanofluids: a review, *International Journal of Thermal Sciences*, **46**, 1, 1-19

47. Yang X.F., Liu Z.H., 2011, Pool boiling heat transfer of functionalized nanofluid under sub-atmospheric pressures, *International Journal of Thermal Sciences*, **50**, 12, 2402-2412

48. Yang Z., Dinh T.-N., Nourgaliev R., Sehgal B., 2001, Numerical investigation of bubble growth and detachment by the lattice-Boltzmann method, *International Journal of Heat and Mass Transfer*, **44**, 1, 195-206

49. You S., Kim J., Kim K., 2003, Effect of nanoparticles on critical heat flux of water in pool boiling heat transfer, *Applied Physics Letters*, **83**, 16, 3374-3376

50. Yuan P., Schaefer L., 2006, Equations of state in a lattice Boltzmann model, *Physics of Fluids*, **18**, 4, 042101

51. Zeinali Heris S., 2011, Experimental investigation of pool boiling characteristics of low-concentrated CuO/ethylene glycol-water nanofluids, *International Communications in Heat and Mass Transfer*, **38**, 10, 1470-1473

52. Zhang R., Chen H., 2003, Lattice Boltzmann method for simulations of liquid-vapor thermal flows, *Physical Review E*, **67**, 6, 066711

53. Zheng H., Shu C., Chew Y.-T., 2006, A lattice Boltzmann model for multiphase flows with large density ratio, *Journal of Computational Physics*, **218**, 1, 353-371

Manuscript received March 25, 2015; accepted for print November 27, 2015

JOURNAL OF THEORETICAL AND APPLIED MECHANICS
54, 3, pp. 827-838, Warsaw 2016
DOI: 10.15632/jtam-pl.54.3.827

GENERALIZED THERMOELASTIC INTERACTIONS DUE TO AN INCLINED LOAD AT A TWO-TEMPERATURE HALF-SPACE

Ahmed E. Abouelregal

Department of Mathematics, Faculty of Science, Mansoura University, Mansoura 35516, Egypt and
Department of Mathematics, College of Science and Arts, Aljouf University, Al-Qurayat, Saudi Arabia

Ashraf M. Zenkour

Department of Mathematics, Faculty of Science, King Abdulaziz University, Jeddah, Saudi Arabia and
Department of Mathematics, Faculty of Science, Kafrelsheikh University, Kafr El-Sheikh, Egypt
e-mail: zenkour@sci.kfs.edu.eg

The article presents a two-temperature theory to study the thermally insulated stress-free surface of a thermoelastic solid half-space due to an inclined load. The inclined load is a linear combination of a normal load and a tangential load. The normal mode analysis has been employed to solve the present problem. Variations of conductive and thermodynamic temperatures, displacements, and stresses distributions with the horizontal distance have been presented graphically. Some comparisons have been made to estimate the effects due to the two-temperature parameter and the inclination angle on the field quantities. Results of earlier works have been deduced from the present investigation as special cases.

Keywords: thermoelasticity, conductive and thermodynamic temperatures, half-space, inclined load

1. Introduction

Classical thermoelasticity theory is based on Fourier's law of heat conduction, which, when combined with other fundamental field equations, leads to coupled hyperbolic-parabolic governing equations. These equations imply that thermal effects are to be felt instantaneously far away from the external thermo-mechanical load. Therefore, this theory admits infinite speeds of propagation of thermoelastic disturbances. This paradox becomes especially evident in problems involving very short time intervals or high rates of heat flux.

The heat equations for both the classical uncoupled theory and the coupled one by Biot (1956) of the diffusion type predict infinite speeds of propagation for heat waves contrary to physical observations. The classical uncoupled theory states that the elastic changes have no effect on temperature. So, Biot (1956) formulated his theory to eliminate this paradox. At present, there are several theories of hyperbolic thermoelasticity (Lord and Shulman, 1967; Green and Lindsay, 1972) with one and two relaxation times. Both of these theories ensure finite speeds of propagation for the heat wave. Green and Naghdi (1993) formulated another generalized thermoelasticity theory without energy dissipation. It included isothermal displacement gradients among its independent constitutive variables. Recently, Zenkour (2015) presented a unified theory that included different generalized and coupled thermoelasticity theories.

Sherief and Hamza (1996) solved a 2-D problem in spherical regions. Sherief and El-Maghraby (2003, 2005) solved two problems including cracks in an infinite thermoelastic solid. A 2-D problem for a half-space and for a thick plate under the action of body forces was solved by El-Maghraby (2008, 2009). Allam *et al.* (2009) studied a 2-D problem of electromagneto-thermoelasticity for a homogeneous isotropic perfectly conducting thick plate. Abouelregal and

Zenkour (2013) presented the effect of fractional thermoelasticity in a rotating fibre-reinforced thermoelastic medium. Zenkour and Abouelregal (2015) investigated a thermoelastic problem of an axially moving microbeam subjected to an external transverse excitation.

The present article is concerned with investigations related to analytical expressions for displacement, stress, and temperature distributions on the free surface of a thermoelastic medium subjected to an inclined load. The governing equations are taken in the two-temperature generalized thermoelasticity model (for the two-temperature model, one can refer to (Chen and Gurtin, 1968; Chen *et al.*, 1969; Boley, 1956; Abbas and Zenkour, 2014; Zenkour and Abouelregal, 2014a,b). Some comparisons are graphically shown to estimate the effect of the inclination angle and the two-temperature parameters on all the studied fields.

2. Basic equations

The basic equations of motion for a linear, homogeneous and isotropic thermoelastic material in the context of generalized thermoelasticity with two temperatures in the absence of the body force take the following forms

$$\mu\nabla^2\mathbf{u} + (\lambda+\mu)\nabla\,\mathrm{div}\,\mathbf{u} - \gamma\nabla\theta = \rho\ddot{\mathbf{u}} \tag{2.1}$$

where $\mathbf{u}$ denotes the displacement vector, $\theta = T - T_0$ denotes the thermodynamical temperature, T_0 is the reference temperature, λ and μ are Lamé's constants, $\gamma = (3\lambda+2\mu)\alpha_t$, α_t is the coefficient of thermal expansion and ρ is the mass density. Note that the direct vector/tensor notation is employed; also, an over dot denotes partial derivative with respect to the time variable t.

The stress tensor $\boldsymbol{\sigma}$ associated with $\mathbf{u}$ and θ is given by the constitutive equation

$$\boldsymbol{\sigma} = \lambda(\,\mathrm{div}\,\mathbf{u})\mathbf{I} + \mu[\nabla\mathbf{u} + (\nabla\mathbf{u})^{\mathrm{T}}] - \gamma\theta\mathbf{I} \tag{2.2}$$

where $\mathbf{I}$ is the identity tensor and the suffix T is the transpose of the given vector.

The strain-displacement relations are

$$e_{ij} = \frac{1}{2}(u_{i,j} + u_{j,i}) \tag{2.3}$$

where e_{ij} is the strain tensor.

The equation of entropy (energy equation) is

$$\rho T_0\frac{\partial\eta}{\partial t} = -q_{i,i} + Q \tag{2.4}$$

where η is the entropy per unit volume measured from the entropy of the reference state, q_i are the components of the heat flow vector, and Q is the applied heat flux.

The entropy-strain-temperature relation is

$$\rho\eta = \gamma e_{kk} + \frac{\rho C_E}{T_0}\theta \tag{2.5}$$

where C_E is the specific heat at constant strain and $e_{kk} = \mathrm{div}\,\mathbf{u} = e$ is the cubical dilatation.

The modified Fourier law is

$$q_i + \tau_0\frac{\partial q_i}{\partial t} = -K\varphi_{,i} \tag{2.6}$$

where τ_0 is the thermal relaxation time which will ensure that the heat conduction equation will predict finite speeds of heat propagation, K is the thermal conductivity, and φ is the conductive temperature measured from the temperature φ_0 ($\varphi_0 = T_0$), which satisfies the relation

$$\theta = \varphi - a\varphi_{,ii} \tag{2.7}$$

where a is the two-temperature parameter (temperature discrepancy).Then the heat conduction equation takes the form

$$(K\varphi_{,i})_{,i} = \Big(1 + \tau_0 \frac{\partial}{\partial t}\Big)\Big(\rho C_E \frac{\partial \theta}{\partial t} + \gamma T_0 \frac{\partial e}{\partial t} - Q\Big) \tag{2.8}$$

3. Statement of the problem

Let us consider a homogeneous thermoelastic half-space with two-temperatures occupying the region $z \geqslant 0$. The z-axis is taken perpendicular to the bounding plane pointing inwards. It is assumed that the initial state of the medium is quiescent. The surface of the medium is subjected to an inclined load. The inclined load is assumed to be a linear combination of the normal and tangential load. A Cartesian coordinate system (x, y, z) is used. The present study is restricted to plane strain parallel to the xz-plane. The problem is thus two-dimensional with all functions considered depending on the spatial variables x and z as well as on the time variable t. The problem is considered within the context of the theory of two temperature thermoelasticity.

The displacement vector $\mathbf{u}$, thus, has the form

$$\mathbf{u} = [u, 0, w] \tag{3.1}$$

For the 2-D problem in the xz-plane, Eq. (2.1) can be written as

$$\begin{aligned} &(\lambda + 2\mu)\frac{\partial^2 u}{\partial x^2} + (\lambda + \mu)\frac{\partial^2 w}{\partial x \partial z} + \mu \frac{\partial^2 u}{\partial z^2} - \gamma \frac{\partial \theta}{\partial x} = \rho \frac{\partial^2 u}{\partial t^2} \\ &(\lambda + 2\mu)\frac{\partial^2 w}{\partial z^2} + (\lambda + \mu)\frac{\partial^2 u}{\partial x \partial z} + \mu \frac{\partial^2 w}{\partial x^2} - \gamma \frac{\partial \theta}{\partial z} = \rho \frac{\partial^2 w}{\partial t^2} \end{aligned} \tag{3.2}$$

The generalized equation of heat conduction, Eq. (2.8), is written in the xz-plane as

$$K\Big(\frac{\partial^2 \varphi}{\partial x^2} + \frac{\partial^2 \varphi}{\partial z^2}\Big) = \Big(1 + \tau_0 \frac{\partial}{\partial t}\Big)\Big(\rho C_E \frac{\partial \theta}{\partial t} + \gamma T_0 \frac{\partial e}{\partial t}\Big) \tag{3.3}$$

and, Eq. (2.7) becomes

$$\theta - \varphi = -a\Big(\frac{\partial^2 \varphi}{\partial x^2} + \frac{\partial^2 \varphi}{\partial z^2}\Big) \tag{3.4}$$

In addition, the constitutive relations may be reduced to

$$\begin{aligned} \sigma_{xx} &= (\lambda + 2\mu)\frac{\partial u}{\partial x} + \lambda \frac{\partial w}{\partial z} - \gamma\theta & \sigma_{yy} &= \lambda\Big(\frac{\partial u}{\partial x} + \frac{\partial w}{\partial z}\Big) - \gamma\theta \\ \sigma_{zz} &= (\lambda + 2\mu)\frac{\partial w}{\partial z} + \lambda \frac{\partial u}{\partial x} - \gamma\theta & \sigma_{xz} &= \mu\Big(\frac{\partial u}{\partial z} + \frac{\partial w}{\partial x}\Big) \end{aligned} \tag{3.5}$$

4. Solution of the problem

Let us define displacement potentials Φ and Ψ which are related to the displacements u and w as

$$u = \frac{\partial \Phi}{\partial x} - \frac{\partial \Psi}{\partial z} \qquad w = \frac{\partial \Phi}{\partial z} + \frac{\partial \Psi}{\partial x} \tag{4.1}$$

Using the above relations in the governing equations, one obtains

$$\begin{aligned} &c_1^2 \nabla^2 \Phi - \frac{\partial^2 \Phi}{\partial t^2} = \frac{\gamma}{\rho}(\varphi - a\nabla^2 \varphi) \qquad c_2^2 \nabla^2 \Psi - \frac{\partial^2 \Psi}{\partial t^2} = 0 \\ &K\nabla^2 \varphi = \Big(1 + \tau_0 \frac{\partial}{\partial t}\Big)\Big(\rho C_E \frac{\partial}{\partial t}[\varphi - a\nabla^2 \varphi] + \gamma T_0 \frac{\partial}{\partial t}(\nabla^2 \Phi)\Big) \end{aligned} \tag{4.2}$$

and

$$\begin{aligned} &\sigma_{xx} = \lambda \nabla^2 \Phi + 2\mu \frac{\partial}{\partial x}\Big(\frac{\partial \Phi}{\partial x} - \frac{\partial \Psi}{\partial z}\Big) - \gamma[\varphi - a\nabla^2 \varphi] \qquad \sigma_{yy} = \lambda \nabla^2 \Phi - \gamma[\varphi - a\nabla^2 \varphi] \\ &\sigma_{zz} = \lambda \nabla^2 \Phi + 2\mu \frac{\partial}{\partial z}\Big(\frac{\partial \Psi}{\partial x} + \frac{\partial \Phi}{\partial z}\Big) - \gamma[\varphi - a\nabla^2 \varphi] \qquad \sigma_{xz} = 2\mu \frac{\partial^2 \Phi}{\partial x \partial z} + \mu\Big(\frac{\partial^2 \Psi}{\partial x^2} - \frac{\partial^2 \Psi}{\partial z^2}\Big) \end{aligned} \tag{4.3}$$

where

$$c_1^2 = \frac{\lambda + 2\mu}{\rho} \qquad c_2^2 = \frac{\mu}{\rho} \qquad \nabla^2 = \frac{\partial^2}{\partial x^2} + \frac{\partial^2}{\partial z^2} \tag{4.4}$$

The initial conditions are given by

$$\begin{aligned} &u(x,z,0) = w(x,z,0) = 0 \qquad \frac{\partial u}{\partial t} = \frac{\partial w}{\partial t} = 0 \\ &\theta(x,z,0) = \varphi(x,z,0) = 0 \qquad \frac{\partial \varphi}{\partial t} = \frac{\partial \theta}{\partial t} = 0 \end{aligned} \tag{4.5}$$

The following dimensionless variables are introduced

$$\begin{aligned} &\{x', z', u', w'\} = \frac{\eta_0}{c_1}\{x, z, u, w\} \qquad \{t', \tau_0'\} = \eta_0\{t, \tau_0\} \qquad \eta_0 = \frac{\rho C_E c_1^2}{K} \\ &\{\Phi', \Psi', a'\} = \Big(\frac{\eta_0}{c_1}\Big)^2\{\Phi, \Psi, a\} \qquad \{\theta', \varphi'\} = \frac{\gamma}{\rho c_1^2}\{\theta, \varphi\} \qquad \sigma_{ij}' = \frac{\sigma_{ij}}{\mu} \end{aligned} \tag{4.6}$$

into Eqs. (4.2). After removing the primes, one obtains

$$\begin{aligned} &\nabla^2 \Phi - \frac{\partial^2 \Phi}{\partial t^2} = \varphi - a\nabla^2 \varphi \qquad \nabla^2 \Psi - \beta^2 \frac{\partial^2 \Psi}{\partial t^2} = 0 \\ &\Big[1 + \eta_0 a \frac{\partial}{\partial t}\Big(1 + \tau_0 \frac{\partial}{\partial t}\Big)\Big]\nabla^2 \varphi = \eta_0 \Big(1 + \tau_0 \frac{\partial}{\partial t}\Big)\Big(\frac{\partial \varphi}{\partial t} + \varepsilon \frac{\partial}{\partial t}(\nabla^2 \Phi)\Big) \end{aligned} \tag{4.7}$$

where ε is the dimensionless thermoelastic coupling constant and β is the ratio of the longitudinal waves speed to the shear waves speed

$$\varepsilon = \frac{\gamma^2 T_0}{\rho C_E(\lambda + 2\mu)} \qquad \beta^2 = \frac{\lambda + 2\mu}{\mu}$$

Here, we restrict our attention to the constitutive relations given by Eqs. $(4.3)_{3,4}$. They become

$$\begin{aligned} &\sigma_{zz} = 2\frac{\partial}{\partial z}\Big(\frac{\partial \Psi}{\partial x} + \frac{\partial \Phi}{\partial z}\Big) + (1 - 2\beta^2)\nabla^2 \Phi - \beta^2[\varphi - a\nabla^2 \varphi] \\ &\sigma_{xz} = 2\frac{\partial^2 \Phi}{\partial x \partial z} + \frac{\partial^2 \Psi}{\partial x^2} - \frac{\partial^2 \Psi}{\partial z^2} \end{aligned} \tag{4.8}$$

5. Normal mode analysis

The normal mode analysis is used to give exact solutions without any assumed restrictions on temperature, displacement, and stress distributions (Cheng and Zhang, 2000; Allam *et al.*, 2009). The solution of the present field quantities can be decomposed in terms of the normal modes as

$$[u, w, \varphi, \Phi, \Psi, \sigma_{ij}](x, y, t) = [u^*, w^*, \varphi^*, \Phi^*, \Psi^*, \sigma^*_{ij}](x)\mathrm{e}^{(\omega t + \mathrm{i}\zeta z)} \tag{5.1}$$

where ω is the complex frequency, $\mathrm{i} = \sqrt{-1}$, ζ is the wave number in the z-direction, and $u^*(x)$, $w^*(x)$, $\varphi^*(x)$, $\Phi^*(x)$, $\Psi^*(x)$ and $\sigma^*_{ij}(x)$ are the amplitudes of the field quantities. Using Eq. (34), Eqs. (4.7) take the forms

$$(D^2 - \alpha_1)\Phi^* = -a(D^2 - \alpha_2)\varphi^* \qquad q\varepsilon(D^2 - \zeta^2)\Phi^* = (D^2 - \alpha_3)\varphi^* \qquad (D^2 - k_3^2)\Psi^* = 0 \tag{5.2}$$

where

$$\alpha_1 = \zeta^2 + \omega^2 \qquad \alpha_2 = \zeta^2 + \frac{1}{a} \qquad \alpha_3 = \zeta^2 + q \qquad k_3^2 = \zeta^2 + \omega^2\beta^2$$
$$q = \frac{\omega\eta_0(1 + \tau_0\omega)}{1 + \eta_0 a\omega(1 + \tau_0\omega)} \qquad D = \frac{\mathrm{d}}{\mathrm{dx}} \tag{5.3}$$

Eliminating $\varphi^*(x)$ or $\Phi^*(x)$ in Eqs. $(5.2)_{1,2}$, one gets the following fourth-order differential equation for $\varphi^*(x)$ or $\Phi^*(x)$

$$(D^4 - AD^2 + B)\{\varphi^*(x), \Phi^*(x)\} = 0 \tag{5.4}$$

where

$$A = \frac{\alpha_1 + \alpha_3 - q\varepsilon a(\zeta^2 + \alpha_2)}{1 - q\varepsilon a} \qquad B = \frac{\alpha_1\alpha_3 - q\varepsilon a\zeta^2\alpha_2}{1 - q\varepsilon a} \tag{5.5}$$

Introducing k_i $(i = 1, 2, 3)$ into Eq. (5.4), one finds

$$(D^2 - k_1^2)(D^2 - k_2^2)\{\varphi^*(x), \Phi^*(x)\} = 0 \tag{5.6}$$

where k_1^2 and k_2^2 are the roots of the characteristic equation

$$k^4 - Ak^2 + B = 0 \tag{5.7}$$

The roots of Eqs. (5.6) are given by

$$k_1^2 = \frac{1}{2}\Big[2A + \sqrt{A^2 - 4B}\Big] \qquad k_2^2 = \frac{1}{2}\Big[2A + \sqrt{A^2 - 4B}\Big] \tag{5.8}$$

Keeping in mind that $\varphi^*, \Phi^* \to 0$ as $x \to \infty$ for surface waves, the solution to Eq. (5.6) has the form

$$\{\varphi^*(x), \Phi^*(x)\} = \sum_{n=1}^{2}\{m_n(a, \omega), M_n(a, \omega)\}\mathrm{e}^{-k_n x} \tag{5.9}$$

where $m_n(a, \omega)$ and $M_n(a, \omega)$ are specific functions depending on a and ω. Substituting Eqs. (5.9) into Eqs. $(5.2)_2$, one obtains the following relation

$$M_n(a, \omega) = H_n m_n(a, \omega) \qquad n = 1, 2 \tag{5.10}$$

where

$$H_n = \frac{k_n^2 - \alpha_3}{q\varepsilon(k_n^2 - \zeta^2)} \qquad n = 1, 2 \tag{5.11}$$

Thus, one has

$$\{\varphi^*(x), \Phi^*(x)\} = \sum_{n=1}^{2} \{1, H_n\} m_n(a, \omega) \mathrm{e}^{-k_n x} \tag{5.12}$$

From the regularity condition, one obtains

$$\Psi^*(x) = m_3(a, \omega) \mathrm{e}^{-k_3 x} \tag{5.13}$$

where $m_3(a, \omega)$ is specific function depending on a and ω. Making use of solutions given in Eqs. (5.12) and (5.13), one gets

$$u^* = -\sum_{n=1}^{2} k_n H_n m_n \mathrm{e}^{-k_n x} - \mathrm{i}\zeta m_3 \mathrm{e}^{-k_3 x} \qquad w^* = \mathrm{i}\zeta \sum_{n=1}^{2} H_n m_n \mathrm{e}^{-k_n x} - k_3 m_3 \mathrm{e}^{-k_3 x} \tag{5.14}$$

Using Eqs. (3.4) and (5.9), one obtains

$$\theta^* = \sum_{n=1}^{2} [(1 + a\zeta^2) - a k_n^2] m_n \mathrm{e}^{-k_n x} \tag{5.15}$$

Substituting Eqs. (5.12) and (5.13) into Eqs. (4.8), we obtain

$$\begin{aligned} \sigma_{zz}^* &= \sum_{n=1}^{2} L_n m_n \mathrm{e}^{-k_n x} - 2\mathrm{i}\zeta k_3 m_3 \mathrm{e}^{-k_3 x} \\ \sigma_{xz}^* &= -2\mathrm{i}\zeta \sum_{n=1}^{2} k_n H_n m_n \mathrm{e}^{-k_n x} + (\zeta^2 + k_3^2) m_3 \mathrm{e}^{-k_3 x} \end{aligned} \tag{5.16}$$

where

$$L_n = [-2\zeta^2 + (1 - 2\beta^2)(k_n^2 - \zeta^2)] H_n - \beta^2 [1 - a(k_n^2 - \zeta^2)] \tag{5.17}$$

6. Applications

In what follows, the parameters m_j $(j = 1, 2, 3)$ will be determined. In a physical problem, we should suppress the positive exponentials that are unbounded at infinity. Suppose that an inclined line load F_0 is acting along the interface on the x-axis and its inclination angle with the z-axis is θ_0.

The normal line load F_1 is considered to be acting in the positive x direction on the surface $x = 0$ along the z-axis, and the tangential load F_2 is acting at the origin in the positive x direction, then the boundary conditions on the surface $y = 0$ are

$$\{\sigma_{zz}(0, z, t), \sigma_{xy}(0, z, t)\} = -\{F_1, F_2\} \mathrm{e}^{(\omega t + \mathrm{i}\zeta z)} \tag{6.1}$$

where for the inclined line load F_0 we have $F_1 = F_0 \cos\theta_0$ and $F_2 = F_0 \sin\theta_0$.

The surface $x = 0$ is thermally insulated, i.e. it satisfies the boundary condition

$$\frac{\partial \varphi(0, z, t)}{\partial x} = 0 \tag{6.2}$$

Using the above boundary conditions, one readily obtains the following equations

$$\begin{aligned} &\sum_{n=1}^{2} L_n m_n - 2\mathrm{i}\zeta k_3 m_3 = -F_1 \qquad\qquad -2\mathrm{i}\zeta \sum_{n=1}^{2} k_n H_n m_n + (\zeta^2 + k_3^2) m_3 = -F_2 \\ &\sum_{n=1}^{2} k_n m_n(a,\omega) = 0 \end{aligned} \tag{6.3}$$

They may be written in the matrix form

$$\begin{Bmatrix} m_1 \\ m_2 \\ m_3 \end{Bmatrix} = \begin{bmatrix} L_1 & L_2 & -2\mathrm{i}\zeta k_3 \\ -2\mathrm{i}\zeta k_1 H_1 & -2\mathrm{i}\zeta k_2 H_2 & \zeta^2 + k_3^2 \\ k_1 & k_2 & 0 \end{bmatrix}^{-1} \begin{Bmatrix} -F_1 \\ -F_2 \\ 0 \end{Bmatrix} \tag{6.4}$$

which gives values of the three constants m_j $(j = 1, 2, 3)$. Therefore, the physical quantities of the medium will be fully determined.

7. Numerical results

Numerical results of the thermodynamical temperature, conductive temperature, displacements and stresseswill be presented here. In the present work, the thermoelastic solid half-space due to an inclined load is analyzed by considering the medium made of Copper. The physical properties of Copper is presented in Table 1.

Table 1. Physical data of Copper

Quantity	Unit	Value
K	$\mathrm{W/(m\,K)}$	368
ρ	$\mathrm{kg/m^3}$	8954
C_E	$\mathrm{J/(kg\,K)}$	383.1
α_t	$\mathrm{1/K}$	$1.78 \cdot 10^{-5}$
λ	$\mathrm{N/m^2}$	$7.76 \cdot 10^{10}$
μ	$\mathrm{N/m^2}$	$3.86 \cdot 10^{10}$
T_0	K	293

The computations are carried out on the surface $z = 1.0$ at $t = 0.15$. The graphical results for the dimensionless temperature distribution θ, conductive temperature φ, normal displacement u, transverse displacement w, normal stress σ_{zz}, and tangential stress σ_{zx} are shown in Figs. 1 and 2 with $F_0 = 1$, $\omega = \omega_0 + \mathrm{i}\xi$, $\omega_0 = 2$, $\xi = 0.1$, $\zeta = 2.1$. All the functions have been evaluated inside the medium on the z-axis ($z = 1.0$) as functions of x.

A number of special cases are pertinent in this contribution:

- The equations of the coupled thermoelasticity (CTE) theory with one temperature are obtained when $\tau_0 = 0$ and $a \to 0$.
- The equations of the coupled thermoelasticity (CTE theory) with two temperatures are obtained when $\tau_0 = 0$ and $a > 0$.
- The equations of the Lord-Shulman (LS) theory with one relaxation time are retrieved when $\tau_0 > 0$ and $a \to 0$.
- The equations of the generalized thermoelasticity with two temperatures are obtained when $\tau_0 > 0$ and $a > 0$.

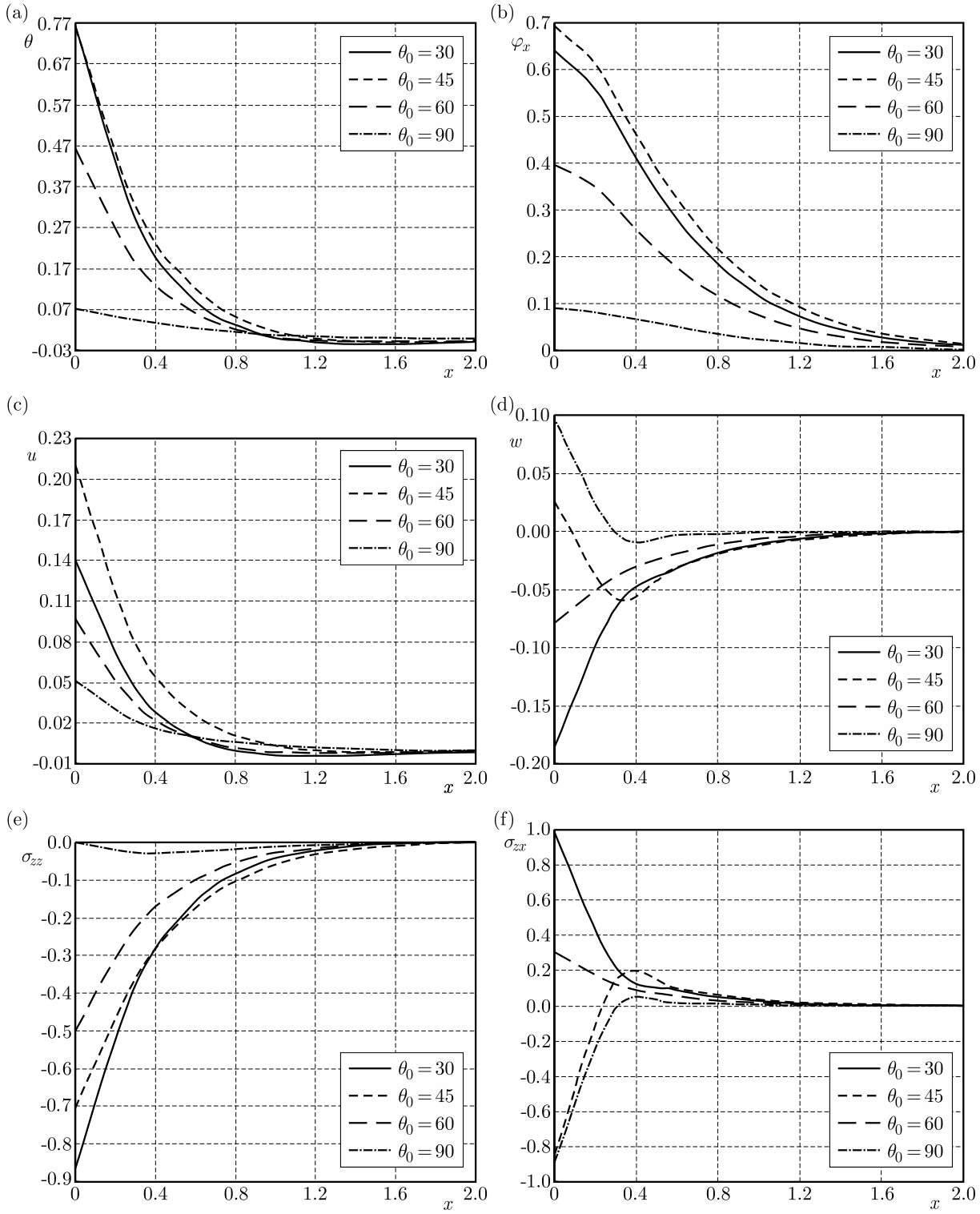

Fig. 1. Variation of dimensionless (a) temperature distribution θ, (b) conductive φ, (c) normal displacement u, (d) tangential displacement w, (e) normal force stress σ_{zz}, (f) tangential force stress σ_{zx} with distance x for different values of angle of inclination θ_0

Figures 1a-1f give a comparison of the results obtained for the normal displacement u, tangential displacement v, transverse normal stress σ_{zz}, tangential shear stress σ_{zx}, temperature distribution θ and conductive temperature φ against the x direction for different values of the angle of inclination θ_0 (orientation of source) and the temperature discrepancy parameter remains constant.

We can see that the angle of inclination θ_0 has significant effects on all the studied fields. It has been observed that θ_0 plays a vital role on the development of temperature, stress, and displacement fields, in which the following is observed:

1. A significant difference in values of the studied fields is noticed for different values of the angle of inclination θ_0.
2. Values of temperature, conductive temperature and normal displacement in the fixed point (x, z) increase when $0 \leqslant \theta \leqslant \pi/4$ and decrease when $\pi/3 \leqslant \theta \leqslant \pi/2$ for the whole time t.
3. The maximum points of displacements w increase when θ_0 increases.
4. Figure 1d shows that the behavior due to $\theta_0 = 45^\circ$ and $\theta_0 = 90^\circ$ is similar, and so for $\theta_0 = 30^\circ$ and $\theta_0 = 60^\circ$.
5. The angle of inclination θ_0 has large effects on the value of the tangential shear stress σ_{zx} which means that σ_{zx} decreases with θ_0.
6. Values of the normal stress σ_{zz} in the fixed point (x, z) decrease when $0 \leqslant \theta \leqslant \pi/4$ and increase when $\pi/3 \leqslant \theta \leqslant \pi/2$ at any moment t.

Figures 2a-2f show how the field results vary with different values of the dimensionless temperature discrepancy. The case $a \to 0$ indicates the old situation (one temperature 1TT) and the cases $a > 0$ indicate the two-temperature theory (2TT).

The variation is very sensitive to the response of all field quantities. When $a = 0$, all quantities exhibit different behavior. This shows the difference between the one temperature generalized thermoelasticity of LS (1TT) and the two-temperature generalized thermoelasticity (2TT). Also, Figs. 2a-2f show that this parameter has significant effects on all the field quantities. The waves reach the steady state depending on the value of the temperature discrepancy. It can be observed that $a > 0$ corresponds to a slower rate of decay than the case when $a = 0$. Once again, the behavior of 2TT model may differ from that of 1TT model near the boundary plane. The model of thermoelasticity with two temperatures predicts a finite speed of wave propagation, which makes the generalized theorem of thermoelasticity more agreeable with physical properties of the material.

8. Conclusions

Analysis of normal displacement, tangential displacement, transverse normal stress, tangential shear stress, temperature distribution and conductive temperature due to mechanical load in a semi-infinite generalized thermoelastic medium is an interesting problem of mechanics. The generalized two-temperature theory of thermoelasticity in the context of Lord and Shulman's (LS) model is used to solve this problem. A normal mode technique has been used which is applicable to a wide range of problems of thermoelasticity. This method gives exact solutions without any assumed restrictions on the actual physical quantities that appear in the governing equations of the problem considered. The effects of the angle of inclination as well as the two-temperature parameter on the field variables are investigated. The results concluded from the above analysis can be summarized as follows:

- It is seen that the values of all the field variables are significantly dependent on the two-temperature parameter.
- According to the theory of thermoelasticity with two temperatures, we have to construct a new classification for materials according to their fractional parameter. This parameter becomes a new indicator of the material ability to conduct heat under the effect of thermoelastic properties.

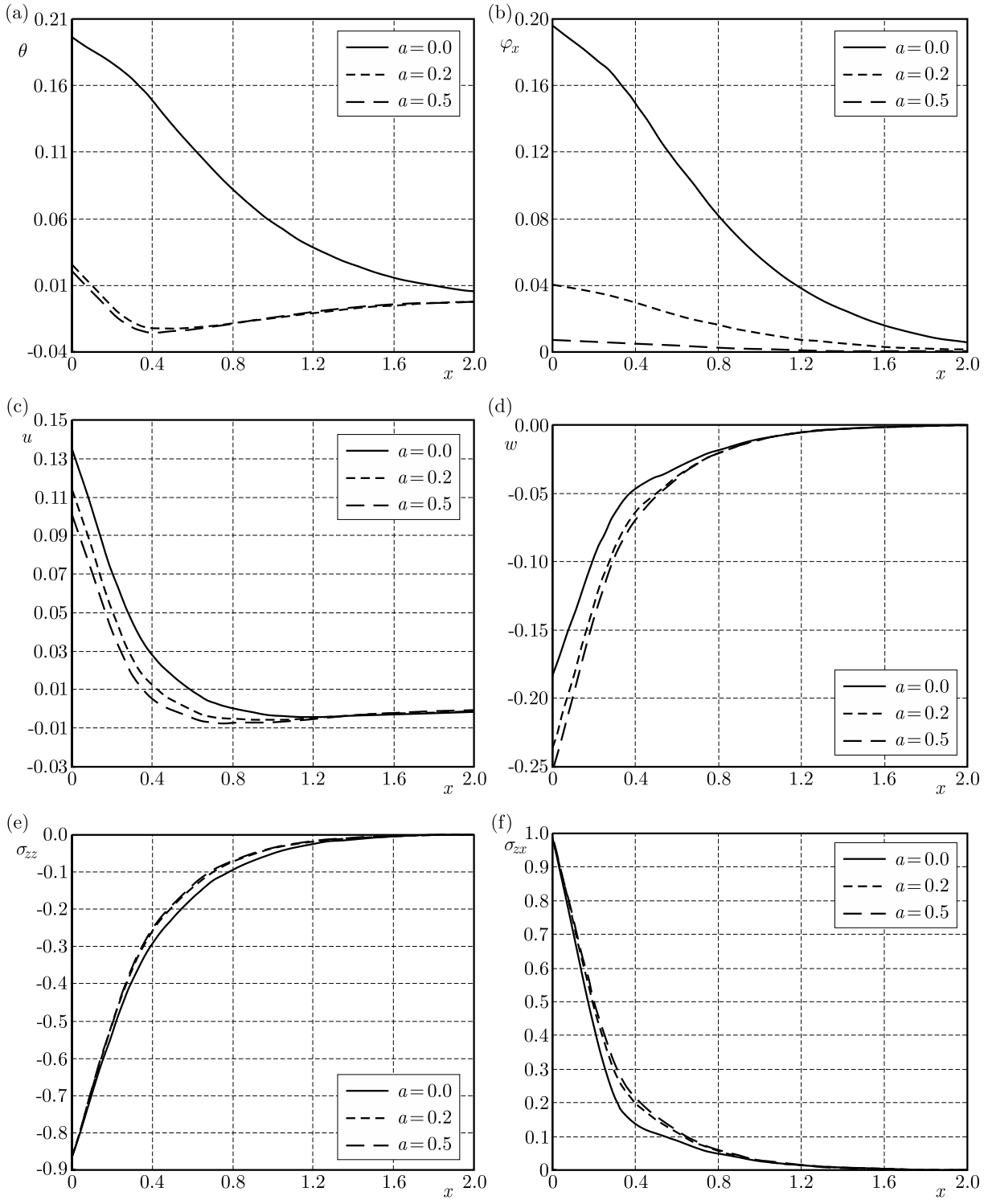

Fig. 2. Variation of dimensionless (a) temperature distribution θ, (b) conductive φ, (c) normal displacement u, (d) tangential displacement w, (e) normal force stress σ_{zz}, (f) tangential stress σ_{zx} with distance x for different values of temperature discrepancy parameter a

- It is also observed that the theories of coupled thermoelasticity and generalized thermoelasticity with one relaxation time can be obtained as limit cases.
- According to this work, one can consider the theory of two-temperature generalized thermoelasticity as an improvement of the study on elastic materials.

- The properties of the body largely depend on the direction of symmetry and the inclination of the applied source.
- Significant difference in values of the studied fields is noticed for different values of the angle of inclination.

References

1. Abbas I.A., Zenkour A.M., 2014, Two-temperature generalized thermoelastic interaction in an infinite fiber-reinforced anisotropic plate containing a circular cavity with two relaxation times, *Journal of Computational and Theoretical Nanoscience*, **11**, 1, 1-7
2. Abouelregal A.E., Zenkour A.M., 2013, Effect of fractional thermoelasticity on a two-dimensional problem of a mode I crack in a rotating fibre-reinforced thermoelastic medium, *Chinese Physics B*, **22**, 10, 108102
3. Allam M.N., Elsibai K.A., Abouelregal A.E., 2009, Electromagneto-thermoelastic problem in a thick plate using Green and Naghdi theory, *International Journal of Engineering Science*, **47**, 680-690
4. Biot M.A., 1956, Thermoelasticity and irreversible thermodynamics, *Journal of Applied Physics*, **27**, 240-253
5. Boley M., 1956, Thermoelastic and irreversible thermo dynamics, *Journal of Applied Physics*, **27**, 240-253
6. Chen P.J., Gurtin M.E., 1968, On a theory of heat conduction involving two temperatures, *Zeitschrift für angewandte Mathematik und Physik ZAMP*, **19**, 614-627
7. Chen P.J., Gurtin M.E., Willams W.O., 1969, On the thermodynamics of non-simple elastic material with two temperatures, *Zeitschrift für angewandte Mathematik und Physik ZAMP*, **20**, 107-112
8. Cheng J.C., Zhang S.Y., 2000, Normal mode expansion method for laser generated ultrasonic lamb waves in orthotropic thin plates, *Applied Physics B*, **70**, 57-63
9. El-Maghraby N.M., 2008, A Two-dimensional generalized thermoelasticity problem for a half-space under the action of a body force, *Journal of Thermal Stresses*, **31**, 557-568
10. El-Maghraby N.M., 2009, Two-dimensional thermoelasticity problem for a thick plate under the action of a body force in two relaxation times, *Journal of Thermal Stresses*, **32**, 863-876
11. Green A.E., Lindsay K.A., 1972, Thermoelasticity, *Journal of Elasticity*, **2**, 1-7
12. Green A.E. Naghdi P.M., 1993, Thermoelasticity without energy dissipation, *Journal of Elasticity*, **31**, 189-208
13. Lord H.W., Shulman Y., 1967, A generalized dynamical theory of thermoelasticity, *Journal of the Mechanics and Physics of Solids*, **15**, 299-309
14. Sherief H., Hamza F., 1996, Generalized two dimensional thermoelastic problems in spherical regions under axisymmetric distributions, *Journal of Thermal Stresses*, **19**, 55-76
15. Sherief H.H., El-Maghraby N., 2003, An internal penny-shaped crack in an infinite thermoelastic solid, *Journal of Thermal Stresses*, **26**, 333-352
16. Sherief H.H., El-Maghraby N., 2005, A mode-I crack in an Infinite Space in Generalized Thermoelasticity, *Journal of Thermal Stresses*, **28**, 465-484
17. Zenkour A.M., 2015, Three-dimensional thermal shock plate problem within the framework of different thermoelasticity theories, *Composite Structures*, **132**, 1029-1042
18. Zenkour A.M., Abouelregal A.E., 2014a, State-space approach for an infinite medium with a spherical cavity based upon two-temperature generalized thermoelasticity theory and fractional heat conduction, *Zeitschrift für angewandte Mathematik und Physik ZAMP*, **65**, 1, 149-164

19. Zenkour A.M., Abouelregal A.E., 2014b, The effect of two temperatures on a functionally graded nanobeam induced by a sinusoidal pulse heating, *Structural Engineering and Mechanics*, **51**, 2, 199-214

20. Zenkour A.M., Abouelregal A.E., 2015, Thermoelastic problem of an axially moving microbeam subjected to an external transverse excitation, *Journal of Theoretical and Applied Mechanics*, **53**, 167-178

Manuscript received December 25, 2014; accepted for print November 29, 2015

JOURNAL OF THEORETICAL AND APPLIED MECHANICS
54, 3, pp. 839-846, Warsaw 2016
DOI: 10.15632/jtam-pl.54.3.839

EXPERIMENTAL STUDY ON AMPLITUDE-FREQUENCY CHARACTERISTIC AND BASIN STABILITY OF HORIZONTALLY DRIVEN PENDULUM

Ji Jia
School of Science, Beijing University of Posts and Telecommunications, Beijing, China

Ye Wu
School of Science, Beijing University of Posts and Telecommunications, Beijing, China
State Key Lab of Information Photonics and Optical Communications, Beijing University of Posts and Telecommunications, Beijing, China

Weiqing Liu
School of Science, Jiangxi University of Science and Technology, Ganzhou, China

Jinghua Xiao
School of Science, Beijing University of Posts and Telecommunications, Beijing, China
State Key Lab of Information Photonics and Optical Communications, Beijing University of Posts and Telecommunications, Beijing, China; e-mail: jhxiaobupt@163.com

In this article, an inverted pendulum system is set up to explore the dynamics of a horizontally driven pendulum which exhibits a great variety of dynamical behavior and appears in a wide range of applications in the field of engineering. The facility is efficient to experimentally explore two kinds of coexisting movement patterns in the horizontally driven pendulum, i.e. in-phase and anti-phase patterns between the angular velocity of the pendulum rod and the direction of the driving forces. Theoretical analysis is applied to reveal the regimes of the coexistence of the two movement patterns, which is promising to control the system to a desired pattern.

Keywords: horizontally driven pendulum system, bifurcation, basin stability

1. Introduction

The study of pendulum motion is a classical problem in physics since it reveals the basic movement in the world of nature (Mokha *et al.*, 1991; Wu *et al.*, 2012a), ranging from physics, chemistry ecology and economics to biology (Wu *et al.*, 2012b). Without additional driving and damping, an isolated pendulum swings in a simple period mode. With various types of additional driving and damping, driven pendulum models are widely used since they often capture the key dynamics of many complicated dynamical systems (Leven and Koch, 1981; Sauer *et al.*, 1999; Masoud *et al.*, 2004). For instance, through vertical shaking of the pendulum pivot point, a lot of chaotic motions are observed in the driving pendulum (Heng and Martienssen, 1992; Baker, 1995). However, a group of pendulums driven by horizontal forces has been recently examined in experiments and widely applied in engineering (Thakur *et al.*, 2008), yet the basic dynamical behavior is still unclear and need further concentrations. The most noteworthy is that horizontal driving may lead the pendulum to angular vibration of a non-zero mean value (Schmitt and Bayly, 1998) and a variety of dynamical characteristics such as the existence of bi-stability (Nakamura *et al.*, 2011; Yan *et al.*, 2012).

A series of equipment such as driving stepper motors, poles of metal and conveyor belts are used to set up the device. It can be observed in the experiment that the special parameters

lead the top and bottom ends of the rod of the pendulum to in-phase or anti-phase oscillating. In our experiment, the amplitude-versus-frequency curve is studied, dynamic analysis of the system and numerical simulation is carried out, and the basins and their stability of the two coexisting periodic oscillation states are considered. Moreover, it is noticeable that there is a certain difficulty to control the switching between the two coexisting movement patterns. In reaction of this phenomenon, a possible explanation is given in theory, and it is hopeful to benefit for more experiments and applications.

This paper is arranged as follows. In Section 2, the experimental setup is introduced. In Section 3, we present the experimental results and analysis. In Section 4, the theoretical model and analysis are introduced in detail. The results of numerical simulations are presented in Section 5. Finally, in Section 6, we recommend some other significant applications and draw a conclusion.

2. Experimental setup

A schematic of the physical pendulum system we consider, as shown in Fig. 1, consists of an inverted pendulum system and an acquisition system linked with a computer. The system is mainly composed of a driving stepper motor, conveyor belt, horizontal track, slider, and swinging rod. The slider is confined on the horizontal track and can move freely in the direction of the horizontal track. Applying a sine signal to the driving motor, the slider may exhibit a simple harmonic movement in the direction of the horizontal track through the conveyor belt connected to the motor. The swinging rod connected with the slider through a rotating axis (perpendicular to the trace of the slider) can swing freely in the vertical plane.

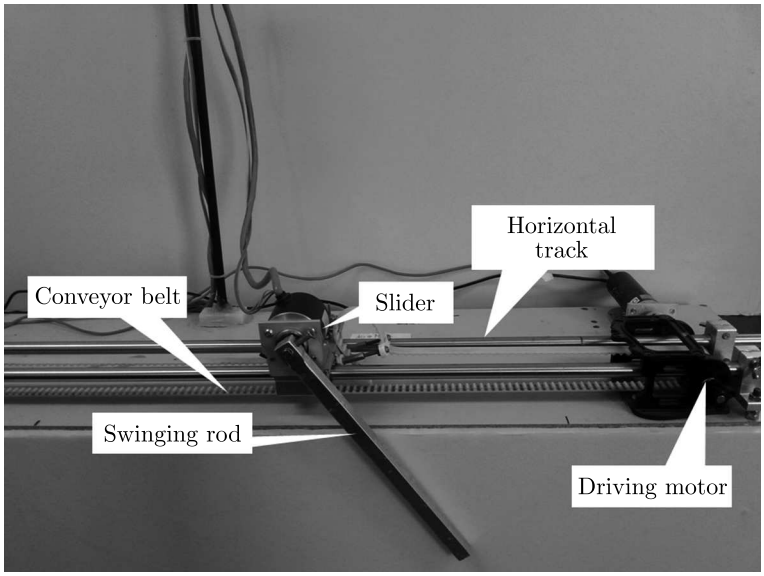

Fig. 1. Experimental setup

Several sensors are set up on the rotating axis. The sensors record the data of the rotating angle of the rotating axis and the horizontal displacement of the slider, and then transmits those data to the computer for further analysis (Wu *et al.*, 2014). The corresponding experimental parameters are set as follows. Length of the rod is 0.193 m, and the driving frequency varies from 0.6 Hz to 2.0 Hz. The time interval of acquisition is 0.01 s.

3. Experimental results and analysis

Under driving with the sine signal, the movements of the slider and the swinging rod are coupled together. To describe the movement of the slider and the swinging rod, the displacement $x(t)$ and the angular displacement $\theta(t)$ are defined by selecting the balance point of the simple harmonic movement and the vertical line through the rotor axis as a reference, respectively. The time series of the displacement $x(t)$ and the angular displacement $\theta(t)$ recorded by the sensors reveal the dynamics of the slider and the swinging rod as shown in Fig. 2a,b. Two kinds of movement patterns are observed as (a) in-phase pattern, and (b) anti-phase pattern for different initial values. When the coupled movement is in the in-phase (anti-phase) pattern, the slider and the swing rod move in the same (opposite) directions.

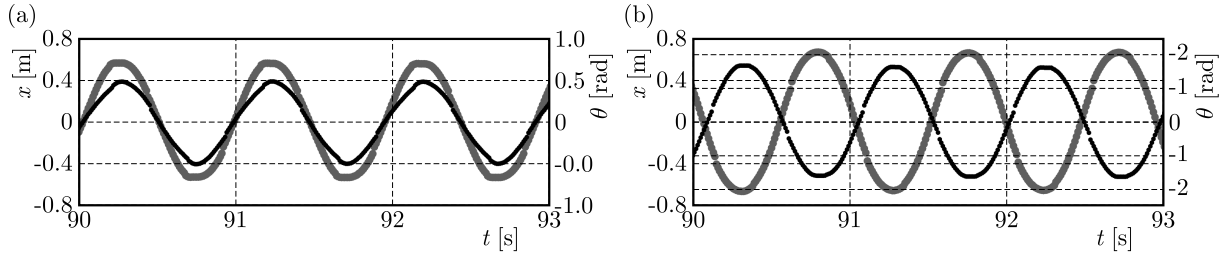

Fig. 2. Time series of the horizontal displacement of the slider (expressed by x and plotted by the thin black line) and the pivot angle of the rod (expressed by θ and plotted by the thick gray line). (a) In-phase oscillation state with the initial value $(x, \theta) = (0.93, 0.52)$, (b) anti-phase oscillation state with the initial value $(x, \theta) = (-0.49, 1.74)$

According to the experimental set up, the driving signal has obvious influence on the amplitude of the movement of the slider and the swinging rod. To reveal the effects of the frequency of the driving signals on the movements, the amplitude-frequency characteristics of the driven oscillators are recorded. Since there are two coexisting patterns, it is necessary to check if the amplitude-frequency curves of those two patterns are different. The maximal swing angle of the rod is recorded for all given frequencies of the driving signal as shown in Fig. 3. Interestingly, in a particular range of the parameter $f \in [0.722, 1.139]$, there are two quite different amplitude-frequency curves for different patterns. When the system is in the anti-phase pattern, the maximal swing angle is quite larger than that when the system is in the in-phase pattern.

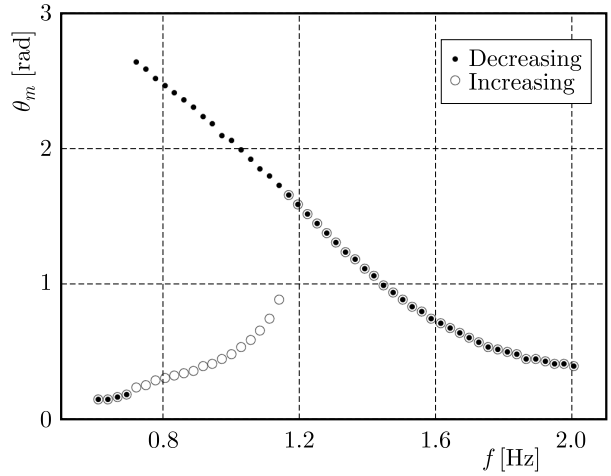

Fig. 3. Amplitude-frequency curves of the horizontally driven pendulum. The circles and dots denote the increasing and decreasing processes of frequency, respectively

4. Theoretical model

We consider a horizontally driven pendulum system whose rotation axis is driven by a horizontal force. The rod is rigid and uniform, the mass is m, and the length is l. The upper end is fixed on a slider which can move horizontally at a particular rate along the track when driven by a motor. A model diagram is shown in Fig. 4.

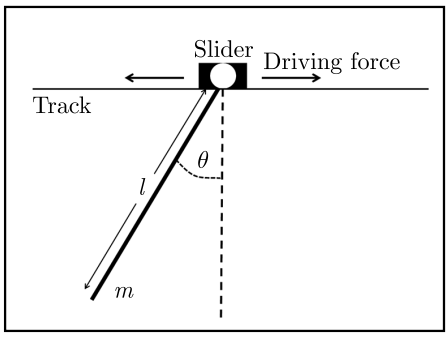

Fig. 4. Sketch of the model. A rod of mass m and length l is subjected to a horizontal driving force and angular displacement θ from the vertical direction

We control the driving signal of the driving motor and let the speed of the slider satisfy the following equation

$$\dot{x}(t) = A_m \sin(2\pi f t) \tag{4.1}$$

where A_m is the maximum value of the speed and f is the frequency of driving force. When the slider moves at the speed $\dot{x}(t)$ in equation (4.1), the rod hinged in the slider will swing according to the driving signal. The equation of dynamics of the system can be written as the following Euler-Lagrange equation

$$L = \frac{1}{2}m\Big(\dot{x}^2 + \frac{1}{3}l^2\dot{\theta}^2 + \dot{x}l\dot{\theta}\cos\theta\Big) - \frac{1}{2}mgl(1-\cos\theta) \tag{4.2}$$

As a consequence, the kinematical equation of the system can be expressed as a second order nonlinear differential equation

$$\frac{1}{3}ml^2\ddot{\theta} + \pi f m l A_m \cos(2\pi f t)\cos\theta + \frac{1}{2}mgl\sin\theta + C\dot{\theta} = 0 \tag{4.3}$$

In equations (4.2) and (4.3), m and l are the mass and length of the rod respectively, θ is the swing angle of the rod, g is the acceleration of gravity, and C is the damping coefficient.

5. The results of numerical simulations

5.1. In-phase and anti-phase periodic oscillation

There are four parameters to be confirmed in equation (4.3). In order to ensure the simulation results coincide with the experimental data, the parameters should be measured as accurately as possible. The mass and length of the rod can be directly measured and the results are $m = 0.05631$ and $l = 0.193$ (in SI). The maximum speed of the slider can be precisely adjusted by the computer and the value is fixed as $A_m = 0.3544$ so that the moving slider can be kept in a proper range. Comparing the numerical simulation repeatedly with experimental results is necessary to confirm the damping coefficient. Without the horizontal driving force, the system is underdamped. If the rod is released from the horizontal direction, it will oscillate for a few

periods and end up vertically stationary due to the action of damping. Through experiments, we record the duration of the underdamped system and the number of times the rod passesthe stable point. Thus, it can be found in the simulation after several repeated attempts that for the damping coefficient is $C = 0.001$, the number of oscillations and the total time of the motion are both consistent with the experimental results. Hence, the above values are determined to be used in our following simulations.

We obtain the dynamics under different initial conditions by numerical calculation based on the 4th-order Runge-Kutta method. There is also a coexistence of the in-phase and anti-phase patterns in the system as shown in Fig. 5. The numerical results excellently agree with the experimental phenomena given in Fig. 2. Figures 5a and 5b are numerical results of time series of the in-phase and anti-phase oscillation state, respectively.

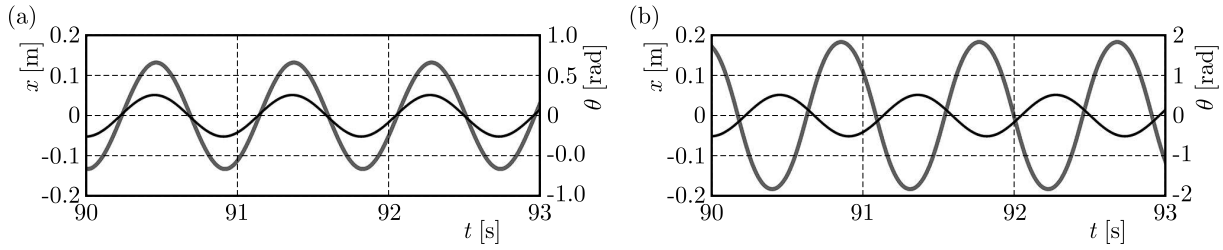

Fig. 5. Numerical simulation results of two kinds of the oscillation state. The displacement of the top end of the rod is plotted by the thin black line and the pivot angle of the rod is plotted by the thick grey line. (a) The in-phase oscillation state, (b) the anti-phase oscillation state

5.2. Bifurcation phenomenon

Let us consider the amplitude-frequency curve of the horizontally driven pendulum system numerically. We record the maximal values of the swing angle of the rod with a quasi-static method, i.e. we start from the driving frequency $f = 0.7\,\mathrm{Hz}$ ($2.0\,\mathrm{Hz}$), then slightly increase (decrease) the driving frequency and take the final states with tiny noise as the initial value for a new f. Since there are two coexisting states when $f = 0.7\,\mathrm{Hz}$, two branches of the amplitude-frequency curves can be obtained. Compared with the amplitude-frequency of the experimental results, the numerical one coincides with the experimental one well as shown in Fig. 6. The black solid line and the grey dashed line are the numerical results while the black triangles and the grey circles are experimental results.

Furthermore, the final state of the horizontally driven pendulum system is so sensitive to the initial values that obvious uncertainty and unpredictability exist in the experiment. Two very closing initial values may lead to quite different states. It is extremely difficult to make the initial values exactly the same when repeating the practical experiments. There is always a slight difference and interference during the experiments. Therefore, prediction and control of the final state of the system become a noteworthy problem in the experiment.

5.3. Basin and its stability

It is meaningful to explore the basin stability of the two coexisting patterns since detailed information of the basin stability is important in predicting the dynamical fate of the coupled system. With the fixed parameters $l = 0.193$, $A_m = 0.3544$, $C = 0.001$, $f = [0.607, 1.1763]\,\mathrm{Hz}$, the system has two coexisting patterns (in-phase or anti-phase patterns). To observe the basin of those two coexisting patterns in detail, we recorded and dotted all initial values $(\theta_0, \dot{\theta}_0)$ with which the system finally transits to the in-phase pattern for a given driving frequency f. According to the results shown in Figs. 7a-7h, one may find that the basins of the two patterns

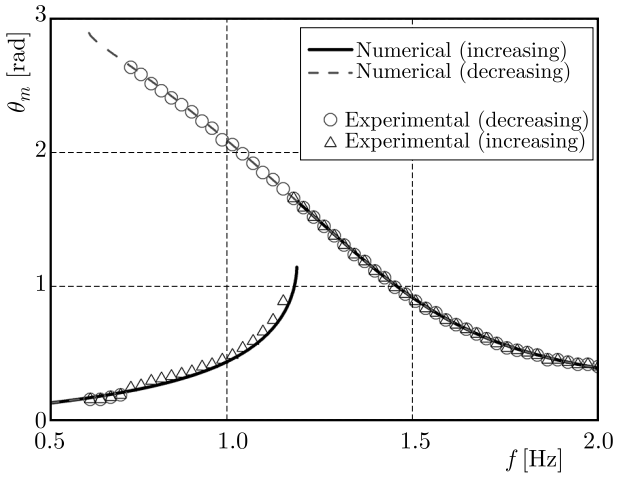

Fig. 6. Amplitude-frequency curves of the numerical and experimental results. The upper branch is for the anti-phase oscillation state, and the lower branch if for the in-phase state. The triangles (increasing) and circles (decreasing) are the experimental results while the solid (increasing) and dash (decreasing) lines are the numerical ones

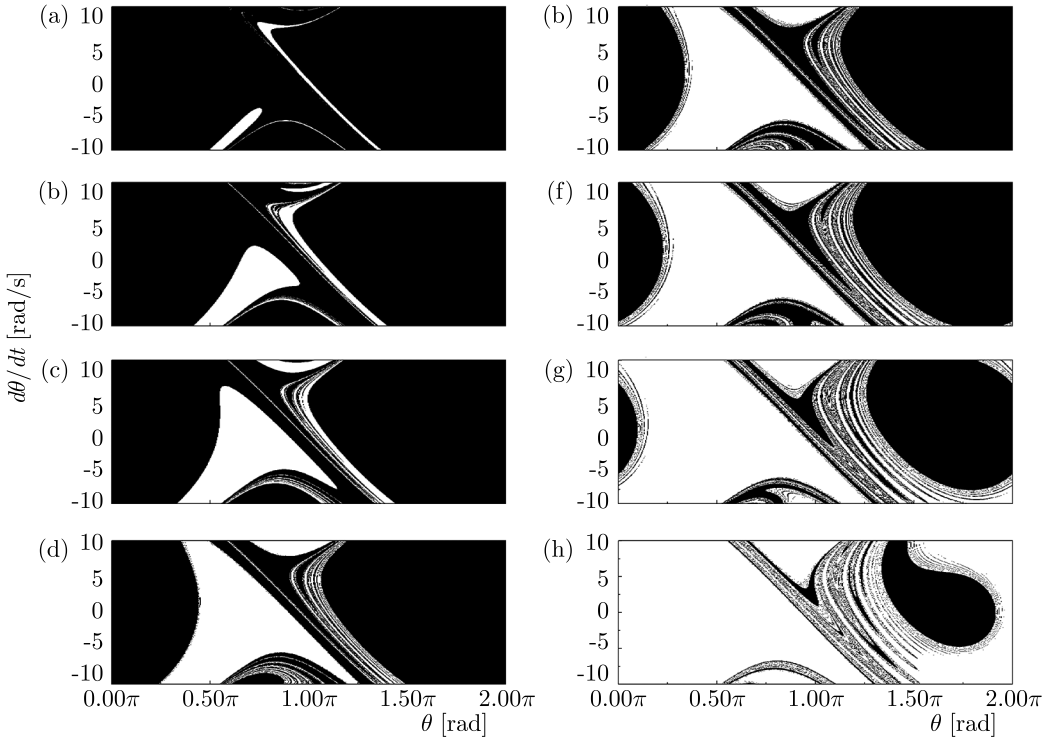

Fig. 7. Basins of the system with different frequencies. From (a) to (h), the driving frequency of the system changes from 0.8 Hz to 1.15 Hz by step of 0.05 Hz

are possible and riddled in some phase space of $(\theta, \dot{\theta})$. Moreover, with an increment in the driving frequency, the basins of the in-phase pattern shrink with that of the anti-phase one expanding.

With detailed information on the basin, it is helpful to determine the final state of the bistable system in the sense of the control experiment. Since is convenient to set the angular velocity to be zero, one may take more attention to the basin when the initial angular velocity is zero. For example, in this experiment, if the information on the basin is known as in Fig. 7h for $f = 1.15$ Hz, then we can surely get the anti-phase dynamics by pulling the swinging rod to a certain point of angle (less than $\pi/2$) and then releasing it from the stationary state. However,

the final state is hard to predict when the basins are riddled since tiny noise tends to change the fate of the final state (Aguirre and Sanjuan, 2002), for example, if we initially pull the rod to a position between $\theta = [\pi, 1.5\pi]$ for $f = 1.15\,\mathrm{Hz}$, the final state is possible in-phase or anti-phase in the experiment with small noise.

Owing to the interweave of basins of different states and inevitable systematic noise as well as experimental error, it is wise to calculate the basin stability based on the method presened by Menck *et al.* (2013). Applying it, we can calculate the basin stability for the anti-phase S_{BA} and in-phase pattern S_{BI} by estimating the volume of the basin in a relatively sensitive subset of the state volume $Q \in (\theta, \dot{\theta})$. Therefore, according to the basin stability for different parameters, the possibility of the system to reach the final state can be easily determined by the following forms

$$S_{BA} = \frac{Vol(B_A \cap Q)}{Vol(Q)} \qquad S_{BI} = \frac{Vol(B_I \cap Q)}{Vol(Q)}$$

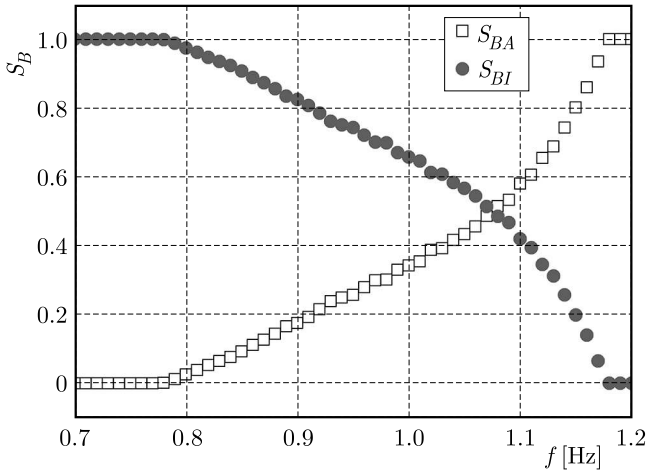

Fig. 8. Basin stability of the system

The basin stabilities of the two coexisting patterns of the system versus the driving frequency f are calculated with the subset volume $Q = 50000$ points for each $f \in [0.7, 1.2]\,\mathrm{Hz}$ as shown in Fig. 8. When $f < 0.78\,\mathrm{Hz}$, all initial values will lead to an in-phase pattern. With an increment in the frequency f, the basin stability of the in-phase pattern continuously decreases till $f > 1.17\,\mathrm{Hz}$.

6. Conclusion

Experimental tests and nonlinear numerical analyses reveal a great deal of results that seem to be interesting from the research point of view. In this paper, a simple experimental device of a horizontally driven pendulum is set up to explore rich dynamics such as the bistability and bifurcation phenomenon in a specific range of the driving frequency. Two kinds of patterns, i.e. in--phase and anti-phase patterns coexisting with each other are observed. They have corresponding branches of amplitude-frequency characteristics. The riddled basins are observed, which makes it difficult to predict the final state in the experiment on a real system. The basin of stability is calculated and applied to predict the final states of the multi-stable system for different driving frequencies. When the driving frequency is low, the system has a unique in-phase oscillation state; the basin of stability of the in-phase state decreases with an increment in the driving frequency till the in-phase state disappears when the driving frequency is larger than a certain value.

Finally, we verified the experimental results by numerical simulation. Some suggestions were also brought out from theory, which facilitated in the experiment the controlling of the final state of the system and switching it between two kinds of oscillation states. Moreover, we hope that our study of the horizontally driven pendulum system can play a guiding role in thr control and synchronization problems of driven damping systems and coupled oscillatory systems in real life.

Acknowledgment

This work was jointly supported by the National Natural Science Foundation of China (Grant No. 11375033) and the project of high school of Jiangxi province (KJLD14047), and the training plan of young scientists of Jiangxi Province.

References

1. Aguirre J., Sanjuan M.A.F., 2002, Unpredictable behavior in the Duffing oscillator: Wada basins, *Physica D*, **171**, 1/2, 41-51
2. Baker G.L., 1995, Control of the chaotic driven pendulum, *American Journal of Physics*, **63**, 9, 832-838
3. Heng H., Martienssen W., 1992, Analysing the chaotic motion of a driven pendulum, *Chaos, Solitons and Fractals*, **2**, 3, 323-334
4. Leven R.W., Koch B.P., 1981, Chaotic behavior of paramentrically excited damped pendulum, *Physics Letters A*, **86**, 2, 71-74
5. Masoud Z.N., Nayfeh A.H., Mook D.T., 2004, Cargo pendulation reduction of ship-mounted cranes, *Nonlinear Dynamics*, **35**, 3, 299-311
6. Menck P.J., Heitzig J., Marwan N., Kurths J., 2013, How basin stability complements the linear-stability paradigm, *Nature Physics*, **9**, 2, 89-98
7. Mokha A., Constantinou M.C., Reinhorn A.M., Zayas V.A., 1991, Experimental study of friction-pendulum isolation systeme, *Journal of Ftructural Engineering*, **117**, 4, 1201-1217
8. Nakamura Y., Saruta M., Wada A., Takeuchi T., Hikone S., Takahashi T., 2011, Development of the core-suspended isolation system, *Earthquake Engineering and Structural Dynamics*, **40**, 4, 429-447
9. Sauer I.M., Frank J., Bucherl E.S., 1999, Proposal of a new electromechanical total artificial heart: the TAH Serpentina, *Aritificial Organs*, **23**, 3, 290-291
10. Schmitt J.M., Bayly P.V., 1998, Bifurcations in the mean angle of a horizontally shaken pendulum: analysis and experiment, *Nonlinear Dynamics*, **15**, 1, 1-14
11. Thakur R.B., English L.Q., Sievers A.J., 2008, Driven intrinsic localized modes in a coupled pendulum array, *Journal of Physics D-Applied Physics*, **41**, 1, 015503
12. Wu Y., Song Z., Liu W., Jia J., Xiao J., 2014, Experimental and numerical study on the basin stability of the coupled metronomes, *European Physical Journal-Special Topics*, **223**, 4, 697-705
13. Wu Y., Wang N.C., Li L.X., Xiao J., 2012, Anti-phase synchronization of two coupled mechanical metronomes, *Chaos*, **22**, 2, 5
14. Wu Y., Xiao J.H., Hu G., Zhan M., 2012, Synchronizing large number of nonidentical oscillators with small coupling, *Europhysics Letters*, **97**, 4, 6
15. Yan X., Tristram J.A., Harvinder S.S., 2012, Instability dynamics of a horizontally shaken pendulum, *Australian and New Zealand Industrial and Applied Mathematics*, **53** (EMAC2011), C325-C339

Manuscript received January 28, 2015; accepted for print December 2, 2015

JOURNAL OF THEORETICAL AND APPLIED MECHANICS
54, 3, pp. 847-857, Warsaw 2016
DOI: 10.15632/jtam-pl.54.3.847

EFFECT OF INITIAL STRESS AND GRAVITY FIELD ON MICROPOLAR THERMOELASTIC SOLID WITH MICROTEMPERATURES

Mohamed I.A. Othman

Zagazig University, Department of Mathematics, Faculty of Science, Zagazig, Egypt
Taif University, Department of Mathematics, Faculty of Science, Taif, Saudi Arabia
e-mail: m_i_a_othman@yahoo.com

Ramadan S. Tantawi

Zagazig University, Department of Mathematics, Faculty of Science, Zagazig, Egypt
e-mail: ramadan_tantawi1@yahoo.com

Mohamed I.M. Hilal

Zagazig University, Department of Mathematics, Faculty of Science, Zagazig, Egypt
Sinai University, Department of Basic Sciences, Faculty of Engineering Sciences, El-Arish, Egypt
e-mail: mimhilal@yahoo.com

The purpose of the present article is the study of the effect of the gravity field on an initially stressed micropolar thermoelastic medium with microtemperatures. The analytical method used to obtain the formula of the physical quantities is the normal mode analysis. The comparisons are established graphically in the presence and the absence of gravity, initial stress and micropolar thermoelasticity. The main conclusions state that the gravity, initial stress and the micropolar thermoelasticity are effective physical operators on the variation of the physical quantities. The microtemperatures are very useful theory in the field of geophysics and earthquake engineering.

Keywords: gravity, initial stress, micropolar thermoelasticity, microtemperatures

1. Introduction

The theory of elastic micropolar materials was introduced by Eringen (1966). The theory of continuum micropolar mechanics takes into consideration the microstructure of materials. Description of the micropolar materials is useful for fibrous, lattice or, in general, materials having microstructural construction having in each point extra rotational degrees of freedom independent of translation. The material, however, can transmit couple stress. Smith (1967) studied wave propagation in micropolar elastic solids. Parfitt and Eringen (1971) investigated reflection of plane waves from a flat boundary of a micropolar elastic half-space. Ariman (1972) also studied wave propagation in a micropolar elastic half-space solid. Eringen (1999) presented the microcontinuum field theory. Kumar and Ailawalia (2005) studied the response of a micropolar cubic crystal due to various sources. Kumar and Gupta (2010) studied propagation of waves in a transversely isotropic micropolar generalized thermoelastic half-space. Abbas and Kumar (2013) studied deformation due to a thermal source in micropolar thermoelastic media with the two-temperature effect. Recently, Othman *et al.* (2014) established the effect of rotation on a micropolar thermo-elastic solid with two temperatures. Abouelregal and Zenkour (2015) studied a thermoelastic problem of an axially moving micro beam subjected to an external transverse excitation. The concept of microtemperatures means that microelements of a thermoelastic body have different temperatures and depend homogeneously on microcoordinates of the microelements, which are based on the

microstructure of the continuum. Grot (1969) established the thermodynamic theory of elastic materials with inner structures, in which microdeformations and particles possess microtemperatures. Eringen and Kafadar (1976) presented the basis for the microelements with microtemperatures. Riha (1979) presented a study of heat conduction in materials with inner structures. Iesan and Quintanilla (2000) constructed the linear theory of thermoelasticity for materials with inner structure whose particles, in addition to the classical displacement and temperature fields, possess microtemperatures. Iesan (2001, 2004) presented the mathematical model of theory of micromorphic elastic solids with microtemperatures, in which microelements possess microtemperatures and can stretch and contract independently of their translations. Casas and Quintanilla (2005) studied exponential stability in thermoelasticity with microtemperatures. Scalia and Svanadze (2006) discussed solutions of the theory of thermoelasticity with microtemperatures. Iesan (2006, 2007) presented a study of thermoelastic bodies with a microstructure and microtemperatures.

The effect of gravity on wave propagation in an elastic medium was first considered by Bromwich (1898) who treated the force of gravity as a type of a body force. Love (1965) extended the work of Bromwich investigating the influence of gravity on superficial waves and showed that the Rayleigh wave velocity is affected by the gravitational field. Sezawa (1927) studied dispersion of elastic waves propagating on curved surfaces. Othman *et al.* (2013a,b) investigated two models on the effect of the gravitational field on thermoelastic solids. The presence of initial stresses in solid materials has a substantial effect on their subsequent response to applied loads that is very different from the corresponding response in the absence of initial stresses. In geophysics, as an example, high stress developed below the Earth's surface due to gravity has a strong influence on the propagation speed of elastic waves. While in soft biological tissues initial (or residual), stresses in artery walls ensure that the circumferential stress distribution through thickness of the artery wall is close to uniform at typical physiological blood pressures. Initial stresses may arise, for example, from applying loads, as in the case of gravity, processes of growth and development in living tissue or, in the case of engineering components, from the manufacturing process. Ames and Straughan (1999) derived continuous dependence results for initially pre-stressed thermoelastic bodies. Montanaro (1999) investigated isotropic linear thermoelasticity with hydrostatic initial stress. Wang and Slattery (2002) formulated thermoelastic equations without energy dissipation for initially stressed bodies. Iesan (2008) presented a theory of Cosserat thermoelastic solids with initial stresses. Recently, Othman *et al.* (2015) discussed the effect of initial stress on a thermoelastic rotating medium with laser pulse heating.

This investigation studies the 2D problem of linear, isotropic, homogeneous initially stressed micropolar thermoelastic solid influenced by the gravity field. The application of the present model cannot be ignored in geophysics and earthquake engineering due to the importance of the microtemperature properties. The normal mode analysis is the analytical method used to obtain the solutions of the considered physical quantities which are graphically represented in the absence and presence of the studied physical effects.

2. Basic equations

Consider the linear theory of thermodynamics for isotropic elastic materials with inner structure. According to Eringen (1999), Isean (2007) and Montanaro (1999), the field equations and the constitutive relations for a linear, homogeneous, isotropic initially stressed micropolar thermoelastic solid with microtemperatures without body forces, body couples, heat sources and first heat source moment, can be considered as

$$\begin{aligned}
&\frac{\partial \sigma_{ij}}{\partial x_i} = \rho \frac{\partial^2 u_j}{\partial t^2} \qquad \frac{\partial m_{ij}}{\partial x_i} + \varepsilon_{ijr}\sigma_{ir} - \mu_1 \frac{\partial w_j}{\partial x_i} = J\rho \frac{\partial^2 \phi_j}{\partial t^2} \\
&k_6 \frac{\partial^2 w_i}{\partial x_j^2} + (k_4 + k_5)\frac{\partial^2 w_j}{\partial x_i \partial x_j} + \mu_1 \frac{\partial}{\partial t}\frac{\partial \phi_j}{\partial x_i} - k_2 w_i - b\frac{\partial w_i}{\partial t} - k_3 \frac{\partial T}{\partial x_i} = 0 \\
&k\frac{\partial^2 T}{\partial x_i^2} - \rho C_e \frac{\partial T}{\partial t} - \gamma_1 T_0 \frac{\partial}{\partial t}\frac{\partial u_i}{\partial x_i} + k_1 \frac{\partial w_i}{\partial x_i} = 0
\end{aligned} \tag{2.1}$$

and

$$\begin{aligned}
&\sigma_{ij} = \lambda \frac{\partial u_r}{\partial x_r}\delta_{ij} + \mu\Big(\frac{\partial u_i}{\partial x_j} + \frac{\partial u_j}{\partial x_i}\Big) + k^*\Big(\frac{\partial u_i}{\partial x_j} - \varepsilon_{ijr}\phi_r\Big) - \gamma_1 T\delta_{ij} - p(\delta_{ij} + \omega_{ij}) \\
&m_{ij} = \alpha \frac{\partial \phi_r}{\partial x_r}\delta_{ij} + \beta \frac{\partial \phi_i}{\partial x_j} + \gamma \frac{\partial \phi_j}{\partial x_i} \qquad q_i = k\frac{\partial T}{\partial x_i} + k_1 w_i \\
&q_{ij} = -k_4 \frac{\partial w_k}{\partial x_k}\delta_{ij} - k_5 \frac{\partial w_i}{\partial x_j} - k_6 \frac{\partial w_j}{\partial x_i} \qquad Q_i = (k_1 - k_2)w_i + (k - k_3)\frac{\partial T}{\partial x_i} \\
&e_{ij} = \frac{1}{2}\Big(\frac{\partial u_i}{\partial x_j} + \frac{\partial u_j}{\partial x_i}\Big) \qquad \omega_{ij} = \frac{1}{2}\Big(\frac{\partial u_j}{\partial x_i} - \frac{\partial u_i}{\partial x_j}\Big)
\end{aligned} \tag{2.2}$$

where λ and μ are Lamé constants, α, β, γ, and k^* are micropolar constants, $\gamma_1 = (3\lambda + 2\mu + k^*)\alpha_t$, while α_t is the linear thermal expansion coefficient, ρ is density, C_e – specific heat, k – thermal conductivity, u_i – displacement vector, T – absolute temperature, T_0 – reference temperature chosen so that $|(T - T_0)/T_0| \ll 1$, ϕ_j is the microrotation vector, σ_{ij} are components of stresses, e_{ij} are components of strains, δ_{ij} is the Kronecker delta, ε_{ijr} is the permutation symbol, p – pressure, m_{ij} are couple stresses, J is microinertia, w_i – microtemperature vector, μ_1, b, k_i $(i = 1, 2, \ldots, 6)$ are constitutive coefficients, q_i is heat flux moment, q_{ij} – first heat flux moment and Q_i is the mean heat flux vector.

3. Formulation and solution of the problem

Consider an isotropic, linear, homogeneous, initially stressed micropolar thermoelastic solid with microtemperatures. Consider also a half-space $(y \geqslant 0)$ and the rectangular Cartesian coordinate system (x, y, z) originated in the surface $z = 0$. For a two-dimensional problem, assume the dynamic displacement vector as $u_i = (u, v, 0)$. The microrotation vector ϕ_j will be $\phi_j = (0, 0, \phi_3)$, consequently the microtemperature vector w_i willbe $w_i = (w_1, w_2, 0)$. All quantities will be a function of the time variable t and coordinates x and y. In the equations, comma denotes derivatives with respect to coordinates system.

Equations (2.1) under the effect of the gravitational field can be stated as

$$\begin{aligned}
&\Big(\mu + k^* - \frac{p}{2}\Big)\nabla^2 u + \Big(\lambda + \mu + \frac{p}{2}\Big)\frac{\partial e}{\partial x} + k^*\frac{\partial \phi_3}{\partial y} - \gamma_1 \frac{\partial T}{\partial x} + \rho g \frac{\partial v}{\partial x} = \rho \frac{\partial^2 u}{\partial t^2} \\
&\Big(\mu + k^* - \frac{p}{2}\Big)\nabla^2 v + \Big(\lambda + \mu + \frac{p}{2}\Big)\frac{\partial e}{\partial y} - k^*\frac{\partial \phi_3}{\partial x} - \gamma_1 \frac{\partial T}{\partial y} - \rho g \frac{\partial u}{\partial x} = \rho \frac{\partial^2 v}{\partial t^2} \\
&\gamma \nabla^2 \phi_3 - 2k^*\phi_3 + (k^* - p)\Big(\frac{\partial v}{\partial x} - \frac{\partial u}{\partial y}\Big) - \mu_1\Big(\frac{\partial w_2}{\partial x} - \frac{\partial w_1}{\partial y}\Big) = J\rho \frac{\partial^2 \phi_3}{\partial t^2} \\
&k_6 \nabla^2 w_1 + (k_4 + k_5)\frac{\partial}{\partial x}\Big(\frac{\partial w_1}{\partial x} + \frac{\partial w_2}{\partial y}\Big) + \mu_1 \frac{\partial}{\partial t}\frac{\partial \phi_3}{\partial y} - k_2 w_1 - b\frac{\partial w_1}{\partial t} - k_3 \frac{\partial T}{\partial x} = 0 \\
&k_6 \nabla^2 w_2 + (k_4 + k_5)\frac{\partial}{\partial y}\Big(\frac{\partial w_1}{\partial x} + \frac{\partial w_2}{\partial y}\Big) - \mu_1 \frac{\partial}{\partial t}\frac{\partial \phi_3}{\partial x} - k_2 w_2 - b\frac{\partial w_2}{\partial t} - k_3 \frac{\partial T}{\partial y} = 0 \\
&k\nabla^2 T - \rho C_e \frac{\partial T}{\partial t} - \gamma_1 T_0 \frac{\partial e}{\partial t} + k_1\Big(\frac{\partial w_1}{\partial x} + \frac{\partial w_2}{\partial y}\Big) = 0
\end{aligned} \tag{3.1}$$

where g is the acceleration of gravity and e is dilatation.

Define non-dimensional variables by expressions

$$\begin{aligned}
&x_i' = \frac{\omega_1^*}{c_0}x_i && u_i' = \frac{\rho c_0\omega_1^*}{\gamma_1 T_0}u_i && \phi_3' = \frac{\rho c_0^2}{\gamma_1 T_0}\phi_3\\
&w_i' = \frac{c_0}{\omega_1^*}w_i && m_{ij}' = \frac{\omega_1^*}{\gamma_1 c_0 T_0}m_{ij} && q_{ij}' = \frac{\mu c_0^2}{\omega_1^*}q_{ij}\\
&(T', p_2') = \frac{1}{T_0}(T, p_2) && (\sigma_{ij}', p_1') = \frac{1}{\gamma_1 T_0}(\sigma_{ij}, p_1) && t' = \omega_1^* t\\
&g' = \frac{g}{c_0\omega_1^*} && \omega_1^* = \frac{\rho C_e c_0^2}{k} && c_0^2 = \frac{\lambda + 2\mu + k^*}{\rho}
\end{aligned} \tag{3.2}$$

Assuming the potential functions $\psi_1(x,y,t)$, $\psi_2(x,y,t)$, $q_1(x,y,t)$ and $q_2(x,y,t)$ in dimensionless form, we have

$$u = \frac{\partial\psi_1}{\partial x} + \frac{\partial\psi_2}{\partial y} \qquad v = \frac{\partial\psi_1}{\partial y} - \frac{\partial\psi_2}{\partial x} \qquad w_1 = \frac{\partial q_1}{\partial x} + \frac{\partial q_2}{\partial y} \qquad w_2 = \frac{\partial q_1}{\partial y} - \frac{\partial q_2}{\partial x} \tag{3.3}$$

To get the solution for the physical quantities, consider it in form of the normal mode as

$$[\psi_1, \psi_2, \phi_3, q_1, q_2, T](x,y,t) = [\psi_1^*, \psi_2^*, \phi_3^*, q_1^*, q_2^*, T^*](y)\mathrm{e}^{\mathrm{i}(ax-\xi t)} \tag{3.4}$$

where $[\psi_1^*, \psi_2^*, \phi_3^*, q_1^*, q_2^*, T^*](y)$ are amplitudes of the physical quantities, ξ is the angular frequency, $\mathrm{i} = \sqrt{-1}$ and a is the wave number in the x direction.

Apply equations (3.2)-(3.4) into equations (3.1) and drop the prime to obtain

$$\begin{aligned}
&[\mathrm{D}^2 - N_3]\psi_1^* - N_4\psi_2^* - N_5T^* = 0 && N_6\psi_1^* + [\mathrm{D}^2 - N_7]\psi_2^* + c_2\phi_3^* = 0\\
&-c_6[\mathrm{D}^2 - a^2]\psi_2^* + [\mathrm{D}^2 - N_8]\phi_3^* + c_7[\mathrm{D}^2 - a^2]q_2^* = 0\\
&[\mathrm{D}^2 - N_9]q_1^* - N_{10}T^* = 0 && N_{11}\phi_3^* + [\mathrm{D}^2 - N_{12}]q_2^* = 0\\
&N_{14}[\mathrm{D}^2 - a^2]\psi_1^* + c_{16}[\mathrm{D}^2 - a^2]q_1^* + [\mathrm{D}^2 - N_{13}]T^* = 0
\end{aligned} \tag{3.5}$$

where $\mathrm{D} = d/dy$. All the constants are given in Appendix B.

Eliminating ψ_1^*, ψ_2^*, ϕ_3^*, q_1^*, q_2^* and T^* from equations (3.5), enables one to obtain the following differential equations

$$[\mathrm{D}^{12} - \lambda_1\mathrm{D}^{10} + \lambda_2\mathrm{D}^8 - \lambda_3\mathrm{D}^6 + \lambda_4\mathrm{D}^4 - \lambda_5\mathrm{D}^2 + \lambda_6]\{\psi_1^*(y), \psi_2^*(y), \phi_3^*(y), q_1^*(y), q_2^*(y), T^*(y)\} = 0 \tag{3.6}$$

where λ_n $(n = 1, 2, \ldots, 6)$ are constants.

Equation (3.6) can be factored as

$$\begin{aligned}
&[(\mathrm{D}^2 - S_1^2)(\mathrm{D}^2 - S_2^2)(\mathrm{D}^2 - S_3^2)(\mathrm{D}^2 - S_4^2)(\mathrm{D}^2 - S_5^2)(\mathrm{D}^2 - S_6^2)]\\
&\quad \cdot \{\psi_1^*(y), \psi_2^*(y), \phi_3^*(y), q_1^*(y), q_2^*(y), T^*(y)\} = 0
\end{aligned} \tag{3.7}$$

where S_n^2 $(n = 1, 2, \ldots, 6)$ are the roots of the characteristic equation of (3.7).

The general solution to equation (3.7) bounded at $y \to \infty$ is given by

$$\begin{aligned}
&u(x,y,t) = \sum_{n=1}^{6} G_{1n}R_n\mathrm{e}^{-S_ny+\mathrm{i}(ax-\xi t)} && v(x,y,t) = \sum_{n=1}^{6} G_{2n}R_n\mathrm{e}^{-S_ny+\mathrm{i}(ax-\xi t)}\\
&\phi_3(x,y,t) = \sum_{n=1}^{6} A_{2n}R_n\mathrm{e}^{-S_ny+\mathrm{i}(ax-\xi t)} && T(x,y,t) = \sum_{n=1}^{6} A_{5n}R_n\mathrm{e}^{-S_ny+\mathrm{i}(ax-\xi t)}\\
&m_{xz}(x,y,t) = \sum_{n=1}^{6} G_{9n}R_n\mathrm{e}^{-S_ny+\mathrm{i}(ax-\xi t)} && w_2(x,y,t) = \sum_{n=1}^{6} G_{4n}R_n\mathrm{e}^{-S_ny+\mathrm{i}(ax-\xi t)}\\
&\sigma_{xy}(x,y,t) = \sum_{n=1}^{6} G_{7n}R_n\mathrm{e}^{-S_ny+\mathrm{i}(ax-\xi t)} && q_{xy}(x,y,t) = \sum_{n=1}^{6} G_{12n}R_n\mathrm{e}^{-S_ny+\mathrm{i}(ax-\xi t)}
\end{aligned} \tag{3.8}$$

Here R_n $(n = 1, 2, \ldots, 6)$ are some coefficients. The other field quantities are given in Appendix A.

4. Applications

Consider the following non-dimensional boundary conditions to determine the coefficients R_n $(n = 1, 2, \ldots, 6)$ and neglect the positive exponentials to avoid unbounded solutions at infinity. The surface of the medium satisfies the following conditions $y = 0$:

- The mechanical boundary conditions are
  - normal stress condition (mechanically stressed by the constant force p_1), so that

$$\sigma_{yy} = -p_1 \mathrm{e}^{\mathrm{i}(ax-\xi t)} - p \tag{4.1}$$

  - tangential stress condition (stress free)

$$\sigma_{xy} = 0 \tag{4.2}$$

- Condition of couple stress (couple stress is constant in the y-direction) implying that

$$m_{xz} = 0 \tag{4.3}$$

- Thermal condition (half-space subjected to thermal shock with constant temperature p_2 applied to the boundary) leading to

$$T = p_2 \mathrm{e}^{\mathrm{i}(ax-\xi t)} \tag{4.4}$$

- Normal and tangential heat flux moments are free, so that

$$q_{yy} = q_{xy} = 0 \tag{4.5}$$

Substituting the expressions of the considered quantities into boundary conditions (4.1)-(4.5), one obtains equations satisfied by the coefficients R_n $(n = 1, 2, \ldots, 6)$. Applying the inverse of matrix method to the raised system of equations, one finds values of the coefficients R_n $(n = 1, 2, \ldots, 6)$ as

$$\begin{bmatrix} R_1 \\ R_2 \\ R_3 \\ R_4 \\ R_5 \\ R_6 \end{bmatrix} = \begin{bmatrix} G_{61} & G_{62} & G_{63} & G_{64} & G_{65} & G_{66} \\ G_{71} & G_{72} & G_{73} & G_{74} & G_{75} & G_{76} \\ G_{91} & G_{92} & G_{93} & G_{94} & G_{95} & G_{96} \\ A_{51} & A_{52} & A_{53} & A_{54} & A_{55} & A_{56} \\ G_{111} & G_{112} & G_{113} & G_{114} & G_{115} & G_{116} \\ G_{121} & G_{122} & G_{123} & G_{124} & G_{125} & G_{126} \end{bmatrix}^{-1} \begin{bmatrix} -p_1 \\ 0 \\ 0 \\ p_2 \\ 0 \\ 0 \end{bmatrix} \tag{4.6}$$

Thus, we obtain expressions for the physical quantities of the plate surface.

5. Particular cases

In the present study, we consider the following particular cases:

(i) Absence of gravity by taking $g = 0$ in equations (4.1) and (4.2).

(ii) Non-initial stress effect by taking $p = 0$ in equation (4.5).

(iii) Absence of micropolar by taking α, β, γ, k^* and $j = 0$ in equations (4.1)-(4.5).

6. Numerical results and discussion

In order to illustrate the obtained theoretical results in the preceding Section, according to Eringen (1984), the magnesium crystal-like thermoelastic micropolar material has been chosen for the purpose of calculations. The used parameters are given in SI units. The constants are taken as $\lambda = 9.4 \cdot 10^{10}\,\mathrm{N/m^2}$, $\mu = 4 \cdot 10^{10}\,\mathrm{N/m^2}$, $k = 1.7 \cdot 10^2\,\mathrm{N/(s\,K)}$, $\rho = 1.74 \cdot 10^3\,\mathrm{kg/m^3}$, $\alpha_t = 7.4033 \cdot 10^{-7}\,\mathrm{/K}$, $C_e = 1.04 \cdot 10^3\,\mathrm{J/(kg\,K)}$, $k* = 1 \cdot 10^{10}\,\mathrm{N/m^2}$, $\gamma = 7.779 \cdot 10^{-8}\,\mathrm{N}$, $J = 2 \cdot 10^{-20}\,\mathrm{m^2}$, $T_0 = 298\,\mathrm{K}$, $k_1 = 0.0035\,\mathrm{N/s}$, $k_2 = 0.0045\,\mathrm{N/s}$, $k_3 = 0.0055\,\mathrm{N/(s\,K)}$, $k_4 = 0.065\,\mathrm{N/(s\,m^2)}$, $k_5 = 0.076\,\mathrm{N/(s\,m^2)}$, $k_6 = 0.096\,\mathrm{N/(s\,m^2)}$, $\mu_1 = 0.0085\,\mathrm{N}$, $b = 0.15 \cdot 10^{-9}\,\mathrm{N}$, $p_1 = 1\,\mathrm{N/m^2}$, $p_2 = 2\,\mathrm{K}$, $a = 1.5\,\mathrm{m}$, $t = 0.5\,\mathrm{s}$, $\xi = \eta + i\eta_1$, $\eta = 0.9\,\mathrm{rad/s}$, $\eta_1 = 2.9\,\mathrm{rad/s}$, $x = 0.5\,\mathrm{m}$, $0 \leqslant y \leqslant 6\,\mathrm{m}$.

The variation of real parts of each displacement v, microtemperature vector w_2, temperature T, stress σ_{xy}, couple stress m_{xz}, microrotation ϕ_3 and the first heat flux moment q_{xy} are obtained and represented by the distance y.

Figures 1-3 represent the behavior of these physical quantities against the distance y in 2D when $p = 5\,\mathrm{N/m}$ and $g = 9.8\,\mathrm{m/s^2}$. Figures 4a and 4b show the behavior of these physical quantities against the distance y in 2D for $g = 9.8\,\mathrm{m/s^2}$ in the case of $p = 5\,\mathrm{N/m}$. Figures 5a and 5b depict the variation of these physical quantities against the distance y in 2D in the case of presence and absence of micropolar thermoelasticity when the gravity and the initial stress are present.

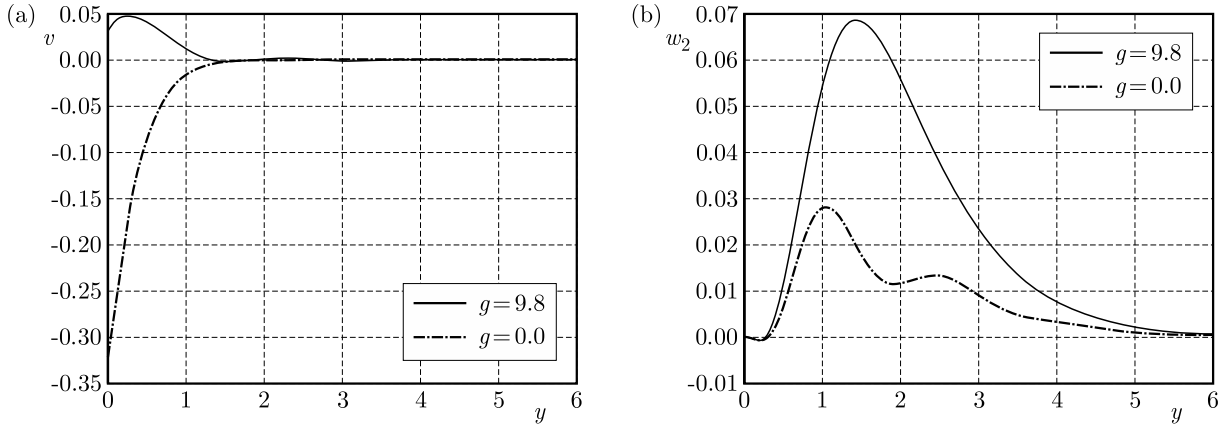

Fig. 1. Variation of displacement v (a) and of microtemperature vector w_2 (b) against y

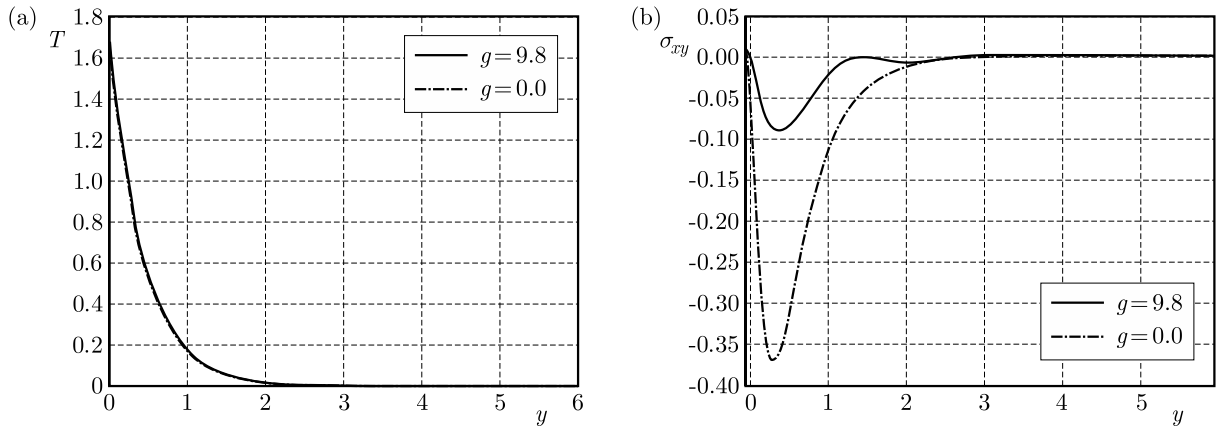

Fig. 2. Variation of temperature T (a) and of stress σ_{xy} (b) against y

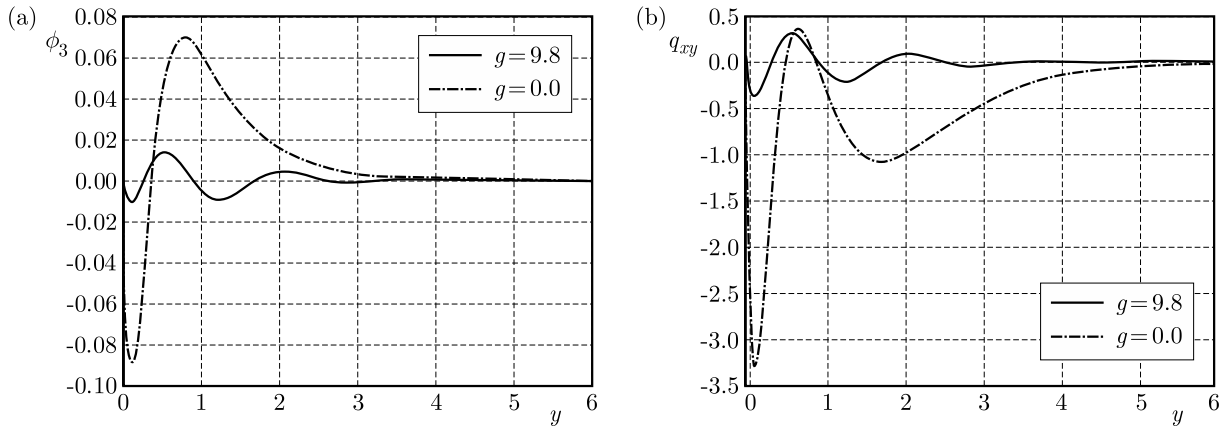

Fig. 3. Variation of microrotation vector ϕ_3 (a) and of the first heat flux moment q_{xy} (b) against y

Figure 1a shows that the variation of the displacement component v increases with an increase in gravity for $y \geqslant 0$. Figure 1b clarifies the variation of the microtemperature vector w_2 which decreases with an increase in gravity for $y \geqslant 0$. It is clear from Fig. 2a that the variation of temperature T decreases with an increase in gravity for $y \geqslant 0$, but for very small values it seems to be identical. This means that the effect of gravity has a small influence on the variation of temperature. Figure 2b depicts the variation of the shearing stress σ_{xy} which increases with an increase in gravity for $y \geqslant 0$. Figure 3a explains that the variation of the microrotation vector ϕ_3 increases in the interval $0 \leqslant y \leqslant 0.5$, while it decreases in the interval $0.5 \leqslant y \leqslant 6$, with an increase in gravity. Figure 3b determines the variation of the heat flux moment q_{xy} which increases at the intervals $0 \leqslant y \leqslant 0.6$ and $1 \leqslant y \leqslant 6$, but decreases at the interval $0.6 \leqslant y \leqslant 1$ with an increase in gravity. The gravity has an effective role in the variation of all physical quantities of the problem. One can notice a change in the variation of the physical quantities while gravity is present or absent.

Figure 4a shows that the variation of the displacement component v decreases in the intervals $0 \leqslant y \leqslant 0.4$, $1 \leqslant y \leqslant 1.8$ and $2.8 \leqslant y \leqslant 6$, while it increases in the intervals $0.4 \leqslant y \leqslant 1$ and $1.8 \leqslant y \leqslant 2.8$ with an increase in the initial stress. Figure 4b clarifies the variation of the microtemperature vector w_2 which increases with an increase in the initial stress for $y \geqslant 0$. It is clear that all functions are continuous and all the curves converge to zero. The initial stress has a significant role in the variation of all physical quantities in the problem. This can be deduced from changing of the manner of variation of the physical quantities while the effect of the initial stress is present or absent.

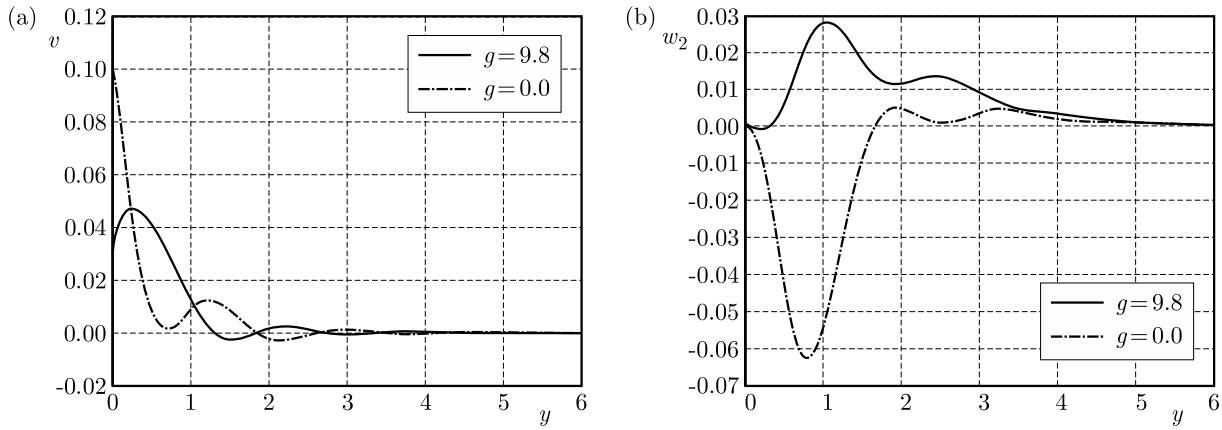

Fig. 4. Variation of displacement v (a) and of microtemperature vector w_2 (b) against y

Figure 5a shows that the variation of the displacement component v increases in the intervals $0 \leqslant y \leqslant 2$ and $4.4 \leqslant y \leqslant 6$, while it decreases in the interval $2 \leqslant y \leqslant 4.4$ with an increase in the micropolar thermoelasticity. It is clear from Fig. 5b that the variation of temperature T decreases with an increase of the micropolar thermoelasticity for $y \geqslant 0$ in observable behavior. It is clear that all functions are continuous and all the curves converge to zero. The micropolar thermoelasticity plays an important role in the variation of all physical quantities in the problem. The micropolar thermoelasticity is a very important property in thermoelastic materials with a microstructure.

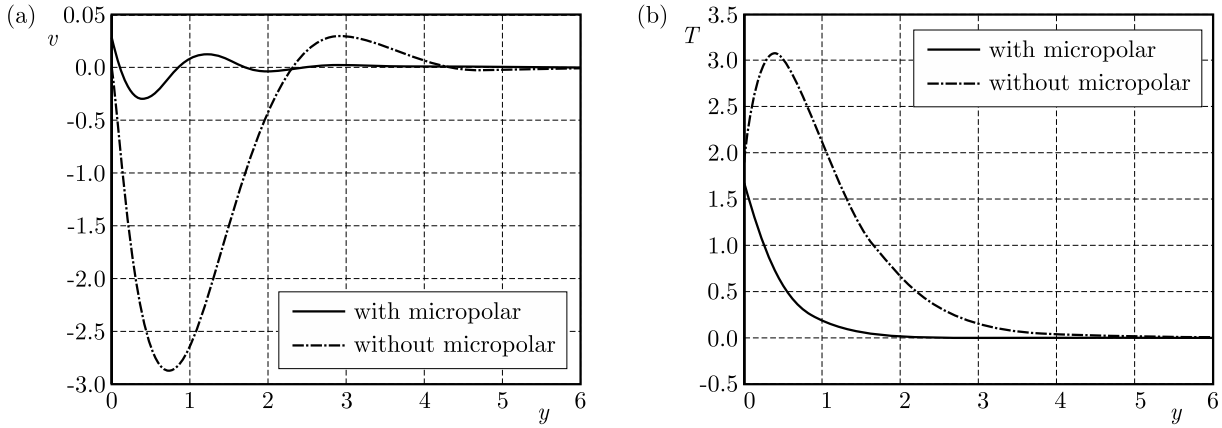

Fig. 5. Variation of displacement v (a) and of temperature T (b) against y with and without micropolar

The 3D curves of the quantities v and w_1 are shown in Figs. 6a and 6b for $g = 9.8\,\mathrm{m/s^2}$ and $p = 5\,\mathrm{N/m}$ with the presence of the micropolar thermoelasticity at $t = 0.5\,\mathrm{s}$. These figures depict the dependence of these quantities on the distances x and y while they are moving during wave propagation.

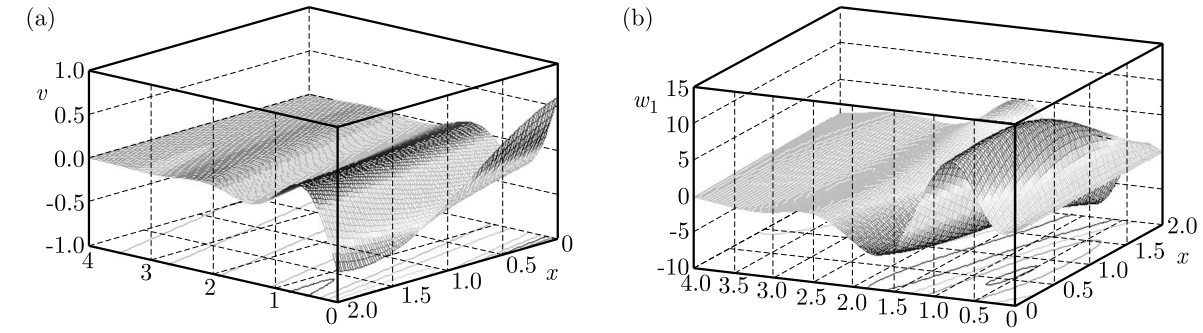

Fig. 6. Variation of displacement v (a) and of microtemperature vector w_1 (b) versus distances x and y

7. Conclusion

From the above analytical solutions, we conclude that:

1. Gravity and initial stress are effective physical factors having an important role in the variation of the physical quantities.
2. The micropolar thermoelasticity is an important property. The presence or the absence of this property is an observable effect in the variation of the considered physical quantities, for example in the variation of temperature.
3. The microtemperature is a very useful theory in the field of geophysics and earthquake engineering and for seismologists working in the field of mining tremors and drilling into the earth's crust.

4. Values of all physical quantities converge to zero with an increase in the distance y, and all functions are continuous.

Appendix A

$$\psi_1(x,y,t)=\sum_{n=1}^{6}R_n\mathrm{e}^{-S_ny+\mathrm{i}(ax-\xi t)} \qquad \psi_2(x,y,t)=\sum_{n=1}^{6}A_{1n}R_n\mathrm{e}^{-S_ny+\mathrm{i}(ax-\xi t)}$$

$$q_1(x,y,t)=\sum_{n=1}^{6}A_{3n}R_n\mathrm{e}^{-S_ny+\mathrm{i}(ax-\xi t)} \qquad q_2(x,y,t)=\sum_{n=1}^{6}A_{4n}R_n\mathrm{e}^{-S_ny+\mathrm{i}(ax-\xi t)}$$

$$w_1(x,y,t)=\sum_{n=1}^{6}G_{3n}R_n\mathrm{e}^{-S_ny+\mathrm{i}(ax-\xi t)} \qquad \sigma_{xx}(x,y,t)=\sum_{n=1}^{6}G_5nR_n\mathrm{e}^{-S_ny+\mathrm{i}(ax-\xi t)}$$

$$\sigma_{yy}(x,y,t)=\sum_{n=1}^{6}G_{6n}R_n\mathrm{e}^{-S_ny+\mathrm{i}(ax-\xi t)} \qquad \sigma_{xz}(x,y,t)=\sigma_{yz}(x,y,t)=0$$

$$m_{yz}(x,y,t)=\sum_{n=1}^{6}G_{8n}R_n\mathrm{e}^{-S_ny+\mathrm{i}(ax-\xi t)} \qquad m_{xz}(x,y,t)=\sum_{n=1}^{6}G_{9n}R_n\mathrm{e}^{-S_ny+\mathrm{i}(ax-\xi t)}$$

$$q_{xz}(x,y,t)=0 \qquad q_{xx}(x,y,t)=\sum_{n=1}^{6}G_{10n}R_n\mathrm{e}^{-S_ny+\mathrm{i}(ax-\xi t)}$$

$$q_{yy}(x,y,t)=\sum_{n=1}^{6}G_{11n}R_n\mathrm{e}^{-S_ny+\mathrm{i}(ax-\xi t)} \qquad q_{yz}(x,y,t)=0$$

Appendix B

$$N_1=c_1+1 \qquad N_2=c_9+1 \qquad N_3=a^2-\frac{c_3\xi^2}{N_1} \qquad N_4=\frac{\mathrm{i}ac_4}{N_1}$$

$$N_5=\frac{c_3}{N_1} \qquad N_6=\mathrm{i}ac_4 \qquad N_7=a^2-c_3\xi^2 \qquad N_8=a^2+2c_5-c_7\xi^2$$

$$N_9=a^2+\frac{c_{11}-\mathrm{i}\xi c_{12}}{N_2} \qquad N_{10}=\frac{c_{13}}{N_2} \qquad N_{11}=-\mathrm{i}\xi c_{10} \qquad N_{12}=a^2+c_{11}-\mathrm{i}\xi c_{12}$$

$$N_{13}=a^2-\mathrm{i}\xi c_{14} \qquad N_{14}=\mathrm{i}\xi c_{15} \qquad A_{1n}=\frac{S_n^6-l_1S_n^4+l_2S_n^2-l_3}{N_4S_n^4-l_4S_n^2+l_5}$$

$$A_{2n}=\frac{-N_6-A_{1n}(S_n^2-N_7)}{c_2} \qquad A_{3n}=\frac{N_{10}A_{5n}}{S_n^2-N_9} \qquad A_{4n}=\frac{-N_{11}A_{2n}}{S_n^2-N_{12}}$$

$$A_{5n}=\frac{-N_{14}S_n^4+(N_9N_{14}+N_{14}a^2)S_n^2+N_9N_{14}a^2}{S_n^4-(N_9+N_{13}+c_{16}N_{10})S_n^2+N_9N_{13}-c_{16}N_{10}a^2}$$

$$A_{6n}=c_{14}(\mathrm{i}aH_{1n}-S_nH_{2n})+\mathrm{i}ac_{15}H_{1n}-A_{5n} \qquad A_{9n}=-c_{18}S_nA_{2n}$$

$$A_{7n}=c_{14}(\mathrm{i}aH_{1n}-S_nH_{2n})-S_nc_{15}H_{2n}-A_{5n} \qquad A_{10n}=\mathrm{i}ac_{18}A_{2n}$$

$$A_{8n}=c_{16}(-S_nH_{1n}+\mathrm{i}aH_{2n})+c_{17}(\mathrm{i}aH_{2n}-A_{2n}) \qquad c_1=\frac{2(\lambda+\mu)+p}{2(\mu+k^*)-p}$$

$$c_2=\frac{2k^*}{2(\mu+k^*)-p} \qquad c_3=\frac{2\rho c_0^2}{2(\mu+k^*)-p} \qquad c_4=\frac{2\rho g c_0^2}{2(\mu+k^*)-p}$$

$$c_5=\frac{2k^*c_0^2}{\gamma\omega_1^{*2}} \qquad c_6=\frac{c_0^2(k^*-p)}{\gamma\omega_1^{*2}} \qquad c_7=\frac{\rho\mu_1c_0^4}{\gamma\gamma_1T_0\omega_1^{*2}} \qquad c_8=\frac{j\rho c_0^2}{\gamma}$$

$$c_9=\frac{k_4+k_5}{k_6} \qquad c_{10}=\frac{\mu_1\gamma_1T_0}{\rho\omega_1^*k_6} \qquad c_{11}=\frac{k_2c_0^2}{k_6\omega_1^{*2}} \qquad c_{12}=\frac{bc_0}{k_6\omega_1^*}$$

$$c_{13}=\frac{k_3T_0c_0^2}{k_6\omega_1^{*2}} \qquad c_{14}=\frac{\rho C_ec_0^2}{k\omega_1^*} \qquad c_{15}=\frac{\gamma_1^2T_0}{\rho k\omega_1^*} \qquad c_{16}=\frac{k_1}{kT_0} \qquad c_{17}=\frac{\lambda}{\rho c_0^2}$$

$$c_{18}=\frac{2\mu+k^*}{\rho c_0^2} \qquad c_{19}=\frac{\mu+p}{2\rho c_0^2} \qquad c_{20}=\frac{2(k^*+\mu)-p}{2\rho c_0^2} \qquad c_{21}=\frac{k^*}{\rho c_0^2}$$

$$c_{22}=\frac{\gamma\omega_1^{*2}}{\rho c_0^4} \qquad c_{23}=-k_4\mu\omega_1^* \qquad c_{24}=-(k_5+k_6)\mu\omega_1^* \qquad c_{25}=-k_5\mu\omega_1^*$$

$$c_{26}=-k_6\mu\omega_1^* \qquad l_1=N_3+N_9+N_{13}-c_{16}N_{10}-N_5N_{14}$$

$$l_2=N_3(N_9+N_{13}-c_{16}N_{10})+N_9N_{13}-c_{16}N_{10}a^2-N_5N_{14}(N_9+a^2)$$

$$l_3=N_3(N_9N_{13}-c_{16}N_{10}a^2)-N_5N_9N_{14}a^2 \qquad l_4=N_4(N_9+N_{13}-c_{16}N_{10})$$

$$l_5=N_4(N_9N_{13}-c_{16}N_{10}a^2) \qquad G_{1n}=(\mathrm{i}a-S_nA_{1n}) \qquad G_{2n}=-(S_n+\mathrm{i}aA_{1n})$$

$$G_{3n}=\mathrm{i}aA_{3n}-S_nA_{4n} \qquad G_{5n}=c_{17}(\mathrm{i}aG_{1n}-S_nG_{2n})+\mathrm{i}ac_{18}G_{1n}-A_{5n}-p$$

$$G_{4n}=-(S_nA_{3n}+\mathrm{i}aA_{4n}) \qquad G_{6n}=c_{17}(\mathrm{i}aG_{1n}-S_nG_{2n})-S_nc_{18}G_{2n}-A_{5n}-p$$

$$G_{7n}=-c_{19}S_nG_{1n}+\mathrm{i}ac_{20}G_{2n}-c_{21}A_{2n} \qquad G_{8n}=-c_{22}S_nA_{2n}$$

$$G_{9n}=\mathrm{i}ac_{22}A_{2n} \qquad G_{10n}=c_{23}(\mathrm{i}aG_{3n}-S_nG_{4n})+\mathrm{i}ac_{24}G_{3n}$$

$$G_{11n}=c_{23}(\mathrm{i}aG_{3n}-S_nG_{4n})-S_nc_{24}G_{4n} \qquad G_{7n}=-c_{15}S_nG_{3n}+\mathrm{i}ac_{26}G_{4n}$$

$$n=1,2,\ldots,6$$

References

1. Abbas I.A., Kumar R., 2013, Deformation due to thermal source in micropolar thermoelastic media with thermal and conductive temperatures, *Journal of Computational and Theoretical Nanosciences*, **10**, 2241-2247
2. Abouelregal A.E., Zenkour A.M., 2015, Thermoelastic problem of an axially moving micro beam subjected to an external transverse excitation, *Journal of Theoretical and Applied Mechanics*, **53**, 167-178
3. Ariman T., 1972, Wave propagation in a micropolar elastic half-space, *Acta Mechanica*, **13**, 11-20
4. Ames K., Straughan B., 1999, Continuous dependence results for initially prestressed thermoelastic bodies, *International Journal of Engineering Sciences*, **30**, 7-13
5. Bromwich T.J., 1898, On the influence of gravity on elastic waves and in particular on the vibrations of an elastic globe, *Proceedings of the London Mathematical Society*, **30**, 98-120
6. Casas P.S., Quintanilla R., 2005, Exponential stability in thermoelasticity with microtemperatures, *International Journal of Engineering Sciences*, **43**, 33-47
7. Eringen A.C., 1966, Linear theory of micropolar elasticity, *Journal of Mathematics and Mechanics*, **15**, 909-924
8. Eringen A.C., 1984, Plane wave in nonlocal micropolar elasticity, *International Journal of Engineering Sciences*, **22**, 1113-1121
9. Eringen A.C., 1999, *Microcontinuum Field Theory I: Foundations and Solids*, Springer-Verlag, Berlin
10. Eringen A.C., Kafadar C.B., 1976, Polar field theories, [In:] *Continuum Physics IV*, Eringen A.C. (Edit.), Academic Press, New York
11. Grot R., 1969, Thermodynamics of continuum with microstructure, *International Journal of Engineering Sciences*, **7**, 801-814

12. Iesan D., 2001, On a theory of micromorphic elastic solids with microtemperatures, *Journal of Thermal Stresses*, **24**, 737-752

13. Iesan D., 2004, *Thermoelastic Models of Continua*, Springer Netherlands

14. Iesan D., 2006, Thermoelasticity of bodies with microstructure and microtemperatures, *International Journal of Solids and Structures*, **43**, 3414-3427

15. Iesan D., 2007, Thermoelasticity of bodies with microstructure and microtemperatures, *International Journal of Solids and Structures*, **44**, 8648-8662

16. Iesan D., 2008, A theory of prestressed thermoelastic Cosserat continua, *Journal of Applied Mathematics and Mechanics*, **88**, 306-319

17. Iesan D., Quintanilla R., 2000, On a theory of thermoelasticity with micro- temperatures, *Journal of Thermal Stresses*, **23**, 199-215

18. Kumar R., Ailawalia P., 2005, Deformation in micropolar cubic crystal due to various sources, *International Journal of Solids and Structures*, **42**, 5931-5944

19. Kumar R. Gupta R.R., 2010, Propagation of waves in transversely isotropic micropolar generalized thermoelastic half space, *International Communications in Heat and Mass Transfer*, **37**, 1452-1458

20. Love A.E.H., 1965, *Some Problems of Geodynamics*, Cambridge University Press, London

21. Montanaro A., 1999, On singular surfaces in isotropic linear thermoelasticity with initial stress, *Journal of Acoustical Society of America*, **106**, 1586-1588

22. Othman M.I.A, Elmaklizi J.D., Saied S.M., 2013a, Generalized thermoelastic medium with temperature dependent properties for different theories under the effect of gravity field, *International Journal of Thermophysics*, **34**, 521-537

23. Othman M.I.A., Hasona W.M., Abd-Elaziz E.M., 2014, Effect of rotation on micro-polar generalized thermoelasticity with two temperature using a dual-phase-lag model, *Canadian Journal of Physics*, **92**, 148-159

24. Othman M.I.A, Zidan M.E.M., Hilal M.I.M., 2013b, The influence of gravitational field and rotation on thermoelastic solid with voids under Green-Naghdi theory, *Journal of Physics*, **2**, 22-34

25. Othman M.I.A, Zidan M.E.M., Hilal M.I.M., 2015, The effect of initial stress on thermoelastic rotating medium with voids due to laser pulse heating with energy dissipation, *Journal of Thermal Stresses*, **38**, 835-853

26. Parfitt V.R., Eringen A.C., 1971, Reflection of plane waves from a flat boundary of a micropolar elastic half-space, *The Journal of Acoustical Society of America*, **45**, 1258-1272

27. Riha P., 1979, On the microcontinuum model of heat conduction in materials with inner structure, *International Journal of Engineering Sciences*, **14**, 529-535

28. Scalia A., Svanadze M., 2006, On the representation of solutions of the theory of thermoelasticity with microtemperatures, *Journal of Thermal Stresses*, **29**, 849-863

29. Sezawa K., 1927, Dispersion of elastic waves propagated on the surface of stratified bodies and on curved surfaces, *Bull Earthquake Research Institute Tokyo*, **3**, 1-18

30. Smith A.C., 1967, Waves in micropolar elastic solids, *International Journal of Engineering Sciences*, **5**, 741-746

31. Wang J., Slattery P., 2002, Thermoelasticity without energy dissipation for initially stressed bodies, *International Journal of Mathematics and Mathematical Sciences*, **31**, 329-337

Manuscript received September 3, 2015; accepted for print December 3, 2015

JOURNAL OF THEORETICAL AND APPLIED MECHANICS
54, 3, pp. 859-870, Warsaw 2016
DOI: 10.15632/jtam-pl.54.3.859

AN APPROACH TO FREE VIBRATION ANALYSIS OF AXIALLY GRADED BEAMS

Stanisław Kukla, Jowita Rychlewska
Czestochowa University of Technology, Institute of Mathematics, Czestochowa, Poland
e-mail: stanislaw.kukla@im.pcz.pl; jowita.rychlewska@im.pcz.pl

In this study, the solution to the free vibration problem of axially graded beams with a non-uniform cross-section has been presented. The proposed approach relies on replacing functions characterizing functionally graded beams by piecewise exponential functions. The frequency equation has been derived for axially graded beams divided into an arbitrary number of subintervals. Numerical examples show the influence of the parameters of the functionally graded beams on the free vibration frequencies for different boundary conditions.

Keywords: axially graded beam, non-uniform beam, free vibration

1. Introduction

Functionally graded materials (FGMs) are a novel class of composites which have continuous variation of material properties from one constituent to another. As a result, they have various advantages over the classical composite laminates. For example, using FGMs, we avoid stress concentrations typical for heterogeneous structures with jump a discontinuity between dissimilar materials. For this reason, FGMs are widely used in mechanical, nuclear, aerospace, biomedical and civil engineering. Simultaneously, because of wide applications of FGMs, it is very important to study static and dynamic analysis of functionally graded structures, such as plates, shells and beams. In this paper, the object of consideration is the problem of free vibration of functionally graded (FG) beams. For FG beams, the gradient variation may be oriented in the axial and/or in the cross-section direction.

The literature on vibration analysis of FG beams with thickness-wise gradient variation is very extensive. For example, Anandrao *et al.* (2012) made free vibration analysis of functionally graded beams using the principle of virtual work to obtain a finite element system of equations. The variation of material properties across the thickness of the beam was governed by a power law distribution. The same type of variation of the beam properties was also assumed by Sina *et al.* (2009). They solved the resulting system of ordinary differential equations of free vibration analysis by using an exact method. An analytical solution to study free vibration of exponential functionally graded beams with a single delamination was developed by Liu and Shu (2014). Pradhan and Chakraverty (2013) used the Rayleigh-Ritz model to analyse free vibration of FG beams with material properties that continuously vary in the thickness direction according to the power-law exponent form. This type of gradation was also assumed by Wattanasakulpong and Ungbhakorn (2012). They applied the differential transformation method to solve the governing equation of free vibration of FG beams supported by various types of general boundary conditions. The line spring model to solve the free vibration problem of an exponentially graded cracked beam was employed by Matbuly *et al.* (2009).

Free vibration analysis for axially graded beams has become more complicated because of the governing equation with variable coefficients. For example, Wu *et al.* (2005) applied the semi-inverse method to find solutions to the dynamic equation of axially functionally graded

simply supported beams. Huang and Li (2010) studied free vibration of axially functionally graded beams by using the Fredholm integral equations. Hein and Feklistova (2011) applied the Haar wavelet approach to analyse free vibration of axially functionally graded beams. The differential transform element method and differential quadrature element method of the lowest order were used to solve free vibration and stability problems of FG beams by Shahba and Rajasekaran (2012). The exact solution to free vibration of exponentially axially graded beams was presented by Li *et al.* (2013). Explicit frequency equations of free vibration of exponentially FG Timoshenko beams were derived by Tang *et al.* (2014). Huang *et al.* (2013) presented a new approach to the investigation of free vibration of axially functionally graded Timoshenko beams. By applying auxiliary functions, they transformed the coupled governing equations into a single governing equation. Moreover, there are some studies related with the problem of free vibration of FG beams where the gradation of the material is assumed to be along any of the possible Cartesian coordinates, see Alshorbagy *et al.* (2011), by Shahba *et al.* (2013). A review of researches on FG beam type structures can be found in Chauhan and Khan (2014).

In this contribution, we propose a new approach to free vibration analysis of FG beams with arbitrary axial inhomogeneity. The main idea presented in this paper is to approximate an FG beam by an equivalent beam with piece-wise exponentially varying material and geometrical properties. Considerations are carried out in the framework of the Euler-Bernoulli beam theory. Taking into account various boundary conditions associated with clamped, pinned and free ends, numerical solutions are obtained for different functions describing gradient variation of material/geometrical properties of an FG beam. The effectiveness of the proposed approach is confirmed by comparing the obtained numerical results with other numerical solutions available in the existing literature for homogeneous and nonhomogeneous beams. The proposed method is a certain generalization of the approach presented by Kukla and Rychlewska (2014).

2. Equations of motion

An axially graded and non-uniform beam of length L is considered. In this contribution, the material properties and/or cross-section of the beam are assumed to vary continuously along the axial direction. Based on the Euler-Bernoulli beam theory, Lebed and Karnovsky (2000), the governing differential equation is given by

$$\frac{\partial^2}{\partial x^2}\Big[E(x)I(x)\frac{\partial^2 w}{\partial x^2}\Big] + \rho(x)A(x)\frac{\partial^2 w}{\partial t^2} = 0 \qquad 0 < x < L \tag{2.1}$$

where x is the axial coordinate, $A(x)$ is the cross-section area, $I(x)$ is the moment of inertia, $E(x)$ denotes the modulus of elasticity, $\rho(x)$ is the material density and $w(x,t)$ is the transverse deflection at the position x and time t.

In order to investigate free vibration of the beam, we assume that

$$w(x,t) = W(x)\sin\omega t \tag{2.2}$$

where $W(x)$ is the amplitude of vibration and ω is the circular frequency of vibration. Substituting (2.2) into (2.1) and introducing the non-dimensional coordinate $\xi = x/L$, we can transform governing equation (2.1) into

$$\frac{d^2}{d\xi^2}\Big[E(\xi)I(\xi)\frac{d^2 W}{d\xi^2}\Big] - L^4\omega^2\rho(\xi)A(\xi)W = 0 \qquad 0 < \xi < 1 \tag{2.3}$$

In the subsequent analysis, it is assumed that

$$E(\xi)I(\xi) = d_0 g(\xi) \qquad \rho(\xi)A(\xi) = m_0 h(\xi) \qquad 0 < \xi < 1 \tag{2.4}$$

where $d_0 = E(0)I(0)$ and $m_0 = \rho(0)A(0)$. Subsequently, we shall approximate the FG beam under consideration by an equivalent beam with piecewise exponentially varying geometrical and material properties, setting

$$g(\xi) \cong d_i \mathrm{e}^{2\beta_i \xi} \qquad h(\xi) \cong m_i \mathrm{e}^{2\beta_i \xi} \qquad \xi_{i-1} < \xi < \xi_i \qquad i = 1, \ldots, n \tag{2.5}$$

where $\xi_0 = 0$ and $\xi_n = 1$. The coefficients d_i, m_i, β_i, $i = 1, \ldots, n$ we determine by using the following relationships $(i = 1, \ldots, n)$

$$g(\xi_{i-1}) = d_i \mathrm{e}^{2\beta_i \xi_{i-1}} \qquad g(\xi_i) = d_i \mathrm{e}^{2\beta_i \xi_i} \qquad g(\xi_0) = 1 \tag{2.6}$$

and $(i = 1, \ldots, n)$

$$h\Big(\frac{\xi_i + \xi_{i-1}}{2}\Big) = m_i \mathrm{e}^{\beta_i(\xi_i + \xi_{i-1})} \qquad h(\xi_0) = 1 \tag{2.7}$$

Hence $(i = 1, \ldots, n)$

$$\begin{aligned} &\beta_i = \frac{1}{2(\xi_i - \xi_{i-1})} \ln \frac{g(\xi_i)}{g(\xi_{i-1})} \qquad d_i = g(\xi_i)\mathrm{e}^{-2\beta_i \xi_i} \\ &m_i = h\Big(\frac{\xi_i + \xi_{i-1}}{2}\Big)\mathrm{e}^{-\beta_i(\xi_i + \xi_{i-1})} \end{aligned} \tag{2.8}$$

We shall also assume that the transverse deflection of the beam has the form

$$W(\xi) = W_i(\xi) \qquad \xi_{i-1} < \xi < \xi_i \qquad i = 1, \ldots, n \tag{2.9}$$

Hence, the governing system of equations for such a piecewise beam can be expressed by

$$\frac{d^2}{d\xi^2}\Big[d_0 d_i \mathrm{e}^{2\beta_i \xi} \frac{d^2 W_i}{\partial \xi^2}\Big] - L^4 \omega^2 m_0 m_i \mathrm{e}^{2\beta_i \xi} W_i = 0 \qquad \begin{matrix} \xi_{i-1} < \xi < \xi_i \\ i = 1, \ldots, n \end{matrix} \tag{2.10}$$

Introducing denotations

$$\Omega^2 = \frac{m_0 m_1}{d_0 d_1} L^4 \omega^2 \qquad \mu_i^2 = \frac{m_i d_1}{m_1 d_i} \tag{2.11}$$

equations (2.10) can be rewritten as

$$\frac{d^2}{d\xi^2}\Big[\mathrm{e}^{2\beta_i \xi} \frac{d^2 W_i}{d\xi^2}\Big] - \Omega^2 \mu_i^2 \mathrm{e}^{2\beta_i \xi} W_i = 0 \qquad \xi_{i-1} < \xi < \xi_i \qquad i = 1, \ldots, n \tag{2.12}$$

After some manipulations. equations (2.12) reduce to the form

$$\frac{d^4 W_i}{d\xi^4} + 4\beta_i \frac{d^3 W_i}{d\xi^3} + 4\beta_i^2 \frac{d^2 W_i}{d\xi^2} - \Omega^2 \mu_i^2 W_i = 0 \qquad \begin{matrix} \xi_{i-1} < \xi < \xi_i \\ i = 1, \ldots, n \end{matrix} \tag{2.13}$$

The parameters β_i in equations (2.8) have been determined from the function $g(\cdot)$ corresponding to the stiffness of the beam. These parameters can be determined also by using the function $h(\cdot)$ corresponding to mass of the beam. In this case, we assume that

$$h(\xi_{i-1}) = m_i \mathrm{e}^{2\beta_i \xi_{i-1}} \qquad h(\xi_i) = m_i \mathrm{e}^{2\beta_i \xi_i} \qquad h(\xi_0) = 1 \qquad i = 1, \ldots, n \tag{2.14}$$

and

$$g\Big(\frac{\xi_i + \xi_{i-1}}{2}\Big) = d_i \mathrm{e}^{\beta_i(\xi_i + \xi_{i-1})} \qquad g(\xi_0) = 1 \qquad i = 1, \ldots, n \tag{2.15}$$

Then we have

$$\begin{aligned} &\beta_i = \frac{1}{2(\xi_i - \xi_{i-1})} \ln \frac{h(\xi_i)}{h(\xi_{i-1})} \qquad m_i = h(\xi_i)\mathrm{e}^{-2\beta_i \xi_i} \\ &d_i = g\Big(\frac{\xi_i + \xi_{i-1}}{2}\Big)\mathrm{e}^{-\beta_i(\xi_i + \xi_{i-1})} \qquad i = 1, \ldots, n \end{aligned} \tag{2.16}$$

Differential equation (2.13) is valid also for d_i, m_i, β_i, given by formulae (2.16).

3. Solution to the free vibration problem

On the assumption $\beta_i^2 < \mu_i \Omega$, the general solution to equations (2.13) has the form

$$W_i(\xi) = \mathrm{e}^{-\beta_i \xi}(A_i \cos \delta_i \xi + B_i \sin \delta_i \xi + C_i \cosh \overline{\delta}_i \xi + D_i \sinh \overline{\delta}_i \xi) \qquad \xi_{i-1} < \xi < \xi_i \tag{3.1}$$

where $\delta_i = \sqrt{\mu_i \Omega - \beta_i^2}$, $\overline{\delta}_i = \sqrt{\mu_i \Omega + \beta_i^2}$, $A_i, B_i, C_i, D_i \in R$, $i = 1, \ldots, n$.

In order to analyse the free vibration of functionally graded beams, solution (3.1) has to be applied to certain boundary conditions. In this paper we shall consider the following types of boundary conditions:

— clamped-clamped beam (C-C)

$$W_1(0) = 0 \qquad \frac{dW_1}{d\xi}(0) = 0 \qquad W_n(1) = 0 \qquad \frac{dW_n}{d\xi}(1) = 0 \tag{3.2}$$

— pinned-pinned beam (P-P)

$$W_1(0) = 0 \qquad \frac{d^2W_1}{d\xi^2}(0) = 0 \qquad W_n(1) = 0 \qquad \frac{d^2W_n}{d\xi^2}(1) = 0 \tag{3.3}$$

— clamped-pinned beam (C-P)

$$W_1(0) = 0 \qquad \frac{dW_1}{d\xi}(0) = 0 \qquad W_n(1) = 0 \qquad \frac{d^2W_n}{d\xi^2}(1) = 0 \tag{3.4}$$

— pinned-clamped beam (P-C)

$$W_1(0) = 0 \qquad \frac{d^2W_1}{d\xi^2}(0) = 0 \qquad W_n(1) = 0 \qquad \frac{dW_n}{d\xi}(1) = 0 \tag{3.5}$$

— clamped-free beam (C-F)

$$W_1(0) = 0 \qquad \frac{dW_1}{d\xi}(0) = 0 \qquad \frac{d^2W_n}{d\xi^2}(1) = 0 \qquad \frac{d}{d\xi}\Big(\mathrm{e}^{2\beta\xi}\frac{d^2W_n}{d\xi^2}\Big)(1) = 0 \tag{3.6}$$

— free-clamped beam (F-C)

$$\frac{d^2W_1}{d\xi^2}(0) = 0 \qquad \frac{d}{d\xi}\Big(\mathrm{e}^{2\beta\xi}\frac{d^2W_1}{d\xi^2}\Big)(0) = 0 \qquad W_n(1) = 0 \qquad \frac{dW_n}{d\xi}(1) = 0 \tag{3.7}$$

The matching conditions between two connecting elements of the piecewise beams satisfy the following continuity conditions

$$\begin{aligned} &W_i(\xi_i) = W_{i+1}(\xi_i) && \frac{dW_i}{d\xi}(\xi_i) = \frac{dW_{i+1}}{d\xi}(\xi_i) \\ &\frac{d^2W_i}{d\xi^2}(\xi_i) = \frac{d^2W_{i+1}}{d\xi^2}(\xi_i) && \frac{d^3W_i}{d\xi^3}(\xi_i) = \frac{d^3W_{i+1}}{d\xi^3}(\xi_i) \qquad i = 1, \ldots, n-1 \end{aligned} \tag{3.8}$$

Substituting functions (3.1) into one of the set of boundary conditions (3.2)-(3.7) and continuity conditions given by equations (3.8), we obtain a system of 4n equations which can be written in the matrix form

$$\mathbf{A}(\omega)\mathbf{X} = \mathbf{0} \tag{3.9}$$

where $\mathbf{X} = [A_1, B_1, C_1, D_1, \ldots, A_n, B_n, C_n, D_n]^{\mathrm{T}}$ and $\mathbf{A}(\omega) = [a_{kj}]_{4n\times 4n}$. The matrix $\mathbf{A}$ can be expressed as

$$\mathbf{A}(\omega) = \begin{bmatrix} \mathbf{B}_1 \\ \mathbf{C}_1 \\ \mathbf{C}_2 \\ \vdots \\ \mathbf{C}_{n-1} \\ \mathbf{B}_n \end{bmatrix}_{4n\times 4n} \tag{3.10}$$

where the matrices $\mathbf{B}_1, \mathbf{B}_n$ of size $(2 \times 4n)$ represent the boundary conditions and matrices $\mathbf{C}_i$, $i = 1, \ldots, n-1$ of size $(4 \times 4n)$ represent the continuity conditions. The matrices associated with the boundary conditions corresponding to the four kinds of end supports can be written as follows:

— clamped-clamped beams

$$\begin{aligned} \mathbf{B}_1 &= \begin{bmatrix} 1 & 0 & 1 & 0 & 0 & \cdots & 0 \\ -\beta_1 & \delta_1 & -\beta_1 & \overline{\delta}_1 & 0 & \cdots & 0 \end{bmatrix}_{2\times 4n} \\ \mathbf{B}_n &= \begin{bmatrix} 0 & \cdots & 0 & \cos\delta_n & \sin\delta_n & \cosh\overline{\delta}_n & \sinh\overline{\delta}_n \\ 0 & \cdots & 0 & a_{4n,4n-3} & a_{4n,4n-2} & a_{4n,4n-1} & a_{4n,4n} \end{bmatrix}_{2\times 4n} \end{aligned} \tag{3.11}$$

where

$$\begin{aligned} a_{4n,4n-3} &= -\beta_n \cos\delta_n - \delta_n \sin\delta_n \\ a_{4n,4n-2} &= -\beta_n \sin\delta_n + \delta_n \cos\delta_n \\ a_{4n,4n-1} &= -\beta_n \cosh\overline{\delta}_n + \overline{\delta}_n \sinh\overline{\delta}_n \\ a_{4n,4n} &= -\beta_n \sinh\overline{\delta}_n + \overline{\delta}_n \cosh\overline{\delta}_n \end{aligned} \tag{3.12}$$

— pinned-pinned beams

$$\begin{aligned} \mathbf{B}_1 &= \begin{bmatrix} 1 & 0 & 1 & 0 & 0 & \cdots & 0 \\ \beta_1^2 - \delta_1^2 & -2\beta_1\delta_1 & \beta_1^2 + \overline{\delta}_1^2 & -2\beta_1\overline{\delta}_1 & 0 & \cdots & 0 \end{bmatrix}_{2\times 4n} \\ \mathbf{B}_n &= \begin{bmatrix} 0 & \cdots & 0 & \cos\delta_n & \sin\delta_n & \cosh\overline{\delta}_n & \sinh\overline{\delta}_n \\ 0 & \cdots & 0 & a_{4n,4n-3} & a_{4n,4n-2} & a_{4n,4n-1} & a_{4n,4n} \end{bmatrix}_{2\times 4n} \end{aligned} \tag{3.13}$$

where

$$\begin{aligned} a_{4n,4n-3} &= 2\beta_n\delta_n \sin\delta_n + (\beta_n^2 - \delta_n^2)\cos\delta_n \\ a_{4n,4n-2} &= -2\beta_n\delta_n \cos\delta_n + (\beta_n^2 - \delta_n^2)\sin\delta_n \\ a_{4n,4n-1} &= -2\beta_n\overline{\delta}_n \sinh\overline{\delta}_n + (\beta_n^2 + \overline{\delta}_n^2)\cosh\overline{\delta}_n \\ a_{4n,4n} &= -2\beta_n\overline{\delta}_n \cosh\overline{\delta}_n + (\beta_n^2 + \overline{\delta}_n^2)\sinh\overline{\delta}_n \end{aligned} \tag{3.14}$$

— free-clamped beams

$$\mathbf{B}_1 = \begin{bmatrix} \beta_1^2 - \delta_1^2 & -2\beta_1\delta_1 & \beta_1^2 + \overline{\delta}_1^2 & -2\beta_1\overline{\delta}_1 & 0 & \cdots & 0 \\ \beta_1^3 + \beta_1\delta_1^2 & -\beta_1^2\delta_1 - \delta_1^3 & \beta_1^3 - \beta_1\overline{\delta}_1^2 & -\beta_1^2\overline{\delta}_1 + \overline{\delta}_1^3 & 0 & \cdots & 0 \end{bmatrix}_{2\times 4n} \tag{3.15}$$

the matrix $\mathbf{B}_n$ is given by $(3.11)_2$

— clamped-free beams
the matrix $\mathbf{B}_1$ is given by $(3.11)_1$

$$\mathbf{B}_n = \begin{bmatrix} 0 & \cdots & 0 & a_{4n-1,4n-3} & a_{4n-1,4n-2} & a_{4n-1,4n-1} & a_{4n-1,4n} \\ 0 & \cdots & 0 & a_{4n,4n-3} & a_{4n,4n-2} & a_{4n,4n-1} & a_{4n,4n} \end{bmatrix}_{2\times 4n} \tag{3.16}$$

where

$$\begin{aligned}
a_{4n-1,4n-3} &= 2\beta_n\delta_n \sin\delta_n + (\beta_n^2 - \delta_n^2)\cos\delta_n \\
a_{4n-1,4n-2} &= -2\beta_n\delta_n \cos\delta_n + (\beta_n^2 - \delta_n^2)\sin\delta_n \\
a_{4n-1,4n-1} &= -2\beta_n\overline{\delta}_n \sinh\overline{\delta}_n + (\beta_n^2 + \overline{\delta}_n^2)\cosh\overline{\delta}_n \\
a_{4n-1,4n} &= -2\beta_n\overline{\delta}_n \cosh\overline{\delta}_n + (\beta_n^2 + \overline{\delta}_n^2)\sinh\overline{\delta}_n \\
a_{4n,4n-3} &= (\beta_n^2\delta_n + \delta_n^3)\sin\delta_n + (\beta_n^3 + \beta_n\delta_n^2)\cos\delta_n \\
a_{4n,4n-2} &= -(\beta_n^2\delta_n + \delta_n^3)\cos\delta_n + (\beta_n^3 + \beta_n\delta_n^2)\sin\delta_n \\
a_{4n,4n-1} &= (-\beta_n^2\overline{\delta}_n + \overline{\delta}_n^3)\sinh\overline{\delta}_n + (\beta_n^3 - \beta_n\overline{\delta}_n^2)\cosh\overline{\delta}_n \\
a_{4n,4n} &= (-\beta_n^2\overline{\delta}_n + \overline{\delta}_n^3)\cosh\overline{\delta}_n + (\beta_n^3 - \beta_n\overline{\delta}_n^2)\sinh\overline{\delta}_n
\end{aligned} \tag{3.17}$$

For clamped-pinned and pinned-clamped beams, the matrices $\mathbf{B}_1$, $\mathbf{B}_n$ are given by equations $(3.11)_1$-$(3.13)_2$ and $(3.13)_1$-$(3.11)_2$, respectively. The matrices associated with the continuity conditions are represented by

$$\mathbf{C}_i = \begin{bmatrix} 0 & \cdots & 0 & a_{4i-1,4i-3} & \cdots & a_{4i-1,4i+4} & 0 & \cdots & 0 \\ 0 & \cdots & 0 & a_{4i,4i-3} & \cdots & a_{4i,4i+4} & 0 & \cdots & 0 \\ 0 & \cdots & 0 & a_{4i+1,4i-3} & \cdots & a_{4i+1,4i+4} & 0 & \cdots & 0 \\ 0 & \cdots & 0 & a_{4i+2,4i-3} & \cdots & a_{4i+2,4i+4} & 0 & \cdots & 0 \end{bmatrix}_{4\times 4n} \qquad i = 1, \ldots, n-1 \tag{3.18}$$

The non-zero elements of these matrices are given in Appendix.

The determinant of the matrix $\mathbf{A}$ has to vanish for a non-trivial solution of equation (3.9) to exist. The frequency equation

$$\det \mathbf{A}(\omega) = 0 \tag{3.19}$$

is then solved numerically using an approximate method.

4. Numerical results

The numerical computations have been carried out for an FG beam which was divided into n segments of the same length. The functions $g(\cdot)$, $h(\cdot)$ introduced into equations (2.4) are assumed in the form $g(\xi) = (1+\gamma\xi)^\alpha$, $h(\xi) = 1+\gamma\xi$. In the computations, the formulae given by equation (2.8) have been used. The first three non-dimensional free vibration frequencies obtained in the present study for $n = 100$ are listed in Tables 1 and 2 in comparison with those presented by Huang and Li (2010) and calculated by using a power series expansion. From Tables 1-2, it can be seen that the present results are in good agreement with the existing results. For $\gamma = 0$, we have the case of a homogeneous beam. It is seen in Tables 1 and 2 that in this case the agreement is excellent.

Table 1. The first three non-dimensional free vibration frequencies for $g(\xi) = (1+\gamma\xi)^3$, $h(\xi) = 1+\gamma\xi$, clamped-clamped beam

γ	Power series method	Huang and Li (2010)	Present study
−0.1	21.2409777868	21.24097778688	21.242905
	58.5500545739	58.55005461550	58.567526
	114.780241659	114.78027750905	114.824704
0	22.3732854478	22.37328544806	22.373285
	61.6728228676	61.67282294761	61.672823
	120.903391727	120.90340027002	120.903392
0.1	23.4796072481	23.47960724845	23.460013
	64.7210676329	64.72106768601	64.678046
	126.878016311	126.87805071630	126.802905
0.2	24.5634175322	24.5634175326	24.508817
	67.7047553171	67.7047553184	67.596273
	132.723976757	132.7240684027	132.546612

Table 2. The first three non-dimensional free vibration frequencies for $g(\xi) = (1+\gamma\xi)^3$, $h(\xi) = 1+\gamma\xi$, clamped-pinned beam

γ	Power series method	Huang and Li (2010)	Present study
−0.1	14.8488960557	14.84889605539	14.844562
	47.6370371901	47.63703719174	47.647237
	99.171635183	99.17165323722	99.206918
0	15.4182057169	15.41820571698	15.418206
	49.964862032	49.96486203816	49.964862
	104.247696458	104.24770194514	104.247696
0.1	15.968709884	15.96870988416	15.950015
	52.2372268871	52.23722689317	52.198883
	109.202352455	109.20235370558	109.134912
0.2	16.5028988943	16.50289889399	16.445277
	54.4614625302	54.46146253076	54.360368
	114.051623344	114.05163085534	113.888586

The effects of parameters α, γ and the number of segments n on the first three non-dimensional frequencies for different boundary conditions are presented in Tables 3-5. It can be observed that an increase in the value of the parameter α causes an increase in the difference between the results obtained for $n = 5$, $n = 10$ and $n = 20$, respectively.

Figure 1 presents the first free vibration frequencies calculated for the functions $g(\xi) = (1+\gamma\xi)^\alpha$ and $h(\xi) = 1+\gamma\xi$ for $\alpha = 1$, $\alpha = 2$ and $\alpha = 3$. The calculations have been performed for six types of boundary conditions. It can be noticed that variation of the parameter γ has a significant effect on the free vibration frequency. For the clamped-free beams, the greatest impact of the parameter γ occurs for $\alpha = 1$, and for all the other boundary conditions under considerations it is for $\alpha = 3$. For the clamped-clamped and pinned-pinned beams, the differences between the values of free vibration frequencies for $\alpha = 1$ are negligible.

Table 3. The first non-dimensional free vibration frequency for different boundary conditions, $g(\xi) = (1+\gamma\xi)^{\alpha}$, $h(\xi) = 1+\gamma\xi$

BC	n	$\alpha = 1$		$\alpha = 2$		$\alpha = 3$	
		$\gamma = -0.5$	$\gamma = 0.5$	$\gamma = -0.5$	$\gamma = 0.5$	$\gamma = -0.5$	$\gamma = 0.5$
C-C	5	22.03982	22.264535	19.265636	24.165700	16.814251	26.214186
	10	22.051059	22.262618	19.048822	24.459508	16.441212	26.863566
	20	22.053796	22.261942	18.935593	24.609820	16.247100	27.197036
P-P	5	9.583045	9.773619	8.177437	10.524969	6.896407	11.294071
	10	9.588353	9.772740	8.086959	10.653015	6.746380	11.574244
	20	9.589777	9.772464	8.039484	10.718554	6.667729	11.718081
C-P	5	15.838604	14.907051	14.080008	15.909067	12.483974	16.939622
	10	15.845921	14.905829	13.922110	16.102144	12.209467	17.358429
	20	15.847897	14.905405	13.839671	16.201108	12.066042	17.573873
P-C	5	14.448440	15.749301	12.216596	17.289925	10.244436	18.957895
	10	14.456396	15.747708	12.079634	17.500534	10.017769	19.429126
	20	14.458368	15.747212	12.008080	17.608138	9.899795	19.670529
C-F	5	4.379586	3.121248	4.321434	3.188805	4.234717	3.251220
	10	4.380502	3.120991	4.252879	3.232930	4.103112	3.342365
	20	4.380745	3.120903	4.222757	3.254157	4.045646	3.386566
F-C	5	2.887779	3.995266	2.290903	4.643804	1.807925	5.384977
	10	2.889157	3.994728	2.270108	4.689088	1.774671	5.492166
	20	2.889508	3.994563	2.257891	4.715110	1.755475	5.553767

Table 4. The second non-dimensional free vibration frequency for different boundary conditions, $g(\xi) = (1+\gamma\xi)^{\alpha}$, $h(\xi) = 1+\gamma\xi$

BC	n	$\alpha = 1$		$\alpha = 2$		$\alpha = 3$	
		$\gamma = -0.5$	$\gamma = 0.5$	$\gamma = -0.5$	$\gamma = 0.5$	$\gamma = -0.5$	$\gamma = 0.5$
C-C	5	61.187699	61.527290	53.563835	66.810777	46.705060	72.453327
	10	61.220229	61.522622	52.964685	67.624175	45.679608	74.250130
	20	61.227661	61.520754	52.649784	68.039773	45.140471	75.171899
P-P	5	39.248490	39.415763	34.281704	42.767233	29.772507	46.312345
	10	39.265508	39.411680	33.896833	43.288075	29.121704	47.465112
	20	39.270192	39.410436	33.695664	43.554164	28.779150	48.054717
C-P	5	50.300388	49.461958	44.282315	53.482420	38.806190	57.735593
	10	50.321872	49.457835	43.792788	54.127769	37.971984	59.156518
	20	50.327702	49.456336	43.532945	54.460171	37.525512	59.890410
P-C	5	48.939014	50.267141	42.517999	54.777959	36.759687	59.599505
	10	48.964462	50.262091	42.035739	55.451783	35.941623	61.097469
	20	48.970497	50.260490	41.785685	55.792915	35.517228	61.857034
C-F	5	23.381744	21.158807	21.233450	22.452525	19.191540	23.771357
	10	23.393474	21.157385	20.890872	22.761849	18.565383	24.434588
	20	23.396111	21.156800	20.740129	22.911071	18.295994	24.757241
F-C	5	20.476134	22.847483	17.187639	25.342189	14.317750	28.060961
	10	20.488032	22.845673	17.036003	25.587931	14.064074	28.609593
	20	20.490837	22.844949	16.945280	25.728924	13.914191	28.926634

Table 5. The third non-dimensional free vibration frequency for different boundary conditions, $g(\xi) = (1+\gamma\xi)^{\alpha}$, $h(\xi) = 1+\gamma\xi$

BC	n	$\alpha = 1$		$\alpha = 2$		$\alpha = 3$	
		$\gamma = -0.5$	$\gamma = 0.5$	$\gamma = -0.5$	$\gamma = 0.5$	$\gamma = -0.5$	$\gamma = 0.5$
C-C	5	120.319511	120.746274	105.344423	131.127496	91.681928	142.145173
	10	120.392769	120.740300	104.218260	132.739432	89.853340	145.728137
	20	120.407372	120.736681	103.598604	133.555211	88.792805	147.537078
P-P	5	88.594258	88.779880	77.531290	96.389774	67.426814	104.429449
	10	88.629715	88.770369	76.684167	97.575681	66.023866	107.072172
	20	88.639792	88.767515	76.229088	98.175746	65.248530	108.403315
C-P	5	104.554645	103.740552	91.766692	112.472339	80.084560	121.703952
	10	104.597719	103.733256	90.815730	113.815304	78.503258	124.685866
	20	104.609566	103.730098	90.278366	114.513546	77.584066	126.231330
P-C	5	103.144606	104.556740	90.048791	113.706807	78.140870	123.417530
	10	103.202283	104.546600	89.029672	115.147269	76.462403	126.629660
	20	103.214761	104.543267	88.499082	115.856814	75.558342	128.206906
C-F	5	62.982515	60.852831	56.140476	65.522940	49.819399	70.432539
	10	63.020704	60.849312	55.256707	66.417417	48.227924	72.379515
	20	63.028371	60.847560	54.856960	66.851872	47.524147	73.333012
F-C	5	60.136355	62.488331	51.918494	68.523131	44.593816	75.023941
	10	60.171203	62.485112	51.449765	69.200653	43.789492	76.516820
	20	60.178811	62.483270	51.173617	69.581994	43.319244	77.363991

The presented numerical results have been obtained by using coefficients d_i, m_i, β_i, $i = 1, \ldots, n$, given by equations (2.8). Numerical computations show that the application of equations (2.16) leads to results which are in good agreement with the obtained by using equations (2.8).

5. Conclusions

In the paper, a solution to the free vibration problem of axially functionally graded beams is presented. An exact solution is derived for axially piece-wise exponential graded beams. The frequency equation for beams with various combinations of clamped, pinned and free ends has been obtained. In this approach, the distributed parameters which describe continuous axial changes of the material properties of the beam are approximated by piecewise exponential functions. The non-dimensional free vibration frequencies for a chosen function characterizing the functionally graded beams have been numerically computed. An improvement of the accuracy of the numerical results for a larger number of beam subsections applied in the method has been demonstrated. A high agreement of the numerical results obtained by using the presented method with the results obtained by using the power series method as well as with results given by other authors has also been observed. The numerical investigation shows that the beam stiffness distribution in the axial direction significantly effects free vibration frequencies of the system.

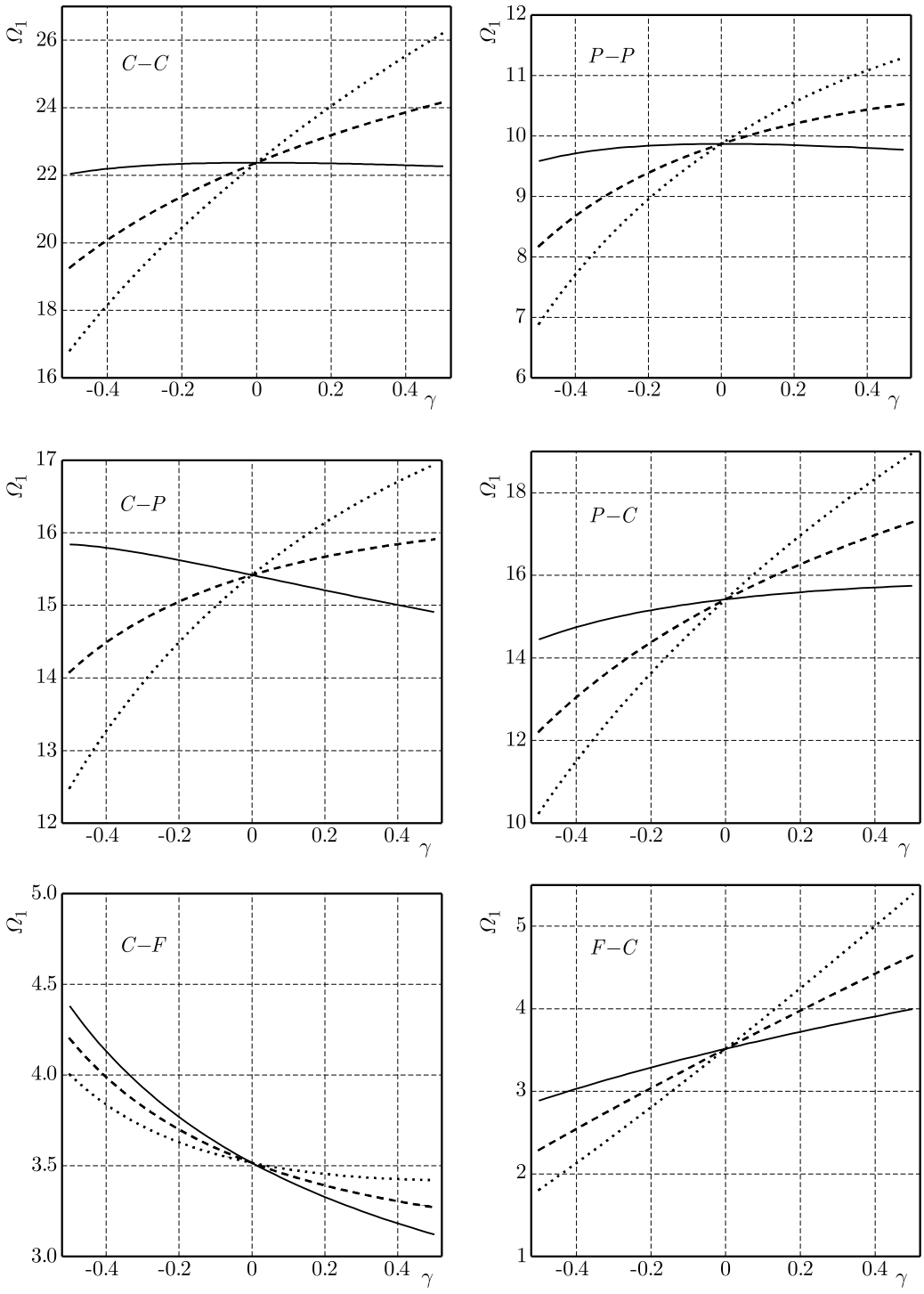

Fig. 1. The first non-dimensional free vibration frequency as a function of γ for $\alpha = 1$ (solid line), $\alpha = 2$ (dashed line), $\alpha = 3$ (dotted line) for different boundary conditions

Appendix

Let us denote $exi = \mathrm{e}^{\xi_i}(\beta_{i+1} - \beta_i)$, $ci = \cos(\delta_i \xi_i)$, $si = \sin(\delta_i \xi_i)$, $chi = \cosh(\overline{\delta}_i \xi_i)$, $shi = \sinh(\overline{\delta}_i \xi_i)$, $ci1 = \cos(\delta_{i+1} \xi_i)$, $si1 = \sin(\delta_{i+1} \xi_i)$, $chi1 = \cosh(\overline{\delta}_{i+1} \xi_i)$, $shi1 = \sinh(\overline{\delta}_{i+1} \xi_i)$.

The non-zero elements of the matrix $\mathbf{C}_i$, $i = 1, \ldots, n-1$, which occur in equation (3.18) are given by

$$a_{4i-1,4i-3} = exi \cdot ci \qquad a_{4i-1,4i-2} = exi \cdot si \qquad a_{4i-1,4i-1} = exi \cdot chi$$
$$a_{4i-1,4i} = exi \cdot shi \qquad a_{4i-1,4i+1} = -ci1 \qquad a_{4i-1,4i+2} = -si1$$
$$a_{4i-1,4i+3} = -chi1 \qquad a_{4i-1,4i+4} = -shi1$$
$$a_{4i,4i-3} = -exi(\beta_i ci + \delta_i si) \qquad a_{4i,4i-2} = -exi(\beta_i si - \delta_i ci)$$
$$a_{4i,4i-1} = -exi(\beta_i chi - \overline{\delta}_i shi) \qquad a_{4i,4i} = -exi(\beta_i shi - \overline{\delta}_i chi)$$
$$a_{4i,4i+1} = \beta_{i+1} ci1 + \delta_{i+1} si1 \qquad a_{4i,4i+2} = \beta_{i+1} si1 - \delta_{i+1} ci1$$
$$a_{4i,4i+3} = \beta_{i+1} chi1 + \overline{\delta}_{i+1} shi1 \qquad a_{4i,4i+4} = \beta_{i+1} shi1 - \overline{\delta}_{i+1} chi1$$
$$a_{4i+1,4i-3} = exi[(\beta_i^2 - \delta_i^2)ci + 2\beta_i\delta_i si]$$
$$a_{4i+1,4i-2} = exi[(\beta_i^2 - \delta_i^2)si - 2\beta_i\delta_i ci]$$
$$a_{4i+1,4i-1} = exi[(\beta_i^2 + \overline{\delta}_i^2)chi - 2\beta_i\overline{\delta}_i shi]$$
$$a_{4i+1,4i} = exi[(\beta_i^2 + \overline{\delta}_i^2)shi - 2\beta_i\overline{\delta}_i chi]$$
$$a_{4i+1,4i+1} = -2\beta_{i+1}\delta_{i+1} si1 + (-\beta_{i+1}^2 + \delta_{i+1}^2)ci1$$
$$a_{4i+1,4i+2} = 2\beta_{i+1}\delta_{i+1} ci1 + (-\beta_{i+1}^2 + \delta_{i+1}^2)si1$$
$$a_{4i+1,4i+3} = 2\beta_{i+1}\overline{\delta}_{i+1} shi1 - (\beta_{i+1}^2 + \overline{\delta}_{i+1}^2)chi1$$
$$a_{4i+1,4i+4} = 2\beta_{i+1}\overline{\delta}_{i+1} chi1 - (\beta_{i+1}^2 + \overline{\delta}_{i+1}^2)shi1$$
$$a_{4i+2,4i-3} = -exi[(\beta_i^2 - 3\delta_i^2)\beta_i ci + (3\beta_i^2 - \delta_i^2)\delta_i si]$$
$$a_{4i+2,4i-2} = -exi[(\beta_i^2 - 3\delta_i^2)\beta_i si + (-3\beta_i^2 + \delta_i^2)\delta_i ci]$$
$$a_{4i+2,4i-1} = -exi[(\beta_i^2 + 3\overline{\delta}_i^2)\beta_i chi - (3\beta_i^2 + \overline{\delta}_i^2)\overline{\delta}_i shi]$$
$$a_{4i+2,4i} = -exi[(\beta_i^2 + 3\overline{\delta}_i^2)\beta_i shi - (3\beta_i^2 + \overline{\delta}_i^2)\overline{\delta}_i chi]$$
$$a_{4i+2,4i+1} = (\beta_{i+1}^2 - 3\delta_{i+1}^2)\beta_{i+1} ci1 - (-3\beta_{i+1}^2 + \delta_{i+1}^2)\delta_{i+1} si1$$
$$a_{4i+2,4i+2} = (\beta_{i+1}^2 - 3\delta_{i+1}^2)\beta_{i+1} si1 + (-3\beta_{i+1}^2 + \delta_{i+1}^2)\delta_{i+1} ci1$$
$$a_{4i+2,4i+3} = -(3\beta_{i+1}^2 + \overline{\delta}_{i+1}^2)\overline{\delta}_{i+1} shi1 + (\beta_{i+1}^2 + 3\overline{\delta}_{i+1}^2)\beta_{i+1} chi1$$
$$a_{4i+2,4i+4} = -(3\beta_{i+1}^2 + \overline{\delta}_{i+1}^2)\overline{\delta}_{i+1} chi1 + (\beta_{i+1}^2 + 3\overline{\delta}_{i+1}^2)\beta_{i+1} shi1$$

References

1. Alshorbagy A.E., Eltaher M.A., Mahmoud F.F., 2011, Free vibration characteristics of a functionally graded beam by finite element method, *Applied Mathematical Modelling*, **35**, 412-425
2. Anandrao K.S., Gupta R.K., Ramachandran P., Rao G.V., 2012, Free vibration analysis of functionally graded beams, *Defence Science Journal*, **62**, 3, 139-146
3. Chauhan P.K., Khan I.A., 2014, Review on analysis of functionally graded material beam type structure, *International Journal of Advanced Mechanical Engineering*, **4**, 3, 299-306
4. Hein H., Feklistova L., 2011, Free vibrations of non-uniform and axially functionally graded beams using Haar wavelets, *Engineering Structures*, **33**, 3696-3701
5. Huang Y., Li X.-F., 2010, A new approach for free vibration of axially functionally graded beams with non-uniform cross-section, *Journal of Sound and Vibration*, **329**, 2291-2303
6. Huang Y., Yang L.-E., Luo Q.-Z., 2013, Free vibration of axially functionally graded Timoshenko beams with non-uniform cross-section, *Composites: Part B*, **45**, 1493-1498
7. Kukla S., Rychlewska J., 2014, Free vibration of axially functionally graded Euler-Bernoulli beams, *Journal of Applied Mathematics and Computational Mechanics*, **13**, 1, 39-44
8. Lebed O.I., Karnovsky I.A., 2000, *Formulas for Structural Dynamics*, Mc Graw-Hill

9. Li X.-F., Kang Y.-A., Wu J.-X., 2013, Exact frequency equations of free vibration of exponentially functionally graded beams, *Applied Acoustics*, **74**, 413-420

10. Liu Y., Shu D.W., 2014, Free vibrations analysis of exponential functionally graded beams with a single delamination, *Composites: Part B*, **59**, 166-172

11. Matbuly M.S., Ragb O., Nassar M., 2009, Natural frequencies of a functionally graded cracked beam using the differential quadrature method, *Applied Mathematics and Computation*, **215**, 2307-2316

12. Pradhan K.K., Chakraverty S., 2013, Free vibration of Euler and Timoshenko functionally graded beams by Rayleigh-Ritz method, *Composites: Part B*, **51**, 175-184

13. Shahba A., Attarnejad R., Zarrinzadeh H., 2013, Free vibration analysis of centrifugally stiffened tapered functionally graded beams, *Mechanics of Advanced Materials and Structures*, **20**, 331-338

14. Shahba A., Rajasekaran S., 2012, Free vibration and stability of tapered Euler-Bernoulli beams made of axially functionally graded materials, *Applied Mathematical Modelling*, **36**, 3094-3111

15. Sina S.A., Navazi H.M., Haddadpour H., 2009, An analytical method for free vibration analysis of functionally graded beams, *Materials and Design*, **30**, 741-747

16. Tang A.-Y., Wu J.-X., Li X.-F., Lee K.Y., 2014, Exact frequency equations of free vibration of exponentially non-uniform functionally graded Timoshenko beams, *International Journal of Mechanical Sciences*, **89**, 1-11

17. Wattanasakulpong N., Ungbhakorn V., 2012, Free vibration analysis of functionally graded beams with general elastically end constraints by DTM, *World Journal of Mechanics*, **2**, 297-310

18. Wu L., Wang Q., Elishakoff I., 2005, Semi-inverse method for axially functionally graded beams with an anti-symmetric vibration mode, *Journal of Sound and Vibration*, **284**, 1190-1202

Manuscript received July 8, 2015; accepted for print December 4, 2015

JOURNAL OF THEORETICAL AND APPLIED MECHANICS
54, 3, pp. 871-879, Warsaw 2016
DOI: 10.15632/jtam-pl.54.3.871

NUMERICAL AND FIELD INVESTIGATIONS OF TRACK DYNAMIC BEHAVIOR CAUSED BY LIGHT AND HEAVY RAILWAY VEHICLES

Jabbar Ali Zakeri, Seyed Ali Mosayebi, Morteza Esmaeili

School of Railway Engineering, The Center of Excellence in Railway Transportation, Iran University of Science and Technology, Tehran, Iran

e-mail: zakeri@iust.ac.ir; mosayebi@iust.ac.ir; m_esmaeili@iust.ac.ir

Dynamic behavior of a track-train system is a function of axle loads and support stiffness because of non-linear supports. Therefore, it is expected that the support stiffness affects the behavior of the railway track during passing of a light or heavy car body. Since the effects of axle loads caused by light and heavy railway vehicles and support stiffness of ballasted railway tracks due to passing railway vehicles have not been studied adequately, therefore the present study focused on this issue. For this purpose, this issue was first investigated by passing a light and heavy car body including bogies with three axle loads as field tests. Then, numerical analyses of the railway track caused by the passing of these railway vehicles were studied, and the numerical results were compared with the field results. There was a good agreement between the values of field responses and numerical analyses. Subsequently, a series of sensitivity analyses on effects of the axle loads caused by light or heavy loading and support conditions was done on the ballasted railway track. The results indicated that the maximum vertical displacements increased by axle loads, increased sleeper distances and decreases support stiffness. Finally, equations of track behavior based on support stiffness and axle loads were derived.

Keywords: numerical and field investigation, railway track, track dynamics, railway vehicles

1. Introduction

In order to understand the mechanism of railway tracks and reduction of maintenance costs, the dynamic behavior of the railway track should be investigated. Since it was difficult to measure responses of the railway track directly in field, therefore models of railway tracks were investigated usually. The available technical literature indicated that different models and methods were presented for the analysis of railway tracks by various researchers. Usually, numerical models for analyzing the railway track are: one-dimensional model of a railway including lumped masses, two-dimensional model of a track including beam on an elastic foundation with continuous supports or discrete supports. There are many researchers in the field of modeling and dynamic analysis of railway tracks. In these studies, several models have been proposed for investigating the railway track and its components. Generally, the research fields of these researchers could be divided into three categories: dynamic analysis of railway tracks, simulation of the vehicle and railway track, and train-track interaction. Some of the most prominent researchers who studied these fields are: Cai (1992), Zhai and Sun (1994), Knothe (1995), Zhai and Cai (1997), Fryba (1999), Zakeri (2000), Popp *et al.* (2003), Zakeri and Xia (2008), Bogacz and Czyczuła (2008), Dahlberg (2010) and Zakeri and Ghorbani (2011). Among the most important parameters in the analysis of railway tracks, axle loads of railway vehicles and support conditions of ballasted railway tracks could be pointed out. Some of researchers worked in the field of the effects of stiffness of railway track components. For example, Kerr (2003) investigated the behavior of the rail on elastic supports due to moving load. Zhai *et al.* (2004) studied vibrations of the railway

ballast in tracks. Witt (2008) studied the behavior of under sleeper pads in railway tracks. Puzavac *et al.* (2012) investigated vertical stiffness of the railway track due to passing loads. Zakeri and Abbasi (2012) investigated stiffness of the railway track in desert areas. Also, Esmaeili *et al.* (2014) studied the sand fouled ballast on train induced vibrations. In the mentioned studies and the available technical literature, the effects of a passing light railway vehicle (Draisine) and a heavy railway vehicle including bogies with three axle loads on ballasted railway tracks have not been studied adequately. Also considering that the behavior of the railway track support is nonlinear and depends on train loads, the effects of various passing train loads including the light and heavy railway vehicles have been studied in this paper. Therefore, the simulation of light and heavy car bodies has been explained in this paper. Afterward, a series of field tests by using light or heavy loading was done for validating the numerical analyses. After validation and in continuation, the effects of axle loads caused by light and heavy railway vehicles and support stiffness of the railway track were studied. Finally, equations of the track behavior based on the support stiffness and then the axle loads were derived.

2. Modeling of the railway track

In modeling of the railway track with the concept of railway tracks on a viscoelastic foundation, two models can be considered. These are: (a) railway track with one layer including a continuous rail, (b) railway track with two layers including the rail and sleepers. In Fig. 1, the railway track with two layers is presented. The first layer is the rail as a continuous support and the second layer are sleepers as discrete supports.

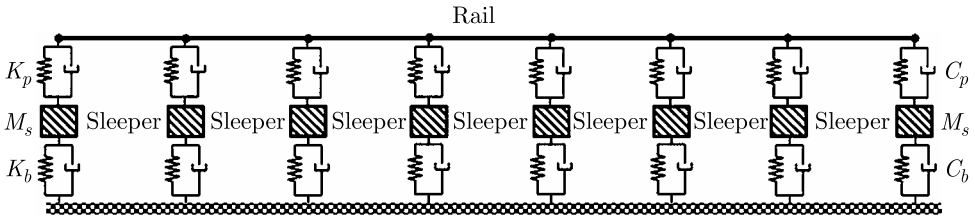

Fig. 1. Railway track with two layers (rail and sleeper)

As can be observed from Fig. 1, the sleepers are modeled as a series of lumped masses. In this figure, K_p and K_b are pad and support stiffnesses, respectively. Figure 2 shows the rail and sleeper in the model of the railway track with two layers.

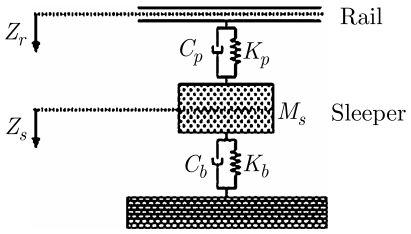

Fig. 2. Rail and sleeper in the railway track model

By using the finite element method, the rail is divided into several elements, and the matrix of each element is derived. Then the total matrix of the rail is derived by assembling all rail elements. In each element of the rail, vertical stiffness of rail pads is considered in beam joints. Also, stiffness, damping and mass matrix of the railway track with two layers can be considered as a submatrix of the whole system (Zakeri, 2000).

3. Modeling of railway vehicles

In this Section, the passing railway vehicles including light and heavy railway car bodies are simulated. In this regard and by using the finite element method, the equations of motion of all components of the light and heavy railway vehicles are derived and their matrices are formed. Then by assembling the matrices of railway vehicles and tracks, the derived equation is solved with available numerical methods. Next, the models of light and heavy railway vehicles are presented.

3.1. Heavy railway vehicle

In order to model a rail vehicle for heavy loading, a car body including bogies with three axle loads is considered, see Fig. 3.

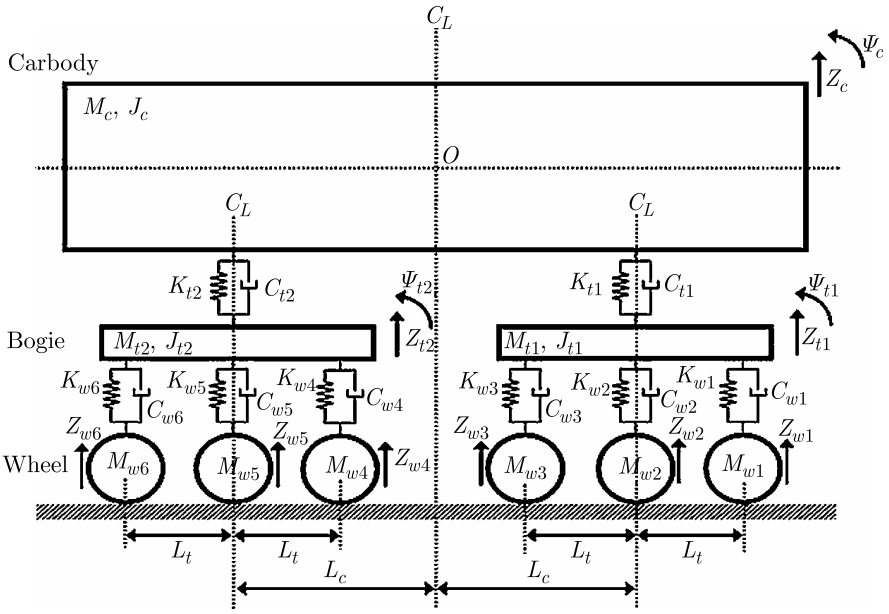

Fig. 3. Heavy railway car body including bogies with three axle loads

In Fig. 3, L_c and L_t are halves of the bogies and wheels axes, respectively. In this figure, M_c is car body mass, M_t – bogie mass, M_w – wheel mass, J_c – car body rotational inertia and J_t is bogie rotational inertia. As can be seen in Fig. 3, the car body has bogies with three axle loads. C_w, K_w, C_t and K_t are primary and secondary suspension damping and stiffness, respectively. So, Zc is the vertical displacement of the car body, ψ_c – rotation of the car body, Z_t – vertical displacement of the bogie, ψ_t – rotation of the bogie and Z_w is vertical displacement of the wheel.

3.2. Light railway vehicle

Also, in order to model a railway vehicle for ight loading, a draisine with two axle loads is considered as shown in Fig. 4.

In Fig. 4, M_D and J_D are mass and rotational inertia of the draisine, respectively. K_w and C_w are suspension system damping and stiffness, respectively. Also, Z_D is the vertical displacement of the draisine, ψ_D – its rotation and Z_w is the vertical displacement of the wheel. In the following, the procedure of field tests caused by a passing light draisine and a heavy car body is presented.

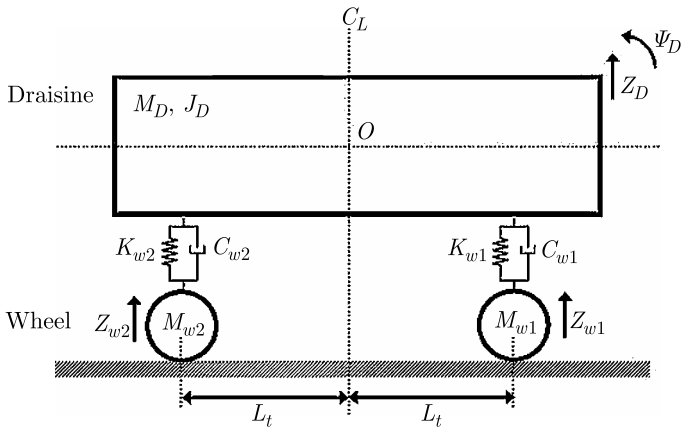

Fig. 4. Light railway draisine with two axle loads

4. Field tests

For investigating the behavior of a ballasted railway track in field, a railway track was selected in Iran. In order to obtain time histories of the vertical displacement of the railway track in field tests, two types of railway vehicles including light and heavy railway vehicles were utilized. For applying light loading, a draisine with two axle loads was used. Specifications of that draisine were: total weight 4 tons, axle load 2 tons, wheel load 1 ton, length 4 m and vehicle speed 30 km/h. Also, locomotive GT26CW was used to apply heavy loading. Specifications of the locomotive were: total weight 110 tons, axle load 18.3 tons, wheel load 9.2 tons, length 18 m and vehicle speed 30 km/h (Zakeri and Abbasi, 2012). Figure 5 indicates the passing of the light and heavy railway vehicles.

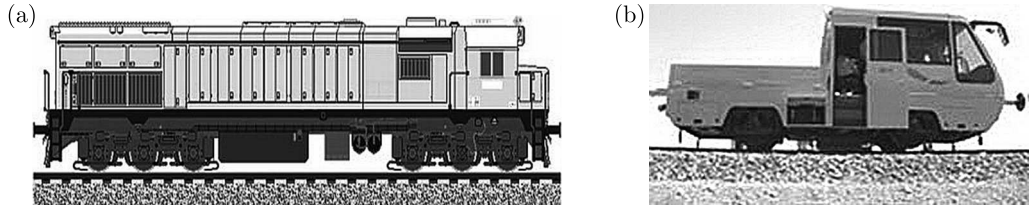

Fig. 5. Railway vehicles for field tests; (a) GT26CW locomotive including bogies with three axle loads, (b) draisine with two axle loads

For measuring the vertical displacement of the railway track caused by the rail vehicles, linear variable differential transformers (LVDT's) located on sleepers were utilized (Fig. 6).

Fig. 6. Linear variable differential transformer (LVDT) for measuring the vertical displacement of the railway track

In next Section, results of numerical analyses are compared and validated with the responses from field tests.

5. Validation of the railway model

In order to validate the results of numerical analyses, they have been compared and validated with the results of field tests. Figure 7 shows numerical and field vertical displacement time histories of the railway track caused by the car bodies.

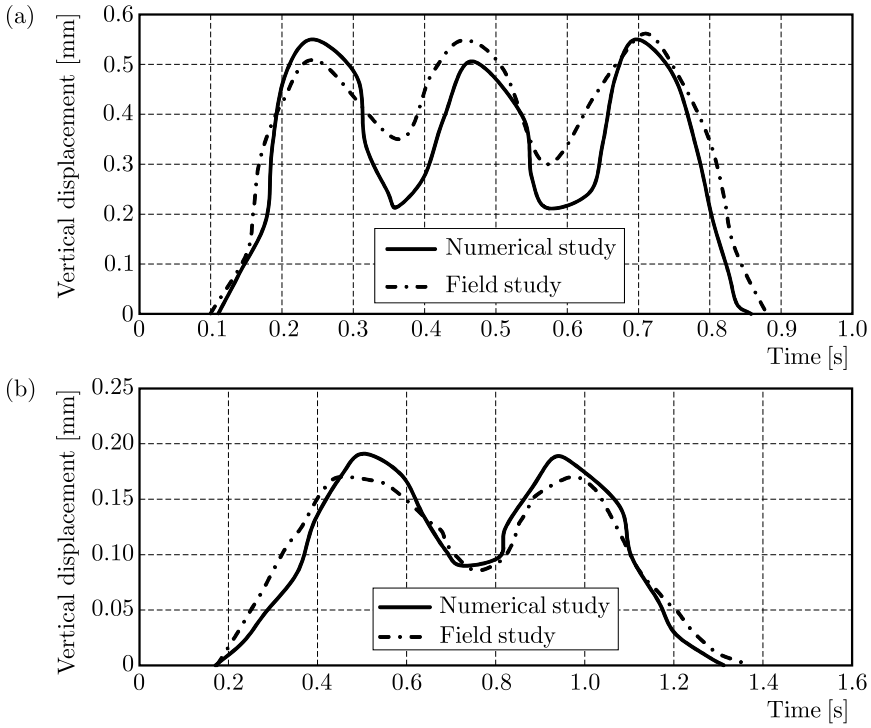

Fig. 7. Vertical displacement time histories of the railway track caused by railway vehicles; (a) heavy vehicle, (b) light vehicle

By observing and comparing vertical displacement time histories of the railway track caused by passing railway vehicles and those obtained from numerical simulation and field studies, two important points could be extracted. Firstly, the range of field responses is in a good agreement with the values of numerical analyses. Secondly, the trend of field responses shows a good agreement with the numerical analyses. Hence, it could be concluded that the modeling and numerical analyses of the railway track caused by a light draisine and a heavy car body have been done correctly. In the next Section, equations of the railway track according to the support stiffness and axle loads are derived.

6. Track behavior versus support stiffness

In this Section, effects of axle loads of light and heavy car bodies are investigated in terms of the behavior of a ballasted railway track. Figure 8 indicates a sample of the vertical displacement time history of the railway track due to passing of light and heavy railway vehicles.

As can be observed in Fig. 8, the vertical displacement time history of the railway track has two and six peaks due to passing of a light draisine and a heavy car body, respectively. Figure 9 shows the ratio of the maximum vertical displacement with respect to the light and heavy axle loads [mm/ton] against the support stiffness [MN/m] for various distances between the sleepers.

As can be seen in Fig. 9, the maximum vertical displacement per unit axle load is constant for higher support stiffness. The maximum vertical displacements decrease for growing axle loads. Also, the increase of the sleeper distances and decreasing of the support stiffness make them

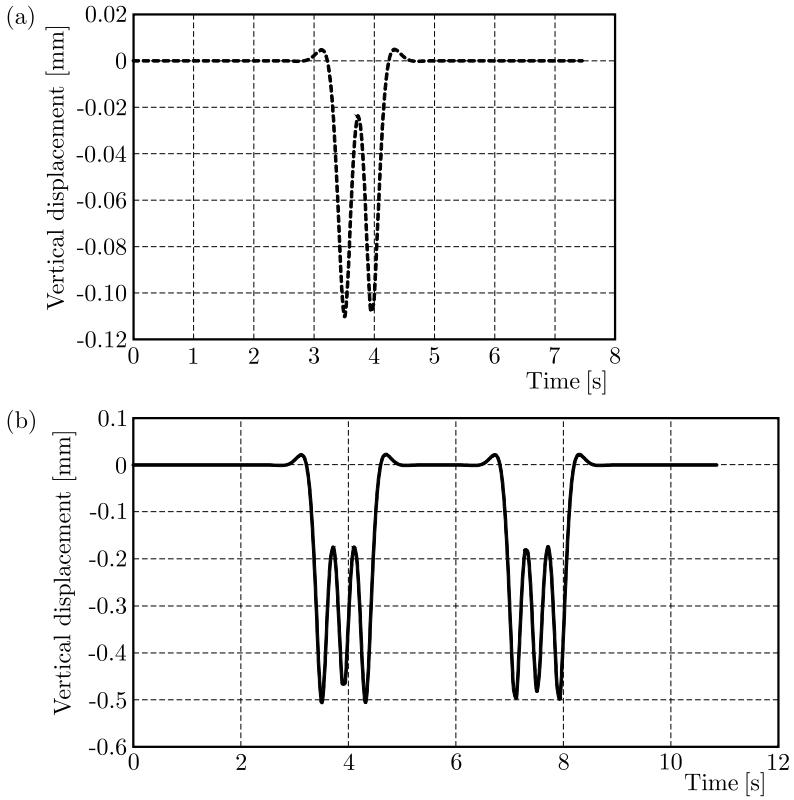

Fig. 8. Vertical displacement time history of ballasted railway track; (a) passing of a light draisine, (b) passing of heavy car body

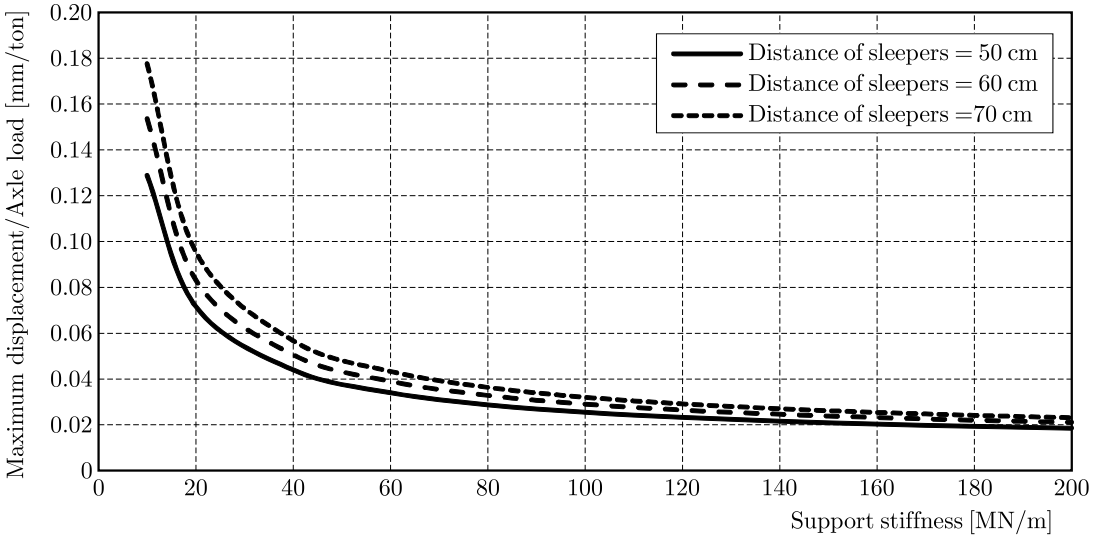

Fig. 9. Ratio of the maximum vertical displacement with respect to light and heavy axle loads versus the support stiffness

greater. The effect of the sleeper distance is significant as it decreases the support stiffness. The trend observed in Fig. 9 is close to the power equation as $y = ax^b$. The corresponding equations are presented in Table 1.

Table 1 indicates that the coefficients of the equations increase with the increasing distance of the sleepers.

Table 1. Equations of the maximum vertical displacement per unit axle load against the support stiffness

Distance of sleepers	Equations	R-Squared
50 cm	$y = 0.5x^{-0.63}$	$R^2 = 0.98$
60 cm	$y = 0.6x^{-0.64}$	$R^2 = 0.98$
70 cm	$y = 0.73x^{-0.66}$	$R^2 = 0.98$

* x and y are the support stiffness [MN/m] and the maximum vertical displacement per unit load [mm/ton], respectively

7. Track behavior versus axle loads

In the previous Section it has been shown that by increasing axle loads, the track behavior may be stabilised by increasing the support stiffness. Figure 10 indicates the maximum vertical displacement [mm] versus the axle load [ton] for various distances between the sleepers.

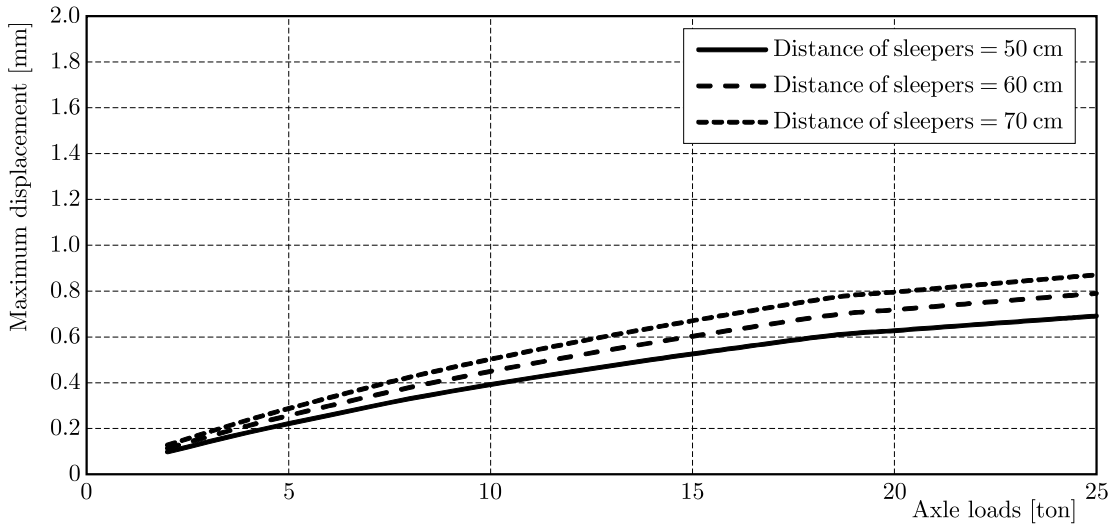

Fig. 10. The maximum vertical displacement for light and heavy axle loads

As can be observed is Fig. 10, the maximum vertical displacements increase with an increase in the axle loads. Also, they grow for greater sleeper distances. The effect of the sleeper distance is significant as it increases the values of axle loads. The trend of the diagrams is close to a logarithmic equation $y = a\ln(x) + b$. The corresponding equations are given in Table 2.

Table 2. Equations for the maximum vertical displacement versus axle loads

Distance of sleepers	Equations	R-Squared
50 cm	$y = 0.25\ln(x) - 0.15$	$R^2 = 0.97$
60 cm	$y = 0.29\ln(x) - 0.17$	$R^2 = 0.97$
70 cm	$y = 0.32\ln(x) - 0.18$	$R^2 = 0.97$

* x and y are axle loads [ton] and the maximum vertical displacement [mm], respectively

In Table 2, the coefficients of the equations increase with the distance between the sleepers.

8. Conclusion

A review of technical literature indicates that the behavior of track supports is nonlinear and depends on train loads. For this reason, the effects of passing light and heavy railway vehicles have been studied in this paper. So, the simulation procedure of light and heavy car bodies has been explained. Afterward, results of a series of field tests with two light and heavy loadings have been presented for validating the numerical analyses. After validation, the effects of axle loads of light and heavy railway vehicles as well as support stiffness have been studied. The important findings of the present study can be summarized as follows:

- The range of the field responses is in a good agreement with the values of numerical analyses. Also, the trend of field responses is in a good agreement with the numerical analyses.
- By increasing the distance between the sleepers from 50 to 70 cm, the ratio of the maximum vertical displacement with respect to the axle load increased by 33 and 25 percent at the support stiffness of 20 and 120 MN/m, respectively.
- For the sleeper spacing 60 cm, the ratio of the maximum vertical displacement with respect to the axle load decreased by 68 percent due to increasing of the support stiffness from 20 to 120 MN/m.
- The trend of the ratio of the maximum vertical displacement with respect to the axle load against the support stiffness is close to a power equation $y = ax^b$. The coefficient a in this equation is 0.5, 0.6 and 0.73 for the distance of between sleepers of 50, 60 and 70 cm, respectively. Correspondingly, the coefficient b is -0.63, -0.64 and -0.66, respectively.
- By increasing the axle loads from 8 to 18.5 tons, the maximum vertical displacement increased the 83 percent for sleeper spacing 60 cm.
- By increasing the distance between the sleepers from 50 to 70 cm, the maximum vertical displacement increased by 30 and 27 percent at the axle loads of 2 and 20 tons, respectively.
- The trend of the maximum vertical displacement against the axle loads is close to a logarithmic equation $y = a\ln(x) + b$. The coefficient a in this equation is 0.25, 0.29 and 0.32 for the distance between the sleepers 50, 60 and 70 cm, respectively. Correspondingly, the coefficient b is -0.15, -0.17 and -0.18, respectively.

Acknowledgment

The authors are grateful to dr. S. Mohammadzadeh for his help in this study. The authors would like to thank technical engineers, R. Abbasi, M. Mehrali and M. Nouri, for their assistance during the course of this project.

References

1. Bogacz R., Czyczuła W., 2008, Response of beam on visco-elastic foundation to moving distributed load, *Journal of Theoretical and Applied Mechanics*, **46**, 4, 763-775
2. Cai Z., 1992, Modeling of rail track dynamics and wheel rail interaction, PhD Thesis, Department of Civil Engineering, Queen's University, Kingston, Ontario, Canada
3. Dahlberg T., 2010, Railway track stiffness variations – consequences and countermeasures, *International Journal of Civil Engineering*, **8**, 1, 1-12
4. Esmaeili M., Zakeri J.A., Mosayebi S.A., 2014, Effect of sand-fouled ballast on train-induced vibration, *International Journal of Pavement Engineering*, **15**, 7, 635-644
5. Fryba L., 1999, *Vibrations of Solids and Structures under Moving Loads*, English co-edition published by Thomas Telford

6. Kerr A.D., 2003, *Fundamentals of Railway Track Engineering*, Simmons-Boardman Books, Inc.
7. Knothe K., 1995, Past and future of vehicle/track interaction, *Vehicle System Dynamics*, **24**, 3-6
8. Popp K., Kaiser I., Kruse H., 2003, System dynamics of railway vehicles and track, *Archive of Applied Mechanics*, **72**, 949-961
9. Puzavac L., Popovic Z., Lazarevic L., 2012, Influence of track stiffness on track behavior under vertical load, *Scientific Journal on Traffic and Transportation Research*, **24**, 5, 405-412
10. Witt S., 2008, *The Influence of Under Sleeper Pads on Railway Track Dynamics*, Department of Management and Engineering, Division of Solid Mechanics, Linköping University, Sweden
11. Zakeri J.A., 2000, Computer simulation for dynamics of railway track structures, PhD Thesis, School of Civil Engineering, Beijing Jiaotong University, Beijing
12. Zakeri J.A., Abbasi R., 2012, Field investigation of variation of rail support modulus in ballasted railway track, *Latin American Journal of Solids and Structures*, **9**, 6, 643-656
13. Zakeri J.A., Ghorbani V., 2011, Investigation on dynamic behavior of railway track in transition zone, *Journal of Mechanical Science and Technology*, **25**, 2, 287-292
14. Zakeri J.A., Xia H., 2008, Sensitivity analysis of track parameters in train-track interaction, *Journal of Mechanical Science and Technology*, **22**, 7, 1299-1304
15. Zhai W.M., Cai Z., 1997, Dynamic interaction between a lumped mass vehicle and a discretely supported continuous rail track, *Computers and Structures*, **63**, 5, 987-997
16. Zhai W.M., Sun X., 1994, A detailed model for investigating vertical interaction between railway vehicle and track, *Vehicle System Dynamics*, **23**, 1, 603-615
17. Zhai W.M., Wang K.Y., Lin J.H., 2004, Modelling and experiment of railway ballast vibrations, *Journal of Sound and Vibration*, **270**, 4/5, 673-683

Manuscript received January 25, 2015; accepted for print December 4, 2015

JOURNAL OF THEORETICAL AND APPLIED MECHANICS
54, 3, pp. 881-892, Warsaw 2016
DOI: 10.15632/jtam-pl.54.3.881

ANALYSIS OF PRESSURE BEHAVIOR IN A TEMPERATURE CONTROLLED MOLECULAR DYNAMIC FLOW

Hamed R. Najafi, S.M. Hossein Karimian

Department of Aerospace Engineering, Amirkabir University of Technology, Tehran, Iran

e-mail: hamedramezani@aut.ac.ir; hkarim@aut.ac.ir

Thermo-fluid properties are required for numerical modeling of nano/micro devices. These properties are mostly obtained from results of molecular dynamics (MD) simulations. Therefore, efforts have been put in developing methods for numerical evaluation of fluid properties, such as pressure. In this paper, the pressure behavior in a controllable nanochannel flow is investigated. The nanoflow field is created by imposing a gradient of a macroscopic property such as temperature. Details of the pressure calculation method in a molecular system and its sensitivity to the approximations made are described first. The effect of temperature rise in a uniform flow on the pressure field is studied next. Then, in the flow under a fixed mean velocity condition, the effect of temperature gradient as a controllable property on the pressure field of nanoflow is studied. Velocity, pressure and molecular density of nanoflows with various temperature gradients and different temperature levels are investigated as well. It has been found that the temperature level at which the temperature gradient is imposed, is important. A fixed temperature gradient will not always lead to the same pressure gradient at different temperature levels. Furthermore, quite interestingly, it is observed that at a fixed temperature gradient, with the variation of mean velocity the pressure field also varies.

Keywords: nanofluid, molecular dynamics, pressure, bin size, sampling, periodic flow

1. Introduction

Flow behavior at micro and nano scales has been a subject of interest in the recent years. The flow in a nanochannel, as a typical reduced-size fluid flow system, can demonstrate different aspects of nanofluid systems. This is why many studies can be found in literature focusing on the simulation of nanochannel flows (Mi and Chwang, 2003).

Molecular Dynamics (MD) is a deterministic method to calculate position of molecules and their dynamic properties. Different potential functions have been introduced to represent molecular forces in MD simulations (see for example Leach, 1999; Sadus, 2002). Extracting macroscopic properties such as velocity, temperature and pressure from microscopic data has been also a challenging issue for scientists (Allen and Tildesley, 1987; Karniadakis *et al.*, 2002; Karimian *et al.*, 2011). In earlier studies, the boundary of the domain was not of primary importance and simple. Periodic boundary conditions were used (Stillinger and Rahman, 1974; Travis and Evans, 1977; Koplik *et al.*, 1989; Travis and Gubbins, 2000; Nagayama and Cheng, 2004). Implementation of boundary conditions in MD simulation has been the center of attention in the recent years, especially in the field of mechanics (Sun and Ebner, 1992; Huang *et al.*, 2004, 2006; Hanasaki and Nakatani, 2006). In addition to the inlet/outlet boundary conditions, different approaches exist in the literature to implement wall boundary conditions in molecular dynamics. The most usual choice is to model walls by two rows of molecules. Wall molecules are allowed to oscillate about their initial positions at which they are fixed. This is done either by assigning heavy weights to the wall molecules (Koplik *et al.*, 1988), rescaling the velocity of wall molecules to their initial values (Huang *et al.*, 2004) or using fictitious springs (Fan *et al.*, 2002; Huang *et*

al., 2006; Sofos *et al.*, 2009; Branam and Micci, 2009; Kamali and Kharazmi, 2011). In addition to these, some studies can be found where the walls were modeled differently. For example, see the work of Ziarani and Mohamad (2005), where the walls were modeled as reflective. Since wall boundary conditions are not the subject of this paper, interested scientists are encouraged to read the above-mentioned references.

Boundary conditions at the inlet and outlet have been also a subject of research. With proper boundary conditions, the desired flow field can be created within a nanochannel. There are different methods in the literature to create controllable nanoflow. These methods are classified in four categories. Creating a flow with an external force or acceleration to move molecules in a specified direction is the most simple and straightforward method. Note that the extra energy added to the flow field due to external force must be taken out of the domain to hold the energy balance (Koplik *et al.*, 1988; Fan *et al.*, 2002; Ziarani and Mohamad, 2005; Sofos *et al.*, 2009; Kamali and Kharazmi, 2011).

Another method found in the literature makes use of motion of a piston or plate upstream of the inlet to create the flow. In this method, the solution domain is extended to provide extra space between the piston and the inlet. To control flow condition in the outlet as well, sometimes a piston and the required extra space is added to the end of the solution domain. In this case, there is no need to implement periodic boundary conditions or insert and delete molecules at the inlet or outlet of the solution domain. This approach works well for dense systems. Since additional molecules are to be taken into account in these added spaces, extra computational effort is required in these methods. The other disadvantage is that the solution is limited to the time in which the piston moves in the space between its initial position and the inlet/outlet (Huang *et al.*, 2004, 2006; Hanasaki and Nakatani, 2006).

The third method involves using a temperature gradient to create a nanoflow. In this approach, hot and/or cold walls are embedded within the domain along the flow direction (Han, 2008; Liu and Li, 2010; Darbandi *et al.*, 2011). The role of the temperature gradient is to change the kinetic energy of the fluid. At high temperatures, the kinetic energy and therefore the pressure of the fluid increase. This pressure gradient causes the fluid to move downstream. The energy balance can be established between hot and cold plates to prevent accumulation of extra energy in the domain. It should be noted that in practice, hot or cold temperature walls cannot be easily mounted within the flow and, therefore, implementation of this approach is not straightforward.

The fourth method creates a flow by wall motion. In this approach, walls of a channel move in opposite or parallel directions with a constant velocity to create the flow (Zhang *et al.*, 2009; Kim *et al.*, 2010).

While all of the above-mentioned methods achieve the goal of creating a molecular flow in nanochannels, they fail to offer a proper approach to produce the predefined flow. The goal of the present research is to investigate pressure behavior in a controllable nanochannel flow created by a gradient of a macroscopic property such as temperature. In the following sections, we first introduce the calculation method used here to evaluate pressure in a nanoflow. Then we will discuss details about the nanoflows controlled by the temperature gradient, especially the behavior of pressure.

2. Molecular dynamics

In molecular dynamics, positions of molecules are determined using Newton's second law. Intermolecular fluid-fluid forces are calculated using the Lennard-Jones 12-6 potential equation (Rapaport, 2004)

$$U_{ij} = 4\varepsilon\Big[\Big(\frac{\sigma}{r_{ij}}\Big)^{12} - \Big(\frac{\sigma}{r_{ij}}\Big)^{6}\Big] \tag{2.1}$$

In this equation, U_{ij} is the Lennard-Jones potential, r_{ij} is the distance between two interacting molecules i and j, ε is the energy scale, and σ is the finite distance at which the intermolecular potential is zero. The derivative of the L-J potential with respect to r_{ij} represents the intermolecular force

$$f_{ij} = -\frac{dU_{ij}}{dr_{ij}} \qquad f_{ij} = \frac{48\varepsilon}{r_{ij}^2}\Big[\Big(\frac{\sigma}{r_{ij}}\Big)^{12} - \frac{1}{2}\Big(\frac{\sigma}{r_{ij}}\Big)^{6}\Big]r_{ij} \tag{2.2}$$

In the above equation, f_{ij} is the force of molecule j acting on molecule i. It is common to enforce this equation within a cut-off distance to reduce the computational cost. We chose a cut-off distance of $r_c = 2.5\sigma$ herein, which is usually used in other references to simulate the argon flow (Koplik *et al.*, 1989; Priezjev, 2007; Sofos *et al.*, 2009).

3. Pressure formula

In a macroscopic analysis, pressure is calculated solely based on the virial equation of state. In a microscopic system however, pressure is calculated from the virial equation of state on all atoms plus summation of intermolecular forces multiplied by corresponding distances between them. For pair-additive force fields, the fluid pressure P can be estimated through the virial equation of state given below (Allen and Tildesly, 1987)

$$P = \frac{Nk_BT}{V} + \frac{1}{3V}\sum_{i=1}^{N}\sum_{j>i}^{N} r_{ij}f_{ij} \tag{3.1}$$

where N is the number of molecules in the computational domain, k_B is Boltzmann's constant, and V and T are volume and temperature of the computational domain, respectively. The first term in Eq. (3.1) is called the kinetic term and contains temperature of the computational domain. In a microscopic view, temperature is defined as

$$T = \frac{m}{3Nk_B}\sum_{n=1}^{N}\sum_{i=1}^{3}(V_{n_i} - \overline{V}_i)^2 \tag{3.2}$$

where n denotes the molecule number in the domain, $i = 1, 2, 3$ denote the x, y, and z components of the atomic velocity $\mathbf{V}_n$, $\overline{V}_i$ is the i-th component of the mean flow velocity $\mathbf{V}$, and m is the atom mass. The mean velocity can be obtained from any of the several averaging methods like SAM (Tysanner and Garcia, 2004), CAM (Tysanner and Garcia, 2005) or SMC (Karimian *et al.*, 2011) that reduces statistical errors in its calculation. In this paper, the SMC method is used to calculate the mean velocity. As can be observed in Eq. (3.2), temperature is related to the kinetic energy of molecules in the microscopic view, which is always positive. The velocity difference within parentheses that represents instantaneous velocity due to thermal fluctuations is called the virial velocity.

The second term in Eq. (3.1) includes the effect of forces between the molecules; this term is called the potential term. The kinetic term is always positive but the potential term may be positive or negative. A zero force exists between two molecules at a distance of $2^{1/6}$ based on the L-J potential model. If the distance between two molecules is higher than this value, the sign of the pair-additive force will be negative and the molecules attract each other. On the other hand, when the distance between two molecules is less than this value, the force is of repellant nature.

The pressure calculation method defined by Eqs. (3.1) and (3.2) is implemented in an in-house, MD code to determine pressure values from the results of MD simulations. Please note that this code is used in authors' previous works in which its accuracy in calculation of macroscopic properties were demonstrated (Karimian *et al.*, 2011; Karimian and Namvar, 2012; Namvar and Karimian, 2012; Karimian and Izadi, 2013).

4. Pressure calculation

The purpose of this Section is to validate the pressure calculation. According to Eq. (3.1), pressure has two parts, kinetic and potential terms. Our experience shows that precautions should be taken in calculation of pressure in MD simulation. This is demonstrated by considering a cubic region with its molecules in equilibrium, which is a constant Number, Volume and Energy (NVE) simulation. We know that pressure would be the same all over this region. The size of this cube is $L = 45\,\text{Å}$ and it contains $N = 1728$ mono atomic noble gas molecules of Argon. Atomic diameter of Argon is $\sigma = 3.4\,\text{Å}$ and its energy parameter is $\varepsilon = 1.67 \cdot 10^{-21}$ J. A periodic boundary condition is applied in all directions. Argon molecules are initially arranged in a lattice form of Face-Centered Cube (FCC). MD simulation of Argon molecules starts from the initial temperature of 120 K, and the mean velocity of zero. The equation of motion is integrated over time with $\Delta t = 10^{-15}$ s, using Verlet's scheme (Verlet, 1967). The number of molecules is constant during the simulation. Macroscopic properties at any point of the molecular domain is extracted via sampling and averaging of molecular properties within the control region around that point, called a bin (Kamiadakis *et al.*, 2002). Four bins with different sizes are selected for sampling and averaging of flow properties. As shown in Fig. 1, the largest bin covers the whole cube and contains all argon molecules. Other bins are smaller cubes with lateral sizes of 3/4, 1/2 and 1/4 of the lateral size of the whole domain. In volumetric fraction, these cubes are 27/64, 1/8, and 1/64 of the whole domain, respectively. Note that the periodic boundary condition is applied on the cube boundaries. Therefore, similar to other three bins, bin 1/1 is also simulated as if it is in the middle of the domain. Obviously, pressure obtained from all bin sizes should be equal. The molecular dynamics simulation is continued for 30000 time steps of 10^{-15} s, when equilibrium is reached. Although pressure as a macroscopic property should be independent of the bin size, the results show that different pressure values are obtained. The origin of this difference is in the potential part of the pressure equation.

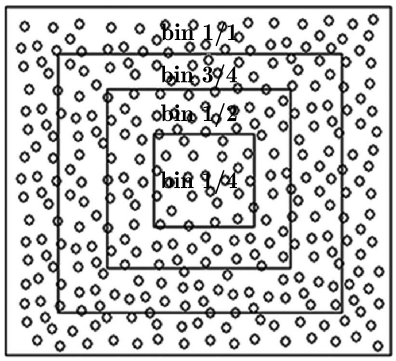

Fig. 1. Bin sizes for pressure calculation in a periodic stationary molecular flow

The kinetic part of pressure, which is solely based on the properties of atoms and is independent of molecular interactions, converges to the value of 27 MPa in all bins with different sizes. The potential part of pressure, however, converges to different values of −22.3, −18.4, −1.2, and 5.9 MPa in bins with sizes of 1/1, 3/4, 1/2, and 1/4, respectively. This part of pressure is calculated from summation of all pair-additive forces between molecules multiplied by the distance between them. In this approach, no cut-off distance is considered for the molecules. More numerical tests have shown that inclusion of the cut-off distance cannot resolve this problem of pressure calculation, unless the influence of the molecules outside the calculation bin within the cut-off distance from its boundaries is taken into account. Having implemented this, calculated pressures in all of the bins converge to the value of 31.4 MPa at the equilibrium state with minor pressure oscillations and differences in bins with sizes of 1/4 and 1/2 due to the bin size. Note

that the number of molecules within a bin plays an important role in calculation of pressure. More details about the effect of bin size on sampling and averaging can be found in (Karimian and Izadi, 2013). Calculation of pressure in bin 1/1 with LAMMPS (Plimpton, 1995) converged to the same value with less than a 3 percent difference, which verifies the present method for calculation of pressure in MD simulation.

5. Control of pressure by temperature

As noted, macroscopic properties can be extracted from microscopic properties of molecules, calculated by MD simulation. In contrast to this, here we would like to set a macroscopic property in the solution domain. For this purpose, consider a periodic flow in a nanochanel with length of $L = 144.6\,\text{Å}$ and cross-section of $36.15\,\text{Å}\times 36.15\,\text{Å}$. This flow contains $N = 940$ mono-atomic noble gas molecules of Argon. Periodic boundary conditions are applied on the boundaries of the domain. Argon molecules are initially arranged in a FCC lattice form, and solution starts from the initial temperature and velocity of 120 K and 5 m/s, respectively. As shown in Fig. 2, the solution domain is divided into 8 equal bins. We are going to set a desired pressure within the domain and study its effects on the solution; but before that, the solution is proceeded for 400000 time steps of $\Delta t = 10^{-15}\,\text{s}$ to reach equilibrium. During the solution, temperature of 120 K and mean velocity of 5 m/s are continuously enforced in the first bin. At each time step, the mean velocity in this bin is updated by adding the difference between desired and calculated mean velocities to the velocity of each molecule inside the bin. In a similar fashion, at each time step, temperature in the bin is updated by rescaling the virial velocity of molecules. As expected, temperature and flow velocity within the whole solution domain reach 120 K and 5 m/s respectively, at the equilibrium. The averaging method of SMC (Karimian *et al.*, 2011) is applied to calculate pressure using Eq. (3.1) at each time step. Solution convergence for velocity and pressure in all 8 bins is shown in Fig. 3.

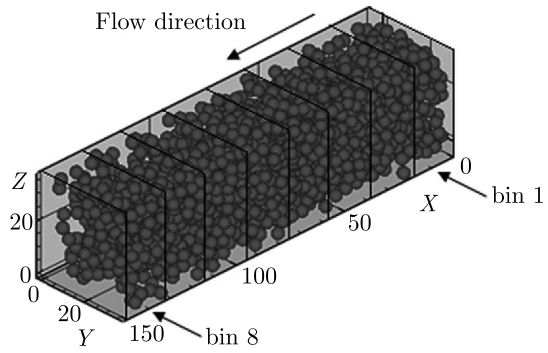

Fig. 2. Periodic flow including 940 molecules with 8 bins along the x direction

As expected, the mean velocity has converged to a value of 5 m/s in all of the bins. The convergence of the mean velocity values is faster than that for the pressure. We believe that this is because the mean velocity is weakly dependent on interactions between molecules. In Fig. 3b, pressure has converged to a value of 2.9 MPa.

Now we would like to set a new value for pressure in the solution domain. For a fixed number of molecules, pressure can be set to a new value by changing temperature of molecules. As noted above, temperature can be set by rescaling the virial velocity of molecules. To examine this, temperature is raised up from 120 K to 150 K in the first bin of this periodic flow at time $4 \cdot 10^{-10}\,\text{s}$; i.e. in the time step of 400001. Then solution is continued for an extra 400000 time steps. The enforced mean velocity is still 5 m/s in the first bin. Analysis of the solution shows that pressure increases in the first bin and consequently propagates to the rest of the periodic

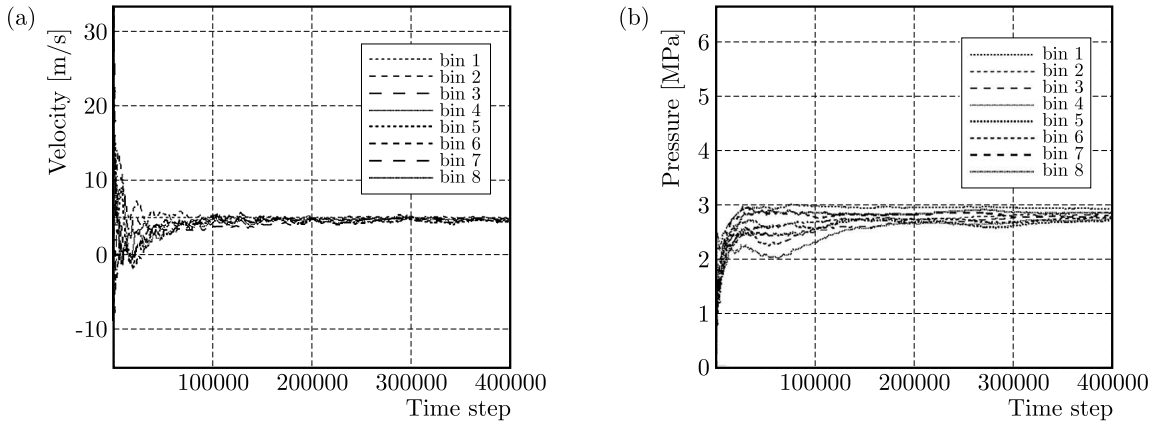

Fig. 3. Solution convergence in bins for: (a) velocity in a periodic flow with enforced velocity of 5 m/s in bin 1, and (b) pressure in a periodic flow with enforced temperature of 120 K in bin 1

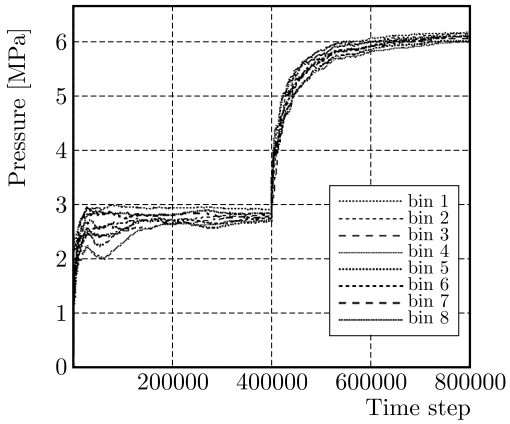

Fig. 4. Convergence of pressure in different bins of the periodic flow with the mean flow velocity of 5 m/s. A raise in temperature from 120 K to 150 K is enforced in the first bin at the time step 400001

flow until the equilibrium is reached. The convergence of pressure in all of the bins is shown in Fig. 4. At the equilibrium, pressure reaches 6.1 MPa all over the solution domain. Again, the mean flow velocity also reaches the value of 5 m/s.

In the next step, we would like to see how effectively the temperature gradient along a periodic flow can alter pressure, or how quick would be the response of pressure to the temperature gradient along the flow. In the first 400000 time steps, the flow field reaches its equilibrium for the enforced temperature and mean flow velocity of 120 K and 5 m/s, respectively, in the first bin. Then, at the time step 400001, a temperature difference of 30 K is applied between bins 3 and 7, by setting temperature values to 180 K and 150 K, respectively.

During the first 400000 time steps, SMC averaging uses all solution data from the first time step. However, after the implementation of temperature change at the time step 400001, we cannot include much data from the previous time steps in SMC averaging. If we start SMC averaging promptly from the time step 400001, undesirable pressure fluctuations will appear in the results. In this case, noticeable extra time steps would be required to resolve this inconsistency in SMC averaging. Our experience shows that very good results can be obtained if only a small portion of data before the time step at which the temperature change is applied (i.e. 400001), is involved in SMC averaging. Here, pressure data of 30 time steps are enough. This means that SMC averaging uses the data from the time step 399971 and after that. Convergence rates of pressure in all of the bins are shown in Fig. 5. As can be seen, pressure increases from 2.9 MPa at temperature of 120 K to 7.90 MPa and 7.15 MPa at temperatures of 180 K and 150 K in bins 3

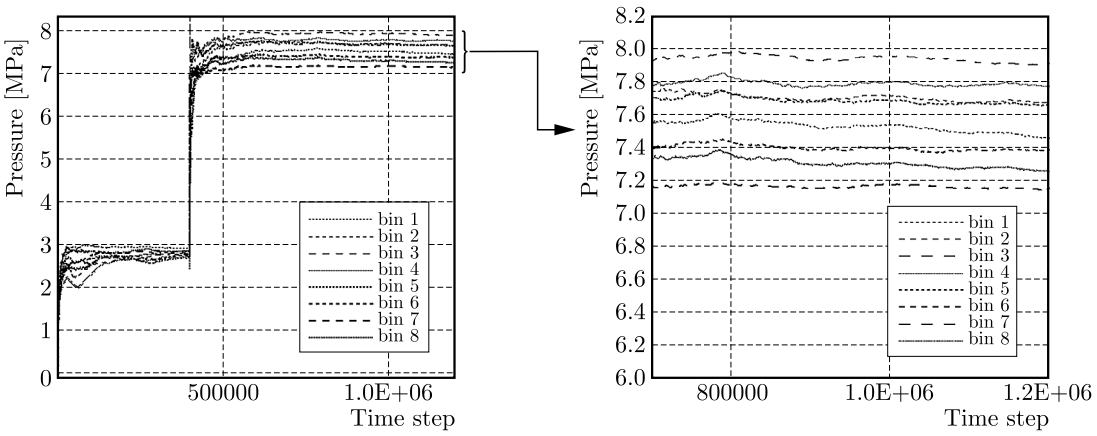

Fig. 5. Convergence of pressure in different bins of the periodic flow with the mean flow velocity of 5 m/s. A temperature gradient of 30 K is enforced between bin 3 with 180 K and bin 7 with 150 K at the time step 400001

and 7, respectively. It can also be seen that pressures in other bins are between these two values. In the next Section, results of this case including pressure, density, and velocity gradients in the periodic flow will be discussed in details. At this point, we conclude that pressure can be effectively set to a desired value at anytime or anywhere in the solution domain by setting the temperature of molecules. This finding can be very useful in applying flow boundary conditions in the inlet or the outlet of the solution domain.

6. Creating a periodic flow with a temperature gradient

In this Section, we would like to analyze a flow field and gradients of its variables in a periodic flow that is created by a temperature gradient. Consider the flow field from the previous Section that has been created by a temperature gradient enforced between bins 3 and 7. The mean velocity was set to 5 m/s in the third bin, and temperature values of 180 K and 150 K were set in bins 3 and 7, respectively. Having assumed periodic boundary conditions at the inlet and outlet, bins 3 and 7 fall exactly in the middle of the flow field. It means that the distance from bin 3 to bin 7 is equal to the distance from bin 7 to bin 3 in the periodic domain. From the time step 400001, 800000 time steps of 10^{-15} s are taken to arrive at the equilibrium in the flow field. The implemented temperature gradient of 30 K has resulted in pressure, mean flow velocity, and molecular density variations shown in Fig. 6. In Fig. 6a, the mean flow velocity decreases from 5 m/s in bin 3 to 3.3 m/s in bin 7. Furthermore, pressure has reached its maximum value of 7.9 MPa in bin 3 and its minimum value of 7.15 MPa in bin 7 (Fig. 6b).

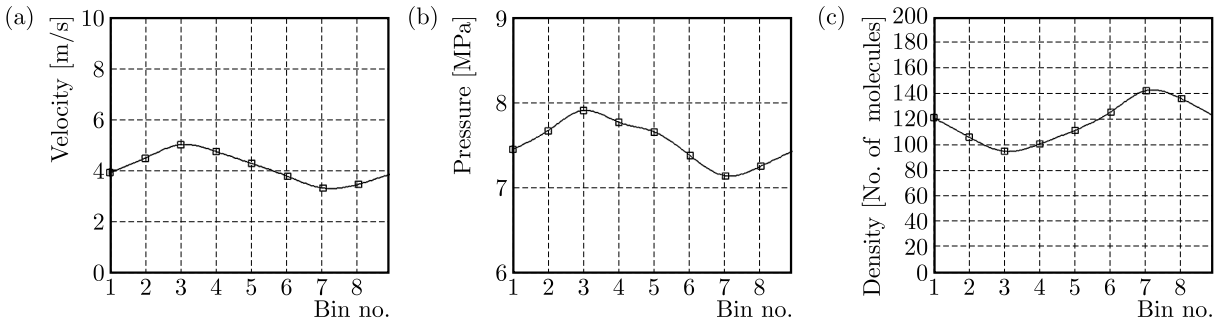

Fig. 6. Variations of flow variables along the periodic flow generated by temperature gradient of 30 K, (a) velocity, (b) pressure and (c) molecular density

As shown in Fig. 6c, the lowest value of molecular density occurs in bin 3 where temperature value is set to 180 K. This is the highest temperature in the channel. The molecules move with a high virial velocity in this bin and, therefore, they push each other to the outside of the bin. This is why the lowest molecular density occurs here. According to Eq. (3.1), while pressure increases with temperature only through the first term and the effect of molecular density appears in both terms, temperature has the dominant role in determining the pressure value and its variation. Therefore, as seen in Fig. 6b, the highest pressure occurrs at the bin with the highest temperature.

In the next step, we would like to investigate the effect of the temperature gradient on the flow field at different temperature levels. We believe that the temperature level at which the temperature gradient is applied, is important. Variations of velocity, pressure and molecular density for a temperature gradient of 30 K between bins 3 and 7, and at different fluid temperature values are shown in Fig. 7. The results are obtained for fixed temperatures of 150 K, 180 K, 210 K, 240 K, and 270 K at bin 3. The mean flow velocity of 5 m/s is still forced at bin 3.

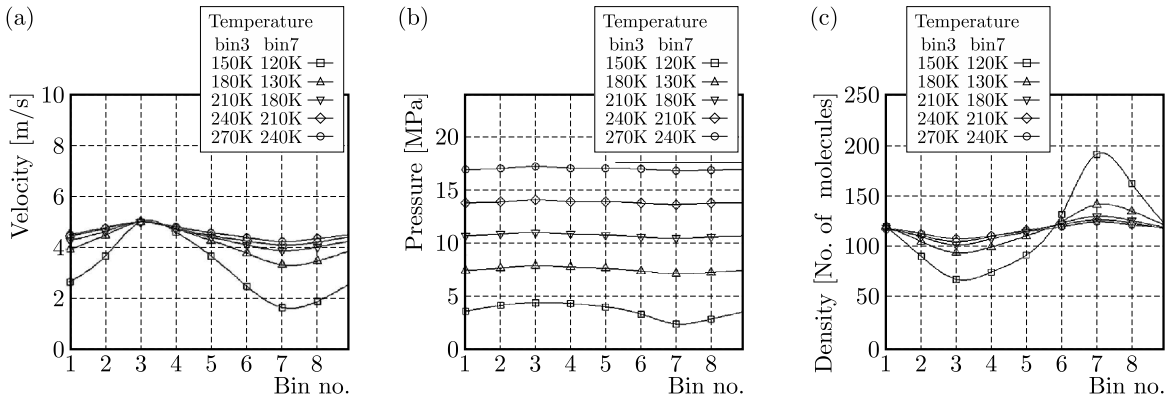

Fig. 7. Variations of flow variables along the channel generated by a temperature gradient of 30 K at different fluid temperatures, (a) mean flow velocity, (b) pressure and (c) molecular density

In comparison to the level of fluid temperature, the results show that a 30 K temperature gradient becomes less effective at higher fluid temperature levels. In other words, the 30 K temperature gradient at the fluid temperature of 150 K has a higher effect on the flow characters than it does at a fluid temperature of 270 K, for instance. Therefore, it can be seen in Fig. 7 that as the temperature level increases, the mean flow velocity profile and molecular density profile become smoother. In a similar fashion, the pressure profile becomes almost flat at higher temperature values. Furthermore, in Figs. 7a and 7c, the profiles converge to a single avergage value. This is not the case with the average pressure value which continuously increases with temperature throughout the channel.

From Eq. (3.1), one can conclude that the mean flow velocity will not affect the pressure values since it has no direct contribution in the equation. To study this, the values of temperature in bins 3 and 7 are set to 150 K and 300 K, respectively enforcing a high temperature gradient of 150 K in the domain. The molecular flow is solved for this temperature gradient at different mean flow velocities of 5, 10, 15, 20, 25, 30, 35, 40, and 45 meters per second in bin 3. The profiles of velocity, pressure and molecular density as well as temperature in these experiments are shown in Figs. 8a-8d. In addition, the average temperature value of the molecules in the whole domain has been calculated and plotted in Fig. 8e.

It can be seen in Fig. 8b that pressure decreases uniformly with an increase in the mean flow velocity. This is in contrast with the above-mentioned statement. To further understand the reason behind this behavior, let us analyze the results shown in Fig. 8. From Figs. 8c and 8d, we observe that molecular density is at its maximum in the lower temperature zone of the domain.

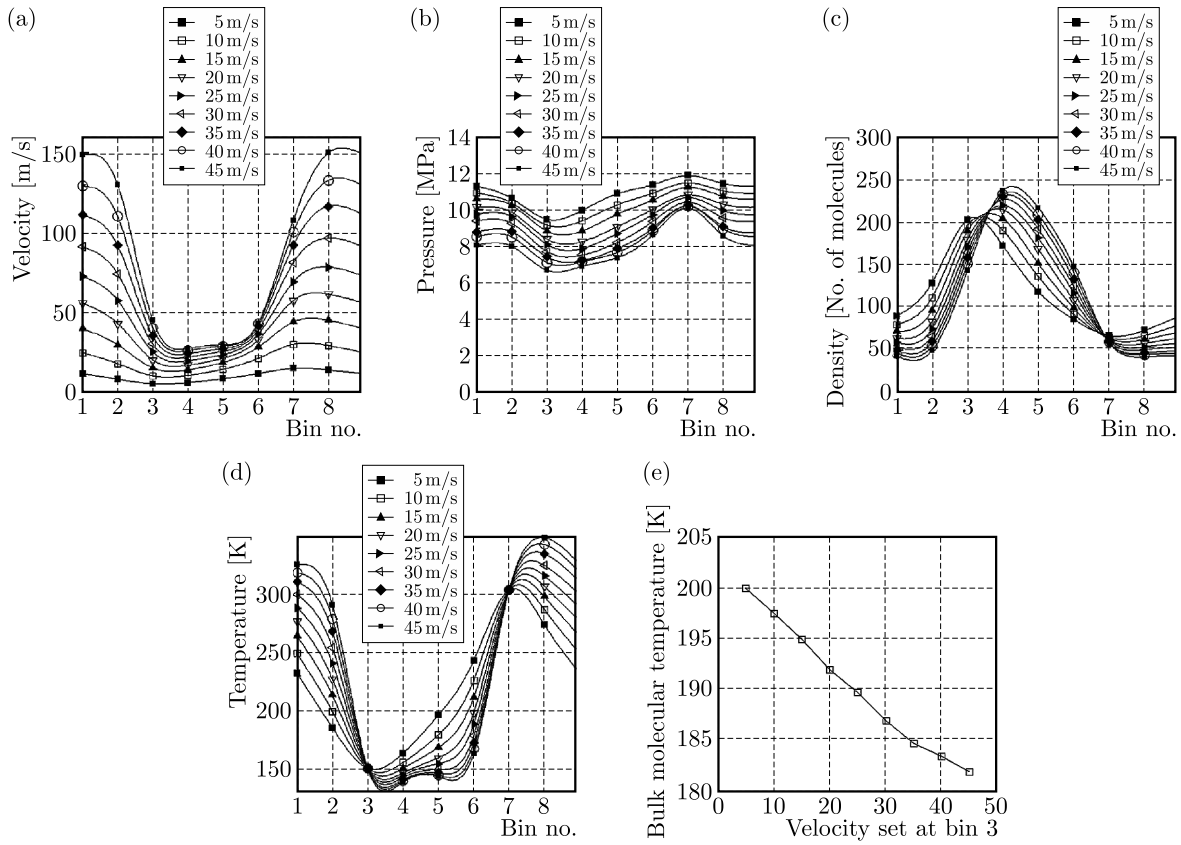

Fig. 8. Variations of flow variables along the channel generated by a temperature gradient of 150 K at different mean flow velocities. Variations of (a) velocity, (b) pressure and (c) molecular density, (d) temperature, (e) average temperature of molecules in the whole channel

This trend is more pronounced when the mean flow velocity increases. This means that the number of molecules with lower temperature values increases in the solution domain with the mean flow velocity. As a result, the bulk molecular temperature of the domain decreases with the mean flow velocity (Fig. 8e). Since temperature has the dominant influence on pressure, it can be justified that the reduction of pressure in the domain is a direct result of the reduction in the bulk molecular temperature.

The effect of the temperature gradient on the flow field is also studied here. Different temperature gradient values are examined by setting temperature of bin 7 at 175 K, 200 K, 225 K, 250 K, 275 K, 300 K, 325 K, and 350 K. A mean flow velocity of 5 m/s and temperature of 150 K are set at bin 3. Variations of velocity, pressure and molecular density for different temperature gradients between bins 3 and 7 are shown in Fig. 9.

At higher temperature values, the virial velocity of molecules increases and, therefore, molecules repel each other. As a result, the molecular density decreases. In addition, the mean flow velocity of molecules increases since at low molecular density values, fewer obstacles exist on their ways. Based on this argument, the behavior of velocity and density profiles in Figs. 9a and 9c can be easily justified.

As seen in Fig. 9b, pressure in the whole domain rises with the temperature gradient. An increase in the temperature gradient increases the average temperature of the flow field globally and, therefore, pressure rises in the whole channel. The behavior of pressure profiles can be explained locally as well. In bin 3 for instance, pressure rises due to an increase in molecular density although temperature is constant. In bin 7, however, pressure rises due to an increase in temperature although molecular density reduces. Once again, note that temperature has the

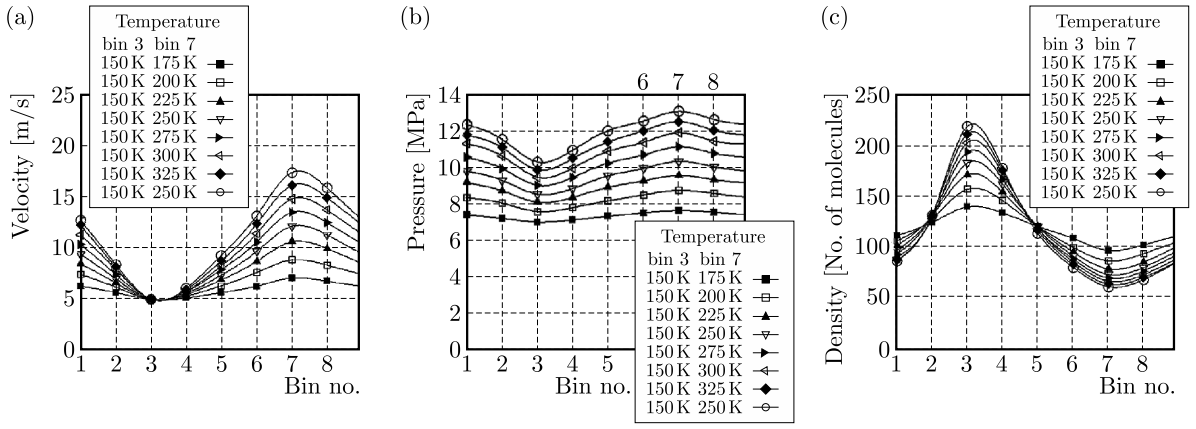

Fig. 9. Variations of flow variables along the channel generated by different temperature gradients at a mean flow velocity of 5 m/s in bin 3. Variations of (a) velocity, (b) pressure and (c) molecular density

primary role in variation of the pressure value and its behavior. Therefore, pressure increases from bin 3 to bin 7.

The last test case has been repeated with a fixed temperature of 180 K (instead of 150 K) to investigate the flow behavior at a different temperature level. The results are not reported here to limit the length of the present paper; but similar behavior has been observed. At the end, it is worth to mention that while more accurate methods for pressure calculation in inhomogeneous fluids can be found in the literature (Todd *et al.*, 1995), we believe that employment of such methods will not lead to different conclusions than those made herein.

7. Conclusion

Details of pressure calculation in a molecular system and its sensitivity to approximations have been studied herein. It has been shown that for molecules near boundaries, inclusion of all molecules within their cut-off region including those outside of the domain boundary is crucial for correct calculation of pressure.

In this paper, a method has been introduced to create a flow by controlling macroscopic properties in two different regions. Temperature values have been imposed at two selected regions along the flow, and the mean flow velocity has been imposed at one of these regions. Having applied these conditions to the periodic flow and conducting parametric study on it, the following results have been obtained.

- Temperature and its gradient have the most dominant role on the variation of the pressure value and its gradient in the periodic flow.
- In the periodic flow, the pressure gradient established as a result of a constant temperature gradient is not always the same at different temperature levels. In fact, both the temperature gradient and the temperature at which this gradient is applied, determine the pressure gradient in the flow.
- Since the mean velocity does not appear in the pressure formula, it is expected that variations of the mean velocity would not change pressure in the periodic flow. However, the results show that for a constant temperature gradient, pressure changes inversely with the mean flow velocity. Based on our analysis, this is because the mean flow velocity directly changes the average temperature of the flow within the channel.

References

1. Allen M.P., Tildesley D.J., 1987, *Computer Simulation of Liquids Oxford*, New York
2. Branam R.D., Micci M.M., 2009, Comparison of wall models for the molecular dynamics simulation of microflows, *Nanoscale and Microscale Thermophysical Engineering*, **13**, 1-12
3. Darbandi M., Abbassi H.R., Khaledi Alidusti R., Sabouri M., 2011, Molecular dynamics simulation of nano channel as nanopumps, *ICNMM*, Edmonton, Alberta, Canada
4. Fan X.J., Phan-Thien N., Teng Yong N., Diao X., 2002, Molecular dynamics simulation of a liquid in a complex nano channel flow, *Physics of Fluids*, **14**, 3, 1146-1153
5. Han M., 2008, Thermally-driven nanoscale pump by molecular dynamics simulation, *Journal Title: Journal of Mechanical Science and Technology*, **22**, 157-165
6. Hanasaki I., Nakatani A., 2006, Fluidized piston model for molecular dynamics simulations of hydrodynamics flow, *Modelling and Simulation in Materials Science and Engineering*, **14**, S9-S20
7. Huang C., Choi P.Y.K., Nandakumar K., Kostiuk L.W., 2006, Molecular dynamics simulation of a pressure-driven liquid transport process in a cylindrical nanopore using two self-adjusting plates, *Journal of Chemical Physics*, **124**, 234701
8. Huang C., Nandakumar K., Kwok D.Y., 2004, Non-equilibrium injection flow in a nanometer capillary channel, *ICMENS'04*, 374-378
9. Kamali R., Kharazmi A., 2011, Molecular dynamics simulation of surface roughness effects on nanoscale flows, *International Journal of Thermal Sciences*, **50**, 3, 226-232
10. Karniadakis G.E., Beskok A., Aluru N., 2002, *Micro Flows and Nanoflows*, Springer, New York, 641-648
11. Karimian S.M.H., Izadi S., 2013, Bin size determination for the measurement of mean flow velocity in molecular dynamics simulation, *International Journal For Numerical Methods In Fluids*, **71**, 7, 930-938
12. Karimian S.M.H., Izadi S., Barati Farimani A., 2011, A study on the measurement of mean velocity and its convergence in molecular dynamics simulations, *International Journal for Numerical Methods in Fluids*, **67**, 12, 2130-2140
13. Karimian S.M.H., Namvar S., 2012, Implementation of SMC averaging method in a channeled molecular flow of liquids and gases, *Journal of Physics: Conference Series*, **362**, 1, 2029
14. Kim B.H., Beskok A., Cagin T., 2010, Viscous heating in nanoscale shear driven liquid flows, *Microfluid Nanofluid*, **9**, 31-40
15. Koplik J., Banavar J., Willemsen J., 1988, Molecular dynamics of poiseuille flow and moving contact lines, *Physical Review Letters*, **60**, 1282-1285
16. Koplik J., Banavar J. R., Willemsen J.F., 1989, Molecular dynamics of fluid flow at solid surfaces, *Physics of Fluids A*, **1**, 781-794
17. Leach A.R., 1999, *Molecular Modeling: Principles and Applications*, Longman
18. Liu C., Li Z., 2010, Molecular dynamics simulation of composite nanochannels as nanopumps driven by symmetric temperature gradients, *Physical Review Letters*, **105**, 174501
19. Mi X.B., Chwang A. T., 2003, Molecular dynamics simulations of nanochannel flows at low Reynolds numbers, *Molecules*, **8**, 193-206
20. Nagayama G., Cheng P., 2004, Effects of interface wettability on microscale flow by molecular dynamics simulation, *International Journal of Heat and Mass Transfer*, **47**, 501-513
21. Namvar S., Karimian S.M.H., 2012, Detailed investigation on the effect of wall spring stiffness on velocity profile in molecular dynamics simulation, *Journal of Physics: Conference Series*, **362**, 1, 2039

22. Plimpton S.J., 1995, Fast parallel algorithms for short-range molecular dynamics, *Journal of Computational Physics*, **117**, 1

23. Priezjev N.V., 2007, Effect of surface roughness on rate-dependent slip in simple fluids, *Journal of Chemical Physics*, **127**, 144708

24. Rapaport D.C., 2004, *The Art of Molecular Dynamics Simulation*, Cambridge University Press

25. Sadus R.J., 2002, *Molecular Simulation of Fluids: Theory, Algorithms and Object-Orientation*, Elsevier

26. Sofos F., Karakasidas T.E., Liakopoulos A., 2009, Non-equilibrium molecular dynamics investigation of parameters affecting planar nanochannel flows, *Contemporary Engineering Sciences*, **2**, 6, 283-298

27. Stillinger F.H., Rahman A., 1974, Improved simulation of liquid water by molecular dynamics, *Journal of Chemical Physics*, **60**, 1545-1557

28. Sun M., Ebner C., 1992, Molecular-Dynamics simulation of compressible fluid flow in two--dimensional channels, *Physical Review A*, **46**, 4813

29. Todd B.D., Evans D.J., Davis P.J., 1995, Pressure tensor for inhomogeneous fluids, *Physical Review E*, **52**, 1627

30. Travis K.P., Evans D.J., 1997, Molecular spin in a fluid undergoing Poiseuille flow, *Physical Review E*, **55**, 1566-1572

31. Travis K.P., Gubbins K.E., 2000, Poiseuille flow of Lennard-Jones fluids in narrow slit pores, *Journal of Chemical Physics*, **112**, 1984-1994

32. Tysanner M.W., Garcia A.L., 2004, Measurement bias of fluid velocity in molecular simulations, *Journal of Computational Physics*, **196**, 173-183

33. Tysanner M.W., Garcia A.L., 2005, Non-equilibrium behavior of equilibrium reservoirs in molecular simulations, *International Journal of Numerical Methods in Fluids*, **2050**, 1-12

34. Verlet L., 1967, Computer "experiments" on classical fluids. I. Thermodynamical properties of Lennard-Jones molecules, *Physical Review*, **159**, 98

35. Zhang Z.Q., Zhang H.W., Ye H.F., 2009, Pressure-driven flow in parallel-plate nanochannels, *Applied Physics Letters*, **95**, 154101

36. Ziarani A.S., Mohamad A.A., 2005, A Molecular dynamics study of perturbed Poiseuille flow in a nanochannel, *Microfluid Nanofluid*, **2**, 12-20

Manuscript received February 12, 2015; accepted for print December 10, 2015

JOURNAL OF THEORETICAL AND APPLIED MECHANICS
54, 3, pp. 893-907, Warsaw 2016
DOI: 10.15632/jtam-pl.54.3.893

EVALUATION OF THE JET DAMPING EFFECT ON FLIGHT DYNAMICS OF A HOMING GUIDED MISSILE

Grzegorz Kowaleczko
Air Force Institute of Technology, Warsaw, Poland
e-mail: g.kowaleczko@chello.pl

The paper presents evaluation of the jet damping effect on spatial motion of a homing guided missile with variable mass. The mathematical model of motion including effects generated by the burning fuel are presented – changes of mass characteristics as well as the jet damping effect are taken into account. Both the influences of inertia forces/moments and changes of the position of mass center are calculated. The damping effect generating additional forces and moments acting on the missile is also determined. The obtained set of equations of motion allows one to analyze a wide spectrum of various problems, e.g. the influence of jet damping on the homing guided missile trajectory or the dynamic response of the missile to atmospheric disturbances. Exemplary results of simulations are shown.

Keywords: missile dynamics, variable mass system, jet damping effect, numerical simulations

1. Introduction

During the phase of engine working, a missile should be treated as a variable mass system (Davis *et al.*, 1958; Dimitrevskii, 1972; Quarelli *et al.*, 2014; Thomson, 1965a,b, 1986). The combustion process causes a change in the mass center – all mass characteristics of the missile change. Simultaneously produced gases reach high speed inside the engine. In the case of pitching or yawing motion of the missile, these moving gases are a source of the "jet damping" effect. This effect influences rotational motion of the missile. Usually, this effect is ignored because the burning phase is short and the blast-off parameters are stable. In particular, it concerns the angular velocities which are equal to zero. But in the case of a homing guided missile with a long burning process, it may be possible to observe its maneuvers when the engine still works and angular velocities are different from zero. It means that the jet damping effect occurs. It should be assessed whether it is important for the dynamics of missile flight and for precision of target hitting.

To calculate the jet damping effect one has to know the velocity distribution of combustion gases inside the engine. Because the engine consists of two parts – a combustion chamber and an exhaust nozzle, we have to determine these distributions inside both engine components. In the case of the combustion chamber, the combustion law and the geometry of the fuel rod have to be taken into account, and usually an analytical formula describing velocity can be determined. For the exhaust nozzle, thermodynamic laws for supersonic de Laval nozzle are included into consideration. In this case, the velocity profile can be determined numerically – an analytical formula is not possible because of various descriptions of nozzle geometry.

2. Geometry and kinematics of missile motion

2.1. Geometry of the missile

The following right-handed rectangular coordinate systems are applied in order to determine the set of equations of motion:

1. $O_I x_I y_I z_I$ inertial coordinate system with the origin at any point in space;
2. $O_Z x_I y_I z_I$ – coordinate system with the origin at the center of the Earth parallel to $O_I x_I y_I z_I$;
3. $O_g x_g y_g z_g$ – moving coordinate system with the origin O_g at the Earth surface;
4. $O x_g y_g z_g$ – moving coordinate system parallel to $O_g x_g y_g z_g$ with the origin O at any fixed point of the missile;
5. $Oxyz$ – moving coordinate system with the origin at any fixed point of the missile.

2.2. Transformations of coordinate systems

If one has components of any vector in any coordinate system, its components in another system can be calculated using a transformation matrix. This matrix is determined using elementary angles of rotation. These angles define the relative position of two coordinate systems.

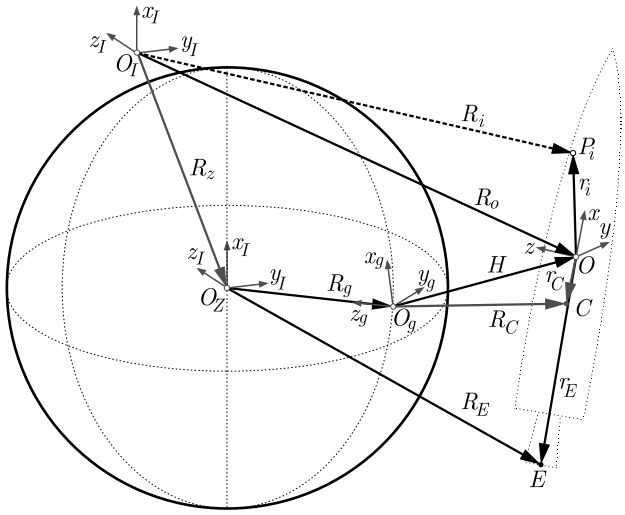

Fig. 1. Coordinate systems $O_I x_I y_I z_I$, $Oxyz$ and basic vectors

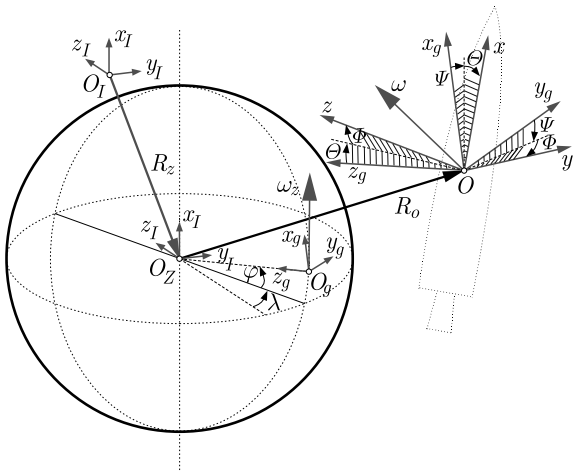

Fig. 2. Transformations of the coordinate systems

For the transformation from $O_Z x_I y_I z_I$ to $O_g x_g y_g z_g$, the following angles (see Fig. 2) are used: λ – azymuth, φ – declination. For the systems $O_g x_g y_g z_g$ and $Oxyz$, the following angles are used: Ψ – yaw, Θ – pitch, Φ – roll. The transformation matrices have the form, respectively

$$\mathbf{L}_{g/I} = \begin{bmatrix} \cos\phi & -\sin\phi\sin\lambda & \sin\phi\cos\lambda \\ 0 & \cos\lambda & \sin\lambda \\ -\sin\phi & -\cos\phi\sin\lambda & \cos\phi\cos\lambda \end{bmatrix}$$
$$\mathbf{L}_{m/g} = \begin{bmatrix} \cos\Psi\cos\Theta & \sin\Psi\cos\Theta & -\sin\Theta \\ \cos\Psi\sin\Theta\sin\Phi - \sin\Psi\cos\Phi & \sin\Psi\sin\Theta\sin\Phi + \cos\Psi\cos\Phi & \cos\Theta\sin\Phi \\ \cos\Psi\sin\Theta\cos\Phi + \sin\Psi\sin\Phi & \sin\Psi\sin\Theta\cos\Phi - \cos\Psi\sin\Phi & \cos\Theta\cos\Phi \end{bmatrix} \tag{2.1}$$

2.3. Velocities

2.3.1. Angular velocities

We define the following angular velocities: ω_z – angular velocity of $O_g x_g y_g z_g$ relative to $O_g x_I y_I z_I$. This velocity in $O_g x_I y_I z_I$ has the following components: $\boldsymbol{\omega}_z = [\omega_z, 0, 0]^{\mathrm{T}}$; $\boldsymbol{\omega}$ – angular velocity of $Oxyz$ relative to $O_g x_g y_g z_g$. This velocity in $Oxyz$ has the following components: $\boldsymbol{\omega} = [P, Q, R]^{\mathrm{T}}$; $\boldsymbol{\Omega}$ – angular velocity of $Oxyz$ relative to the inertial coordinate system. It is equal to the sum of two velocities $\boldsymbol{\Omega} = \boldsymbol{\omega} + \boldsymbol{\omega}_z$.

2.3.2. Linear velocities

In further analysis, one assumes that the inertial system with the origin at the center of the Earth is the reference coordinate system (i.e. $\mathbf{R}_Z = \mathbf{0}$). The translational and rotational motion of the missile is represented by a change of the vector $\mathbf{R}_O$. The absolute velocity of any point of the missile P_i is defined by the expression

$$\mathbf{V}_i = \mathbf{V}_{O/g} + \mathbf{V}_{rel\_i} + \boldsymbol{\omega} \times \mathbf{r}_i + \boldsymbol{\omega}_z \times \mathbf{R}_i \tag{2.2}$$

where $\mathbf{V}_{O/g} = [U, V, W]^{\mathrm{T}}$ is the velocity of the pole O, $\mathbf{V}_{rel\_i} = d'\mathbf{r}_i/dt$ is the relative velocity in the case if the point P_i represents a gas particle, which after fuel burning moves inside the missile body in the direction to the nozzle – in this case, this motion causes a change of the vector $\mathbf{r}_i$. If the angular velocity of the Earth is omitted, the last component is equal to zero.

2.4. Accelerations

Newton's laws hold true in the inertial system. The absolute acceleration of the point P_i in this system is equal to

$$\begin{aligned} \mathbf{a}_i = {} & \mathbf{a}_{O/g} + \boldsymbol{\omega} \times \mathbf{V}_{O/g} + \boldsymbol{\varepsilon} \times \mathbf{r}_i + \mathbf{a}_{rel\_i} + \boldsymbol{\omega} \times (\boldsymbol{\omega} \times \mathbf{r}_i) + 2(\boldsymbol{\omega} + \boldsymbol{\omega}_z) \times \mathbf{V}_{rel\_i} \\ & + 2\boldsymbol{\omega}_z \times \mathbf{V}_{O/g} + 2(\boldsymbol{\omega}_z \times \boldsymbol{\omega}) \times \mathbf{r}_i + 2\boldsymbol{\omega} \times (\boldsymbol{\omega}_z \times \mathbf{r}_i) + \boldsymbol{\omega}_z \times (\boldsymbol{\omega}_z \times \mathbf{R}_i) \end{aligned} \tag{2.3}$$

where $\mathbf{a}_{O/g} = d'\mathbf{V}_{O/g}/dt$ is the acceleration of the pole O in $O_g x_g y_g z_g$; $\boldsymbol{\varepsilon} = d'\boldsymbol{\omega}/dt$ is the angular acceleration of the missile; $\mathbf{a}_{rel\_i} = d\mathbf{V}_{rel\_i}/dt$ is the relative acceleration of a particle moving inside the missile. For missiles of short and medium-range, the issues related to the angular velocity of the Earth can be omitted. In this case, the absolute acceleration is equal to

$$\mathbf{a}_i = \mathbf{a}_O + \boldsymbol{\omega} \times \mathbf{V}_O + \boldsymbol{\varepsilon} \times \mathbf{r}_i + \mathbf{a}_{rel\_i} + \boldsymbol{\omega} \times (\boldsymbol{\omega} \times \mathbf{r}_i) + 2\boldsymbol{\omega} \times \mathbf{V}_{rel\_i} \tag{2.4}$$

In this case, $O_g x_g y_g z_g$ is the inertial frame. Accordingly, in the above formula, the subscript O/g is replaced by O.

3. Mass and mass center of the missile

The missile is a system of variable mass. Its mass is the sum of all elementary masses contained in a given time within its body. During the active phase of flight, this mass includes: fuselage, fuel, gases contained in the combustion chamber and in the nozzle: $m = m_{fus} + m_{fuel} + m_{chamber} + m_{nozzle}$. The position of the center of mass in the inertial system is determined by the vector $\mathbf{R}_C = \left(\sum_i \mathbf{R}_i m_i\right)/m$. However, in the moving system $Oxyz$, the position of the center of mass is determined by the formula $\mathbf{r}_C = \mathbf{S}/m$, where $\mathbf{S}$ is the vector of static moments

$$\mathbf{S} = \sum_i \mathbf{r}_i m_i = \left[\sum_i x_i m_i, \sum_i y_i m_i, \sum_i z_i m_i\right]^{\mathrm{T}}$$

4. The equations of translatory motion of the missile with variable mass

The momentum of the missile with variable mass and with one outlet nozzle is

$$\mathbf{p}(t) = m\mathbf{V}_C + \dot{m}(\mathbf{R}_C - \mathbf{R}_E) \tag{4.1}$$

where $\dot{m} = dm/dt$ is the mass flow rate; $\mathbf{V}_C = d\mathbf{R}_C/dt$ is the absolute velocity of the center of mass; $\mathbf{R}_E = \mathbf{R}_O + \mathbf{r}_E$ is the vector determining the position of the nozzle. On the basis of equation (4.1), one can calculate the total differential of momentum for the mass inside the body

$$d\mathbf{p}_1(t) = \left[\dot{m}\mathbf{V}_C + m\frac{d\mathbf{V}_C}{dt} + \ddot{m}(\mathbf{R}_C - \mathbf{R}_E) + \dot{m}(\mathbf{V}_C - \mathbf{V}_E)\right]dt \tag{4.2}$$

For the mass $\dot{m}dt$, which lefts the missile body with the absolute velocity $\mathbf{V}_e^*$, the total differential of momentum is equal to $d\mathbf{p}_2(t) = -\dot{m}dt\mathbf{V}_e^*$[1]. Finally, the change of momentum of both the missile as well as the mass $\dot{m}dt$ is equal to

$$d\mathbf{p} = d\mathbf{p}_1 + d\mathbf{p}_2 = \left[m\frac{d\mathbf{V}_C}{dt} + \ddot{m}(\mathbf{R}_C - \mathbf{R}_E) + \dot{m}(2\mathbf{V}_C - \mathbf{V}_E - \mathbf{V}_e^*)\right]dt \tag{4.3}$$

According to the second Newton law, the change of momentum of the missile is equal to the impulse of the external force $\mathbf{F}$

$$d\mathbf{p}(t) = \mathbf{F}dt \tag{4.4}$$

On the basis of expressions (4.3) and (4.4) one can obtain

$$m\frac{d\mathbf{V}_C}{dt} + \ddot{m}(\mathbf{R}_C - \mathbf{R}_E) + \dot{m}(2\mathbf{V}_C - \mathbf{V}_E - \mathbf{V}_e^*) = \mathbf{F} \tag{4.5}$$

Without taking into account the angular velocity of the Earth rotation, the absolute velocities of points C and E are defined by expressions

$$\mathbf{V}_C = \mathbf{V}_O + \frac{d'\mathbf{r}_C}{dt} + \boldsymbol{\omega} \times \mathbf{r}_C \qquad \mathbf{V}_E = \mathbf{V}_O + \boldsymbol{\omega} \times \mathbf{r}_E \tag{4.6}$$

The second component of $\mathbf{V}_C$ is a relative velocity of the center of mass due to its motion as a result of the burning process $\mathbf{V}_{rel\_C} = d'\mathbf{r}_C/dt$. It does not occur in $\mathbf{V}_E$ because the position of the exit nozzle relative to the pole O is fixed. The absolute velocity of the gases leaving the

[1]The sign "–" shows that the mass of the missile decreases and the value of the mass flow rate is negative.

outlet nozzle $\mathbf{V}_e^*$ is equal to the sum of the nozzle exit velocity $\mathbf{V}_E$ and the relative velocity $\mathbf{U}_{rel}$, which is a result of the thermodynamic processes inside the nozzle

$$\mathbf{V}_e^* = \mathbf{V}_E + \mathbf{U}_{rel} = \mathbf{V}_O + \boldsymbol{\omega} \times \mathbf{r}_E + \mathbf{U}_{rel} \tag{4.7}$$

Taking into account the above terms in equation (4.5), we obtain

$$m\frac{d\mathbf{V}_C}{dt} + \ddot{m}(\mathbf{r}_C - \mathbf{r}_E) + 2\dot{m}[\mathbf{V}_{rel\_C} + \boldsymbol{\omega} \times (\mathbf{r}_C - \mathbf{r}_E)] = \mathbf{F} + \mathbf{T} \tag{4.8}$$

where the thrust of the engine is $\mathbf{T} = \dot{m}\mathbf{U}_{rel}$. The thrust $\mathbf{T}$ is positive because in the system $Oxyz$ both the value of the mass flow rate $\dot{m}$ as well as the relative velocity $\mathbf{U}_{rel}$ are negative.

Taking into account formula (2.4) related to the center of mass, on the basis of (4.8), one can determine the equation of translatory motion of the missile with variable mass

$$\begin{aligned} &m\Big(\frac{d'\mathbf{V}_O}{dt} + \boldsymbol{\omega} \times \mathbf{V}_O\Big) + \boldsymbol{\varepsilon} \times \mathbf{S} + \boldsymbol{\omega} \times (\boldsymbol{\omega} \times \mathbf{S}) + m\mathbf{a}_{rel\_C} + 2m\boldsymbol{\omega} \times \mathbf{V}_{rel\_C} \\ &\quad + \ddot{m}(\mathbf{r}_C - \mathbf{r}_E) + 2\dot{m}[\mathbf{V}_{rel\_C} + \boldsymbol{\omega} \times (\mathbf{r}_C - \mathbf{r}_E)] = \mathbf{F} + \mathbf{T} \end{aligned} \tag{4.9}$$

If the thrust has only one component $T_x = T$, the missile is axisymmetric and the center of mass and the center of the missile nozzle exit are all the time on the axis of the missile, then we have three scalar equations

$$\begin{aligned} &m(\dot{U} + QW - RV) - S_x(Q^2 + R^2) + ma_{x\_rel\_C} + \ddot{m}(x_C - x_E) + 2\dot{m}U_{rel\_C} = F_x + T \\ &m(\dot{V} + RU - PW) + S_x(PQ + \dot{R}) + 2mRU_{rel\_C} + 2\dot{m}R(x_C - x_E) = F_y \\ &m(\dot{W} + PV - QU) + S_x(PR - \dot{Q}) - 2mQU_{rel\_C} - 2\dot{m}Q(x_C - x_E) = F_z \end{aligned} \tag{4.10}$$

5. The equations of rotational motion of the missile with variable mass

For rotational motion the second law of dynamics relates to the derivative (with respect to time) of the angular momentum of the system of material points. Consideration should be taken for the same mass particles at two successive moments of time.

- At the time t, the system consists of mass $m = \sum_i m_i$. Locations of elementary masses mi are determined by vectors $\mathbf{R}_i$ (in the inertial system) or by vectors $\mathbf{r}_i$ (in the moving system). The absolute velocity is $\mathbf{V}_i$. The angular momentum $\mathbf{K}_O$ determined in relation to the pole O (Fig. 1) is equal to

$$\mathbf{K}_O(t) = \sum_i \mathbf{K}_{Oi} = \sum_i \mathbf{r}_i \times \mathbf{p}_i = \sum_i \mathbf{r}_i \times m_i\mathbf{V}_i \tag{5.1}$$

- At the time $t + \Delta t$, the system consists of two parts:
  - mass $m = \sum_i (m_i - \Delta m_i)$ that does not leave the body of the missile. The change of mass is equal to $\Delta m_i = -\dot{m}_i \Delta t$. Locations of the elementary masses are determined by vectors $\mathbf{R}_i + \Delta\mathbf{R}_i$ (in the inertial system) or by vectors $\mathbf{r}_i + \Delta\mathbf{r}_i$ (in the moving system). The absolute velocity is $\mathbf{V}_i + \Delta\mathbf{V}_i$. The angular momentum is equal to $\mathbf{K}_{O\_1}(t + \Delta t) = \sum_i (\mathbf{r}_i + \Delta\mathbf{r}_i) \times (m_i - \Delta m_i)(\mathbf{V}_i + \Delta\mathbf{V}_i)$.
  - mass $m = \sum_i \Delta m_i$ that leaves the missile body with absolute velocity $\mathbf{V}_i + \mathbf{U}_{rel\_i}$. If the missile is driven by the engine with one nozzle outlet, this velocity is defined by formula (4.7). The angular momentum of this mass is equal to $\mathbf{K}_{O\_2}(t + \Delta t) = \sum_i (\mathbf{r}_i + \Delta\mathbf{r}_i) \times \Delta m_i(\mathbf{V}_i + \mathbf{U}_{rel\_i})$.

The change of the angular momentum of the system is equal to

$$\begin{aligned}\Delta\mathbf{K}_O &= \mathbf{K}_{O\_1}(t+\Delta t) + \mathbf{K}_{O\_2}(t+\Delta t) - \mathbf{K}_O(t) = \sum_i \mathbf{r}_i \times m_i \Delta\mathbf{V}_i \\ &+ \sum_i \Delta\mathbf{r}_i \times m_i\mathbf{V}_i + \sum_i \mathbf{r}_i \times \Delta m_i \mathbf{U}_{rel\_i}\end{aligned} \tag{5.2}$$

On the basis of (5.2), it is possible to calculate the derivative of the angular momentum $\mathbf{K}_O$ with respect to time

$$\frac{d\mathbf{K}_O}{dt} = \sum_i \mathbf{r}_i \times m_i \frac{d\mathbf{V}_i}{dt} + \sum_i \mathbf{V}_{P_i/O} \times m_i\mathbf{V}_i - \sum_i \mathbf{r}_i \times \dot{m}_i \mathbf{U}_{rel\_i} \tag{5.3}$$

The same derivative can be calculated directly by differentiating expression (5.1)

$$\frac{d\mathbf{K}_O}{dt} = \sum_i \mathbf{V}_{P_i/O} \times m_i\mathbf{V}_i + \sum_i \mathbf{r}_i \times \frac{d(m_i\mathbf{V}_i)}{dt} \tag{5.4}$$

The second component in (5.4) is the moment of external forces acting on the missile relative to the pole O. This moment has the following components in the system $Oxyz$ $\mathbf{M}_O = [L, M, N]$.

By comparing expressions (5.3) and (5.4), we obtain

$$\mathbf{M}_O = \sum_i \mathbf{r}_i \times m_i \frac{d\mathbf{V}_i}{dt} - \sum_i \mathbf{r}_i \times \dot{m}_i \mathbf{U}_{rel\_i} \tag{5.5}$$

If one takes into account expression (2.4) defining the absolute acceleration of any point of the missile, and assumes that the missile has one nozzle, equation (5.5) takes the final form

$$\begin{aligned}&\mathbf{S} \times \Big(\frac{d'\mathbf{V}_0}{dt} + \boldsymbol{\omega} \times \mathbf{V}_O\Big) + \mathbf{I}\boldsymbol{\varepsilon} + \boldsymbol{\omega} \times (\mathbf{I}\boldsymbol{\omega}) + \sum_i m_i \mathbf{r}_i \times \mathbf{a}_{rel\_i} \\ &+ 2\sum_i m_i \mathbf{r}_i \times (\boldsymbol{\omega} \times \mathbf{V}_{rel\_i}) = \mathbf{M}_O + \mathbf{M}_T\end{aligned} \tag{5.6}$$

where $\mathbf{M}_T$ is the moment of thrust $\mathbf{M}_T = \sum_i \mathbf{r}_i \times \dot{m}_i \mathbf{U}_{rel\_i} = \mathbf{r}_E \times \dot{m}\mathbf{U}_{rel}$. This moment has the following components in the system $Oxyz$: $\mathbf{M}_T = [L_T, M_T, N_T]$. $\mathbf{I}$ is the matrix of inertia moments.

Equations (5.6) can be simplified by taking into account the assumption of axial symmetry of the missile. If the thrust lies on the axis of the missile, the final scalar form of this equation is as follows

$$\begin{aligned}&I_x\dot{P} = L \\ &I_y\dot{Q} + PR(I_x - I) - S_x(\dot{W} + PV - QU) + 2Q\sum_i m_i x_i U_{rel\_i} = M \\ &I_z\dot{R} + PQ(I - I_x) + S_x(\dot{V} + RU - PW) + 2R\sum_i m_i x_i U_{rel\_i} = N\end{aligned} \tag{5.7}$$

6. The final form of the equations of motion

Motion of the axisymmetric missile is described by equations (4.10) and (5.7) complemented with kinematic relations - we have the system of twelve differential equations

$$\mathbf{A}\dot{\mathbf{x}} = \mathbf{f} \tag{6.1}$$

where $\mathbf{x}$ is the vector of flight parameters $\mathbf{x} = [U, V, W, P, Q, R, \Phi, \Theta, \Psi, x_O, y_O, z_O]^{\mathrm{T}}$.

Non-zero elements of the matrix **A** are equal to

$$\begin{aligned} &A_{11} = m && A_{22} = m && A_{26} = S_x && A_{33} = m \\ &A_{35} = -S_x && A_{44} = I_x && A_{53} = -S_x && A_{55} = I_y \\ &A_{62} = S_x && A_{66} = I_y \end{aligned} \tag{6.2}$$

whereas, the vector **f** is defined as follows

$$\begin{aligned} f_1 &= F_x + T + m(RV - QW) + S_x(Q^2 + R^2) - ma_{x\_rel\_C} - \dot{m}(x_C - x_E) - 2\dot{m}U_{rel\_C} \\ f_2 &= F_y + m(PW - RU) - S_xPQ - 2mRU_{rel\_C} - 2\dot{m}R(x_C - x_E) \\ f_3 &= F_z + m(QU - PV) - S_xPR + 2mQU_{rel\_C} + 2\dot{m}Q(x_C - x_E) \\ f_4 &= L \\ f_5 &= M + PR(I_y - I_x) + S_x(PV - QU) - 2Q\sum_i m_i x_i U_{rel\_i} \\ f_6 &= N + PQ(I_y - I_x) + S_x(PW - RU) - 2R\sum_i m_i x_i U_{rel\_i} \\ f_7 &= P + (Q\sin\Phi + R\cos\Phi)\tan\Theta \\ f_8 &= Q\cos\Phi - R\sin\Phi \\ f_9 &= \frac{Q\sin\Phi + R\cos\Phi}{\cos\Theta} \\ f_{10} &= U\cos\Psi\cos\Theta + V(\cos\Psi\sin\Theta\sin\Phi - \sin\Psi\cos\Phi) + W(\cos\Psi\sin\Theta\cos\Phi + \sin\Psi\sin\Phi) \\ f_{11} &= U\sin\Psi\cos\Theta + V(\sin\Psi\sin\Theta\sin\Phi + \cos\Psi\cos\Phi) + W(\sin\Psi\sin\Theta\cos\Phi - \cos\Psi\sin\Phi) \\ f_{12} &= -U\sin\Theta + V\cos\Theta\sin\Phi + W\cos\Theta\cos\Phi \end{aligned} \tag{6.3}$$

In equations (4.10), there are elements associated with relative motion of the mass center, while in equations (5.7) there are elements associated with motion of gas particles inside the body of the missile. They require determination of the relative velocity of mass center of the gas inside the missile. This will be described below.

7. Determination of gas parameters inside the missile engine

Due to the combustion process, mass m, static moments S_i and inertia moments I_x, I_y of the missile change. The quantity of fuel decreases in the combustion chamber and burning products leave the interior of the missile through the convergent-divergent nozzle (Fig. 3).

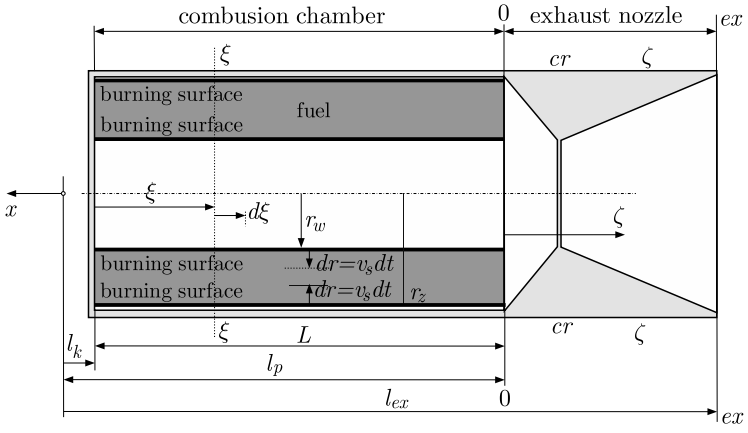

Fig. 3. Scheme of the solid fuel engine

To determine the rule of change of fuel and these products, assumptions on the shape of the fuel and the space filled by gas should be made. Knowledge about physical parameters such as gas pressure p, temperature T, density ρ and velocity U is also necessary.

The following analysis will be carried out in which uniform velocity distribution of flow in each section of the missile engine is assumed (Mattingly, 2006; Torecki, 1984, Turner, 2009). This velocity remains parallel to the axis of the missile (the engine)[2]. In the calculations, the local coordinate systems associated with the combustion chamber (ξ) and the nozzle (ζ) are introduced. This analysis also assumes that the mass flow rate is the same in each section of the nozzle. This means that the initial and final phases of the engine operation are omitted.

7.1. The exhaust nozzle

Energy of gases produced in the combustion chamber is converted into kinetic energy in the exhaust nozzle (Torecki, 1984). This nozzle is a supersonic de Laval nozzle, which means that the gas velocity increases in both the convergent as well as in the divergent parts. At the narrowest cross-section the gas velocity reaches the speed of sound. It is assumed that the flow in the nozzle is adiabatic and isentropic. As the gas velocity increases, and inside the nozzle is several times higher than the velocity at the inlet of the nozzle, it is assumed that the parameters at the inlet cross-section are stagnation parameters density ρ_0, temperature T_0, pressure p_0. Knowing the adiabatic index k, on the basis of the above assumptions, one can calculate velocity, density and temperature in any section of the nozzle inlet

$$U = \sqrt{\frac{2k}{k-1}\frac{p_0}{\rho_0}\Big[1-\Big(\frac{p}{p_0}\Big)^{\frac{k-1}{k}}\Big]} \qquad \rho = \rho_0\Big(\frac{p}{p_0}\Big)^{\frac{1}{k}} \qquad T = T_0\Big(\frac{p}{p_0}\Big)^{\frac{k-1}{k}} \tag{7.1}$$

If the geometry $F(\zeta)$ of the nozzle is known, the pressure ratio p/p_0 can be found from the relation

$$\frac{F}{F_{cr}} = \Big(\frac{2k}{k+1}\Big)^{\frac{1}{k-1}}\sqrt{\frac{k-1}{k+1}}\frac{1}{\sqrt{\Big(\frac{p}{p_0}\Big)^{\frac{2}{k}}-\Big(\frac{p}{p_0}\Big)^{\frac{k+1}{k}}}} \tag{7.2}$$

The mass flow rate in the nozzle can be described by the relation

$$\dot{m}_{nozzle} = F_{cr}\Big(\frac{2}{k+1}\Big)^{\frac{1}{k-1}}\sqrt{\frac{2k}{k+1}}\sqrt{p_0\rho_0} = F_{cr}\frac{\Big(\frac{2}{k+1}\Big)^{\frac{1}{k-1}}\sqrt{\frac{2k}{k+1}}}{\sqrt{RT_0}}p_0 = CF_{cr}p_0 \tag{7.3}$$

where C is the discharge coefficient depending on the fuel type and geometry of the nozzle, R – gas constant of combustion products.

7.2. The combustion chamber

The analysis assumes that the fuel has shape of a hollow cylinder with length of L, see Fig. 3. The initial inner and outer radii are respectively equal to r_{w0} and r_{z0}. It is assumed that the combustion takes place on the inner and outer surface of the cylinder with the burning speed v_{burn}. At the time dt, its inner radius increases and the outer radius decreases by a value

[2]This is relative velocity occurring in equations $(5.7)_{2,3}$ taken with the sign $(-)$. For clarity, the indexing is abandoned, i.e. instead of $-U_{rel\_i}$ we apply U.

$dr = v_{burn}dt$. After the time t, radii r_w and r_z, cross-sectional area F of the space occupied by the products of combustion and the burning surface S are equal to

$$\begin{aligned} r_w(t) &= r_{w0} + \int_0^t v_{burn}\, d\tau \qquad & r_z(t) &= r_{z0} - \int_0^t v_{burn}\, d\tau \\ F(t) &= \pi[r_w^2 + (r_{z0}^2 - r_z^2)] \qquad & S &= 2\pi(r_{w0} + r_{z0})L \end{aligned} \tag{7.4}$$

The latter formula shows that the combustion surface is constant. Whereas, the cross-sectional area $F(t)$ changes because of the change of r_w and r_z.

It is assumed that the pressure p_0 and temperature T_0 is the same in the entire combustion chamber, and the burning speed is determined by a power series combustion law $v_{burn} = Ap_0^n + B$ (Kurov and Dolzhaskii, 1961), where A, B and n depend inter alia on the chemical composition of the fuel and temperature of the initial charge. The mass flow rate of the gas into the combustion chamber is equal to $\dot{m}_{chamber} = \rho_{fuel} v_{burn} S$, where ρ_{fuel} is the fuel density. In the initial and final stages of the fuel combustion process $\dot{m}_{chamber} \neq \dot{m}_{nozzle}$, which means that the flow is non-stationary and the pressure in the combustion chamber is changed. However, the fundamental phase of missile engine working is done with $\dot{m}_{chamber} = \dot{m}_{nozzle}$. This is a result of the so-called self-adjustment of the engine, which keeps a constant pressure in the combustion chamber.

Using the continuity equation for sections 0-0 and *cr-cr* and, further, applying the equation of the state of gas, the gas velocity at the end of the combustion chamber can be calculated as

$$U_0(L,t) = \frac{CF_{cr}p_0}{\rho_0 F(t)} = \frac{CF_{cr}}{F(t)} RT_0 \tag{7.5}$$

It is noted here that the velocity U_0 changes during the combustion process since the cross-sectional area $F(t)$ increases due to changes in both the inner radius r_w and outer radius r_z according to formula (7.4).

In order to calculate the change of velocity along the combustion chamber, it is considered that the gas velocity increases with proximity to the outlet. In the section $d\xi$ over time dt the burned fuel mass is equal to $dm = dSv_{burn}dt\rho_{fuel}$ (dS is an elementary surface of combustion for the $d\xi$ section). An increase in the mass flow rate inside the combustion chamber is $d\dot{m} = v_{burn}\rho_{fuel}dS$. Simultaneously, taking into account the constant velocity distribution in the cross section of the chamber ξ-ξ, the increase is equal to $d\dot{m} = \rho_0 F dU$. Comparing these expressions, one can determine the change of velocity $dU = [v_{burn}\rho_{fuel}/(\rho_0 F)]dS$. In order to calculate the velocity U, it is necessary to know the relationship for the sectional area F and for the combustion surface S as a function of the coordinate ξ. We have

$$U(\xi,t) = \frac{v_{burn}\rho_{fuel}}{\rho_0} \frac{1}{F(t)} \int_0^{\xi} \frac{\partial S(x,t)}{\partial x}\, dx$$

If the fuel has shape of a hollow cylinder, then on the basis of (7.4), one has $\partial S/\partial x = 2\pi(r_{w0} + r_{z0})$. Taking into account the expression for the cross-sectional area $F(t)$ and performing integration, one can calculate the gas velocity at ξ

$$U(\xi,t) = 2v_{burn}\frac{\rho_{fuel}}{\rho_0} \frac{(r_{w0} + r_{z0})L}{r_w^2 + (r_{z0}^2 - r_z^2)} \frac{\xi}{L} = U_0 \frac{\xi}{L} \tag{7.6}$$

This formula takes into account boundary conditions: $U = 0$ for $\xi = 0$ and $U = U_0$ for $\xi = L$.

8. Changes of the missile mass parameters

8.1. The change of the speed of mass

In the time interval dt, along the entire length of the load, the mass occupying the volume $Sv_{burn}dt$ is combusted. Knowing density ρ_{fuel}, one can calculate this mass $dm = 2\pi(r_{w0} + r_{z0})Lv_{burn}dt\rho_{fuel}$. So, the rate of change of fuel mass as well as of missile mass is equal to $\dot{m} = \dot{m}_{fuel} = 2\pi(r_{w0}+r_{z0})Lv_{burn}\rho_{fuel}$. As can be seen, this rate is constant, which means that the component of equation $(4.10)_1$ comprising the second derivative is equal to zero $\ddot{m} = \ddot{m}_{fuel} = 0$.

8.2. Mass of the fuel and missile

Knowing the rate $\dot{m}$, we can calculate the fuel and missile masses at any point of time. If at the beginning they are m_{fuel_0} and m_0, respectively, we have

$$\begin{aligned} m_{fuel}(t) &= m_{fuel\_0} - 2\pi(r_{w0} + r_{z0})L\rho_{fuel}v_{burn}t \\ m(t) &= m_0 - 2\pi(r_{w0} + r_{z0})L\rho_{fuel}v_{burn}t \end{aligned} \tag{8.1}$$

8.3. Motion of the center of mass of the missile

Equations (4.10) require determination of changes in the position of the center of mass and the relative velocity U_{rel_C} and its relative acceleration $a_{x\_rel\_C}$. During operation of the engine, the fuel mass decreases, while the remaining mass is unchanged. At the same time, the center of the decreasing fuel mass is constant. It means that

$$x_C(t) = \frac{x_{fus}m_{fusel} + x_{fuel}m_{fuel}(t) + x_{chamber}m_{chamber} + x_{nozzle}m_{nozzle}}{m} \tag{8.2}$$

The first and second derivatives of the above expression give the relative velocity and acceleration

$$U_{rel\_C} = \dot{m}_{fuel}\frac{x_{fuel} - x_C}{m} \qquad a_{x\_rel\_C} = -2\frac{\dot{m}_{fuel}}{m}U_{rel\_C} \tag{8.3}$$

8.4. Static and inertia moments

On the adopted assumptions concerning the shape and way of the burning process, the static moment and inertia moments can be calculated. For all parts of the missile – fuselage, fuel and gases filling the combustion chamber and the nozzle it is necessary to know the distribution of mass. Table 1 shows necessary formulas which allow one to calculate all static and inertia moments.

9. Members of the equations of motion depending on the relative velocity and relative acceleration

There are elements comprising the relative velocity U_{rel} of the gases moving inside the body of the missile in equations $(6.3)_{2,3}$. They are determined below assuming an uniform distribution of the relative speed in all sections of the engine. Calculations are performed for the combustion chamber and nozzle.

Table 1

Static and inertia moments	Elementary mass for calculation	Formula
Total static moment S_x	$S_x = S_{x\_fusel} + S_{x\_fuel} + S_{x\_chamber} + S_{x\_nozzle}$	
S_{x_fusel}	dm	$S_{x\_fusel} = \iiint\limits_{fuselage} x\, dm$
S_{x_fuel}	$dm = \rho_{fuel}\pi(r_z^2 - r_w^2)dx$	$S_{x\_fuel} = \frac{1}{2}\rho_{fuel}\pi(r_z^2 - r_w^2)(l_k^2 - l_p^2)$
$S_{x_{chamber}}$	$dm = \rho_0 F dx$	$S_{x\_chamber} = \frac{1}{2}\rho_0\pi[r_w^2 + (r_{z0}^2 - r_z^2)](l_k^2 - l_p^2)$
$S_{x_{nozzle}}$	$dm = \rho(x)F(x)dx$	$S_{x\_nozzle} = \rho_0 \int\limits_{l_{ex}}^{l_p} F(x)\left(\frac{p}{p_0}\right)^{\frac{1}{k}} x\, dx$
Total inertia moment I_x	$I_x = I_{x\_fusel} + I_{x\_fuel}$	
I_{x_fusel}	dm	$I_{x\_fusel} = \iiint\limits_{fuselage} r^2\, dm$
I_{x_fuel}	$dm = \rho_{fuel}2\pi r L dr$	$I_{x\_fuel} = \frac{1}{2}\pi\rho_{fuel}L(r_z^4 - r_w^4)$
Total inertia moment I_y	$I_y = I_{y\_fusel} + I_{y\_fuel} + I_{y\_chamber} + I_{y\_nozzle}$	
I_{y_fusel}	dm	$I_{y\_fusel} = \iiint\limits_{fuselage} x^2\, dm$
I_{y_fuel}	$dm = \rho_p\pi(r_z^2 - r_w^2)dx$	$I_{y\_fuel} = \frac{1}{3}\rho_{fuel}\pi(r_z^2 - r_w^2)(l_k^3 - l_p^3)$
$I_{y\_chamber}$	$dm = \rho_0\pi[r_w^2 + (r_{z0}^2 - r_z^2)]dx$	$I_{y\_chamber} = \frac{1}{3}\rho_0\pi[r_w^2 + (r_{z0}^2 - r_z^2)](l_k^3 - l_p^3)$
I_{y_nozzle}	$dm = \rho(x)F(x)dx$	$I_{y\_nozzle} = \rho_0 \int\limits_{l_{ex}}^{l_p} F(x)\left(\frac{p}{p_0}\right)^{\frac{1}{k}} x^2\, dx$

The combusion chamber

Elementary mass of the gas in the section dx of the combustion chamber is equal to $dm = \rho_0\pi[r_w^2 + (r_{z0}^2 - r_z^2)]dx$. Its velocity is given by (7.6). Taking into account this relationship, one can obtain

$$\sum_i m_i x_i U_{rel\_i} = \pi v_s \rho_p (r_{w0} + r_{z0})\Big(l_k l_p^2 - \frac{1}{3}l_k^3 - \frac{2}{3}l_p^3\Big)$$

The exhaust nozzle

The sought expressions for the nozzle can be found based on the knowledge of density distribution $\rho(x)$ and velocity distribution $U_{rel}(x)$ along the nozzle. We have

$$\sum_i m_i x_i U_{rel\_i} = \int\limits_{-l_{ex}+l_p}^{0} (\zeta - l_p)\rho F U_{rel}\, d\zeta$$

This integral can be efficiently calculated applying numerical methods and solving the issue of gas flow through the nozzle, as described in Section 7.1.

10. Determination of external forces acting on the missile

The right-hand side of equations (6.1) includes components of the resultant external force $\mathbf{F}$ acting on the missile and the resultant moment of external forces $\mathbf{M}_O$ relative to the pole O. The external force $\mathbf{F}$ is the sum of the weight $\mathbf{Q}$ and the aerodynamic force $\mathbf{R}$. Whereas, the moment $\mathbf{M}_O$ relative to the pole O is the sum of the moments generated by the weight $\mathbf{M}_Q = \mathbf{r}_C \times \mathbf{Q}$ and the aerodynamic moment $\mathbf{M}_{aer}$

$$\mathbf{F} = \mathbf{Q} + \mathbf{R} \qquad \mathbf{M}_O = \mathbf{M}_Q + \mathbf{M}_{aer} \tag{10.1}$$

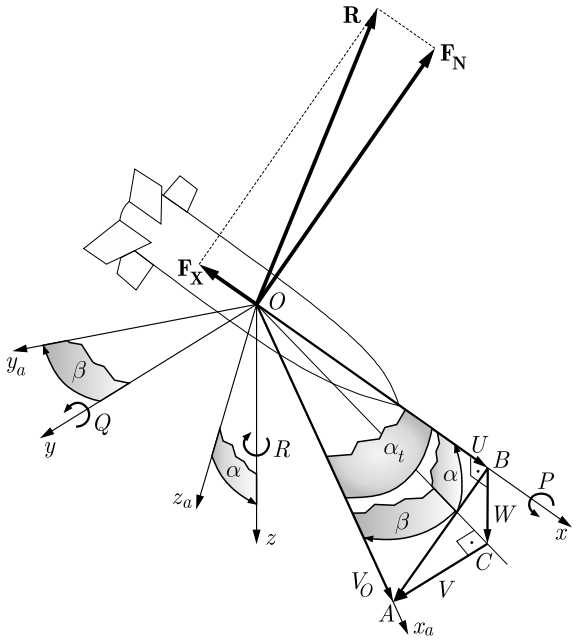

Fig. 4. Coordinate systems, aerodynamic forces, velocities and angles

The aerodynamic forces and moments can be divided into static and dynamic. The static forces and moments are determined on the basis of the value of the nutation angle α_t (Fig. 4). At the same time, the dynamic forces and moments are created when the missile is rotating. They have a damping character. The resultant aerodynamic force $\mathbf{R}$ is equal to the sum of forces: axial force $\mathbf{F}_X$ and normal force $\mathbf{F}_N$, $\mathbf{R} = \mathbf{F}_X + \mathbf{F}_N$ (Davis *et al.*, 1958; McCoy, 2012; Rosser *et al.*, 1947). The final expressions defining the components of the external force and moments are as follows

$$\begin{aligned}
F_x &= -mg\sin\Theta - C_x\frac{\rho V_{air}^2}{2}S \\
F_y &= mg\cos\Theta\sin\Phi + \frac{\rho V_{air}^2}{2}S\Big[C_{N\delta}\Big(\frac{-V}{V_{air}}\Big) + \Big(\frac{Pd}{V_{air}}\Big)C_{N_p\delta}\Big(\frac{W}{V_{air}}\Big) + \Big(\frac{Rd}{V_{air}}\Big)\Big(C_{Nq} + C_{N\dot\alpha}\Big)\Big] \\
F_z &= mg\cos\Theta\cos\Phi - \frac{\rho V_{air}^2}{2}S\Big[C_{N\delta}\Big(\frac{-W}{V_{air}}\Big) + \Big(\frac{Pd}{V_{air}}\Big)C_{N_p\delta}\Big(\frac{-V}{V_{air}}\Big) + \Big(\frac{-Qd}{V_{air}}\Big)\Big(C_{Nq} + C_{N\dot\alpha}\Big)\Big] \\
L &= \frac{\rho V_{aer}^2}{2}SdC_{lp}\Big(\frac{Pd}{V_{aer}}\Big) \\
M &= -x_C mg\cos\Theta\cos\Phi + \frac{\rho V_{air}^2}{2}Sd\Big[C_{M\delta}\Big(\frac{W}{V_{air}}\Big) + \Big(C_{Mq} + C_{M\dot\alpha}\Big)\Big(\frac{Qd}{V_{air}}\Big) \\
&\quad + \Big(\frac{Pd}{V_{air}}\Big)C_{M_{p\delta}}\Big(\frac{V}{V_{air}}\Big)\Big]
\end{aligned} \tag{10.2}$$

$$N = x_C mg\cos\Theta\sin\Phi + \frac{\rho V_{air}^2}{2}Sd\Big[C_{M\delta}\Big(\frac{-V}{V_{air}}\Big) + \Big(C_{Mq} + C_{M\dot{\alpha}}\Big)\Big(\frac{Rd}{V_{air}}\Big) + \Big(\frac{Pd}{V}\Big)C_{M_{p\delta}}\Big(\frac{W}{V_{air}}\Big)\Big]$$

V_{air} is the velocity at which the missile moves relative to the air $\mathbf{V}_{air} = \mathbf{V}_O - \mathbf{V}_{wind}$. All coefficients in brackets [...] determine the aerodynamic forces and moments. They depend on the nutation angle and the Mach number.

11. Numerical example and conclusions

Formulas $(6.2)_1$-$(6.2)_5$ show that during the combustion process there are additional forces and moments which depend on the mass flow rate, relative speed of the combustion products and their mass. In particular, there are additional moments depending on the angular velocities: $-2Q\sum_i m_i x_i U_{rel\_i}$ and $-2R\sum_i m_i x_i U_{rel\_i}$. They have a damping character as well as the aerodynamic damping moments (members containing $(C_{Mq} + C_{M\dot{\alpha}})$ in expressions $(10.2)_5$ and $(10.2)_6$). To compare both damping moments, the following derivatives are analyzed

$$M_{aer}^Q = (C_{Mq} + C_{M\dot{\alpha}})\frac{\rho V_{air}}{2}Sd^2 \qquad M_{jet}^Q = -2\sum_i m_i x_i U_{rel\_i} \tag{11.1}$$

To do it, numerical simulation of flight for a homing guided missile has been performed. For this reason, additionally control laws are also determined on the basis of methods described in (Krasovskii, 1969, 1973; Locke, 1955; Neupokoev, 1991; Shneyder, 1998; Siouris, 2004). A lot of various variants of the initial conditions both for the missile and for the maneuvering target are used. Below, exemplary results for one variant of target flight are presented – a turn maneuver with increasing altitude. It is assumed that the target is detected by the missile at the distance of 30 km and initial altitude of 5 km. Its velocity is 100 m/s. The initial conditions for the missile (class Patriot MIM-104) are as follows: pitch angle 45°, yaw angle 0°. The working time of the engine is 12 s. The initial mass of the missile is 910 kg, mass of the fuel is 508 kg. The control system starts to work two seconds after blast-off.

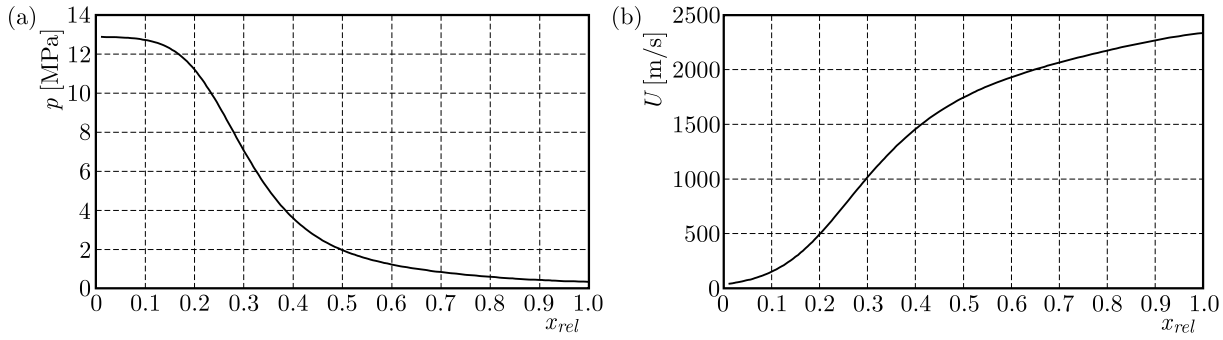

Fig. 5. Gas pressure (a) and gas velocity (b) along exhaust nozzle

It is assumed that the combustion temperature for nitrocellulose solid propellant grain is $T_0 = 2500$ K. The calculations show that for this temperature the pressure in the combustion chamber is $p_0 = 12.9$ MPa, the burning speed $v_{burn} = 8$ mm/s and the relative velocity at the nozzle exit is $Ur_{rel} = 2336$ m/s. These parameters give a thrust equal to $T = 107.08$ kN. Exemplary changes of gas parameters in the exhaust nozzle are shown in Figs. 5a and 5b. The defined by (11.1) derivatives are presented in Fig. 6a. We can see that the derivative M_{jet}^Q is constant during the combustion process. The absolute value of the derivative M_{aer}^Q depends nonlinearly on V_{air} because the coefficients $(C_{Mq} + C_{M\dot{\alpha}})$ depend on the Mach number (Fig. 6b). Figure 6a proves that the aerodynamic derivative M_{aer}^Q is many times greater than M_{jet}^Q. Therefore, any

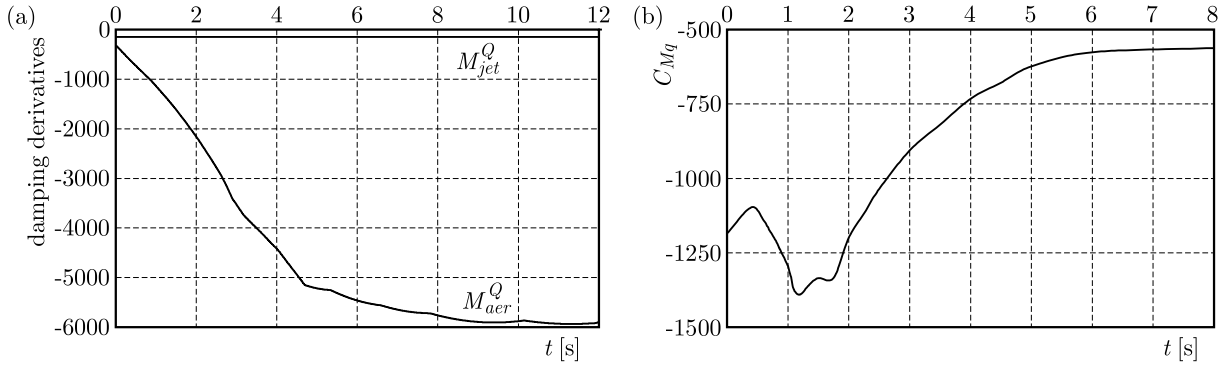

Fig. 6. (a) Damping derivatives; (b) coefficient C_{Mq}

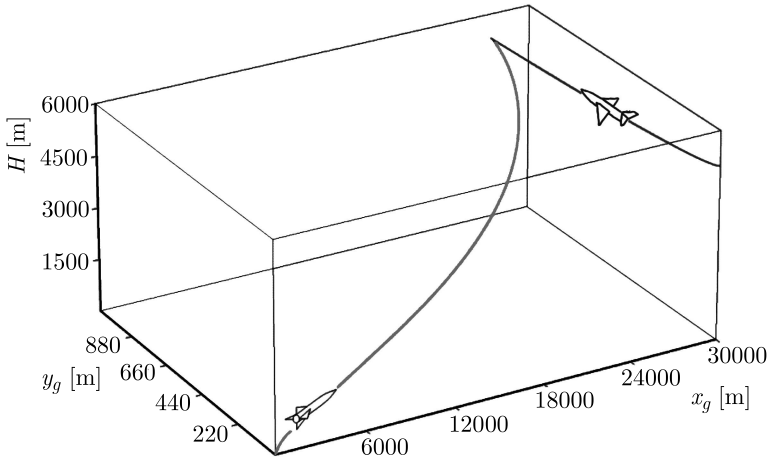

Fig. 7. Missile and target trajectories

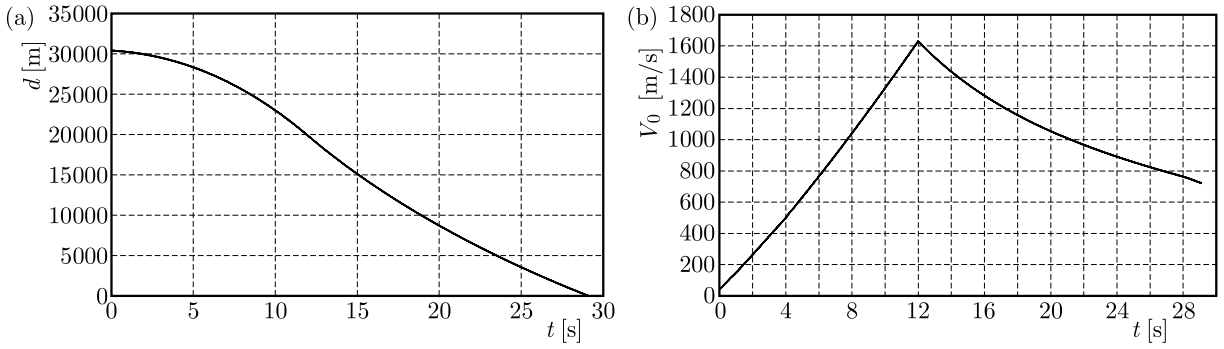

Fig. 8. (a) Missile-target distance; (b) missile velocity

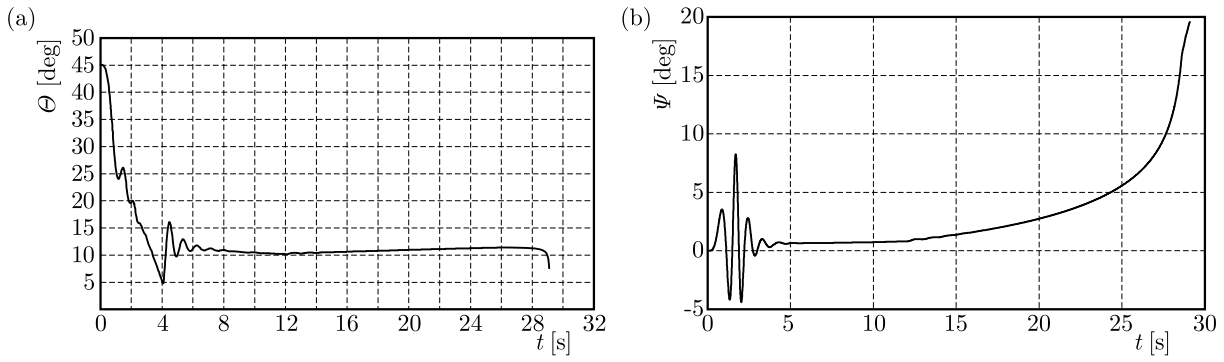

Fig. 9. (a) Pitch angle; (b) yaw angle

important influence of the jet damping effect on the missile atmospheric flight has not been found. The trajectories of the missile and the target are shown in Fig. 7. We can see that the maneuvering target is hit – a distance between the missile and the target decreases to zero, see Fig. 8a. Figure 8b presents velocity of the missile which grows during engine operation and next decreases. The pitch and yaw angles are presented in Figs. 9a and 9b.

Other obtained results also show that the jet damping effect can be neglected for maneuvering missiles when angular velocities are not equal to zero. The aerodynamic forces and moments are still of minor importance.

References

1. Davis L., Follin J.W., Blitzer L., 1958, *Exterior Ballistics of Rockets*, D. Van Nostrad Company Inc.
2. Dimitrevski A.A., 1972, *Exterior Ballistics* (in Russian), Publishing House "Maschinostroenie"
3. Krasovsky A.A., 1969, *Analytical Design of Aircraft Control Loops* (in Russian), Publishing House "Maschinostroenie"
4. Krasovsky A.A., 1973, *Systems of the Automatic Flight Control and its Analytical Design* (in Russian), Publishing House "Nauka"
5. Kurov V.D., Dolzhansky J.M., 1961, *Fundamentals of Solid Propellant Rockets* (in Russian), State Scientific and Technical Publishing "Oborongiz"
6. Locke A.S., 1955, *Guidance*, D. Van Nostrad Company Inc.
7. Mattingly J.D., 2006, *Elements of Propulsion: Gas Turbines and Rockets*, AIAA Education Series
8. McCoy R.L., 2012, *Modern Exterior Ballistics*, Schifler Publishing Ltd.
9. Neypokoev F.K., 1991, *Firing of anti-aircraft missiles* (in Russian), Voennoe Izdatelstvo
10. Quarelli M.B., Cameron J., Balaram B., Baranwal M., Bruno A., 2014, Modeling and simulation of flight dynamics of variable mass system, *AIAA Space Conference and Exposition*, San Diego, 2014-4454
11. Rosser J., Newton R., Gross G., 1947, *Mathematical Theory of Rocket Flight*, McGraw Hill Book Company Inc.
12. Thomson W.T., 1965a, Equations of motion for the variable mass system, *AIAA Journal*, **4**, 4, 766-768
13. Thomson W.T., 1965b, Jet damping of solid rocket: theory and flight results, *AIAA Journal*, **3**, 3, 413-417
14. Thomson W.T., 1986, *Introduction to Space Dynamics*, Dover Publications Inc.
15. Torecki S., 1984, *Rocket engines* (in Polish), Wydawnictwa Komunikacji i Łączności
16. Turner M., 2009, *Rocket and Spacecraft Propulsion – Principles, Practice and New Developments*, Springer Verlag
17. Shneydor N.A., 1998, *Missile Guidance and Pursuit: Kinematics, Dynamics and Control*, Horwood Publishing
18. Siouris G.M., 2004, *Missile Guidance and Control Systems*, Springer Verlag

Manuscript received November 4, 2015; accepted for print December 15, 2015

JOURNAL OF THEORETICAL AND APPLIED MECHANICS
54, 3, pp. 909-919, Warsaw 2016
DOI: 10.15632/jtam-pl.54.3.909

A SMOOTH MODEL OF THE RESULTANT FRICTION FORCE ON A PLANE CONTACT AREA

Grzegorz Kudra, Jan Awrejcewicz

Lodz University of Technology, Department of Automation, Biomechanics and Mechatronics, Łódź, Poland
e-mail: grzegorz.kudra@p.lodz.pl

A class of smooth approximations of the total friction force occurring on a plane finite contact surface is presented. It is assumed that the classical Coulomb friction law is valid on any infinitesimal element of the contact region. The models describe the stick phase, the fully developed sliding and the transition between these two modes. They take into account different values of static and dynamic friction coefficients. The models are applied in simulation of a dynamical system performing translational and rotational stick-slip oscillations, and then they are verified by comparison with the corresponding results in which an event-driven discontinuous model of friction is used.

Keywords: friction modelling, Coulomb-Contensou model, stick-slip, plane contact

1. Introduction

Contensou (1963) derived the integral model of resultant friction forces between two contacting bodies on the assumption of validity of the Coulomb friction law on each element of a circular contact area, Hertzian contact stresses and fully developed sliding. He pointed out that the normal component of relative angular velocity cannot be neglected in the model of friction forces for a certain class of mechanical systems.

Howe and Cutkosky (1996), for practical purposes of robotics, proposed an approximation of this problem in the form of ellipsoid description of the limit surface bounding the zone of admissible tangential loadings of the contact. However, it is not a direct description of the relation between the components of sliding and friction. Some researchers proposed Padé approximations as a convenient substitution of the integral model of friction forces (Zhuravlev, 1998; Zhuravlev and Kireenkov, 2005). Then the Padé approximants (Kireenkov, 2008) and hyperbolic tangent functions (Kudra and Awrejcewicz, 2011b) were used in the modelling of friction forces in the case of a circular contact zone and presence of rolling resistance. Kosenko and Aleksandrov (2009) developed a piece-wise linear approximation of the integral model of friction in the case of elliptical contact zone and Hertzian contact stresses. Kudra and Awrejcewicz (2012a, 2013) presented approximations which can be understood as a certain kind of generalizations and modifications of the Padé approximants, and applied them to the above problems including the case of the circular contact with uniform contact pressure distribution as well as elliptical one with the presence of rolling resistance.

The above mentioned models approximate the friction forces during the fully developed sliding or their limits in the stick mode. The simulation requires also models describing the transition between these two modes. The assumption of negligibly short time of duration of this transition results in a non-smooth dynamical system. They can often be modelled by the use of piecewise smooth differential equations (PWS). Then the PWS systems are sometimes divided in the following way (Leine and Nijmeijer, 2004): a) systems with a continuous but non-smooth

vector field; b) systems with a continuous but non-smooth state; c) systems with a discontinuous state.

Existence and uniqueness of the solution are guaranteed only for systems belonging to group (a), known also as Filippov type systems (Filippov, 1964, 1988; Leine and Nijmeijer, 2004). For example, a mechanical system with dry friction modelled as a discontinuous function of time belongs to group (b). For instance, the assumption of rigidity of contacting bodies and the friction force dependent on normal load, which is not known in advance, can lead in some cases to inconsistency of the solution, known as the Painlevé paradox (Jellet, 1872; Painlevé, 1895; Génot and Brogliato, 1999). Such cases should be interpreted in such a way that the mathematical model and solution concept do not correspond to the real physical phenomenon.

The techniques of simulation of non-smooth systems can be divided in the following way (Leine and Nijmeijer, 2004): (i) event-driven integration methods; (ii) time-stepping methods. Acary and Brogliato (2010) presented a comprehensive review of the event-driven and time-stepping numerical methods for simulation of non-smooth dynamical systems. Sometimes as another way of dealing with the non-smooth dynamical systems are regularization or smoothing methods.

Event driven methods (Leine and Nijmeijer, 2004) use classical integration methods between two successive events (switches between two different modes) when a system behaves smoothly. The integration stops if the event is detected. Then the system may undergo a step change and the next mode is determined. Special rules for the system change can be constructed in order to avoid inconsistency of the solution mentioned above. Kudra and Awrejcewicz (2012a) developed an event driven simulation algorithm of a mechanical system with circular frictional contact with a uniform contact pressure distribution and the Coulomb friction law. The scheme uses approximations of the integral friction model for both the fully developed sliding and stick phase (for determination of the end of the stick mode), but different values of static and (constant) dynamic friction coefficients are used. The combined translational and rotational stick-slip oscillations are presented.

Time-stepping methods are special numerical schemes which do not require detection of the events (Moreau, 1988; Stewart and Trinkle, 1996; Jean, 1999; Awrejcewicz and Lamarque, 2003). Some authors (Leine and Glocker, 2003; Möller *et al.*, 2009) constructed such algorithms with appropriate approximations of the friction forces for a finite circular contact area with the Hertz stress distribution and Coulomb friction law on each element of the contact.

The regularization methods are modifications of the mathematical model leading to a lower degree of "non-smoothness" of the dynamical system. Particularly, they can result in a smooth dynamical system, allowing for the use of classical integration methods. In the case of dry friction modelling, a common approach is to replace the set-valued friction force in the stick mode by the force of action of a stiff spring with some saturation threshold, usually supplemented with additional damping elements or with additional state variables resulting in better description of the real phenomenon (Do *et al.*, 2007). In the instance of a one-dimensional dry friction problem (i.e. either pure translational or rotational relative displacement of the contact), one can encounter smooth approximations of the friction force, where the signum function is replaced by such functions like arctangent or hyperbolic tangent. If this function is multiplied by another expression describing the changes of the dynamic friction coefficient during motion, then the phenomenon when the friction coefficient decreases at the beginning of the movement can be modelled (Awrejcewicz and Olejnik, 2003; Pilipchuk and Tan, 2004; Awrejcewicz *et al.*, 2008).

The drawback of the above mentioned regularizations may be stiffness of the resulting ordinary differential equations. Sometimes they may change some properties of the model, especially may change properties or destroy the equilibrium related to the stick mode. Also, in some regularized models, the loos of stability of the equilibrium and occurrence of artificial oscillations is possibly. On the other hand, the regularizations in general decrease the risk of the occurrence of

problems with the solution inconsistency. In particular, if the friction force is not a discontinuous function of sliding velocity (it may be a non-smooth function), the system belongs to the above mentioned group (a) and the solution uniqueness and existence are guaranteed. There are many works in which the influence of the friction model on the properties of the resulting mechanical system, including stability and bifurcations of the related solutions, is investigated (Bogacz and Sikora, 1990; Sikora and Bogacz, 1993; Leine *et al.*, 2000).

In the case of combined translational and rotational relative displacement of a finite contact, there are smooth models developed in which singularities of the expressions are avoided by the addition of a small positive parameter in special places of approximations of the integral models (Kudra and Awrejcewicz, 2011b, 2012b). However, these constructions do not assume the possibility for the friction coefficient to decrease in the beginning of slip. Stamm and Fidlin (2007, 2008) developed a regularized two-dimensional model based on the elastic-plastic theory and being a generalization of similar approaches for one-dimensional contact. It requires, however, discretization of the contact area (in contrast to the other above-referred models for two-dimensional contact), leading to much higher computational cost.

In this paper, we present smooth approximations of the friction force and torque appearing between two bodies contacting on a plane contact area of an arbitrary shape. They are applied to a special mechanical system in which combined translational and rotational stick-slip oscillations appear and the results are compared to those obtained by the event-driven numerical algorithm (Kudra and Awrejcewicz, 2012a). A part of the present work was previously presented in a shortened version (Kudra and Awrejcewicz, 2011a).

2. Integral model of friction

Let us consider the plane contact area F whose dimensionless form is presented in Fig. 1a. The Cartesian coordinate system $Axyz$ is introduced, where the axes x and y lie in the contact plane. The dimensionless length is related to the real characteristic dimension of the contact $\widehat{a}$, therefore the dimensionless coordinates of the point situated on the contact plane are $x = \widehat{x}/\widehat{a}$ and $y = \widehat{y}/\widehat{a}$, where $\widehat{x}$ and $\widehat{y}$ are the corresponding real coordinates. The non-dimensional elementary friction force acting on the element dF of the contact area is defined as $d\mathbf{T} = d\widehat{\mathbf{T}}/(\mu\widehat{N})$, where $d\widehat{\mathbf{T}}_s$ is its real counterpart, $\widehat{N}$ is the real normal component of the total force of interaction between two bodies, while μ is the dry friction coefficient during slip. The moment of the force $d\mathbf{T}$ about the point A (center of contact) reads $d\mathbf{M} = \boldsymbol{\rho} \times d\mathbf{T} = d\widehat{\mathbf{M}}/(\widehat{a}\mu\widehat{N})$, where $d\widehat{\mathbf{M}}$ is the real counterpart of $d\mathbf{M}$. The dimensionless contact pressure distribution is defined as $\sigma(x,y) = \widehat{\sigma}(x,y)\widehat{a}^2/\widehat{N}$, where $\widehat{\sigma}(x,y)$ is the real pressure. For the purpose of compatibility with the dimensionless model of the mechanical system presented in Section 5, we additionally introduce the dimensionless time $t = \alpha\widehat{t}$, where $\widehat{t}$ denotes its real counterpart.

It is assumed that the contact F can only operate in the two modes: the stick and the fully developed sliding (the transition between these two modes is infinitely short). During the sliding, local relative motion of the contacting bodies can be assumed as plane motion of the rigid body. Moreover, we assume that the spatial Coulomb friction law is valid on each element dF

$$d\mathbf{T} \in \begin{cases} -\sigma(x,y)\dfrac{\mathbf{v}_P}{\|\mathbf{v}_P\|}dF & \text{for} \quad \mathbf{v}_P \neq \mathbf{0} \\ \{\mathbf{u} \in \mathbb{R}^2 : \ \|\mathbf{u}\} \leqslant \eta\sigma(x,y)dF\} & \text{for} \quad \mathbf{v}_P = \mathbf{0} \end{cases} \tag{2.1}$$

where η is the ratio of the static friction coefficient to the dynamic one, and $\mathbf{v}_P$ is velocity of the element dF (see Fig. 1b).It is *a priori* assumed that the elementary friction force $d\mathbf{T}$ as well as the relative sliding velocity $\mathbf{v}_P$ lie in the plane of the contact F, so the problem described by Eq. (2.1) is in fact the two-dimensional one.

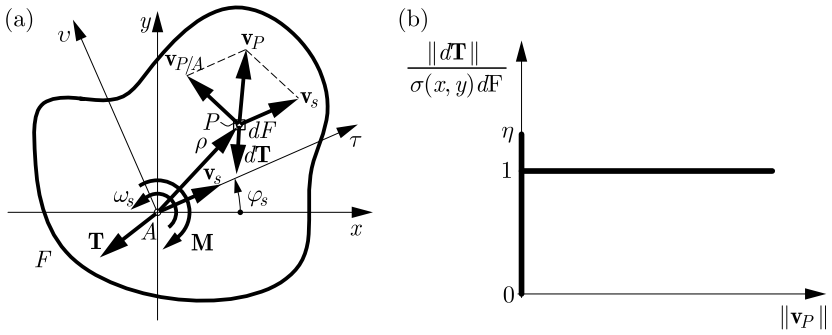

Fig. 1. The plane contact area (a) and the magnitude of the elementary friction force as a function of the magnitude of relative velocity (b)

The system of elementary friction forces can be reduced to the force $\mathbf{T} = T_x\mathbf{e}_x + T_y\mathbf{e}_y = T_\tau\mathbf{e}_\tau + T_\upsilon\mathbf{e}_\upsilon$ acting at the point A and the corresponding moment $\mathbf{M} = M\mathbf{e}_z$, where $\mathbf{e}_x$, $\mathbf{e}_y$, $\mathbf{e}_z$, $\mathbf{e}_\tau$ and $\mathbf{e}_\upsilon$ are the unit vectors of the corresponding axes.

During the slip mode, relative motion of the contact area is described by the use of the following quantities: $\mathbf{v}_s = \widehat{\mathbf{v}}_s/(\alpha\widehat{a}) = v_{sx}\mathbf{e}_x + v_{sy}\mathbf{e}_y = v_s\mathbf{e}_\tau$ – dimensionless linear velocity of the pole A, $\boldsymbol{\omega}_s = \widehat{\boldsymbol{\omega}}_s/\alpha = \omega_s\mathbf{e}_z$ – dimensionless angular velocity of the contact ($\widehat{\mathbf{v}}_s$ and $\widehat{\boldsymbol{\omega}}_s$ denote the corresponding real counterparts). Then the components of the friction force and moment can be obtained by the use of the following integrals

$$
\begin{aligned}
T_x &= -T_{sx}(\theta_s,\varphi_s) = -\iint_F \sigma(x,y)\frac{\cos\theta_s\cos\varphi_s - y\sin\theta_s}{\sqrt{(\cos\theta_s\cos\varphi_s - y\sin\theta_s)^2 + (\cos\theta_s\sin\varphi_s + x\sin\theta_s)^2}}\,dx\,dy\\
T_y &= -T_{sy}(\theta_s,\varphi_s) = -\iint_F \sigma(x,y)\frac{\cos\theta_s\cos\varphi_s + x\sin\theta_s}{\sqrt{(\cos\theta_s\cos\varphi_s - y\sin\theta_s)^2 + (\cos\theta_s\sin\varphi_s + x\sin\theta_s)^2}}\,dx\,dy\\
M &= -M_s(\theta_s,\varphi_s) = -\iint_F \sigma(x,y)\frac{(x^2+y^2)\sin\theta_s + x\cos\theta_s\sin\varphi_s - y\cos\theta_s\cos\varphi_s}{\sqrt{(\cos\theta_s\cos\varphi_s - y\sin\theta_s)^2 + (\cos\theta_s\sin\varphi_s + x\sin\theta_s)^2}}\,dx\,dy
\end{aligned}
\tag{2.2}
$$

where the angles θ_s and φ_s are defined in such a way, that

$$
\begin{aligned}
&v_s = \lambda_s\cos\theta_s \qquad \omega_s = \lambda_s\sin\theta_s \qquad \lambda_s = \sqrt{v_s^2+\omega_s^2}\\
&v_{sx} = v_s\cos\varphi_s \qquad v_{sy} = v_s\sin\varphi_s
\end{aligned}
\tag{2.3}
$$

The signs of the functions T_{sx}, T_{sy} and M_s are changed in order to simplify the further notation.

Then the full model of the friction forces can be defined as

$$
\begin{bmatrix} T_x \\ T_y \\ M \end{bmatrix} \in \begin{cases} -\begin{bmatrix} T_{sx}(\theta_s,\varphi_s) \\ T_{sy}(\theta_s,\varphi_s) \\ M_s(\theta_s,\varphi_s) \end{bmatrix} & \text{for} \quad \lambda_s > 0 \\ \{\mathbf{u}^3 \in \mathbb{R}^3 :\ \xi_{s'}(\mathbf{u}) \leqslant \eta\} & \text{for} \quad \lambda_s = 0 \end{cases}
\tag{2.4}
$$

where the bottom part of the expression concerns the stick mode. In this case the scalar function $\xi_{s'}(\mathbf{u}) \geqslant 0$ is defined as a part of the solution $(\xi_{s'}, \theta_{s'}, \varphi_{s'})$ to the following set of algebraic equations

$$
\mathbf{u} = -\xi_{s'}\begin{bmatrix} T_{sx}(\theta_{s'},\varphi_{s'}) \\ T_{sy}(\theta_{s'},\varphi_{s'}) \\ M_s(\theta_{s'},\varphi_{s'}) \end{bmatrix}
\tag{2.5}
$$

In Eq. (2.5), the angles $\theta_{s'}$ and $\varphi_{s'}$ can be interpreted in such a way that $\lambda_{s'}\cos\theta_{s'}\cos\varphi_{s'} = v_{s'x}$, $\lambda_{s'}\cos\theta_{s'}\sin\varphi_{s'} = v_{s'y}$ and $\lambda_{s'}\sin\theta_{s'} = \omega_{s'}$ ($\lambda_{s'} > 0$) are the components of virtual (possible sliding) in the event that the friction coefficient is sufficiently small. The above construction of the part of the model concerning the stick phase is motivated by the fact that during the stick mode the components of the friction force and moment (T_x, T_y, M) lie inside the zone bounded by a surface parametrically described by the functions $T_x = -\eta T_{sx}(\theta_s, \varphi_s)$, $T_y = -\eta T_{sy}(\theta_s, \varphi_s)$ and $M = -\eta M_s(\theta_s, \varphi_s)$. Since this zone is convex, there always exists one solution to equations (2.4) for $\xi_{s'} \geqslant 0$. The solution to Eq. (2.5) can be obtained numerically by the use of Newtons' method using a proper starting point. Then the first component of the solution $(\xi_{s'}, \theta_{s'}, \varphi_{s'})$ is used for detection of the possible end of the stick mode for $\xi_{s'}(\mathbf{u}) = \eta$. The two remaining components $(\theta_{s'}, \varphi_{s'})$ define the direction of slip in the beginning of the possible sliding. The criterion $\xi_{s'}(\mathbf{u}) = \eta$ can also be interpreted as the yield surface.

3. Approximations of the integral model of sliding friction

An exact integral model of friction forces (2.2) is computationally expensive and inconvenient for use in numerical simulations. Kudra and Awrejcewicz (2013) proposed different families of its approximations. Some of them can be presented in the following form

$$f^{(I_n)}(\theta_s, \varphi_s) = \frac{\sum\limits_{i=0}^{n} a_{f,i}\cos^{n-i}\theta_s \sin^i\theta_s}{\Big(|\cos\theta_s|^{mn} + b^m|\sin\theta_s|^{mn}\Big)^{m^{-1}}} \tag{3.1}$$

where $f = T_{sx}$, T_{sy}, M_s, and n is the order of the approximation. For the assumed model of the contact pressure distribution $\sigma(x, y)$, the functions $a_{f,i} = a_{f,i}(\varphi_s, \operatorname{sgn}(\cos\theta_s), \operatorname{sgn}(\sin\theta_s))$ (it occurs that for an even number n they do not depend on signs of $\cos\theta_s$ and $\sin\theta_s$) are found in such a way, that the following conditions are fulfilled

$$\begin{aligned} &\frac{\partial^i f^{(I_n)}}{\partial\cos^i\theta_s} = \frac{\partial^i f}{\partial\cos^i\theta_s} \qquad \text{for} \quad \cos\theta_s = 0 \quad \text{and} \quad i = 0, 1, \ldots, n_1 \\ &\frac{\partial^i f^{(I_n)}}{\partial\sin^i\theta_s} = \frac{\partial^i f}{\partial\sin^i\theta_s} \qquad \text{for} \quad \sin\theta_s = 0 \quad \text{and} \quad i = 0, 1, \ldots, n_2 \end{aligned} \tag{3.2}$$

where $n_1 + n_2 = n - 1$. The other constants $m \geqslant 0$ and $b \geqslant 0$ do not influence conditions (3.2) and they can be found in the process of optimization of fitting the approximate model to the integral components, or identified experimentally.

Taking into account relations (2.3), approximations (3.1) take the form as follows

$$f^{(I_n)}(v_s, \omega_s, \varphi_s) = \frac{\sum\limits_{i=0}^{n} a_{f,i} v_s^{n-i}\omega_s^i}{\Big(|v_s|^{mn} + b^m|\omega_s|^{mn}\Big)^{m^{-1}}} \tag{3.3}$$

For $n_1 = 0$, $n_2 = 0$ ($n = 1$), one gets the following form of the approximation

$$\begin{aligned} T_{sx}^{(I_{0,0})} &= \frac{v_{sx} - bc_{0,1,1}^{(x,y)}\omega_s}{\Big(|v_s|^m + b^m|\omega_s|^m\Big)^{m^{-1}}} \qquad T_{sy}^{(I_{0,0})} = \frac{v_{sy} + bc_{1,0,1}^{(x,y)}\omega_s}{\Big(|v_s|^m + b^m|\omega_s|^m\Big)^{m^{-1}}} \\ M_s^{(I_{0,0})} &= \frac{bc_{0,0,-1}^{(x,y)}\omega_s - c_{0,1,0}^{(x,y)}v_{sx} + c_{1,0,0}^{(x,y)}v_{sy}}{\Big(|v_s|^m + b^m|\omega_s|^m\Big)^{m^{-1}}} \end{aligned} \tag{3.4}$$

where

$$c_{i,j,k}^{(x,y)} = \iint\limits_F x^i y^j (x^2+y^2)^{-\frac{k}{2}} \sigma(x,y)\, dx\, dy$$

and the alternative notation $f^{(I_{n1,n2})}$ have been introduced.

For a circularly symmetric contact pressure distribution $T_\upsilon = 0$, we use notation $T_s = T_{s\tau} = -T_\tau$. In this case, we can also write that $T_{sx} = T_s \cos\varphi_s$ and $T_{sy} = T_s \sin\varphi_s$. Now $c_{0,1,1}^{(x,y)} = c_{1,0,1}^{(x,y)} = c_{0,1,0}^{(x,y)} = c_{1,0,0}^{(x,y)} = 0$, and approximations (3.4) take the following form

$$T_s^{(I_{0,0})} = \frac{v_s}{\left(|v_s|^m + b^m|\omega_s|^m\right)^{m^{-1}}} \qquad M_s^{(I_{0,0})} = \frac{bc_{0,0,-1}^{(x,y)}\omega_s}{\left(|v_s|^m + b^m|\omega_s|^m\right)^{m^{-1}}} \tag{3.5}$$

where $T_s^{(I_{0,0})}$ is the approximation of T_s ($T_{sx}^{(I_{0,0})} = T_s^{(I_{0,0})}\cos\varphi_s$ and $T_{sy}^{(I_{0,0})} = T_s^{(I_{0,0})}\sin\varphi_s$).

4. Regularized model

In the special case of $\omega_s = 0$ or $\widehat{a} = 0$, models(2.2) and (3.3)-(3.5) are $T_s = T_s^{(I_n)} = \operatorname{sgn} v_s$ ($T_s = -T_\tau$, $T_\upsilon = 0$, $M_s = M_s^{(I_n)} = 0$). For the purpose of numerical simulations, often the regularization of the sign function is performed by the use of arctan or tanh functions (Awrejcewicz and Lamarque, 2003; Awrejcewicz and Olejnik, 2003; Kudra and Awrejcewicz, 2011b). We propose another way of regularization of the sign function

$$T_{s\varepsilon} = T_{s\varepsilon}^{(I_n)} = \frac{v_s}{\sqrt{v_s^2+\varepsilon^2}} \tag{4.1}$$

where ε is a small numerical parameter.

In order to model the stick-slip oscillations, when the static friction coefficient is higher than the corresponding coefficient during the slip, one can develop model (4.1) in the following way

$$T_{s\varepsilon_2} = T_{s\varepsilon_2}^{(I_n)} = v_s\left(\frac{1}{\sqrt{v_s^2+\varepsilon^2}} + \eta'\frac{\varepsilon^3}{(v_s^2+\varepsilon^2)^2}\right) \tag{4.2}$$

where the parameter η' is a certain function of the coefficient $\eta = \max|T_{s\varepsilon_2}|$. The function $\eta' = \eta'(\eta)$ does not depend on ε and can be approximated as $\eta' \approx -13.607 + 30.893\eta - 22.01\eta^2 + 5.878\eta^3$ for $\eta \in [1, 1.3]$ and $\eta' \approx -2.41 + 3.985\eta - 0.3581\eta^2 + 0.0493\eta^3$ for $\eta \in [1.3, 2.7]$, where the error is $|\Delta\eta| < 0.001$. Figure 2 exhibits the exemplary plots of model (4.2).

Trying to generalize the above results and applying them to model (3.3), we assume in what follows

$$f_{\varepsilon_2}^{(I_n)}(v_s,\omega_s,\varphi_s) = \sum_{i=0}^{n} a_{f,i} v_s^{n-i}\omega_s^i\left(\frac{1}{\sqrt{\lambda_{sb}^2+\varepsilon^2}} + \eta'\frac{\varepsilon^3}{(\lambda_{sb}^2+\varepsilon^2)^2}\right) \tag{4.3}$$

where

$$\lambda_{sb} = \left(|v_s|^{mn} + b^m|\omega_s|^{mn}\right)^{m^{-1}}$$

In the special case of $n = 1$ ($n_1 = 0$, $n_2 = 0$, see Eq. (3.4)), one gets

$$\begin{aligned} &T_{sx\varepsilon_2}^{(I_{0,0})} = (v_{sx} - b, c_{0,1,1}^{(x,y)}\omega_s)\lambda_{sb\varepsilon_2}^{(1)} \qquad T_{sy\varepsilon_2}^{(I_{0,0})} = (v_{sy} + bc_{1,0,1}^{(x,y)}\omega_s)\lambda_{sb\varepsilon_2}^{(1)} \\ &M_{s\varepsilon_2}^{(I_{0,0})} = (bc_{0,0,-1}^{(x,y)}\omega_s - c_{0,1,0}^{(x,y)}v_{sx} + c_{1,0,0}^{(x,y)}v_{sy})\lambda_{sb\varepsilon_2}^{(1)} \end{aligned} \tag{4.4}$$

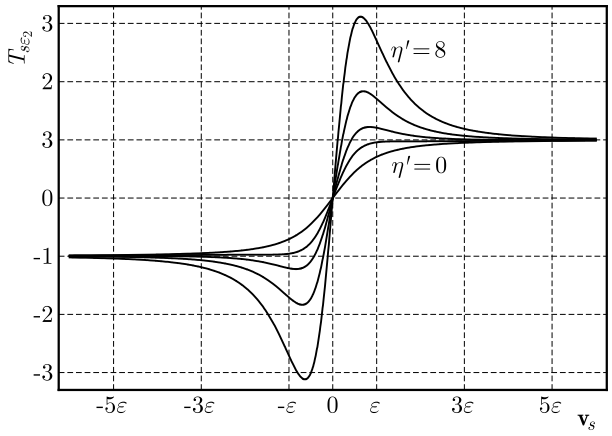

Fig. 2. The regularized model of friction (4.2) for $\eta'=0$, $\eta'=1$, $\eta'=2$, $\eta'=4$ and $\eta'=8$

where

$$\lambda^{(1)}_{sb\varepsilon_2}=\frac{1}{\sqrt{\left(|v_s|^m+b^m|\omega_s|^m\right)^{\frac{2}{m}}+\varepsilon^2}}+\eta'\frac{\varepsilon^3}{\left(\left(|v_s|^m+b^m|\omega_s|^m\right)^{\frac{2}{m}}+\varepsilon^2\right)^2}$$

For a circularly symmetric contact pressure distribution (see Eq. (3.5)) and $m=2$, relations (4.4) take the following form

$$\begin{aligned}T^{(I_{0,0})}_{s\varepsilon_2}&=v_s\left(\frac{1}{\sqrt{v_s^2+b^2\omega_s^2+\varepsilon^2}}+\eta'\frac{\varepsilon^3}{(v_s^2+b^2\omega_s^2+\varepsilon^2)^2}\right)\\ M^{(I_{0,0})}_{s\varepsilon_2}&=bc^{(x,y)}_{0,0,-1}\omega_s\left(\frac{1}{\sqrt{v_s^2+b^2\omega_s^2+\varepsilon^2}}+\eta'\frac{\varepsilon^3}{(v_s^2+b^2\omega_s^2+\varepsilon^2)^2}\right)\end{aligned}\tag{4.5}$$

5. Example of application

Here we recall the model of a mechanical system described and analysed in the work by Kudra and Awrejcewicz (2012a). The system, shown in Fig. 3, consists of a disk of radius $\widehat{r}=\widehat{a}$, mass $\widehat{m}$ and moment of inertia $\widehat{B}$. The disk is situated on a moving belt of velocity $\widehat{v}_b$. The position of the disk is defined by two co-ordinates: $\widehat{x}$ and φ describing the linear and angular positions, respectively. The disk is joined with the support by the use of four elasto-damping cords winding the disk as shown in Fig. 3, where $\widehat{k}_1/2$, $\widehat{k}_2/2$, $\widehat{c}_1/2$ and $\widehat{c}_2/2$ are the corresponding coefficients of stiffness and damping.

It is assumed that the contact pressure distribution is circularly symmetric and $\widehat{\mathbf{T}}=\mu\widehat{N}T\mathbf{e}_\tau$ ($T=T_\tau=T_x$, $T_v=T_y=0$) as well as $\widehat{\mathbf{M}}=\mu\widehat{N}\widehat{r}M\mathbf{e}_z$. Dynamics of the system is then governed by the following non-dimensional equations

$$\begin{bmatrix}1&0\\0&m\end{bmatrix}\begin{Bmatrix}\ddot{x}\\\ddot{\varphi}\end{Bmatrix}+\begin{bmatrix}c&c_{12}\\c_{12}&c\end{bmatrix}\begin{Bmatrix}\dot{x}\\\dot{\varphi}\end{Bmatrix}+\begin{bmatrix}1&k_{12}\\k_{12}&1\end{bmatrix}\begin{Bmatrix}x\\\varphi\end{Bmatrix}=\begin{Bmatrix}\Gamma\\\Omega\end{Bmatrix}\tag{5.1}$$

where the symbol $(\dot{\bullet})$ stands for derivative with respect to the non-dimensional time t.

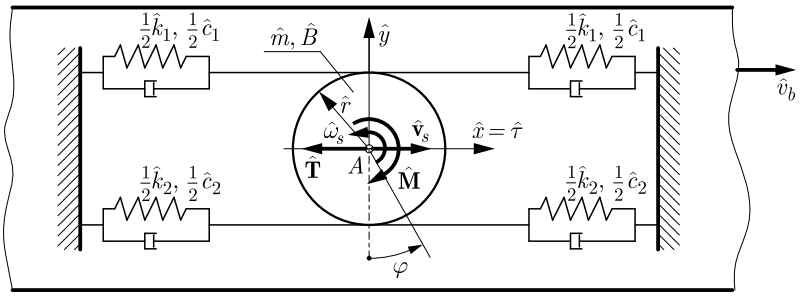

Fig. 3. The investigated mechanical system

The dimensionless variables used in Eq. (5.1) are defined in the following way

$$\begin{aligned} &x=\frac{\widehat{x}}{\widehat{r}} \qquad m=\frac{\widehat{B}}{\widehat{m}\widehat{r}^2} \qquad k_{12}=\frac{\widehat{k}_2-\widehat{k}_1}{\widehat{k}_1+\widehat{k}_2} \qquad \Gamma=\overline{\mu}T \qquad \Omega=\overline{\mu}M \\ &c=\frac{\widehat{c}_1+\widehat{c}_2}{\sqrt{\widehat{m}(\widehat{k}_1+\widehat{k}_2)}} \qquad c_{12}=\frac{\widehat{c}_2-\widehat{c}_1}{\sqrt{\widehat{m}(\widehat{k}_1+\widehat{k}_2)}} \qquad v_b=\frac{\widehat{v}_b}{\alpha\widehat{r}} \qquad t=\alpha\widehat{t} \end{aligned} \tag{5.2}$$

where

$$\alpha=\sqrt{\frac{\widehat{k}_1+\widehat{k}_2}{\widehat{m}}} \qquad \overline{\mu}=\frac{\mu\widehat{m}g}{\widehat{r}(\widehat{k}_1+\widehat{k}_2)}$$

and where Γ and Ω are the non-dimensional friction force and moment, respectively. Since $v_s=\alpha^{-1}\widehat{r}^{-1}\widehat{v}_s$ and $\omega_s=\alpha^{-1}\widehat{\omega}_s$, we get $v_s=\dot{x}-v_b$ and $\omega_s=\dot{\varphi}$, where $\dot{x}$ and $\dot{\varphi}$ are the dimensionless velocities of the disk.

In the work by Kudra and Awrejcewicz (2012a), a special event-driven scheme for numerical solution of equations (5.1) with the set-valued elements Γ and Ω was developed. The solution is composed of segments obtained by the use of classical integration methods for stick or sliding modes. Each segment starts and ends with the events, i.e. switches between the two successive modes which are detected during simulation. The integral model of friction used for simulation of the sliding mode as well as detection of the end of the stick mode (see Section 2) is approximated by the use of Eq. (3.5) for $c^{(x,y)}_{0,0,-1}=2/3$ (uniform contact pressure distribution), $m=2$ and $b=1$.

In the present work, we test simulation of the above presented dynamical system using the regularized model of friction (4.5). Figure 4 exhibits two examples of periodic stick-slip attractors obtained for the following parameters of the system: $m=90$, $k_{12}=0.85$, $c=10^{-4}$, $c_{12}=0$, $v_b=0.15$, $\overline{\mu}=5$. The friction coefficient during the stick mode is defined by the use of $\eta=4.98$ ($\eta'=13.7627$) for the first attractor (a)-(b) and $\eta=2.7$ ($\eta'=6.7627$) for the second orbit (c)-(d). Each attractor is obtained two times through the event-driven scheme (Kudra and Awrejcewicz, 2012a) and presented in the current work as a regularized model, and then plotted two times. Since there is no visible difference between them (the plots cover each other), one can conclude that the proposed smooth model of friction works correctly. In the event-driven numerical algorithm, the threshold of detection of the singularity $\lambda_s=0$ during the sliding mode equals 10^{-7}. For integration of the differential equations between the two successive events, we use the explicit Runge-Kutta (4,5) formula (Dormand-Prince) with relative and absolute tolerances equal to 10^{-10}. In the case of integration of stiff differential equations with the regularized friction model, in which it is assumed $\varepsilon=10^{-5}$, we use a multistep implicit scheme based on numerical differential formulas with relative and absolute tolerances set to 10^{-10}. The value of the parameter ε should be chosen based on numerical experiments.

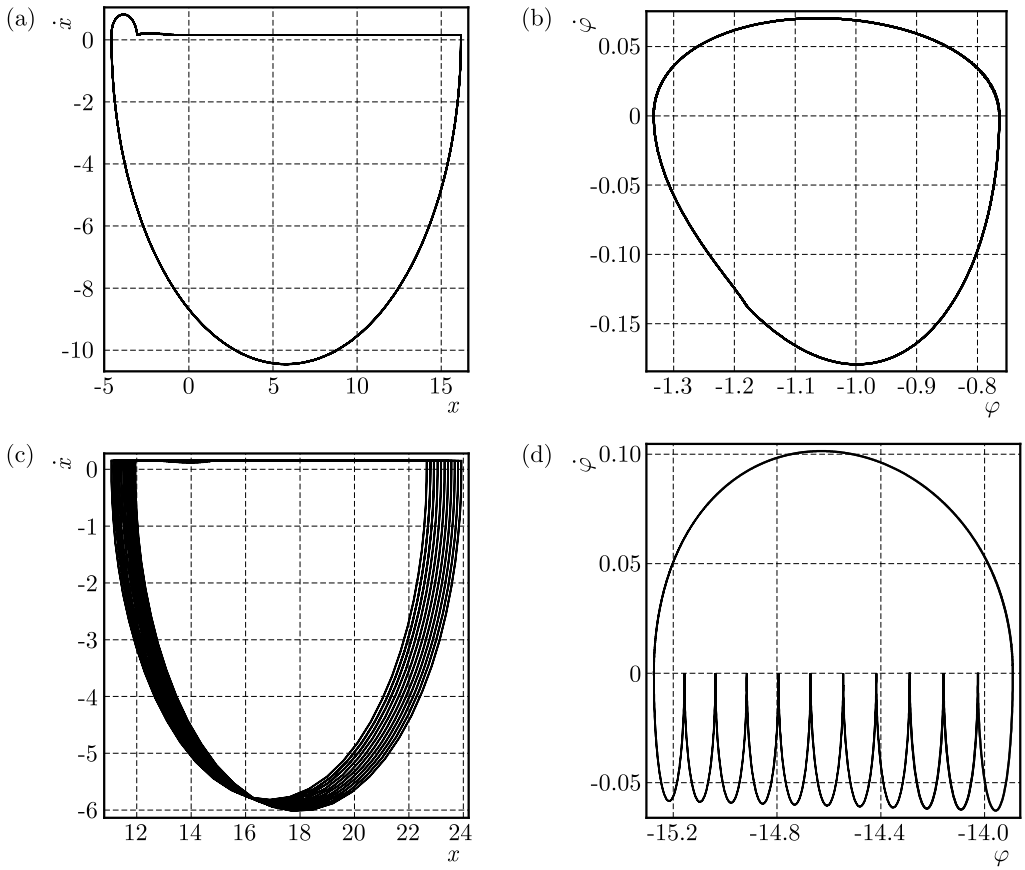

Fig. 4. Two examples of periodic attractors for $\eta = 4.98$ (a)-(b) and $\eta = 2.7$ (c)-(d) obtained from two different methods: event-driven scheme (Kudra and Awrejcewicz, 2012a) and regularization of the friction model

6. Concluding remarks

In the work, a new kind of regularized approximate model of the coupled friction force and torque for the general plane contact has been presented and tested. The developed here model approximates the "exact" integral model in which the classical Coulomb friction law on each element of the contact area and sudden switches between the stick mode and the fully developed sliding are assumed.

The main properties of the new model are: i) avoidance of the problem of time consuming integration over the contact area at each time step of integration of the differential equations, ii) avoidance of singularity problems or set-valued friction forces in the original model of friction and possibility of the use of classical algorithms for integration of the differential equations, iii) possibility to model static friction higher than the sliding one and stick-slip oscillations, iv) parameters of the approximate model can be found based on optimization of the fitting to the integral model or can be identified experimentally (independently of the integral friction model). The above pointed out properties can be understood as advantages. The new model possesses also a drawback, i.e. it makes the resulting differential equations stiff and thus requires special numerical methods.

The proposed model of friction has been applied to the modelling and simulation of a special mechanical system in which two-dimensional (linear and rotational) stick slip oscillation occur. The comparison of the results with those obtained by the event-driven method leads to the conclusion that the new model operates correctly.

Acknowledgments

This work has been supported by the Polish National Science Centre, MAESTRO 2, No. 2012/04/A/ST8/00738. A part of this work was presented at the 11th Conference on Dynamical SystemsTheory and Applications, December 5-8, 2011, Łódź, Poland.

References

1. Acary V., Brogliato, B., 2010, *Numerical Methods for Nonsmooth Dynamical Systems*, Springer
2. Awrejcewicz J., Lamarque C.-H., 2003, *Bifurcation and Chaos in Nonsmooth Mechanical Systems*, World Scientific, Singapore
3. Awrejcewicz J., Olejnik P., 2003, Stick-slip dynamics of a two-degree-of-freedom system, *International Journal of Bifurcation and Chaos*, **13**, 4, 843-861
4. Awrejcewicz J., Supeł B., Lamarque C.-H., Kudra G., Wasilewski G., Olejnik P., 2008, Numerical and experimental study of regular and chaotic motion of triple physical pendulum, *International Journal of Bifurcation and Chaos*, **18**, 10, 2883-2915
5. Bogacz, R., Sikora, J., 1990, On stability of periodic solutions of a discrete system with many degrees of freedom and dry friction, *Proceedings of the Vibrations in Physical Systems*, 57-59, Poznan, Poland
6. Contensou P., 1963,Couplage entre frottement de glissement et de pivotement dans la théorie de la toupe, [In:] *Kreiselprobleme Gyrodynamic*, Ziegler H. (Ed.), *IUTAM Symposium*, Celerina, 1962, Springer-Verlag, Berlin, 201-216
7. Do N.B., Ferri A.A., Bauchau O.A., 2007, Efficient simulation of a dynamic system with LuGre friction, *Journal of Computational and Nonlinear Dynamics*, **2**, 4, 281-289
8. Filippov A.F., 1964, Differential equations with discontinuous right-hand side, *American Mathematical Society Translations*, **42**, 199-231
9. Filippov A.F., 1988, *Differential Equations with Discontinuous Right-Hand Sides*, Kluwer Academic, Dordrecht
10. Génot F., Brogliato B., 1999, New results on Painlevé Paradoxes, *European Journal of Mechanics – A/Solids*, **18**, 653-677
11. Howe R.D., Cutkosky M.R., 1996, Practical force-motion models for sliding manipulation, *International Journal of Robotics Research*, **15**, 6, 557-572
12. Jean M., 1999, The non-smooth contact dynamics method, *Computer Methods in Applied Mechanics and Engineering*, **177**, 235-257
13. Jellet J.H., 1872, *Treatise on the Theory of Friction*, Hodges, Foster and Co, Dublin
14. Kireenkov A.A., 2008, Combined model of sliding and rolling friction in dynamics of bodies on a rough plane, *Mechanicsof Solids*, **43**, 3, 412-425
15. Kosenko I., Aleksandrov E., 2009, Implementation of the Contensou-Erisman model of friction in frame of the Hertz contact problem on Modelica, *7th Modelica Conference*, Como, Italy, 288-298
16. Kudra G., Awrejcewicz J., 2011a, Regularized model of coupled friction force and torque for circularly-symmetric contact pressure distribution, *Proceedings of the 11th Conference on Dynamical Systems – Theory and Applications*, 353-358
17. Kudra G., Awrejcewicz J., 2011b, Tangenshyperbolicus approximations of the spatial model of friction coupled with rolling resistance, *International Journal of Bifurcation and Chaos*, **21**, 10, 2905-2917
18. Kudra G., Awrejcewicz J., 2012a, Bifurcational dynamics of a two-dimensional stick-slip system, *Differential Equations and Dynamical Systems*, **20**, 3, 301-322

19. Kudra G., Awrejcewicz J., 2012b, Celtic stone dynamics revisited using dry friction and rolling resistance, *Shock and Vibration*, **19**, 5, 1115-1123

20. Kudra G., Awrejcewicz J., 2013, Approximate modelling of resulting dry friction forces and rolling resistance for elliptic contact shape, *European Journal of Mechanics – A/Solids*, **42**, 358-375

21. Leine R.I., van Campen D.H., Van De Vrande B.L., 2000, Bifurcations in nonlinear discontinuous systems, *Nonlinear Dynamics*, **23**, 2, 105-164

22. Leine R.I., Glocker Ch., 2003, A set-valued force law for spatial Coulomb-Contensou friction, *European Journal of Mechanics – A/Solids*, **22**, 2, 193-216

23. Leine R.I., Nijmeijer H., 2004, *Dynamics and Bifurcations of Non-smooth Mechanical Systems*, Springer

24. Moreau J.J., 1988, Unilateral contact and dry friction in finite freedom dynamics, *Nonsmooth Mechanics and Applications*, 1-82, Springer-Verlag, Wien

25. Möller M., Leine R.I., Glocker Ch., 2009, An efficient approximation of orthotropic set-valued laws of normal cone type, *Proceedings of the 7th EUROMECH Solid Mechanics Conference*, Lisbon, Portugal

26. Painlevé P., 1895, *Leçon sur le frottement*, Hermann, Paris

27. Pilipchuk V.N., Tan C.A., 2004, Creep-slip capture as a possible source of squeal during decelerated sliding, *Nonlinear Dynamics*, **35**, 259-285

28. Sikora, J., Bogacz, R., 1993, On dynamics of several degrees of freedom system, *ZAMM – Journal of Applied Mathematics and Mechanics*, **73**, T118-T122

29. Stamm W., Fidlin A., 2007, Regularization of 2D frictional contacts for rigid body dynamics, *IUTAM Symposium on Multiscale Problems in Multibody System Contacts*, 291-300, Springer

30. Stamm W., Fidlin A., 2008, Radial dynamics of rigid friction disks with alternating sticking and sliding, *Proceedings of the 6th EUROMECH Nonlinear Dynamics Conference*, Saint Perersburg

31. Stewart D., Trinkle J.C., 1996, An implicit time-stepping scheme for rigid body dynamics with inelastic collisions and Coulomb friction, *International Journal of Numerical Methods in Engineering*, **39**, 2673-2691

32. Zhuravlev V.P., 1998, The model of dry friction in the problem of the rolling of rigid bodies, *Journal of Applied Mathematics and Mechanics*, **62**, 5, 705-710

33. Zhuravlev V.P., Kireenkov A.A., 2005, Padé expansions in the two-dimensional model of Coulomb friction, *Mechanics of Solids*, **40**, 2, 1-10

Manuscript received January 29, 2015; accepted for print December 18, 2015

JOURNAL OF THEORETICAL AND APPLIED MECHANICS
54, 3, pp. 921-933, Warsaw 2016
DOI: 10.15632/jtam-pl.54.3.921

NUMERICAL AND EXPERIMENTAL ANALYSIS OF RESIDUAL STRESSES INDUCED IN METAL COATINGS THERMALLY DEPOSITED (HVOF) ON Al_2O_3 SUBSTRATES

Jolanta Zimmerman

Warsaw University of Technology, Institute of Mechanics and Printing, Warszawa, Poland

e-mail: jolz@wip.pw.edu.pl

The study is concerned with the modeling of residual stresses in thin coatings thermally deposited with a high speed on a substrate. The modeling includes two stages: solution of the particle-target impact problem using FEM and simulation of the spraying process with the use of a thermo-mechanical model in which the coating has been built layer-by-layer. The samples used in the calculations are comprised of Ti, Cu, and Ni coatings deposited on Al_2O_3 substrate by the HVOF method. The numerical model is verified experimentally by measuring the deflections of the samples after spraying, and measuring the stresses using the XRD method.

Keywords: metal coatings, Al_2O_3 substrate, thermal spraying, FEM simulation, residual stress

1. Introduction

Advanced ceramic materials are increasingly used in many industrial branches such as the aircraft, automotive, energy, and chemical industries. The industrial application of ceramics as electric insulators or substrates requires joining them with metals. One of the cheapest methods of joining ceramics with metals is thermal spraying (Chmielewski *et al.* 2013; Zimmerman *et al.*, 2013; Zimmerman, 2014). The high velocity oxy flame (HVOF) spray is a particle deposition process in which heated micro-size particles are propelled and deposited on a substrate at high speeds to form a thin layer of lamellar coating. The final stress state through the coating/substrate system is determined by superposition of stresses of different nature induced during the spray process: rapid cooling of the softened powder particles after their hitting the substrate and previously deposited sub-layer (quenching stresses), thermal mismatch between the substrate and the coating materials, stresses generated when the particles hit the substrate (peening stresses), and stresses induced during the final cooling of the entire system (Lyphout *et al.*, 2008). The unfavorable distribution of residual stresses in the coating as well as at the coating/substrate interface may adversely affect the service life of the ceramic/metal joint or the operational surface leading even to its delamination during exploitation (Hutchinson and Evans, 2002). Moreover, ceramic materials have low thermal conductivity and poor diffusivity, which constitutes a barrier to the flow of heat. In effect, high temporary temperature gradients may occur in the ceramic material resulting in the generation of thermal stresses and, in consequence, an increase in the risk of micro-cracking (Golanski, 1996).

There is a variety of methods used for estimating the residual stress state induced in the coating/substrate systems, such as experimental methods (Toparli *et al.*, 2007; Lyphout *et al.*, 2008; Luzin *et al.*, 2011), analytical methods (Stokes and Looney, 2003; Tsui and Clyne, 1997; Feng *et al.*, 2007), hybrid methods (Salbut *et al.*, 1999), and numerical models. Analytical methods are usually used for simple systems and do not take into account the plastic behavior of the metal. Some studies devoted to the numerical modeling of the residual

stress state in coating/substrate systems, often using the finite element method (FEM), considered axisymmetric (Wenzelburger *et al.*, 2004; Kamara and Davey, 2007; Toparli *et al.*, 2007) or plate models (Yilbas and Arif, 2007) with the coating modeled as a single layer and with stresses examined only when the entire system was cooled after the deposition of the coating. In other numerical studies, the growth of the sprayed coating was modeled by activating the successive sub-layers deposited on the substrate (Ng and Gan, 2005; Zimmerman *et al.*, 2013; Zimmerman, 2014). Still, other authors concentrate on the modeling of the impacts of individual particles on a metallic substrate (Bansal *et al.*, 2006; Lyphout *et al.*, 2008; Kim *et al.*, 2010) and on the effect of the impact velocity on the microstructure of the coating.

A description of the complex thermal spraying process in physical terms is difficult and the existing numerical models which describe the deposition of the coating and generation of residual stresses, require further improvements. These models take no account of how the magnitude of the final residual stresses depends on the mechanical stresses induced during the high-velocity impact of the coating particles. The present study considers this problem. The objective of this study is to evaluate the final residual stress distributions in the Ti, Ni, and Cu coatings deposited on an Al_2O_3 substrate by the HVOF method. The results of calculations have been verified by measuring experimentally the central deflections of the samples after they were cooled. The residual stresses have been found by using X-ray diffraction method.

Thin metallic layers formed on an Al_2O_3 substrate can serve as the aim of metallizing the ceramic surface or function as a transition layer in joining the ceramic with metals (Chmielewski *et al.*, 2013). They can also play the role of protective coatings against the action of environmental factors such as high temperatures, aggressive environments or mechanical action (Chmielewski and Golański, 2011).

2. Spraying process

The experiments include a deposition of titanium, copper, and nickel coatings on an Al_2O_3 substrate by the HVOF method using HV-50 system with JP-5000 torch. The process parameters are given in Table 1.

Table 1. The parameters of HVOF thermal spraying applied for coating Al_2O_3 ceramic with metals

Powder	Oxygen flow [l/h]	Kerosene flow [l/h]	Nitrogen flow [l/min]	Spraying distance [mm]
Ni	849	24	9.5	370
Cu	932	26.5	9.9	370
Ti	932	26.5	14	370

The starting materials are powders with a grain size between 0.04-0.05 mm. The Al_2O_3 substrates are circular plates 27 mm in diameter and 0.6 mm thick. The average thickness of the deposited coatings is $th_{\mathrm{Ti}} = 0.12$ mm, $th_{\mathrm{Ni}} = 0.13$ mm, and $th_{\mathrm{Cu}} = 0.1$ mm. Exemplary photographs of the microstructure of the Ti, and Cu coatings deposited on the Al_2O_3 substrate are shown in Fig. 1a and 1b, respectively. It can be seen that the coatings have a lamellar structure, which is a result of successive depositions of the individual sub-layers on the substrate. The porosity of the coatings is low and they well adhere to the substrate.

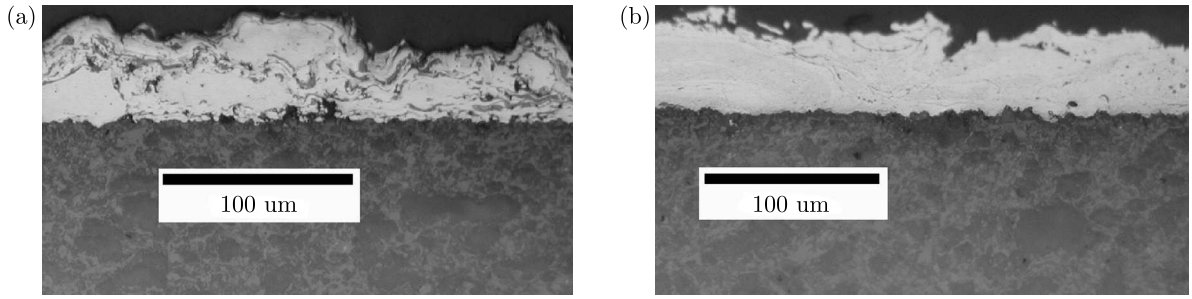

Fig. 1. Microstructure of: (a) the Ti coating (about 60 μm thick), (b) the Cu coating (about 50 μm thick) deposited on an Al_2O_3 substrate by the HVOF method

3. Modeling methods

In view of the complexity of the spraying process, certain physical simplifications have been assumed in the designing of the numerical model intended for the FE analysis of the residual stresses active in the coating/substrate system. The assumptions underlying the numerical model include:

- The droplet deposition process proceeds in two phases: impact of the particle and its spreading on the substrate. The duration of these two phases is much shorter than that necessary for the droplet to solidify and, thus, the initial spreading phase can be neglected (Amon *et al.*, 1996). This assumption decouples the problem from the fluid dynamics and permits it to be simplified to a thermo-mechanical problem. The time interval when the particles are in the impact, heating, and cooling phases is shorter by at least two orders of magnitude than the duration of the spraying cycle (Watanabe *et al.*, 1992). In effect, the next particles impinge on the previously deposited sub-layer when it is already solidified. The substrate and the earlier deposited sub-layers are modeled as being in the solid state with a defined temperature field, and their mechanical and physical properties depend on temperature.
- The high-velocity impact of the particles onto the substrate results in their substantial deformation and transforms 70% of their kinetic energy into heat energy. The particles are flattened and arranged approximately in a parallel layer structure, and during the successive passes of the torch, new particles are deposited on them.
- The contact between the substrate and the subsequently deposited sub-layers is ideal so as there are no thermal barriers between them.

The modeling of the residual stresses generated during the spraying process is divided into two stages. In the first stage the problem of the dynamic impact of spherical powder particles on the substrate is solved using FEM ADINA 8.6 software in the explicit dynamics mode. In the next modeling stage, the coating is built of successively grown 'discs' at time intervals defined by the spraying process parameters until the coating achieved the required thickness and, then, the entire coating/substrate system is cooled to room temperature. This problem is solved using ADINA 8.6 software in the thermo-mechanical mode. The flow chart of modeling the residual stresses induced in the coatings thermally sprayed on the substrate is shown in Fig. 2. As can be seen, the data calculated in the initial stage concerning the dynamic impact of the particle on the substrate, such as temperature, and the vertical deceleration of the particle are introduced at the appropriate calculation stages into the thermal and mechanical models.

During the coupled analysis, the coating is built step-by-step to the desired thickness, which is accompanied by the development of residual stresses in the coating/substrate system.

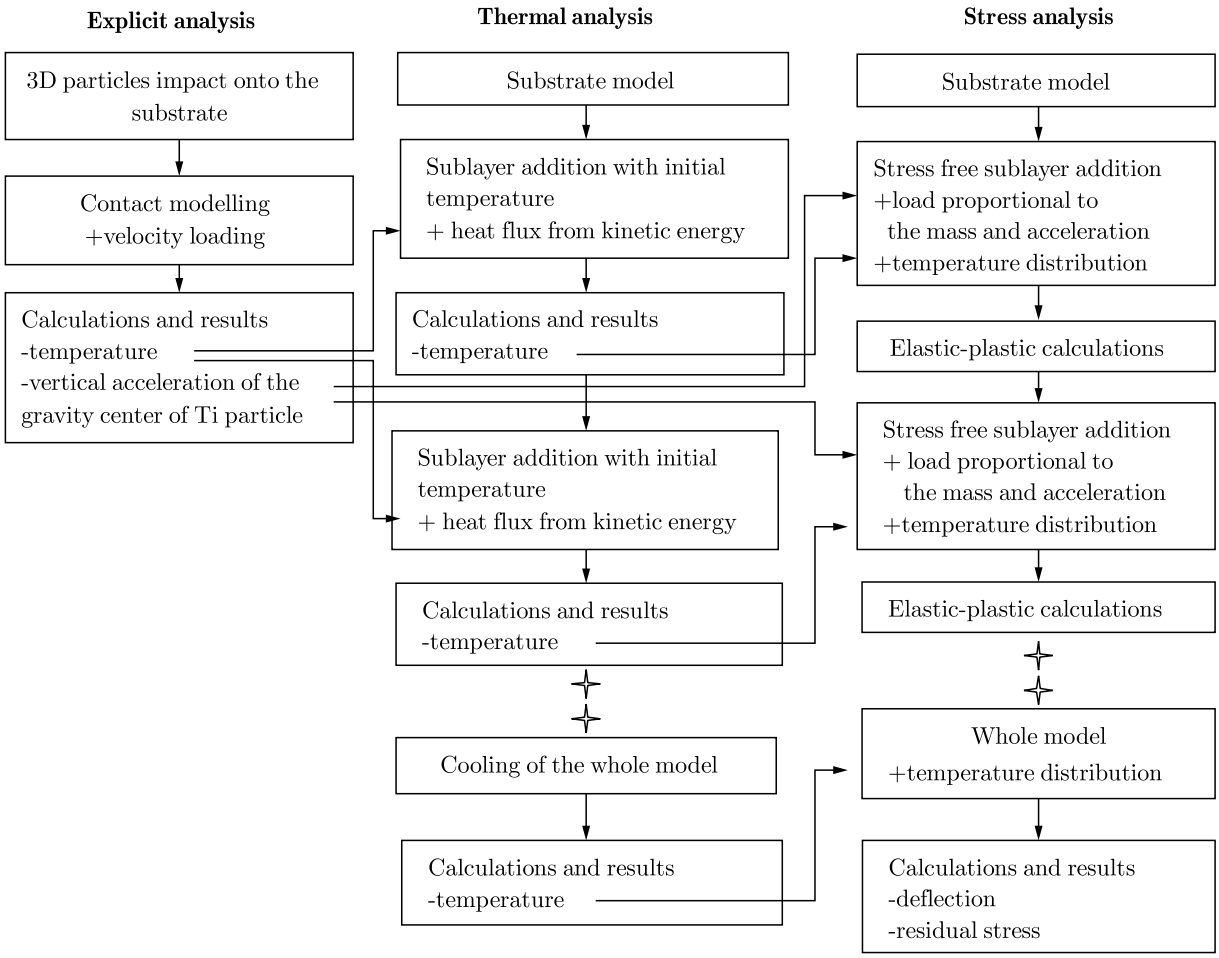

Fig. 2. Flow chart of the FEM simulation used for determining the residual stress distribution in HVOF-sprayed coatings

3.1. The particle impact model and calculation results

Despite their small masses, the particles hitting the substrate with a high velocity deform, to some extent, the previously deposited sub-layers, which generates a stress field and has a significant effect on the final residual stress state (Bansal *et al.*, 2006; Toparli *et al.*, 2007; Lyphout *et al.*, 2008). Therefore, the present study is focused on the modeling of the particle impact. Li *et al.* (2006) showed that during thermal spraying by the industrial HVOF method, the individual powder particles can be considered to be separated from one another and they do not coagulate during their flight. The spatial (3D) model used in the present study has been developed to simulate the deformation and changes in the velocity and acceleration of the individual spherical particles of the coating powder, which impinge on the substrate. During the deformation, the particles block one another forming thereby a flat splat almost parallel to the substrate. In the modeling of the dynamics of the particle motion, it is assumed for simplicity that the particles have the same velocity perpendicular to the substrate and, when hitting the substrate, they form a hexagonal configuration which ensures their most tight packing. The contact planes are situated in the model to block the successive rows of particles. The model utilized the planes of symmetry, which permitted reducing the size of the problem. A schematic representation of the section geometry together with the displacement-blocking planes and the entire FEM mesh are shown in Fig. 3. The numerical calculations have been made using ADINA 8.6 FEM software in the dynamics-explicit analysis mode. The impact velocity of the particles was 600 m/s as

estimated based on the process parameters and calculations reported by Li *et al.* (2006) for the powder with the particle diameter $d = 40\text{-}50\,\mu$m.

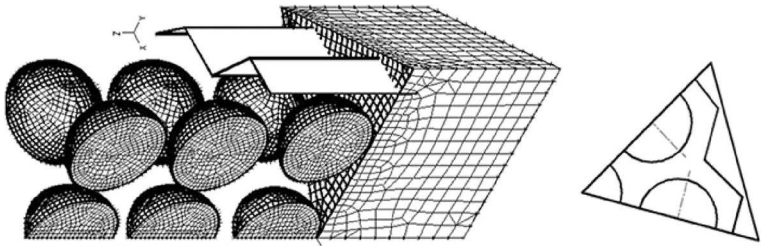

Fig. 3. Geometry and the final element mesh of the model representing the particles impact onto a substrate

Some exemplary calculation results obtained for Ti particles, which impinge on a ceramic substrate, are presented. The properties of titanium are taken to be those valid at a temperature of 300°C, and the elastic-plastic model of the material with the Young modulus 123800 MPa, yield stress 233 MPa, hardening modulus 600 MPa, and the specific gravity 4.54 g/cm^3. The ceramic substrate is modeled as an elastic material with the specific gravity 3.9 g/cm^3 and the Young modulus 318200 MPa. The model assumes that the particles are in contact with one another, with the substrate and with the blocking planes (40 contact pairs in total). The thickened mesh lines indicate the contact surfaces in Fig. 3.

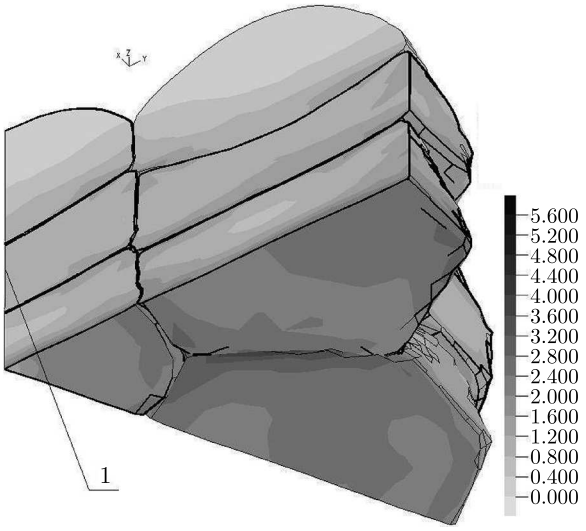

Fig. 4. Bands of the equivalent plastic strains in the titanium particles after their impact

Figure 4 shows the distribution of plastic deformations of Ti particles (which after impinging on the Al_2O_3 substrate form a sub-layer of the coating) after a time of 70 ns when their velocity decreased to zero. The maximum strains of 500% are located near the stiffer substrate and near the contact zone. The particles are flattened, come in contact with one another and fill the free spaces between them. The analysis reveals that after the impact of a particle 50 μm in diameter, the already-deposited particles which are in immediate contact with the substrate change their shapes into discs with a diameter of 12 μm. Figures 5a and 5b show the changes of the velocity and acceleration, respectively, of the center of mass of the Ti particle ('1' indicated in the Fig. 4) after its impact on the substrate. The plot of acceleration of the particle mass center, proportional to the derivative of the momentum, is obtained by double numerical differentiation of time-variation of the displacement. Upon the impact of a particle onto the Al_2O_3 substrate, its acceleration reaches a value of about $-36000\,\mu$m/s^2. The oscillations of the particle acceleration visible in

Fig. 5b are due to inhomogeneity of the deformation and vibrations induced by the high-velocity impact of the particle on the substrate accompanied by phenomena wavy in character.

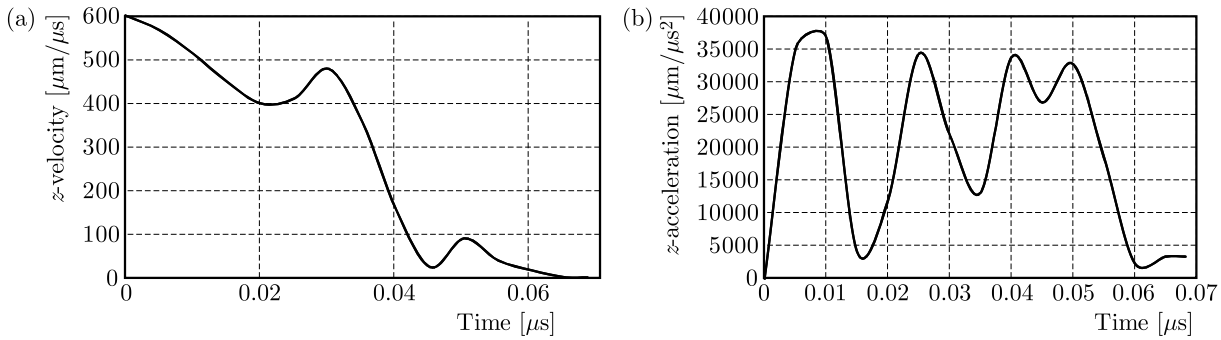

Fig. 5. FEM-calculated (a) velocity, (b) acceleration of the mass center of the centrally-positioned Ti particle after its impact onto the Al_2O_3 substrate

3.2. Thermo-mechanical model

The thermal spraying process is simulated using an axisymmetric model. The modeling is divided into several stages and the calculations conducted during each stage are based on the equations of transient heat flow. The layer deposition interval is taken to be 1s and has been estimated from the torch movements during the spraying process. The real coating is built of five sub-layers.

The boundary and initial conditions adopted in the thermal model are as follows. The heat exchange between the HVOF stream of the torch and the newly-deposited top sub-layers of the coating proceeds through convection. The convection coefficient is taken to be $h_b = 100\,\mathrm{Wm^{-2}K^{-1}}$ (Toparli *et al.*, 2007) and the air temperature from the side of the approaching particles to be $T_b = 150°\mathrm{C}$. The heat exchange between the bottom side of the substrate and the ambience proceeds through convection with the convection coefficient $h_a = 10\,\mathrm{Wm^{-2}K^{-1}}$. The ambient temperature is assumed to be $T_a = 25°\mathrm{C}$. The initial temperature of the individual coating sub-layers are for titanium $T_{init-\mathrm{Ti}} = 450°\mathrm{C}$ (Kim *et al.*, 2010), for nickel $T_{init-\mathrm{Ni}} = 400°\mathrm{C}$, and for copper $T_{init-\mathrm{Cu}} = 350°\mathrm{C}$. The interfaces between the substrate and the first-deposited sub-layer as well as between successive sub-layers are loaded with the heat flux q which acts for $t_q = 1\,\mu\mathrm{s}$ and is activated upon the appearance of the next new sub-layer. The heat flux is assumed to be such that it corresponds to the transformation of kinetic energy into heat energy at a spraying speed of 600 m/s. After achieving the required thickness of the coating, the entire system is cooled down to room temperature. Figure 6a shows a schematic physical and thermo-mechanical description of the HVOF process.

The problem of the temperature field induced in the thermally sprayed coatings has been solved using ADINA 8.6 FE thermal module. The mesh consists of 25480 4-node conducting elements for the substrate and coating materials, and 3640 2-node convection elements at the edges. The finest mesh has been introduced to each layer of the metal coating. The conductive elements of the newly deposited sub-layer and the convection elements of its upper surface are activated at the time intervals $t = 1\,\mathrm{s}$, while at the same time, the convection elements in-between sub-layers are deactivated. Hence, the temperature field induced in the spraying process is the problem with a moving boundary condition in which the outer surface of the coating grows at the time intervals dependent on the spraying frequency. Figure 6b presents a fragment of the mesh of the layer-by-layer model indicating the initial and boundary conditions upon the activation of the 5-th sub-layer.

The stress analysis (mechanical model) included a comparison between the results obtained for two different loads applied to the model. In the first case (FEM1), the load is assumed to

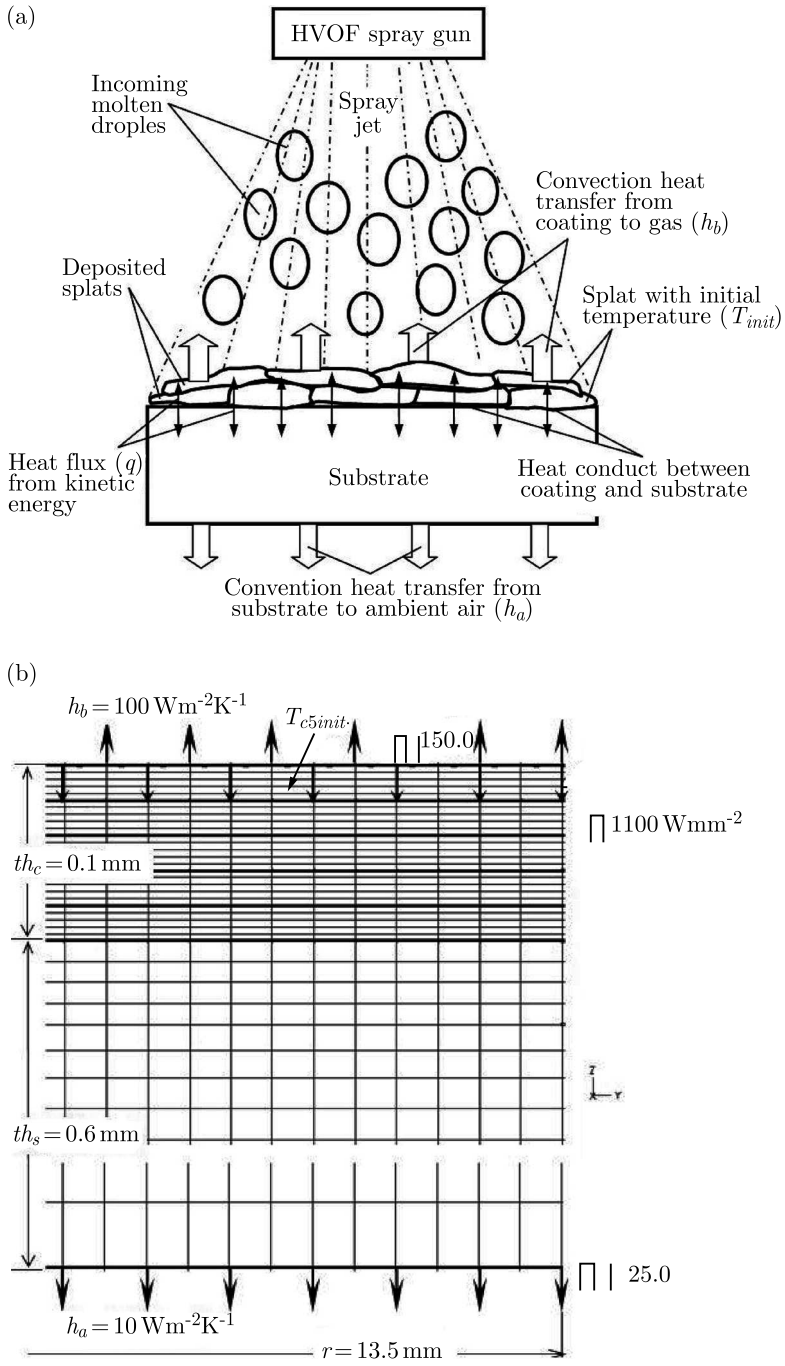

Fig. 6. Schematic physical and thermo-mechanical description of the HVOF process (a), part of the FEM mesh of the layer-by-layer model with the boundary conditions upon the activation of the 5-th sub-layer (b)

be the temperature field obtained in the solution of the problem of transient heat flow during the successive time increments in which current and stress-free sub-layers onto the initially stressed system have been added. In the other case (FEM2), the temperature field is added with a load (active for 0.1 μs) proportional to the mass and acceleration of each newly incoming sub-layer. The acceleration is estimated based on the time variation of the displacement of the center of mass of the centrally-positioned particle (point 1 indicated in Fig. 4), a diagram of which has been obtained from the solution to the particle impact dynamic problem. This approach enables taking into account the influence of the impact of coating particles on the

substrate and the earlier-deposited sub-layer on the final residual stress state. The magnitudes of particle impact pressure are assumed to be 170 MPa, 200 MPa and 300 MPa for systems with Ni, Cu and Ti coatings, respectively. In the modeling, it is assumed that behavior of the ceramic substrate is elastic, whereas the metallic materials are described by the elastic-plastic model. The temperature-dependent properties (specific heat capacity, thermal conductivity, Young's modulus, yield strength, hardening modulus, thermal expansion coefficient) for Ti, Ni, and Cu coatings and the Al_2O_3 substrate are presented in Table 2 based on data taken after Boyer *et al.* (1994), Dobrzanski (2002), Dorf (2004) and Goldsmith *et al.* (1961).

Table 2. Material properties of the substrate and coatings

	Ti					Al_2O_3 (substrate)				
T [°C]	27	127	227	327	427	27	127	227	327	427
C [Jkg^{-1}K^{-1}]	523	546	561	597	632	754	951	1005	1089	1130
k [Wm^{-1}K^{-1}]	21.9	21.0	20.4	19.7	19.4	34.6	25.1	19.0	14.7	11.2
E [GPa]	130	129	127	124	120	318.3	317	315	313	310
Y [MPa]	380	285	250	205	170	not considered (elastic model)				
E_t [MPa]	880	760	640	600	580	not considered (elastic model)				
α [10^{-6}K^{-1}]	8.4	8.7	9.1	9.4	9.7	5.9	6.5	7.1	7.6	8.0
	Ni					Cu				
T [°C]	27	127	227	327	427	27	127	227	327	427
C [Jkg^{-1}K^{-1}]	462	505	554	599	526	385	398	408	417	425
k [Wm^{-1}K^{-1}]	90.5	80.1	72.1	65.5	65.3	398	392	388	383	377
E [GPa]	208	204	197	190	183	130	128	124	119	112
Y [MPa]	150	157	145	143	120	210	205	195	140	85
E_t [MPa]	670	660	690	670	340	250	230	200	150	100
α [10^{-6}K^{-1}]	13.9	14.4	14.9	15.5	16.0	15.4	15.9	16.6	17.1	18.5

C – specific heat, k – thermal conductivity, α – CTE
E – Young's modulus, Y – yield strength, E_t – hardening modulus

4. Measurements of residual stresses

The samples, i.e. Al_2O_3 substrates with Ti, Ni, and Cu coatings, are deflected in various ways after thermal spraying. Their deflections are measured using a specially designed device with a digital dial gauge. The measurement is conducted at the center of the sample on the substrate side. The indication of the dial gauge has been calibrated to zero for each ceramic substrate before the deposition. Table 3 compares the deflections of the samples at their center between those measured and those calculated by FEM. The results appear to be in agreement within the limits of admissible error in case FEM2.

Table 3. The measured and calculated by FEM central deflection of analyzed samples

Coating	Mean coating thickness [mm]	Sample deflection [mm]		
		measured	calculated FEM1	calculated FEM2
Ti	0.119	0.064 ± 0.018	0.078	0.066
Ni	0.133	0.069 ± 0.011	0.073	0.062
Cu	0.105	0.060 ± 0.023	0.061	0.049

The stresses generated in the sprayed coatings, are also estimated by the X-ray method using filtered CoKα radiation ($\lambda = 1.79026$). The measurement of the residual stresses has been

preceded by the X-ray phase analysis. All the measurements have been made using a Brucker D8 Discover diffractometer equipped with a Lynx Eye position-sensitive detector with the 2.6° angular detection range and a Poly Cup primary beam-measuring optics with a pinhole-type collimator and an aperture of 1.0 mm.

The stress characteristics are determined in the sub-surface layer at a small depth (to about 20 μm) in a region with the surface area of about 2 mm^2 located in the center of the sample. The stresses are measured in the plane of the coating. The values of the principal stresses active in the coating plane (determined by the $\sin^2\varphi$ method) are given in Table 4.

Table 4. The magnitude of principal stresses in sprayed coatings obtained by the X-ray diffraction method

Coating	Principal stress [MPa]	
	σ_1	σ_2
Ti	192.0 ± 55.0	350.0 ± 60.0
Ni	84.0 ± 5.0	93.0 ± 6.0
Cu	109.0 ± 7.0	87.0 ± 9.0

5. Calculation results

Figure 7 shows temperature distributions calculated for the time intervals in which the Ti, Ni and Cu coating are deposited on the ceramic substrate. We can see that temperature of the successive sub-layers rapidly decreases while the substrate is slowly heated up.

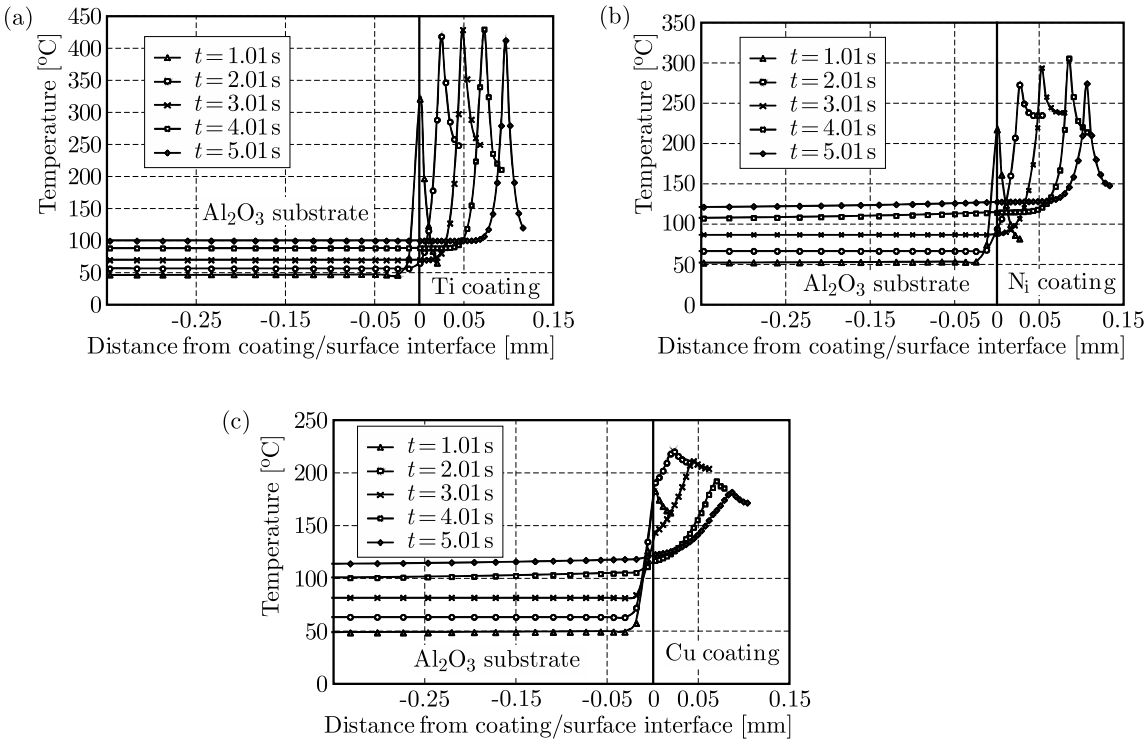

Fig. 7. FEM-calculated temperature distribution along the vertical axis of Ti (a), Ni (b), Cu (c) coating/substrate system versus the distance from the ceramic/metal interface during the successive time intervals of sub-layer activation

The calculated (using FEM1 and FEM2 models) and measured distributions of the radial residual stresses active in the Ti/Al_2O_3, Cu/Al_2O_3, and Ni/Al_2O_3 systems as a function of the

distance from the coating/substrate interface are shown in Figs. 8a, 8b, 8c, respectively. The figures also show the magnitudes of stresses measured by the X-ray method.

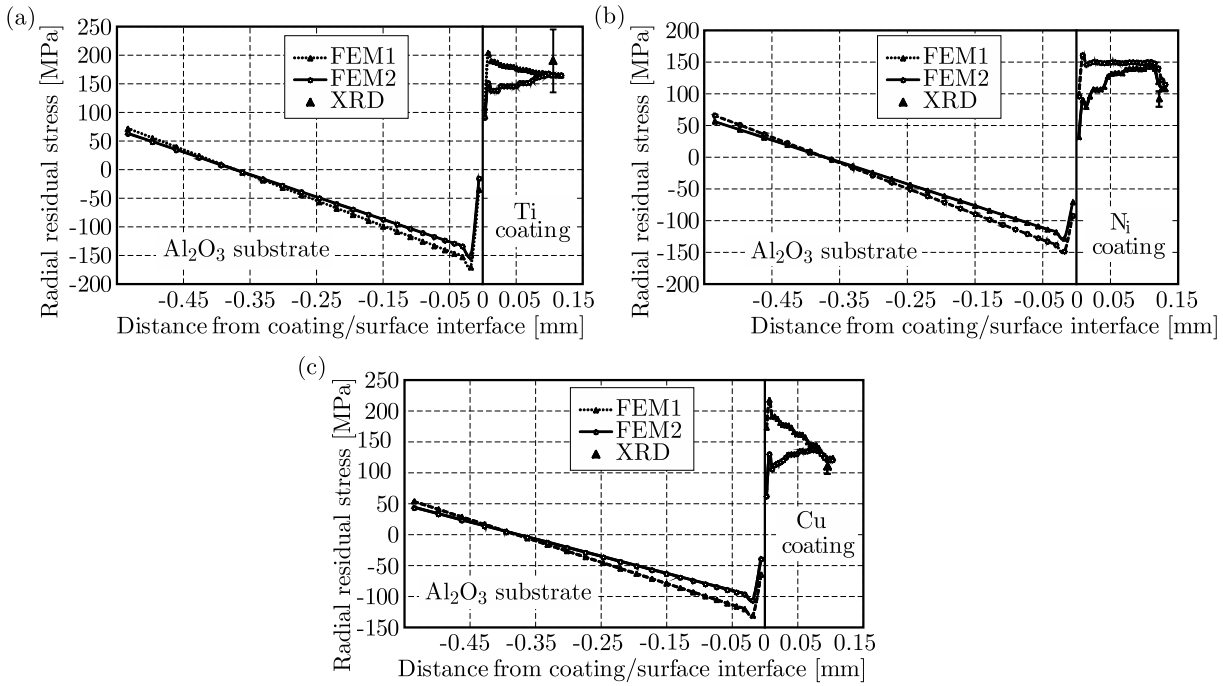

Fig. 8. Radial residual stress profiles along the sample axis as a function of the distance from the Ti/AlO3 (a), Ni/AlO_3 (b), Cu/AlO_3 (c) interface

As expected, the stresses induced in the metallic coatings are tensile, since the thermal contraction of a given sub-layer is limited by the cold substrate and the earlier-deposited sub-layers that are in contact with it. In the ceramic substrate, the radial stresses are compressive in the vicinity of the coating/substrate interface and, then, as the distance from it increases, they change into tensile.

In the model assuming the load in form of a temperature field and particle high-velocity impact onto the substrate (FEM2), the magnitude of the residual stresses is lower, especially in the region of the interface, than that in the model loaded with the temperature field only (FEM1). Additional loading in model FEM2 derived from the particle impact results in higher plastic deformation of metal coatings and lower residual stress amplitude at the coating/substrate interface. The zone of plastic deformation is wider in the case of Ti and Cu coatings. The plastic deformation is responsible for partial redistribution of stress and decreases the deflection of the overall system. The graph in Fig. 9 shows a change in the effective plastic strains along thickness of Ti, Ni and Cu coatings for both FEM1 and FEM2 models. The plastic deformation reaches maximum in the region around the coating/substrate interface.

6. Summary and conclusions

Distributions of the residual stresses active in Ti, Cu, and Ni coatings deposited on Al_2O_3 substrates by the HVOF method are examined. The stress distributions are simulated using a developed numerical model of coating/substrate system based on the finite element method (FEM). The coatings are modeled as growing layer-by-layer during time intervals defined by spraying procedures. The calculations are performed for two different loads imposed on the mechanical coating/substrate model. In the first case, the model is loaded with a temperature field only and, in the other case, the temperature field is added with a load (acting for 0.1 μs)

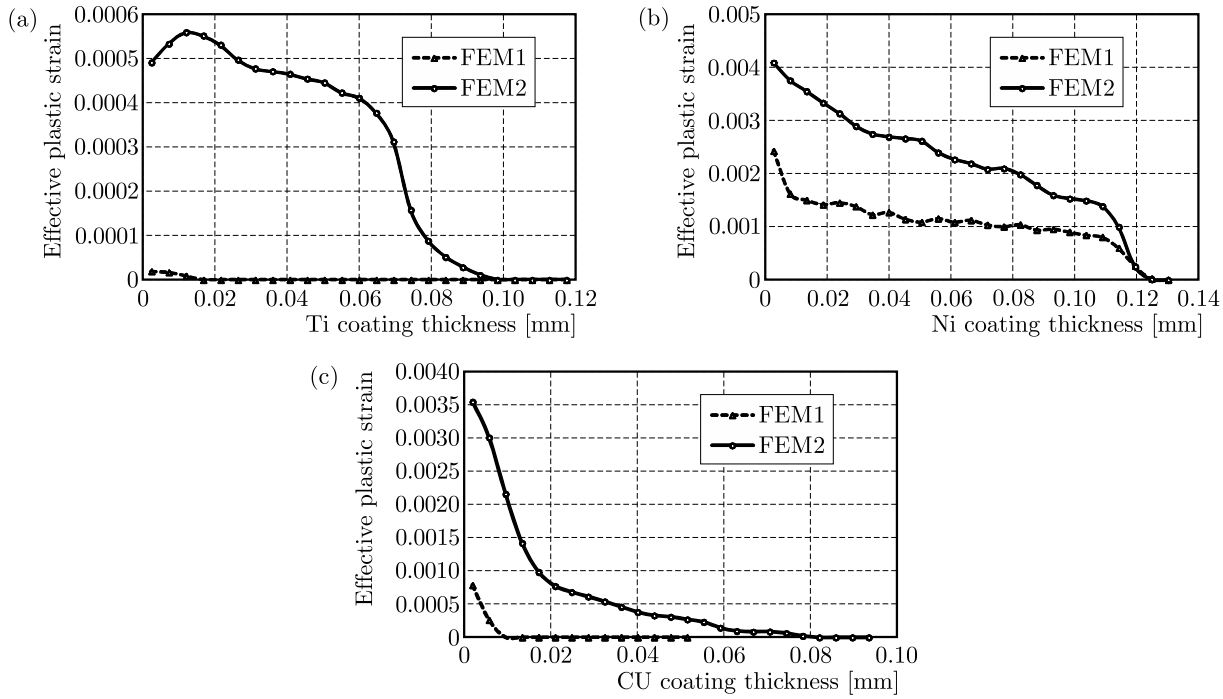

Fig. 9. FEM1, FEM2-calculated effective plastic strain profiles as a function of the Ti (a), Ni (b), Cu (c) coating thickness

proportional to the mass and acceleration of each newly-deposited sub-layer. The acceleration is estimated from the time-variation of the displacement of the center of mass of the centrally--positioned spherical coating particle, which is obtained in the solution to the dynamic particle impact problem. This enables taking into account the effect of high-velocity impact of a coating particle on the final magnitude of residual stresses in the coating/substrate system. The main results can be summarized as follows:

- The deflection of the coating/substrate system simulated using the model loaded with the temperature field and particle impact energy (FEM2) is smaller, and the stresses induced in the vicinity of the coating/substrate interface are lower compared to those simulated in the model loaded by the temperature field only (FEM1).
- The radial stresses active in the ceramic substrate near the coating/substrate interface are compressive and those near the Ti, Cu, and Ni coatings are tensile. The FEM model with additional particle impact loading (FEM2) results in a lower residual stress amplitude at the coating/substrate interface.
- The measured deflections of the real samples are in agreement, within the limits of tolerances, with the deflections calculated using the numerical analysis (FEM2).
- In constructing metal/ceramic joints, it is advantageous to use metals with a lower yield stress ($Re_{Ni} = 140\,MPa$, $Re_{Cu} = 240\,MPa$, $Re_{Ti} = 380\,MPa$) since then redistribution of stresses is greater and, thereby, the residual stress level in the system is lower. In the Ti and Cu coatings, the stress magnitudes determined at a depth of about $20\,\mu m$ by X-ray diffraction are in agreement with their FEM2-calculated values (within the measurement error), whereas in the Ni coatings they are lower by about 12%.
- The X-ray analysis used in the present study gives satisfactory results when measuring stresses at very small depths. In order to verify the proposed model, the stresses induced near the coating/substrate interface should be more thoroughly measured by other methods.

Acknowledgments

This work has been supported by the National Science Centre under project No. N N519 652840.

References

1. Amon C.H., Merz R., Prinz F.B., Schmaltz K.S., 1996, Numerical and experimental investigation of interface bonding via substrate melting of an impinging molten metal droplet, *Journal of Heat Transfer*, **118**, 164-172
2. Bansal P., Shipway P.H., Leen S.B., 2006, Effect of particle impact on residual stress development in HVOF sprayed coatings, *Journal of Thermal Spray Technology*, **15**, 4, 570-575
3. Boyer R., Welsch G., Collings E., 1994, *Materials Property Handbook: Titanium Alloys*, ASM International, Materials Park, OH
4. Chmielewski T., Golański D., 2011, New method of in-situ fabrication of protective coatings based on Fe-Al intermetallic compounds, *Proceedings of the Institution of Mechanical Engineers, Journal of Engineering Manufacture, Part B*, **225** (B4), 611-616
5. Chmielewski T., Golański D., Włosiński W., 2013, Characterization of thermally sprayed titanium coatings on alumina substrate, [In:] *Mechanics and Materials*, S. Jemioło, M. Lutomirska (edit.), Publishing House of Warsaw University of Technology, 173-192
6. Dobrzański L.A., 2002, *Podstawy nauki o materiałach i metaloznawstwo. Materiały inżynierskie z podstawami projektowania materiałowego*, WNT
7. Dorf R.C. (ed.), 2004, *Handbook of Engineering Tables*, CRC Press LLC
8. Feng X., Huang Y., Rosakis A.J., 2007, On the Stoney formula for a thin film/substrate system with nonuniform substrate thickness, *Transactions of the ASME*, **74**, 1276-1281
9. Golanski D., 1996, Temperature distribution in a cylindrical Al_2O_3-steel joint during the vacuum brazing cycle, *Journal of Materials Processing Technology*, **56**, 1/4, 945-954
10. Goldsmith A., Waterman T.E., Hirchorn H.J., 1961, *Handbook of Thermophysical Properties of Solid Materials*, New York
11. Hutchinson J.W., Evans A.G., 2002, On the delamination of thermal barrier coatings in a thermal gradient, *Surface and Coatings Technology*, **149**, 179-184
12. Kamara A.M., Davey K., 2007, A numerical and experimental investigation into residual stress in thermally sprayed coatings, *Solid and Structures*, **44**, 8532-8555
13. Kim K., Kuroda S., Watanabe M., 2010, Microstructural development and deposition behavior of titanium powder particles in warm spraying process: from single splat to coating, *Journal of Thermal Spray Technology*, **19**, 6, 1244-1254
14. Li M., Panagiotis D., Christofides P., 2006, Computational study of in-flight behavior in the HVOF thermal spray process, *Chemical Engineering Science*, **61**, 6540-6552
15. Luzin V., Spencer K., Zhang M.-X., 2011, Residual stress and thermo-mechanical properties of cold spray metal coatings, *Acta Materialia*, **59**, 1259-1270
16. Lyphout C., Nyle'n P., Manescu A., Pirling T., 2008, Residual stresses distribution through thick HVOF sprayed Inconel 718 coatings, *Journal of Thermal Spray Technology*, **17**, 5/6, 915-923
17. Ng H.W., Gan Z., 2005, A finite element analysis technique for predicting as-sprayed residual stress generated by plasma spray coating process, *Finite Elements in Analysis and Design*, **41**, 1235-1254
18. Salbut L., Kujawinska M., Jozwik M., Golanski D., 1999, Investigation of ceramic-to-metal joint properties by hybrid moire interferometry/FEM analysis, *Interferometry'99: Applications. Book Series: Proceedings of The Society of Photo-Optical Instrumentation engineers (SPIE)*, Juptner W.P.O, Patorski K. (edit.), **3745**, 298-306

19. Stokes J., Looney L., 2003, Residual stress in HVOF thermally sprayed thick deposits, *ICMCTF*

20. Toparli M., Sen F., Culha O., Celik E., 2007, Thermal stress analysis of HVOF sprayed WC-Co/NiAl multilayer coatings on stainless steel substrate using finite elements methods, *Journal of Materials Processing Technology*, **190**, 23-32

21. Tsui Y.C., Clyne T.W., 1997, An analytical model for predicting residual stresses in progressively deposited coatings. Part 1: Planar geometry, *Thin Solid Films*, **306**, 23-33

22. Watanabe T., Kuribayashi I., Honda T., Kanzawa A., 1992, Deformation and solidification of a droplet on a cold substrate, *Chemical Engineering. Science A*, **47**, 3059-3065

23. Wenzelburger M., Escribano M., Gadow R., 2004, Modeling of thermally sprayed coatings on light metal substrates: layer growth and residual stress formation, *Surface and Coatings Technology*, **180-181**, 429-435

24. Yilbas B.S., Arif A.F.M., 2007, Residual stress analysis for diamalloy 1005 coating 0n Ti-6Al-4V alloy, *Surface and coating Technology*, **202**, 559-568

25. Zimmerman J., 2014, Finite element modelling of the residual stresses induced in thermally deposited coating, *Archives of Metallurgy and Materials*, **59**, 2, 603-609

26. Zimmerman J., Lindemann Z., Golański D., Chmielewski T., Wlosinski W., 2013, Modeling of the residual stresses generated in thermally sprayed Ti coatings on Al_2O_3 substrate, *Bulletin of the Polish Academy of Science Technical Sciences*, **61**, 515-525

Manuscript received December 12, 2014; accepted for print December 18, 2015

JOURNAL OF THEORETICAL AND APPLIED MECHANICS
54, 3, pp. 935-944, Warsaw 2016
DOI: 10.15632/jtam-pl.54.3.935

TREFFTZ METHOD FOR POLYNOMIAL-BASED BOUNDARY IDENTIFICATION IN TWO-DIMENSIONAL LAPLACIAN PROBLEMS

Leszek Hożejowski
Kielce University of Technology, Faculty of Management and Computer Modelling, Kielce, Poland
e-mail: hozej@tu.kielce.pl

The paper addresses a two-dimensional boundary identification (reconstruction) problem in steady-state heat conduction. Having found the solution to the Laplace equation by superpositioning T-complete functions, the unknown boundary of a plane region is approximated by polynomials of an increasing degree. The provided examples indicate that sufficient accuracy can be obtained with a use of polynomials of a relatively low degree, which allows avoidance of large systems of nonlinear equations. Numerical simulations for assessing the performance of the proposed algorithm show better than 1% accuracy after a few iterations and very low sensitivity to small data errors.

Keywords: inverse geometry problem, boundary identification, Trefftz method, Laplace equation

1. Introduction

Inverse problems appear in many areas of engineering research. They contain, among others, problems of partly unknown geometry where we seek for the shape and location of the boundary of a considered domain (or a part of the boundary) and try to determine it from the information available at the known portion of the boundary. A number of these problems, referred to as inverse geometry problems (IGPs), arise in engineering practice. The intensive study of IGPs in the past decades has resulted in many propositions of efficient solution algorithms. Although purely computational aspects are crucial to many publications in this area, researchers usually indicate possible industrial applications of their theoretical results. Illustrative examples could be non-destructive detection of defects like voids, cracks or inclusions (Cheng and Chang, 2003a,b; Karageorghis *et al.*, 2014), locating the 1150°C isotherm in a blast furnace hearth (Gonzalez and Goldschmit, 2006), or non-destructive evaluation of corrosion (Lesnic *et al.*, 2002; Mera and Lesnic, 2005; Liu, 2008) – to name but a few.

The problem of numerical identification (reconstruction) of geometrical characteristics of the studied object can be solved by a variety of computational methods. For example, Hsieh and Kassab (1986) presented a general solution method which led to a nonlinear algebraic equation, or a nonlinear ordinary differential equation solved numerically by the Newton-Raphson method. Cheng and Chang (2003a,b) used a computational technique based on the conjugate-gradient method for the recovery of inner voids within a solid body, assuming different kinds of data prescribed on the outer surface. Huang and Liu (2010) estimated interfacial configurations in a 3D composite domain by the conjugate gradient method and commercial package CFD-ACE+. Lesnic *et al.* (2002) treated an inverse geometric problem for the Laplace equation by the boundary element method in conjunction with the Tikhonov first-order regularization. Mera *et al.* (2004) modelled the same problem as variational and minimized a defect functional by a real coded genetic algorithm combined with the function specification method. Kazemzadeh-Parsi and Daneshmand (2009) applied the smoothed fixed grid finite element method for the problem

of cavity detection. Liu *et al.* (2008) proposed a new algorithm, named the regularized integral equation method, which employed Lavrentiev regularization and a second kind Fredholm integral equation to ultimately attain the unknown boundary from a nonlinear algebraic equation by the bisection method.

A good reason for the choice of a method is the claim to avoid mesh generation. One could point to several numerical schemes which meet this requirement and perform well in inverse problems, among them the radial basis functions method and the method of fundamental solutions (MFS), both enjoying growing interest recently, as well as the Trefftz method (TM) dating back to the 1920s (Trefftz, 1926).

MFS has been extensively used in scientific computation and simulation over the last two decades. A comprehensive survey of its application to inverse problems (including inverse geometric problems) can be found in Karageorghis *et al.* (2011a,b).

TM and MFS, which are equivalent for Laplace and biharmonic equations (Chen *et al.*, 2007), share the same concept of expressing the solution to a differential equation by a linear combination of basis functions satisfying the governing equation. The coefficients of the bases (T-complete functions) have to be selected to make the solution satisfy, in some sense, all imposed conditions. A broad discussion of the method together with a tutorial on the applications can be found in Li *et al.* (2008). Clearly, TM suits for solving different kinds of inverse problems (Ciałkowski and Grysa, 2010).

There have been quite a few Trefftz-type approaches to a boundary identification problem. Karageorghis *et al.* (2014) proposed collocation TM for reconstruction of the void(s) whose centre(s) is (are) unknown, solving the proceeding non-linear least squares problem with a use of a suitable predefined routine in MATLAB. The collocation Trefftz method, modified by Liu (2007) and further referred as to modified collocation Trefftz method (MCTM), was applied by Fan *et al.* (2012) to a Laplacian problem to infer the spatial position of the unknown part of the boundary from the Dirichlet condition. The authors adopted the exponentially convergent scalar homotopy algorithm (ECSHA) to solve the resulting system of nonlinear equations. A similar problem, but with the Neumann condition on the unknown part of the boundary, was solved by Fan and Chan (2011) using the same technique. A combination of MCTM and ECSHA proved successful also in boundary detection problems for a modified Helmholtz equation (Chan and Fan, 2011); Fan *et al.*, 2014) and biharmonic equation (Chan and Fan, 2013).

In this study, we propose a fast converging computational algorithm based on TM to solve a two-dimensional boundary identification problem for the Laplace equation (excluding, however, highly complicated domains). In the first stage of computationm we approximate the solution to the Laplace equation with a linear combination of harmonic polynomials so that it satisfies the prescribed conditions in the least-squares sense. The reconstruction of an unknown boundary is through the adjustment of parameters of an approximating polynomial curve. It is demonstrated by numerical examples that relatively low degree polynomials could provide, at a small computational cost, sufficient accuracy of boundary identification. Moreover, computation with simulated errors exhibited very low sensitivity to small disturbances of the data. The approach allows immediate extension to problems governed by other linear differential equations.

2. Boundary reconstruction problem for the Laplace equation

Consider a two-dimensional inverse problem in a domain Ω whose boundary $\partial\Omega$ consists of two segments: Γ, which is known, and γ whose shape and position is not known and, therefore, being detected. The governing equation is

$$\Delta T = 0 \qquad \text{in} \quad \Omega \tag{2.1}$$

where Δ is Laplace operator, and it satisfies corresponding conditions prescribed on the domain boundary. The problem could be regarded as a steady-state heat conduction problem. To compensate for the missing information about the geometry of the boundary, an overspecified condition will be imposed on the known part of the boundary. Hence, we have

$$T = T_\Gamma \qquad \text{and} \qquad \frac{\partial T}{\partial n} = q_\Gamma \qquad \text{on} \quad \Gamma \tag{2.2}$$

where $\partial/\partial n$ denotes differentiation along the outward normal n. On the remaining part of the boundary, we assume

$$\alpha T + \beta \frac{\partial T}{\partial n} = g_\gamma \qquad \text{on} \quad \gamma \tag{2.3}$$

where α and β denote arbitrary constants which are not zero simultaneously. In other words, a condition of Dirichlet, Neumann or Robin type can be imposed at the boundary γ.

Rather than discuss the problem in full generality, let us look at a particular situation when the problem domain Ω is an area under the curve γ. It can always be assumed that in appropriate coordinates x varies from 0 to 1, so γ can be described by an explicit equation

$$y = f(x) \qquad x \in \langle 0, 1 \rangle \tag{2.4}$$

For this particular case, the problem specified by equations (2.1)-(2.3) is presented in Fig. 1.

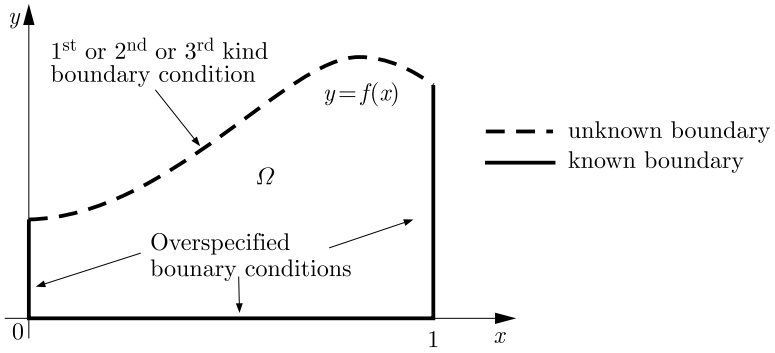

Fig. 1. A diagram of the boundary identification problem

Both boundary curves Γ (known) and γ (unknown), meet at points $(0, y_0)$ and $(1, y_1)$, hence, we can write

$$f(0) = y_0 \qquad f(1) = y_1 \tag{2.5}$$

As stated before, the aim of the study is to determine the shape and location of the unknown part of the boundary γ.

3. Solution methodology

In the first step, we approximate the solution to Laplace equation (2.1) with a combination of the T-complete functions $V_k(x, y)$

$$T(x, y) \approx \Theta(x, y) = \sum_0^K c_k V_k(x, y) \tag{3.1}$$

with coefficients c_k to be found. In the case under consideration, the functions $V_k(x,y)$ which satisfy the Laplace equation will be taken from the set

$$\{1, \mathrm{Re}z^k, \mathrm{Im}z^k, k = 1, 2, \ldots\} \tag{3.2}$$

where $z = x + \mathrm{i}y$ is a complex number. These basis functions are termed harmonic polynomials.

Coefficients c_k in expansion (3.1) will be chosen to minimize, along the boundary Γ, squared differences between true values of the function T and of its normal derivative and the corresponding values provided by the model. Hence, we minimize the following functional

$$J(c_0, c_1, \ldots, c_K) = \int\limits_{\Gamma} \Big(\sum_0^K c_k V_k \Big|_{\Gamma} - T_{\Gamma} \Big)^2 \, d\Gamma + \int\limits_{\Gamma} \Big(\sum_0^K c_k \frac{\partial V_k}{\partial n} \Big|_{\Gamma} - q_{\Gamma} \Big)^2 \, d\Gamma \tag{3.3}$$

The necessary condition for the minimum of $J(c_0, c_1, \ldots, c_K)$ is

$$\frac{\partial J}{\partial c_k} = 0 \qquad k = 0, 1, \ldots, K \tag{3.4}$$

which gives a system of $K+1$ linear equations with $K+1$ variables. In order to avoid problems with numerical stability, the coordinates x and y of the points of Ω should range from 0 to 1. To meet this requirement, one can use a proper change of variables when building a mathematical model of the problem. Alternatively, basis functions (3.2) could be modified by taking z/L instead of z, where L denotes the characteristic length. The latter reminds modification of the corresponding T-complete functions in polar coordinates proposed by Liu (2007).

Having found the coefficients c_k, we can now focus our attention directly on identification of the unknown boundary γ assumed to be a graph of the function $f(x)$. The function $f(x)$ can be approximated with a polynomial of degree N, denoted by $P^{(N)}(x)$ or shortly $P(x)$, if there is no danger of misunderstanding. Since $P(x)$ has the form

$$P(x) = a_0 + a_1 x + a_2 x^2 + \ldots + a_N x^N \tag{3.5}$$

we only need to determine the coefficients a_n to know the approximate values of $f(x)$ in the whole interval $\langle 0, 1 \rangle$. Conditions (2.6) applied to $P(x)$ give

$$P(0) = y_0 \qquad \text{and} \qquad P(1) = y_1 \tag{3.6}$$

In consequence, any two a_n can be expressed as functions of the remaining coefficients.

Further proceeding must include a prescribed boundary condition (2.3) on the sought curve γ. Since $\Theta(x,y) \approx T(x,y)$ and $P(x) \approx f(x)$, we can rewrite equation (2.3) in terms of the approximated functions as

$$\alpha\Theta(x, P(x)) + \beta \frac{\partial \Theta}{\partial n}(x, P(x)) = g_{\gamma}(x) \tag{3.7}$$

where

$$\frac{\partial \Theta}{\partial n} = \frac{1}{\sqrt{1 + [P'(x)]^2}} \Big(-P'(x) \frac{\partial \Theta}{\partial x}(x, P(x)) + \frac{\partial \Theta}{\partial y}(x, P(x)) \Big) \tag{3.8}$$

Equation (3.7) formally holds for all $x \in (0,1)$ but depending on the amount of information available on γ could be given only for $x \in \{x_1, x_2, \ldots, x_M\}$. The polynomial $P(x)$ will be selected so as to minimize the functional

$$J(a_0, a_1, \ldots, a_N) = \int\limits_0^1 \Big(\alpha\Theta(x, P(x)) + \beta \frac{\partial \Theta}{\partial n}(x, P(x)) - g_{\gamma}(x) \Big)^2 \, dx \tag{3.9}$$

In the case of discrete data, integration contained in functional (3.9) has to be changed into summation spanning over all x_m.

Minimization of $J(a_0, a_1, \ldots, a_N)$ results in solving simultaneous equations

$$\frac{\partial J}{\partial a_n} = 0 \qquad n = 0, 1, \ldots, N \tag{3.10}$$

which are nonlinear. We propose an iterative algorithm for finding the coefficients of the polynomial $P^{(N)}(x)$. The computation always starts with $N = 1$ (i.e. a polynomial of degree 1). Note that conditions (3.6) automatically determine the first approximation $P^{(1)}(x)$. We now check whether boundary condition (3.7) is satisfied. More precisely, we want to estimate the goodness of fit for (3.7). For this purpose, we introduce a measure of inaccuracy defined by

$$Er^{(1)} = \frac{1}{\|g_\gamma\|}\left\| \alpha\Theta\big|_{y=P^{(1)}(x)} + \beta\frac{\partial\Theta}{\partial n}\Big|_{y=P^{(1)}(x)} - g_\gamma \right\| \qquad \|\cdot\| \ - \ L^2 \text{ norm} \tag{3.11}$$

assuming either continuous or discrete range of variation of x. In the latter case, both the numerator and the denominator of (3.11) contain the norm of the M-dimensional vector.

If the value of $Er^{(1)}$ is sufficiently close to zero, the computational procedure ends and $P^{(1)}(x)$ is the solution. Otherwise, we increase the polynomial degree by 1 and numerically solve (3.10) for a_2 (since a_0 and a_1 can be expressed as functions of a_2). Numerical root-finding methods require a first guess which we suggest by plotting J versus a_2. Once the coefficients of $P^{(2)}(x)$ are determined, we compute the error $Er^{(2)}$ defined similarly to $Er^{(1)}$. In general, when solving for the coefficients of a polynomial $P^{(N+1)}(x)$, our initial guess are a_n from the previous step and $a_{N+1} = 0$. Having determined $P^{(N+1)}(x)$, we compute $Er^{(N+1)}$. The procedure is continued to achieve the desired accuracy of fulfilment of (3.7), i.e. until $Er^{(N+1)}$ becomes less than the desired level. In geometrical terms, the algorithm allows one to approach the unknown boundary γ with successive polynomial curves. An alternative to the stopping criterion based on $Er^{(N)}$, may well be the rule saying that the iteration stops when the distance between the successive approximations $P^{(N-1)}(x)$ and $P^{(N)}(x)$ is sufficiently small, which gives that either $\|P^{(N)}(x) - P^{(N-1)}(x)\|$ or relative measure $\|P^{(N)}(x) - P^{(N-1)}(x)\| \cdot \|P^{(N-1)}(x)\|^{-1}$ must be less than the user-specified tolerance.

We must emphasise that the proposed method, when compared to the existing approaches using MCTM (Chan and Fan, 2011, 2013; Fan and Chan, 2011; Fan *et al.*, 2012, 2014), differs not only in the representation of the sought boundary (a continuous curve rather than a set of discrete points) but it also uses a different computation scheme. We employ two systems of equations: a linear system to determine the coefficients of T-complete functions and a nonlinear system to adjust the coefficients of a polynomial approximation, the latter having relatively few unknowns. In the cited papers, both coefficients of T-complete functions and the unknown boundary points are obtained from one nonlinear system of equations. In practice, such a system must be large, especially when we use a high-order Trefftz solution for better accuracy and a large number of boundary points for more precise boundary reconstruction. Consequently, the more boundary points we wish to determine, the larger system we obtain, unlike using the present method which allows one to recover infinitely many boundary points at the cost of solving only a small system of equations.

4. Numerical examples

In this Section, some examples will be shown to test the developed theoretical method. Although the boundary detection problem originates from realistic applications, a number of studies proposing efficient solution algorithms, among them those based on MCTM which are cited in

the previous paragraph, validate the proposed computational methods on numerical simulations (synthetic data). Likewise, the present method will be tested on data coming from numerical simulations. The results will be shown for the function $T(x,y) = \mathrm{e}^{2x}\cos(2y)$, which is an analytical solution to the Laplace equation in the domain Ω defined by inequalities

$$0 \leqslant x \leqslant 1 \qquad \text{and} \qquad 0 \leqslant y \leqslant f(x) \tag{4.1}$$

where the graph of $y = f(x)$ represents the unknown boundary γ.

In expansion (3.1), we took $K = 14$, and the values of T_γ, q_γ and g_γ are specified at $M = 49$ distinct points. The resulting simultaneous nonlinear equations are solved using the Levenberg-Marquardt method.

For quantitative evaluation of the final results, we introduce ε, a non-negative number defined by

$$\varepsilon = \frac{\|P(x) - f(x)\|}{\|f(x)\|} \tag{4.2}$$

which can be interpreted as a mean error which is made when replacing the original boundary γ with its polynomial approximation $P(x)$.

Example 1

The unknown boundary is inferred from the Dirichlet condition on γ. We take $f(x) = (1+x-\sin 4x)\mathrm{e}^{-x}$. In Fig. 2, the true boundary is compared with its polynomial approximation.

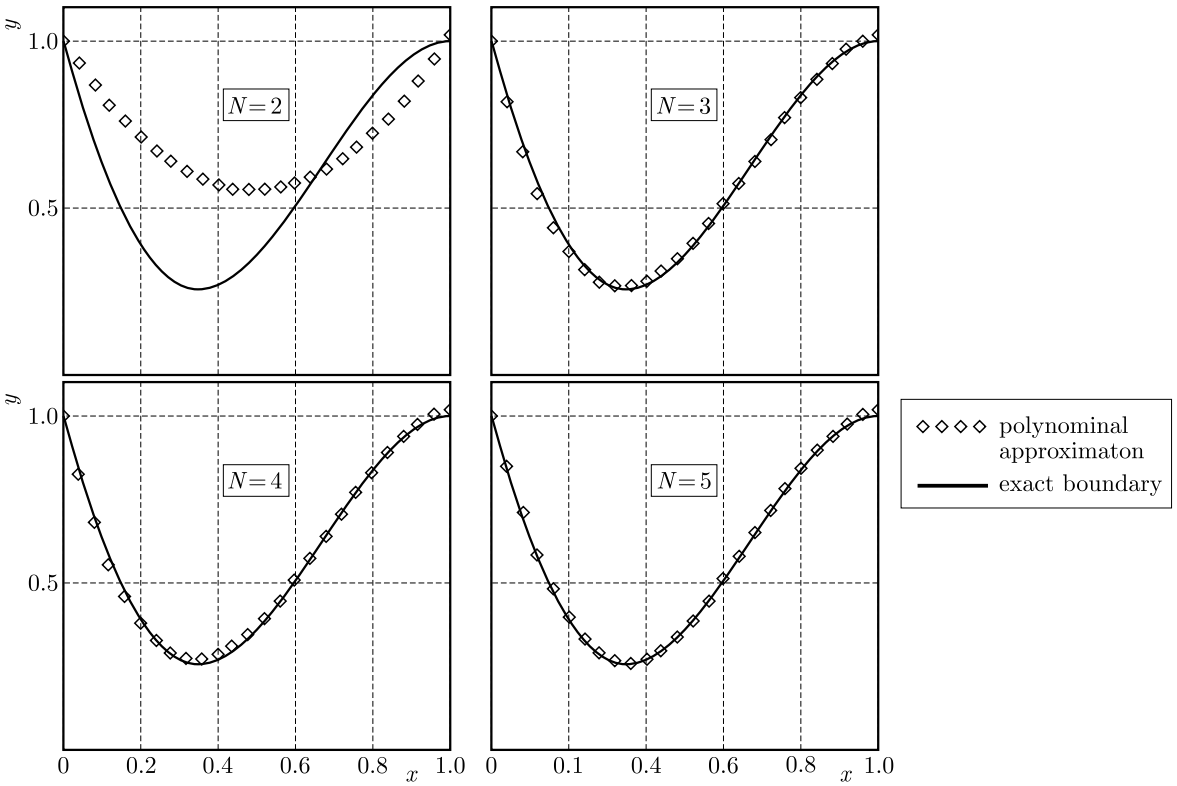

Fig. 2. Boundary shape identification by polynomials of degree $N = 2, 3, 4, 5$

Table 1 gives information about the accuracy of the presented approximations.

Table 1. Mean error of boundary shape identification for $f(x) = (1 + x - \sin 4x)\mathrm{e}^{-x}$

Polynomial degree	$N = 2$	$N = 3$	$N = 4$	$N = 5$
Error ε	32%	2.6%	1.9%	0.1%

Example 2

The computations have been performed for the case of the Neumann condition on γ. Figure 3 shows the results of boundary reconstruction when $f(x) = (1 + x^2)(2 + x^5)^{-1}$.

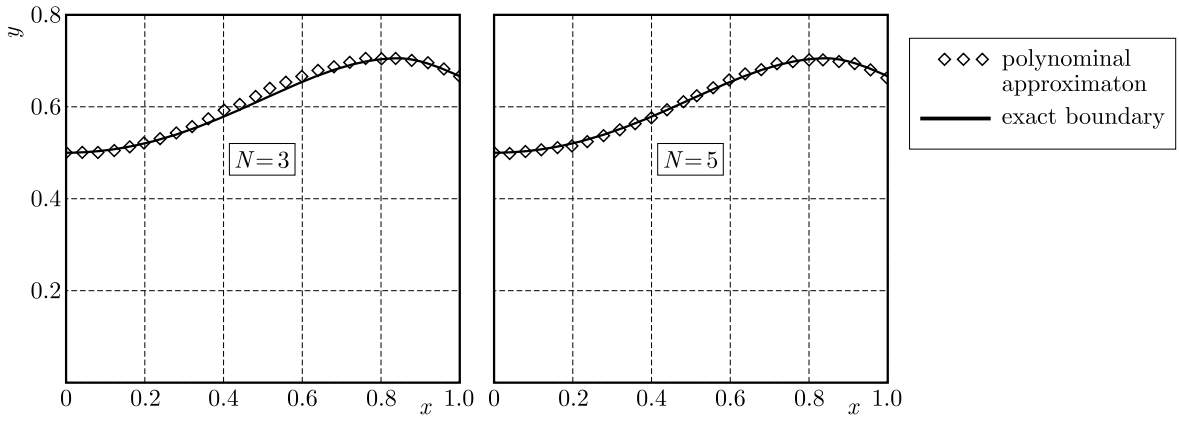

Fig. 3. Boundary shape identification by polynomials of degree $N = 3$ and $N = 5$

The approximation errors ε, concerning the case of the Neumann condition, are listed in Table 2.

Table 2. Mean error of boundary shape identification for $f(x) = (1 + x^2)(2 + x^5)^{-1}$

Polynomial degree	$N = 2$	$N = 3$	$N = 4$	$N = 5$
Error ε	11.9%	1.2%	1.0%	0.4%

Example 3

Finally, we present the results referring to the case of the Robin condition on γ with $\alpha = 1$ and $\beta = -3$ in (2.3). The true boundary γ is a curve $f(x) = (2 + \cos 4x)(x^3 + 2)^{-1}$ and its approximation is presented in Fig. 4.

The approximation errors ε, concerning the case of the Robin boundary condition, are listed in Table 3.

All examples included in this Section prove the effectiveness of the proposed computational procedure for boundary identification. It has been enough to use a 5th degree polynomial to approach the true boundary with an error less than 1%.

5. Stability analysis

The computation results shown in the previous Section have been performed on the exact functions T_γ, q_γ and g_γ. In order to examine the sensitivity of the method to changes in the inputs, one has to introduce random noise to the given functions and then evaluate the impact of such changes on the final boundary detection.

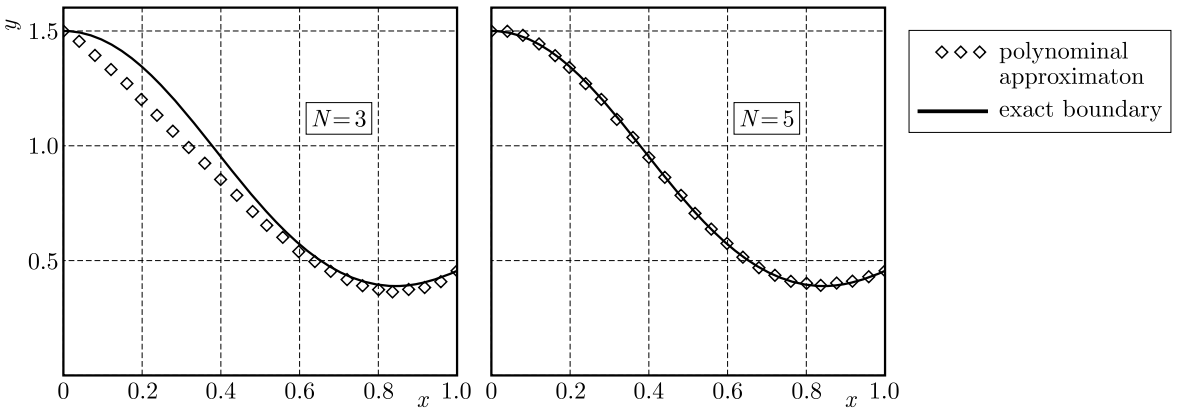

Fig. 4. Boundary shape identification by polynomials of degree $N = 3$ and $N = 5$

Table 3. Mean error of boundary shape identification for $f(x) = (2 + \cos 4x)(x^3 + 2)^{-1}$

Polynomial degree	$N = 2$	$N = 3$	$N = 4$	$N = 5$
Error ε	18.0%	8.6%	1.8%	0.4%

The values of T_γ, q_γ and g_γ are assumed to be given only at M discrete locations. In order to simulate measurement errors, we generate M random numbers having a normal distribution with a mean of 0 and a standard deviation of $\sigma = 0.025$. With such σ, approximately 95% of the simulated errors lie between -5% and 5%.

One can evaluate the influence of the introduced errors on the final results of boundary detection in a variety of ways. For the purpose of stability analysis, we use a measure Δ, defined as

$$\Delta = \frac{\|P_{noisy}(x) - P(x)\|}{\|P(x)\|} \tag{5.1}$$

where $P_{noisy}(x)$ denotes a polynomial approximation of the unknown boundary γ, derived from the noisy data. Since we perform a sequence of computations, each giving a successive approximation to γ, the input data errors might accumulate from step to step. Therefore, it seems reasonable to pay special attention to those solution inaccuracies which occur in the last iteration. Consequently, our discussion of numerical stability is based on the value of Δ calculated for $N = 5$.

For a better insight into the problem, we have recorded Δ in 10 runs of the computational procedure, each with different random noise. The values of Δ in the respective numerical examples are presented in Table 4.

Table 4. Relative changes (Δ) between the solutions derived from exact and disturbed data

	Example 1	Example 2	Example 3
Δ	0.13%-0.84%	0.24%-0.88%	0.06%-0.29%

It turns out that changes in the final results are even smaller than changes in the inputs, as far as percent errors are concerned. A possible explanation is that a polynomial curve, which we fit to a large number of discrete points by least squares, is forced to follow the changes introduced by random errors. Therefore, it should be shifted up at some locations but, on the other hand, shifted down at others. A low-degree polynomial is not very 'flexible', so it remains almost unchanged.

6. Conclusions and final remarks

We proposed a method for the solution of a two-dimensional boundary identification problem governed by the Laplace equation. In contrast to approaches which derive coordinates of unknown boundary points from a large system of nonlinear equations, the proposed algorithm does not require solving large systems and yet it delivers a very accurate reconstruction of the unknown boundary. Its basic advantage is the reduction of the amount of computational work. The provided numerical results exhibit not only high accuracy, but fast convergence of the method. Testing the sensitivity of the algorithm to input data errors showed very low risk of large impact of possible errors in the input data on predicted model outputs. The presented solution procedure can be applied without changes to problems governed by other linear differential equations, provided the appropriate Trefftz functions are known. The only limitation concerns the geometry of a domain, because global Trefftz solutions could provide poor results when used on very complicated domains.

References

1. Chan H.-F., Fan C.-M., 2013, The modified collocation Trefftz method and exponentially convergent scalar homotopy algorithm for the inverse boundary determination problem for the biharmonic equation, *Journal of Mechanics*, **29**, 2, 363-372

2. Chan H.-F., Fan C.-M., and Yeih W., 2011, Solution of inverse boundary optimization problem by Trefftz method and exponentially convergent scalar homotopy algorithm, *CMC: Computers, Materials and Continua*, **24**, 2, 125-142

3. Chen J.-T., Wu Y.-T., Lee Y.-T., Chen K.-H., 2007, On the equivalence of the Trefftz method and method of fundamental solutions for Laplace and biharmonic equations, *Computers and Mathematics with Applications*, **53**, 6, 851-879

4. Cheng C.-H., Chang M.-H., 2003a, A simplified conjugate-gradient method for shape identification based on thermal data, *Numerical Heat Transfer, Part B: Fundamentals*, **43**, 5, 489-507

5. Cheng C.-H., Chang M.-H., 2003b, Shape identification by inverse heat transfer method, *Journal of Heat Transfer*, **125**, 2, 224-231

6. Ciałkowski M., Grysa K., 2010, Trefftz method in solving the inverse problems, *Journal of Inverse and Ill-Posed Problems*, **18**, 6, 595-616

7. Fan C.-M., Chan H.-F., 2011, Modified collocation Trefftz method for the geometry boundary identification problem of heat conduction, *Numerical Heat Transfer, Part B: Fundamentals*, **59**, 1, 58-75

8. Fan C.-M., Chan H.-F., Kuo C.-L., Yeih W., 2012, Numerical solutions of boundary detection problems using modified collocation Trefftz method and exponentially convergent scalar homotopy algorithm, *Engineering Analysis with Boundary Elements*, **36**, 1, 2-8

9. Fan C.-M., Liu Y.-C., Chan H.-F., Hsiao S.-S., 2014, Solutions of boundary detection problems for modified Helmholz equation by Trefftz method, *Inverse Problems in Science and Engineering*, **22**, 2, 267-281

10. Gonzalez M., Goldschmit M., 2006, Inverse geometry heat transfer problem based on radial basis functions geometry representation, *International Journal for Numerical Methods in Engineering*, **65**, 8, 1243-1268

11. Hsieh C.K., Kassab A.J., 1986, A general method for the solution of inverse heat conduction problems with partially unknown system geometries, *International Journal of Heat and Mass Transfer*, **29**, 1, 47-58

12. Huang C.-H., Liu C.-Y., 2010, A three-dimensional inverse geometry problem in estimating simultaneously two interfacial configurations in a composite domain, *International Journal of Heat and Mass Transfer*, **53**, 1/3, 48-57

13. Karageorghis A., Lesnic D., Marin L., 2011a, A survey of applications of the MFS to inverse problems, *Inverse Problems in Science and Engineering*, **19**, 3, 309-336

14. Karageorghis A., Lesnic D., Marin L., 2011b, The MFS for inverse geometric problems, [In:] *Inverse Problems and Computational Mechanics*, L. Munteanu, L. Marin and V. Chiroiu (Eds.), Vol. 1, Editura Academiei, Bucharest, 191-216

15. Karageorghis A., Lesnic D., Marin L., 2014, Regularized collocation Trefftz method for void detection in two-dimensional steady-state heat conduction problems, *Inverse Problems in Science and Engineering*, **22**, 3, 395-418

16. Kazemzadeh-Parsi M.J., Daneshmand F., 2009, Solution of geometric inverse conduction problems by smoothed fixed grid finite element method, *Finite Elements in Analysis and Design*, **45**, 10, 599-611

17. Lesnic D., Berger J.R., Martin P.A., 2002, A boundary element regularization method for the boundary determination in potential corrosion damage, *Inverse Problems in Engineering*, **10**, 2, 163-182

18. Li Z.-C., Lu T.-T., Hu H.-Y., Cheng A. H.-D., 2008, *Trefftz and Collocation Methods*, WIT Press, Southampton, Boston

19. Liu C.-S., 2007, A modified Trefftz method for two-dimensional Laplace equation considering the domain's characteristic length, *CMES: Computer Modeling in Engineering and Sciences*, **21**, 1, 53-66

20. Liu C.-S., 2008, A highly accurate MCTM for inverse Cauchy problems of Laplace equation in arbitrary plane domains, *CMES: Computer Modeling in Engineering and Sciences*, **35**, 2, 91-111

21. Liu C.-S., Chang C.-W., Chiang C.Y., 2008, A regularized integral equation method for the inverse heat conduction problem, *International Journal of Heat and Mass Transfer*, **51**, 21/22, 5380-5388

22. Mera N.S., Lesnic D., 2005, A three-dimensional boundary determination problem in potential corrosion damage, *Computational Mechanics*, **36**, 2, 129-138

23. Mera N.S., Eliott L., Ingham D.B., 2004, Numerical solution of a boundary detection problem using genetic algorithms, *Engineering Analysis with Boundary Elements*, **28**, 4, 405-411

24. Trefftz E., 1926, Ein Gegenstck zum Ritzschen Verfahren, *Verhandlungen des II. Kongress für technische Mechanik*, Zürich, 131-137

Manuscript received October 29, 2015; accepted for print December 22, 2015

JOURNAL OF THEORETICAL AND APPLIED MECHANICS
54, 3, pp. 945-961, Warsaw 2016
DOI: 10.15632/jtam-pl.54.3.945

GEOMETRICALLY NONLINEAR VIBRATIONS OF THIN VISCO-ELASTIC PERIODIC PLATES ON A FOUNDATION WITH DAMPING: NON-ASYMPTOTIC MODELLING

Jarosław Jędrysiak

Lodz University of Technology, Department of Structural Mechanics, Łódź, Poland
e-mail: jarek@p.lodz.pl

The objects under consideration are thin visco-elastic periodic plates with moderately large deflections. Geometrically nonlinear vibrations of these plates are investigated. In order to take into account the effect of microstructure size on behaviour of these plates a non-asymptotic modelling method is proposed. Using this method, called the tolerance modelling, model equations with constant coefficients involving terms dependent on the microstructure size can be derived. In this paper, only theoretical considerations of the problem of nonlinear vibrations of thin visco-elastic periodic plates resting on a foundation with damping are presented.

Keywords: thin visco-elastic periodic plates, nonlinear vibrations, effect of microstructure size, analytical tolerance modelling

1. Introduction

In this paper, thin visco-elastic plates with a periodic structure in planes parallel to the plate midplane, interacting with a periodically heterogeneous foundation are considered. These plates consist of many identical small elements, called periodicity cells (they are distinguished by dotted lines in Fig. 1). Plates of this kind can have deflections of the order of their thickness. Dynamic problems of these plates are described by nonlinear partial differential equations with coefficients being highly oscillating, periodic and non-continuous functions of x_1, x_2. Hence, these equations are not a good tool to analyse various special problems of the plates under consideration. In order to obtain governing equations with constant coefficients, various simplified approaches are proposed, which introduce effective plate properties. Amongst them, it is necessary to mention those based on the asymptotic homogenization, see Kohn and Vogelius (1984). Unfortunately, the governing equations of these models usually neglect the effect of the microstructure size on the plate behaviour.

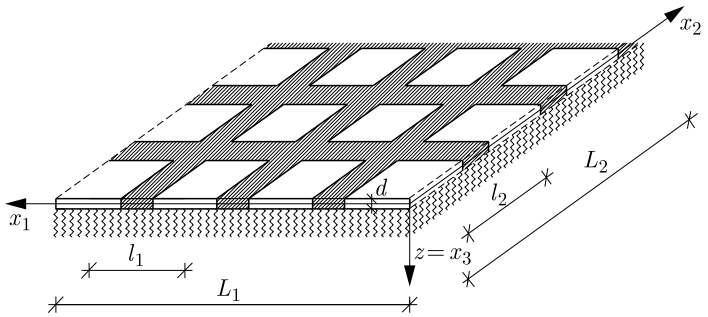

Fig. 1. A fragment of a thin periodic plate on a foundation under consideration

Other various methods are also applied to describe different mechanical problems of periodic structures and composites. Multiscale models were applied to describe composite materials reinforced by micro-particles by Lurie *et al.* (2005); the two-scale asymptotic homogenization method was used to analyse honeycomb sandwich composite shells by Saha *et al.* (2007); a relationship between the 3D and the homogenised Euler-Bernoulli beam limit was shown by Dallot *et al.* (2009), where the homogenisation procedure was also justified using the asymptotic expansion method. Results suggesting the relevance of the proposed algorithm towards the efficient multiscale modelling of periodic materials such as woven composites were obtained by De Carvalho *et al.* (2011); a two-dimensional analytical solution of a multilayered rectangular plate with a small periodic structure along one in-plane direction was obtained by He *et al.* (2013), where the two--scale asymptotic expansion method was employed to develop a homogenized model of each layer in the plate and then the state-space approach was used. Heterogeneous plates were investigated by Schmitz and Horst (2014) using a finite element unit-cell method. The two-dimensional stationary temperature distribution in a periodically stratified composite layer was analysed by Matysiak and Perkowski (2014) within the framework of the homogenized model with microlocal parameters. An asymptotic dispersive method for description of the problem of shear-wave propagation in a laminated composite was proposed by Brito-Santana *et al.* (2015).

Mechanical problems of thin plates under moderately large deflections are described by the known geometrically nonlinear equations presented by e.g. Timoshenko and Woinowsky-Krieger (1959) and Woźniak (2001). Equations of von Kármán-type plates were derived from equations of the three-dimensional nonlinear continuum mechanics by Meenen and Altenbach (2001). Bending problems of such plates can be analysed using various methods, e.g. proposed by Levy (1942) or Timoshenko and Woinowsky-Krieger (1959). However, other new or modified methods are also presented in a lot of papers. Some of them are mentioned below. An asymptotic approach for thin rectangular plates with variable thickness clamped on all edges was used by Huang (2004). Theoretical, numerical and experimental analysis of the stability and ultimate load of multi--cell thin-walled columns of rectangular cross-sections was shown by Królak *et al.* (2009). Teter (2011) analysed the dynamic critical load for buckling of columns, but global and local buckling of sandwich beams and plates was examined by Jasion *et al.* (2012). The nonlinear bending behaviour of moderately thick functionally graded plates on a two-parameter elastic foundation was studied by Golmakani and Alamatian (2013), where the dynamic relaxation method and the finite difference discretization technique were used to solve equations based on the first order shear deformation theory and von Kármán theory.

Problems of nonlinear vibrations and/or visco-elastic damping of composite structures such as beams, plates and shells, are considered by many researchers, applying various methods. The influence of damping and/or stiffness on vibrations of nonlinear periodic plates was shown by Reinhall and Miles (1989). Large amplitude flexural vibration characteristics of composite plates using von Kármán's assumptions and Galerkin's method were obtained by Singha *et al.* (2009). Geometrically nonlinear vibrations of free-edge circular plates with geometric imperfections described by von Kármán equations with using an expansion onto the eigenmode basis of the perfect plate to discretise the equations of motion were analysed by Camier *et al.* (2009). An approximate frequency equation of clamped visco-elastic rectangular plates with thickness variations was derived by using the Rayleigh-Ritz technique by Gupta *et al.* (2009). Magnucka-Blandzi (2010) carried out a certain nonlinear analysis of dynamic stability of a circular plate. Some oscillations of visco-elastic Timoshenko beams were investigated by Manevich and Kołakowski (2011). The variational method was used in nonlinear free vibration and post-buckling analysis of functionally graded beams resting on a nonlinear elastic foundation by Fallah and Aghdam (2011). Damping and forced vibrations of three-layered laminated composite beams described in the framework of the higher-order zig-zag theories were investigated by Youzera *et al.* (2012). Nonlinear free vibrations of orthotropic shells with variable thickness were analysed

by Awrejcewicz *et al.* (2013). Lei *et al.* (2013) used a transfer function method to obtain a closed-form and uniform solution for damped visco-elastic vibrations of Euler-Bernoulli beams. A linearized updated mode method was applied to solve nonlinear equations of geometrically nonlinear free vibrations of laminated composite rectangular plates with curvilinear fibers by Houmat (2013). Natural frequencies of free vibrations for functionally graded annular plates resting on a Winkler's foundation were predicted using the differential quadrature method and the Chebyshev collocation technique by Yajuvindra and Lal (2013). Yaghoobi and Torabi (2013) presented large amplitude vibrations of functionally graded beams on a nonlinear elastic foundation. Nonlinear bending vibrations of sandwich plates with a visco-elastic core were investigated by Mahmoudkhani *et al.* (2014), where the 5th-order method of multiple scales was applied to solve the equations of motion.

Usually, those proposed modelling approaches for microstructured media lead to governing equations neglecting the effect of the microstructure size which can play a crucial role in dynamical problems of such media, e.g. for periodic plates under consideration, see Jędrysiak (2003, 2009). In order to take into account this effect, some special methods are adopted sometimes to analyse particular problems. For example, Zhou *et al.* (2014) investigated the problem of free flexural vibration of periodic stiffened thin plates using Bloch's theorem and the center finite difference method.

However, in order to obtain equations of the model, which describe the aforementioned effect, new non-asymptotic models of thin periodic plates based on the nonlinear theory were proposed by Domagalski and Jędrysiak (2012, 2015). These models are called the tolerance models and are obtained in the framework of a certain general modelling approach called the tolerance averaging technique, see Woźniak *et al.* (2008, 2010). The derived equations, in contrary to the exact ones, have constant coefficients. Some of them explicitly depend on the characteristic size of the periodicity cell.

The tolerance method is general and is useful to model various problems described by differential equations with highly oscillating non-continuous functional coefficients. It can be applied in analysis of various thermo-mechanical problems of microheterogeneous solids and structures. Some applications of this method for different periodic structures were presented in a series of papers, e.g. for dynamics of plane periodic structures by Wierzbicki and Woźniak (2000); for dynamics with near-boundary phenomena in stratified layers by Wierzbicki *et al.* (2001); for vibrations of periodic wavy-type plates by Michalak (2001); for thin plates reinforced by a system of periodic stiffeners by Nagórko and Woźniak (2002); for stability problems of periodic thin plates by Jędrysiak (2000); for stability analysis of periodic shells by Tomczyk (2007); for vibrations of periodic plates by Jędrysiak (2003, 2009); for dynamics problems of medium thickness plates on a periodic foundation by Jędrysiak and Paś (2014); for vibrations of thin functionally graded plates with plate thickness small comparing to the microstructure size by Kaźmierczak and Jędrysiak (2011) and for stability of such plates by Jędrysiak and Michalak (2011); for vibrations of thin functionally graded plates with the microstructure size of an order of the plate thickness by Jędrysiak (2013); for stability of thin functionally graded annular plates on an elastic heterogeneous subsoil by Perliński *et al.* (2014). Moreover, the tolerance method is also used to analyse damped vibrations of periodic plate strips by Marczak and Jędrysiak (2014) and nonlinear vibrations of periodic beams resting on a visco-elastic foundation by Domagalski and Jędrysiak (2014). An extended list of papers can be found in the books by Woźniak *et al.* (2008, 2010).

The main aim of this theoretical contribution is to formulate and discuss the nonlinear tolerance and asymptotic models of dynamic problems for thin visco-elastic periodic plates with moderately large deflections resting on a foundation with damping, on various levels of accuracy. These new tolerance models are an extension and generalization of the tolerance models

presented and applied by Domagalski and Jędrysiak (2012, 2014, 2015), Marczak and Jędrysiak (2014).

2. Fundamental equations

Let us denote by $0x_1x_2x_3$ the orthogonal Cartesian co-ordinate system in the physical space and by t the time co-ordinate. Let the subscripts $\alpha, \beta, \ldots$ $(i, j, \ldots)$ run over 1, 2 (over 1, 2, 3) and the indices $A, B, \ldots$ $(a, b, \ldots)$ run over $1, \ldots, N$ $(1, \ldots, n)$. The summation convention holds for all aforementioned indices. Denote also $\mathbf{x} \equiv (x_1, x_2)$ and $z \equiv x_3$. Let us assume that the undeformed plate occupies the region $\Omega \equiv \{(\mathbf{x}, z) : -d(\mathbf{x})/2 < z < d(\mathbf{x})/2, \mathbf{x} \in \Pi\}$, where Π is the midplane with length dimensions L_1, L_2 along the x_1- and x_2-axis, respectively, and $d(\mathbf{x})$ is plate thickness.

It is assumed that plates under consideration have a periodic structure along the x_1- and x_2-axis directions with periods l_1, l_2, respectively, in planes parallel to the plate midplane. The periodicity basic cell on $0x_1x_2$ plane is denoted by $\Delta \equiv [-l_1/2, l_1/2] \times [-l_2/2, l_2/2]$. It is assumed that the cell size is described by a parameter $l \equiv [(l_1)^2 + (l_2)^2]1/2$, satisfying the condition $\max(d) \ll l \ll \min(L_1, L_2)$. Thus, l will be called the microstructure parameter. Let us denote partial derivatives with respect to a space co-ordinate by $(\cdot)_{,\alpha} \equiv \partial/\partial x_\alpha$.

Moreover, thickness $d(\mathbf{x})$ can be a periodic function in $\mathbf{x}$, elastic moduli $a_{ijkl} = a_{ijkl}(\mathbf{x}, z)$ and mass density $\rho = \rho(\mathbf{x}, z)$ can be also periodic functions in $\mathbf{x}$. In general, these plate properties are not assumed to be even functions in z. Let $a_{\alpha\beta\gamma\delta}$, $a_\alpha\beta33$, a_{3333} be non-zero components of the elastic moduli tensor. Denote $c_{\alpha\beta\gamma\delta} \equiv a_{\alpha\beta\gamma\delta} - a_{\alpha\beta33}a_{\gamma\delta33}(a_{3333})^{-1}$. Proper visco-elastic moduli are denoted by $\widetilde{c}_{\alpha\beta\gamma\delta}$.

It is also assumed that the periodic plates interact with a periodic visco-elastic foundation which rests on a rigid undeformable base, see Vlasov and Leontiev (1960). A fragment of such a plate is presented in Fig. 1. The heterogeneous foundation is assumed to be periodic in planes parallel to the plate midplane, i.e. along the x_1- and x_2-axis directions with periods l_1 and l_2, respectively; however, it has constant properties along the z-axis direction. Hence, the foundation properties, i.e. mass density per unit area $\widehat{\mu} = \widehat{\mu}(\mathbf{x})$, Winkler's coefficient $k = k(\mathbf{x})$ and the damping parameter $c = c(\mathbf{x})$ can be periodic functions in $\mathbf{x} = (x_1, x_2)$. These foundation parameters can be defined following the book by Vlasov and Leontiev (1960). It is also assumed that the plate cannot be torn off from the foundation.

Denote displacements, strains and stresses by u_i, e_{ij} and s_{ij}, respectively; virtual displacements and virtual strains by $\overline{u}_i$ and $\overline{e}_{ij}$; loadings (along the z-axis) by p.

Now, the fundamental relations of the nonlinear thin plates theory, see Levy (1942) and Woźniak *et al.* (2001), are reminded.

- Kinematic assumptions of thin plates

$$u_\alpha(\mathbf{x}, z, t) = u^0_\alpha(\mathbf{x}, t) - z\partial_\alpha w(\mathbf{x}, t) \qquad u_3(\mathbf{x}, z, t) = w(\mathbf{x}, t) \tag{2.1}$$

with $w(\mathbf{x}, t)$ as the deflection of the midplane, $u^0_\alpha(\mathbf{x}, t)$ as the in-plane displacement. Similarly, these are for virtual displacements

$$\overline{u}_\alpha(\mathbf{x}, z) = \overline{u}^0_\alpha(\mathbf{x}) - z\partial_\alpha\overline{w}(\mathbf{x}) \qquad \overline{u}_3(\mathbf{x}, z) = \overline{w}(\mathbf{x}) \tag{2.2}$$

- Strain-displacement relations

$$e_{\alpha\beta} = u_{(\alpha,\beta)} + \frac{1}{2}u_{3,\alpha}u_{3,\beta} \tag{2.3}$$

- Stress-strain relations (it is assumed that the plane of elastic symmetry is parallel to the plane $z = 0$)

$$s_{\alpha\beta} = c_{\alpha\beta\gamma\delta} e_{\gamma\delta} + \widetilde{c}_{\alpha\beta\gamma\delta} \dot{e}_{\gamma\delta} \tag{2.4}$$

with

$$\begin{aligned} c_{\alpha\beta\gamma\delta} &= a_{\alpha\beta\gamma\delta} - a_{\alpha\beta 33} a_{33\gamma\delta}/a_{3333} \qquad & c_{\alpha 3\gamma 3} &= a_{\alpha 3\gamma 3} - a_{\alpha 333} a_{33\gamma 3}/a_{3333} \\ \widetilde{c}_{\alpha\beta\gamma\delta} &= \widetilde{a}_{\alpha\beta\gamma\delta} - \widetilde{a}_{\alpha\beta 33} \widetilde{a}_{33\gamma\delta}/\widetilde{a}_{3333} \qquad & \widetilde{c}_{\alpha 3\gamma 3} &= \widetilde{a}_{\alpha 3\gamma 3} - \widetilde{a}_{\alpha 333} \widetilde{a}_{33\gamma 3}/\widetilde{a}_{3333} \end{aligned} \tag{2.5}$$

- The virtual work equation

$$\begin{aligned} &\int_{\Pi} \int_{-d/2}^{d/2} \rho \ddot{u}_i \overline{u}_i \, dz \, da + \int_{\Pi} \int_{-d/2}^{d/2} s_{\alpha\beta} \overline{e}_{\alpha\beta} \, dz \, da = \int_{\Pi} p \overline{u}_3\Big(\mathbf{x}, \frac{d}{2}\Big) \, da \\ &\quad - \int_{\Pi} (k u_3 + \widehat{\mu} \ddot{u}_3 + c \dot{u}_3) \overline{u}_3\Big(\mathbf{x}, -\frac{d}{2}\Big) \, da \end{aligned} \tag{2.6}$$

is satisfied for arbitrary virtual displacements (2.2), assuming these displacements neglect the plate boundary; moreover: $da = dx_1 dx_2$; the virtual displacements are sufficiently regular, independent functions.

The plate properties are periodic functions in $\mathbf{x}$, i.e. stiffness tensors: $b_{\alpha\beta\gamma\delta}$, $d_{\alpha\beta\gamma\delta}$, $h_{\alpha\beta\gamma\delta}$, visco-elastic tensors: $\widetilde{b}_{\alpha\beta\gamma\delta}$, $\widetilde{d}_{\alpha\beta\gamma\delta}$, $\widetilde{h}_{\alpha\beta\gamma\delta}$, and inertia properties: μ, j, i are defined as

$$\begin{aligned} b_{\alpha\beta\gamma\delta}(\mathbf{x}) &= \int_{-d/2}^{d/2} c_{\alpha\beta\gamma\delta}(\mathbf{x}, z) \, dz \qquad & d_{\alpha\beta\gamma\delta}(\mathbf{x}) &= \int_{-d/2}^{d/2} c_{\alpha\beta\gamma\delta}(\mathbf{x}, z) z^2 \, dz \\ h_{\alpha\beta\gamma\delta}(\mathbf{x}) &= \int_{-d/2}^{d/2} c_{\alpha\beta\gamma\delta}(\mathbf{x}, z) z \, dz \qquad & \widetilde{b}_{\alpha\beta\gamma\delta}(\mathbf{x}) &= \int_{-d/2}^{d/2} \widetilde{c}_{\alpha\beta\gamma\delta}(\mathbf{x}, z) \, dz \\ \widetilde{d}_{\alpha\beta\gamma\delta}(\mathbf{x}) &= \int_{-d/2}^{d/2} \widetilde{c}_{\alpha\beta\gamma\delta}(\mathbf{x}, z) z^2 \, dz \qquad & \widetilde{h}_{\alpha\beta\gamma\delta}(\mathbf{x}) &= \int_{-d/2}^{d/2} \widetilde{c}_{\alpha\beta\gamma\delta}(\mathbf{x}, z) z \, dz \\ \mu(\mathbf{x}) &= \int_{-d/2}^{d/2} \rho(\mathbf{x}, z) \, dz \qquad & j(\mathbf{x}) &= \int_{-d/2}^{d/2} \rho(\mathbf{x}, z) z^2 \, dz \qquad & i(\mathbf{x}) &= \int_{-d/2}^{d/2} \rho(\mathbf{x}, z) z \, dz \end{aligned} \tag{2.7}$$

Using assumptions (2.1)-(2.4) of the nonlinear two-dimensional thin plate theory, applying the divergence theorem and the du Bois-Reymond lemma to equation (2.6), after some manipulations the governing equations of thin visco-elastic plates resting on foundations with damping can be written in the form:
— constitutive equations

$$\begin{aligned} m_{\alpha\beta} &= -h_{\alpha\beta\gamma\delta} u_{\gamma,\delta} + d_{\alpha\beta\gamma\delta} w_{,\gamma\delta} - \frac{1}{2} h_{\alpha\beta\gamma\delta} w_{,\gamma} w_{,\delta} - \widetilde{h}_{\alpha\beta\gamma\delta} \dot{u}_{\gamma,\delta} + \widetilde{d}_{\alpha\beta\gamma\delta} \dot{w}_{,\gamma\delta} \\ &\quad + \frac{1}{2} \widetilde{h}_{\alpha\beta\gamma\delta} (\dot{w}_{,\gamma} w_{,\delta} + w_{,\gamma} \dot{w}_{,\delta}) \\ n_{\alpha\beta} &= b_{\alpha\beta\gamma\delta} u_{\gamma,\delta} - h_{\alpha\beta\gamma\delta} w_{,\gamma\delta} + \frac{1}{2} b_{\alpha\beta\gamma\delta} w_{,\gamma} w_{,\delta} + \widetilde{b}_{\alpha\beta\gamma\delta} \dot{u}_{\gamma,\delta} - \widetilde{h}_{\alpha\beta\gamma\delta} \dot{w}_{,\gamma\delta} \\ &\quad + \frac{1}{2} \widetilde{b}_{\alpha\beta\gamma\delta} (\dot{w}_{,\gamma} w_{,\delta} + w_{,\gamma} \dot{w}_{,\delta}) \end{aligned} \tag{2.8}$$

— equilibrium equations

$$\begin{aligned} &m_{\alpha\beta,\alpha\beta} - (n_{\alpha\beta}w_{,\alpha})_{,\beta} + \mu\ddot{w} - j\ddot{w}_{,\alpha\alpha} + kw + \widehat{\mu}\ddot{w} + c\dot{w} + i\ddot{u}_{\alpha,\alpha} = p \\ &- n_{\alpha\beta,\beta} + \mu\ddot{u}_{\alpha} - i\ddot{w}_{,\alpha} = 0 \end{aligned} \tag{2.9}$$

or after substituting equations (2.8) into (2.9) as

$$\begin{aligned} &\Big\{-h_{\alpha\beta\gamma\delta}\Big(u^0_{\gamma,\delta} + \frac{1}{2}w_{,\gamma}w_{,\delta}\Big) + d_{\alpha\beta\gamma\delta}w_{,\gamma\delta} - \widetilde{h}_{\alpha\beta\gamma\delta}\Big[\dot{u}^0_{\gamma,\delta} - \frac{1}{2}(\dot{w}_{,\gamma}w_{,\delta} + w_{,\gamma}\dot{w}_{,\delta})\Big] \\ &\quad + \widetilde{d}_{\alpha\beta\gamma\delta}\dot{w}_{,\gamma\delta}\Big\}_{,\alpha\beta} - \Big\{\Big[b_{\alpha\beta\gamma\delta}\Big(u^0_{\gamma,\delta} + \frac{1}{2}w_{,\gamma}w_{,\delta}\Big) - h_{\alpha\beta\gamma\delta}w_{,\gamma\delta} \\ &\quad + \widetilde{b}_{\alpha\beta\gamma\delta}\Big[\dot{u}^0_{\gamma,\delta} + \frac{1}{2}(\dot{w}_{,\gamma}w_{,\delta} + w_{,\gamma}\dot{w}_{,\delta})\Big] - \widetilde{h}_{\alpha\beta\gamma\delta}\dot{w}_{,\gamma\delta}\Big]w_{,\alpha}\Big\}_{,\beta} \\ &\quad + \mu\ddot{w} - j\ddot{w}_{,\alpha\alpha} + kw + \widehat{\mu}\ddot{w} + c\dot{w} + i\ddot{u}^0_{\alpha,\alpha} = p \\ &- \Big\{b_{\alpha\beta\gamma\delta}\Big(u^0_{\gamma,\delta} + \frac{1}{2}w_{,\gamma}w_{,\delta}\Big) - h_{\alpha\beta\gamma\delta}w_{,\gamma\delta} + \widetilde{b}_{\alpha\beta\gamma\delta}\Big[\dot{u}^0_{\gamma,\delta} + \frac{1}{2}(\dot{w}_{,\gamma}w_{,\delta} + w_{,\gamma}\dot{w}_{,\delta})\Big] \\ &\quad - \widetilde{h}_{\alpha\beta\gamma\delta}\dot{w}_{,\gamma\delta}\Big\}_{,\beta} + \mu\ddot{u}^0_{\alpha} - i\ddot{w}_{,\alpha} = 0 \end{aligned} \tag{2.10}$$

It can be observed that coefficients of equations (2.8) and (2.9) (or (2.10)) can be discontinuous and highly oscillating, periodic functions in $\mathbf{x}$, cf. (2.7). Hence, solutions to these equations are very difficult to obtain.

The main aim of this paper is to propose a replacement of original equations with approximate models, which describe (or not) the information about the microstructure of considered plates by using systems of equations with constant coefficients.

3. Outline of the tolerance modelling

3.1. Introductory concepts

In the tolerance modelling, certain introductory concepts are used. Following Woźniak *et al.* (2008, 2010) some of them are reminded below.

A cell at $\mathbf{x} \in \Pi_{\Delta}$ is denoted by $\Delta(\mathbf{x}) = \mathbf{x} + \Delta$, $\Pi_{\Delta} = \{\mathbf{x} \in \Pi : \Delta(\mathbf{x}) \subset \Pi\}$. The fundamental concept of the modelling technique is the averaging operator, defined by

$$\langle\phi\rangle(\mathbf{x}) = \frac{1}{l_1 l_2}\int\limits_{\Delta(\mathbf{x})} f(y_1, y_2)\, dy_1\, dy_2 \qquad \mathbf{x} \in \Pi_{\Delta} \qquad \mathbf{y} \in \Delta(\mathbf{x}) \tag{3.1}$$

for an integrable function φ. If the function φ is periodic in $\mathbf{x}$, its averaged value calculated from (3.1) is constant.

Let δ be an arbitrary positive number and X be a linear normed space. The tolerance relation $\approx$ for a certain positive constant δ, called the tolerance parameter, is defined by

$$(\forall(\mathbf{x}_1, \mathbf{x}_2) \in X^2) \quad [\mathbf{x}_1 \approx \mathbf{x}_2 \Leftrightarrow \|\mathbf{x}_1 - \mathbf{x}_2\|_X \leqslant \delta] \tag{3.2}$$

Let $\partial^k\varphi$ denote the k-th gradient of the function $\varphi = \varphi(\mathbf{x})$, $\mathbf{x} \in \Pi$, $k = 0, 1, \ldots, \alpha$, $\alpha \geqslant 0$, and $\partial^0\varphi \equiv \varphi$. Let $\widetilde{\phi}^{(k)}(\mathbf{x}, \cdot)$ be a function defined in $\overline{\Pi} \times R^m$, and δ be the tolerance parameter. Introduce also $\Pi_{\mathbf{x}} \equiv \Pi \cap \bigcup\limits_{\mathbf{z} \in \Delta(\mathbf{x})} \Delta(\mathbf{z})$, $\mathbf{x} \in \overline{\Pi}$.

The function $\varphi \in H^\alpha(\Pi)$ is called the tolerance-periodic function (with respect to cell Δ and tolerance parameter δ), $\varphi \in TP^\alpha_\delta(\Pi, \Delta)$, if for $k = 0, 1, \ldots, \alpha$, the following conditions are satisfied

$$\begin{aligned} &(i) \quad (\forall \mathbf{x} \in \Pi)(\exists \widetilde{\phi}^{(k)}(\mathbf{x}, \cdot) \in H^0(\Delta))\Big[\Big\|\partial^k \phi\Big\|_{\Pi_\mathbf{x}}(\cdot) - \widetilde{\phi}^{(k)}(\mathbf{x}, \cdot)\Big\|_{H^0(\Pi_\mathbf{x})} \leqslant \delta\Big] \\ &(ii) \quad \int\limits_{\Delta(\cdot)} \widetilde{\phi}^{(k)}(\cdot, \mathbf{z})\, d\mathbf{z} \in C^0(\overline{\Pi}) \end{aligned} \tag{3.3}$$

The function $\widetilde{\varphi}^{(k)}(\mathbf{x}, \cdot)$ is a periodic approximation of $\partial^k \varphi$ in $\Delta(\mathbf{x})$, $\mathbf{x} \in \Pi$, $k = 0, 1, \ldots, \alpha$.

The function $F \in H^\alpha(\Pi)$ is a slowly-varying function, $F \in SV^\alpha_\delta(\Pi, \Delta)$, if

$$\begin{aligned} &(i) \quad F \in TP^\alpha_\delta(\Pi, \Delta) \\ &(ii) \quad (\forall \mathbf{x} \in \Pi)\Big[\widetilde{F}^{(k)}(\mathbf{x}, \cdot)\Big|_{\Delta(\mathbf{x})} = \partial^k F(\mathbf{x}),\ k = 0, \ldots, \alpha\Big] \end{aligned} \tag{3.4}$$

The function $\phi \in H^\alpha(\Pi)$ is a highly oscillating function, $\phi \in HO^\alpha_\delta(\Pi, \Delta)$, if

$$\begin{aligned} &(i) \quad \phi \in TP^\alpha_\delta(\Pi, \Delta) \\ &(ii) \quad (\forall \mathbf{x} \in \Pi)\Big[\widetilde{\phi}^{(k)}(\mathbf{x}, \cdot)\Big|_{\Delta(\mathbf{x})} = \partial^k \widetilde{\phi}(\mathbf{x}),\ k = 0, \ldots, \alpha\Big] \\ &(iii) \quad \forall F \in SV^\alpha_\delta(\Pi, \Delta) \quad \exists \varphi = \phi F \in TP^\alpha_\delta(\Pi, \Delta) \\ &\qquad \widetilde{\varphi}^{(k)}(\mathbf{x}, \cdot)\Big|_{\Delta(\mathbf{x})} = F(\mathbf{x}) \partial^k \widetilde{\phi}(\mathbf{x})\Big|_{\Delta(\mathbf{x})},\ k = 1, \ldots, \alpha \end{aligned} \tag{3.5}$$

For $\alpha = 0$, let us denote $\widetilde{\varphi} \equiv \widetilde{\varphi}^{(0)}$.

Let us introduce two highly oscillating functions defined on $\overline{\Pi}$, $f(\cdot)$, $g(\cdot)$, $f \in HO^1_\delta(\Pi, \Delta)$, $g \in HO^2_\delta(\Pi, \Delta)$.

Let the function $f(\cdot)$ be continuous and have a piecewise continuous and bounded gradient $\partial^1 f$. The function $f(\cdot)$ is a fluctuation shape function of the 1st kind, $FS^1_\delta(\Pi, \Delta)$, if it depends on l as a parameter and the conditions hold

$$\begin{aligned} &(i) \quad \partial^k f \in O(l^{\alpha - k}) \ \text{ for } \ k = 0, \alpha,\ \alpha = 1,\ \partial^0 f \equiv f \\ &(ii) \quad \langle f \rangle(\mathbf{x}) \approx 0\ \forall \mathbf{x} \in \Pi_\Delta \end{aligned} \tag{3.6}$$

where l is the microstructure parameter. Condition $(3.6)_{(ii)}$ can be replaced by $\langle \mu f \rangle(\mathbf{x}) \approx 0$ for every $\mathbf{x} \in \Pi_\Delta$, where $\mu > 0$ is a certain tolerance-periodic function.

However, let $g(\cdot)$ be a continuous function together with the gradient $\partial^1 g$ and with the piecewise continuous and bounded gradient $\partial^2 g$. The function $g(\cdot)$ is a fluctuation shape function of the 2-nd kind, $FS^2_\delta(\Pi, \Delta)$, if it depends on l as a parameter and the conditions hold

$$\begin{aligned} &(i) \quad \partial^k g \in O(l^{\alpha - k}) \ \text{ for } \ k = 0, 1, \ldots, \alpha,\ \alpha = 2,\ \partial^0 g \equiv g \\ &(ii) \quad \langle g \rangle(\mathbf{x}) \approx 0\ \forall \mathbf{x} \in \Pi_\Delta \end{aligned} \tag{3.7}$$

where l is the microstructure parameter. Condition $(3.7)_{(ii)}$ can be replaced by $\langle \mu g \rangle(\mathbf{x}) \approx 0$ for every $\mathbf{x} \in \Pi_\Delta$, where $\mu > 0$ is a certain tolerance-periodic function.

3.2. Fundamental assumptions of the tolerance modelling

The tolerance modelling is based on two fundamental modelling assumptions which are formulated in general form in the books by Woźniak *et al.* (2008, 2010). Here, they are shown below in the form for thin periodic plates.

The micro-macro decomposition is the first assumption in which it is assumed that the deflection and the in-plane displacements can be decomposed as

$$\begin{aligned} &w(\mathbf{x},t) = W(\mathbf{x},t) + g^A(\mathbf{x})V^A(\mathbf{x},t) && A=1,\ldots,N \\ &u^0_\alpha(\mathbf{x},t) = U_\alpha(\mathbf{x},t) + f^a(\mathbf{x})T^a_\alpha(\mathbf{x},t) && a=1,\ldots,m \end{aligned} \tag{3.8}$$

and the functions $W(\cdot,t), V^A(\cdot,t) \in SV^2_\delta(\Pi,\Delta)$, $U_\alpha(\cdot,t), T^a_\alpha(\cdot,t) \in SV^1_\delta(\Pi,\Delta)$ are the basic unknowns; $g^A(\cdot) \in FS^2_\delta(\Pi,\Delta)$, $f^a(\cdot) \in FS^1_\delta(\Pi,\Delta)$ are the known fluctuation shape functions. The functions $W(\cdot,t)$ and $U_\alpha(\cdot,t)$ are called the macrodeflection and the in-plane macrodisplacements, respectively; $V^A(\cdot,t)$ and $T^a_\alpha(\cdot,t)$ are called the fluctuation amplitudes of the deflection and the in-plane displacements, respectively. The fluctuation shape function can be obtained as solutions to eigenvalue problems posed on the periodicity cell, cf. Jędrysiak (2009). However, in most cases, they are assumed in an approximate form as: trigonometric functions (g^A) or saw-type functions (f^a), see Jędrysiak (2003, 2013).

Moreover, similar assumptions to (3.8) are introduced for virtual displacements $\overline{w}(\cdot)$, $\overline{u}^0_\alpha(\cdot)$

$$\begin{aligned} &\overline{w}(\mathbf{x}) = \overline{W}(\mathbf{x}) + g^A(\mathbf{x})\overline{V}^A(\mathbf{x}) && A=1,\ldots,N \\ &\overline{u}^0_\alpha(\mathbf{x}) = \overline{U}_\alpha(\mathbf{x}) + f^a(\mathbf{x})\overline{T}^a_\alpha(\mathbf{x}) && a=1,\ldots,m \end{aligned} \tag{3.9}$$

with slowly-varying functions $\overline{W}(\cdot), \overline{V}^A(\cdot) \in SV^2_\delta(\Pi,\Delta)$, $\overline{U}_\alpha(\cdot), \overline{T}^a_\alpha(\cdot) \in SV^1_\delta(\Pi,\Delta)$.

In the tolerance averaging approximation, the terms $O(\delta)$ are assumed to be negligibly small in the course of modelling, i.e. they can be omitted in the following formulas

$$\begin{aligned} &(i) \quad \langle\varphi\rangle(\mathbf{x}) = \langle\widetilde{\varphi}(\mathbf{x}) + O(\delta) \\ &(ii) \quad \langle\varphi\rangle F\rangle(\mathbf{x}) = \langle\varphi\rangle(\mathbf{x})F(\mathbf{x}) + O(\delta) \\ &(iii) \quad \langle\varphi\rangle(gF)_{,\gamma}(\mathbf{x}) = \langle\varphi\rangle g_{,\gamma}(\mathbf{x})F(\mathbf{x}) + O(\delta) \\ &\mathbf{x}\in\Pi; \quad \gamma=1,\alpha; \quad \alpha=1,2; \quad 0<\delta\ll 1; \\ &\varphi\in TP^\alpha_\delta(\Pi,\Delta); \quad F\in SV^\alpha_\delta(\Pi,\Delta); \quad g\in FS^\alpha_\delta(\Pi,\Delta) \end{aligned} \tag{3.10}$$

3.3. The modelling procedure

The above concepts and fundamental assumptions are used in the modelling procedure. This procedure can be divided into four steps.

In the first step, micro-macro decompositions (3.8) and (3.9) are substituted into virtual work equation (2.6) of such a plate resting on a foundation. Then, in the second step, the averaging operation is used to average the resulting equation over the periodicity cell, see Jędrysiak (2003).

In the next step, we arrive at the tolerance averaged virtual work equation after using formulas (3.10) of the tolerance averaging approximation (Jędrysiak, 2003). Applying the following denotations of some averaged parameters, being averaged constitutive relations

$$
\begin{aligned}
&M_{\alpha\beta} \equiv -\Big\langle \int\limits_{-d/2}^{d/2} s_{\alpha\beta} z \, dz \Big\rangle && M^A \equiv -\Big\langle g^A_{,\alpha\beta} \int\limits_{-d/2}^{d/2} s_{\alpha\beta} z \, dz \Big\rangle \\
&N_{\alpha\beta} = \Big\langle \int\limits_{-d/2}^{d/2} s_{\alpha\beta} \, dz \Big\rangle && N^a_\alpha \equiv \Big\langle \int\limits_{-d/2}^{d/2} s_{\alpha\beta} f^a_{,\beta} \, dz \Big\rangle \\
&Q^A_\alpha \equiv \Big\langle \int\limits_{-d/2}^{d/2} s_{\alpha\beta} g^A_{,\beta} \, dz \Big\rangle && R^{AB} \equiv \Big\langle \int\limits_{-d/2}^{d/2} s_{\alpha\beta} g^A_{,\alpha} g^B_{,\beta} \, dz \Big\rangle
\end{aligned}
\tag{3.11}
$$

this tolerance averaged virtual work equation can be written as

$$
\begin{aligned}
&\int\limits_\Pi (\langle\mu\rangle \ddot{W} + \langle\mu g^B\rangle \ddot{V}^B)\delta W \, da + \int\limits_\Pi (\langle\mu g^A\rangle \ddot{W} + \langle\mu g^A g^B\rangle \ddot{V}^B)\delta V^A \, da \\
&\quad + \int\limits_\Pi (\langle\mu\rangle \ddot{U}_\alpha + \langle\mu f^b\rangle \ddot{T}^b_\alpha - \langle i\rangle \ddot{W}_{,\alpha} - \langle i g^B_{,\alpha}\rangle \ddot{V}^B)\delta U_\alpha \, da \\
&\quad + \int\limits_\Pi (\langle\mu f^a\rangle \ddot{U}_\alpha + \langle\mu f^a f^b\rangle \ddot{T}^b_\alpha - \langle i f^a\rangle \ddot{W}_{,\alpha} - \langle i f^a g^B_{,\alpha}\rangle \ddot{V}^B)\delta T^a_\alpha \, da \\
&\quad - \int\limits_\Pi (-\langle i\rangle \ddot{U}_{\alpha,\alpha} - \langle i f^b\rangle \ddot{T}^b_{\alpha,\alpha} + \langle j\rangle \ddot{W}_{,\alpha\alpha} + \langle j g^B_{,\alpha}\rangle \ddot{V}^B_{,\alpha})\delta W \, da \\
&\quad + \int\limits_\Pi (-\langle i g^A_{,\alpha}\rangle \ddot{U}_\alpha - \langle i f^b g^A_{,\alpha}\rangle \ddot{T}^b_\alpha + \langle j g^A_{,\alpha}\rangle \ddot{W}_{,\alpha} + \langle j g^A_{,\alpha} g^B_{,\alpha}\rangle \ddot{V}^B)\delta V^A \, da \\
&\quad - \int\limits_\Pi N_{\alpha\beta,\beta}\delta U_\alpha \, da + \int\limits_\Pi N^a_\alpha \delta T^a_\alpha \, da \\
&\quad + \int\limits_\Pi [M_{\alpha\beta,\alpha\beta} - (N_{\alpha\beta} W_{,\alpha} + Q^A_\beta V^A)_{,\beta}]\delta W \, da \\
&\quad + \int\limits_\Pi (M^A + Q^A_\alpha W_{,\alpha} + R^{AB} V^B)\delta V^A \, da \\
&\quad = \int\limits_\Pi p\delta W \, da - \int\limits_\Pi (\langle k\rangle W + \langle k g^B\rangle V^B)\delta W \, da \\
&\quad - \int\limits_\Pi (\langle k g^A\rangle W + \langle k g^A g^B\rangle V^B)\delta V^A \, da \\
&\quad - \int\limits_\Pi (\langle\widehat{\mu}\rangle \ddot{W} + \langle\widehat{\mu} g^B\rangle \ddot{V}^B)\delta W \, da - \int\limits_\Pi (\langle\widehat{\mu} g^A\rangle \ddot{W} + \langle\widehat{\mu} g^A g^B\rangle \ddot{V}^B)\delta V^A \, da \\
&\quad - \int\limits_\Pi (\langle c\rangle \dot{W} + \langle c g^B\rangle \dot{V}^B)\delta W \, da - \int\limits_\Pi (\langle c g^A\rangle \dot{W} + \langle c g^A g^B\rangle \dot{V}^B)\delta V^A \, da
\end{aligned}
\tag{3.12}
$$

Then, using the divergence theorem and the du Bois-Reymond lemma to equation (3.12), after some manipulations, governing equations of the proposed approximate tolerance model can be obtained.

4. Governing equations

4.1. Tolerance model equations

Let us introduce denotations

$$
\begin{aligned}
&B_{\alpha\beta\gamma\delta} \equiv \langle b_{\alpha\beta\gamma\delta}\rangle && B^{a}_{\alpha\beta\gamma} \equiv \langle b_{\alpha\beta\gamma\delta} f^{a}_{,\delta}\rangle\\
&B^{ab}_{\alpha\gamma} \equiv \langle b_{\alpha\beta\gamma\delta} f^{a}_{,\beta} f^{b}_{,\delta}\rangle && D_{\alpha\beta\gamma\delta} \equiv \langle d_{\alpha\beta\gamma\delta}\rangle\\
&D^{A}_{\alpha\beta} \equiv \langle d_{\alpha\beta\gamma\delta} g^{A}_{,\gamma\delta}\rangle && D^{AB} \equiv \langle d_{\alpha\beta\gamma\delta} g^{A}_{,\alpha\beta} g^{B}_{,\gamma\delta}\rangle\\
&F^{ABC}_{\alpha} \equiv l^{-3}\langle b_{\alpha\beta\gamma\delta} g^{A}_{,\beta} g^{B}_{,\gamma} g^{C}_{,\delta}\rangle && F^{A}_{\alpha\beta\gamma} \equiv l^{-1}\langle b_{\alpha\beta\gamma\delta} g^{A}_{,\delta}\rangle\\
&F^{AB}_{\alpha\beta} \equiv l^{-2}\langle b_{\alpha\beta\gamma\delta} g^{A}_{,\gamma} g^{B}_{,\delta}\rangle && F^{aB}_{\alpha\gamma} \equiv l^{-1}\langle b_{\alpha\beta\gamma\delta} f^{a}_{,\beta} g^{B}_{,\delta}\rangle\\
&F^{aBC}_{\alpha} \equiv l^{-2}\langle b_{\alpha\beta\gamma\delta} f^{a}_{,\beta} g^{B}_{,\gamma} g^{C}_{,\delta}\rangle && F^{ABCD} \equiv l^{-4}\langle b_{\alpha\beta\gamma\delta} g^{A}_{,\alpha} g^{B}_{,\beta} g^{C}_{,\gamma} g^{D}_{,\delta}\rangle\\
&G^{A}_{\alpha\beta\gamma} \equiv l^{-1}\langle h_{\alpha\beta\gamma\delta} g^{A}_{,\delta}\rangle && G^{AB}_{\alpha\beta} \equiv l^{-2}\langle h_{\alpha\beta\gamma\delta} g^{A}_{,\gamma} g^{B}_{,\delta}\rangle\\
&G^{AB}_{\gamma} \equiv l^{-1}\langle h_{\alpha\beta\gamma\delta} g^{A}_{,\alpha\beta} g^{B}_{,\delta}\rangle && G^{ABC} \equiv l^{-2}\langle h_{\alpha\beta\gamma\delta} g^{A}_{,\alpha\beta} g^{B}_{,\gamma} g^{C}_{,\delta}\rangle\\
&H_{\alpha\beta\gamma\delta} \equiv \langle h_{\alpha\beta\gamma\delta}\rangle && H^{A}_{\alpha\beta} \equiv \langle h_{\alpha\beta\gamma\delta} g^{A}_{,\gamma\delta}\rangle\\
&H^{a}_{\alpha\gamma\delta} \equiv \langle h_{\alpha\beta\gamma\delta} f^{a}_{,\beta}\rangle && H^{aB}_{\alpha} \equiv \langle h_{\alpha\beta\gamma\delta} f^{a}_{,\beta} g^{B}_{,\gamma\delta}\rangle\\
&\widetilde{B}_{\alpha\beta\gamma\delta} \equiv \langle \widetilde{b}_{\alpha\beta\gamma\delta}\rangle && \widetilde{B}^{a}_{\alpha\beta\gamma} \equiv \langle \widetilde{b}_{\alpha\beta\gamma\delta} f^{a}_{,\delta}\rangle\\
&\widetilde{B}^{ab}_{\alpha\gamma} \equiv \langle \widetilde{b}_{\alpha\beta\gamma\delta} f^{a}_{,\beta} f^{b}_{,\delta}\rangle && \widetilde{D}_{\alpha\beta\gamma\delta} \equiv \langle \widetilde{d}_{\alpha\beta\gamma\delta}\rangle\\
&\widetilde{D}^{A}_{\alpha\beta} \equiv \langle \widetilde{d}_{\alpha\beta\gamma\delta} g^{A}_{,\gamma\delta}\rangle && \widetilde{D}^{AB} \equiv \langle \widetilde{d}_{\alpha\beta\gamma\delta} g^{A}_{,\alpha\beta} g^{B}_{,\gamma\delta}\rangle\\
&\widetilde{F}^{ABC}_{\alpha} \equiv l^{-3}\langle \widetilde{b}_{\alpha\beta\gamma\delta} g^{A}_{,\beta} g^{B}_{,\gamma} g^{C}_{,\delta}\rangle && \widetilde{F}^{A}_{\alpha\beta\gamma} \equiv l^{-1}\langle \widetilde{b}_{\alpha\beta\gamma\delta} g^{A}_{,\delta}\rangle\\
&\widetilde{F}^{AB}_{\alpha\beta} \equiv l^{-2}\langle \widetilde{b}_{\alpha\beta\gamma\delta} g^{A}_{,\gamma} g^{B}_{,\delta}\rangle && \widetilde{F}^{aB}_{\alpha\gamma} \equiv l^{-1}\langle \widetilde{b}_{\alpha\beta\gamma\delta} f^{a}_{,\beta} g^{B}_{,\delta}\rangle\\
&\widetilde{F}^{aBC}_{\alpha} \equiv l^{-2}\langle \widetilde{b}_{\alpha\beta\gamma\delta} f^{A}_{,\beta} g^{B}_{,\gamma} g^{C}_{,\delta}\rangle && \widetilde{F}^{ABCD} \equiv l^{-4}\langle \widetilde{b}_{\alpha\beta\gamma\delta} g^{A}_{,\alpha} g^{B}_{,\beta} g^{C}_{,\gamma} g^{D}_{,\delta}\rangle\\
&\widetilde{G}^{A}_{\alpha\beta\gamma} \equiv l^{-1}\langle \widetilde{h}_{\alpha\beta\gamma\delta} g^{A}_{,\delta}\rangle && \widetilde{G}^{AB}_{\alpha\beta} \equiv l^{-2}\langle \widetilde{h}_{\alpha\beta\gamma\delta} g^{A}_{,\gamma} g^{B}_{,\delta}\rangle\\
&\widetilde{G}^{AB}_{\gamma} \equiv l^{-1}\langle \widetilde{h}_{\alpha\beta\gamma\delta} g^{A}_{,\alpha\beta} g^{B}_{,\delta}\rangle && \widetilde{G}^{ABC} \equiv l^{-2}\langle \widetilde{h}_{\alpha\beta\gamma\delta} g^{A}_{,\alpha\beta} g^{B}_{,\gamma} g^{C}_{,\delta}\rangle\\
&\widetilde{H}_{\alpha\beta\gamma\delta} \equiv \langle \widetilde{h}_{\alpha\beta\gamma\delta}\rangle && \widetilde{H}^{A}_{\alpha\beta} \equiv \langle \widetilde{h}_{\alpha\beta\gamma\delta} g^{A}_{,\gamma\delta}\rangle\\
&\widetilde{H}^{a}_{\alpha\gamma\delta} \equiv \langle \widetilde{h}_{\alpha\beta\gamma\delta} f^{a}_{,\beta}\rangle && \widetilde{H}^{aB}_{\alpha} \equiv \langle \widetilde{h}_{\alpha\beta\gamma\delta} f^{a}_{,\beta} g^{B}_{,\gamma\delta}\rangle\\
&m \equiv \langle \mu\rangle && m^{A} \equiv l^{-2}\langle \mu g^{A}\rangle\\
&m^{AB} \equiv l^{-4}\langle \mu g^{A} g^{B}\rangle && \vartheta \equiv \langle j\rangle\\
&\vartheta^{A}_{\alpha} \equiv l^{-1}\langle j g^{A}_{,\alpha}\rangle && \vartheta^{AB}_{\alpha\beta} \equiv l^{-2}\langle j g^{A}_{,\alpha} g^{B}_{,\beta}\rangle\\
&\theta \equiv \langle i\rangle && \theta^{a} \equiv l^{-1}\langle i f^{a}\rangle\\
&\theta^{A}_{\alpha} \equiv l^{-1}\langle i g^{A}_{,\alpha}\rangle && \theta^{aA}_{\alpha} \equiv l^{-2}\langle i f^{a} g^{A}_{,\alpha}\rangle\\
&C \equiv \langle c\rangle && C^{A} \equiv l^{-2}\langle c g^{A}\rangle\\
&C^{AB} \equiv l^{-4}\langle c g^{A} g^{B}\rangle && K \equiv \langle k\rangle\\
&K^{A} \equiv l^{-2}\langle k g^{A}\rangle && K^{AB} \equiv l^{-4}\langle k g^{A} g^{B}\rangle\\
&\widehat{m} \equiv \langle \widehat{\mu}\rangle && \widehat{m}^{A} \equiv l^{-2}\langle \widehat{\mu} g^{A}\rangle\\
&\widehat{m}^{AB} \equiv l^{-4}\langle \widehat{\mu} g^{A} g^{B}\rangle && \overline{m}^{a} \equiv l^{-1}\langle \mu f^{a}\rangle\\
&\overline{m}^{ab} \equiv l^{-4}\langle \mu f^{a} f^{b}\rangle && P \equiv \langle p\rangle \qquad P^{A} \equiv l^{-2}\langle p g^{A}\rangle
\end{aligned}
\tag{4.1}
$$

Using the tolerance modelling procedure, a system of equations for the in-plane macrodisplacements U_α, fluctuation amplitudes of the in-plane macrodisplacements T^a_α, macrodeflection W, fluctuation amplitudes of the deflection V^A can be derived:

— constitutive equations

$$
\begin{aligned}
M_{\alpha\beta} &= -H_{\alpha\beta\gamma\delta}\Big(U_{\gamma,\delta}+\frac{1}{2}W_{,\gamma}W_{,\delta}\Big) - H^a_{\alpha\beta\gamma}T^a_\gamma + D_{\alpha\beta\gamma\delta}W_{,\gamma\delta} + D^A_{\alpha\beta}V^A \\
&\quad - lG^A_{\alpha\beta\gamma}[W_{,\gamma}V^A + (\dot W_{,\gamma}V^A + W_{,\gamma}\dot V^A)] - \frac{1}{2}l^2G^{AB}_{\alpha\beta}[V^AV^B + (\dot V^AV^B + V^A\dot V^B)] \\
&\quad - \widetilde H_{\alpha\beta\gamma\delta}\Big[\dot U_{\gamma,\delta} - \frac{1}{2}(\dot W_{,\gamma}W_{,\delta} + W_{,\gamma}\dot W_{,\delta})\Big] - \widetilde H^a_{\alpha\beta\gamma}\dot T^a_\gamma + \widetilde D_{\alpha\beta\gamma\delta}\dot W_{,\gamma\delta} + \widetilde D^A_{\alpha\beta}\dot V^A \\
M^A &= -H^A_{\alpha\beta}\Big(U_{\gamma,\delta}+\frac{1}{2}W_{,\gamma}W_{,\delta}\Big) - H^{aA}_\alpha T^a_\alpha + D^A_{\alpha\beta}W_{,\gamma\delta} + D^{AB}V^B \\
&\quad - lG^{AB}_\gamma W_{,\gamma}V^B - \frac{1}{2}l^2G^{ABC}V^BV^C - \widetilde H^A_{\alpha\beta}\Big[\dot U_{\gamma,\delta} + \frac{1}{2}(\dot W_{,\gamma}W_{,\delta} + W_{,\gamma}\dot W_{,\delta})\Big] \\
&\quad - \widetilde H^{aA}_\alpha\dot T^a_\alpha + \widetilde D^A_{\alpha\beta}\dot W_{,\gamma\delta} + \widetilde D^{AB}\dot V^B - l\widetilde G^{AB}_\gamma(\dot W_{,\gamma}V^B + W_{,\gamma}\dot V^B) \\
&\quad - \frac{1}{2}l^2\widetilde G^{ABC}(\dot V^BV^C + V^B\dot V^C) \\
N_{\alpha\beta} &= B_{\alpha\beta\gamma\delta}\Big(U_{\gamma,\delta}+\frac{1}{2}W_{,\gamma}W_{,\delta}\Big) + B^a_{\alpha\beta\gamma}T^a_\gamma - H_{\alpha\beta\gamma\delta}W_{,\gamma\delta} - H^A_{\alpha\beta}V^A + lF^A_{\alpha\beta\gamma}W_{,\gamma}V^A \\
&\quad + \frac{1}{2}l^2F^{AB}_{\alpha\beta}V^AV^B + \widetilde B_{\alpha\beta\gamma\delta}\Big[\dot U_{\gamma,\delta} + \frac{1}{2}(\dot W_{,\gamma}W_{,\delta} + W_{,\gamma}\dot W_{,\delta})\Big] + \widetilde B^a_{\alpha\beta\gamma}\dot T^a_\gamma - \widetilde H_{\alpha\beta\gamma\delta}\dot W_{,\gamma\delta} \\
&\quad - \widetilde H^A_{\alpha\beta}\dot V^A + l\widetilde F^A_{\alpha\beta\gamma}(\dot W_{,\gamma}V^A + W_{,\gamma}\dot V^A) + \frac{1}{2}l^2\widetilde F^{AB}_{\alpha\beta}(\dot V^AV^B + V^A\dot V^B) \\
N^a_\alpha &= B^a_{\alpha\gamma\delta}\Big(U_{\gamma,\delta}+\frac{1}{2}W_{,\gamma}W_{,\delta}\Big) + B^{ab}_{\alpha\gamma}T^b_\gamma - H^a_{\alpha\gamma\delta}W_{,\gamma\delta} - H^{aB}_\alpha V^B + lF^{aB}_{\alpha\gamma}W_{,\gamma}V^B \\
&\quad + \frac{1}{2}l^2F^{aBC}_\alpha V^BV^C + \widetilde B^a_{\alpha\gamma\delta}\Big[\dot U_{\gamma,\delta} + \frac{1}{2}(\dot W_{,\gamma}W_{,\delta} + W_{,\gamma}\dot W_{,\delta})\Big] + \widetilde B^{ab}_{\alpha\gamma}\dot T^b_\gamma - \widetilde H^a_{\alpha\gamma\delta}\dot W_{,\gamma\delta} \\
&\quad - \widetilde H^{aB}_\alpha\dot V^B + l\widetilde F^{aB}_{\alpha\gamma}(\dot W_{,\gamma}V^B + W_{,\gamma}\dot V^B) + \frac{1}{2}l^2\widetilde F^{aBC}_\alpha(\dot V^BV^C + V^B\dot V^C) \\
Q^A_\alpha &= lF^A_{\alpha\gamma\delta}\Big(U_{\gamma,\delta}+\frac{1}{2}W_{,\gamma}W_{,\delta}\Big) + lF^{aA}_{\alpha\gamma}T^a_\gamma - lG^A_{\alpha\gamma\delta}W_{,\gamma\delta} - lG^{AB}_\alpha V^B + l^2F^{AB}_{\alpha\gamma}W_{,\gamma}V^B \\
&\quad + \frac{1}{2}l^3F^{ABC}_\alpha V^BV^C + l\widetilde F^A_{\alpha\gamma\delta}\dot U_{\gamma,\delta} + l\widetilde F^{aA}_{\alpha\gamma}\Big[\dot T^a_\gamma + \frac{1}{2}(\dot W_{,\gamma}W_{,\delta} + W_{,\gamma}\dot W_{,\delta})\Big] \\
&\quad - l\widetilde G^A_{\alpha\gamma\delta}\dot W_{,\gamma\delta} - l\widetilde G^{AB}_\alpha\dot V^B + l^2\widetilde F^{AB}_{\alpha\gamma}(\dot W_{,\gamma}V^B + W_{,\gamma}\dot V^B) + \frac{1}{2}l^3\widetilde F^{ABC}_\alpha(\dot V^BV^C + V^B\dot V^C) \\
R^{AB} &= l^2F^{AB}_{\gamma\delta}\Big(U_{\gamma,\delta}+\frac{1}{2}W_{,\gamma}W_{,\delta}\Big) + l^2F^{aAB}_\gamma T^a_\gamma - l^2G^{AB}_{\gamma\delta}W_{,\gamma\delta} - l^2G^{ABC}V^C + l^3F^{ABC}_\gamma W_{,\gamma}V^C \\
&\quad + \frac{1}{2}l^4F^{ABCD}V^CV^D + l^2\widetilde F^{AB}_{\gamma\delta}\Big[\dot U_{\gamma,\delta} + \frac{1}{2}(\dot W_{,\gamma}W_{,\delta} + W_{,\gamma}\dot W_{,\delta})\Big] + l^2\widetilde F^{aAB}_\gamma\dot T^a_\gamma - l^2\widetilde G
\end{aligned}
\tag{4.2}
$$

— equilibrium equations

$$
\begin{aligned}
&M_{\alpha\beta,\alpha\beta} - (N_{\alpha\beta}W_{,\alpha} + Q^A_\beta V^A)_{,\beta} + (m+\widehat m)\ddot W + l^2(m^A+\widehat m^A)\ddot V^A - \vartheta\ddot W_{,\alpha\alpha} - l\vartheta^A_\alpha\ddot V^A_{,\alpha} \\
&\quad + KW + l^2K^AV^A + C\dot W + l^2C^A\dot V^A + \theta\ddot U_{\alpha,\alpha} + l\theta^a\ddot T^a_{\alpha,\alpha} = P \\
&M^A + Q^A_\alpha W_{,\alpha} + R^{AB}V^B + l^2(m^A+\widehat m^A)\ddot W + l\vartheta^A_\alpha\ddot W_{,\alpha} + l^2(l^2m^{AB} + l^2\widehat m^{AB} + \vartheta^{AB}_{\alpha\beta})\ddot V^B \\
&\quad + l^2K^AW + l^4K^{AB}V^B + l^2C^A\dot W + l^4C^{AB}\dot V^B - l\theta^A_\alpha\ddot U_\alpha - l^2\theta^{aA}_\alpha\ddot T^a_\alpha = l^2P^A \\
&-N_{\alpha\beta,\beta} + m\ddot U_\alpha + l\overline m^a\ddot T^a_\alpha - \theta\ddot W_{,\alpha} - l\theta^A_\alpha\ddot V^A = 0 \\
&N^a_\alpha + l\overline m^a\ddot U_\alpha + l^2\overline m^{ab}\ddot T^b_\alpha - l\theta^a\ddot W_{,\alpha} - l^2\theta^{aA}_\alpha\ddot V^A = 0
\end{aligned}
\tag{4.3}
$$

Equations (4.2) and (4.3) together with micro-macro decompositions (3.8) constitute the nonlinear tolerance model of thin visco-elastic periodic plates resting on a foundation with damping if the plate properties are not even functions of z. This model describes the effect of the microstructure size on the overall plate behaviour by terms with the microstructure

parameter l. For the considered plates, boundary conditions have to be formulated only for the macrodeflection W and the in-plane macrodisplacements U_α. Moreover, the basic unknowns of equations (4.2) and (4.3) have to satisfy the following conditions: $W(\cdot,t), V^A(\cdot,t) \in SV^2_\delta(\Pi,\Delta)$, $U_\alpha(\cdot,t), T^a_\alpha(\cdot,t) \in SV^1_\delta(\Pi,\Delta)$, i.e. they are slowly-varying functions in x.

In the next considerations, it is assumed that the plate properties are even functions of z, i.e. plates under consideration have the symmetry plane $z=0$. Hence, some coefficients (4.1) are equal to zero

$$\begin{aligned}
&H_{\alpha\beta\gamma\delta} = H^A_{\alpha\beta} = H^a_{\alpha\gamma\delta} = H^{aB}_{\alpha} = G^A_{\alpha\beta\gamma} = G^{AB}_{\alpha\beta} = G^{AB}_{\gamma} = G^{ABC} = 0\\
&\widetilde{H}_{\alpha\beta\gamma\delta} = \widetilde{H}^A_{\alpha\beta} = \widetilde{H}^a_{\alpha\gamma\delta} = \widetilde{H}^{aB}_{\alpha} = \widetilde{G}^A_{\alpha\beta\gamma} = \widetilde{G}^{AB}_{\alpha\beta} = \widetilde{G}^{AB}_{\gamma} = \widetilde{G}^{ABC} = 0\\
&\theta = \theta^a = \theta^A_\alpha = \theta^{aA}_\alpha = 0
\end{aligned} \tag{4.4}$$

Equations (4.2) and (4.3) take the following form:

— constitutive equations

$$\begin{aligned}
M_{\alpha\beta} &= D_{\alpha\beta\gamma\delta}W_{,\gamma\delta} + D^A_{\alpha\beta}V^A + \widetilde{D}_{\alpha\beta\gamma\delta}\dot{W}_{,\gamma\delta} + \widetilde{D}^A_{\alpha\beta}\dot{V}^A\\
M^A &= D^A_{\alpha\beta}W_{,\gamma\delta} + D^{AB}V^B + \widetilde{D}^A_{\alpha\beta}\dot{W}_{,\gamma\delta} + \widetilde{D}^{AB}\dot{V}^B\\
N_{\alpha\beta} &= B_{\alpha\beta\gamma\delta}\Big(U_{\gamma,\delta} + \frac{1}{2}W_{,\gamma}W_{,\delta}\Big) + B^a_{\alpha\beta\gamma}T^a_\gamma + lF^A_{\alpha\beta\gamma}W_{,\gamma}V^A + \frac{1}{2}l^2F^{AB}_{\alpha\beta}V^AV^B\\
&\quad + \widetilde{B}_{\alpha\beta\gamma\delta}\Big[\dot{U}_{\gamma,\delta} + \frac{1}{2}(\dot{W}_{,\gamma}W_{,\delta} + W_{,\gamma}\dot{W}_{,\delta})\Big] + \widetilde{B}^a_{\alpha\beta\gamma}\dot{T}^a_\gamma\\
&\quad + l\widetilde{F}^A_{\alpha\beta\gamma}(\dot{W}_{,\gamma}V^A + W_{,\gamma}\dot{V}^A) + \frac{1}{2}l^2\widetilde{F}^{AB}_{\alpha\beta}(\dot{V}^AV^B + V^A\dot{V}^B)\\
N^a_\alpha &= B^a_{\alpha\gamma\delta}\Big(U_{\gamma,\delta} + \frac{1}{2}W_{,\gamma}W_{,\delta}\Big) + B^{ab}_{\alpha\gamma}T^b_\gamma + lF^{aB}_{\alpha\gamma}W_{,\gamma}V^B + \frac{1}{2}l^2F^{aBC}_{\alpha}V^BV^C\\
&\quad + \widetilde{B}^a_{\alpha\gamma\delta}\Big[\dot{U}_{\gamma,\delta} + \frac{1}{2}(\dot{W}_{,\gamma}W_{,\delta} + W_{,\gamma}\dot{W}_{,\delta})\Big] + \widetilde{B}^{ab}_{\alpha\gamma}\dot{T}^b_\gamma\\
&\quad + l\widetilde{F}^{aB}_{\alpha\gamma}(\dot{W}_{,\gamma}V^B + W_{,\gamma}\dot{V}^B) + \frac{1}{2}l^2\widetilde{F}^{aBC}_{\alpha}(\dot{V}^BV^C + V^B\dot{V}^C)\\
Q^A_\alpha &= lF^A_{\alpha\gamma\delta}\Big(U_{\gamma,\delta} + \frac{1}{2}W_{,\gamma}W_{,\delta}\Big) + lF^{aA}_{\alpha\gamma}T^a_\gamma + l^2F^{AB}_{\alpha\gamma}W_{,\gamma}V^B + \frac{1}{2}l^3F^{ABC}_{\alpha}V^BV^C\\
&\quad + l\widetilde{F}^A_{\alpha\gamma\delta}\dot{U}_{\gamma,\delta} + l\widetilde{F}^{aA}_{\alpha\gamma}\Big[\dot{T}^a_\gamma + \frac{1}{2}(\dot{W}_{,\gamma}W_{,\delta} + W_{,\gamma}\dot{W}_{,\delta})\Big] + l^2\widetilde{F}^{AB}_{\alpha\gamma}(\dot{W}_{,\gamma}V^B + W_{,\gamma}\dot{V}^B)\\
&\quad + \frac{1}{2}l^3\widetilde{F}^{ABC}_{\alpha}(\dot{V}^BV^C + V^B\dot{V}^C)\\
R^{AB} &= l^2F^{AB}_{\gamma\delta}\Big(U_{\gamma,\delta} + \frac{1}{2}W_{,\gamma}W_{,\delta}\Big) + l^2F^{aAB}_{\gamma}T^a_\gamma + l^3F^{ABC}_{\gamma}W_{,\gamma}V^C + \frac{1}{2}l^4F^{ABCD}V^CV^D\\
&\quad + l^2\widetilde{F}^{aAB}_{\gamma}\dot{T}^a_\gamma + l^2\widetilde{F}^{AB}_{\gamma\delta}\Big[\dot{U}_{\gamma,\delta} + \frac{1}{2}(\dot{W}_{,\gamma}W_{,\delta} + W_{,\gamma}\dot{W}_{,\delta})\Big]\\
&\quad + l^3\widetilde{F}^{ABC}_{\gamma}(\dot{W}_{,\gamma}V^C + W_{,\gamma}\dot{V}^C) + \frac{1}{2}l^4\widetilde{F}^{ABCD}(\dot{V}^CV^D + V^C\dot{V}^D)
\end{aligned} \tag{4.5}$$

— equilibrium equations

$$\begin{aligned}
&M_{\alpha\beta,\alpha\beta} - (N_{\alpha\beta}W_{,\alpha} + Q^A_\beta V^A)_{,\beta} + (m+\widehat{m})\ddot{W} + l^2(m^A+\widehat{m}^A)\ddot{V}^A - \vartheta\ddot{W}_{,\alpha\alpha} - l\vartheta^A_\alpha\ddot{V}^A_{,\alpha}\\
&\quad + KW + l^2K^AV^A + C\dot{W} + l^2C^A\dot{V}^A = P\\
&M^A + Q^A_\alpha W_{,\alpha} + R^{AB}V^B + l^2(m^A+\widehat{m}^A)\ddot{W} + l\vartheta^A_\alpha\ddot{W}_{,\alpha} + l^2(l^2m^{AB} + l^2\widehat{m}^{AB} + \vartheta^{AB}_{\alpha\beta})\ddot{V}^B\\
&\quad + l^2K^AW + l^4K^{AB}V^B + l^2C^A\dot{W} + l^4C^{AB}\dot{V}^B = l^2P^A\\
&-N_{\alpha\beta,\beta} + m\ddot{U}_\alpha + l\overline{m}^a\ddot{T}^a_\alpha = 0\\
&N^a_\alpha + l\overline{m}^a\ddot{U}_\alpha + l^2\overline{m}^{ab}\ddot{T}^b_\alpha = 0
\end{aligned} \tag{4.6}$$

Similarly to equations (4.2) and (4.3), equations (4.5) and (4.6) together with micro-macro decompositions (3.8) constitute the nonlinear tolerance model of thin visco-elastic periodic plates resting on a foundation with damping, but only for plates with the symmetry plane $z = 0$. It can be observed that all above equations (4.2), (4.3) and (4.5), (4.6) have constant coefficients.

4.2. Asymptotic model equations

The asymptotic model equations can be obtained, from the formal point of view, using the asymptotic modelling procedure, see Woźniak *et al.* (2010). Below, this is done by simply neglecting terms of the order of $O(l^n)$, $n = 1, 2, \ldots$, in equations (4.2), (4.3) and (4.5), (4.6).

Hence, from equations (4.2) and (4.3), the equations of the nonlinear asymptotic model take the form:

— constitutive equations

$$
\begin{aligned}
M_{\alpha\beta} &= -H_{\alpha\beta\gamma\delta}\Big(U_{\gamma,\delta} + \frac{1}{2}W_{,\gamma}W_{,\delta}\Big) - H^{a}_{\alpha\beta\gamma}T^{a}_{\gamma} + D_{\alpha\beta\gamma\delta}W_{,\gamma\delta} + D^{A}_{\alpha\beta}V^{A} \\
&\quad - \widetilde{H}_{\alpha\beta\gamma\delta}\Big[\dot{U}_{\gamma,\delta} - \frac{1}{2}(\dot{W}_{,\gamma}W_{,\delta} + W_{,\gamma}\dot{W}_{,\delta})\Big] - \widetilde{H}^{a}_{\alpha\beta\gamma}\dot{T}^{a}_{\gamma} + \widetilde{D}_{\alpha\beta\gamma\delta}\dot{W}_{,\gamma\delta} + \widetilde{D}^{A}_{\alpha\beta}\dot{V}^{A} \\
M^{A} &= -H^{A}_{\alpha\beta}\Big(U_{\gamma,\delta} + \frac{1}{2}W_{,\gamma}W_{,\delta}\Big) - H^{aA}_{\alpha}T^{a}_{\alpha} + D^{A}_{\alpha\beta}W_{,\gamma\delta} + D^{AB}V^{B} \\
&\quad - \widetilde{H}^{A}_{\alpha\beta}\Big[\dot{U}_{\gamma,\delta} + \frac{1}{2}(\dot{W}_{,\gamma}W_{,\delta} + W_{,\gamma}\dot{W}_{,\delta})\Big] - \widetilde{H}^{aA}_{\alpha}\dot{T}^{a}_{\alpha} + \widetilde{D}^{A}_{\alpha\beta}\dot{W}_{,\gamma\delta} + \widetilde{D}^{AB}\dot{V}^{B} \\
N_{\alpha\beta} &= B_{\alpha\beta\gamma\delta}\Big(U_{\gamma,\delta} + \frac{1}{2}W_{,\gamma}W_{,\delta}\Big) + B^{a}_{\alpha\beta\gamma}T^{a}_{\gamma} - H_{\alpha\beta\gamma\delta}W_{,\gamma\delta} - H^{A}_{\alpha\beta}V^{A} \\
&\quad + \widetilde{B}_{\alpha\beta\gamma\delta}\Big[\dot{U}_{\gamma,\delta} + \frac{1}{2}(\dot{W}_{,\gamma}W_{,\delta} + W_{,\gamma}\dot{W}_{,\delta})\Big] + \widetilde{a}B^{a}_{\alpha\beta\gamma}\dot{T}^{a}_{\gamma} - \widetilde{H}_{\alpha\beta\gamma\delta}\dot{W}_{,\gamma\delta} - \widetilde{H}^{A}_{\alpha\beta}\dot{V}^{A} \\
N^{a}_{\alpha} &= B^{a}_{\alpha\gamma\delta}\Big(U_{\gamma,\delta} + \frac{1}{2}W_{,\gamma}W_{,\delta}\Big) + B^{ab}_{\alpha\gamma}T^{b}_{\gamma} - H^{a}_{\alpha\gamma\delta}W_{,\gamma\delta} - H^{aB}_{\alpha}V^{B} \\
&\quad + \widetilde{B}^{a}_{\alpha\gamma\delta}\Big[\dot{U}_{\gamma,\delta} + \frac{1}{2}(\dot{W}_{,\gamma}W_{,\delta} + W_{,\gamma}\dot{W}_{,\delta})\Big] + \widetilde{B}^{ab}_{\alpha\gamma}\dot{T}^{b}_{\gamma} - \widetilde{H}^{a}_{\alpha\gamma\delta}\dot{W}_{,\gamma\delta} - \widetilde{H}^{aB}_{\alpha}\dot{V}^{B} \\
Q^{A}_{\alpha} &= 0 \qquad\qquad R^{AB} = 0
\end{aligned}
\tag{4.7}
$$

— equilibrium equations

$$
\begin{aligned}
&M_{\alpha\beta,\alpha\beta} - (N_{\alpha\beta}W_{,\alpha} + Q^{A}_{\beta}V^{A})_{,\beta} + (m + \widehat{m})\ddot{W} - \vartheta\ddot{W}_{,\alpha\alpha} + KW + C\dot{W} + \theta\ddot{U}_{\alpha,\alpha} = P \\
&M^{A} = 0 \qquad\qquad - N_{\alpha\beta,\beta} + m\ddot{U}_{\alpha} - \theta\ddot{W}_{,\alpha} = 0 \qquad\qquad N^{a}_{\alpha} = 0
\end{aligned}
\tag{4.8}
$$

where all coefficients are constant.

It can be observed that equations (4.7) and (4.8) with micro-macro decompositions (3.8) constitute the nonlinear asymptotic model of thin visco-elastic periodic plates resting on a foundation with damping for plates without the symmetry plane $z = 0$.

On the other side, from equations (4.5) and (4.6), similar equations of the nonlinear asymptotic model can be derived in the form:

— constitutive equations

$$
\begin{aligned}
M_{\alpha\beta} &= D_{\alpha\beta\gamma\delta}W_{,\gamma\delta} + D^{A}_{\alpha\beta}V^{A} + \widetilde{D}_{\alpha\beta\gamma\delta}\dot{W}_{,\gamma\delta} + \widetilde{D}^{A}_{\alpha\beta}\dot{V}^{A} \\
M^{A} &= D^{A}_{\alpha\beta}W_{,\gamma\delta} + D^{AB}V^{B} + \widetilde{D}^{A}_{\alpha\beta}\dot{W}_{,\gamma\delta} + \widetilde{D}^{AB}\dot{V}^{B} \\
N_{\alpha\beta} &= B_{\alpha\beta\gamma\delta}\Big(U_{\gamma,\delta} + \frac{1}{2}W_{,\gamma}W_{,\delta}\Big) + B^{a}_{\alpha\beta\gamma}T^{a}_{\gamma} \\
&\quad + \widetilde{B}_{\alpha\beta\gamma\delta}\Big[\dot{U}_{\gamma,\delta} + \frac{1}{2}(\dot{W}_{,\gamma}W_{,\delta} + W_{,\gamma}\dot{W}_{,\delta})\Big] + \widetilde{B}^{a}_{\alpha\beta\gamma}\dot{T}^{a}_{\gamma} \\
N^{a}_{\alpha} &= B^{a}_{\alpha\gamma\delta}\Big(U_{\gamma,\delta} + \frac{1}{2}W_{,\gamma}W_{,\delta}\Big) + B^{ab}_{\alpha\gamma}T^{b}_{\gamma} + \widetilde{B}^{a}_{\alpha\gamma\delta}\Big[\dot{U}_{\gamma,\delta} + \frac{1}{2}(\dot{W}_{,\gamma}W_{,\delta} + W_{,\gamma}\dot{W}_{,\delta})\Big] + \widetilde{B}^{ab}_{\alpha\gamma}\dot{T}^{b}_{\gamma} \\
Q^{A}_{\alpha} &= 0 \qquad R^{AB} = 0
\end{aligned}
\tag{4.9}
$$

— equilibrium equations

$$\begin{aligned} &M_{\alpha\beta,\alpha\beta} - (N_{\alpha\beta}W_{,\alpha})_{,\beta} + (m+\widehat{m})\ddot{W} - \vartheta\ddot{W}_{,\alpha\alpha} + KW + C\dot{W} = P \\ &M^A = 0 \qquad\qquad - N_{\alpha\beta,\beta} + m\ddot{U}_\alpha = 0 \qquad\qquad N^a_\alpha = 0 \end{aligned} \tag{4.10}$$

with all coefficients constant.

It is necessary to observe that equations (4.9) and (4.10) and micro-macro decompositions (3.8) constitute the nonlinear asymptotic model of thin visco-elastic periodic plates resting on a foundation with damping for plates with the symmetry plane $z = 0$.

5. Final remarks

A new nonlinear non-asymptotic model for dynamic problems of thin visco-elastic periodic plates resting on a foundation with damping is proposed in this note. This model is based on the assumptions of von Kármán nonlinear thin plate theory. In order to derive the model governing equations, the tolerance modelling is applied.

Summarizing, it can be concluded that:

- The proposed approach replaces governing equations of plates having highly oscillating, periodic, non-continuous functional coefficients by the model equations with constant coefficients, which can be solved using suitable well-known methods. Thus, the nonlinear tolerance model can be a useful tool in investigations of various dynamic phenomena of the considered plate structures.
- In contrast to the original formulations, the new proposed nonlinear tolerance model introduces some averaged, effective properties of the plate structure.
- Dynamic behaviour of the plates under consideration is described in this model by some new unknowns as averaged deflections (macrodeflections) and averaged in-plane displacements (in-plane macrodisplacements) and amplitudes of their disturbances due to inhomogeneity of the structure. These new kinematic unknowns have to be slowly-varying functions in $\mathbf{x}$, which constitutes conditions of physical reliability of the solutions.
- The very important feature of the proposed nonlinear tolerance model is that its governing equations involve terms with the microstructure parameter. Hence, this tolerance model makes it possible to investigate the effect of the microstructure size on the overall dynamic behaviour of thin visco-elastic periodic plates resting on a foundation with damping in the framework of von Kármán nonlinear thin plate theory. Using this model, some phenomena in dynamic problems caused by the internal periodic structure of the plates under consideration can be investigated.
- It can be observed that the transition from the governing equations of geometrically nonlinear tolerance models to the equations of the linear tolerance models may take place on two levels – micro, when the effect of nonlinear terms with fluctuation amplitudes is omitted, and micro-macro, when all nonlinear terms are neglected.
- It should be noted that the proposed model is a kind of generalization in relation to the known tolerance models shown by Domagalski and Jędrysiak (2012, 2015), where some bending nonlinear problems of thin periodic plates were described. Domagalski and Jędrysiak (2014) analysed nonlinear vibrations of slender periodic beams resting on a foundation with damping, wherreas Marczak and Jędrysiak (2014) investigated damped vibrations of plate strips with periodically distributed concentrated masses.

Various applications of the proposed tolerance and asymptotic models to dynamics of thin visco-elastic periodic plates with moderately large deflections resting on a foundation with damping will be analysed in the forthcoming papers.

References

1. Awrejcewicz J., Kurpa L., Shmatko T., 2013, Large amplitude free vibration of orthotropic shallow shells of complex shapes with variable thickness, *Latin American Journal of Solids and Structures*, **10**, 149-162
2. Brito-Santana H., Wang Y.S., Rodrguez-Ramos R., Bravo-Castillero J., Guinovart-Díaz R., Volnei Tita, 2015, A dispersive nonlocal model for shear wave propagation in laminated composites with periodic structures, *European Journal of Mechanics – A/Solids*, **49**, 35-48
3. Camier C., Touzé C., Thomas O., 2009, Non-linear vibrations of imperfect free-edge circular plates and shells, *European Journal of Mechanics – A/Solids*, **28**, 500-515
4. Dallot J., Sab K., Foret G., 2009, Limit analysis of periodic beams, *European Journal of Mechanics – A/Solids*, **28**, 166-178
5. De Carvalho N.V., Pinho S.T., Robinson P., 2011, Reducing the domain in the mechanical analysis of periodic structures, with application to woven composites, *Composites Science and Technology*, **71**, 969-979
6. Domagalski Ł., Jędrysiak J., 2012, On the elastostatics of thin periodic plates with large deflections, *Meccanica*, **41**, 1659-1671
7. Domagalski Ł., Jędrysiak J., 2014, Nonlinear vibrations of periodic beams, *Journal of Vibrations in Physical Systems*, **26**, 73-78
8. Domagalski Ł., Jędrysiak J., 2015, On the tolerance modelling of geometrically nonlinear thin periodic plates, *Thin-Walled Structures*, **87**, 183-190
9. Fallah A., Aghdam M.M., 2011, Nonlinear free vibration and post-buckling analysis of functionally graded beams on nonlinear elastic foundation, *European Journal of Mechanics – A/Solids*, **30**, 571-583
10. Golmakani M.E., Alamatian J., 2013, Large deflection analysis of shear deformable radially functionally graded sector plates on two-parameter elastic foundations, *European Journal of Mechanics – A/Solids*, **42**, 251-265
11. Gupta A.K., Khanna A., Gupta D.V., 2009, Free vibration of clamped visco-elastic rectangular plate having bi-direction exponentially thickness variations, *Journal of Theoretical and Applied Mechanics*, **47**, 2, 457-471
12. He W.M., Chen W.Q., Qiao H., 2013, Two-scale analytical solutions of multilayered composite rectangular plates with in-plane small periodic structure, *European Journal of Mechanics – A/Solids*, **40**, 123-130
13. Houmat A., 2013, Nonlinear free vibration of laminated composite rectangular plates with curvilinear fibers, *Composites Structures*, **106**, 211-224
14. Huang J.Y., 2004, Uniformly valid asymptotic solutions of the nonlinear unsymmetrical bending for orthotropic rectangular thin plate of four clamped edges with variable thickness, *Applied Mathematics and Mechanics*, **25**, 817-826
15. Jasion P., Magnucka-Blandzi E., Szyc W., Magnucki K., 2012, Global and local buckling of sandwich circular and beam-rectangular plates with metal foam core, *Thin-Walled Structures*, **61**, 154-161
16. Jędrysiak J., 2000, On the stability of thin periodic plates, *European Journal of Mechanics – A/Solids*, **19**, 3, 487-502
17. Jędrysiak J., 2003, Free vibrations of thin periodic plates interacting with an elastic periodic foundation, *International Journal of Mechanical Sciences*, **45**, 8, 1411-1428
18. Jędrysiak J., 2009, Higher order vibrations of thin periodic plates, *Thin-Walled Structures*, **47**, 890-901

19. Jędrysiak J., 2013, Modelling of dynamic behaviour of microstructured thin functionally graded plates, *Thin-Walled Structures*, **71**, 102-107

20. Jędrysiak J., Michalak B., 2011, On the modelling of stability problems for thin plates with functionally graded structure, *Thin-Walled Structures*, **49**, 627-635

21. Jędrysiak J., Paś A., 2014, Dynamics of medium thickness plates interacting with a periodic Winkler's foundation: non-asymptotic tolerance modelling, *Meccanica*, **49**, 1577-1585

22. Kaźmierczak M., Jędrysiak J., 2011, Tolerance modelling of vibrations of thin functionally graded plates, *Thin-Walled Structures*, **49**, 1295-1303

23. Kohn R.V., Vogelius M., 1984, A new model of thin plates with rapidly varying thickness, *International Journal of Solids and Structures*, **20**, 333-350

24. Królak M., Kowal-Michalska K., Mania R.J., Świniarski J., 2009, Stability and load carrying capacity of multi-cell thin-walled columns of rectangular cross-sections, *Journal of Theoretical and Applied Mechanics*, **47**, 1, 435-456

25. Lei Y., Murmu T., Adhikari S., Friswell M.I., 2013, Dynamic characteristics of damped viscoelastic nonlocal Euler-Bernoulli beams, *European Journal of Mechanics – A/Solids*, **42**, 125-136

26. Levy S., 1942, Bending of rectangular plates with large deflections, NACA Rep No. 737. NACA Tech Note No. 846

27. Lurie S.A., Belov P.A., Tuchkova N.P., 2005, The application of the multiscale models for description of the dispersed composites, *Composites Part A: Applied Science and Manufacturing*, **36**, 2, 145-152

28. Magnucka-Blandzi E., 2010, Non-linear analysis of dynamic stability of metal foam circular plate, *Journal of Theoretical and Applied Mechanics*, **48**, 1, 207-217

29. Mahmoudkhani S., Haddadpour H., Navazi H.M., 2014, The effects of nonlinearities on the vibration of viscoelastic sandwich plates, *nternational Journal of Non-Linear Mechanics*, **62**, 41-57

30. Manevich A., Kołakowski Z., 2011, Free and forced oscillations of Timoshenko beam made of viscoelastic material, *Journal of Theoretical and Applied Mechanics*, **49**, 1, 3-16

31. Marczak J., Jędrysiak J., 2014, Analysis of vibrations of plate strip with concentrated masses using tolerance averaging technique, *Journal of Vibrations in Physical Systems*, **26**, 161-168

32. Matysiak S.J., Perkowski D.M., 2014, Temperature distributions in a periodically stratified layer with slant lamination, *Heat Mass Transfer*, **50**, 75-83

33. Meenen J., Altenbach H., 2001, A consistent deduction of von Kármán-type plate theories from three-dimensional nonlinear continuum mechanics, *Acta Mechanica*, **147**, 1-17

34. Michalak B., 2001, The meso-shape functions for the meso-structural models of wavy-plates, *ZAMM*, **81**, 639-641

35. Nagórko W., Woźniak C., 2002, Nonasymptotic modelling of thin plates reinforced by a system of stiffeners, *Electronic Journal of Polish Agricultural Universities – Civil Engineering*, **5**, 2

36. Perliński W., Gajdzicki M., Michalak B., 2014, Modelling of annular plates stability with functionally graded structure interacting with elastic heterogeneous subsoil, *Journal of Theoretical and Applied Mechanics*, **52**, 2, 485-498

37. Reinhall P.G., Miles R.N., 1989, Effect of damping and stiffness on the random vibration of non-linear periodic plates, *Journal of Sound and Vibration*, **132**, 33-42

38. Saha G.C., Kalamkarov A.L., Georgiades A.V., 2007, Effective elastic characteristics of honeycomb sandwich composite shells made of generally orthotropic materials, *Composites Part A: Applied Science and Manufacturing*, **38**, 6, 1533-1546

39. Schmitz A., Horst P., 2014, A finite element unit-cell method for homogenised mechanical properties of heterogeneous plates, *Composites Part A: Applied Science and Manufacturing*, **61**, 23-32

40. Singha M.K., Rupesh Daripa, 2009, Nonlinear vibration and dynamic stability analysis of composite plates, *Journal of Sound and Vibration*, **328**, 541-554

41. Teter A., 2011, Dynamic critical load based on different stability criteria for coupled buckling of columns with stiffened open cross-sections, *Thin-Walled Structures*, **49**, 589-595

42. Timoshenko S., Woinowsky-Krieger S., 1959, *Theory of Plates and Shells*, McGraw-Hill, New York

43. Tomczyk B., 2007, A non-asymptotic model for the stability analysis of thin biperiodic cylindrical shells, *Thin-Walled Structures*, **45**, 941-944

44. Vlasov W.Z., Leontiev N.N., 1960, *Beams, Plates and Shells on Rigid Subsoil* (in Russian), Gos. Izd. Fiz.-Mat. Lit., Moskva

45. Wierzbicki E., Woźniak C., 2000, On the dynamics of combined plane periodic structures, *Archive of Applied Mechanics*, **70**, 6, 387-398

46. Wierzbicki E., Woźniak C., Woźniak M., 2001, On the modelling of transient micro-motions and near-boundary phenomena in a stratified elastic layer, *International Journal of Engineering Science*, **39**, 13, 1429-1441

47. Woźniak C. (edit.), 2001, *Mechanics of Elastic Plates and Shells* (in Polish), PWN, Warsaw

48. Woźniak C., *et al.* (edit.), 2010, *Mathematical Modelling and Analysis in Continuum Mechanics of Microstructured Media*, Silesian Techn. Univ. Press, Gliwice

49. Woźniak C., Michalak B., Jędrysiak J. (edit.), 2008, *Thermomechanics of Microheterogeneous Solids and Structures. Tolerance Averaging Approach*, Lodz Univ. Techn. Press, Lodz

50. Yajuvindra Kumar, Lal R., 2013, Prediction of frequencies of free axisymmetric vibration of two-directional functionally graded annular plates on Winkler foundation, *European Journal of Mechanics – A/Solids*, **42**, 219-228

51. Yaghoobi H., Torabi M., 2013, An analytical approach to large amplitude vibration and post-buckling of functionally graded beams rest on non-linear elastic foundation, *Journal of Theoretical and Applied Mechanics*, **51**, 1, 39-52

52. Youzera H., Meftah S.A., Challamel N., Tounsi A., 2012, Nonlinear damping and forced vibration analysis of laminated composite beams, *Composites Part B: Engineering*, **43**, 1147-1154

53. Zhou X.Q., Yu D.Y., Shao X., Wang S., Tian Y.H., 2014, Band gap characteristics of periodically stiffened-thin-plate based on center-finite-difference-method, *Thin-Walled Structures*, **82**, 115-123

Manuscript received September 23, 2015; accepted for print December 22, 2015

JOURNAL OF THEORETICAL AND APPLIED MECHANICS
54, 3, pp. 963-973, Warsaw 2016
DOI: 10.15632/jtam-pl.54.3.963

SUGGESTION OF AN EQUATION OF MOTION TO CALCULATE THE DAMPING RATIO DURING EARTHQUAKE BASED ON A CYCLIC PROCEDURE

H. Naderpour
Semnan University, Faculty of Civil Engineering, Semnan, Iran
e-mail: naderpour@semnan.ac.ir

R.C. Barros
University of Porto(FEUP), Faculty of Engineering, Porto, Portugal

S.M. Khatami
Semnan University, Faculty of Civil Engineering, Semnan, Iran

Large horizontal relative displacements are naturally caused by seismic excitation, which is able to provide collisions between two adjacent buildings due to insufficient separation distance and severe damages due to impacts, especially in tall buildings. In this paper, the impact is numerically simulated and two needed parameters are calculated, including the impact force and energy absorption. In order to calculate the mentioned parameters, mathematical study is carried out to model an unreal link element, which is logically assumed to be a spring and dashpot to determine the lateral displacement and damping ratio of the impact. For the determination of the dynamic response of the impact, a new equation of motion is theoretically suggested to the evaluate impact force and energy dissipation. In order to confirm the rendered equation, a series of parametric studies are performed and the accuracy of the formulas is confirmed.

Keywords: pounding, impact, dissipated rnergy, coefficient of restitution

1. Introduction

During earthquake, buildings commonly collide with each other due to different dynamic characteristics of adjacent buildings, insufficient gap between them and vibrate out of phase. This phenomenon is called "building pounding". The pounding is experimentally shown by an instance of rapid strong pulsation, which causes severe damage and is repeated by decreasing stiffness of the building after each collision. Consequently, as it is obviously seen, there are many tall buildings constructed with a small gap size. The effectiveness of pounding must be considered to avoid collisions or decline impact forces when adjacent buildings are designed and built. Importance of the mentioned subject has been understood by some researchers, who tried to report their studies about pounding. Anagnostopolos (1995, 1996, 2004) was among the first researchers who explained possible dangers due to building pounding. He presented an equation of motion to calculate the impact damping ratio. Kasai and Maison (1997) presented a formulation and simulated multiple-degree-of-freedom equations of motion for floor-to-floor pounding between two 15-storey and 8-storey buildings. The influence of building separation, relative mass, and contact location properties were assessed by them. Jankowski (2008) carried out the most studies about pounding in two different terms, which were experimental and numerical analyses. Jankowski (2009, 2010, 2012) suggested efficient methods to calculate the impact ratio by justifying different equations and also substantially implemented different experimental tests to predict impact velocity by focusing on dropping balls onto a rigid surface. Muthukumar and

DesRoches (2006) introduced an equation of motion to generate an impact and determine the damping coefficient. Ye *et al.* (2009) and Yu and Gonzalez (2008) theoretically explained two equations of motions in order to determine the impact damping ratio by focusing on stiffness of the spring and also impact velocity. They coordinated a stereo-mechanical model with energy loss during the impact. Komodromos *et al.* (2007) expressed an equation of motion to create an impact between two bodies, which could estimate the impact damping ratio. The base isolation systems have recently been described by Komodromos and Polycarpou (2011, 2012) and the pounding was numerically investigated. Barros and Khatami (2012a) parametrically evaluated different damping equations to show the optimum formula to calculate the impact force. They also examined a new model of impact to coordinate the results among numerical and experimental studies (Barros and Khatami, 2013). Furthermore, the effectiveness of concrete shear wall was considered to reduce collision between adjacent buildings by Barros and Khatami (2012b). Naderpour *et al.* (2013) investigated results of all represented formulas and compared them in terms of dissipated energy. They also suggested an approximate trend to select the coefficient of restitution, which became equal with the impact velocity (Barros *et al.*, 2013). Subsequently, a new equation of motion has been suggested to simulate the impact and figure damping terms out of collision (Naderpour *et al.*, 2014). Nevertheless, it seems that there is lack of calculating the impact force and energy dissipation, which could be satisfied by selecting different coefficients of restitutions and various situations. It leads to introdution different equations with different results, and it can not be accepted. So, there is a need to use an equation which could be a response to all questions about the pounding. In this paper, a new mathematical program, called CRVK, submitted by Naderpour *et al.* (2014) at the FEUP, is specifically developed to model the impact between two bodies. Subsequently, an equation of motion is numerically suggested and the accuracy of the formula is confirmed by comparison between the dissipated energy and the energy loss.

2. Past equations to calculate the impact damping ratio

The contact element is an unreal element to model the impact between two bodies, which commonly includes a spring and dashpot and is called "Hertz contact element". It is widely used to calculate the impact force and energy absorption. The impact is parametrically modeled when the relative displacement exceeds the separation distance and the contact element is activated to simulate collision between two bodies and to calculate the impact force. For this challenge, an equation of motion is numerically considered to simulate the impact, which becomes

$$F_{imp}(t) = k_s \delta^n(t) + c_d \dot{\delta}(t) \tag{2.1}$$

where k_s is stiffness of the spring, c_d denotes the damping ratio of the dashpot, δ and $\dot{\delta}$ describe the lateral displacement and velocity, respectively. The power of n is recommended to be 1 or 1.5, which depends significantly on the model.

In this equation, the damping ratio has been related by different equations which are individually investigated. In order to introduce the equations, the coefficient of restitution (CR) is used, which is defined as the ratio of relative velocities before and after the impact, and is written as

$$0 < CR = \frac{\dot{\delta}_{before}}{\dot{\delta}_{after}} < 1 \tag{2.2}$$

The first equation of motion was suggested by Anagnostopolos (2004) to calculate the damping ratio and solve equation (2.1) when the power of n is 1

$$c_{imp} = 2\zeta\sqrt{k_s\frac{m_i m_j}{m_i + m_j}} \qquad \zeta = -\frac{\ln(CR)}{\sqrt{\pi^2 + [\ln(CR)]^2}} \tag{2.3}$$

where m_i, m_j are the colliding masses and ζ is the damping ratio. Here, the dashpot is still activated when two bodies are separated and the system shows a negative impact, which is not clearly justified.

Jankowski *et al.* (2009) introduced an equation to calculate the damping coefficient, which can be focused on the coefficient of restitution and solved it when $n = 1.5$. He found that for the impact between two bodies, the negative force and dissipated energy have to disappear as it was pointed out. It was not inherently confirmed by physical explanation. Therefore, the impact force in the contact element may be expressed based on the given formula

$$c_{imp} = 2\zeta\sqrt{\beta\sqrt{\delta(t)}\frac{m_i m_j}{m_i + m_j}} \qquad \zeta = \frac{9\sqrt{5}}{2}\frac{1 - CR^2}{CR[CR(9\pi - 16) + 16]} \tag{2.4}$$

where β is the impact stiffness parameter depending on material properties of the colliding bodies.

Barros *et al.* (2013) simulated an impact and justified an equation to determine the impact damping ratio based on the coefficient of restitution. The equation yields better behavior in terms of the impact against equation $(2.3)_2$ and $(2.4)_2$, when the accuracy of the mentioned equation is compared with each other

$$\zeta = \left(\frac{1 - CR^2}{CR\left[\sqrt{\pi}\left(\frac{1}{2}CR + \frac{1}{\pi}\right) - CR\right]}\right)^2 \tag{2.5}$$

An improved equation of motion to find the damping ratio was considered by Muthukumar and DisRocher (2006). They believed that the damping ratio of the dashpot was not dependent on the contact element and the behavior of spring had an important effect on the coefficient of damping ratio. They presented a new equation, which depended on three parameters, including the coefficient of restitution, stiffness of the spring and impact velocity. They demonstrated that energy loss during the impact had to be equal by energy absorption during an impact. It is worth to mention that the power of n was suggested to be 1.5

$$c_{imp} = \zeta\delta^n \qquad \zeta = \frac{3k_s(1 - CR^2)}{4\dot{\delta}_{imp}} \tag{2.6}$$

Ye *et al.* (2009) claimed that equation $(2.6)_2$ was incorrect to calculate the damping ratio for simulation of pounding in order to evaluate the impact between two buildings. Despite the mentioned point, three parameters used in equation $(2.6)_2$, the coefficient of restitution (CR), stiffness of the spring and impact velocity were listed to present the impact damping ratio by Ye *et al.* (2009). They numerically indicated that energy loss during the impact should be equal to kinetic energy by the dashpot and is expressed as follows

$$\zeta = \frac{8k_s(1 - CR)}{5CR\dot{\delta}_{imp}} \tag{2.7}$$

In order to obtain equation (2.7), Ye *et al.* (2009) tried to use an approximate relation between lateral displacement and velocity to solve the relation and to confirm the suggested equation, an integration around a hysteresis loop was used.

Naderpour *et al.* (2013) proposed another equation to show the impact between two bodies focusing on impact velocity, stiffness of the spring and the coefficient of restitution

$$\zeta = \frac{2k_h}{5CR^2\dot{\delta}_{imp}}\sqrt{\frac{1-CR}{1+CR}} \tag{2.8}$$

Equation (2.8) completes equation (2.5) in calculating the impact force and energy dissipation.

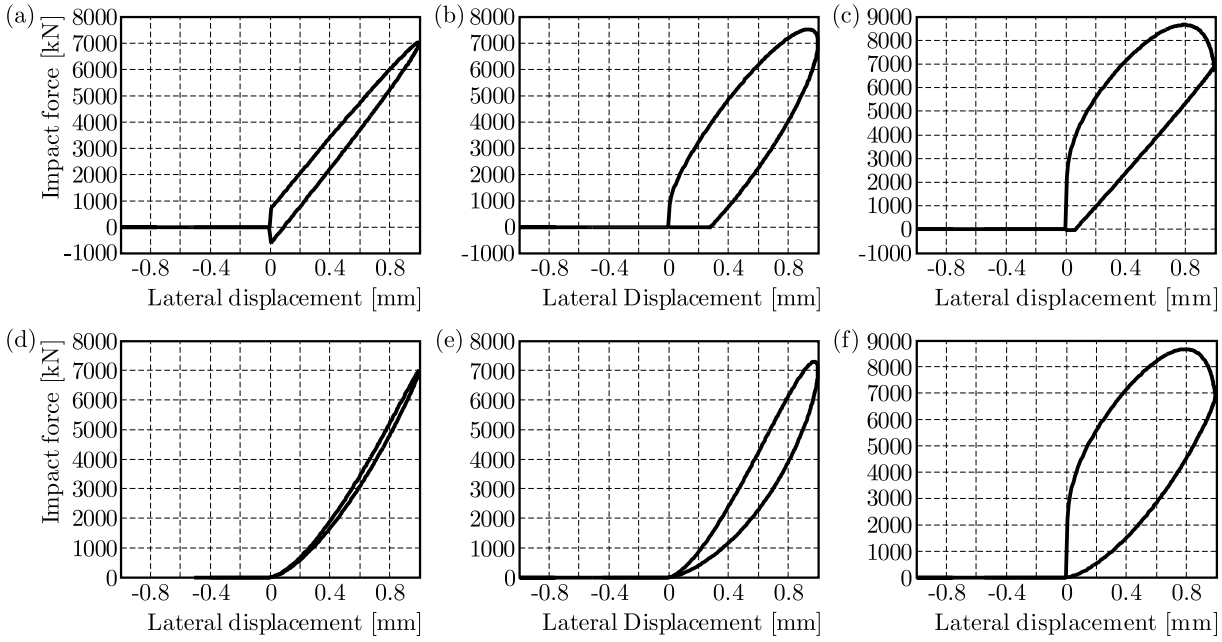

Fig. 1. Impact force versus lateral displacement based on: (a) Eq. $(2.3)_2$, (b) Eq. $(2.4)_2$, (c) Eq. (2.5), (d) Eq. $(2.6)_2$, (e) Eq. (2.7) and (f) Eq. (2.8)

3. The proposed impact damping model

As it has been noted, an efficient method by consideration a new equation in terms of the damping ratio is specially needed to illustrate an impact and solve the damping ratio based on all effectively used parameters in the impact such as lateral displacement, velocity, acceleration, stiffness of the spring, impact velocity and the coefficient of restitution. In order to define the impact damping ratio, which can be obtained from results of simulations and confirmed by numerical analyses, the impact between two bodies is equivalently modeled and a cyclic process for simulation of the structural pounding is numerically considered. In the current study, the impact is mathematically divided into three parts, during the impact, after the impact and when two bodies are completely separated from each other. In the first part, all elements are activated and energy can be absorbed by using the dashpot. In the second part, the dashpot is displayed and energy is not dissipated and, finally, any impact and energy are not shown as the bodies have been separated. For simulation of the impact and to remedy the equation of contact, using CRVK program (Naderpour *et al.*, 2014), the spring and dashpot are activated when the impact takes place and, subsequently, the dashpot is automatically eliminated when the two bodies are detached. The three mentioned parts of the impact can be numerically expressed as below

$$F_{imp} = \begin{cases} k_s\delta^n(t) + c_{imp}\dot{\delta}(t) & \text{for} \quad \delta(t) > 0 \quad \text{and} \quad \dot{\delta}(t) > 0 \\ k_s\delta^n(t) & \text{for} \quad \delta(t) > 0 \quad \text{and} \quad \dot{\delta}(t) < 0 \\ 0 & \text{for} \quad \delta(t) < 0 \end{cases} \tag{3.1}$$

where $n = 1.5$.

In order to determine the impact force and energy dissipation, the impact between two bodies is simulated and the hysteresis loop is depicted. It is assumed that the dissipated energy is approximately expressed by the enclosed area of the hysteresis curve due to the impact. On the other hand, the kinetic energy loss due to the impact was demonstrated by Goldsmith (1960), which was seen as

$$E = \frac{1}{2}\frac{m_i m_j}{m_i + m_j}(1 - CR^2)\dot{\delta}_{imp}^2 \tag{3.2}$$

It is obviously confirmed that the dissipated energy during the impact has to be equal to the kinetic energy calculated by equation (3.2). Undoubtedly, if both energies becomes equal to each other, it shows the accuracy of the impact damping ratio.

As it has been described in the previous part of this paper, many researchers proposed different equations of motion to simulate collision between two bodies and calculate the impact force during earthquake records. As it was shown, all the equations describe the damping coefficient based on some parameters such as CR. It is obviously seen that each equation gives specific results by selecting CR and the results are modified by using another CR. Consequently, it cannot be accepted and the results can not be also confirmed.

In order to provide a new equation in terms of the damping ratio, an unknown parameter is considered to be c_{imp}, which depends on some parameters as

$$c_{imp} \cong \{k_s, m, CR, \dot{\delta}_{imp}, \delta, \dot{\delta}, \ddot{\delta}\} \tag{3.3}$$

To meet this challenge, an unreal link element is considered to be at the level of bodies, which includes a spring and a dashpot to calculate lateral displacement and energy absorption, respectively.

The damping coefficient is defined by the following expression

$$c_{imp} = \zeta_{imp} k_s \delta^n(t) \tag{3.4}$$

where k_s is stiffness of the spring and $\delta(t)$ denotes lateral displacement ($n = 1.5$). The impact damping ratio is given by different terms, and becomes

$$\zeta_{imp} = w_{CR}\frac{1 - CR}{\ddot{\delta}(t)\dot{\delta}(t)\delta(t)}CR_{imp} \tag{3.5}$$

In order to solve equation (3.5), the terms need to be presented based on the mentioned parameters, seen in c_{imp}. So it is estimated to be

$$CR_{imp(i)} = \rho(i)CR^{\eta} \tag{3.6}$$

In equation (3.5), w_{CR} depends on the impact velocity, which is determined as below

$$w_{CR(i)} = \alpha(i)\dot{\delta}_{imp}^{\beta} \tag{3.7}$$

In order to start the simulation of the impact and solve the program to get the impact damping ratio, a value of mass is given and CRVK program calculates lateral displacement, velocity and acceleration of the spring streched between two bodies. Stiffness of the spring is determined and a CR is also selected. The program solves the equations and calculates energy dissipation, which is equal to the area of the hysteresis loop of each impact and compares it with the kinetic energy calculated by equation (3.2). Both energies should be equal if all factors has been correctly selected.

This process is numerically repeated for all considered coefficients of restitution for solving the equations, and the results are frequently compared to confirm equation (3.5).

Firstly, let us know the value of equal masses that is calculated by equation (3.8). Having used the mass, stiffness of the spring is estimated by the given figure

$$m = \frac{m_i m_j}{m_i + m_j} \tag{3.8}$$

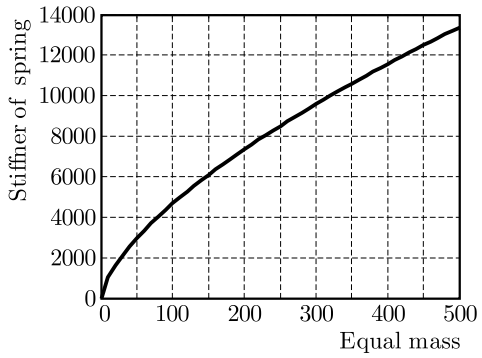

Fig. 2. Stiffness of the spring based on equal masses

Now, the coefficient of restitution (CR) is randomly selected ($0 < CR < 1$). In particular, for $CR = 0$ and 1, we have full energy for a perfectly plastic impact and no energy to show an elastic impact, respectively. After selecting CR and having impact velocity, the coefficient of w_{CR} is calculated based on the selected CR.

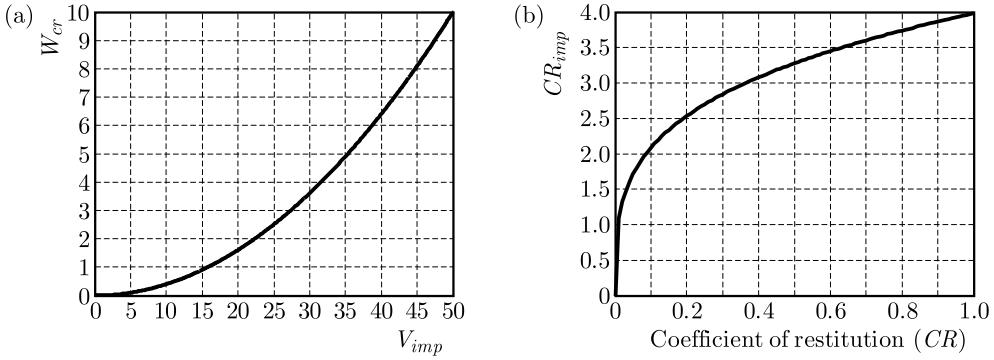

Fig. 3. (a) Coefficient w_{CR} based on impact velocity, (b) coefficient CR_{imp} based on the coefficient of restitution

Now, after selecting CR and getting w_{CR}, by making use of Fig. 3, CR_{imp} is determined.

Based on the energy equilibrium before and after an impact and the energy loss mentioned in equation (3.2) and using all parameters and all CRs, a cyclic process is provided to calculate the kinetic energy loss and available energy. By comparing these energies with each other, one gets an approximate damping term. In order to show a better image from the mentioned cyclic process of calculation of the impact damping ratio, a chart is rendered to determine the impact damping ratio based on all used parameters.

The chart is divided into two different parts. In the first step, it is assumed that the damping coefficient depends on the acceleration, velocity, lateral displacement and also the coefficient of restitution. For this challenge, a value of CR is selected and CR_{imp} is estimated. The hysteresis loop is depicted and also energy absorption A_h is calculated. Kinetic energy and energy absorption are compared with each other, if both become equal, then CR_{imp} has been correctly selected and the system selects a new CR and CR_{imp} automatically.

Finally, the impact damping ratio is also described as

$$\zeta_{imp} = 0.0159\dot{\delta}_{imp}^2 \frac{1 - CR}{\ddot{\delta}(t)\dot{\delta}(t)\delta(t)} CR^{0.2805} \tag{3.9}$$

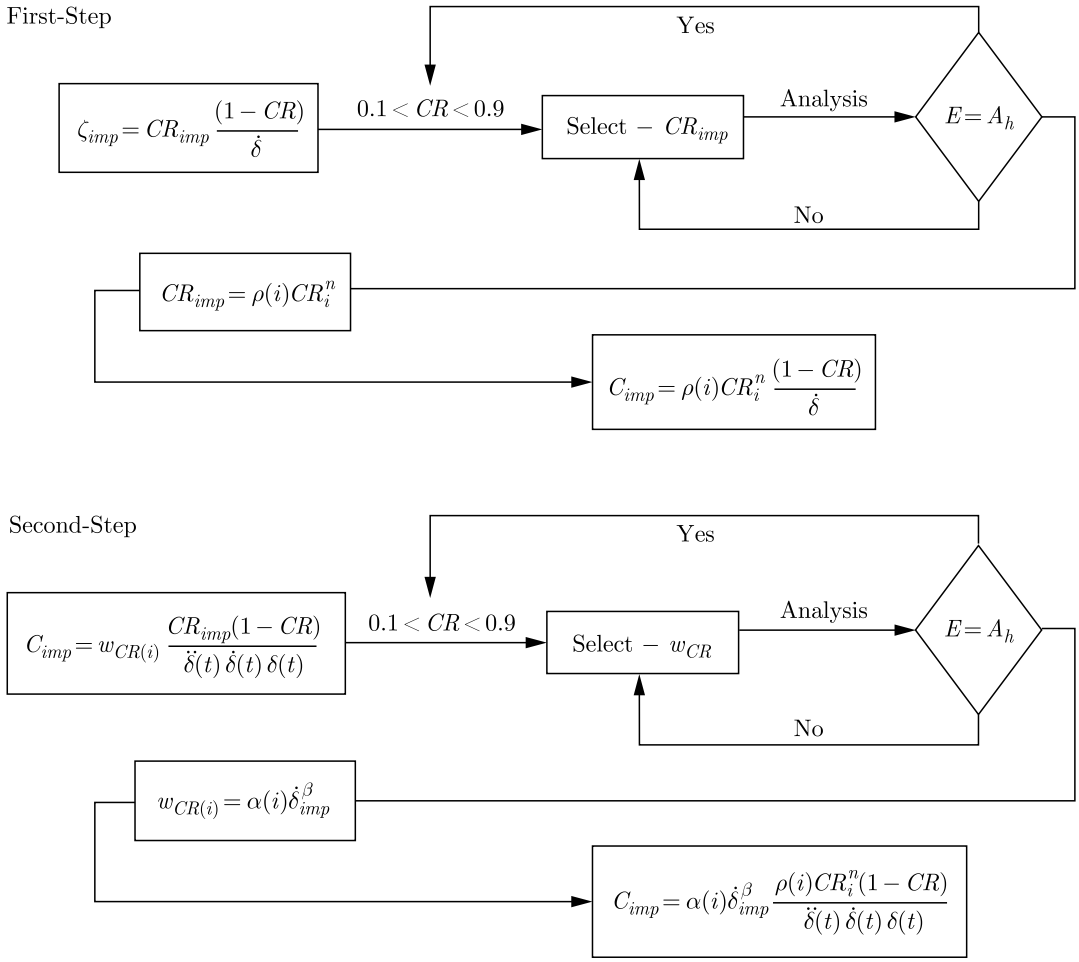

Fig. 4. The iterative procedure to determine the damping coefficient

For example, two SDOF systems are considered which are separated by a 0.2 mm gap from each other. The assumed lateral displacement by the impact velocity equal to 10 m/s is defined, and equal mass of 100 kg and $CR = 0.4$ are taken into account, respectively. So we have: $m = 100$ kg, $k = 6000\,\mathrm{kN}/\sqrt{\mathrm{mm}}$, $\dot{\delta}_{imp} = 10$ m/s, $CR = 0.4$, $CR_{imp} = 1.1903$, $w_{CR} = 2.5269$.

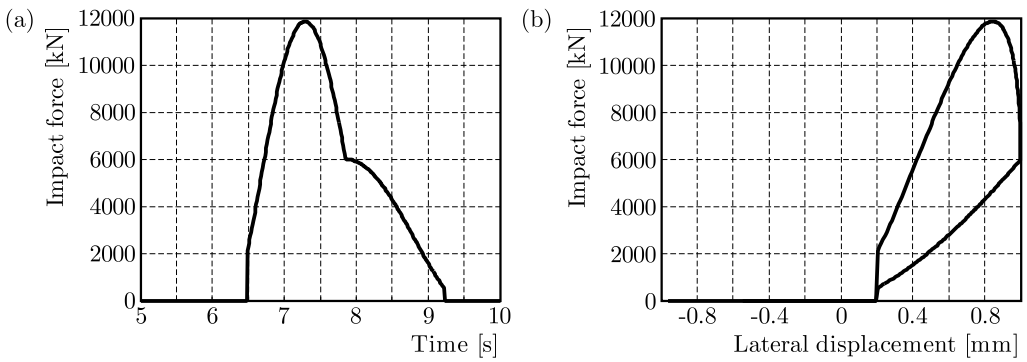

Fig. 5. Impact force versus time and lateral displacement

As it has been shown, the maximum impact force is approximately 12000 kN, and the dissipated energy, which has already been assumed to be the area of the hysteresis loop is 4189 kN·mm. On the other hand, the kinetic energy is calculated to be 4200 kN·mm based on the Goldsmith rule (Eq. (3.5)). It is obviously achieved that both energies are close to each other and the

calculated CR is 0.3527, which shows an error about 0.007%, which is negligible. Based on this process, all CRs are selected and compared as depicted in Fig. 6.

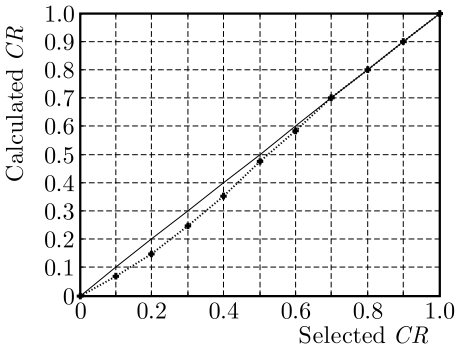

Fig. 6. Accuracy of the proposed damping ratio by numerical analysis

In order to investigate the accuracy of equation (3.9), an experimental test has been carried out to compare the results of experiment and numerical analysis.

Katija *et al.* (2006) carried out an impact test between two steel frames, each frame of 300 kg with a $40 \cdot 40$ cm beam separated by a 10 cm gap. The collision test was implemented using a horizontal hydraulic high-speed loading machine. This machine had a loading capacity of 1000 kN and a maximum loading speed of 3.0 m/s. The collision test was carried out in a line on a guide rail with length of 3000 mm. Two static and hysteresis tests were calibrated by using CRVK program when the impact velocity was 0.68 m/s for the second evaluation.

Both tests are considered and numerically examined to investigate the impact between two the bodies. Equation (3.9) is used and the proposed impact model is also defined to calibrate and compare the results of experimental and numerical analyses.

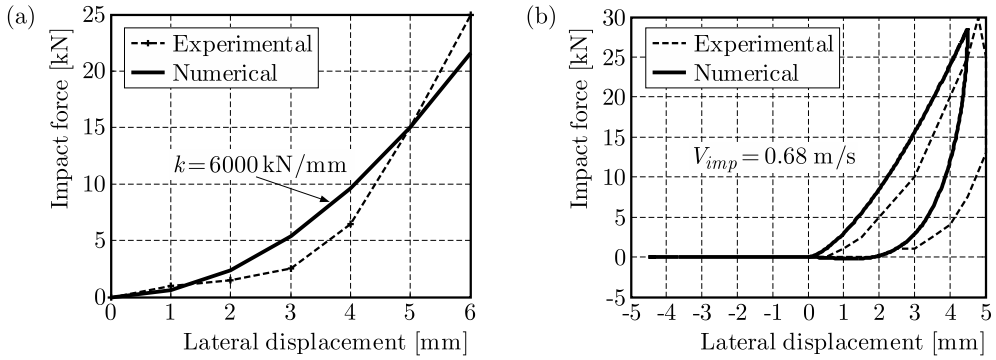

Fig. 7. Accuracy of the proposed damping ratio by calibrating the numerical and experimental analyses

The accuracy of the mentioned equation is confirmed as the trend of both tests is similar, and the maximum impact forces are 29.85 and 28.32 kN, which shows an error about 5%, which is negligible.

4. Numerical study

A parametric study is considered in order to describe the proposed impact damping model. The impact between two bodies is numerically simulated to measure the impact force and dissipated energy during seismic excitation. For this challenge, CRVK program is basically used and developed to perform dynamic analyses under Parkfield (1966), San Fernando (1971), Kobe (1995) and El Centro (1940) earthquake records. These records have different content of excitation

frequencies, different random magnitude of accelerations in time and different earthquake durations. Besides, their place of occurrence and geological conditions are distinct. All mentioned records are directly normalized to investigate the effect of earthquake properties when bodies collide with each other.

Effect of gap size

In order to investigate the effect of separation distance, the gap size is varied from 0 to 20 cm. The link element between the bodies is automatically activated when the gap size exceeds from the considered separation distance between them. Figure 8 depicts the effect of separation distance on the response in terms of the impact force during the four earthquake records. In particular, the curves follow an irregular decrease in the gap size 0 to 20 cm and the impact forces are suddenly reduced in San Fernando and Parkfield records and are slightly declining in the two other records. Therefore, an increase in the separation distance shows an effective decline in the impact force due to collision between the two bodies.

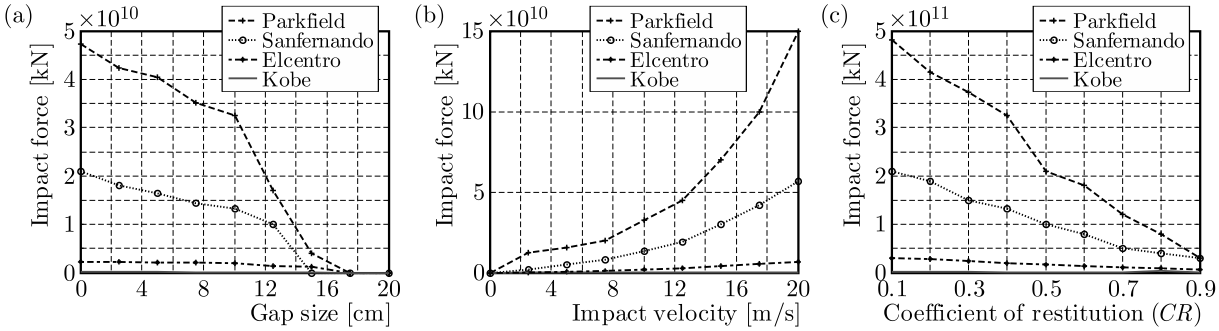

Fig. 8. Impact forces with the increasing (a) gap size, (b) impact velocity and (c) coefficient of restitution

Effect of coefficient of restitution

As the coefficient of restitution has a great effect on calculation of the impact damping ratio, different values of CR are considered to compare the impact forces during earthquakes. Figure 8 shows that the peak impact forces slowly decrease when the coefficient of restitution increases. A similar trend of impact force responses based on the coefficient of restitution is observed as the effect of CR is numerically seen to be linear in the proposed impact damping model. For instance, San Fernando record shows an impact force about $21 \cdot 10^9$ kN and $6.7 \cdot 10^9$ kN for $CR = 0.1$ and 0.9, respectively.

Effect of impact velocity

As it is shown in equations (3.5) and (3.6), the impact damping ratio directly depends on the impact velocity. Figure 8 shows a calm increase with growth of the impact velocity, which seems to be predictable. In order to get the responses of impacts and compare the results of maximum impact forces, different values of the impact velocity are considered from the interval 0 to 20 m/s, and the impact is simulated by different velocities. For example, the impact forces are $7.2 \cdot 10^{10}$, $3.13 \cdot 10^{10}$, $0.41 \cdot 10^{1}0$ and $0.019 \cdot 10^{10}$ kN for 15 m/s of the impact velocity in the Parkfield, San Fernando, El Centro and Kobe, respectively.

5. Conclusion

When two buildings are built close to each other, it is very important to consider pounding phenomena between them due to earthquake. Researchers have introduced an unreal element to calculate the impact force and the dissipated energy during seismic excitation by making use of the spring and the dashpot. Different equations of motion are presented to determine the damping ratio and an estimated value of the impact between the two colliding bodies. Here, a new equation based on all effectiveness parameters has been suggested, and the accuracy of the formula has been numerically evaluated. The effect of stiffness of the spring, impact velocity, coefficient of restitution and also separation distance have been investigated in detail. A parametric analysis has been carried out to show the results of the impact force and dissipated energy which have been then compared with the kinetic energy to confirm the created formula.

Refrences

1. Anagnostopoulos S.A., 1995, Earthquake induced pounding: state of the art, *Proceedings of 10th European Conference on Earthquake Engineering*, Balkema, Rotterdam, 897-905
2. Anagnostopoulos S.A., 1996, Building pounding re-examined: how serious a problem is it? *Eleventh World Conference on Earthquake Engineering*, Pergamon, Elsevier Science Ltd.
3. Anagnostopoulos S.A., 2004, Equivalent viscous damping for modeling inelastic impacts in earthquake pounding problems, *Earthquake Engineering and Structural Dynamics*, **33**, 8, 897-902
4. Barros R.C, Khatami S.M., 2012a, Building pounding forces for different link element models, *CST2011*, 4-7 September, Dubrovnic, Croatia
5. Barros R.C, Khatami S.M., 2012b, Seismic response effect of shear walls in reducing pounding risk of reinforced concrete building pounding subjected to near fault-ground motion, *15th World Conference Earthquake Engineering, 15WCEE*, Lisbon, Portugal
6. Barros R.C., Khatami S.M., 2013, Damping ratios for pounding of adjacent building and their consequence on the evaluation of impact forces by numerical and experimental models, *Mecânica Experimental*, **22**, 119-131
7. Barros R.C., Naderpour H., Khatami S.M., Mortezaei A.R., 2013, Influence of seismic pounding on rc buildings with and without base isolation system subject to near-fault ground motions, *Journal of Rehabilitation in Civil Engineering*, **1**, 39-52
8. Goldsmith W., 1960, *Impact: The Theory and Physical Behavior of Colliding Solids*, 1st ed., Edward Arnold: London U.K.
9. Jankowski R., 2008, Earthquake-induced pounding between equal height buildings with substantially different dynamic properties, *Engineering Structures*, **30**, 10, 2818-2829
10. Jankowski R., 2009, Non-linear FEM analysis of earthquake-induced pounding between the main building and the stairway tower of the Olive View Hospital, *Engineering Structures*, **31**, 8, 1851-1864
11. Jankowski R., 2010, Experimental study on earthquake-induced pounding between structural elements made of different building materials, *Earthquake Engineering and Structural Dynamics*, **39**, 3, 343-354
12. Jankowski R., 2012, Non-linear FEM analysis of pounding-involved response of buildings under non-uniform earthquake excitation, *Engineering Structures*, **37**, 0, 99-105
13. Kajita Y., Kitahara T., Nishimoto, N., 2006, Estimation of maximum impact force on natural rubber during collision, *First European Conference on Earthquake Engineering and Seismologhy*, 1st Ecees, Geneva, Switzland

14. Kasai K., Maison B.F., 1997, Building pounding damage during the 1989 Loma Prieta earthquake, *Engineering Structures*, **19**, 3, 195-207

15. Komodromos P., Polycarpou P., 2011, Numerical investigation of potential mitigation measures for poundings of seismically isolated buildings, *Earthquake and Structures*, **2**, 1, 1-24

16. Komodromos P., Polycarpou P., 2012, A nonlinear impact model for simulating the use of rubber shock absorbers for mitigating the effect of structural pounding during earthquake, *Earthquake Engineering and Structural Dynamics* **42**, 81-100

17. Komodromos P., Polycarpou P.C., Papaloizou L., Phocas M.C., 2007, Response of seismically isolated buildings considering poundings, *Earthquake Engineering and Structural Dynamics*, **36**, 12, 1605-1622

18. Muthukumar S., DesRoches R., 2006, A Hertz contact model with non-linear damping for pounding simulation, *Earthquake Engineering and Structural Dynamics*, **35**, 7, 811-828

19. Naderpour H., Barros R.C, Khatami S.M., 2013, A new equation of motion to calculate the impact force and the energy dissipation, *Proceedings of the Fourteenth International Conference on Civil, Structural and Environmental Engineering Computing*, B.H.V. Topping, P. Iványi (Edit.), Civil-Comp Press, Stirlingshire, UK, Paper 92, Doi:10.4203/ccp.102.92

20. Naderpour H., Barros R.C., Khatami S.M., 2014, A new model for calculating the impact force and the energy dissipation based on cr-factor and impact velocity, *Scientia Iranica*, **1**, 48-63

21. Ye K., Li L., Zhu H., 2009, A note on the Hertz contact model with nonlinear damping for pounding simulation, *Earthquake Engineering and Structural Dynamics*, **38**, 9, 1135-1142

22. Yu Q.K., Gonzalez D., 2008, Lessons learned from the October 15, 2006 Hawaii earthquake and the August 15, 2007 Peru earthquake, *14th World Conference on Earthquake Engineering: Innovation Practice Safety, International Association for Earthquake Engineering*

Manuscript received October 28, 2015; accepted for print January 6, 2016

JOURNAL OF THEORETICAL AND APPLIED MECHANICS
54, 3, pp. 975-986, Warsaw 2016
DOI: 10.15632/jtam-pl.54.3.975

A NONLINEAR ELECTROMECHANICAL PENDULUM ARM WITH A NONLINEAR ENERGY SINK CONTROL (NES) APPROACH

G. Füsun Alışverişçi, Hüseyin Bayiroğlu
Yıldız Technical University, Istanbul, Turkey; e-mail: afusun@yildiz.edu.tr; hbayir@yildiz.edu.tr

Jorge Luis Palacios Felix
UFFS – Federal University of Fronteira Sul, Cerro Largo, RS, Brazil; e-mail: jorge.felix@uffs.edu.br

José M. Balthazar
ITA – Aeronautics Technological Institute, São José dos Campos, SP, Brazil and UNESP-Bauru, SP, Brazil
e-mail: jmbaltha@gmail.com

Reyolando Manoel Lopes Rebello da Fonseca Brasil
Federal University of ABC, Santo André, SP, Brazil; e-mail: reyolando.brasil@ufabc.edu.br

This paper considers the nonlinear dynamics of an electromechanical device with a pendulum arm and a Nonlinear Energy Sink (NES) put on the point of the pendulum suspension. It is shown that the (NES) is capable of absorbing energy from the system. The numerical results are shown in a bifurcation diagram, phase plane, Poincaré map and Lyapunov exponents.

Keywords: nonlinear electromechanical system, bifurcations, nonlinear energy sink

1. Introduction

Mechanical oscillatory systems (e.g., a pendulum system which is a basic subsystem of any robot) are of special interest for research and applications as examples of simple systems that may exhibit complex nonlinear behavior. That is why mechanical pendulum-like models of robot arms and mechanical manipulators have recently drawn attention of researchers (Mogo and Woafo, 2007). An interesting example of a driven pendulum device coupled with an electric circuit through a magnetic field. This enters the class of nonlinear electromechanical devices with a pendulum arm. It has been found that the device displays different nonlinear behavior, including chaos (Mogo and Woafo, 2007). SDRE control and sensibility analysis of a chaotic double pendulum arm excited by a RLC circuit based nonlinear shaker was presented by Tusset *et al.* (2014, 2015). A non-ideal electromechanical damping vibration absorber, the Sommerfeld effect and energy transfer were studied by Felix and Balthazar (2009). The energy pumping, synchronization and beat phenomenon in a non-ideal structure coupled with an essentially nonlinear oscillator were discussed by Felix *et al.* (2009).

This paper deals with a thin rod mounted to a plate to which electrical windings are applied. Connected to an electric circuit (Tusset *et al.*, 2014, 2015), its oscillations are due to the electromagnetic force resulting from two identical and repulsive permanent magnets (Mogo and Woafo, 2007) as well as a Nonlinear Energy Sink. NES has recently drawn attention of many researchers. The NES method represents a new and unique application of strong nonlinearity. The nonlinear energy sink is a local, simple, lightweight subsystem capable of completely altering the global behavior of the primary system to which it is attached (Vakakis *et al.*, 2008). Elimination of chaotic behavior in a non-ideal portal frame structural system using both passive and active controls were described by Tusset *et al.* (2013). Steady-state dynamics of a linear

structure weakly coupled to an essentially nonlinear oscillator was studied by Malatkar and Nayfeh (2007).

Steady state passive nonlinear energy pumping in coupled oscillators was studied by Jiang *et al.* (2003). Introduction of passive nonlinear energy sinks to linear systems was discussed by Vakakis (2001). Energy pumping in nonlinear mechanical oscillators for resonance capture was examined by Vakakis and Gendelman (2001). The energy transfer between linear and non-linear oscillators was investigated by Dantas and Balthazar (2008).

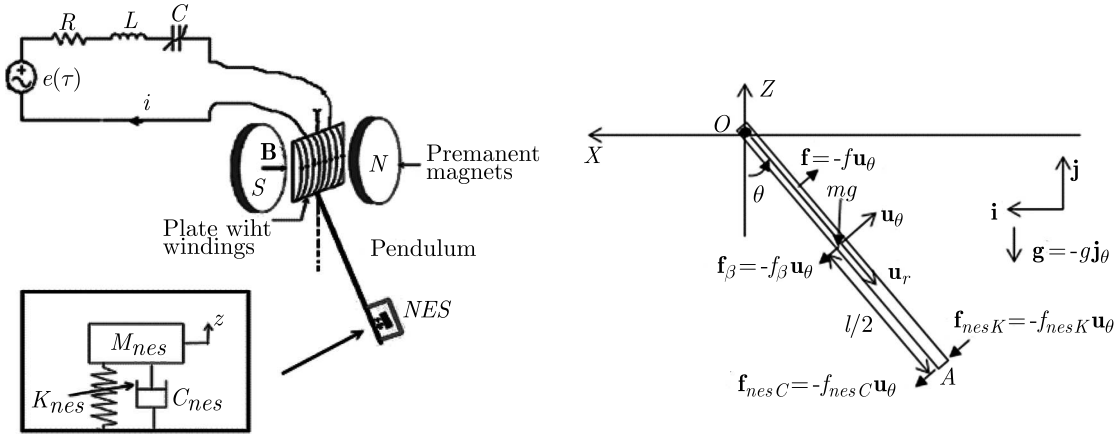

Fig. 1. Idealization of a NES applied to a pendulum arm, $\mathbf{u}_r$ and $\mathbf{u}_\theta$ are the polar unit vectors

In this work, a NES device is applied to the free end of the pendulum (Fig. 1). This set-up is a system with three degrees of freedom: (i) charge q of the nonlinear condenser, (ii) angular displacement θ of the pendulum, (iii) displacement ζ of the M_{nes}.

2. Equations of motion

2.1. Equation of the electric drive

The electric oscillator used to drive the pendulum is an RLC series circuit with a sinusoidal excitation $e(t) = v_0 \cos \Omega t$ (v_0 and Ω being, respectively, the amplitude and frequency, and t time). Denoting the forced mesh current i in the RLC circuit, as shown in Fig. 1, applying Kirchhoff's rules, and taking into account the contribution of Lenz's electromotive voltage for N turns by integrating over θ from zero to $2\pi N$ ($e = -0.5NB\sigma^2 l^2\, d\theta/dt$) one obtains

$$L\frac{di}{dt} + Ri + V_c(q) - e = e(t) \tag{2.1}$$

where $L\,di/dt$, Ri, $V_C(q)$ are the voltages across the selenoid of the inductance L, the resistor R, and the nonlinear capacitor C, respectively. In this electromechanical model, the electrical nonlinear term is introduced by considering that the voltage of the capacitor is a nonlinear function of the instantaneous electrical charge q of the following form

$$V_c(q) = \frac{1}{C_0}q + a_3 q^3 \tag{2.2}$$

where C_0 is the linear value of C and a_3 is the nonlinear coefficient depending on the type of the capacitor used. Inserting Eq. (2.2) in Eq. (2.1), the electric part of the model is described by the following nonlinear differential equation

$$\frac{d^2q}{dt^2} + \frac{R}{L}\frac{dq}{dt} + \omega_e^2 q + \frac{a_3}{L}q^3 + \frac{NB\sigma^2 l^2}{2L}\frac{d\theta}{dt} = \frac{v_0}{L}\cos(\Omega t) \tag{2.3}$$

where $\omega_e^2 = 1/(LC_0)$ is the resonance frequency of the electric oscillator.

2.2. Equation of the pendulum arm and the Nonlinear Energy Sink

In Fig. 1, the forces acting on the pendulum are represented. The mechanism consists of a uniform thin rod OA of mass m and length l, having a plate to which N conducting electric windings of length σl each are applied, with $\sigma = 1/2$. The pendulum is hinged at O about a horizontal axis, with only the portion σl of the rod in the magnetic field. The total mass of the conducting wire and the plate bathing in the magnetic field have been neglected compared to the pendulum mass. The moment of inertia of the output is then reduced to

$$I_O = \frac{1}{3}ml^2 + M_{nes}l^2 \tag{2.4}$$

where m, M_{nes} are mass of the pendulum and NES, respectively. When the current i flows through the conducting wire in the magnetic field, there appear, according to the directions of the current (upward or downward), two identical Laplace forces (direction and intensity) whose resultant f sets the pendulum into motion in a viscous medium with the frictional coefficient β. According to the equation for kinetic moment, the moment of inertia I_O times the angular acceleration equals the sum of torques due to forces applied to the pendulum. The Laplace force $f = NB\sigma l\, dq/dt$ is applied to the center of the plate gravity and friction forces. NES spring and friction forces are applied to the free end of the pendulum.

Thus, the pendulum motion is described by

$$I_O\frac{d^2\theta}{dt^2} = \frac{NB\sigma^2 l^2}{2}\frac{dq}{dt} - \frac{mgl}{2}\sin\theta - \frac{\beta l^2}{4}\frac{d\theta}{dt} - C_{nes}l\Big(l\frac{d\theta}{dt} - \frac{d\zeta}{dt}\Big) - K_{nes}l(l\theta - \zeta)^n \tag{2.5}$$

where $n = 1$ and $n = 3$. It can be divided by the moment of inertia to obtain this equation in the standard form

$$\begin{aligned}
&\frac{d^2\theta}{dt^2} = \frac{NB\sigma^2 l^2}{2\Big(\frac{m}{3} + M_{nes}\Big)l^2}\frac{dq}{dt} - \frac{mgl}{2\Big(\frac{m}{3} + M_{nes}\Big)l^2}\sin\theta - \frac{\beta l^2}{4\Big(\frac{m}{3} + M_{nes}\Big)l^2}\frac{d\theta}{dt}\\
&\quad - \frac{C_{nes}l}{\Big(\frac{m}{3} + M_{nes}\Big)l^2}\Big(l\frac{d\theta}{dt} - \frac{d\zeta}{dt}\Big) - \frac{K_{nes}l}{\Big(\frac{m}{3} + M_{nes}\Big)l^2}(l\theta - \zeta)^n\\
&\frac{d^2\theta}{dt^2} + \omega_m^2\sin\theta + \frac{\beta}{4\Big(\frac{m}{3} + M_{nes}\Big)}\frac{d\theta}{dt} - \frac{NB\sigma^2}{2\Big(\frac{m}{3} + M_{nes}\Big)}\frac{dq}{dt} + \frac{C_{nes}}{\Big(\frac{m}{3} + M_{nes}\Big)l}\Big(l\frac{d\theta}{dt} - \frac{d\zeta}{dt}\Big)\\
&\quad + \frac{K_{nes}}{\Big(\frac{m}{3} + M_{nes}\Big)l}(l\theta - \zeta)^n = 0
\end{aligned} \tag{2.6}$$

where $\omega_m^2 = mg/[2(\frac{m}{3} + M_{nes})l]$ is the resonance frequency of the pendulum, C_{nes} is the damping coefficients of the NES, K_{nes} is the spring coefficient of the NES.

According to Newton's second law, the NES motion is described by

$$M_{nes}\frac{d^2\zeta}{dt^2} = -C_{nes}\Big(\frac{d\zeta}{dt} - l\frac{d\theta}{dt}\Big) - K_{nes}(\zeta - l\theta)^n \tag{2.7}$$

It can be divided by mass of the NES to obtain this equation in the standard form

$$\frac{d^2\zeta}{dt^2} + \frac{C_{nes}}{M_{nes}}\Big(\frac{d\zeta}{dt} - l\frac{d\theta}{dt}\Big) + \frac{K_{nes}}{M_{nes}}(\zeta - l\theta)^n = 0 \tag{2.8}$$

2.3. Nondimensional equations and values of the parameter

Using the transformation

$$\begin{aligned}
&x=\frac{q}{Q_0} && y=\frac{\theta}{\theta_0} && z=\frac{\zeta}{l\theta_0} && \tau=\omega_e t\\
&\frac{dq}{dt}=Q_0\omega_e\frac{dx}{d\tau} && \frac{d\theta}{dt}=\theta_0\omega_e\frac{dy}{d\tau} && \frac{d\zeta}{dt}=l\theta_0\omega_e\frac{dz}{d\tau} &&\\
&\frac{d^2q}{dt^2}=Q_0\omega_e^2\frac{d^2x}{d\tau^2} && \frac{d^2\theta}{dt^2}=\theta_0\omega_e^2\frac{d^2y}{d\tau^2} && \frac{d^2\zeta}{dt^2}=l\theta_0\omega_e^2\frac{d^2z}{d\tau^2} &&
\end{aligned} \tag{2.9}$$

where x, y, τ are dimensionless variables, Q_0 is the reference charge of the condenser, and θ_0 is the reference pendulum angular displacement. The equations of motion of the complete system can be written as follows

$$\begin{aligned}
&\frac{d^2x}{d\tau^2}+\frac{R}{L\omega_e}\frac{dx}{d\tau}+x+\frac{a_3Q_0^2}{L\omega_e^2}x^3+\frac{NB\sigma^2l^2\theta_0}{2LQ_0\omega_e}\frac{dy}{d\tau}=\frac{v_0}{Q_0\omega_e^2L}\cos\Big(\frac{\Omega}{\omega_e}\tau\Big)\\
&\frac{d^2y}{d\tau^2}=\frac{NB\sigma^2}{2\Big(\frac{m}{3}+M_{nes}\Big)\omega_e\theta_0}Q_0\frac{dx}{d\tau}-\frac{mg}{2\Big(\frac{m}{3}+M_{nes}\Big)\theta_0\omega_e^2l}\sin(\theta_0 y)-\frac{\beta}{4\Big(\frac{m}{3}+M_{nes}\Big)\omega_e}\frac{dy}{d\tau}\\
&\quad-\frac{C_{nes}}{\Big(\frac{m}{3}+M_{nes}\Big)\omega_e}\Big(\frac{dy}{d\tau}-\frac{dz}{d\tau}\Big)-\frac{K_{nes}(l\theta_0)^{n-1}}{\Big(\frac{m}{3}+M_{nes}\Big)\omega_e^2}(y-z)^n\\
&\frac{d^2z}{d\tau^2}+\frac{C_{nes}}{M_{nes}\omega_e}\Big(\frac{dz}{d\tau}-\frac{dy}{d\tau}\Big)+\frac{K_{nes}(l\theta_0)^{n-1}}{M_{nes}\omega_e^2}(z-y)^n=0
\end{aligned} \tag{2.10}$$

and

$$\begin{aligned}
&x''+\mu_1x'+x+\alpha x^3+\gamma_1y'=E\cos(\omega\tau)\\
&y''+\mu_2y'+\omega_2^2\sin(\theta_0'y)-\gamma_2x'+c_{2nes}(y'-z')+k_{2nes}(y-z)^n=0\\
&z''+c_{1nes}(z'-y')+k_{1nes}(z-y)^n=0
\end{aligned} \tag{2.11}$$

where the prime denotes a derivative with respect to τ and

$$\begin{aligned}
&\mu_1=\frac{R}{L\omega_e} && \alpha=\frac{a_3Q_0^2}{L\omega_e^2} && E=\frac{v_0}{LQ_0\omega_e^2}\\
&\omega=\frac{\Omega}{\omega_e} && \gamma_1=\frac{NB\sigma^2l^2\theta_0}{2LQ_0\omega_e} && \mu_2=\frac{\beta}{4\Big(\frac{m}{3}+m_{nes}\Big)\omega_e}\\
&\omega_2^2=\frac{\omega_m^2}{\omega_e^2\theta_0} && \gamma_2=\frac{NB\sigma^2Q_0}{2\Big(\frac{m}{3}+m_{nes}\Big)\omega_e\theta_0} && c_{1nes}=\frac{C_{nes}}{m_{nes}\omega_e}\\
&c_{2nes}=\frac{C_{nes}}{\Big(\frac{m}{3}+M_{nes}\Big)\omega_e} && k_{1nes}=\frac{K_{nes}(l\theta_0)^{n-1}}{M_{nes}\omega_e^2} && k_{2nes}=\frac{K_{nes}(l\theta_0)^{n-1}}{\Big(\frac{m}{3}+M_{nes}\Big)\omega_e^2}
\end{aligned}$$

The physical parameters used are the following: $C_0=0.11$ F, $a_3=158\,\mathrm{VC}^{-3}$, $Q_0=0.24$ C, $R=0.97\ \Omega$, $L=1.15$ H, $B=0.02$ T, $N=685$, $\theta_0=\pi$ rad, $l=0.465$ m, $g=9.81\ \mathrm{m/s^2}$, $m=1$ kg, $M_{nes}=0.1$ kg, $\beta=0.49$ Ns/m, $\Omega=5.6$ rad/s, $\sigma=0.5$, $K_{nes}=1.5$ N/m, $C_{nes}=0.3$ Ns/m.

This gives the following values for non-dimensional constants: $\omega=2$, $\omega_2=1$, $\mu_1=0.30$, $\mu_2=0.1$, $\alpha=1$, $\gamma_1=1.5$, $\gamma_2=0.1$, $c_{1nes}=1$, $c_{2nes}=5$, $k_{1nes}=2$, $k_{2nes}=8$.

2.4. Bifurcation structures and basin of chaoticity

The aim of this subsection is to find how chaos arises in our electromechanical model as the parameters of the system evolve. For this purpose, we numerically solve equations of motion (2.11) and plot the resulting bifurcation diagrams, Lyapunov exponents, phase planes and Poincare maps as E, ω, ω_2, α, μ_1, μ_2, γ_1, γ_2, c_{1nes}, c_{2nes}, k_{1nes}, k_{2nes} varies. Figures 2 and 3 show the non-dimensional amplitude diagram for the pendulum arm as the other non-dimensional

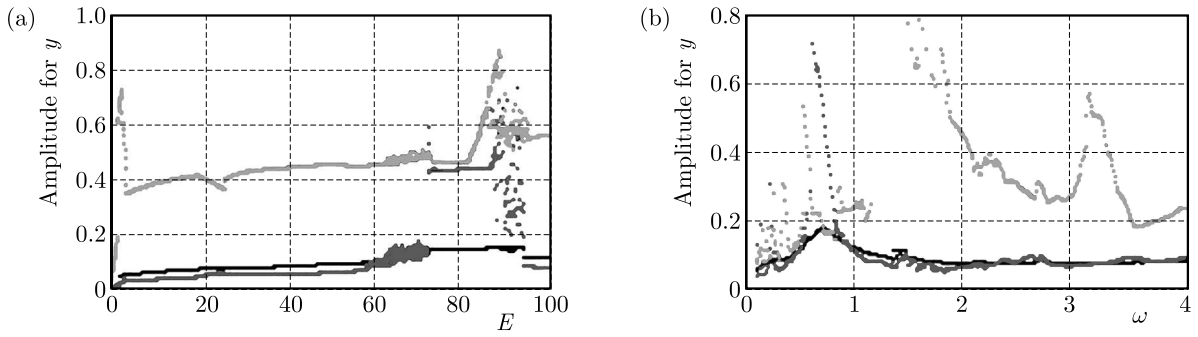

Fig. 2. Amplitude of the pendulum arm versus (a) excitation amplitude E, (b) excitation frequency ω; bleu lines $n = 1$, black lines $n = 3$, grey lines without NES

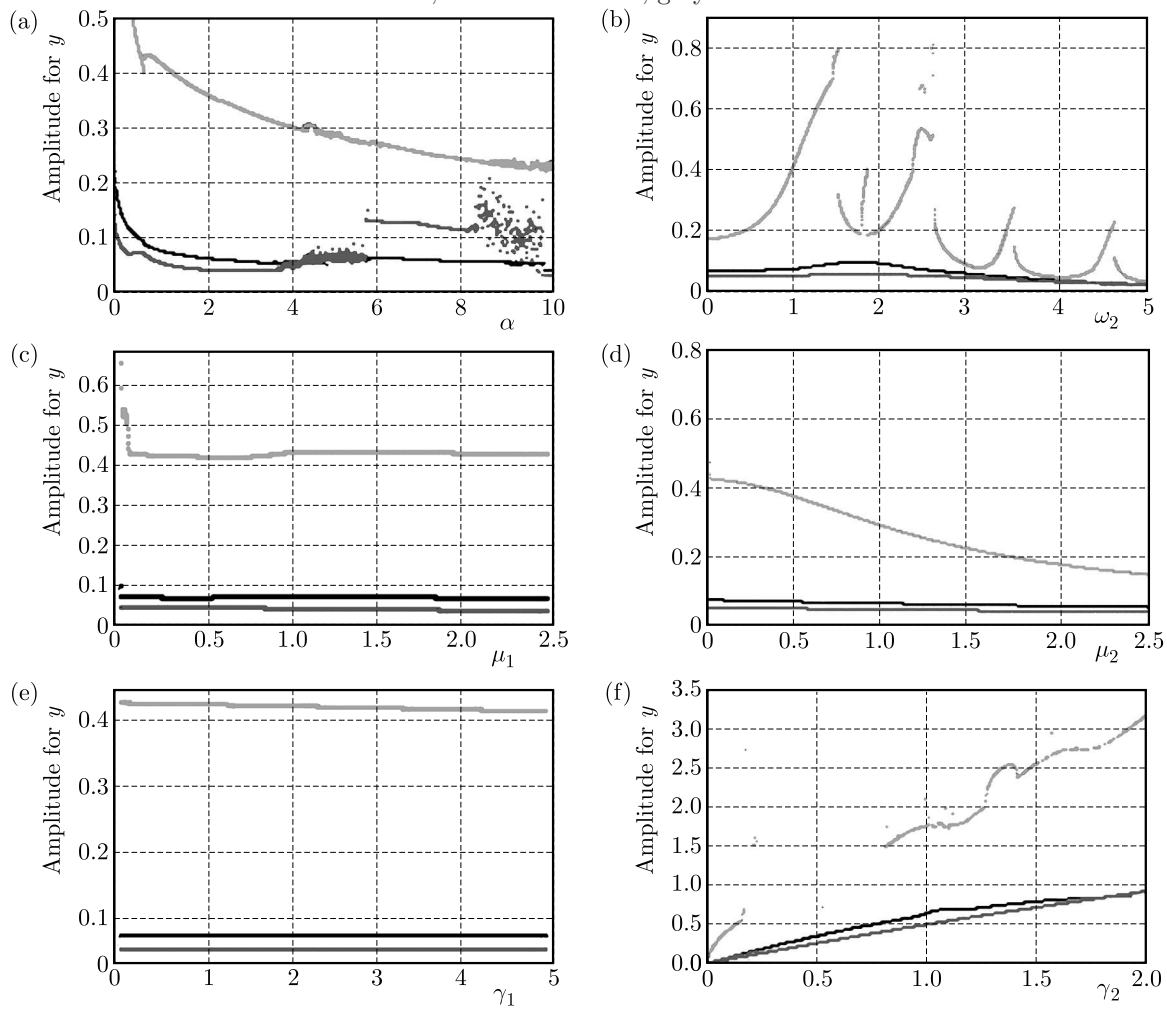

Fig. 3. Amplitude of the pendulum arm versus (a) function of α, (b) function of ω_2, (c) function of μ_1, (d) function of μ_2, (e) function of γ_1, (f) function of γ_2; bleu lines $n = 1$, black lines $n = 3$, grey lines without NES

parameters (E, ω, ω_2, α, μ_1, μ_2, γ_1, γ_2) vary. The dark grey lines are shown for $n = 1$, the black lines for $n = 3$ and the grey ones for without NES. The investigation of these figures shows that the pendulum arm with NES and $n = 3$ diminishes the chaotic effect and amplitude.

Figure 4 shows the non-dimensional amplitude diagram for the pandulum arm as the other non-dimensional parameters (c_{1nes}, c_{2nes}, k_{1nes}, k_{2nes}) vary. The dark grey lines are for $n = 1$, the black lines for $n = 3$. It is clear that for $n = 3$ the chaotic effect and amplitude are diminished.

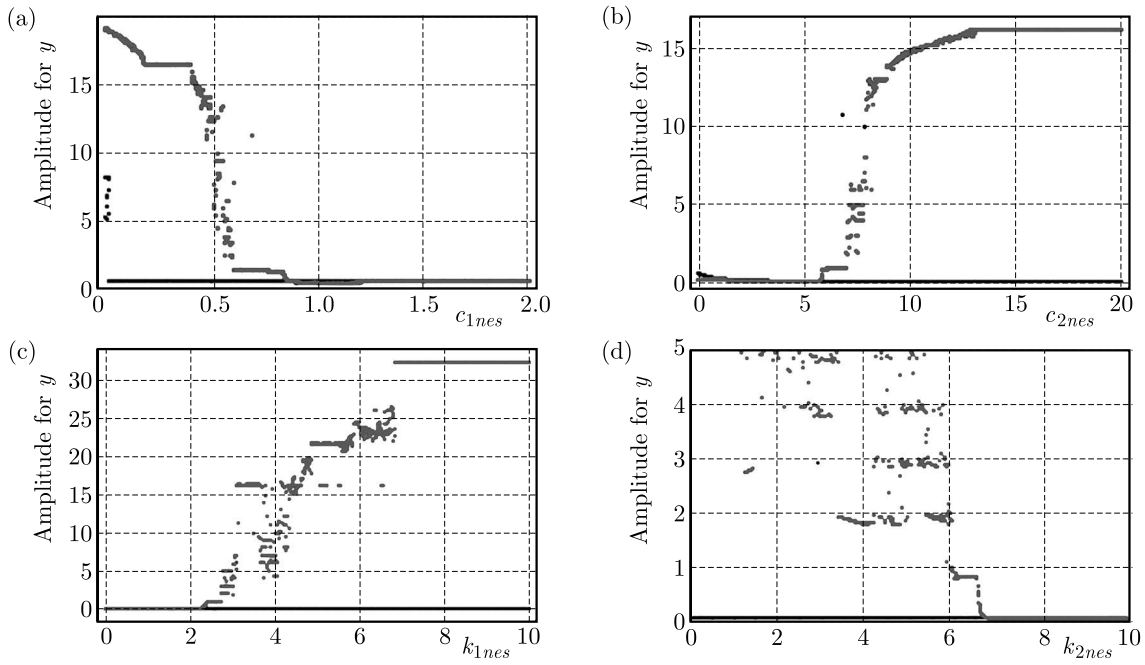

Fig. 4. Amplitude of the pendulum arm versus (a) function of c_{1nes}, (b) function of c_{2nes}, (c) function of k_{1nes}, (d) function of k_{2nes}; dark grey lines $n = 1$, black lines $n = 3$

Table 1 shows the stability condition as a function of E, ω, ω_2, α, γ_2, k_{1nes}, k_{2nes}, c_{1nes}, c_{2nes}. It has been constructed with Figs. 5-8 and Figs. 10-14. According to this Table, the pendulum arm with NES and $n = 3$ diminishes the chaotic effect and amplitude. Figure 9 shows that only for $\mu 1 < 0.01$ the system exhibits chaotic effect without NES.

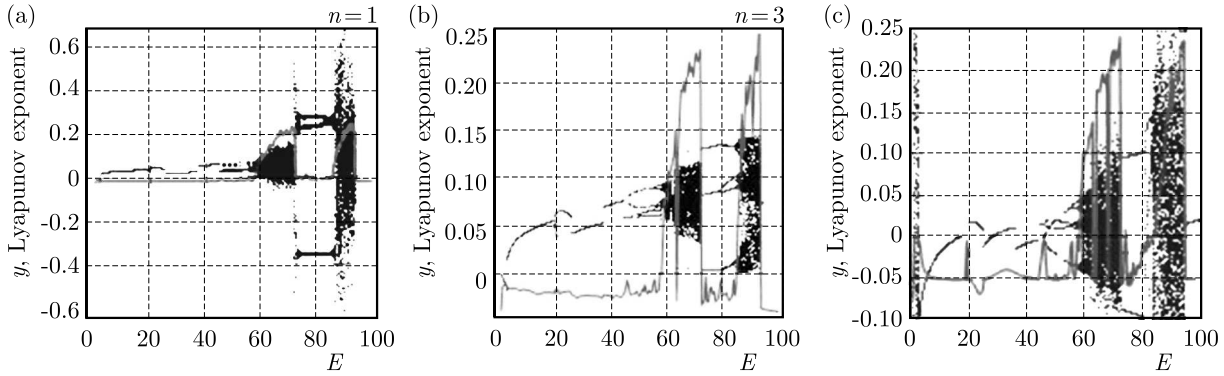

Fig. 5. Bifurcation diagrams and Lyapunov exponents of the pendulum arm as functions of E in the y direction, (a) NES, $n = 1$, (b) NES $n = 3$, (c) without NES. The other parameters are $E = 30$, $\omega = 2$, $\mu_1 = 0.3$, $\mu_2 = 0.1$, $\theta_0 = \pi$, $\gamma_1 = 1.5$, $\gamma_2 = 0.1$, $c_{1nes} = 1$, $c_{2nes} = 5$, $k_{1nes} = 2$, $k_{2nes} = 8$; dark grey line – bifurcation diagram, grey line – Lyapunov exponent

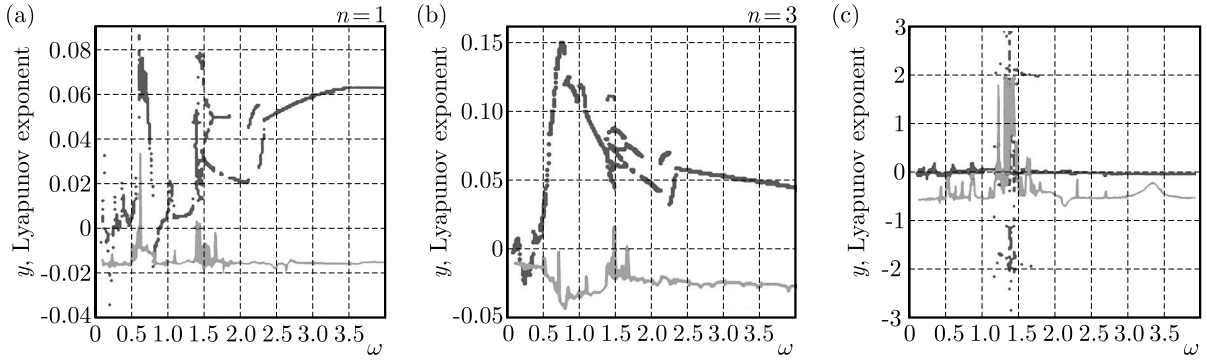

Fig. 6. Bifurcation diagrams and Lyapunov exponents of the pendulum arm as functions of ω in the y direction, (a) NES, $n = 1$, (b) NES $n = 3$, (c) without NES. The other parameters are $E = 30$, $\omega_2 = 1$, $\mu_1 = 0.3$, $\mu_2 = 0.1$, $\theta_0 = \pi$, $\gamma_1 = 1.5$, $\gamma_2 = 0.1$, $c_{1nes} = 1$, $c_{2nes} = 5$, $k_{1nes} = 2$, $k_{2nes} = 8$; dark grey line – bifurcation diagram, grey line – Lyapunov exponent

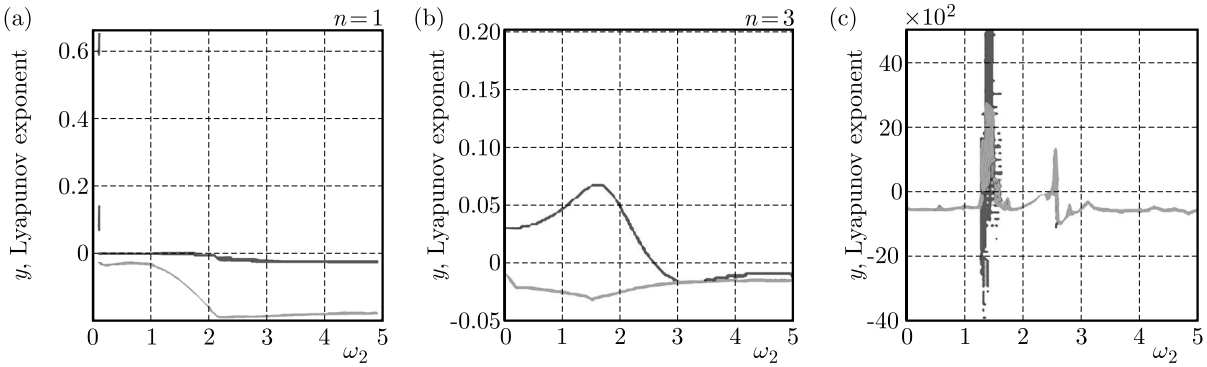

Fig. 7. Bifurcation diagrams and Lyapunov exponents of the pendulum arm as functions of ω_2 in the y direction, (a) NES, $n = 1$, (b) NES $n = 3$, (c) without NES. The other parameters are $E = 30$, $\omega = 2$, $\mu_1 = 0.3$, $\mu_2 = 0.1$, $\theta_0 = \pi$, $\gamma_1 = 1.5$, $\gamma_2 = 0.1$, $c_{1nes} = 1$, $c_{2nes} = 5$, $k_{1nes} = 2$, $k_{2nes} = 8$; dark grey line – bifurcation diagram, grey line – Lyapunov exponent

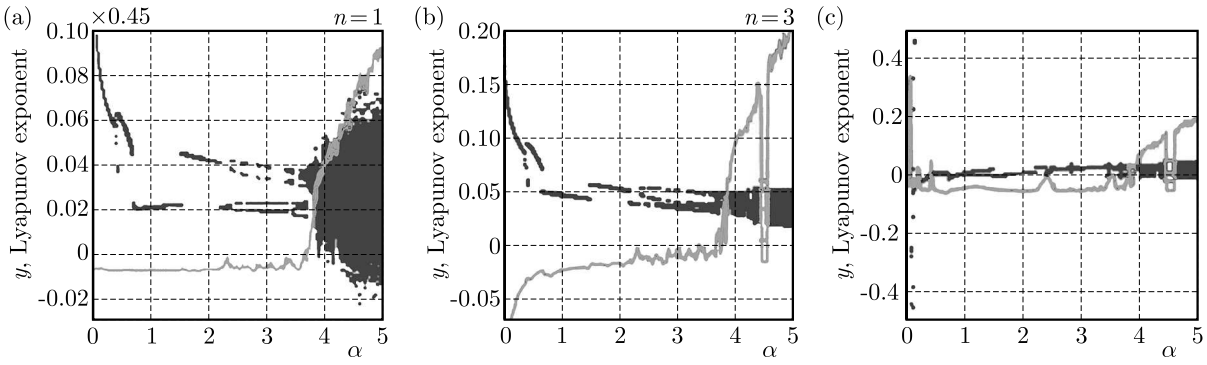

Fig. 8. Bifurcation diagrams and Lyapunov exponents of the pendulum arm as functions of α in the y direction, (a) NES, $n = 1$, (b) NES $n = 3$, (c) without NES. The other parameters are $E = 30$, $\omega = 2$, $\mu_1 = 0.3$, $\mu_2 = 0.1$, $\theta_0 = \pi$, $\gamma_1 = 1.5$, $\gamma_2 = 0.1$, $c_{1nes} = 1$, $c_{2nes} = 5$, $k_{1nes} = 2$, $k_{2nes} = 8$; dark grey line – bifurcation diagram, grey line – Lyapunov exponent

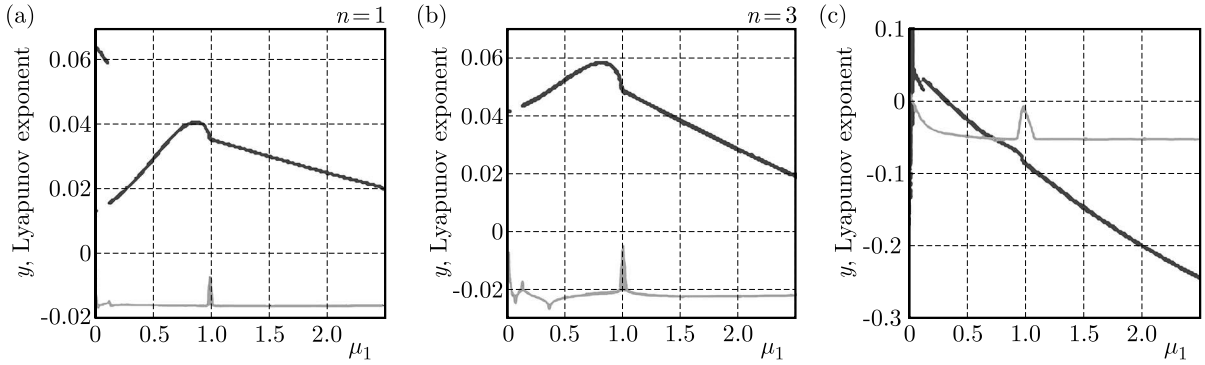

Fig. 9. Bifurcation diagrams and Lyapunov exponents of the pendulum arm as functions of μ_1 in the y direction, (a) NES, $n = 1$, (b) NES $n = 3$, (c) without NES. The other parameters are $E = 30$, $\omega = 2$, $\alpha = 1$, $\mu_2 = 0.1$, $\theta_0 = \pi$, $\gamma_1 = 1.5$, $\gamma_2 = 0.1$, $c_{1nes} = 1$, $c_{2nes} = 5$, $k_{1nes} = 2$, $k_{2nes} = 8$; dark grey line – bifurcation diagram, grey line – Lyapunov exponent

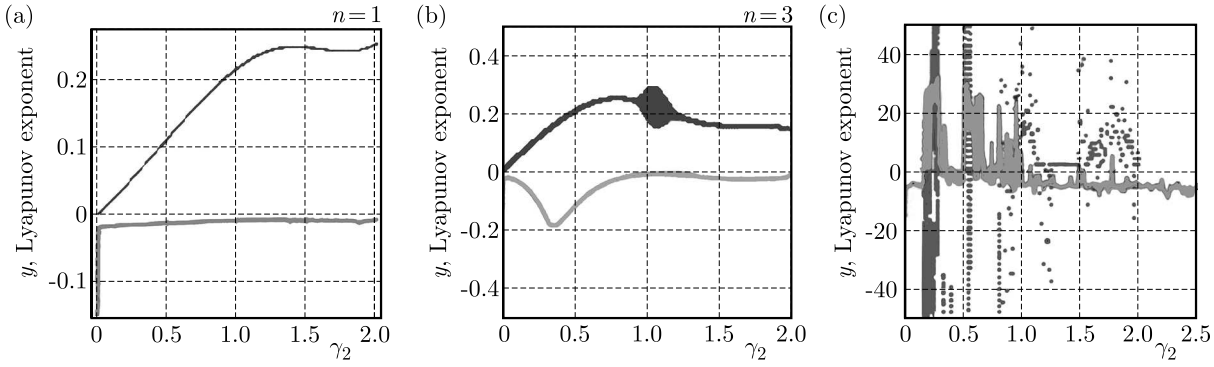

Fig. 10. Bifurcation diagrams and Lyapunov exponents of the pendulum arm as functions of γ_2 in the y direction, (a) NES, $n = 1$, (b) NES $n = 3$, (c) without NES. The other parameters are $E = 30$, $\omega = 2$, $\mu_1 = 0.3$, $\mu_2 = 0.1$, $\theta_0 = \pi$, $\alpha = 1$, $\gamma_1 = 1.5$, $c_{1nes} = 1$, $c_{2nes} = 5$, $k_{1nes} = 2$, $k_{2nes} = 8$; dark grey line – bifurcation diagram, grey line – Lyapunov exponent

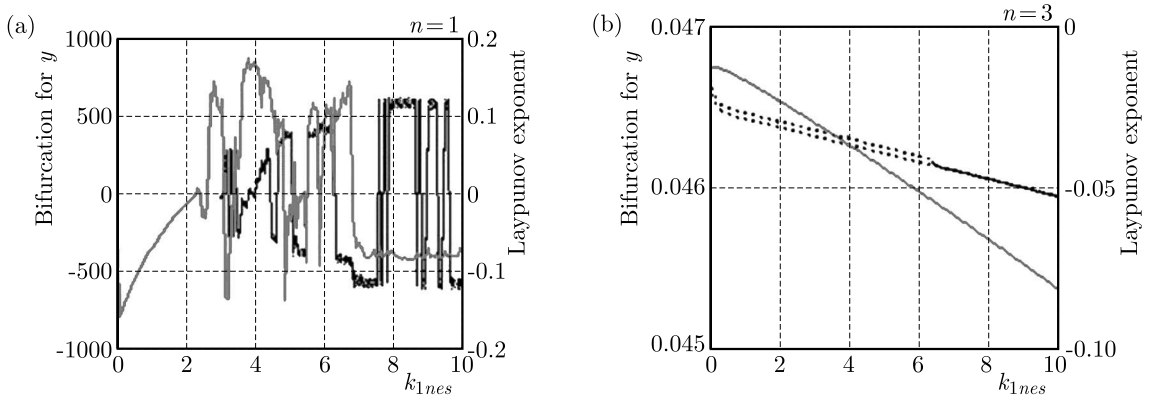

Fig. 11. Bifurcation diagrams and Lyapunov exponents of the pendulum arm as functions of k_{1nes} with NES, (a) $n = 1$, (b) $n = 3$. The other parameters are $E = 30$, $\omega = 2$, $\mu_1 = 0.3$, $\mu_2 = 0.1$, $\theta_0 = \pi$, $\alpha = 1$, $\gamma_2 = 0.1$, $c_{1nes} = 1$, $c_{2nes} = 5$, $k_{2nes} = 8$; dark grey line – bifurcation diagram, grey line – Lyapunov exponent

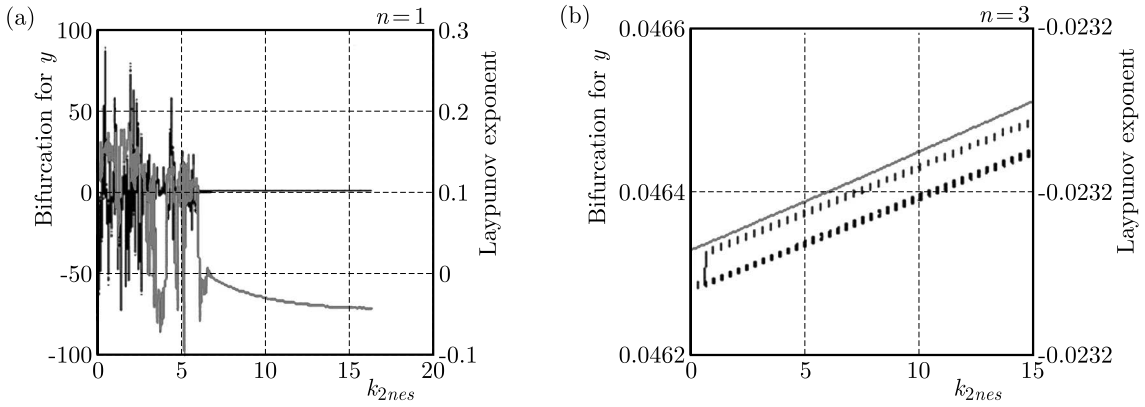

Fig. 12. Bifurcation diagrams and Lyapunov exponents of the pendulum arm as functions of k_{2nes} with NES, (a) $n = 1$, (b) $n = 3$. . The other parameters are $E = 30$, $\omega = 2$, $\mu_1 = 0.3$, $\mu_2 = 0.1$, $\theta_0 = \pi$, $\alpha = 1$, $\gamma_2 = 0.1$, $c_{1nes} = 1$, $c_{2nes} = 5$, $k_{1nes} = 2$; dark grey line – bifurcation diagram, grey line – Lyapunov exponent

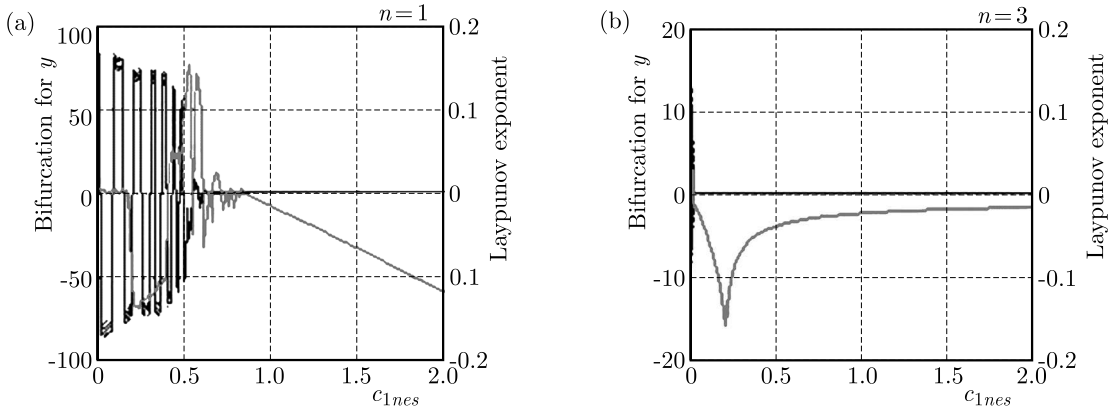

Fig. 13. Bifurcation diagrams and Lyapunov exponents of the pendulum arm as functions of c_{1nes} with NES, (a) $n = 1$, (b) $n = 3$. The other parameters are $E = 30$, $\omega = 2$, $\mu_1 = 0.3$, $\mu_2 = 0.1$, $\theta_0 = \pi$, $\alpha = 1$, $\gamma_2 = 0.1$, $c_{1nes} = 1$, $c_{2nes} = 5$, $k_{1nes} = 2$, $k_{2nes} = 8$; dark grey line – bifurcation diagram, grey line – Lyapunov exponent

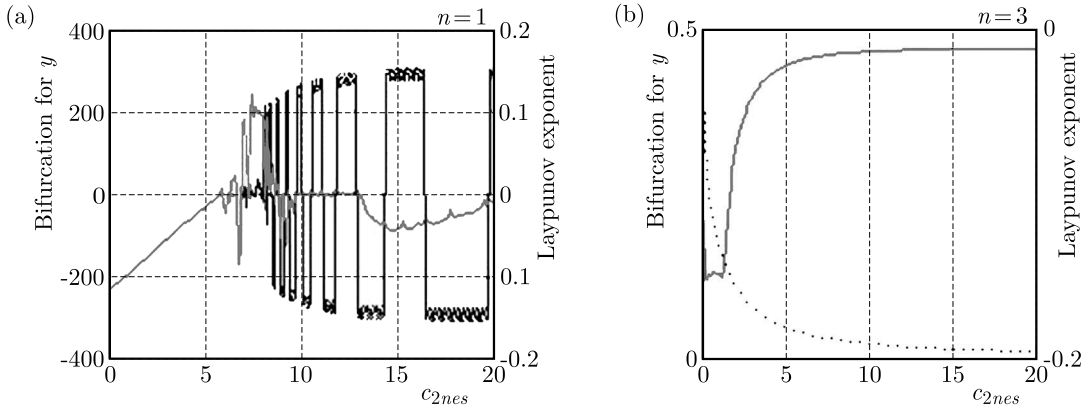

Fig. 14. Bifurcation diagrams and Lyapunov exponents of the pendulum arm as functions of c_{2nes} with NES, (a) $n = 1$, (b) $n = 3$. The other parameters are $E = 30$, $\omega = 2$, $\mu_1 = 0.3$, $\mu_2 = 0.1$, $\theta_0 = \pi$, $\alpha = 1$, $\gamma_2 = 0.1$, $c_{1nes} = 1$, $k_{1nes} = 2$, $k_{2nes} = 8$; dark grey line – bifurcation diagram, grey line – Lyapunov exponent

Table 1. Stability conditions as a function of E, ω, ω_2, α, γ_2, k_{1nes}, k_{2nes}, c_{1nes}, c_{2nes}

	Periodic	Quasi periodic	Chaotic
Fig. 5a, $n = 1$, various E	$E < 45$, $E > 93$	$45 < E < 57$, $73 < E < 87$	$57 < E < 73$, $87 < E < 93$
Fig. 5b, $n = 3$, various E	$E < 20$, $93 < E$, $28 < E < 45$	$20 < E < 28$, $45 < E < 58$, $72 < E < 86$	$58 < E < 72$, $86 < E < 93$
Fig. 5c, without NES, various E	$5 < E < 20$, $E > 95$	$E = 32$, $48 < E < 60$	$E < 5$, $60 < E < 73$, $85 < E < 95$
Fig. 6a, $n = 1$, various ω	$\omega < 0.7$, $\omega > 2.3$	$1.5 < \omega < 1.8$, $2.1 < \omega < 2.3$	$0.7 < \omega < 0.8$, $1.3 < \omega < 1.45$
Fig. 6b, $n = 3$, various ω	$\omega < 1.45$, $\omega > 2.3$	$1.5 < \omega < 1.7$	$1.45 < \omega < 1.5$, $\omega = 1.7$
Fig. 6c, without NES, various ω	$\omega < 0.4$, $\omega > 2.3$	$0.5 < \omega < 0.6$, $0.8 < \omega < 0.9$	$1.2 < \omega < 1.5$, $1.6 < \omega < 1.7$
Fig. 7a, $n = 1$, various ω_2	$0 > \omega_2 < 5$		
Fig. 7b, $n = 3$, various ω_2	$0 > \omega_2 < 5$		
Fig. 7c, without NES, various ω_2	$\omega_2 < 1.3$, $\omega_2 > 2.55$, $1.6 < \omega_2 < 2.5$		$1.3 < \omega_2 < 1.6$, $2.5 < \omega_2 < 2.55$
Fig. 8a, $n = 1$, various α	$\alpha < 2.3$	$2.3 < \alpha < 3.7$	$\alpha > 3.7$
Fig. 8b, $n = 3$, various α	$\alpha < 2.2$	$2.3 < \alpha < 3.7$, $4.4 < \alpha < 4.6$	$3.7 < \alpha < 4.4$, $\alpha > 4.6$
Fig. 8c, without NES, various α	$0.2 < \alpha < 0.4$, $0.5 < \alpha < 1$, $1.4 < \alpha < 2.2$	$1.2 < \alpha < 1.4$, $2.2 < \alpha < 3.4$ $4.4 < \alpha < 4.6$	$0 < \alpha < 0.2$, $0.4 < \alpha < 0.5$, $3.4 < \alpha < 3.6$, $3.8 < \alpha < 4.4$, $4.6 < \alpha < 5$
Fig. 10a, $n = 1$, various γ_2	$0 < \gamma_2 < 2$		
Fig. 10b, $n = 3$, various γ_2	$0 < \gamma_2 < 0.8$, $1.38 < \gamma_2 < 2$		$0.8 < \gamma_2 < 1.3$
Fig. 10c, without NES, various γ_2	$0 < \gamma_2 < 0.15$, $1.35 < \gamma_2 < 1.4$	$1.9 < \gamma_2 < 2.5$	$0.15 < \gamma_2 < 1.1$, $1.8 < \gamma_2 < 1.9$
Fig. 11a, $n = 1$, various k_{1nes}	$0 < k_{1nes} < 2.1$	$3 < k_{1nes} < 3.2$, $4.8 < k_{1nes} < 5$, $6.4 < k_{1nes} < 10$	$2.1 < k_{1nes} < 3$, $3.1 < k_{1nes} < 5$, $5 < k_{1nes} < 6.4$
Fig. 11b, $n = 3$, various k_{1nes}	$6.4 < k_{1nes} < 10$	$0 < k_{1nes} < 6.4$	
Fig. 12a, $n = 1$, various k_{2nes}	$7 < k_{2nes} < 15$		$0 < k_{2nes} < 7$
Fig. 12b, $n = 3$, various k_{2nes}		$0 < k_{2nes} < 15$	

Fig. 13a, $n = 1$, various c_{1nes}	$0.2 < c_{1nes} < 0.4$, $0.7 < c_{1nes} < 2$	$0 < c_{1nes} < 0.2$	$0.4 < c_{1nes} < 0.7$
Fig. 13b, $n = 3$, various c_{1nes}	$0 < c_{1nes} < 2$		
Fig. 14a, $n = 1$, various c_{2nes}	$0 < c_{2nes} < 2$		$2 < c_{2nes} < 20$
Fig. 14b, $n = 3$, various c_{2nes}	$0 < c_{2nes} < 2$		$2 < c_{2nes} < 20$

3. Conclusion

We have studied the effect of the NES on a electro-mechanical device with a pendulum.

The system exhibits complex dynamical behavior such as multi-periodic, quasi-periodic and chaotic responses, and these are strongly dependent on non-dimensional control parameters E, ω and a nonlinearity coefficient α for RLC circuit, and NES parameters c_{1nes}, c_{2nes}, k_{1nes}, k_{2nes}. Moreover, the system without NES exhibits a chaotic response depending on γ_2. The NES parameters (c_{1nes}, c_{2nes}, k_{1nes}, k_{2nes}) for $n = 1$ lead to chaotic responses, but for $n = 3$, they induce periodic and quasi-periodic responses. It is shown that the NES is capable of absorbing energy from the system and decreases the amplitude as well as diminishes the chaotic effect.

References

1. Dantas M.J.H., Balthazar J.M., 2008, On energy transfer between linear and non-linear oscillator, *Journal of Sound and Vibration*, **315**, 4/5, 1047-1070
2. Felix J.L.P., Balthazar J.M., 2009, Comments on a nonlinear and a non-ideal electromechanical damping vibration absorber, sommerfeld effect and energy transfer, *Nonlinear Dynamics*, **55**, 1, 1-11
3. Felix J.L.P., Balthazar J.M., Dantas M.J.H., 2009, On energy pumping, synchronization and beat phenomenon in a non-ideal structure coupled to an essentially nonlinear oscillator, *Nonlinear Dynamics*, **56**, 1, 1-11
4. Jiang X., McFarland D.M., Bergman L.A., Vakakis A.F., 2003, Steady state passive nonlinear energy pumping in coupled oscillators: theoretical and experimental results, *Nonlinear Dynamics*, **33**, 87-102
5. Malatkar P., Nayfeh A.H., 2007, Steady-state dynamics of a linear structure weakly coupled to an essentially nonlinear oscillator, *Nonlinear Dynamics*, **47**, 167-179
6. Mogo J.B., Woafo P., 2007, Dynamics of a nonlinear electromechanical device with a pendulum arm, *Journal of Computational and Nonlinear Dynamics*, **2**, 4, 374-378, DOI: 10.1115/1.2756080
7. Tusset A.M., Balthazar J.M., Felix J.L.P., 2013, On elimination of chaotic behavior in a non-ideal portal frame structural system, using both passive and active controls, *Journal of Vibration and Control*, **19**, 6, 803-813
8. Tusset A.M., Bueno A.M., Sado D., Balthazar J.M., Colón D., 2014, SDRE control and sensibility analysis of a chaotic double pendulum arm excited by a RLC circuit based nonlinear shaker, *Conference on Dynamical Systems Theory and Applications*, Łódź, Poland, 195-204
9. Tusset A.M., Picirillo V., Bueno A.M., Sado D., Balthazar J.M., Felix J.L.P., 2015, Chaos control and sensitivity analysis of a double pendulum arm excited by an RLC circuit based nonlinear shaker, *Journal of Vibration and Control*, 1077546314564782

10. Vakakis A.F., 2001, Inducing passive nonlinear energy sinks in linear vibrating systems, *Journal of Vibration and Acoustics*, **123**, 3, 324-332

11. Vakakis F., Gendelman O., 2001, Energy pumping in nonlinear mechanical oscillators. II: Resonance capture, *Journal of Applied Mechanics*, **68**, 1, 42-48

12. Vakakis A.F., Gendelman O.V., Bergman L.A., McFarland D.M., Kerschen G., Lee Y.S., 2008, *Nonlinear Targeted Energy Transfer in Mechanical and Structural Systems (Solid Mechanics and Its Applications)*, Springer

Manuscript received January 13, 2015; accepted for print January 8, 2016

JOURNAL OF THEORETICAL AND APPLIED MECHANICS
54, 3, pp. 987-1000, Warsaw 2016
DOI: 10.15632/jtam-pl.54.3.987

ADAPTIVE FUZZY CONTROL FOR A CLASS OF CONSTRAINED NONLINEAR SYSTEMS WITH APPLICATION TO A SURFACE VESSEL

Mehrnush Sadat Jamalzade, Hamid Reza Koofigar, Mohammad Ataei
Department of Electrical Engineering, University of Isfahan, Isfahan, Iran
e-mail: koofigar@eng.ui.ac.ir

In this paper, adaptive control for a class of uncertain nonlinear systems with input constraints is addressed. The main goal is to achieve a self-regulator PID controller whose coefficients are adjusted by using some adaptive fuzzy rules. The constraints on the control signal are taken into account as a saturation operator. The stability of the closed-loop system is analytically proved by using the Lyapunov stability theorem. The proposed method is then applied to a surface vessel with uncertain dynamic equations. The simulation results show the effectiveness of the proposed control strategy.

Keywords: self-regulator, fuzzy PID controller, constraint nonlinear systems, uncertainty, fuzzy estimation

1. Introduction

Dealing with the control problem of uncertain systems, various algorithms have been developed ensuring the robust stability and performance (Petersen and Tempo, 2014). Robust adaptive control has been formulated for a class of uncertain nonlinear systems by output feedback control (Xu and Huang, 2010; Lee, 2011). For nonlinear systems in the strict-feedback form with unknown static parameters, a robust adaptive control law was designed by Montaseri and Mohammad (2012), which guarantees the asymptotic output tracking despite matched and unmatched uncertainties. The neural-network-based robust control design, via an adaptive dynamic programming approach, was investigated in (Wang *et al.*, 2014) to obtain the optimal performance under a specified cost function. Some applications have been also introduced in the literature, in the presence of time-varying uncertainties and disturbances (Koofigar and Amelian, 2013). Nevertheless, taking the input constraint in the controller design procedure is still highly desired.

In the last decade, a considerable attention has been paid to robust control of nonlinear systems with input constraints (Chen *et al.*, 2010, 2014; Lu and Yao, 2014). In such cases, fuzzy logic and neural networks may be some alternative solutions. A direct adaptive fuzzy control approach has been presented for uncertain nonlinear systems in the presence of input saturation by incorporating a new auxiliary design system and Nussbaum gain functions (Li *et al.*, 2013). The problem of adaptive fuzzy tracking control for a class of pure-feedback nonlinear systems with input saturation was studied by Wang *et al.*, (2013a,b). Muñoz and Marquardt (2013) focused on the control design for input-output feedback linearizable nonlinear systems with bounded inputs and state constraints. An indirect adaptive fuzzy control scheme was developed for a wider class of nonlinear systems with the input constraint and unknown control direction by Wuxi *et al.* (2013) and Yongming *et al.* (2014). To this end, a barrier Lyapunov function and an auxiliary design system were employed.

From an application viewpoint, the surface vessels with uncertain nonlinear dynamics may be adopted to demonstrate the effectiveness of various control schemes. Nonlinear strategies

(Daly *et al.*, 2012), adaptive control (Fang *et al.*, 2004), and neural networks (Dai *et al.*, 2015) are samples of control algorithms in the previous investigations. Removing some drawbacks of such works, adaptive intelligent methods as adaptive neural networks, were presented by Li *et al.* (2015). In this study, an adaptive fuzzy algorithm is proposed to achieve the advantages of both intelligent and adaptive mechanisms for ensuring the robustness properties and taking the constraints into account.

Briefly discussing, there may exist some main restrictions in the previous investigations as, i) the fuzzy rules have been designed off-line and the stability and performance may be lost with changing the circumstances, ii) the stability analysis has not been presented in an analytical form, and iii) to ensure the stability of the closed-loop system, the initial value for the controller parameters must be set. To eliminate the aforementioned limitations, a self-regulator fuzzy PID controller is proposed in this paper, which guarantees the robustness properties against the system uncertainties and external disturbances.

This paper is organized as follows. In Section 2, the problem formulation and the constraints on input signal are introduced. In Section 3, an adaptive fuzzy controller is designed for a class of uncertain nonlinear systems with constrained input and the stability proof is given. The proposed method is applied to a surface vessel in Section 4 and the simulation results are presented. The concluding remarks are finally given in Section 5.

2. Problem formulation

Consider a class of nonlinear systems, represented by the state-space description

$$\begin{aligned}
&\dot{\mathbf{X}}_1 = \mathbf{X}_2\\
&\dot{\mathbf{X}}_2 = \mathbf{X}_3\\
&\vdots\\
&\dot{\mathbf{X}}_{n-1} = \mathbf{X}_n\\
&\dot{\mathbf{X}}_n = \mathbf{F}(\mathbf{X}_1, \mathbf{X}_2, \ldots, \mathbf{X}_n) + \mathbf{G}(\mathbf{X}_1, \mathbf{X}_2, \ldots, \mathbf{X}_n)\mathbf{p}(\mathbf{u}) + \mathbf{d}(t)\\
&\mathbf{Y} = \mathbf{X}_1
\end{aligned} \tag{2.1}$$

where $\mathbf{X} \in \mathbb{R}^{n\times m}$ denotes the vector of state variables, $d(t)$ represents the external disturbance, and $\mathbf{p}(\mathbf{u})\in\mathbb{R}^m$ is the vector of constrained inputs.

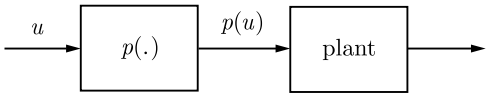

Fig. 1. Block diagram of $p(\mathbf{u})$

As schematically depicted in Fig. 1, the nonlinear operator $p(\mathbf{u})$ acts as a saturation constraint as

$$p(u_i) = \begin{cases} \alpha u_u & \text{for} \quad u_i \geqslant u_u \\ \alpha u_i & \text{for} \quad u_l \leqslant u_i \leqslant u_u \\ \alpha u_l & \text{for} \quad u_i \leqslant u_l \end{cases} \qquad i = 1, 2, \ldots, m \tag{2.2}$$

where u_u, u_l and α denote the parameters of saturation operator.

The saturation operator $p(u_i)$ is described here as

$$p(u_i) = a(u_i)u_i + b(u_i) \tag{2.3}$$

where $a(u_i)$ and $b(u_i)$ are given by

$$a(u_i) = \begin{cases} 0 & \text{for} \quad u_i \geqslant u_u \\ \alpha & \text{for} \quad u_l \leqslant u_i \leqslant u_u \\ 0 & \text{for} \quad u_i \leqslant u_l \end{cases}$$
$$b(u_i) = \begin{cases} \alpha u_u & \text{for} \quad u_i \geqslant u_u \\ 0 & \text{for} \quad u_l \leqslant u_i \leqslant u_u \\ \alpha u_l & \text{for} \quad u_i \leqslant u_l \end{cases} \tag{2.4}$$

Incorporating description (2.3) into (2.1), yields

$$\begin{aligned} &\dot{\mathbf{X}}_1 = \mathbf{X}_2 \\ &\dot{\mathbf{X}}_2 = \mathbf{X}_3 \\ &\vdots \\ &\dot{\mathbf{X}}_{n-1} = \mathbf{X}_n \\ &\dot{\mathbf{X}}_n = \mathbf{F} + \mathbf{G}\mathbf{b}(\mathbf{u}) + \mathbf{G}\mathbf{a}(\mathbf{u})\mathbf{u} + \mathbf{d}(t) = \mathbf{F} + \mathbf{G}\mathbf{b}(\mathbf{u}) + \widehat{\mathbf{G}}_u\mathbf{u} + \mathbf{d}(t) \\ &\mathbf{Y} = \mathbf{X}_1 \end{aligned} \tag{2.5}$$

Remark 1. The only information about the system model is that the invertible matrix $\widehat{\mathbf{G}}_u(\cdot)$, as an estimate of $\mathbf{G_u}(\cdot) = \mathbf{G}(\cdot)a(u)$, is available, see Mclain *et al.* (1999).

The control objective is to design the control input u such that $\mathbf{Y}$ tracks the smooth reference trajectory $\mathbf{Y}_d$. Define the tracking error vector $\mathbf{E} = [e_1, \ldots, e_m]^{\mathrm{T}}$ as

$$\mathbf{E} = \mathbf{X}_1 - \mathbf{Y}_d = \mathbf{Y} - \mathbf{Y}_d \tag{2.6}$$

A PID control structure is adapted here as

$$u_i = k_{Pi}e_i + k_{Ii}\int_0^t e_i(\tau)d\tau + k_{Di}\frac{de_i}{dt} \qquad i = 1, 2, \ldots, m \tag{2.7}$$

where e_i is the i-th component of the error vector $\mathbf{E}$, and k_{Pi}, k_{Ii} and k_{Di} denote respectively the proportional, integral and derivative coefficients.

3. Adaptive fuzzy controller design

3.1. Fuzzy estimation

In this Section, the l-th fuzzy rule of the fuzzy controller for estimating the unknown function $H(x)$ is formed by (Shaocheng *et al.*, 2000)

$$R^l: \quad \text{if} \quad x_1 = A_1^l \quad \wedge \quad x_2 = A_2^l \quad \rightarrow \quad H(x) = \theta_l \tag{3.1}$$

where $\mathbf{x} = [x_1, x_2]^{\mathrm{T}}$ denotes the input vector, A_i^l is the membership function of each input. The fuzzy model for describing $H(\mathbf{x})$ is Mamdani, and the output of the fuzzy system can be obtained by

$$H(\mathbf{x}) = \frac{\sum\limits_{l=1}^{N}\theta_l\prod\limits_{i=1}^{2}\mu_{A_i^l}(x_i)}{\sum\limits_{l=1}^{N}\prod\limits_{i=1}^{2}\mu_{A_i^l}(x_i)} \tag{3.2}$$

where $u_{F_i^l}$ is the fuzzy membership function and N is the number of rules. Now, form the unknown function as

$$H(\mathbf{x}) = \mathbf{\Phi}(\mathbf{x})^{\mathrm{T}}\boldsymbol{\theta} \tag{3.3}$$

where

$$\begin{aligned} &\mathbf{\Phi}(\mathbf{x}) = [\phi_1(\mathbf{x}), \phi_2(\mathbf{x}), \ldots, \phi_N(\mathbf{x})]^{\mathrm{T}} \qquad \phi_l(\mathbf{x}) = \frac{\prod_{i=1}^{2} \mu_{A_i^l}(x_i)}{\sum_{l=1}^{N}\prod_{i=1}^{2} \mu_{A_i^l}(x_i)} \\ &\boldsymbol{\theta} = [\theta_1, \theta_2, \ldots, \theta_N]^{\mathrm{T}} \end{aligned} \tag{3.4}$$

3.2. Controller design

To facilitate the designing procedure, new state variables are defined here as

$$\begin{aligned} &\mathbf{Z}_1 = \int_0^t \mathbf{E}(\tau)\, d\tau \\ &\mathbf{Z_2} = \mathbf{E} \\ &\mathbf{Z}_3 = \frac{d\mathbf{E}}{dt} \\ &\vdots \\ &\mathbf{Z}_{n+1} = \frac{d^{n-1}\mathbf{E}}{dt^{n-1}} \end{aligned} \tag{3.5}$$

by which the dynamic equations (2.1) may be rewritten as

$$\begin{aligned} &\dot{\mathbf{Z}}_1 = \mathbf{Z}_2 \\ &\dot{\mathbf{Z}}_2 = \mathbf{Z}_3 \\ &\vdots \\ &\dot{\mathbf{Z}}_n = \mathbf{Z}_{n+1} \\ &\dot{\mathbf{Z}}_{n+1} = \mathbf{F}_t + \widehat{\mathbf{G}}_u\mathbf{u} \end{aligned} \tag{3.6}$$

where

$$\mathbf{F}_t = \mathbf{F} - \frac{d^n\mathbf{Y}_d}{dt^n} + \mathbf{G}\mathbf{b}(\mathbf{u}) + (\mathbf{G}_u - \widehat{\mathbf{G}}_u)\mathbf{u} + \mathbf{d}(t) \tag{3.7}$$

Hence, input signal (2.7) may be given by

$$\mathbf{u} = \mathbf{K}_I\mathbf{Z}_1 + \mathbf{K}_P\mathbf{Z}_2 + \mathbf{K}_D\mathbf{Z}_3 \tag{3.8}$$

where

$$\begin{aligned} &\mathbf{K}_P = \text{ diag } \begin{bmatrix} k_{P1} & k_{p2} & \cdots & k_{pm} \end{bmatrix} \\ &\mathbf{K}_I = \text{ diag } \begin{bmatrix} k_{I1} & k_{I2} & \cdots & k_{Im} \end{bmatrix} \\ &\mathbf{K}_D = \text{ diag } \begin{bmatrix} k_{D1} & k_{D2} & \cdots & k_{Dm} \end{bmatrix} \end{aligned} \tag{3.9}$$

Now, define an ideal control signal $\mathbf{u}^*$ as

$$\mathbf{u}^* = \mathbf{\Phi}_T^{\mathrm{T}}\mathbf{\Theta}^* = \widehat{\mathbf{G}}_u^{-1}(-\mathbf{F}_t - \mathbf{K}_1\mathbf{Z}_1 - \mathbf{K}_2\mathbf{Z}_2 - \ldots - \mathbf{K}_{n+1}\mathbf{Z}_{n+1}) \tag{3.10}$$

where $\mathbf{u}^*$ is obtained from the feedback linearization of system (3.6).

Remark 2. $\mathbf{K}_i, \quad i = 1, \ldots, n+1$, is chosen such that

$$\mathbf{A}_{cl} = \begin{bmatrix} 0 & I_m & 0 & \cdots & 0 \\ 0 & 0 & I_m & \ddots & \vdots \\ \vdots & \vdots & \ddots & \ddots & 0 \\ 0 & 0 & \cdots & 0 & I_m \\ -K_1 & -K_2 & \cdots & -K_n & -K_{n+1} \end{bmatrix} \tag{3.11}$$

is negative semi-definite.

The input signal u^* is not implementable, as $\mathbf{F}_t$ is unknown. Instead, an approximation of the ideal signal u^* is generated as

$$\widehat{\mathbf{u}} = \mathbf{\Phi}_T^{\mathrm{T}} \widehat{\mathbf{\Theta}} \tag{3.12}$$

where $\widehat{\mathbf{\Theta}}$ is an approximation of $\mathbf{\Theta}^*$.

Then, replacing (3.12) in (3.6), yields

$$\dot{\mathbf{Z}}_{n+1} = \mathbf{F}_t + \widehat{\mathbf{G}}_u \mathbf{\Phi}_T^{\mathrm{T}} \widehat{\mathbf{\Theta}} \tag{3.13}$$

By adding and subtracting $\widehat{\mathbf{G}}_u \mathbf{\Phi}_T^{\mathrm{T}} \mathbf{\Theta}^*$ in (3.13), one can write

$$\dot{\mathbf{Z}}_{n+1} = \mathbf{F}_t + \widehat{\mathbf{G}}_u \mathbf{\Phi}_T^{\mathrm{T}} \widehat{\mathbf{\Theta}} - \widehat{\mathbf{G}}_u \mathbf{\Phi}_T^{\mathrm{T}} \mathbf{\Theta}^* + \widehat{\mathbf{G}}_u \mathbf{\Phi}_T^{\mathrm{T}} \mathbf{\Theta}^* = \mathbf{F}_t + \widehat{\mathbf{G}}_u \mathbf{\Phi}_T^{\mathrm{T}} \widetilde{\mathbf{\Theta}} + \widehat{\mathbf{G}}_u \mathbf{\Phi}_T^{\mathrm{T}} \mathbf{\Theta}^* \tag{3.14}$$

where

$$\widetilde{\mathbf{\Theta}} = \widehat{\mathbf{\Theta}} - \mathbf{\Theta}^* \tag{3.15}$$

denotes the parameter estimation error. By substituting (3.10) into (3.14), one obtains

$$\dot{\mathbf{Z}}_{n+1} = -\mathbf{K}_1 \mathbf{Z}_1 - \mathbf{K}_2 \mathbf{Z}_2 - \ldots - \mathbf{K}_{n+1} \mathbf{Z}_{n+1} + \widehat{\mathbf{G}}_u \mathbf{\Phi}_T^{\mathrm{T}} \widetilde{\mathbf{\Theta}} \tag{3.16}$$

and

$$\dot{\mathbf{Z}} = \mathbf{A}_{cl} \mathbf{Z} + \mathbf{B}_{cl} \mathbf{\Phi}_T^{\mathrm{T}} \widetilde{\mathbf{\Theta}} \tag{3.17}$$

where

$$\mathbf{Z} = [\mathbf{Z}_1, \mathbf{Z}_2, \cdots, \mathbf{Z}_{n+1}]^{\mathrm{T}} \qquad \mathbf{B}_{cl} = [\mathbf{0}, \mathbf{0}, \ldots, \widehat{\mathbf{G}}_u]^{\mathrm{T}} \tag{3.18}$$

Remark 3. $\mathbf{A}_{cl}$ in (3.11) is a negative semi-definite matrix, so the positive definite symmetric matrix $\mathbf{P}$ can be found that satisfy the algebraic Lyapunov equation

$$\mathbf{A}_{cl}^{\mathrm{T}} \mathbf{P} + \mathbf{P} \mathbf{A}_{cl} = -\mathbf{Q} \tag{3.19}$$

for any positive definite symmetric matrix $\mathbf{Q}$.

Theorem. Consider constrained nonlinear system (3.6). By applying the control input $\mathbf{u} = \mathbf{\Phi}_T^{\mathrm{T}} \mathbf{\Theta}$ and adaptive law $\dot{\widehat{\mathbf{\Theta}}} = -2\mathbf{\Gamma}^{\mathrm{T}} \mathbf{\Phi}_T \mathbf{B}_{cl}^{\mathrm{T}} \mathbf{P} \mathbf{Z}$, the closed loop stability and tracking performance are guaranteed.

More precisely

$$\mathbf{u}=\begin{bmatrix}u_1\\u_2\\\vdots\\u_m\end{bmatrix}=\begin{bmatrix}\boldsymbol{\Phi}_{T1}^{\mathrm{T}}\boldsymbol{\Theta}_1\\\boldsymbol{\Phi}_{T2}^{\mathrm{T}}\boldsymbol{\Theta}_2\\\vdots\\\boldsymbol{\Phi}_{Tm}^{\mathrm{T}}\boldsymbol{\Theta}_m\end{bmatrix}=\begin{bmatrix}\boldsymbol{\Phi}_{T1}^{\mathrm{T}}&\mathbf{0}&\mathbf{0}&\mathbf{0}\\\mathbf{0}&\boldsymbol{\Phi}_{T2}^{\mathrm{T}}&\mathbf{0}&\mathbf{0}\\\mathbf{0}&\ddots&\ddots&\mathbf{0}\\\mathbf{0}&\mathbf{0}&\mathbf{0}&\boldsymbol{\Phi}_{Tm}^{\mathrm{T}}\end{bmatrix}\begin{bmatrix}\boldsymbol{\Theta}_1\\\boldsymbol{\Theta}_2\\\vdots\\\boldsymbol{\Theta}_m\end{bmatrix}=\boldsymbol{\Phi}_T^{\mathrm{T}}\boldsymbol{\Theta}\tag{3.20}$$

and

$$u_i=\Phi_i^{\mathrm{T}}\theta_{pi}Z_{2i}+\Phi_i^{\mathrm{T}}\theta_{Ii}Z_{1i}+\Phi_i^{\mathrm{T}}\theta_{Di}Z_{3i}=\boldsymbol{\Phi_{\mathbf{T}i}}^{\mathrm{T}}\boldsymbol{\Theta}_i\tag{3.21}$$

in which

$$\boldsymbol{\Phi}_{Ti}=[\Phi_iZ_{1i},\Phi_iZ_{2i},\Phi_iZ_{3i}]^{\mathrm{T}}\qquad\boldsymbol{\Theta}_i=[\theta_{Ii},\theta_{pi},\theta_{Di}]\tag{3.22}$$

and

$$\begin{aligned}&k_{pi}=g_{pi}\Big(e_i,\frac{de_i}{dt}\Big)=\Phi_i^{\mathrm{T}}\theta_{pi}\qquad k_{Ii}=g_{Ii}\Big(e_i,\frac{de_i}{dt}\Big)=\Phi_i^{\mathrm{T}}\theta_{Ii}\\&k_{Di}=g_{Di}\Big(e_i,\frac{de_i}{dt}\Big)=\Phi_i^{\mathrm{T}}\theta_{Di}\end{aligned}\tag{3.23}$$

Remark 4. The nonlinear functions $g_{pi}(\cdot)$, $g_{Ii}(\cdot)$ and $g_{Di}(\cdot)$ may be obtained by a formulation as $H(\mathbf{x})$ in (3.2).

Proof. Choose the Lyapunov function candidate

$$V(\mathbf{Z},\widetilde{\boldsymbol{\Theta}})=\mathbf{Z}^{\mathrm{T}}\mathbf{P}\mathbf{Z}+\frac{1}{2}\widetilde{\boldsymbol{\Theta}}^{\mathrm{T}}\boldsymbol{\Gamma}^{-1}\widetilde{\boldsymbol{\Theta}}\qquad\boldsymbol{\Gamma}>0\tag{3.24}$$

with $\mathbf{P}>0$ and $\boldsymbol{\Gamma}>0$. The time derivative of V is given by

$$\dot{V}(\mathbf{Z},\widetilde{\boldsymbol{\Theta}})=\dot{\mathbf{Z}}^{\mathrm{T}}\mathbf{P}\mathbf{Z}+\mathbf{Z}^{\mathrm{T}}\mathbf{P}\dot{\mathbf{Z}}+\frac{1}{2}\dot{\widetilde{\boldsymbol{\Theta}}}^{\mathrm{T}}\boldsymbol{\Gamma}^{-1}\widetilde{\boldsymbol{\Theta}}+\frac{1}{2}\widetilde{\boldsymbol{\Theta}}^{\mathrm{T}}\boldsymbol{\Gamma}^{-1}\dot{\widetilde{\boldsymbol{\Theta}}}\tag{3.25}$$

By replacing (3.17) into (3.25) and some manipulations, one can obtain

$$\begin{aligned}\dot{V}(\mathbf{Z},\widetilde{\boldsymbol{\Theta}})&=\mathbf{Z}^{\mathrm{T}}(\mathbf{A}_{cl}^{\mathrm{T}}\mathbf{P}+\mathbf{P}\mathbf{A}_{cl})\mathbf{Z}+2\mathbf{Z}^{\mathrm{T}}\mathbf{P}\mathbf{B}_{cl}\boldsymbol{\Phi}_T^{\mathrm{T}}\widetilde{\boldsymbol{\Theta}}+\dot{\widetilde{\boldsymbol{\Theta}}}^{\mathrm{T}}\boldsymbol{\Gamma}^{-1}\widetilde{\boldsymbol{\Theta}}\\&=-\mathbf{Z}^{\mathrm{T}}\mathbf{Q}\mathbf{Z}+(2\mathbf{Z}^{\mathrm{T}}\mathbf{P}\mathbf{B}_{cl}\boldsymbol{\Phi}_T^{\mathrm{T}}+\dot{\widetilde{\boldsymbol{\Theta}}}^{\mathrm{T}}\boldsymbol{\Gamma}^{-1})\widetilde{\boldsymbol{\Theta}}\end{aligned}\tag{3.26}$$

Then, by adopting the adaptation law

$$\dot{\widetilde{\boldsymbol{\Theta}}}=-2\boldsymbol{\Gamma}^{\mathrm{T}}\boldsymbol{\Phi}_T\mathbf{B}_{cl}^{\mathrm{T}}\mathbf{P}\mathbf{Z}\tag{3.27}$$

one can conclude

$$\dot{V}(\mathbf{Z},\widetilde{\boldsymbol{\Theta}})=-\mathbf{Z}^{\mathrm{T}}\mathbf{Q}\mathbf{Z}<0\tag{3.28}$$

Thus, Barbalat's Lemma (Sastry and Shankar, 1999; Åström and Wittenmark, 2013) ensures that the vector $\mathbf{Z}$ is asymptotically converged to zero.

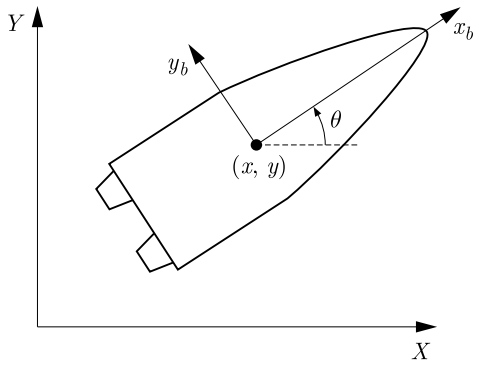

Fig. 2. Surface vessel in the inertial fixed and body fixed frames

4. Simulation

In this Section, the performance of the controller is evaluated in two situations, and the proposed method is applied to a surface vessel schematically shown in Fig. 2.

Such a three-input three-output system may be described by (Fang *et al.*, 2004)

$$\begin{aligned} &m_{11}\dot{v}_x + d_{11}v_x = \tau_1 \\ &m_{22}\dot{v}_y + m_{23}\dot{w} + d_{22}v_v + d_{23}w = \tau_2 \\ &m_{33}\dot{w} + m_{23}\dot{v}_y + d_{23}v_y + d_{33}w = \tau_3 \end{aligned} \tag{4.1}$$

in which (x, y) and θ are respectively the surface vessel position and yaw angle in the inertial coordinate system and (v_x, v_y), and w denote respectively the surface vessel speed and rotational speed in the body coordinate system.

Dynamical equations (4.1) with using a set of simple mathematical operations can be rewritten in the form

$$\mathbf{M}(\mathbf{q})\dot{\mathbf{q}} + \mathbf{C}(\mathbf{q}, \dot{\mathbf{q}})\dot{\mathbf{q}} + \mathbf{G}(\mathbf{q}, \dot{\mathbf{q}}) = \tau^* \tag{4.2}$$

where

$$\begin{aligned} &\mathbf{q} = [x, y, \theta]^{\mathrm{T}} \\ &\mathbf{M}(\mathbf{q}) = \begin{bmatrix} m_{11}\cos^2\theta + m_{22}\sin^2\theta & -m_d\cos\theta\sin\theta & -m_{23}\sin\theta \\ -m_d\cos\theta\sin\theta & m_{22}\cos^2\theta + m_{11}\sin^2\theta & m_{23}\cos\theta \\ -m_{23}\sin\theta & m_{23}\cos\theta & m_{33} \end{bmatrix} \\ &\mathbf{C}(\mathbf{q}, \dot{\mathbf{q}}) = \begin{bmatrix} \dot{\theta}(m_d\cos\theta\sin\theta) & \dot{\theta}(m_{11}\cos^2\theta + m_{22}\sin^2\theta) & 0 \\ -\dot{\theta}(m_{22}\cos^2\theta + m_{11}\sin^2\theta) & -\dot{\theta}(m_d\cos\theta\sin\theta) & 0 \\ -\dot{\theta}(m_{23}\cos\theta) & -\dot{\theta}(m_{23}\sin\theta) & 0 \end{bmatrix} \\ &\mathbf{G}(\mathbf{q}, \dot{\mathbf{q}}) = \mathbf{K}(\mathbf{q})\dot{\mathbf{q}} \\ &\mathbf{K}(\mathbf{q}) = \begin{bmatrix} d_{11}\cos^2\theta + d_{22}\sin^2\theta & -d_d\cos\theta\sin\theta & -d_{23}\sin\theta \\ -d_d\cos\theta\sin\theta & d_{22}\cos^2\theta + d_{11}\sin^2\theta & d_{23}\cos\theta \\ -d_{23}\sin\theta & d_{23}\cos\theta & d_{33} \end{bmatrix} \end{aligned} \tag{4.3}$$

and

$$\boldsymbol{\tau}^* = [\tau_1, \tau_2, \tau_3] \tag{4.4}$$

To facilitate the designing procedure, choose the state variables as

$$\mathbf{X}_1 = \mathbf{q} \qquad \mathbf{X}_2 = \dot{\mathbf{q}} \qquad \mathbf{X}_1, \mathbf{X}_2 \in \mathbb{R}^3 \tag{4.5}$$

The state space representation may be as

$$\dot{\mathbf{X}}_1 = \mathbf{X}_2 \qquad \dot{\mathbf{X}}_2 = \mathbf{F}(\mathbf{X}_1, \mathbf{X}_2) + \mathbf{G}_u(\mathbf{X}_1, \mathbf{X}_2)\mathbf{u} \tag{4.6}$$

where

$$\mathbf{F}(\mathbf{X}_1, \mathbf{X}_2) = -\mathbf{M}^{-1}(\mathbf{X}_1)[\mathbf{C}(\mathbf{X}_1, \mathbf{X}_2)\mathbf{X}_2 + \mathbf{G}(\mathbf{X}_1, \mathbf{X}_2)] \qquad \mathbf{G}_u(\mathbf{X}_1, \mathbf{X}_2) = \mathbf{M}^{-1}(\mathbf{X}_1) \tag{4.7}$$

and

$$\mathbf{u} = \boldsymbol{\tau}^* \qquad \mathbf{u} \in \mathbb{R}^3 \tag{4.8}$$

The numerical values of the model parameters in equation (4.1) are given in Table 1, as given by Fang *et al.* (2004).

Table 1. Model parameter values for the surface vessel

Parameter	Value	Parameter	Value	Parameter	Value
m_{11} [kg]	1.0852	m_{33} [kg]	0.2153	d_{11} [kg/s]	0.08656
m_{22} [kg]	2.0575	d_{11} [kg]	0.08656	d_{22} [kg/s]	0.0762
d_{33} [kg/s]	0.0031	d_{23} [kg/s]	0.151	d_{32} [kg/s]	0.0151

The initial values and eigenvalues of the matrix $\mathbf{A}_{cl} \in \mathbb{R}^{9\times 9}$ are selected as

$$\begin{aligned} &\mathbf{X}_{10} = [1, -1, 0.3]^{\mathrm{T}} \qquad \mathbf{X}_{20} = [0, 0, 0]^{\mathrm{T}} \\ &\boldsymbol{\lambda} = [-1, -1, -1, -1, -1, -1, -1, -1, -1] \end{aligned} \tag{4.9}$$

The matrix $\boldsymbol{\Gamma}$, constant scalars γ_i, $i = 1, 2, 3$ and membership functions are chosen here as

$$\boldsymbol{\Gamma} = \begin{bmatrix} \gamma_1 I_L & 0 & 0 \\ 0 & \gamma_2 I_L & 0 \\ 0 & 0 & \gamma_3 I_L \end{bmatrix} \qquad \gamma_1 = \gamma_2 = 10 \qquad \gamma_3 = 10^3 \tag{4.10}$$

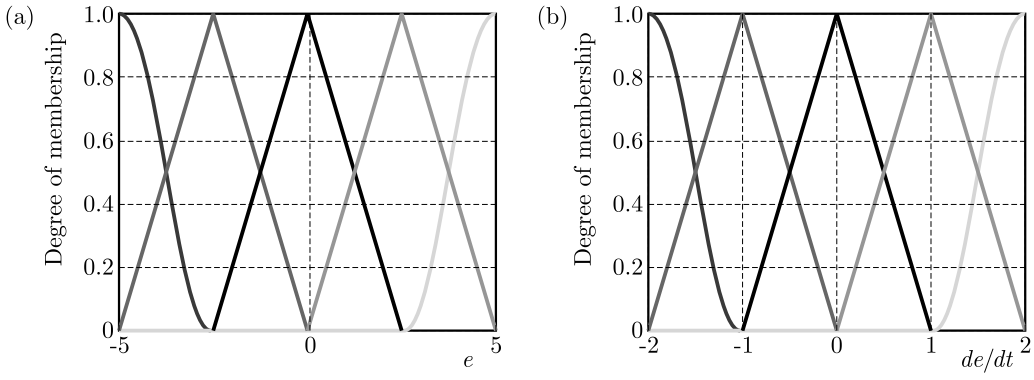

Fig. 3. (a) Membership function of the tracking error, (b) membership function of the derivative of the tracking error

Case *I.* The tracking performance of the proposed constrained control scheme is evaluated here and compared with that of the existing sliding mode method, see Zeinali and Leila (2010). Assume the reference position and the saturation limits are respectively given by $[x_d(t), y_d(t), \theta_d(t)]^{\mathrm{T}} = [3.5\,\mathrm{m}, 2\,\mathrm{m}, 0\,\mathrm{rad}]^{\mathrm{T}}$ and $-2 < \tau_i < 2$, $i = 1, 2, 3$. The external disturbance $\mathbf{d}(t) = (\sin(t) + 1)[1, 1, 1]^{\mathrm{T}}$ also perturb the system at time $t = 5\,\mathrm{s}$.

Figures 4a and 4b show that the tracking of the reference positions for x and y is obtained in the presence of disturbance. Figure 5 shows the capability of the proposed scheme in disturbance rejection compared with the sliding mode control by Zeinali and Notash (2010). The convergence of the controller coefficients K_p, K_D, K_I for tracking $x_d(t)$, $y_d(t)$ and $\theta_d(t)$ are demonstrated in Figs. 6 and 7. The control efforts in the proposed adaptive fuzzy method and the existing sliding controller are illustrated in Fig. 8.

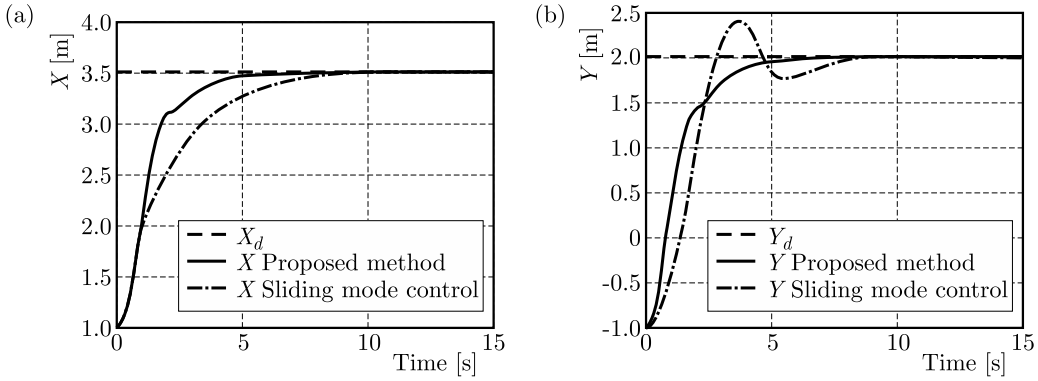

Fig. 4. (a) X direction and (b) Y direction tracking of the surface vessel

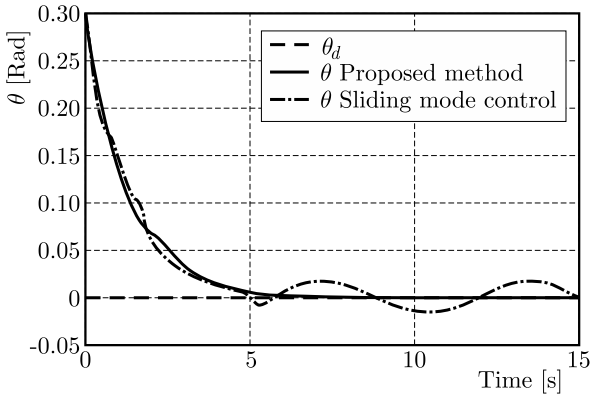

Fig. 5. Tracking of the pitch θ of the surface vessel

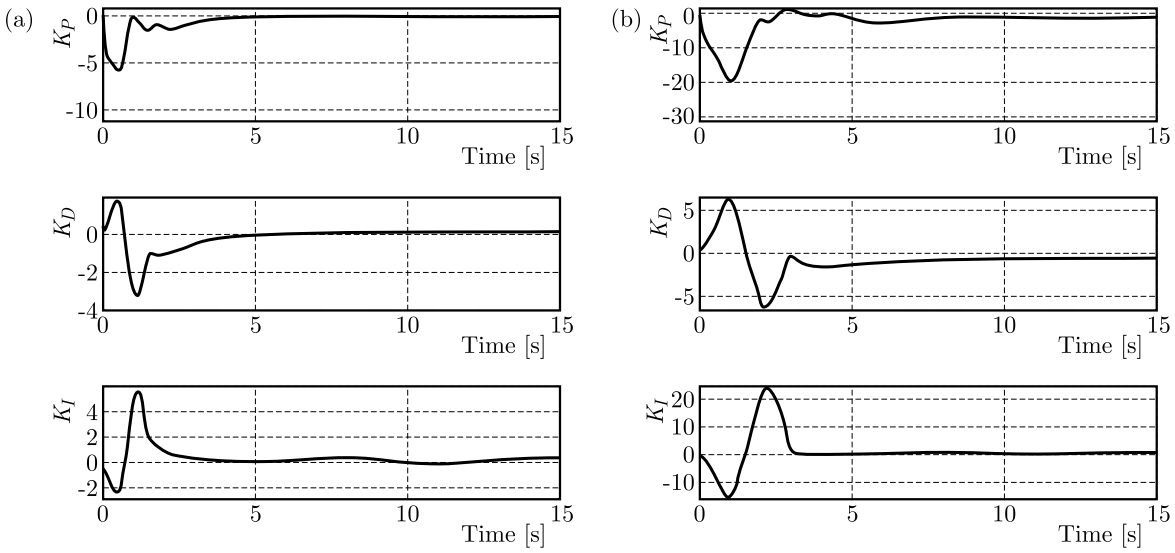

Fig. 6. Convergence of the controller parameters in (a) the x direction, (b) the y direction

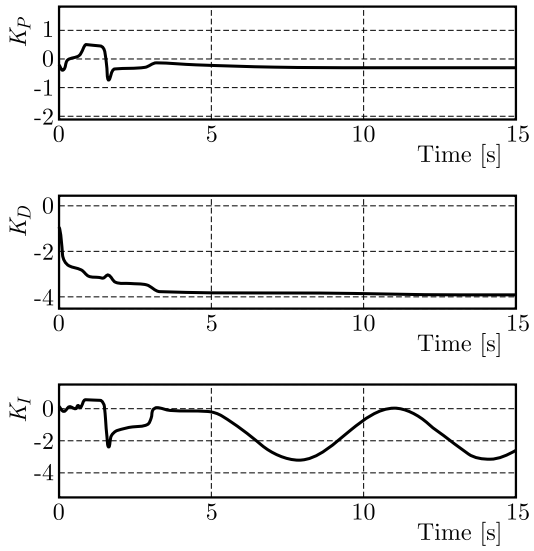

Fig. 7. Convergence of K_p, K_D, K_I for the yaw controller

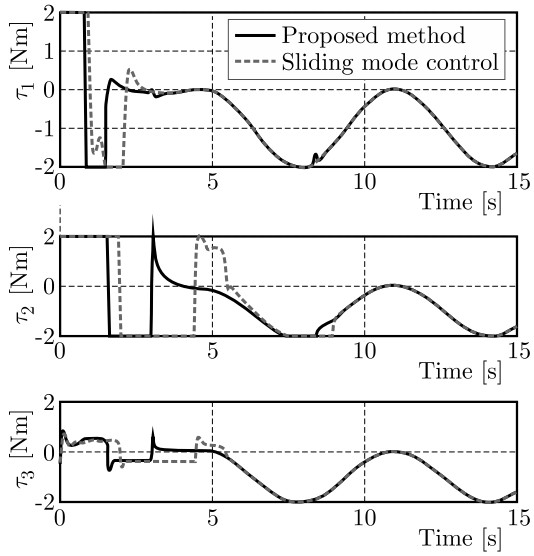

Fig. 8. Control signals in the proposed algorithm and the sliding control

To make a comparison between the designed adaptive fuzzy controller and the existing sliding control (Zeinali and Leila 2010), consider a cost function as

$$J = \int_0^{t_f} (\|e(t)\|^2 + \|u(t)\|^2)\, dt \tag{4.11}$$

The lower cost of the proposed controller, as reported in Table 2, shows the advantage of the proposed approach.

Table 2. The costs of controllers in Case I

Controller	Sliding mode	Proposed method
J	117.1378	61.3327

Case *II*. In this case, the reference signal and the saturation operator parameters are considered respectively as

$$\begin{bmatrix} x_d(t) \\ y_d(t) \\ \theta_d(t) \end{bmatrix} = \begin{bmatrix} \sin(0.5t) \\ \cos(0.5t) \\ 0 \end{bmatrix} \qquad \text{and} \qquad -2 < \tau_i < 2 \qquad i = 1, 2, 3$$

The simulation results, illustrated in Figs. 9 and 10, show that the proposed method gives smoother responses with less tracking error, compared with the sliding mode control (Zeinali and Leila, 2010). In the tracking of the reference output on the channel y, the sliding mode algorithm is unstable, while the proposed method is stable and the tracking error is converged to zero. Figure 11 shows that the control effort of the proposed method is much lower than that in the other method. Unlike the sliding mode, the control signal is zero in the steady state for the proposed method. Comparing the results may be also possible by adopting cost function (4.11), as numerically reported in Table 3.

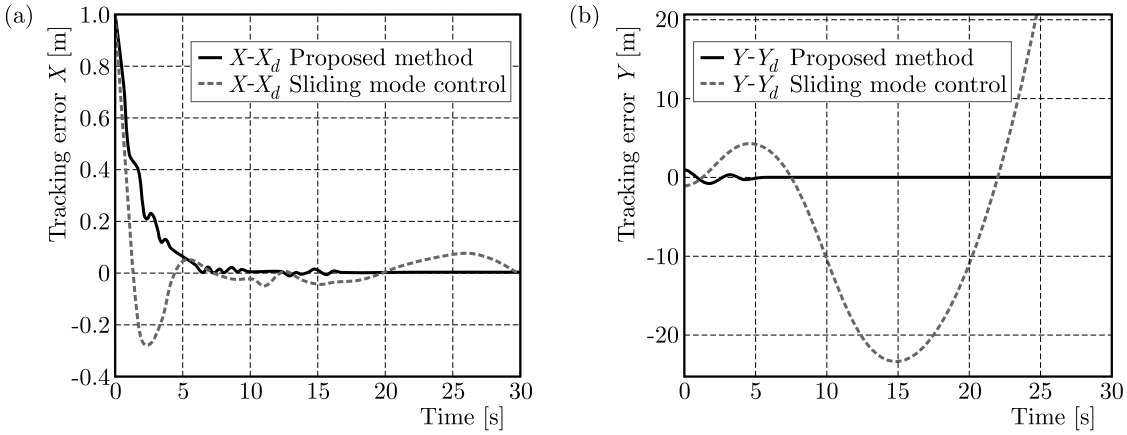

Fig. 9. Tracking error of the (a) the x direction, (b) the y direction

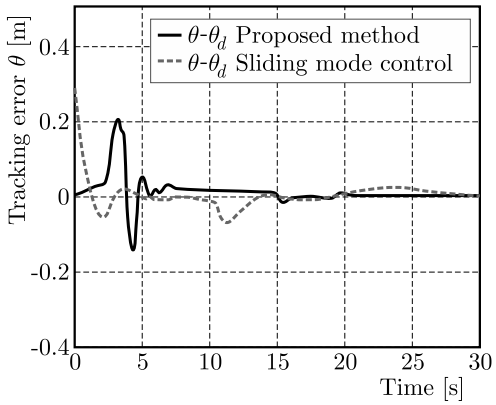

Fig. 10. Tracking error of pitch θ

Table 3. The cost of controllers in Case *II*

Proposed method	Sliding mode	Controller
J	16933.4	77.8

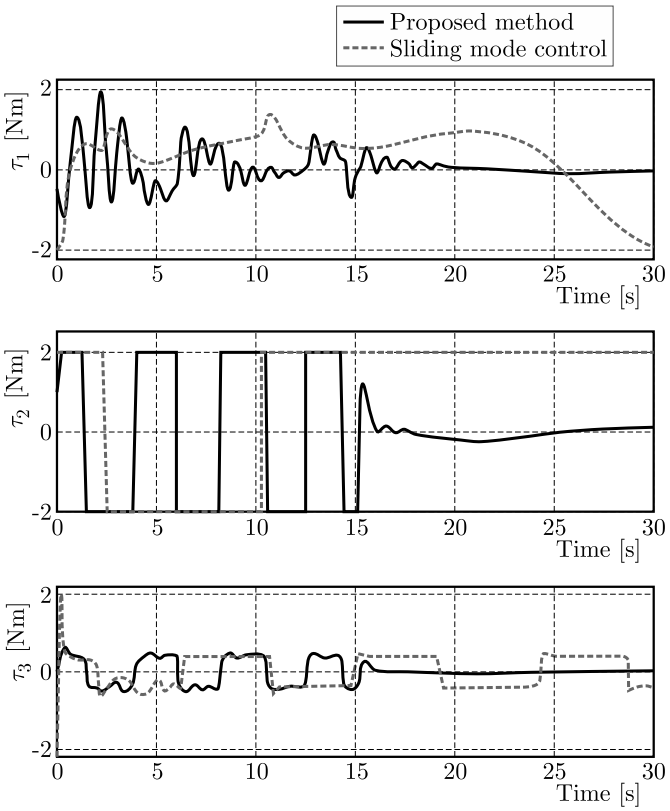

Fig. 11. Control signals

5. Conclusion

Focusing on the constraints on the inputs of nonlinear systems, the problem of robust tracking is investigated here. To solve the problem, an adaptive fuzzy algorithm is proposed for which the robust stability is proved using the Lyapunov stability theorem. As a practical situation, the problem is formulated for a surface vessel, taking the limitations on the control input into account. The designed controller is applied and the simulation results are presented to show the benefits of the method. The existing sliding control is also applied to the vessel and a cost function is defined to compare the results with the proposed scheme. In addition to demonstrations, a cost function is defined, and a numerical comparison is also made to show the benefits of the adaptive fuzzy algorithm.

References

1. Åström K.J., Wittenmark B., 2013, *Adaptive control*, Courier Corporation

2. Chen M., Ge S.S., How B.V.E., 2010, Robust adaptive neural network control for a class of uncertain MIMO nonlinear systems with input nonlinearities, *Neural Networks, IEEE Transactions*, **21**, 5, 796-812

3. Chen M., Zhou Y., Guo W.W., 2014 Robust tracking control for uncertain MIMO nonlinear systems with input saturation using RWNNDO, *Neurocomputing*, **144**, 436-447

4. Dai S.L., Wang M., Wang C., 2015, Neural learning control of marine surface vessels with guaranteed transient tracking performance, *IEEE Transactions on Industrial Electronics*, DOI 10.1109/TIE.2015.2504553

5. Daly J.M., Tribou M.J., Waslander S.L., 2012, A nonlinear path following controller for an underactuated unmanned surface vessel, *IEEE/RSJ International Conference of Intelligent Robots and Systems (IROS)*, 82-87

6. Fang Y., Zergeroglu E., de Queiroz M.S., Dawson D.M., 2004, Global output feedback control of dynamically positioned surface vessels: an adaptive control approach, *Mechatronics*, **14**, 4, 341-356

7. Koofigar H.R., Amelian S., 2013, Robust adaptive vibration control for a general class of structures in the presence of time-varying uncertainties and disturbances, *Journal of Theoretical and Applied Mechanics*, **51**, 3, 533-541

8. Lee H., 2011, Robust adaptive fuzzy control by backstepping for a class of MIMO nonlinear systems, *Fuzzy Systems, IEEE Transactions*, **19**, 2, 265-275

9. Li G., Li W., Hildre H.P., Zhang H., 2015, Online learning control of surface vessels for fine trajectory tracking, *Journal of Marine Science and Technology*, in press, DOI 10.1007/s00773--015-0347-9

10. Li Y., Li T., Jing X., 2014, Indirect adaptive fuzzy control for input and output constrained nonlinear systems using a barrier Lyapunov function, *International Journal of Adaptive Control and Signal Processing*, **28**, 2, 184-199

11. Li Y., Tong S., Li T., 2013, Direct adaptive fuzzy backstepping control of uncertain nonlinear systems in the presence of input saturation, *Neural Computing and Applications*, **23**, 5, 1207-1216

12. Lu L., Yao B., 2014, Online constrained optimization based adaptive robust control of a class of MIMO nonlinear systems with matched uncertainties and input/state constraints, *Automatica*, **50**, 3, 864-873

13. Mclain R.B., Henson M.A., Pottmann M., 1999, Direct adaptive control of partially known nonlinear systems, *IEEE Transactions on Neural Networks*, **10**, 3, 714-721

14. Montaseri G., Yazdanpanah M.J., 2012 Adaptive control of uncertain nonlinear systems using mixed backstepping and Lyapunov redesign techniques, *Communications in Nonlinear Science and Numerical Simulation*, **17**, 8, 3367-3380

15. Muñoz D.A., Marquardt W., 2013, Robust control design of a class of nonlinear input-and state-constrained systems, *Annual Reviews in Control*, **37**, 2, 232-245

16. Petersen I.R., Tempo R., 2014, Robust control of uncertain systems: classical results and recent developments, *Automatica*, **50**, 5, 1315-1335

17. Sastry S., 1999, *Nonlinear Systems: Analysis, Stability, and Control*, **10**, New York: Springer

18. Shaocheng T., Jiantao T., Tao W., 2000, Fuzzy adaptive control of multivariable nonlinear systems, *Fuzzy Sets and Systems*, **111**, 2, 153-167

19. Wang D., Liu D., Li H., Ma H., 2014, Neural-network-based robust optimal control design for a class of uncertain nonlinear systems via adaptive dynamic programming, *Information Sciences*, **282**, 167-179

20. Wang H.Q., Chen B., Lin C., 2013a, Adaptive neural tracking control for a class of stochastic nonlinear systems with unknown dead-zone, *International Journal of Innovative Computing, Information and Control*, **9**, 8, 3257-3269

21. Wang H., Chen B., Liu X., Liu K., Lin C., 2013b, Robust adaptive fuzzy tracking control for pure-feedback stochastic nonlinear systems with input constraints, *Cybernetics, IEEE Transactions*, **43**, 6, 2093-2104

22. Wuxi S., Hongquan W., Furong L., Xiangyu W., 2013, Adaptive fuzzy control for a class of nonlinear systems with input constraint and unknown control direction, *Control and Decision Conference (CCDC), 2013 25th Chinese. IEEE*

23. Xu D., Huang J., 2010, Robust adaptive control of a class of nonlinear systems and its applications, *Circuits and Systems I: Regular Papers, IEEE Transactions*, **57**, 3, 691-702

24. Zeinali M., Notash L., 2010, Adaptive sliding mode control with uncertainty estimator for robot manipulators, *Mechanism and Machine Theory*, **45**, 1, 80-90

Manuscript received June 5, 2015; accepted for print January 13, 2016

JOURNAL OF THEORETICAL AND APPLIED MECHANICS
54, 3, pp. 1001-1012, Warsaw 2016
DOI: 10.15632/jtam-pl.54.3.1001

RESEARCH ON THE DISTURBANCE GENERATED BY A SOLAR ARRAY DRIVE ASSEMBLY DRIVING A FLEXIBLE SYSTEM

Jiangpan Chen, Wei Cheng

School of Aeronautic Science and Engineering, Beijing University of Aeronautics and Astronautics, Beijing, China
e-mail: chenjiangpan@hotmail.com; cheng_wei@buaa.edu.cn

The present work is aimed at presenting the disturbance generated by a solar array drive assembly (SADA) driving a flexible system. Firstly, the vibration equation of SADA is obtained by simplifying and linearizing the electromagnetic torque. Secondly, the disturbance model of SADA driving a discrete flexible system is achieved based on the vibration equation established. Taking a two-dof flexible system as the study object, this disturbance model is simulated and analyzed. Lastly, a continuous flexible system, which is designed to simulate the solar array, is used to illustrate the simulation method of the disturbance emitted by SADA driving a continuous flexible system. All the achievements obtained from this project will provide a theoretical basis for the prediction of the disturbance emitted by the SADA driving solar array on the orbit.

Keywords: solar array drive assembly, disturbance, flexible system, electromagnetic torque, vibration equation

1. Introduction

Micro-vibrations of a satellite, which are characterized by a low amplitude and a wide frequency band, can significantly degrade its pointing accuracy and imaging quality. There are many possible disturbance sources, such as reaction/momentum wheel assembly, control moment gyroscope and SADA (Luo *et al.*, 2013). Due to a longer exposure time than in a low orbit remote sensing satellite, the performance of a high orbit remote sensing satellite is more sensitive to micro-vibrations in the low frequency band. Three reasons make the disturbance emitted by the SADA driving solar array on the orbit extremely complex and mainly in the low frequency band, which are: (1) distribution of the natural frequency of the solar array in the low frequency band is dense (Cui, 2006); (2) exciting energy of SADA in the low frequency band is large, which makes the natural vibration of the solar array easily excited out; (3) vibration attenuation of the solar array in the low frequency band is slow without air damping in space. Therefore, to study the disturbance produced by the SADA driving solar array is imperative. Because of the gravity, the solar array, which has characteristics of low stiffness, large mass and large size (Chen, 2010), is difficult to unfold on the Earth. Testing of the disturbance generated by the SADA driving solar array in the atmospheric environment is hard to carry out. A disturbance model used to predict the disturbance emitted by the SADA driving solar array on the orbit is necessary.

From researches carried out thus far, lots of studies have focused on the disturbance properties of SADA. The mechanism of electromagnetic vibration of SADA was studied by Xia (1994), and the methods to lower the amplitude of the electromagnetic vibration were also proposed, such as using damping (including mechanical damping and electrical damping) and choosing a more appropriate drive circuit. The expression for electromagnetic vibration frequency of SADA was presented in Bodson *et al.* (2006). In Yang *et al.* (2010) and Zhu *et al.* (2015), argued that the electromagnetic field between the stator and rotor of SADA could be equivalent to an

electromagnetic spring-viscous damping system. Stiffness of the electromagnetic spring, named as electromagnetic stiffness, was obtained by experimental testing by Yang *et al.* (2010). Zhu *et al.* (2015) validated feasibility of the equivalent electromagnetic field to an electromagnetic spring-viscous damping system, and also investigated the coupling effect between the solar array and the electromagnetic spring-viscous damping system. Meanwhile, Si *et al.* (2010), Elsodany *et al.* (2011) and Szolc *et al.* (2012) proposed dynamic models of SADA. Among them, the dynamic model proposed by Si *et al.* (2010) was more complete, in which the friction torque and fluctuation torque of SADA were taken into account. The disturbance emitted by SADA driving a rigid system could be obtained by the dynamic models easily. Chen *et al.* (2014) modeled and simulated the disturbance produced by SADA driving a rigid system through a flexible transmission shaft based on the dynamic model of SADA. In this paper, the coupling effect between the electromagnetic stiffness and the flexible transmission shaft was studied by changing the stiffness of the transmission shaft.

However, the electromagnetic stiffness of the electromagnetic spring has not appeared in the dynamic models as an explicit expression up to now, and just has been hidden in the electromagnetic torque, which prevented the establishment of the coupling effect between the electromagnetic stiffness and the flexible system. As the solar array is an extremely complex typical continuous flexible system, the dynamic models existing do not have the ability to describe the disturbance caused by the SADA driving solar array on the orbit precisely and easily.

As a consequence, in this paper, the first part is to establish the vibration equation of SADA; the second part is to model, simulate and analyze the disturbance produced by SADA driving a discrete flexible system; the third part is to introduce the simulation method of the disturbance generated by SADA driving a continuous flexible system; the last part summarizes the paper and states conclusions drawn from this work.

2. Modeling of the vibration equation of SADA

The SADA discussed in this paper is a two-phase hybrid stepper motor. Stepper motors are motors which translate digital pulse sequences to precise movements of the rotor shaft, rather than rotating continuously as conventional motors do (Anish *et al.*, 2012). Because of the advantages of high resolution, high torque and low noise, the stepper motor is widely used in the field of spacecraft (Letchmanan *et al.*, 2005). Both solar array and digital antenna use stepper motors as the driver. The most frequently used dynamic model of SADA at present is given by

$$J_0\ddot{\theta} = T_e - C_0\dot{\theta} - T_l \tag{2.1}$$

where J_0 is the moment of inertia of the rotor, θ is the angular displacement of the rotor, T_e is the electromagnetic torque, C_0 is the viscous damping coefficient and T_l is the load torque.

As to a two-phase hybrid stepper motor, when the linear flux model without saturation effects is assumed, the driving model presented by Kapun *et al.* (2007) can be used in the form

$$\boldsymbol{\varphi} = \mathbf{LI} \qquad T_e = \frac{1}{2}\mathbf{I}^{\mathrm{T}}\frac{\partial\boldsymbol{\varphi}}{\partial\theta} = \frac{1}{2}\mathbf{I}^{\mathrm{T}}\frac{\partial\mathbf{L}}{\partial\theta}\mathbf{I} \tag{2.2}$$

where $\boldsymbol{\varphi}$ is the flux linkage vector, $\mathbf{L}$ is the symmetric inductance matrix and $\mathbf{I}$ is the current vector. The expressions of $\mathbf{I}$ and $\mathbf{L}$ are given by

$$\mathbf{I} = \begin{bmatrix} I_A \\ I_B \\ I_f \end{bmatrix} \qquad \mathbf{L} = \begin{bmatrix} L_{AA} & L_{AB} & L_{Af} \\ L_{BA} & L_{BB} & L_{Bf} \\ L_{fA} & L_{fB} & L_{ff} \end{bmatrix} \tag{2.3}$$

where I_A and I_B signifies the current of phase A and phase B respectively, I_f is the fictitious constant rotor current, L_{ii} $(i = A, B)$ is the self-inductance of the stator winding, $L_{AB} = L_{BA}$ is the mutual inductance between the stator windings, L_{ff} is the self-inductance of the fictitious rotor winding, $L_{if} = L_{fi}$ $(i = A, B)$ is the mutual inductance between the i-th stator winding and the fictitious rotor winding, see Yang *et al.* (2010) and Kapun *et al.* (2007).

Assuming that the mutual inductance between the stator windings is negligible and ignoring the second and more harmonics of the cyclical permeance function, the elements of the inductance matrix $\mathbf{L}$ can be defined as

$$\begin{aligned} &L_{AA} = L_{BB} = L_0 \qquad L_{AB} = L_{BA} = 0 \qquad L_{Af} = L_{fA} = L_{m0} + L_{m1}\cos(z\theta) \\ &L_{Bf} = L_{fB} = L_{m0} + L_{m1}\sin(z\theta) \qquad L_{ff} = L_{f0} + L_{f1}\cos(4z\theta) \end{aligned} \tag{2.4}$$

where z is the rotor teeth number. Substituting equations (2.3) and (2.4) into equation (2.2), the electromagnetic torque can be obtained as

$$T_e = T_m - T_d = K_m[I_B\cos(z\theta) - I_A\sin(z\theta)] - K_d\sin(4z\theta) \tag{2.5}$$

where T_m is the motor torque, T_d is the detent torque, $K_m = zI_fL_{m1}$ and $K_d = 2zI_f^2L_{f1}$ is the motor torque constant and detent torque constant, respectively (Letchmanan *et al.*, 2005).

In general, the detent torque constant K_d is so small that the detent torque T_d is far less than the motor torque T_m, and can be ignored (Yang *et al.*, 2010). Thus, equation (2.5) can be simplified as

$$T_e = K_m[I_B\cos(z\theta) - I_A\sin(z\theta)] \tag{2.6}$$

In order to improve the resolution and running smoothness of the stepper motor, a subdivision driver is frequently used. Yang *et al.* (2007) pointed out that the ladder sine curve current is frequently used as the subdivision driving current in the subdivision driver. Thus, the expression for the two-phase current I_A and I_B after subdivision can be shown as

$$I_A = I\cos(\gamma i) \qquad I_B = I\sin(\gamma i) \tag{2.7}$$

where I is the amplitude of the two-phase current, γ is the electrical step angle after subdivision and $i = 1, 2, \ldots$ is the step number. Substituting equation (2.7) into equation (2.6), the electromagnetic torque can be rewritten as

$$T_e = K_mI\sin(\gamma i - z\theta) = K_mI\sin\Big[z\Big(\frac{\gamma i}{z} - \theta\Big)\Big] = K_mI\sin(z\Delta\theta) \tag{2.8}$$

In equation (2.8), the physical meaning of $\Delta\theta$ is that: $\Delta\theta$ is the included angle between the actual position and theoretical equilibrium position of the rotor during the time period that after the input of the i-th digital pulse signal completed and before the input of $(i+1)$-th digital pulse signal, where $\gamma i/z$ and θ is the theoretical equilibrium position and actual position of the rotor in this time period, respectively. To ensure SADA running without losing step, the range of $\Delta\theta$ is given by

$$-\alpha \leqslant \Delta\theta \leqslant \alpha \tag{2.9}$$

where α is the micro-step angle after subdivision. The expression for α is given by

$$\alpha = \frac{2\pi}{zpn} \tag{2.10}$$

where p is the beat number and n is the subdivision number. The value of p and n of the SADA studied in this paper is 4 and 256, respectively, thus, we can obtain that

$$-\frac{\pi}{512} \leqslant z\Delta\theta \leqslant \frac{\pi}{512} \tag{2.11}$$

A significant result can be obtained from equation (2.11) that: $z\Delta\theta$ is so small that equation (2.8) can be linearized as

$$T_e = K_m I \sin(z\Delta\theta) = K_m I z\Delta\theta = K_m I\gamma i - K_m I z\theta \tag{2.12}$$

Substituting equation (2.12) into equation (2.1), the dynamic model of SADA can be rewritten as

$$J_0\ddot{\theta} + C_0\dot{\theta} + K_0\theta = K_m I\gamma i - T_l \tag{2.13}$$

where $K_0 = K_m I z$ and $K_m I\gamma i$ is called the electromagnetic stiffness and exciting torque, respectively.

From equation (2.13) we can get that: 1) the electromagnetic field between the stator and rotor of SADA can be equivalent to an electromagnetic spring-viscous damping system; 2) the rotor of SADA coupled with the load vibrates with viscous damping under the action of the exciting torque $K_m I\gamma i$. Thus, the equivalent system diagram of SADA can be shown as Fig. 1.

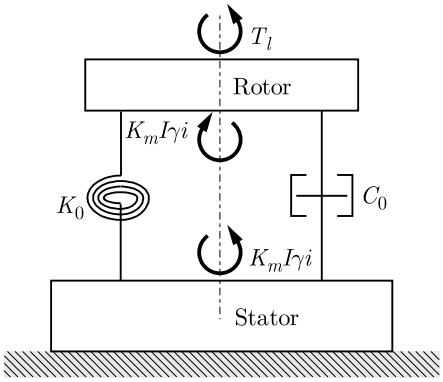

Fig. 1. Equivalent system of SADA

Assuming that the stator of SADA is a rigid body, the disturbance torque generated by SADA acting on the satellite can be defined as

$$T_{dis} = K_m I\gamma i - C_0\dot{\theta} - K_0\theta \tag{2.14}$$

Thus, the disturbance model of SADA can be defined as

$$J_0\ddot{\theta} + C_0\dot{\theta} + K_0\theta = K_m I\gamma i - T_l \qquad T_{dis} = K_m I\gamma i - C_0\dot{\theta} - K_0\theta \tag{2.15}$$

From equation (2.15) we can obtain that the dynamic model of SADA can be redefined as a vibration equation, and the electromagnetic stiffness appears in this vibration equation as an explicit expression which leads to the coupling relationship between the electromagnetic spring-viscous damping system and the solar array easily achieved by establishing the vibration equation of the coupling system. Thus, the disturbance torque aroused by the SADA driving solar array acting on the satellite can be facilely obtained.

3. Disturbance model of SADA driving a discrete flexible system

3.1. Modeling

Assuming that the discrete flexible system is a torsion spring-damping-moment of inertia system with n-dofs, the equivalent system of SADA driving this discrete flexible system is shown in Fig. 2.

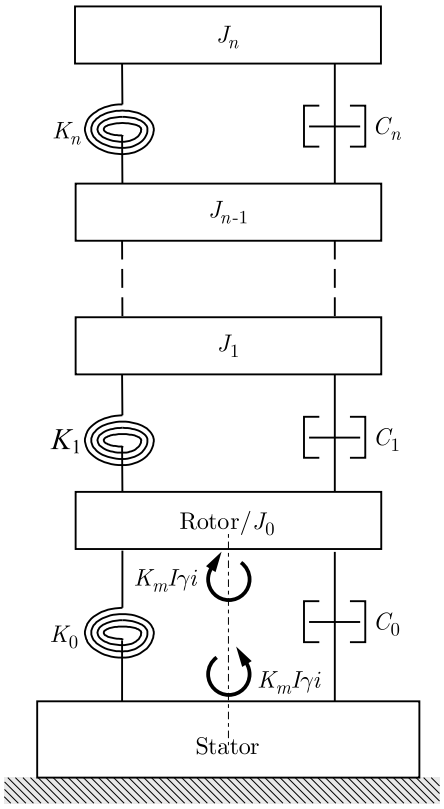

Fig. 2. Equivalent system diagram of SADA driving a discrete flexible system with n-dofs

Thus, the disturbance model of SADA driving this flexible system can be defined as

$$\mathbf{J}\ddot{\boldsymbol{\beta}} + \mathbf{C}\dot{\boldsymbol{\beta}} + \mathbf{K}\boldsymbol{\beta} = \mathbf{F} \qquad T_{dis} = K_m I\gamma i - C_0\dot{\theta} - K_0\theta \tag{3.1}$$

where $\mathbf{J}$, $\mathbf{C}$, $\mathbf{K}$, $\mathbf{F}$ and $\boldsymbol{\beta}$ is the mass matrix, damping matrix, stiffness matrix, excitation vector and angular displacement vector, respectively. All the expressions are shown in equation (3.2)

$$\begin{aligned}
\mathbf{J} &= \begin{bmatrix} J_0 & 0 & \cdots & 0 \\ 0 & J_1 & \cdots & 0 \\ \vdots & \vdots & \ddots & \vdots \\ 0 & 0 & \cdots & J_n \end{bmatrix} \qquad \mathbf{C} = \begin{bmatrix} C_0 + C_1 & -C_1 & \cdots & 0 \\ -C_1 & C_1 + C_2 & \cdots & 0 \\ \vdots & \vdots & \ddots & \vdots \\ 0 & 0 & \cdots & C_n \end{bmatrix} \\
\mathbf{K} &= \begin{bmatrix} K_0 + K_1 & -K_1 & \cdots & 0 \\ -K_1 & K_1 + K_2 & \cdots & 0 \\ \vdots & \vdots & \ddots & \vdots \\ 0 & 0 & \cdots & K_n \end{bmatrix} \qquad \mathbf{F} = \begin{bmatrix} K_m I\gamma i \\ 0 \\ \vdots \\ 0 \end{bmatrix} \qquad \boldsymbol{\beta} = \begin{bmatrix} \theta \\ \theta_1 \\ \vdots \\ \theta_n \end{bmatrix}
\end{aligned} \tag{3.2}$$

3.2. Simulation and analysis

Taking a two-dof torsion spring-damping-moment of inertia system as the simulation object, Matlab/Simulink toolbox is used to simulate the disturbance model of SADA driving this discrete flexible system. Table 1 shows the simulation parameters of SADA and the two-dof flexible system. The simulation time and time step size is 100 s and 1/2048 s, respectively.

Figures 3 to 5 illustrate the simulation results of the disturbance model of SADA driving this two-dof flexible system.

It can be seen from Figs. 3a and 3b that the two-phase currents I_A and I_B are ladder cosine/sine curves, and the amplitude I is 0.3 A.

Table 1. Simulation parameters of SADA and the two-dof flexible system

Parameter	Symbol	Value	Unit
Rotor teeth number	z	300	–
Beat number	p	4	–
Subdivision number	n	256	–
Given angular velocity of rotor	ω_0	0.012	$^\circ/s$
Amplitude of two-phase current	I	0.3	A
Moment of inertia of rotor	J_0	0.0005	kg·m^2
Viscous damping coefficient	C_0	0.01	N·m·s/rad
Motor torque constant	K_m	10	N·m/(A·rad)
Electromagnetic stiffness	K_0	900	N·m/rad
Moment of inertia of flexible system	J_1/J_2	1/4	kg·m^2
Viscous damping coefficient	C_1/C_2	0.02/0.01	N·m·s/rad
Stiffness of torsion spring	K_1/K_2	1000/2000	N·m/rad

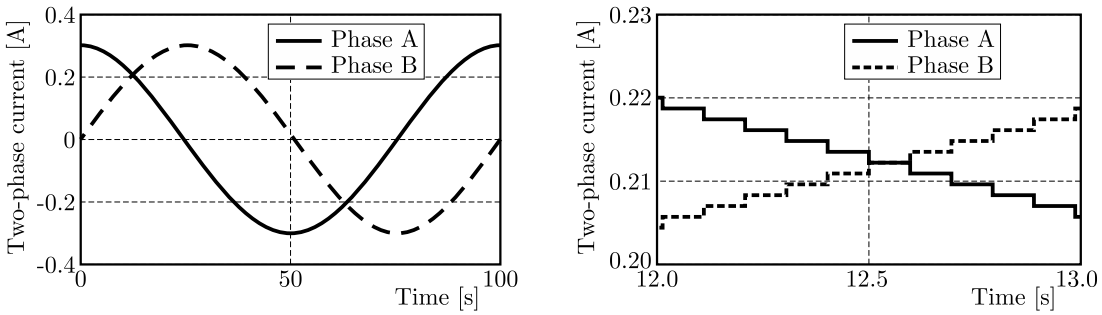

Fig. 3. Simulation results of the two-phase current (a) full view (b) partially enlarged view

As shown in Fig. 4, the simulation result of the rotor angular displacement indicates that after 100 seconds of running, the angular displacement of the rotor is 1.2°, which is equal to the given angular velocity ω_0 (0.012°/s) times the running time (100 s).

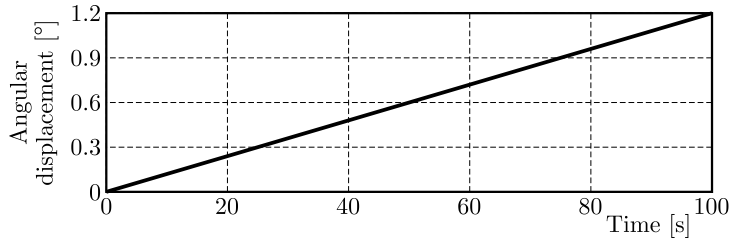

Fig. 4. Simulation result of the angular displacement of the rotor

The simulation result of the disturbance torque shown in Fig. 5 indicates that the disturbance frequencies in the frequency band of 0∼40 Hz are 1.438 Hz, 8.563 Hz, 10.25 Hz, 20.5 Hz and 30.75 Hz. Substituting the parameters shown in Table 1 into equation (3.2), the natural frequency of the equivalent system of SADA driving the two-dof flexible system can be calculated easily, which is demonstrated as

$$f_1 = 1.440\,\text{Hz} \qquad f_2 = 8.558\,\text{Hz} \qquad f_3 = 310.272\,\text{Hz} \tag{3.3}$$

Therefore, the disturbance frequencies 1.438 Hz and 8.563 Hz are the natural frequencies of the equivalent coupling system of SADA driving the flexible system.

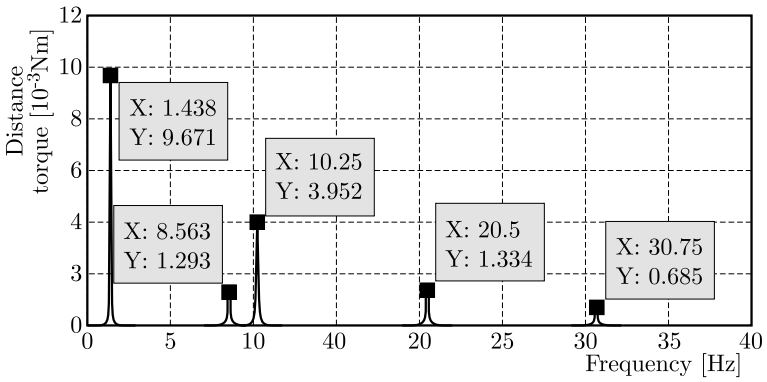

Fig. 5. Simulation result of the disturbance torque

As mentioned above, SADA is to translate digital pulse sequences to precise movements of the rotor shaft. The input frequency of the digital pulse signal is given by

$$f_d = \frac{\frac{\pi\omega_0}{180}}{\alpha} = \frac{\frac{\pi\omega_0}{180}}{\frac{2\pi}{zpn}} = 10.24\,\text{Hz} \tag{3.4}$$

Thus, the disturbance frequencies 10.25 Hz, 20.5 Hz and 30.75 Hz are the input frequency of the digital pulse signal and its harmonics.

As a consequence, we can obtain that the disturbance frequencies of SADA driving a discrete flexible system are mainly consists of two parts: 1) natural frequencies of the equivalent system of SADA driving the flexible system; 2) input frequency of the digital pulse signal and its harmonics. These disturbance frequencies are consistent with those obtained by Yang *et al.* (2010) and Chen *et al.* (2014), which confirmedly validates the effectiveness of the disturbance model proposed in this paper.

4. Simulation method of SADA driving a continuous flexible system

Since the solar array is a typical continuous flexible system, equation (3.1) used to describe vibration of the equivalent system of the SADA driving solar array is difficult to establish. Taking a continuous flexible system, which is designed to simulate the solar array, as the studied object, the simulation method of the disturbance generated by SADA driving a continuous flexible system is demonstrated in this part.

4.1. Continuous flexible system

The continuous flexible system is made of a thin aluminum plate, steel counterweight beam and connecting bracket. The size of the thin aluminum plate is 5 m×1.6 m×0.001 m. The steel counterweight beam is arranged along the four sides of the thin aluminum plate continuously, whose section size is 0.03 m×0.03 m. The connection bracket is composed of two identical steel beams. The length of each steel beam is 1m, and its section size is 0.03 m×0.03 m as well. A schematic diagram of this continuous flexible system is shown in Fig. 6.

ANSYS 12.1 is used to create the finite element model of this continuous flexible system. In the finite element model, element SHELL 181 is used to mesh the thin aluminum plate and element BEAM 4 is used to mesh the steel counterweight beam and the connecting bracket. What is more, a node should be laid in the installation point which is named as *node a*. The modal shape of this finite element model is determined for the boundary condition of constraining all-dofs of *node a*. The calculation results of the modal analysis are listed in Table 2.

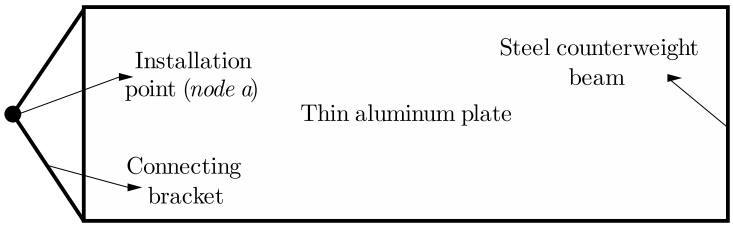

Fig. 6. Schematic diagram of the continuous flexible system

Table 2. Calculation results of the modal

Modal order	Frequency [Hz]	Modal shape
1	0.503	first-order out-of-plane bending
2	1.364	first-order in-plane rocking
3	2.110	first-order torsional
4	2.222	second-order out-of-plane bending

As the former four order modal shapes of the continuous flexible system designed are the same as the actual solar array mentioned in Zhu *et al.* (2014), this continuous flexible system has the ability to simulate the actual solar array.

4.2. Continuous flexible system coupling with SADA

As discussed above, the electromagnetic field between the stator and rotor of SADA can be equivalent to an electromagnetic spring-viscous damping system, thus, the equivalent system of the continuous flexible system coupling with SADA can be shown as in Fig. 7.

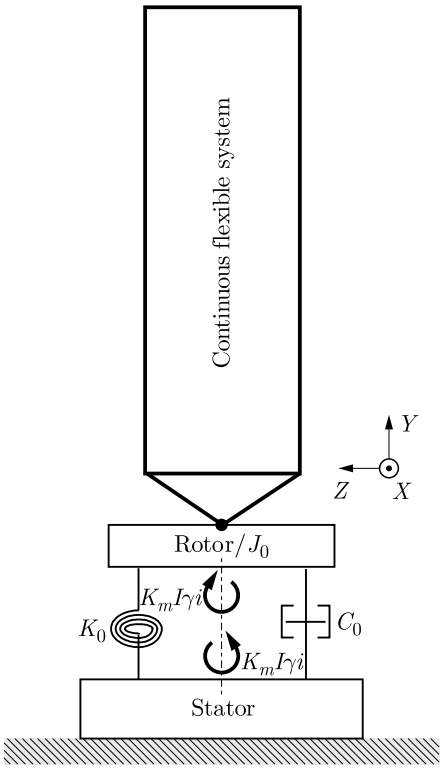

Fig. 7. Equivalent system of the continuous flexible system coupling with SADA

ANSYS 12.1 is used to create the finite element model of this equivalent system. In this finite element model, the moment of inertia of the rotor J_0 is meshed by using element MASS 21; the electromagnetic torsion spring-viscous damping system is meshed by using element COMBIN 14; the finite element model of the continuous flexible system in the equivalent system is the same as the finite element model created above. Element MASS 21, element COMBIN 14 and the finite element model of the continuous flexible system should share one node, which is *node a*. As the rotor of SADA has only one rotation dof, *node a* has only this dof (Y-rotation) as well. Constraining all the other dofs of *node a* and all-dofs of the other node of element COMBIN 14, then the creation process of the finite element model is accomplished.

ANSYS 12.1 is used to find the modal shapes of this coupling finite element model. The calculation results of the modal analysis are presented in Table 3.

Table 3. Calculation results of the modal analysis

Modal order	Frequency [Hz]	Modal shape
1	0.503	first-order out-of-plane bending
2	0.606	first-order torsional
3	1.364	first-order in-plane bending
4	2.222	second-order out-of-plane bending

Comparing with the calculation results shown in Table 2, the natural frequency of the first-order torsional modes moves forward and the other natural frequency remains the same, which is caused by the coupling effect between the continuous flexible system and the electromagnetic spring of SADA.

4.3. Simulation and analysis

ANSYS 12.1/Transient is used to simulate the disturbance emitted by SADA driving the continuous flexible system designed. The simulation process is done on the basis of the coupling finite element model created in Section 4.2. In the simulation processing, firstly, the exciting torque $K_m I\gamma i$ acts on *node a*; secondly, the simulation time and time step size is 20 s and 1/2048 s respectively; thirdly, each substep of the angular displacement and angular velocity of *node a* are written down; lastly, substituting the angular displacement and angular velocity of *node a* into equation (3.1), the disturbance torque of SADA driving this continuous flexible system is obtained. The simulation results are shown in Figs. 8 and 9.

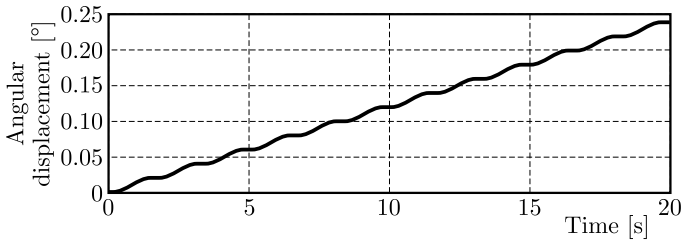

Fig. 8. Simulation result of the angular displacement of the rotor (node a)

It can be seen from Fig. 8 that due to huge torsional vibration of the continuous flexible system coupling with SADA in the low frequency band (0.606 Hz), the angular displacement of the rotor is no longer a straight line. However, after 20 seconds of running, the angular displacement of rotor is very close to 0.24°, which equals to the given angular velocity of the rotor ω_0 (0.012°/s) times the running time (20 s).

What can be obtained from Fig. 9 are the disturbance frequencies in the frequency band of $0 \sim 40$ Hz are 0.625 Hz, 10.25 Hz, 20.5 Hz and 30.75 Hz. Among them, 0.625 Hz is the natural

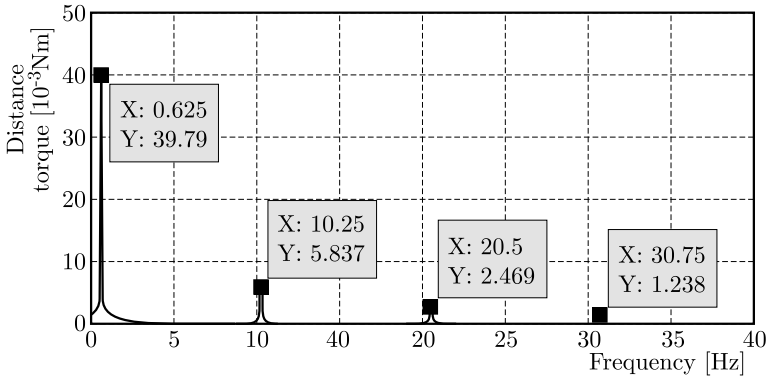

Fig. 9. Simulation result of the disturbance torque

frequency of the first-order torsional mode of the continuous flexible system coupled with SADA shown in Table 3; 10.25 Hz, 20.5 Hz and 30.75 Hz is the input frequency of the digital pulse signal and its harmonics. Due to low exciting energy of the exciting torque $K_m I\gamma i$ beyond the low frequency band and the existence of the viscous damping inner SADA, the natural frequencies of high-order torsional modes of the continuous flexible system coupled with SADA do not appear in the disturbance frequencies.

Therefore, the disturbance frequencies of SADA driving the continuous flexible system mainly consist of two parts: 1) natural frequencies of the torsional mode of the continuous flexible system coupled with SADA in the low frequency band; 2) input frequency of the digital pulse signal and its harmonics. These conclusions are the same as those obtained for SADA driving athe discrete flexible system in Section 3.2. This proves that the simulation method of SADA driving the continuous flexible system demonstrated in this part is right.

4.4. Summarizing

The simulation method of the disturbance aroused by SADA driving the continuous flexible system can be summarized as follows:

- Before the start of simulation, the finite element model of the continuous flexible system coupled with SADA, which can be equivalent to an electromagnetic spring-viscous damping system, should be created firstly, and the coupling node named *node a*. Appropriate boundary conditions should be formulated as well.
- In the process of simulation, the exciting torque $K_m I\gamma i$ should act on *node a*, and each substep of the angular displacement and angular velocity of *node a* should be written down. What is more, an appropriate simulation time and time step size should be chosen.
- After the end of simulation, substituting the angular displacement and angular velocity of *node a* into equation (3.1), the disturbance torque produced by SADA driving the continuous flexible system could be obtained.

5. Conclusions

According to the above discussions, the following conclusions can be drawn:

- By simplifying and linearizing the electromagnetic torque of SADA, the electromagnetic field between the stator and rotor of SADA can be found as equivalent to an electromagnetic spring-viscous damping system, and the vibration equation of SADA can be established.

- The disturbance model of SADA driving a discrete flexible system is achieved based on the vibration equation of SADA. A two-dof flexible system is used to simulate and analyze the disturbance model. The simulation results show that the disturbance frequencies of SADA mainly consist of two parts:

  1) natural frequencies of the equivalent system of SADA driving the flexible system;

  2) input frequency of the digital pulse signal and its harmonics.

- The method to simulate the disturbance emitted by SADA driving the continuous flexible system, which is designed to simulate the solar array, is proposed. And the disturbance frequencies of SADA mainly consist of two parts:

  1) natural frequencies of the low-order torsional mode of the continuous flexible system coupling with SADA in the low frequency band;

  2) input frequency of the digital pulse signal and its harmonics.

In conclusion, all the achievements of this project will provide a theoretical basis for the prediction of disturbances emitted by the SADA driving solar array on the orbit.

References

1. Anish N.K., Krishnan D., Moorthi S., Selvan M.P., 2012, FPGA based microstepping scheme for stepper motor in space-based solar power systems, *Industrial and Information Systems, IEEE Conference*, 1-5
2. Bodson M., Sato J.S., Silver S.R., 2006, Spontaneous speed reversals in stepper motors, *IEEE Transactions on Control Systems Technology*, **14**, 2, 369-373
3. Chen J.P., Cheng W., Han W., 2014, Analysis and simulation of stepper motor disturbance considering structural coupling, *Applied Mechanics and Materials*, **526**, 103-108
4. Chen Y.M., 2010, Application of shape memory alloys to control the vibration of solar panels, *Mechanical Engineering and Automation*, **1**, 173-175
5. Cui G.G., 2006, The satellite modeling and analysis of dynamic characteristic of drive system of solar array, Dissertation for the Master Degree in Engineering of Harbin Institute of Technology
6. Elsodany N.M., Rezeka S.F., Maharem N.A., 2011, Adaptive PID control of a stepper motor driving a flexible rotor, *Alexandria Engineering Journal*, **50**, 2, 127-136
7. Kapun A., Hace A., Jezernik K., 2007, Identification of stepping motor parameters, *International Conference on "Computer as a Tool", IEEE Conference*, 1856-1863
8. Letchmanan R., Economou J.T., Tsourdos A., 2005, Modelling and analysis of geared PM stepping motor for simulation of all-electric off-road vehicles, *Vehicle Power and Propulsion, IEEE Conference*, 301-307
9. Luo Q., Li D., Zhou W., Jiang J., Yang G., Wei X., 2013, Dynamic modelling and observation of micro-vibrations generated by a Single Gimbal Control Moment Gyro, *Journal of Sound and Vibration*, **332**, 19, 4496-4516
10. Si Z.H., Liu Y.W., Li K., 2010, Research on modeling and driver design of solar array drive assembly, *Aerospace Control and Application*, **36**, 2, 13-19
11. Szolc T., Pochanke A., 2012, Dynamic investigations of electromechanical coupling effects in the mechanism driven by the stepping motor, *Journal of Theoretical and Applied Mechanics*, **50**, 2, 653-673
12. Xia L., 1994, The primary research on low-frequency resonate of step-motor and its damping methods, *Journal of Shenyang Polytechnic University*, **16**, 3, 73-78

13. Yang T.Y., Wang H., Xu F., 2007, Micro-stepping drive method study of two-phase step motors, *Micromotors Servo Technique*, **40**, 9, 69-71

14. Yang Y.L., Cheng W., Wu S.J., Wang G.Y., 2010, Experiment and simulation of electromagnetic stiffness for stepper motor, *Applied Mechanics and Materials*, **, 29**, 1567-1573

15. Zhu S.Y., Lei Y.J., Wu X.F., Zhang D.P., 2015, Influence analysis on dynamic characteristic parameters of solar array drive system, *Journal of Vibration Engineering*, **28**, 2, 183-189

16. Zhu S.Y., Xie Y., Lei Y.J., 2014, Characteristic analysis of disturbance aroused by solar array tracking drive, *Journal of National University of Defense Technology*, **36**, 1, 27-33

Manuscript received July 16, 2015; accepted for print January 28, 2016

JOURNAL OF THEORETICAL AND APPLIED MECHANICS
54, 3, pp. 1013-1024, Warsaw 2016
DOI: 10.15632/jtam-pl.54.3.1013

CONTROL OF ANISOTROPIC ROTOR VIBRATION USING FRACTIONAL ORDER CONTROLLER

Mariusz Czajkowski, Magdalena Gertner

Bialystok University of Technology, Department of Automatic Control and Robotics, Bialystok, Poland

e-mail: m.czajkowski@doktoranci.pb.edu.pl; m.gertner@doktoranci.pb.edu.pl

Monika Ciulkin

Bialystok University of Technology, Department of Mechanics and Applied Computer Science, Bialystok, Poland

e-mail: m.ciulkin@doktoranci.pb.edu.pl

This article presents an analysis of a flexible Jeffcott rotor with an active bearing support. The rotor is coupled with lateral and torsional vibrations and a force from the unbalance vector derived from the Lagrangian method. The active support bearing is controlled by FOPID controller. Changing the rotor vibration is followed by shifting rotor angular speed and achieving the natural frequency. Simulation results demonstrate torsional and lateral vibration of thr rotor at the rotating speed near the natural frequency. Consequently, controlling the lateral vibrations mitigates potential damage and improves safety. FOPID controller introduces a new approach to vibration control of a rotating machine.

Keywords: rotor dynamic, active bearings, fractional order controller

1. Introduction

Application of rotors in modern turbomachinery, particularly in the power generation industry, requires continuous diagnosis and control. Although many studies have been conducted dealing with control of vibration in rotating shafts, there is still no ideal method allowing one to eliminate too high vibration of the machines. Observing rotors vibration during operation with different rotating speeds, allows implementation of various lateral damping on bearings depending on the necessity. Consequently, the control of lateral vibrations mitigates potential damage and improves safety.

Two dynamic systems influence each other when they are coupled. Dynamic lateral and torsional rotor vibrations can be considered separately. This approach is permitted if the effect of coupling is weak (Gosiewski, 2008b; Gosiewski and Muszyńska, 1992; Sawicki *et al.*, 2004).

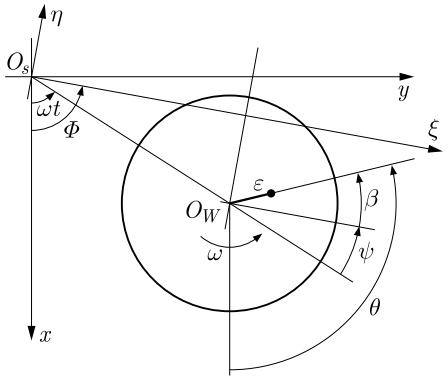

Fig. 1. Section of the rotor in inertial and rotating coordinates

The system is coupled by the unbalance vector in the model of the rotor (Fig. 1). If the rotor is considered as a weakly damped system it has a range of unstable speeds. The speed ranges are unstable when the poles in diagram of both dynamic systems are crossing each other (Gosiewski and Muszyńska, 1992). This article presents phenomena of vibration in classical dynamical systems (Gosiewski and Muszyńska, 1992) and a relationship for the stability of rotor machinery and vibration control in a closed loop when the rotor speed is in the stable and unstable range. For several decades, control applications in industrial processes have been dominated by the PID controller. Its wide popularity results from the simplicity of design and good performance including low overshoot and small settling time for slow process plants (Astrom and Hagglund, 1995; Biswas *et al.*, 2009). Fast changing process plants require a more sophisticated approach – in several research groups, a fractional order calculus has been proposed (Merrikh-Bayat, 2012). Podlubny (1999) proposed a concept of fractional order controllers and demonstrated the effectiveness of such controllers for actuating the responses of fractional order systems. The transfer function of the fractional order $PI^{\lambda}D^{\mu}$ (FOPID) controller is given by Podlubny (1999) as

$$G_c(s) = K_P + K_I s^{-\lambda} + K_D s^{\mu} \tag{1.1}$$

where K_P is the proportional gain, K_I is the integration gain, K_D is the differentiation gain, λ is the order of integrator, μ is the order of differentiator.

2. Rotor mathematical model

The mathematical model, called the Jeffcott rotor (Ma *et al.*, 2013), is described as a flexible rotor consisting of a centrally located unbalanced disk attached to a weightless shaft mounted symmetrically on rigid bearings (Gan *et al.*, 2014; Gosiewski, 2008a,b; Gosiewski and Muszyńska, 1992). The stiffness of the shaft is anisotropic (asymmetric) and the damping due to the air resistance effect is assumed to be viscous. The angular position of the unbalanced vector $\boldsymbol{\varepsilon}$ can be used as an indicator and is given by: $\theta(t) = \omega t + \psi(t) + \beta$, where ω is constant rotating speed of the shaft, $\psi(t)$ is torsional angle, β is the angle between the unbalanced vector and the ξ axis. Kinetic and potential energy of the rotor system exhibiting coupling lateral and torsional vibrations can be expressed by the following equations (Sawicki *et al.*, 2004)

$$T = \frac{m}{2}(x_s^2 + y_s^2) + \frac{I_O}{2}\dot{\theta} \qquad U = \frac{1}{2}[\xi \;\; \eta]\mathbf{K}_I \begin{bmatrix}\xi \\ \eta\end{bmatrix} + \frac{K_T}{2}\psi^2 - mgh \tag{2.1}$$

where $\mathbf{K}_I$ is the shaft stiffness defined by the matrix (Eq. (2.2)) in inertial coordinates for the undisturbed rotor by geometry or influence of the uncracked stiffness $K_{xy} = K_{yx} \equiv 0$. In the case of an unbalanced (anisotropic) rotor, the stiffnesses along the ξ, η directions are not equal ($K_{xx} \neq K_{yy}$). $x_s = x - \varepsilon\cos(\omega t + \beta)$ and $y_s = x + \varepsilon\sin(\omega t + \beta)$ are the coordinates of the centre of mass of the disk in the inertial coordinate system XYZ, $\xi = x\cos(\omega t) + y\sin(\omega t)$ and $\eta = -x\sin(\omega t) + y\cos(\omega t)$ are the coordinates of the geometric centre of the rotor in the rotating coordinate system $\xi\eta\zeta$ following Φ with rotating speed

$$\mathbf{K}_I = \begin{bmatrix}K_{xx} & K_{xy} \\ K_{yx} & K_{yy}\end{bmatrix} \tag{2.2}$$

The Rayleigh dissipation function (Lalanne *et al.*, 1998) in lateral vibrations consists of two components. One of these components defines energy dissipation caused by internal dumping,

the second one describes damping proportional to rotational speed of the rotor in the inertial coordinate system

$$E_r = \frac{1}{2}C_E(\dot{x}^2 + \dot{y}^2) + \frac{1}{2}C_L(\dot{\xi}^2 + \dot{\eta}^2) + C_T\psi^2 \tag{2.3}$$

Using the Euler-Lagrange method, the equations of kinetic and potential energy balance (Eq. (2.1)), the Rayleigh dissipation function (Eq. (2.3)) and the non-linear equations of motion for lateral and torsional vibrations of the rotor system (Eqs. (2.4)) are determined

$$\begin{aligned}
&\ddot{x} - \varepsilon[\dot{\theta}^2\cos(\theta+\beta) + \ddot{\theta}\sin(\theta+\beta)] + \frac{K_{xx}}{m}(x\cos^2\theta + y\sin\theta\cos\theta)\\
&\quad + \frac{K_{yy}}{m}(x\sin^2\theta - y\sin\theta\cos\theta) + \frac{C_E}{m}\dot{x} + \frac{C_L}{m}(\dot{x} + \omega y) = 0\\
&\ddot{y} - \varepsilon[\ddot{\theta}\cos(\theta+\beta) - \dot{\theta}^2\sin(\theta+\beta)] + \frac{K_{xx}}{m}(ysin^2\theta + x\sin\theta\cos\theta)\\
&\quad + \frac{K_{yy}}{m}(y\cos^2\theta - x\sin\theta\cos\theta) - g + \frac{C_E}{m}\dot{y} + \frac{C_L}{m}(\dot{y} + \omega x) = 0\\
&\ddot{\theta} - \frac{m\varepsilon}{I_O}[\ddot{y}\cos(\theta+\beta) - \ddot{x}\sin(\theta+\beta)] + \frac{m\varepsilon^2}{I_O}\ddot{\theta} + \frac{m}{I_O}\Big[\frac{2(K_{xx}-K_{yy})}{m}(x^2-y^2)\sin 2\theta\\
&\quad - \frac{K_{xx}-K_{yy}}{m}xy\cos 2\theta\Big] + \frac{K_T}{I_O}(\theta + \omega t) + \frac{2K_T}{I_O}(\dot{\theta} - \omega) = 0
\end{aligned} \tag{2.4}$$

The next step of modelling is the transition for the non-linear equations of motion in the fixed coordinates to the fixed complex coordinates by specifying the concurrent and backward movement (Eq. (2.5)). Conversion to complex coordinates allows linearisation of the system through coefficients

$$u = x + \mathrm{j}y \qquad \overline{u} = x - \mathrm{j}y \tag{2.5}$$

Thus, having the system of equations of motion in the complex inertial coordinates, it can be linearised assuming that the angle of torsion $\theta = \omega t + \psi$ is close to the angle of rotation $\Phi = \omega t$, where ψ is a relatively small angular displacement describing torsional vibration of the shaft. A linearised Taylor series (Eqs. (2.6)) is used. In this step, the first expressions of decomposition of the exponential function in Eq. $(2.6)_1$ is taken. The non-linear elements have been skipped (Gosiewski and Muszyńska, 1992). As a result of this procedure, we obtain linearised equations of motion in the complex inertial coordinates, and using formulas (Eqs. $(2.6)_{2-5}$), equations in the real rotating coordinates are obtained

$$\begin{aligned}
&\mathrm{e}^{\pm\mathrm{j}\psi} = 1 \pm \mathrm{j}\psi + \ldots \qquad u = w\mathrm{e}^{\mathrm{j}\omega t} \qquad \overline{u} = \overline{w}\mathrm{e}^{-\mathrm{j}\omega t}\\
&w = \xi + \mathrm{j}\eta \qquad \overline{w} = \xi - \mathrm{j}\eta
\end{aligned} \tag{2.6}$$

Then the rotor model is determined by

$$\begin{aligned}
&\ddot{\xi} = 2\omega\dot{\eta} + \omega^2\xi - \frac{C_E}{m}(\dot{\xi} - \omega\eta) - \frac{C_L}{m}\dot{\xi} - \frac{K_{xx}}{m}\xi - \varepsilon\omega^2\psi\sin\beta + 2\varepsilon\omega\dot{\psi}\cos\beta\\
&\quad + \varepsilon\ddot{\psi}\sin\beta + \varepsilon\omega^2\cos\beta + g\sin(\omega t)\\
&\ddot{\eta} = -2\omega\dot{\xi} + \omega^2\eta - \frac{C_E}{m}(\dot{\eta} - \omega\xi) - \frac{C_L}{m}\dot{\eta} - \frac{K_{yy}}{m}\eta - \varepsilon\omega^2\psi\cos\beta + 2\varepsilon\omega\dot{\psi}\sin\beta\\
&\quad + \varepsilon\ddot{\psi}\cos\beta + \varepsilon\omega^2\sin\beta + g\cos(\omega t)\\
&\ddot{\psi} = -\frac{C_T}{I_O} - \frac{m\varepsilon^2}{I_O}\omega^2\psi - \frac{K_T}{I_O}\psi - \frac{\varepsilon}{I_O}K_{yy}\xi\sin\beta + \frac{\varepsilon}{I_O}K_{xx}\eta\cos\beta - \frac{m\varepsilon}{I_O}g\cos(\omega t + \beta)
\end{aligned} \tag{2.7}$$

The coefficients of the rotor dynamic equation obtained in this way are time dependent, which means that vibration of the rotor can be considered as parametric vibration. It is known that vibrations of machines are unstable in a range of parameters. One of the rotor parameter is the angular speed, which is changing while working. For the purpose of solving the eigenvalue problem, free lateral and torsional vibration of the rotor should be determined. Free vibrations are deprived of external excitations and are defined by the following equations

$$\begin{aligned}
\ddot{\xi} &= 2\omega\dot{\eta} + \omega^2\xi - \frac{C_E}{m}(\dot{\xi} - \omega\eta) - \frac{C_L}{m}\dot{\xi} - \frac{K_{xx}}{m}\xi - \varepsilon\omega^2\psi\sin\beta \\
&\quad + 2\varepsilon\omega\dot{\psi}\cos\beta + \varepsilon\ddot{\psi}\sin\beta \\
\ddot{\eta} &= -2\omega\dot{\xi} + \omega^2\eta - \frac{C_E}{m}(\dot{\eta} - \omega\xi) - \frac{C_L}{m}\dot{\eta} - \frac{K_{yy}}{m}\eta - \varepsilon\omega^2\psi\cos\beta \\
&\quad + 2\varepsilon\omega\dot{\psi}\sin\beta + \varepsilon\ddot{\psi}\cos\beta \\
\ddot{\psi} &= -\frac{C_T}{I_O} - \frac{m\varepsilon^2}{I_O}\omega^2\psi - \frac{K_T}{I_O}\psi - \frac{\varepsilon}{I_O}K_{yy}\xi\sin\beta + \frac{\varepsilon}{I_O}K_{xx}\eta\cos\beta
\end{aligned} \tag{2.8}$$

Using the Laplace transformation, differential equations (2.8) take the form of coupled equations with the complex variable $s = -\mathrm{j}\omega$

$$\begin{bmatrix} A_{1d}(s) & -B_d(s) & -D(s) \\ B_d(s) & A_{2d}(s) & -F(s) \\ -H(s) & -K(s) & C(s) \end{bmatrix} \begin{bmatrix} \xi \\ \eta \\ \psi \end{bmatrix} = \begin{bmatrix} 0 \\ 0 \\ 0 \end{bmatrix} \tag{2.9}$$

where

$$\begin{aligned}
A_{1d}(s) &= s^2 + \frac{1}{m}(C_E + C_L)s + \frac{K_{yy}}{m} - \omega^2 & A_{2d}(s) &= s^2 + \frac{1}{m}(C_E + C_L)s + \frac{K_{xx}}{m} - \omega^2 \\
B_d(s) &= 2\omega s + \frac{C_E}{m}\omega & C(s) &= s^2 + \frac{C_T}{I_O}s + \frac{m\varepsilon^2}{I_O}\omega^2 + \frac{K_T}{I_O} \\
D(s) &= \varepsilon\sin\beta s^2 + 2\varepsilon\omega\cos\beta s - \varepsilon\omega^2\cos\beta & F(s) &= \varepsilon\cos\beta s^2 + 2\varepsilon\omega\sin\beta s - \varepsilon\omega^2\cos\beta \\
H(s) &= K_{yy}\frac{\varepsilon}{I_O}\sin\beta & K(s) &= K_{xx}\frac{\varepsilon}{I_O}\cos\beta
\end{aligned} \tag{2.10}$$

The determinant of the main matrix in equation (Eq. (2.9)) is the characteristic polynomial of the rotor model. Comparing this characteristic polynomial to zero, poles of the system are obtained.

Using such a characteristic equation, stability of the system can be determined. When the system is stable, all elements (poles) of the characteristic equation have negative real parts. Checking the roots of the characteristic equation in the rotational speed of the rotor ω characteristic shows that the speed of the rotor is stable. The rotor parameters are chosen to correspond to real machines (Sawicki *et al.*, 2004). The map in Fig. 2 shows the course of the poles depending on the rotating speed. Unstable rotating speed occurs when the poles change the sign in the real part. Furthermore, unstable rotating speed occurs when the imaginary part of the trajectories intersect (Gosiewski, 2008a,b). The first area corresponds to the natural frequency $\omega_1 \cong (\sqrt{K_{xx}/m} + \sqrt{K_{yy}/m})/2$, the second $\omega_2 \cong \sqrt{K_T/I_O} - (\sqrt{K_{xx}/m} + \sqrt{K_{yy}/m})/2$ and the third $\omega_3 \cong \sqrt{K_T/I_O} + (\sqrt{K_{xx}/m} + \sqrt{K_{yy}/m})/2$.

Real parameters listed in Table 1 are chosen for the model in order to emphasize the importance of examining real life applications.

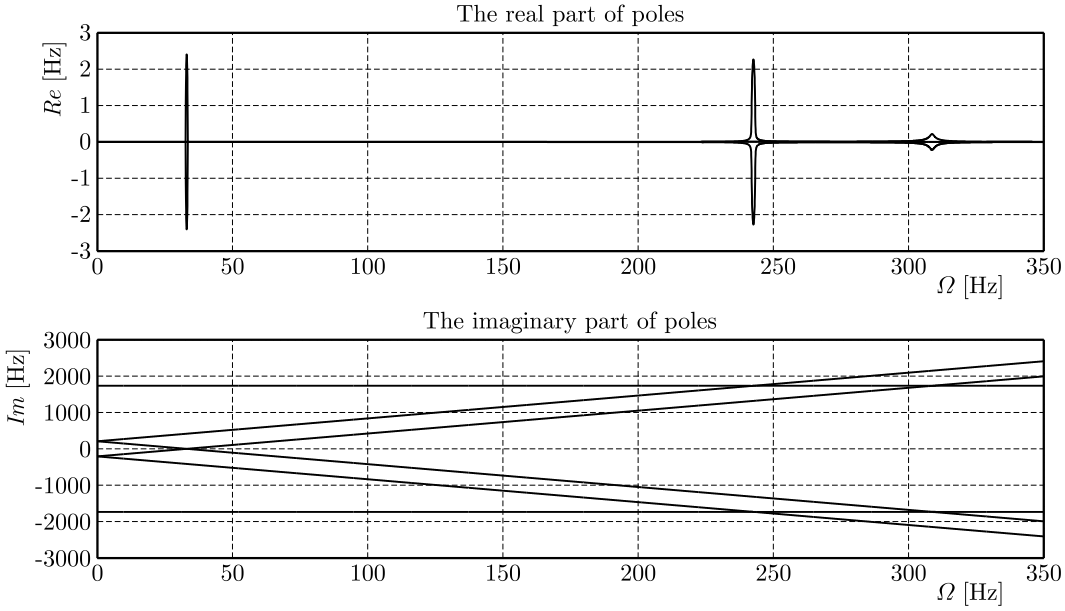

Fig. 2. Distribution poles in the rotation frequency

Table 1. Simulation parameters (Sawicki *et al.*, 2004)

Physical parameters	Value	Units
Disk mass m	20	kg
Disk polar moment of inertia I_O	0.3	kg/m^2
Shaft stiffness K_{xx}	$8.82 \cdot 10^5$	N/m
Shaft stiffness K_{yy}	$8.42 \cdot 10^5$	N/m
Torsional shaft stiffness K_T	$9.00 \cdot 10^5$	N/m
Range of stiffness ΔK	10%	
Unbalance eccentricity ε	$1.5 \cdot 10^{-3}$	m
Unbalance phase angle β	30	degrees
Lateral damping ratio C_L	0.01	–
External damping ratio C_E	0.01	–
Torsional damping ratio C_T	0.001	–

3. Realization of the fractional order controller

There are many methods of finding integer or discrete transfer functions which approximate a fractional derivative. For example, Merrikh-Bayat (2011) approximated the transfer function of controller with an integer order transfer function. Valsa and Brancik (1998) used the inverse Laplace transformations, and more methods can be found in Vinagre *et al.* (2000)

The Oustaloup Recursive Approximation (ORA) is widely used in finding a rational integer--order approximation for fractional-order integrators and differentiators of the form s^r, where $r \in (-1, 1)$ and is defined by Eq. (3.1) (Merrikh, 2012; Oustaloup *et al.*, 2000; Vinagre *et al.*, 2000)

$$s^r \approx k \prod_{n=1}^{N} \frac{1 + \frac{s}{\omega_{z,n}}}{1 + \frac{s}{\omega_{p,n}}} \tag{3.1}$$

where Eq. (3.1) is determined by Eqs. (3.2)

$$\omega_{z,1} = \omega_l\sqrt{\eta} \qquad \omega_{p,n} = \omega_{z,n}\alpha \qquad n = 1,\ldots,N$$
$$\omega_{z,n+1} = \omega_{p,n}\eta, \qquad n = 1,\ldots,N-1 \qquad \alpha = \left(\frac{\omega_h}{\omega_l}\right)^{\frac{r}{N}} \qquad \eta = \left(\frac{\omega_h}{\omega_l}\right)^{\frac{1-r}{N}} \tag{3.2}$$

where N is the number of poles and zeros, ω_h is high transitional frequency, ω_l is low frequency, ω_u is the unit gain frequency and the central values of a band of frequencies geometrically distributed around it and defined by $\omega_u = \sqrt{\omega_l\omega_h}$. The Oustaloup-Recursive-Approximation for a fractional order differentiator enable one to obtain the transfer function of an integral element of the order of 1/2 (Xue *et al.*, 2001). The following variables should be given: r – fractional order as in s^r, where r is a real number, N – order of the finite transfer function approximation for both (num/den), ω_l – low frequency limit of the range of frequency of interest, ω_h – upper frequency limit of the range of frequency of interest. The frequencies ω_l and ω_h should be selected before approximation of the integer element of the fractional $PI^\lambda D$ controller. If the frequency of the input signal is in a different range than ω_l and ω_h, the fractional $PI^\lambda D$ controller will not be able to work properly – the integer part of the controller will not act like a integer.

In further simulation, $\lambda = 1/2$, $\omega_l = 3\cdot 10^4\,\mathrm{Hz}$, $\omega_h = 2\cdot 10^{-4}\,\mathrm{Hz}$ and $N = 1, 5, 11$ are considered.

Figure 3 shows a comparison of a fractional order with the classical order in the Bode characteristic. As it can be seen, the 11-th approximation of the integrator element gives a sufficient result for the factor in the integrator description and gives similar results for the phase characteristic to the classical order. According to the range of frequencies, the systems have different quality of control. If the order of approximation increases, the ripple of phases decreases.

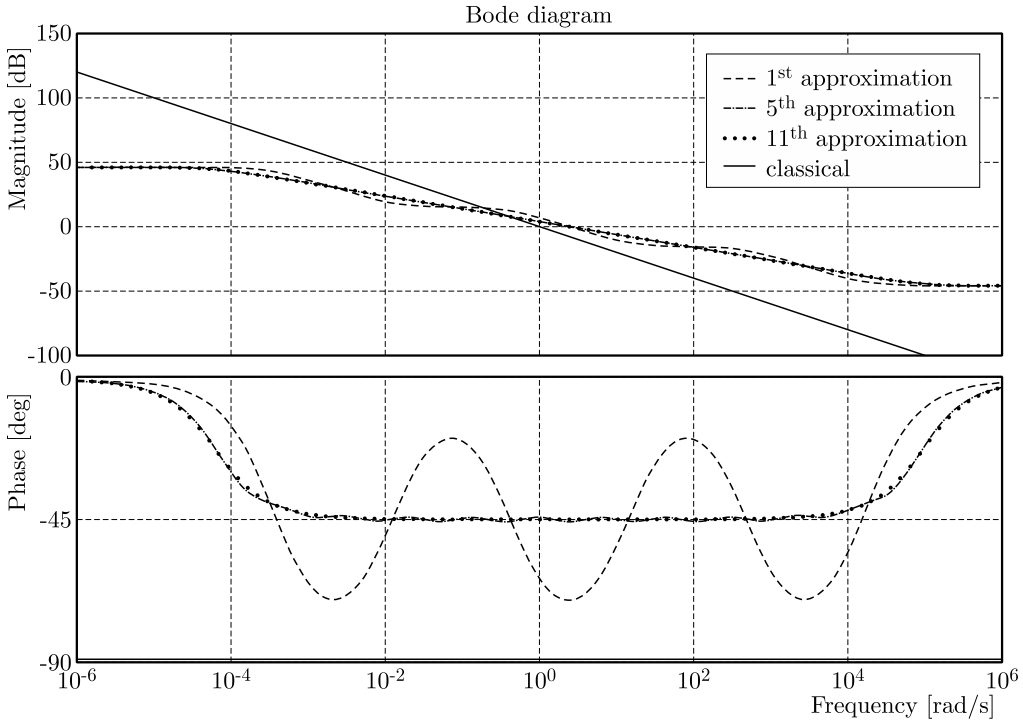

Fig. 3. Comparison of the fractional order with the classical order in the Bode characteristic

In Fig. 4, a comparison of the poles-zeros plot of different approximations of the fractional integer with the classical integer are shown. From this characteristic, several numbers of poles and zeros of the systems have been received. All systems are within stability boundary and do

not have imaginary parts. With increasing approximation, the zeros and poles move closer to the area of stability.

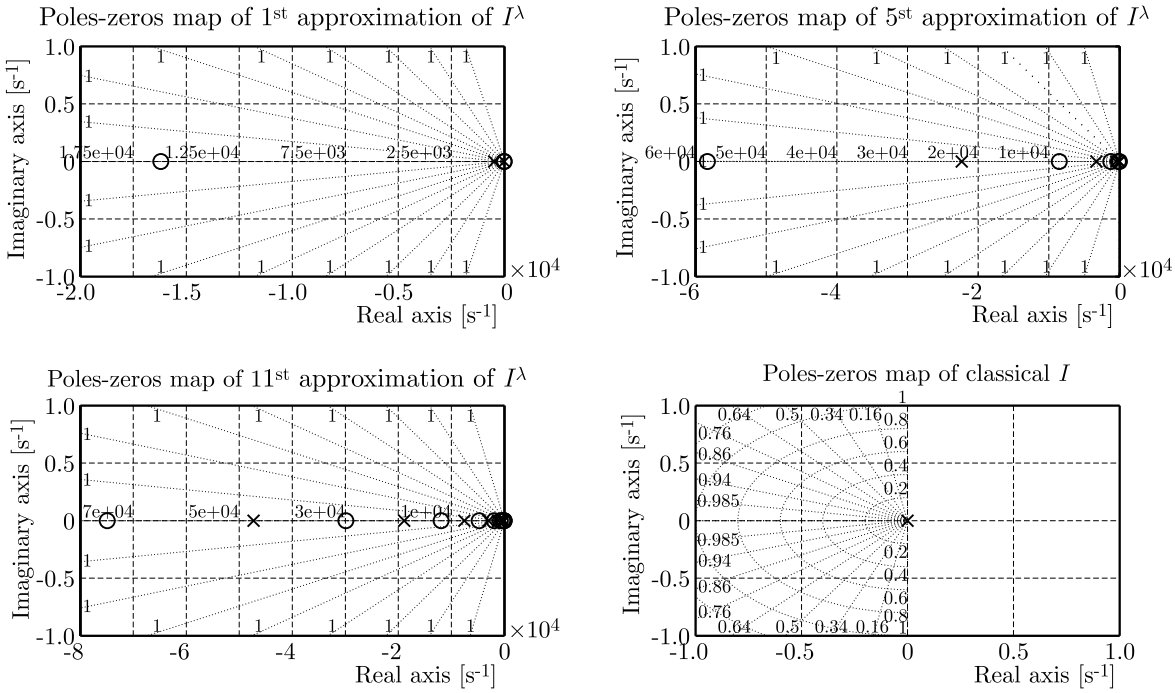

Fig. 4. Comparison of the fractional order with the classical order in poles-zeros map

Figure 5 shows the step response of a different number of approximations of the integrator used in the fractional order controller. The comparison shows that the system with a lower number of approximations achieves faster the set point.

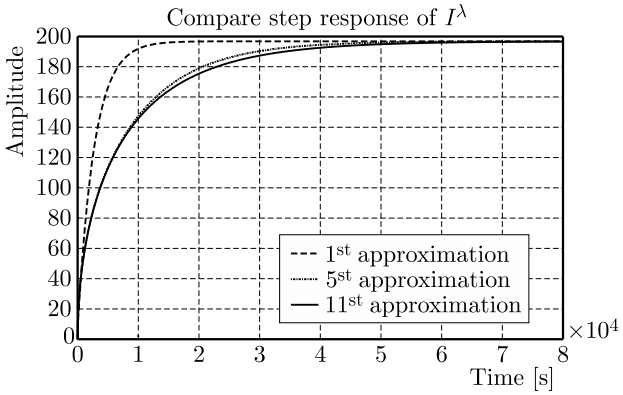

Fig. 5. Comparison of the fractional order with the classical order on the step response

In the low range of frequencies the integral element behave like a proportional element, in the higher range like an object with damped signals. This leads to non-linear action of the integral element which can precipitate internal signal saturation for long prevalence of a fixed offset value and "low pass filter" in the case of a large dynamic offset.

4. Open-loop and closed-loop system

Free vibration at a stable speed (30 Hz), close to the first unstable speed, is shown in Fig. 6. Vibration along the axis η and ξ have similar amplitudes and are shifted in phase by $\pi/2$ rad in

which the controller can work with information about the value ξ. Vibration of ψ depends on η and ξ, so if η and ξ are minimized then, vibration of ψ is also minimized.

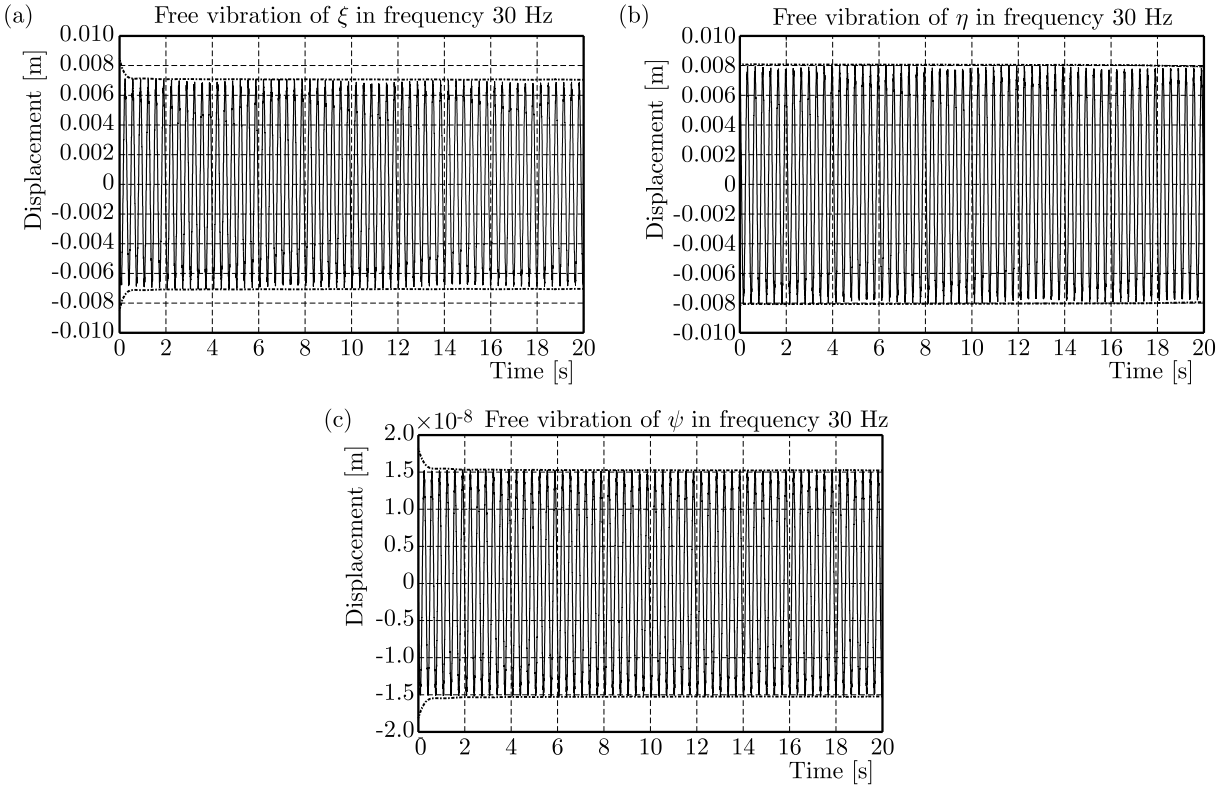

Fig. 6. Free vibration of the rotor, (a) vibration of ξ, (b) vibration of η, (c) vibration of ψ

The classical PID controller and fractional $PI^{\lambda}D$ controller have been designed for stable rotation speed $\omega = 30\,\text{Hz}$. The rotating speed $\omega = 30\,\text{Hz}$ has been selected as a stable speed by the characteristic shown in Fig. 2. This vibrations have the amplitude in constant value (not increasing). Vibrations in the ξ, η axes have similar amplitudes and differ by a phase shift $\pi/2\,\text{rad}$ from each other. The controller measuring the amplitude of vibration in the ξ axis does not need the information in the η axis because of the similarity. Vibrations in the ψ axis are coupled with vibrations in the ξ and η axes by the stiffness matrix (Eq. (2.4)). Minimising the vibrations in the ξ and η vertical axis decreases the vibrations of the ξ and η directions.

The concept of realization of the rotor vibration controller consists in measuring the amplitude of vibration in the ξ axis and varying the stiffness of the active supports within the range ΔK (Fig. 7). The controller changes the transverse stiffness of the system by adding to the initial stiffness K_{xx}, and K_{yy} by adding the processing stiffness ΔK. The final value of stiffness is $\Delta K_{xx} = \Delta K_{yy} = K_{xx} + \Delta K = K_{yy} + \Delta K$ (Fig. 7).

The controller settings for the rotating speed $\omega = 30\,\text{Hz}$ are shown in Table 2. The first case is tuned for the $PI^{\lambda}D$ controller, the second one for a classical PID controller. As the two elements of the controller do not differ in structure and the integral component I acts similarly in both cases, the responses of the controls have been tested for the same two settings.

Simulations have been carried for two stable rotating speeds (30 Hz, 36 Hz) and one unstable rotating speed (32 Hz). The results are shown in Figs. 8-10 and in Table 3.

Simulations of rotor vibrations have been carried out at a constant rotating speed. Simulations present only vibration in the ξ axis. All results of the simulstion are presented in Table 3. To present stable vibrations of the rotor, the operation of the controller has been started at the second second of simulation. In the first simulation at the rotating speed $\omega = 30\,\text{Hz}$ the con-

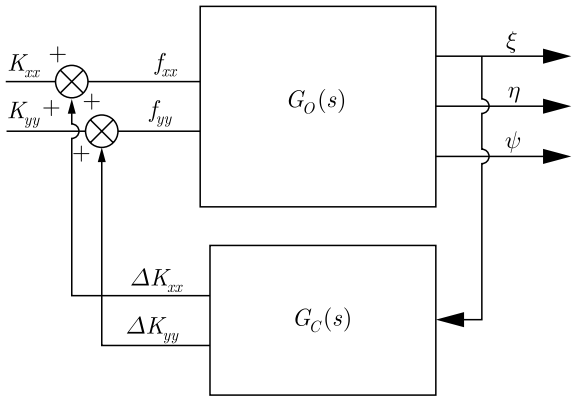

Fig. 7. Close loop system

Table 2. Controller settings

Settings	First case	Second case	Units
k_p	$1.4139 \cdot 10^3$	$2.5194 \cdot 10^3$	–
T_i	14.9496	7.8666	s
k_d	8	8	–
T_d	1.69787	3.8445	s

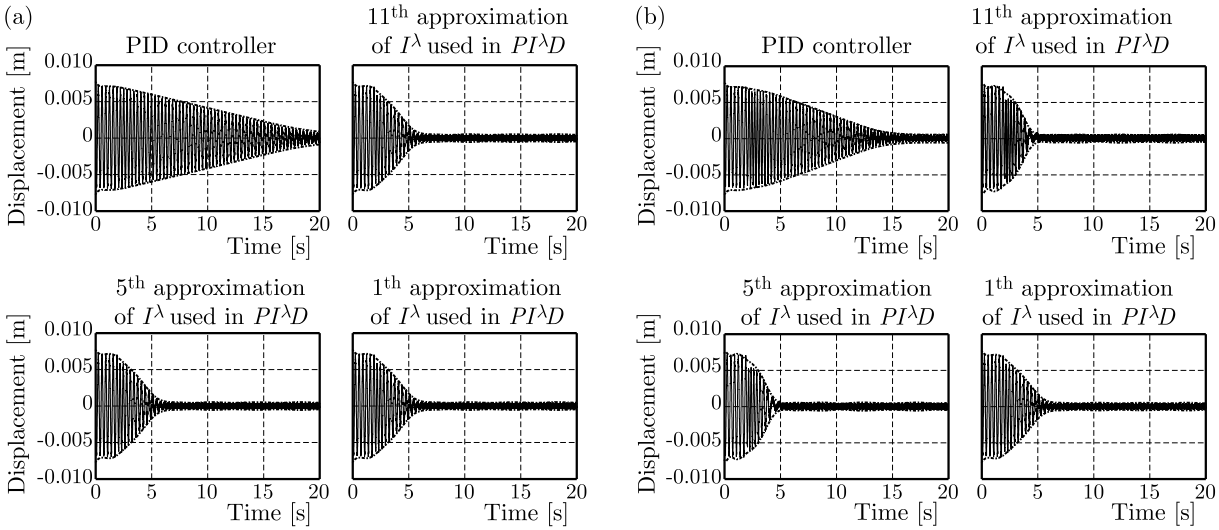

Fig. 8. Comparison of controllers at the rotating speed 30 Hz. Vibration in the ξ direction with controllers with first settings (a) and with second settings (b)

trollers have first settings (Table 2). The settling time in the system with the fractional order controller is shorter than in the classical PID controller (Fig. 9). The response of the system with $PI^\lambda D$ controllers for all order approximations has close settling time. The amplitude of settling vibrations in the system with $FOPID$ controllers is lower than in the system with the classical PID controller.

In the next simulation, the second set of settings of the controllers (Table 2) with the same rotor rotating speed ($\omega = 30$ Hz) has been used. The $FOPID$ controllers are still better than the classical PID controller. The systems with the $FOPID$ controllers have a shorter settling time and lower amplitudes of vibrations.

Next simulations present control vibration at an unstable rotating speed ($\omega = 32$ Hz) (Fig. 9).

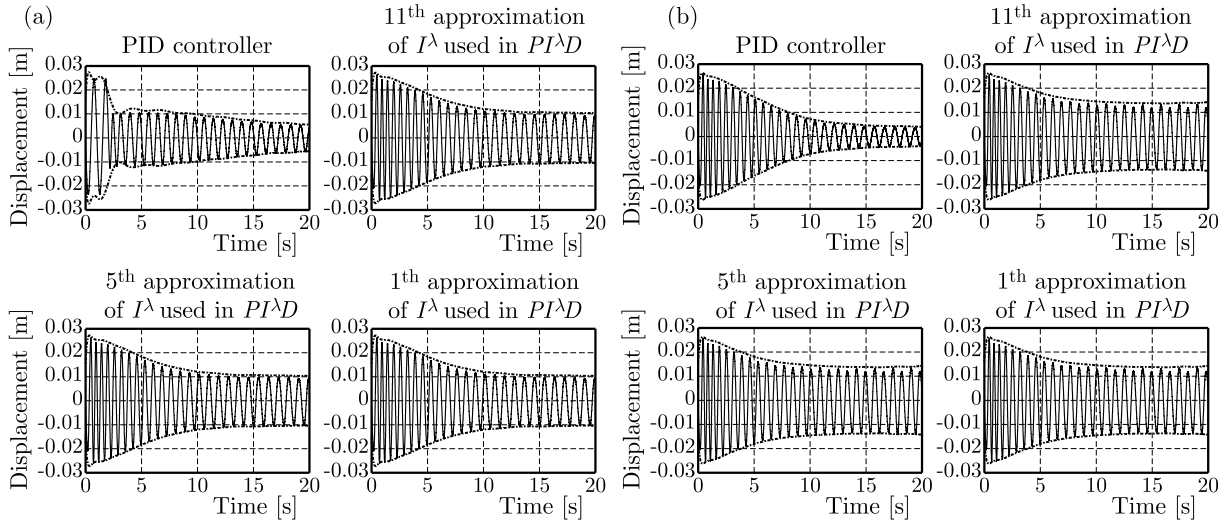

Fig. 9. Comparison of controllers at the rotating speed 32 Hz. Vibration in the ξ direction with controllers with first settings (a) and with second settings (b)

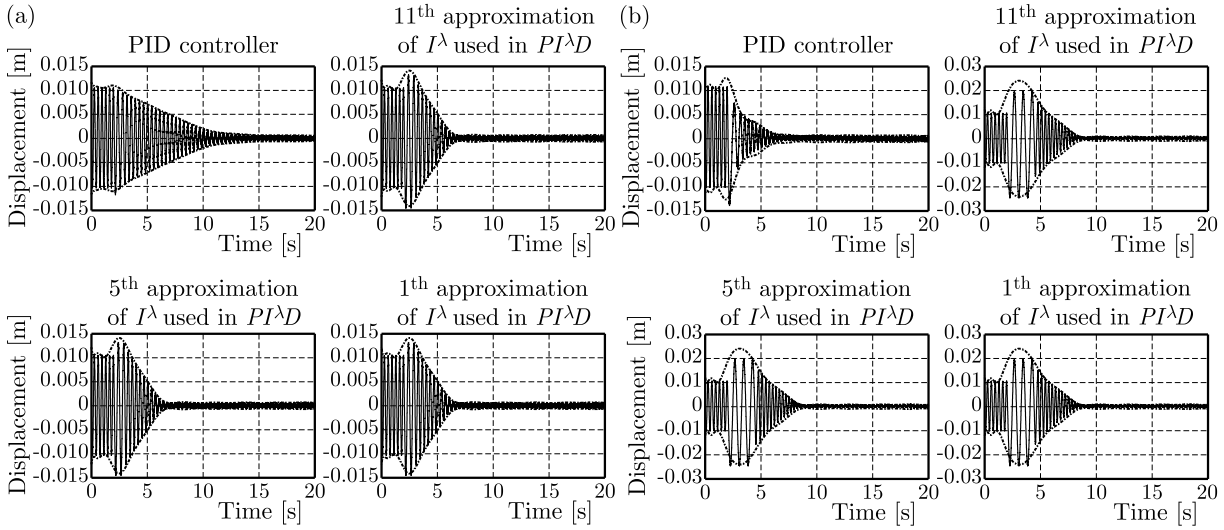

Fig. 10. Comparison of controllers at the rotating speed 36 Hz. Vibration in the ξ direction with controllers with first settings (a) and with second settings (b)

Because the amplitude of vibration goes to infinity, the controllers have been started at the beginning of simulation. The systems with the classical PID controllers are characterized by a better stablisation process. Simulations for systems with different order of approximations of $PI^\lambda D$ present various amplitudes for settling vibrations, but the settling times are constant. With an increase in the order of the approximation, the amplitudes of settling vibrations decrease for all settings of the controller. The systems with classical PID controllers have longer settling times but achieve a lower amplitude of settling vibrations.

In the next part of the numerical research, the response of the close loop systems with controllers have been tested at a stable speed 36 Hz (Fig. 10). This is intended to test how the settings and types of the controllers are resistant to a change in the rotating speed. In both cases, overshoot is observable, but in the classical controller the overshoot has a smaller value than in the fractional order controller. The vibrations in steady states of the system with the fractional order controller reach smaller values.

Table 3. Comparison of the simulations results

Controller	Settings	Order of of approximation	Rotating speed [Hz]	Settling time [s]	Settling vibration [m]
PID	First case		30	18	$9 \cdot 10^{-4}$
			32	19	$5.6 \cdot 10^{-3}$
			36	10	$6.4 \cdot 10^{-4}$
	Second case		30	12	$5.6 \cdot 10^{-4}$
			32	14	$4.1 \cdot 10^{-3}$
			36	4	$6.1 \cdot 10^{-4}$
$PI^{\lambda}D$	First case	1-st, 5-th, 11-th	30	4	$4.6 \cdot 10^{-4}$
		1-st, 5-th	32	12	$1.06 \cdot 10^{-2}$
		11-th	32	12	$1 \cdot 10^{-2}$
		1-st, 5-th, 11-th	36	4.5	$6.8 \cdot 10^{-4}$
	Second case	1-st, 5-th, 11-th	30	3	$5.2 \cdot 10^{-4}$
		1-st	32	10	$1.39 \cdot 10^{-2}$
		5-th	32	10	$1.37 \cdot 10^{-2}$
		11-th	32	10	$1.3 \cdot 10^{-2}$
		1-st, 5-th, 11-th	36	6.5	$6.7 \cdot 10^{-4}$

5. Conclusion

Taking into account the coupling between torsional and bending vibrations for the Jeffcott model, an analytical solution has been developed. The inclusion of Eq. $(2.7)_3$ for torsional vibration is used to achieve this result. Numerical simulations of the anisotropic rotor are carried out by applying an unbalance excitation, gravity forces and a torsional excitation. The torsional and lateral vibrations and the settling time are compared by using a different approach to control theory. The classical controller and the fractional order controller are used in the closed loop system. The investigations have been carried out on the effects of the type of controllers on rotor vibration and revealed that PID controllers are more efficient around the point in which they are tuned and have lower resistance to changes in the speed of rotation. For unstable vibrations, better results give systems with the classical PID controller. The authors concluded that a good approach to controlling vibration of the rotor at a stable speed is to build a system with switching parameters of the $FOPID$ controller relative to the rotational speed. A real life problem may be still the proper choice of actuators corresponding to the reaction to changes in the stiffness control signal of the rotor and, more specifically, in its bearing. However, the proposed concept of a new method of control for an anisotropic rotor using a fractional order controller requires experimental confirmation, which is underway.

Acknowledgements

The authors acknowledge the financial support by Faculty of Mechanical Engineering, Bialystok University of Technology (MB/WM/7/2014).

References

1. Astrom K., Hagglund T., 1995, *PID Controllers: Theory, Design and Tuning*, Instrument Society of America
2. Biswas A., Das S., Abraham A., Dasgupta S., 2009, Design of fractional-order $PI^{\lambda}D^{\mu}$ controllers with an improved differential evolution, *Engineering Applications of Artificial Intelligence*, **22**, 343-350

3. Gan C.B., Wang Y.H., Yang S.X., Cao Y.L., 2014, Nonparametric modeling and vibration analysis of uncertain Jeffcott rotor with disc offset, *International Journal of Mechanical Sciences*, **78**, 126-134

4. Gosiewski Z., 2008a, Analysis of coupling mechanism in lateral/torsional rotor vibrations, *Journal of Theoretical and Applied Mechanics*, **46**, 4, 829-844

5. Gosiewski Z., 2008b, Control-oriented modelling and control of rotor vibration, *Acta Mechanica et Automatica*, **2**, 2, 21-38

6. Gosiewski Z., Muszyńska A., 1992, *Dynamics of Rotating Machinery* (in Polish), Wydaw. Wyższej Szkoły Inżynierskiej, Koszalin

7. Lalanne M., Ferraris G., 1998, *Rotordynamics Prediction in Engineering*, John Wiley & Sons Ltd.

8. Ma H., Li H., Niu H., Song R, Wen B., 2013, Nonlinear dynamic analysis of a rotor-bearing-seal system under two loading conditions, *Journal of Sound and Vibration*, **332**, 6128-6154

9. Merrikh-Bayat F., 2011, Efficient method for time-domain simulation of the linear feedback systems containing fractional order controllers, *ISA Transactions*, **50**, 2, 170-176

10. Merrikh-Bayat F., 2012, Rules for selecting the parameters of Oustaloup recursive approximation for the simulation of linear feedback systems containing $PI^{\lambda}D^{\mu}$ controller, *Communications in Nonlinear Science and Numerical Simulation*, **17**, 1852-1860

11. Oustaloup A., Levron F., Mathieu B., Nanot F., 2000, Frequency-band complex noninteger differentiator: characterization and synthesis, *IEEE Transactions on Circuits and Systems. I: Fundamental Theory and Applications*, **47**, 1, 25-39

12. Podlubny I., 1999, Fractional-order systems and $PI^{\lambda}D^{\mu}$-controllers, *IEEE Transactins on Automatic Control*, **44**, 1

13. Sawicki J.T., Baaklini G.Y., Gyekenyesi A.L., 2004, Dynamic analysis of accelerating cracked flexible rotor, *Turbo ASME Turbo Expo Conference*

14. Valsa J., Brancik L., 1998, Approximate formulae for numerical inversion of Laplace transforms, *International Journal of Numerical Modelling: Electronic Networks, Devices and Fields*, **11**, 153-166

15. Vinagre B.M., Podlubny I., Hernandez H., Feliu V., 2000, Some approximations of fractional order operators used in control theory and applications, *Fractional Calculus and Applied Analysis*, **3**, 3, 231-248

16. Xue D., Chen Y.Q., Atherton D., 2001, Linear feedback control – analysis and design with Matlab 6.5, *Advances in Design and Control*

Manuscript received March 17, 2015; accepted for print December 27, 2015

JOURNAL OF THEORETICAL AND APPLIED MECHANICS
54, 3, pp. 1025-1037, Warsaw 2016
DOI: 10.15632/jtam-pl.54.3.1025

MODELLING OF THE VIBRATION EXPOSURE IN TYPICAL WORKING MACHINES BY MEANS OF RANDOM INPUT SIGNALS

Igor Maciejewski, Tomasz Krzyżyński

Koszalin University of Technology, Faculty of Technology and Education, Koszalin, Poland

e-mail: igor.maciejewski@tu.koszalin.pl; tomasz.krzyzynski@tu.koszalin.pl

The aim of the paper is to formulate a generalized methodology of modelling random vibrations that are experienced by machine operators during their work. In the following paper, spectral characteristics of input vibrations are specified in such a way that the generated excitation signals are representative for different types of working machines. These signals could be used for determination and evaluation of risks from exposure to whole-body vibration.

Keywords: simulated input vibration, random vibration

1. Introduction

There are two basic sources of mechanical vibrations that can disturb proper functioning of machines. The first one relates to systems that during their operation generate vibrations, e.g. engine vibrations in the working machine (Preumont, 2002). The second class concerns systems that vibrate due to external factors, e.g. cab vibrations of the machine that is moving over uneven ground (Maciejewski and Krzyżyński, 2011; Nabaglo *et al.*, 2013). Many sources of vibrations can cause periodic or random reactions of machine elements (Sapiński and Rosół, 2007; Maślanka *et al.*, 2007). In such a situation, resonant states can be obtained and they may cause disturbances in motion of individual machine elements. Resonant vibrations have an adverse effect on machine functioning, and this can lead to their failure. In addition, vibrations have a negative influence on health of operators of working machines.

Machine operators during their work are exposed to vibrations that are caused very often by motion of machinery over uneven ground (Kowal *et al.*, 2008; Snamina *et al.*, 2013). In the case of whole-body vibration, the seat of a vehicle or the platform of a worker vibrates and this motion is transmitted into the human body. Under normal operating conditions, humans occupy the following body positions (Griffin *et al.*, 2006):

- sitting position (mechanical vibrations transmitted through pelvis) that precludes active damping of vibration using lower limbs,
- standing position (mechanical vibrations transmitted through feet) that allows active damping of vibration in the low frequency range.

The basic positions of the human body at work are presented in Fig. 1. Harmful vibrations can be transmitted to the human body in three orthogonal directions: longitudinal x, lateral y and vertical z. Vibrations are defined by their magnitudes and frequencies. The magnitudes of vibration are traditionally expressed as vibration acceleration, because most vibration transducers produce an output that is related to the acceleration signal. Frequencies appearing in the random whole-body vibration environment usually occur between 1 and 20 Hz (Krzyzynski *et al.*, 2004). Exposure to whole-body vibration causes motions and forces within the human body that may cause discomfort, adversely affect working performance and cause health and safety risk (Griffin *et al.*, 2006).

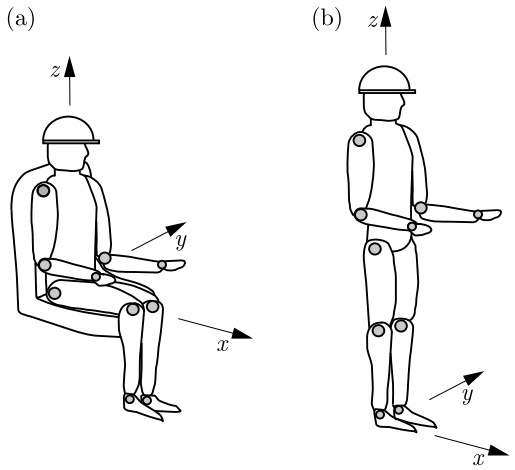

Fig. 1. Positions of the human body at work: sitting position (a), standing position (b)

The basic opportunity to minimise harmful vibrations consists in applying a vibration reduction system that prevents propagation of mechanical vibrations from their source to the isolated body (Kowal *et al.*, 2008). Dynamic characteristics of a vibration isolator should be selected for a specific application in such a way that the vibrations transmitted from the source to the body are minimal (Snamina *et al.*, 2013). In order to analyze dynamics of a vibration isolation system, the excitation signal with specific spectral characteristics should be used. Unfortunately, there are no effective methods for generating signals representing the working of different machinery. In the papers [3], [7], [8], the target spectral characteristics are only standardised for the simulated input vibration test in the vertical direction. There is a lack of effective procedures of generating the time history of random signals with precisely defined spectral properties. In addition, it is not known how to reproduce the excitation signals based on the measured spectral characteristics (Bluthner *et al.*, 2008), especially in horizontal directions (lateral and longitudinal).

In the following paper, an effective method of reproducing random vibration in different types of working machines is proposed for the purpose of selecting dynamic characteristics of vibration reduction systems. At first, machines having similar operational vibration are grouped by virtue of various mechanical characteristics. Then a signal generator is utilized to generate random vibration and an original signal processing technique is used in order to obtain the spectral characteristics representing vibration in a specific group of machines.

2. Modelling of the vibration reduction system

The general model of the vibration reduction system used in typical working machines is presented in Fig. 2. The suspended body is isolated against harmful vibrations in three orthogonal directions: longitudinal x, lateral y and vertical z. The passive visco-elastic elements are used in order to minimise the human exposure to whole-body vibration. Rotation vibrations around each axis of the Cartesian coordinate system (x, y, z) are neglected in this simplified model. Ongoing research (Maciejewski *et al.*, 2011) indicates that the exposure of workers to risks arising from vibration are evaluated for translational axes, therefore in this paper, vibro-isolation properties are discussed for this specific direction. The equation of motion for such a system is formulated in the matrix form

$$\mathbf{M}_i\ddot{\mathbf{q}}_i + \mathbf{D}_i\dot{\mathbf{q}}_i + \mathbf{C}_i\mathbf{q}_i = \mathbf{F}_{si} \qquad i = x, y, z \tag{2.1}$$

where $\mathbf{q}_i$ is the displacement vector of the isolated body, $\mathbf{M}_i$, $\mathbf{D}_i$, $\mathbf{C}_i$ are the inertia, damping and stiffness matrices, respectively, $\mathbf{F}_{si}$ is the vector of exciting forces describing the non-linear vibration isolator.

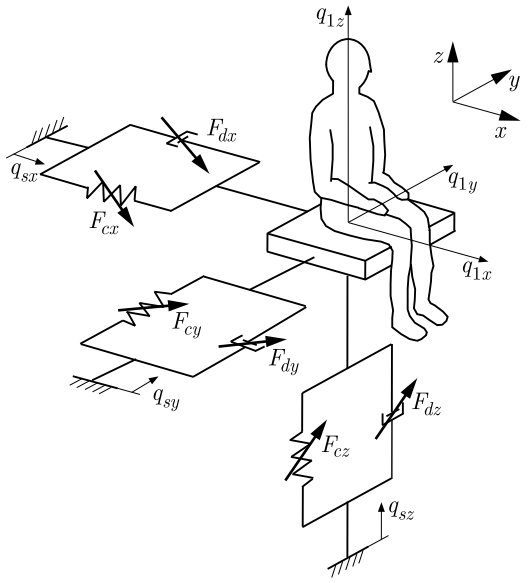

Fig. 2. General model of the non-linear vibration reduction system used in typical working machines

There are dozens of human body models presented in the modern literature (Rutzel *et al.*, 2006; Stein *et al.*, 2007; Toward and Griffin, 2011). Usually, there are multi-degree of freedom lumped parameter models that consider the seating and standing position. In this paper, the generalised mathematical model of vibration reduction system is presented that allows one to use various bio-mechanical structures of the well-known human body models. The n-element vector $\mathbf{q}_i$ represents the movement of elements contained in the bio-mechanical model of the human body

$$\mathbf{q}_i = [q_{1i}, q_{2i}, \ldots, q_{ni}]^{\mathrm{T}} \qquad i = x, y, z \tag{2.2}$$

where: $q_{1i}, q_{2i}, \ldots, q_{ni}$ are displacements of the human body model. The n-element vector of exciting forces $\mathbf{F}_{si}$ is given by the following expression

$$\mathbf{F}_{si} = [F_{si}, 0, \ldots, 0]^{\mathrm{T}} \qquad i = x, y, z \tag{2.3}$$

The particular non-linear exciting forces F_{si} can be described in a general form as follows

$$F_{si} = \sum_{k=1}^{l} F_{dik}(\dot{q}_{1i} - \dot{q}_{si}) + \sum_{k=1}^{l} F_{cik}(q_{1i} - q_{si}) \qquad i = x, y, z \tag{2.4}$$

where: $F_{cik}(q_{1i} - q_{si})$ are non-linear functions including force characteristics of the conservative elements as a function of the system relative displacement $q_{1i} - q_{si}$, $F_{dik}(\dot{q}_{1i} - \dot{q}_{si})$ are non--linear functions including force characteristics of the dissipative elements as a function of the system relative velocity $\dot{q}_{1i} - \dot{q}_{si}$. These non-linear characteristics should be selected especially for well-defined input vibrations by using appropriate element models. Exemplary models can be found in the authors' previous paper (Maciejewski *et al.*, 2011). The input displacement q_{si} and velocity $\dot{q}_{si}$ are modelled as discrete-time random signals that are generated for the specific direction of vibration exposure ($i = x, y, z$).

Modelling of the random vibration acceleration $\ddot{q}_{si}(t)$ occurring in typical working machines is presented in the next part of the following paper. The elaborated signal models allow one to

test a variety of vibration reduction systems by means of the laboratory measurements and/or numerical simulations. The proposed method can be used for generating signals specified by the present test standards, see [3], [7], [8] and also for reproducing signals measured by other authors (Bluthner *et al.*, 2008). The requirements regarding limitations of the vibration simulator (shaker) can be found in International Standards ([3], [7], [8]). Safety requirements for the test person are exhaustively discussed in ISO-2613 [6].

3. Random signal generator

The simulated input vibration is generated using a normally (Gaussian) distributed random numbers (rand) that produces a waveform

$$\ddot{q}_{sij}(t) = \sqrt{\sigma^2_{sij}}\mathrm{rand}\Big(\frac{t_k}{t_s}\Big) \qquad i = x, y, z \qquad j = 1, \ldots, l \tag{3.1}$$

where: $q_{sij}(t)$ is vibration acceleration generated in the direction x, y, z, $j = 1, \ldots, l$ is the number of signal generator, σ^2_{sij} is the variance of random numbers, t is the current time instant, t_k is the computation time, t_s is the time interval between samples.

In order to simulate the effect of white noise with a correlation time near 0 and a flat power spectral density, a sampling time should be much smaller than the fastest dynamics of the system. For intended analysis with high resolution, an acceptable random signal can be achieved by specifying the sampling frequency 100 times (or more) of the maximal frequency of the system to be tested. Therefore, the time interval between samples of the random signal is $t_s = 0.01/f_{max}$, where f_{max} is the maximal frequency of the system in Hz. For generation of vibration up to 20 Hz, the maximal frequency of the random signal is set to 25 Hz.

The probability density function of a normally distributed random signal can be described using the following relation

$$p(\ddot{q}_{sij}(t)) = \frac{1}{\sqrt{2\pi\sigma^2_{sij}}}\exp\Big(-\frac{1}{2\sigma^2_{sij}}\ddot{q}^2_{sij}(t)\Big) \qquad i = x, y, z \qquad j = 1, \ldots, l \tag{3.2}$$

The time plot of a stochastic signal $\ddot{q}_{sij}(t)$ is shown in Fig. 3a, and its histogram on the background of the probability density function is illustrated in Fig. 3b.

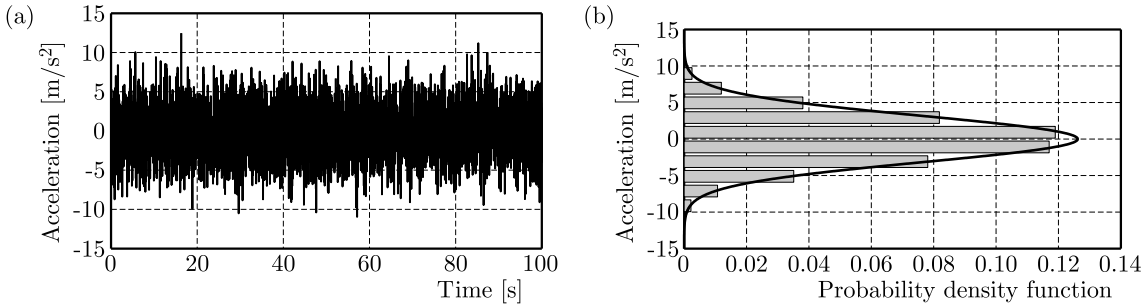

Fig. 3. Input vibration generated as a normally distributed random process (a) and its histogram (grey box) on the background of the probability density function (black line) (b)

The spectral properties of the generated random signal have to be close to white noise, so the power spectral density (PSD) should be flat in the considered frequency range, and the correlation time of a time series shall be close to zero (Bendat and Piersol, 2004). The power spectral density and the normalized auto-correlation of the generated signal are presented in Fig. 4.

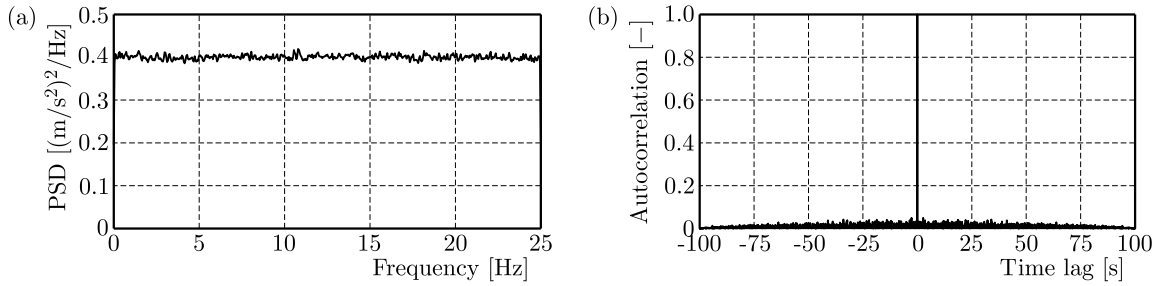

Fig. 4. Power spectral density (a) and normalized autocorrelation (b) of the generated random signal

4. Signal processing technique

An original signal processing technique is proposed in order to obtain specific spectral properties of the generated random signal. This technique involves the making use of a set of the Butterworth filters (high-pass and low-pass). A block diagram of the proposed signal processing technique is shown in Fig. 5.

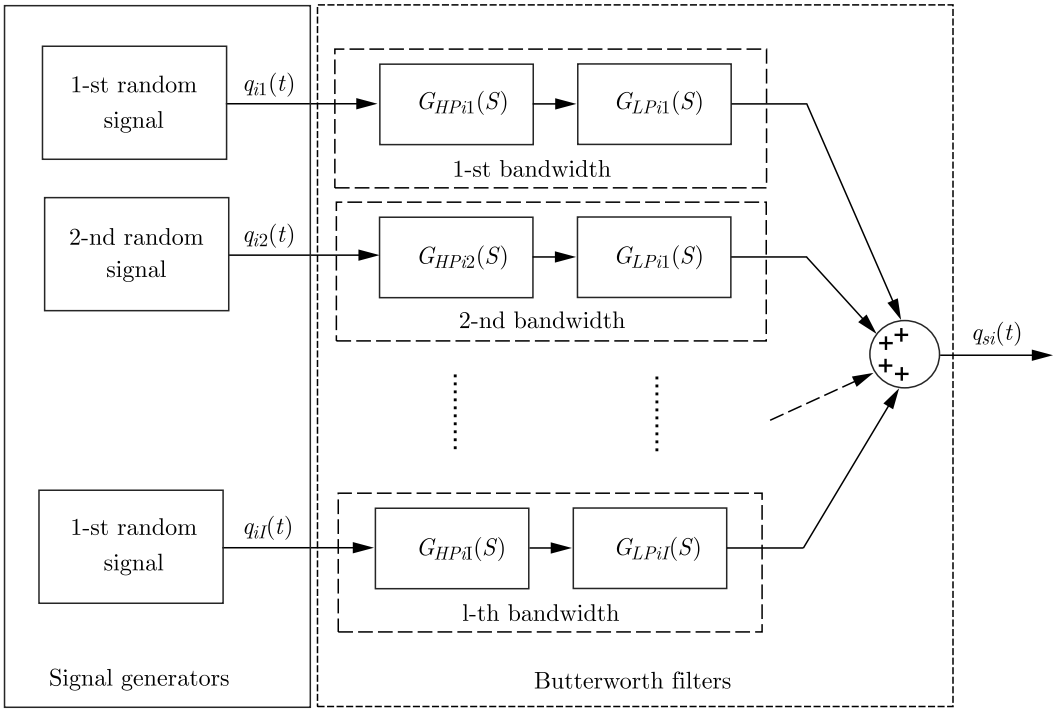

Fig. 5. Block diagram of the proposed signal processing technique

Transfer functions for the linear Butterworth filters are defined in the following way (Parks and Burrus, 1987):

— high-pass filter

$$G_{HPsij}(s) = \frac{s^n}{s^n + a_{n-1}s^{n-1} + \ldots + a_1 s + 1} \qquad i = x, y, z \qquad j = 1, \ldots, l \tag{4.1}$$

— low-pass filter

$$G_{LPsij}(s) = \frac{1}{s^n + a_{n-1}s^{n-1} + \ldots + a_1 s + 1} \qquad i = x, y, z \qquad j = 1, \ldots, l \tag{4.2}$$

where: a_1 to a_n are the coefficients of the Butterworth filter specified in Table 1, n is the order of the filter, s is the Laplace variable, $j = 1, \ldots, l$ is the number of filters used.

Table 1. Coefficients of the Butterworth filter $a_1, \ldots, a_n$ for different filter orders n

n	a_1	a_2	a_3	a_4	a_5	a_6	a_7
2	1.414	–	–	–	–	–	–
3	2.000	2.000	–	–	–	–	–
4	2.613	3.414	2.613	–	–	–	–
5	3.236	5.236	5.236	3.236	–	–	–
6	3.863	7.464	9.141	7.464	3.863	–	–
7	4.493	10.097	14.591	14.591	10.097	4.493	–
8	5.125	13.137	21.846	25.688	21.846	13.137	5.125

The high-pass and low-pass filters (Eqs. (4.1) and (4.2)) allows one to create the required band-pass filter for a specified frequency bandwidth. A combination of the high-pass and low--pass filters at the defined cut-off frequency and filter order provides generating of the input vibration with various spectral characteristics. The transfer function of the total filter is defined as follows

$$G_{si}(s) = \frac{N_{si}(s)}{D_{si}(s)} = \sum_{j=1}^{l} G_{HPsij}(s) G_{LPsij}(s) \qquad i = x, y, z \qquad j = 1, \ldots, l \tag{4.3}$$

where: $N_{si}(s)$ and $D_{si}(s)$ are the numerator and denominator polynomials that represent a combination of the Butterworth filters shown in Fig. 5.

The transfer function (Eq. (4.3)) is especially useful when analyzing the proposed filter stability. If all poles of this transfer function have negative real parts, then the filter is considered as asymptotically stable. However, the filter is unstable when any pole has a positive real part. Therefore, all poles in the complex s-plane should be located in the left half plane to ensure filter stability, which can be described by the following relation

$$\mathrm{Re}(D_{si}(s)) < 0 \qquad i = x, y, z \tag{4.4}$$

Pole distribution in the complex s-plane for unstable and stable filter is shown in Fig. 6.

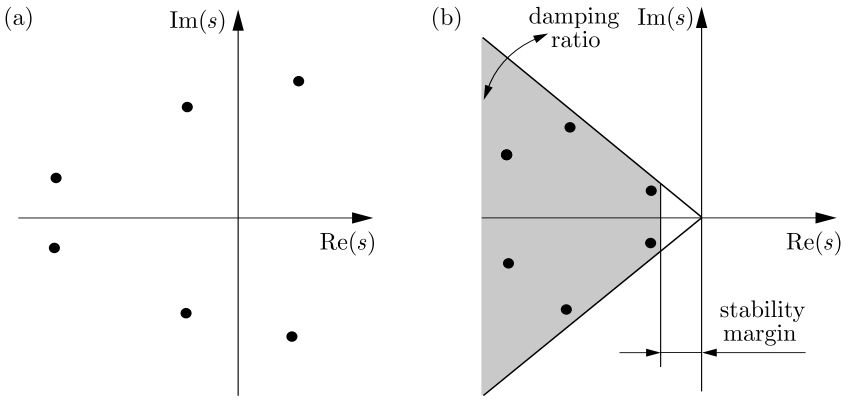

Fig. 6. Pole distribution in the complex s-plane: unstable filter (a), stable filter with stability margin (b)

The input vibration is defined by a power spectral density of the vertical acceleration and by the root mean square value of the acceleration signal. The target magnitude $\mathrm{PSD}_{si}(2\pi f)$ of the power spectral density function can be calculated with the assistance of the following equation

$$\mathrm{PSD}_{si}(2\pi f) = \sum_{j=1}^{l} \frac{2\sigma_{sij}^2}{f_s} \left| (G_{HPsij}(2\pi f))^2 (G_{LPsij}(2\pi f))^2 \right| \qquad \begin{matrix} i = x, y, z \\ j = 1, \ldots, l \end{matrix} \tag{4.5}$$

where: f is the frequency in Hz, σ_{sij}^2 is the signal variance in a specified frequency bandwidth, f_s is the sampling frequency. The curve defined by Eq. (4.5)) consists of target power spectral density to be produced for the simulated input vibration (Fig. 7).

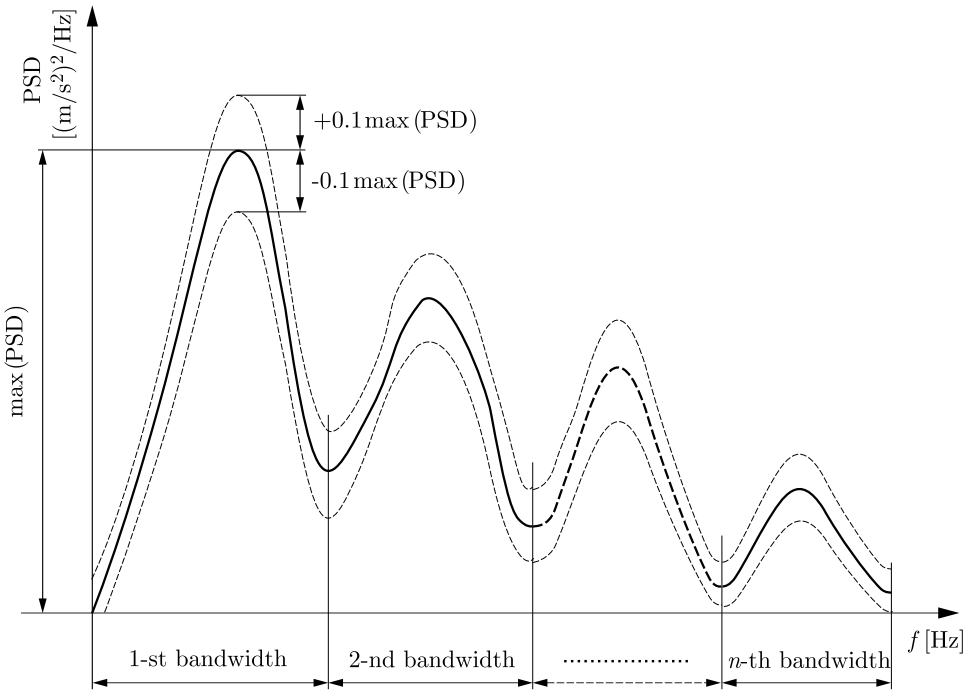

Fig. 7. Target power spectral density of the simulated input vibration

The power spectral density of the simulated acceleration signal is considered to be representative for different types of working machines if and only if ([3], [7], [8]):

- the magnitude of simulated input is within the tolerance of the target power spectral density function $\mathrm{PSD}_{si}(2\pi f) \pm 0.1 \max_f(\mathrm{PSD}_{si}(2\pi f))$,
- the root mean square (RMS) value of simulated input acceleration is within the tolerance of the required value $(\ddot{q}_{si})_{RMS} \pm 0.05(\ddot{q}_{si})_{RMS}$.

The root mean square value of the acceleration signal is defined using the following relation

$$(\ddot{q}_{si})_{RMS} = \sqrt{\frac{1}{t_k}\int_0^{t_k} (\ddot{q}_{si}(t))^2 \, dt} \qquad i = x, y, z \tag{4.6}$$

where: $\ddot{q}_{si}(t)$ is the time history of input vibration and t_k is the duration within which vibration data for analysis is obtained.

5. Spectral estimation method

A novel method is proposed in order to evaluate parameters (signal variances and filter cut-off frequencies) of the system presented in Fig. 5. Such a parametric method allows one to find the system configuration with a magnitude response approximating the desired function (Fig. 8). Therefore, a random signal with the user-defined spectral properties can easily be generated. This is the essence of the importance and novelty of the authors' method in comparison with the spectral estimation methods used by most authors. The proposed method applies the least square error (LSE) minimization technique over the frequency range of the filter response.

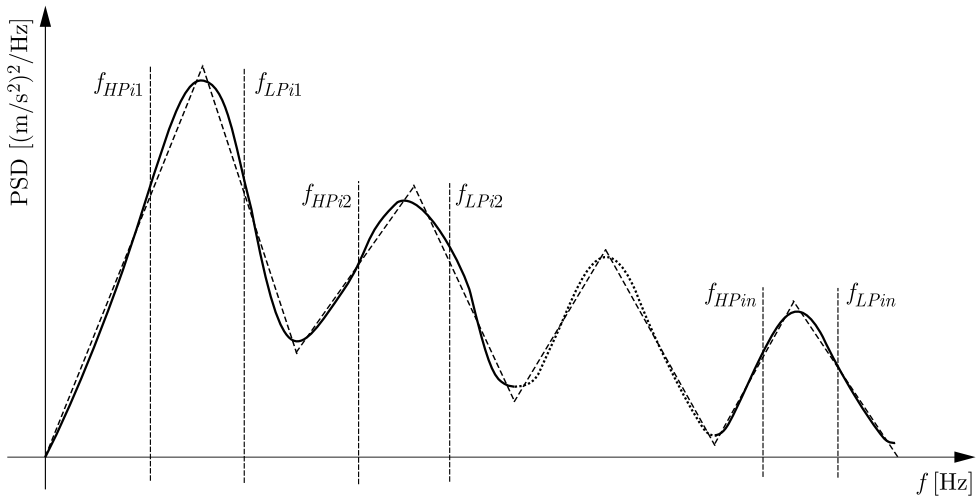

Fig. 8. Magnitude response (—) approximating the desired function (- - -)

The least square error of the specified frequency response is described in the following form

$$\mathrm{LSE}_{si} = \sqrt{\sum_{k=1}^{m}\Big(\mathrm{PSD}_{si}(2\pi f_k) - \widehat{\mathrm{PSD}}_{si}(2\pi f_k)\Big)^2} \qquad i = x, y, z \tag{5.1}$$

where: PSD_{si} and $\widehat{\mathrm{PSD}}_{si}$ are the desired and estimated power spectral densities that are obtained for the same frequency value f_k.

The error minimization includes design parameters having an influence on the spectral characteristics of the generated signal as follows

$$\min_{\sigma^2_{sij}, f_{HPsij}, f_{LPsij}} \mathrm{LSE}_{si}(\sigma^2_{sij}, f_{HPsij}, f_{LPsij}) \qquad i = x, y, z \qquad j = 1, \ldots, l \tag{5.2}$$

where: σ^2_{sij} is the variance of the random signal, f_{HPsij} and f_{LPsij} are the cut-off frequencies of the high-pass and low-pass Butterworth filters, respectively.

The problem of minimizing the objective function (Eq. (5.2)) of several parameters (decision variables) is defined subject to linear inequality constraints on these variables

$$\begin{aligned} &(\sigma^2_{sij})_{min} \leqslant \sigma^2_{sij} \leqslant (\sigma^2_{sij})_{max} \\ &(f_{HPsij})_{min} \leqslant f_{HPsij} \leqslant (f_{HPsij})_{max} \qquad i = x, y, z \qquad j = 1, \ldots, l \\ &(f_{LPsij})_{min} \leqslant f_{LPsij} \leqslant (f_{LPsij})_{max} \end{aligned} \tag{5.3}$$

where: $(\sigma^2_{sij})_{min}$ and $(\sigma^2_{sij})_{max}$ are the lowest and highest value of the signal variance, $(f_{HPsij})_{min}$ and $(f_{HPsij})_{max}$ are the lowest and highest value of the cut-off frequencies of the high-pass filter, $(f_{LPsij})_{min}$ and $(f_{LPsij})_{max}$ are the lowest and highest value of the cut-off frequencies of the low-pass filter.

Additionally, nonlinear inequality constraints are imposed on the objective function (Eq. (5.2)) to restrict the filter cut-off frequencies in the following order

$$f_{HPsi1} \leqslant f_{LPsi1} \leqslant f_{HPsi2} \leqslant f_{LPsi2}, \ldots, \leqslant f_{HPsij} \leqslant f_{LPsij} \qquad \begin{matrix} i = x, y, z \\ j = 1, \ldots, l \end{matrix} \tag{5.4}$$

where: $j = 1, \ldots, l$ is the number of low-pass (LP) and high-pass (HP) filters used to estimate the input vibration in different directions ($i = x, y, z$).

The multiple correlation coefficient (R) is employed in order to measure how successful is the approximation in explaining the variation of the optimisation results. This coefficient is defined as follows

$$R_{si} = \sqrt{1 - \frac{\sum_{k=1}^{m}\left(\widehat{\mathrm{PSD}}_{si}(2\pi f_k) - \mathrm{PSD}_{si}(2\pi f_k)\right)^2}{\sum_{k=1}^{m}\left(\mathrm{PSD}_{si}(2\pi f_k) - \overline{\mathrm{PSD}}_{si}(2\pi f_k)\right)^2}} \qquad i = x, y, z \tag{5.5}$$

where: $\widehat{\mathrm{PSD}}_{si}$ is the estimated power spectral density for the directions x, y, z, PSD_{si} is the desired power spectral density, $\overline{\mathrm{PSD}}_{si}$ is the mean value of the desired power spectral density, f_k is the discrete value of frequency. The coefficient R_{si} can take any value between 0 and 1, with a value closer to 1 indicating a better estimation of the power spectral density.

6. Vertical vibration

The standards ([3], [7], [8]) specify the laboratory simulated vertical vibration (z-axis) that is based on representative measured data from different types of machines in typical working conditions. The input spectral classes are defined for machines having similar mechanical characteristics. The test inputs indicated in these standards are based on a large number of measurements taken in situ of working machines while they were used under severe operating conditions.

International Standard ISO 7096 [7] specifies input vibrations for earth-moving machinery in nine spectral classes (EM1-EM9). British Standard BS EN 13490 [3] defines the input spectral classes required for industrial trucks (IT1-IT4). ISO 5007 standard [8] specifies input vibration in three input spectral classes (AG1-AG3) for agricultural tractors with rubber tyres, unsprung rear axles and no low-frequency cab isolation. Each class defines a group of machines having similar vibration characteristics.

All of these standards completely designate high-pass and low-pass filters of the Butterworth type that are required for generating vibration along the vertical axis. Numerical values of the cut-off frequencies and filter orders are presented in Table 2. The vibration characteristics for selected input spectral classes, i.e. EM1, EM5-EM7, IT2-IT3, AG1-AG2 and their tolerances, are shown in Fig. 9. The desired and obtained root mean square values of the acceleration signal are defined in Table 2.

Table 2. Parameters of the input vibration generated for different types of working machines

			Signal generators			High-pass filters						Low-pass filters						Results	
			σ^2_{sij}, $[(\frac{\mathrm{m}}{\mathrm{s}}{}^2)^2]$			f_{HPsij} [Hz]			n_{HPsij}			f_{LPsij} [Hz]			n_{LPsij}			$(\ddot{q}_{si})_{RMS}$, $[\frac{\mathrm{m}}{\mathrm{s}}{}^2]$	
Type of machines	Input vibration	i	j			j			j			j			j			Desi-	Obta-
			1	2	3	1	2	3	1	2	3	1	2	3	1	2	3	red	ined
Earth moving machinery	EM1	z	282	–	–	1.5	–	–	4	–	–	2.5	–	–	4	–	–	1.71	1.67
	EM5	z	111	–	–	1.5	–	–	4	–	–	3.5	–	–	1	–	–	1.94	2.10
	EM6	z	79	–	–	6.5	–	–	2	–	–	9	–	–	2	–	–	1.65	1.70
	EM7	z	925	–	–	3	–	–	8	–	–	3.5	–	–	8	–	–	2.25	2.27
Industrial trucks	IT2	z	145	–	–	3	–	–	4	–	–	3	–	–	2	–	–	1.05	1.05
	IT3	z	60	–	–	1.5	–	–	4	–	–	3	–	–	4	–	–	0.96	0.94
Agricultural tractors	AG1	z	925	–	–	3	–	–	8	–	–	3.5	–	–	8	–	–	2.26	2.27
	AG2	z	722	–	–	2.1	–	–	8	–	–	2.6	–	–	8	–	–	1.94	1.91
Agricultural tractor	AT1	x	335	51	27.1	2	5.2	9.7	8	4	4	2.4	5.7	12	4	4	4	1.62	1.69
		y	728	165	27.3	1.1	3	7.7	8	4	4	1.3	3.4	10	8	4	4	1.86	1.84
Articulated truck	AL1	x	7.9	6,8	3.7	0.2	1.3	5.7	8	4	4	1.2	2.3	7	8	4	2	0.50	0.49
		y	15.7	21.9	1.8	0.4	2	6	4	8	4	1.5	2.4	14	4	8	2	0.62	0.63

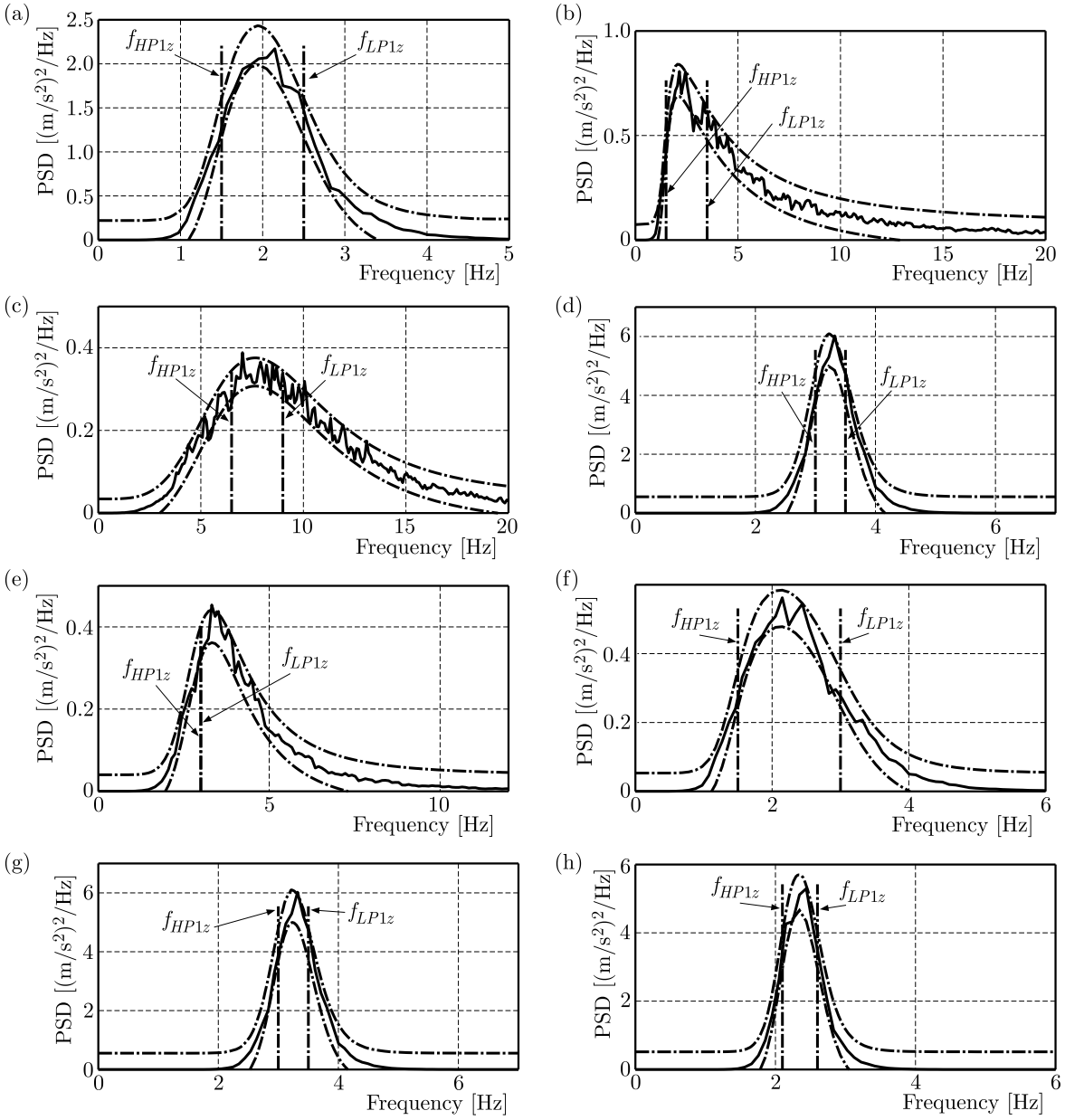

Fig. 9. Power spectral densities of simulated vertical input vibration (—) for spectral classes: EM1 (a), EM5 (b), EM6 (c), EM7 (d), IT2 (e), IT3 (f), AG1 (g), AG2 (h) and their tolerances (- - -)

7. Horizontal vibration

In contrary to vertical vibration, there are no standardised signals available for the horizontal directions (x-axis and y-axis). Therefore, this paper specifies input vibrations for selected spectral classes and each class consisting of longitudinal and lateral cabin floor vibration for particular working machines performing a specific operation. In the paper by Bluthner *et al.* (2008), the test inputs were measured as a part of the study that has been done within the framework of the European research project VIBSEAT. They do not have sufficient magnitudes to cover the majority of actual spectra observable on the field. The determination of representative spectra represents a large amount of work which is not the purpose of this paper.

There are no designated Butterworth filters that are desired for generating vibration along the horizontal axes. Therefore, at first, PSD functions of these signals are determined using the spectral estimation method shown in Section 5. Then the variance of random signals and the cut-off frequencies of filters are evaluated using the objective function described by Eq. (5.2). Numerical values of the design parameters are presented in Table 2. The spectral characteristics of measured, estimated and simulated input vibrations, i.e. AT1, AL1 and their tolerances for the x and y axes, are shown in Fig. 10. The desired and obtained root mean square values of the acceleration signal are defined in Table 2.

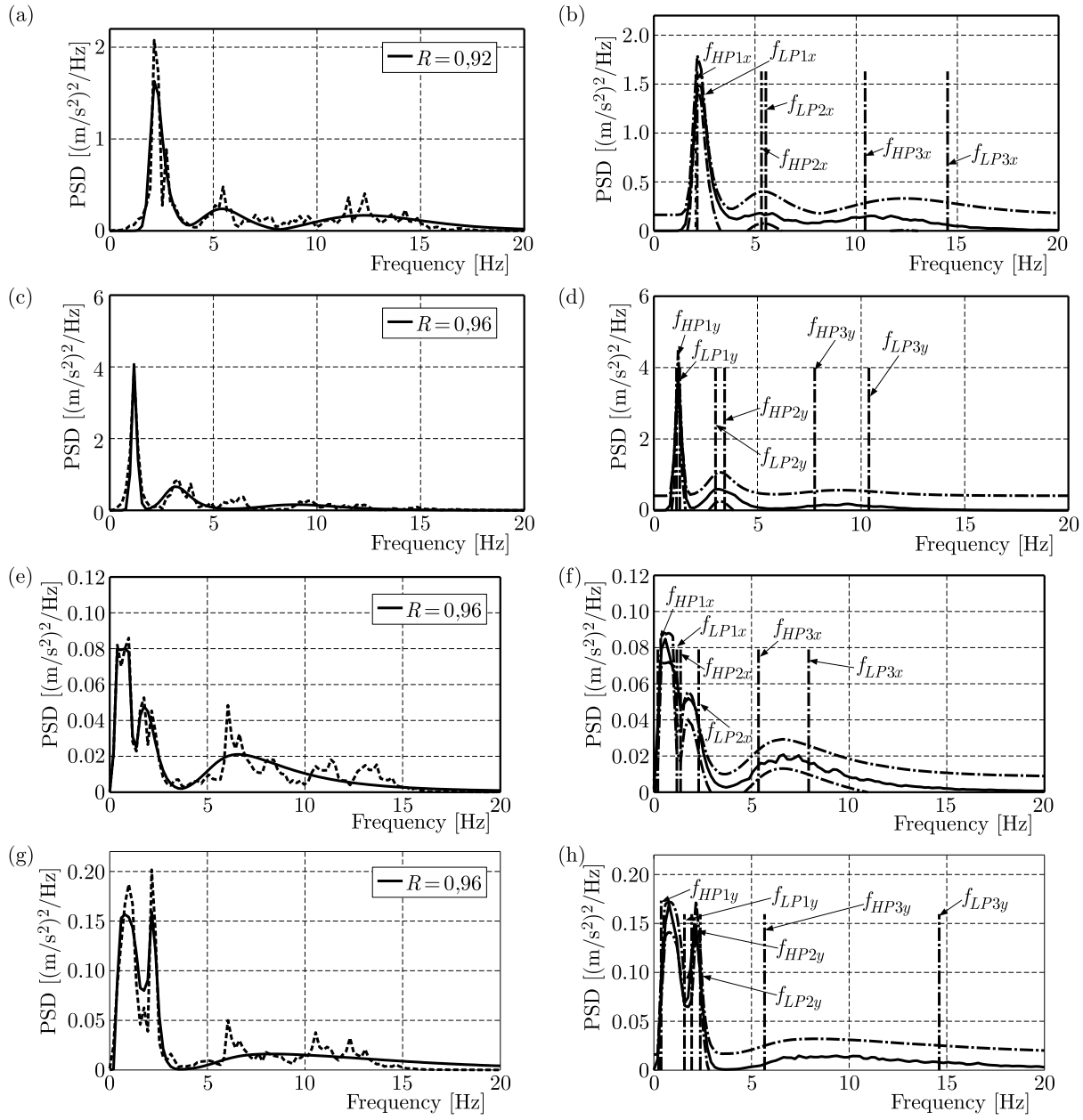

Fig. 10. Power spectral densities of measured (- - -), estimated (—) (left-hand side) and simulated (—) (right-hand side) horizontal input vibrations for spectral classes: AT1 x-axis (a), (b), AT1 y-axis (c), (d), AL1 x-axis (e), (f), AL1 y-axis (g), (h) and their tolerances (-·-·-)

8. Conclusions

In this paper, the theoretical models of simulated input vibrations are developed in such a way that the specific spectral properties of signals are obtained using the original filtration technique. This is the basis of the proposed procedure for generating random vibration that is representative for vibrations affecting the operators at work. The models developed in this paper can be used to reproduce the real working conditions of vibration reduction systems in different types of machines. Investigations carried out using the proposed signals should assist a selection process of vibro-isolation properties of systems for different spectral classes of the input vibrations.

Acknowledgements

The following work has been a part of the research project "Methods and procedures of selecting vibro-isolation properties of vibration reduction systems" funded by the National Science Center of Poland under the contract No. UMO-2013/11/B/ST8/03881.

References

1. Bendat J.S., Piersol A.G., 2004, *Methods for Analysis and Measurement of Random Signals* (in Polish), Polish Scientific Publishers PWN, Warsaw
2. Bluthner R., Seidel H., Hinz B., 2008, Laboratory study as basis of the development for a seat testing procedure in horizontal directions, *International Journal of Industrial Ergonomics*, **38**, 447-456
3. British Standards Institution BS EN 13490, 2002, Mechanical vibration – Industrial trucks – Laboratory evaluation and specification of operator seat vibration, London
4. Directive 2002/44/EC of the European Parliament and of the Council, 2002, On the minimum health and safety requirements regarding the exposure of workers to the risks arising from physical agents (vibration), Official Journal of the European Communities, 13-18
5. Griffin M.J., Howarth H.V.C., Pitts P.M., Fischer S., Kaulbars U., Donati P.M., Bereton P.F., 2006, Guide to good practice on whole-body vibration. Non-binding guide to good practice with a view to implementation of Directive 2002/44/EC on the minimum health and safety requirements regarding the exposure of workers to the risks arising from physical agents (vibrations), European Commission, Luxembourg
6. International Organization for Standardization, 1997, Mechanical vibration and shock – Evolution of human exposure to whole body vibration, ISO 2631, Genewa
7. International Organization for Standardization, 2000, Earth-moving machinery – Laboratory evaluation of operator seat vibration, ISO 7096, Genewa
8. International Organization for Standardization, 2003, Agricultural wheeled tractors – Operator's seat – Laboratory measurement of transmitted vibration, ISO 5007, Genewa
9. Kowal J., Pluta J., Konieczny J., Kot A., 2008, Energy recovering in active vibration isolation system – results of experimental research, *Journal of Vibration and Control*, **14**, 7, 1075-1088
10. Krzyzynski T., Maciejewski I., Chamera S., 2004, Modeling and simulation of active system of truck vibroisolation with biomechanical model of human body under real excitation, *VDI Publications (The Association of German Engineers)*, **1821**, 377-390
11. Maciejewski I., Kiczkowiak T., Krzyzynski T., 2011, Application of the Pareto-optimal approach for selecting dynamic characteristics of seat suspension systems, *Vehicle System Dynamics*, **49**, 12, 1929-1950
12. Maciejewski I., Krzyżyński T., 2011, Control design of semi-active seat suspension, *Journal of Theoretical and Applied Mechanics*, **49**, 4, 1151-1168

13. Maślanka M., Sapiński B., Snamina J., 2007, Experimental study of vibration control of a cable with an attached MR damper, *Journal of Theoritical and Applied Mechanics*, **45**, 4, 893-917

14. Nabaglo T., Kowal J., Jurkiewicz A., 2013, Construction of a parametrized tracked vehicle model and its simulation in MSC.ADAMS program, *Journal of Low Frequency Noise Vibration and Active Control*, **32**, 1/2, 167-173

15. Parks T.W., Burrus C.S., 1987, *Digital Filter Design*, John Wiley & Sons, New York

16. Preumont A., 2002, *Vibration Control of Active Structures An Introduction*, Kluwer Academic Publishers, London

17. Rutzel S., Hinz B., Wolfel H.B., 2006, Modal description – a better way of characterizing human vibration behavior, *Journal of Sound and Vibration*, **298**, 810-823

18. Sapiński B., Rosół M., 2007, MR Damper performance for shock isolation, *Journal of Theorethical and Applied Mechanics*, **45**, 1, 133-145

19. Snamina J., Kowal J., Orkisz P., 2013, Active suspension based on low dynamic stiffness, *Acta Physica Polonica A*, **123**, 6, 1118-1122

20. Stein G.J, Muka P., Chmurny R., Hinz B., Bluthner R., 2007, Measurement and modelling of x-direction apparent mass of the seated human body - cushioned seat system, *Journal of Biomechanics*, **40**, 1493-1503

21. Toward M., Griffin J., 2011, The transmission of vertical vibration through seats: influence of the characteristics of the human body, *Journal of Sound and Vibration*, **330**, 6526-6543

Manuscript received April 28, 2015; accepted for print February 16, 2016

JOURNAL OF THEORETICAL AND APPLIED MECHANICS
54, 3, pp. 1039-1049, Warsaw 2016
DOI: 10.15632/jtam-pl.54.3.1039

DYNAMIC RESPONSE OF A SPUR GEAR SYSTEM WITH UNCERTAIN PARAMETERS

Ahmed Guerine

Laboratory Optimization and Reliability in Structural Mechanics LOFIMS, Mechanical Engineering Department, National Institute of Applied Sciences of Rouen, Cedex, France and
Mechanics, Modelling and Manufacturing Laboratory LA2MP, Mechanical Engineering Department, National School of Engineers of Sfax, Sfax, Tunisia; e-mail: ahmedguerine@gmail.com

Abdelkhalak El Hami

Laboratory Optimization and Reliability in Structural Mechanics LOFIMS, Mechanical Engineering Department, National Institute of Applied Sciences of Rouen, Cedex, France

Lassaad Walha, Tahar Fakhfakh, Mohamed Haddar

Mechanics, Modelling and Manufacturing Laboratory LA2MP, Mechanical Engineering Department, National School of Engineers of Sfax, Sfax, Tunisia

In this paper, we propose a new approach for taking into account uncertainties based on the projection on polynomial chaos. The new approach is used to determine the dynamic response of a spur gear system with uncertainty associated to gear system parameters. The simulation results are obtained by the polynomial chaos approach for dynamic analysis under uncertainty. The proposed approach is an efficient probabilistic tool for uncertainty propagation. It has been found to be an interesting alternative to the parametric studies. The polynomial chaos results are compared with Monte Carlo simulations.

Keywords: uncertainty, spur gear system, polynomial chaos approach, gear parameters

1. Introduction

The gearing is the best solution to transmit rotational motion and torque, which offers numerous advantages (Dalpiaz *et al.*, 1996) including mechanical reliability. Furthermore, its mechanical efficiency is of the order of 0.96 to 0.99. But today, several applications require gear transmissions to be more and more reliable, light and having long service life. This requires control of the acoustic broadcast and vibratory behavior of such gearings (Begg *et al.*, 2000).

Several parametric studies (coefficient of friction, assembly of defects, manufacturing defects, eccentricity default,...) have shown great sensitivity of the dynamic behavior of gear systems. However, these parameters assume strong dispersions (Guerine *et al.* 2015a,b). Therefore, it becomes necessary to take into account the uncertainties to ensure the robustness of the analysis. Also, there are several studies on reliability in vibration structures taking into account these uncertainties (Abo Al-kheer *et al.*, 2011; El Hami *et al.*, 1993, 2009; El Hami and Radi, 1996).

Several methods are proposed in the literature. Monte Carlo (MC) simulation is a well-known technique in this field (Fishman, 1996). It can give the entire probability density function of any system variable, but it is often too costly since a great number of samples are required for reasonable accuracy. Parallel simulation (Papadrakakis and Papadopoulos, 1999) and proper orthogonal decomposition (Lindsley and Beran, 2005) are some solutions proposed to circumvent the computational difficulties of the MC method.

Polynomial chaos expansion (PCE) is presented in the literature as a more efficient probabilistic tool for uncertainty propagation. It was first introduced by Wiener (1938) and pioneered

by Ghanem and Spanos (1991) who used Hermite orthogonal polynomials to model stochastic processes with Gaussian random variables. The exponential convergence of such an expansion was shown by Cameron and Martin (1947) and then was generalized to various continuous and discrete distributions using orthogonal polynomials from the so called Askey-scheme (Askey and Wilson, 1985; Xiu and Karniadakis, 2003).

Polynomial chaos (PC) gives a mathematical framework to separate stochastic components of a system response from deterministic ones. The stochastic Galerkin method (Babuska *et al.*, 2004; Le Maître *et al.*, 2001), collocation and regression methods (Isukapalli *et al.*, 1998a,b; Crestaux *et al.* 2009) are used to compute deterministic components called stochastic modes in an intrusive and non-intrusive manner while random components are concentrated in the polynomial basis used. Non-intrusive procedures prove to be more advantageous for stochastic dynamic systems since they need no modifications of the system model, contrary to the intrusive method. In the latter, Galerkin techniques are used to generate a set of deterministic coupled equations from a stochastic system model, and then a suitable algorithm is adapted to obtain stochastic modes.

The capabilities of polynomial chaos have been tested in numerous applications, such as treating uncertainties in environmental and biological problems (Isukapalli *et al.*, 1998a,b), in multibody dynamic systems (Sandu *et al.*, 2006a,b), in solving ordinary and partial differential equations (Williams, 2006; Xiu and Karniadakis, 2002), in component mode synthesis techniques (El Hami and Radi, 1996, Sarsri *et al.*, 2011) and parameter estimation (Saad*et al.*, 2007; Blanchard *et al.*, 2009; Smith *et al.*, 2007).

The main originality of the present paper is that the uncertainty of gear system parameters in the dynamic behavior study of the one stage gear system is taken into account. The main objective is to investigate the capabilities of the new method to determine the dynamic response of a spur gear system subject to uncertain gear parameters. So, an eight degree of freedom system modelling the dynamic behavior of a spur gear system is considered. The modelling of a one-stage spur gear system is presented in Section 2. In the next Section, the theoretical basis of the polynomial chaos is presented. In Section 4, the equations of motion for the eight degrees of freedom are presented. Numerical results are presented in Section 5. Finally in Section 6, to conclude, some comments are made based on the study carried out in this paper.

2. Modelling of a one-stage gear system

The global dynamic model of a one-stage gear system is shown in Fig. 1. This model is composed of two blocks ($j = 1, 2$). Each block (j) is supported by a flexible bearing whose bending stiffness is k_j^x and the traction-compression stiffness is k_j^y.

Wheels (11) and (22) characterize respectively the motor side and the receiving side. The shafts (j) admit some torsional stiffness k_j^θ.

Angular displacements of each wheel are noticed by $\theta_{(i,j)}$ with the indices $j = 1$ to 2 designating the number of the block, and $i = 1$ to 2 designate the two wheels of each block. Moreover, linear displacements of the bearing denoted by x_j and y_j are measured in the plane which is orthogonal to the wheels axis of rotation.

In this study, we model the gear mesh stiffness variation $k(t)$ by a square wave form (Fig. 2). The gear mesh stiffness variation can be decomposed in two elements: an average component denoted by kc, and a time variant one noted by $kv(t)$ (Walha *et al.*, 2009).

The extreme values of the mesh stiffness are defined by

$$k_{min} = -\frac{kc}{2\varepsilon^\alpha} \qquad k_{max} = -k_{min}\frac{2-\varepsilon^\alpha}{\varepsilon^\alpha - 1} \tag{2.1}$$

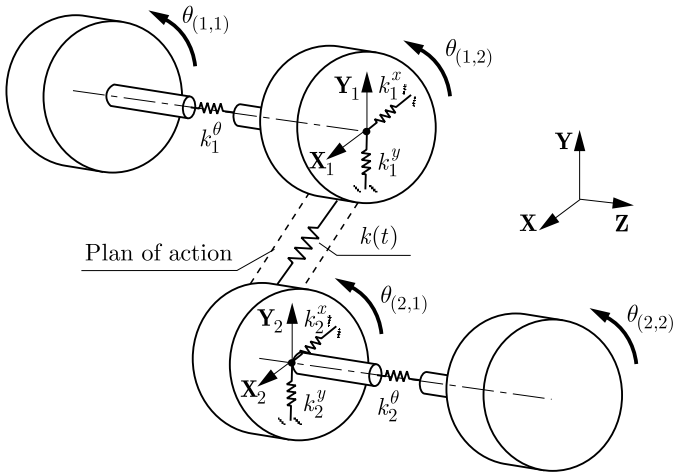

Fig. 1. Global dynamic model of the one stage gear system

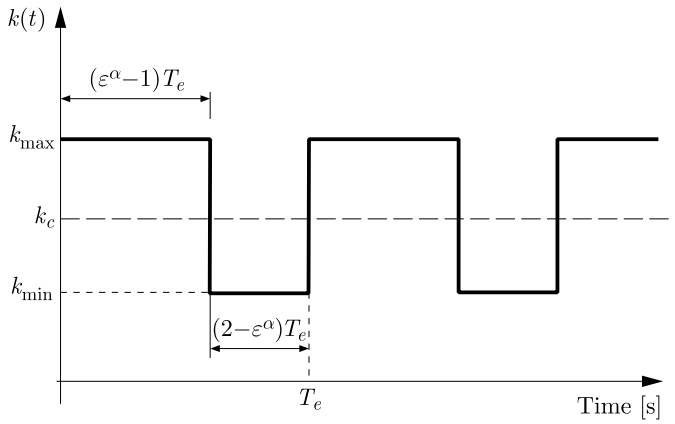

Fig. 2. Modelling of the mesh stiffness variation

where ε^α and Te represent respectively the contact ratio and mesh period corresponding to the two gearmesh contacts.

3. Polynomial chaos approach

In this Section, we propose a new method based on the projection on polynomial chaos. This method consists in projecting stochastic desired solutions on a basis of orthogonal polynomials in which variables are Gaussian orthonormal. The properties of the base polynomial are used to generate a linear system of equations by means of projection. The resolution of this system leads to an expansion of the solution on the polynomial basis, which can be used to calculate the moments of the random solution. With this method, we can easily calculate the dynamic response of a mechanical system.

Let us consider a multi-degrees of freedom linear system with mass and stiffness matrices $\mathbf{M}_T$ and $\mathbf{K}_T$, respectively. The equations of motion describing forced vibration of a linear system are

$$\mathbf{M}_T\ddot{\mathbf{u}}_T(t) + \mathbf{K}_T\mathbf{u}_T(t) = \mathbf{f}_T(t) \tag{3.1}$$

where $\mathbf{u}_T$ is the nodal displacement vector and $\mathbf{f}_T$ is the external excitation.

The chaotic polynomials ψ_m corresponding to the multidimensional Hermite polynomials obtained by formula (3.2)

$$\psi_m(\alpha_1,\ldots,\alpha_P) = (-1)^P \mathrm{e}^{\left(\frac{1}{2}\boldsymbol{\alpha}^{\mathrm{T}}\boldsymbol{\alpha}\right)} \frac{\partial^P \mathrm{e}^{\left(\frac{1}{2}\boldsymbol{\alpha}^{\mathrm{T}}\boldsymbol{\alpha}\right)}}{\partial\alpha_1\cdots\partial\alpha_P} \tag{3.2}$$

where $\boldsymbol{\alpha}$ is the vector grouping the random variables

$$\boldsymbol{\alpha}^{\mathrm{T}} = [\alpha_1,\ldots,\alpha_P] \tag{3.3}$$

The random mass and stiffness matrices $\mathbf{M}_T$ and $\mathbf{K}_T$ of the mechanical system can be written as

$$\mathbf{M}_T = [\mathbf{M}_T]_0 + \widetilde{\mathbf{M}}_T \qquad \mathbf{K}_T = [\mathbf{K}_T]_0 + \widetilde{\mathbf{K}}_T \tag{3.4}$$

where $[\mathbf{M}_T]_0$ and $[\mathbf{K}_T]_0$ are deterministic matrices, $\widetilde{\mathbf{M}}_T$ and $\widetilde{\mathbf{K}}_T$ correspond to the random part of the mass and stiffness matrices. $\widetilde{\mathbf{M}}_T$ and $\widetilde{\mathbf{K}}_T$ are rewritten from an expression of the Karhunen-Loeve type (Ghanem and Spanos, 1991) in the following form

$$\widetilde{\mathbf{M}}_T = \sum_{p=1}^{P} [\mathbf{M}_T]_p \alpha_p \qquad \widetilde{\mathbf{K}}_T = \sum_{p=1}^{P} [\mathbf{K}_T]_p \alpha_p \tag{3.5}$$

where α_p is an independent Gaussian random variable which may correspond to the first polynomial ψ_p, while the matrices $[\mathbf{M}_T]_p$ and $[\mathbf{K}_T]_p$ are deterministic.

We pose $\alpha_0 = 1$, we can write then

$$\mathbf{M}_T = \sum_{p=0}^{P} [\mathbf{M}_T]_p \alpha_p \qquad \mathbf{K}_T = \sum_{p=0}^{P} [\mathbf{K}_T]_p \alpha_p \tag{3.6}$$

In the same way, we can write for $\mathbf{f}_T$

$$\mathbf{f}_T = \sum_{p=0}^{P} \{\mathbf{f}_T\}_p \alpha_p \tag{3.7}$$

The dynamic response is obtained by solving the following equation, knowing that the initial conditions are predefined

$$\mathbf{K}_{eq}\mathbf{u}_T(t+\Delta t) = \mathbf{F}_{eq} \tag{3.8}$$

where

$$\begin{aligned} &\mathbf{K}_{eq} = \mathbf{K}_T + a_0\mathbf{M}_T \\ &\mathbf{F}_{eq} = \mathbf{f}_T(t+\Delta t) + \mathbf{M}_T[a_0\mathbf{u}_T(t) + a_1\dot{\mathbf{u}}_T(t) + a_2\ddot{\mathbf{u}}_T(t)] \end{aligned} \tag{3.9}$$

where

$$a_0 = \frac{1}{A\Delta t^2} \qquad a_1 = \frac{B}{A\Delta t} \qquad a_2 = \frac{1}{A\Delta t} \tag{3.10}$$

A and B are the parameters of the Newmark method. $\mathbf{u}_T(t+\Delta t)$ is decomposed on polynomials to P Gaussian random orthnormal variables, where P is the number of random variables

$$\mathbf{u}_T(t+\Delta t) = \sum_{n=0}^{N} \{\mathbf{u}_T(t+\Delta t)\}_n \, \psi_n(\{\boldsymbol{\alpha}_i\}_{i=1}^{P}) \tag{3.11}$$

where N is the polynomial chaos order. It is the degree of polynomial chaos. $\mathbf{K}_{eq}$ and $\mathbf{F}_{eq}$ are written in the following form

$$\begin{aligned}\mathbf{K}_{eq} &= \sum_{p=0}^{P}[\mathbf{K}_T]_p\alpha_p + a_0\sum_{p=0}^{P}[\mathbf{M}_T]_p\alpha_p = \sum_{p=0}^{P}[\mathbf{K}_{eq2}]_p\alpha_p \\ \mathbf{F}_{eq} &= \sum_{p=0}^{P}\{\mathbf{f}_T(t+\Delta t)\}_p\alpha_p + \sum_{p=0}^{P}[\mathbf{M}_T]_p\alpha_p\Big(a_0\{\mathbf{u}_T(t)\}_0 + a_1\{\dot{\mathbf{u}}_T(t)\}_0 + a_2\{\ddot{\mathbf{u}}_T(t)\}_0\Big) \\ &= \sum_{p=0}^{P}\{\mathbf{F}_{eq2}\}_p\alpha_p\end{aligned} \tag{3.12}$$

Substituting Eqs. (3.11) and (3.12) into Eq. (3.8) and forcing the residual to be orthogonal to the space spanned by the polynomial chaos ψ_m, yields the following system of linear equations

$$\sum_{p=0}^{P}\sum_{n=0}^{N}[\mathbf{K}_{eq2}]_p\{\mathbf{u}_T\}_n\langle\alpha_p\ \psi_n\ \psi_m\rangle = \sum_{p=0}^{P}\{\mathbf{F}_{eq2}\}_p\langle\alpha_p\ \psi_m\rangle \qquad m = 0, 1, \ldots, N \tag{3.13}$$

where $\langle\cdot\ \cdot\rangle$ denotes the inner product defined by the expectation operator.

This algebraic equation can be rewritten in a more compact matrix form as

$$\begin{bmatrix}\mathbf{D}^{00} & \cdots & \mathbf{D}^{0N} \\ & \ddots & \\ \vdots & \mathbf{D}^{ij} & \vdots \\ & \ddots & \\ \mathbf{D}^{N0} & \cdots & \mathbf{D}^{NN}\end{bmatrix}\begin{Bmatrix}\{\mathbf{u}_T(t+\Delta t)\}_0 \\ \vdots \\ \{\mathbf{u}_T(t+\Delta t)\}_j \\ \vdots \\ \{\mathbf{u}_T(t+\Delta t)\}_N\end{Bmatrix} = \begin{Bmatrix}\{\mathbf{f}^{(0)}\} \\ \vdots \\ \{\mathbf{f}^{(j)}\} \\ \vdots \\ \{\mathbf{f}^{(N)}\}\end{Bmatrix} \tag{3.14}$$

where

$$\mathbf{D}^{(ij)} = \sum_{p=0}^{P}[\mathbf{K}_{eq2}]_p\langle\alpha_p\ \psi_i\ \psi_j\rangle \qquad \mathbf{f}^{(j)} = \sum_{p=0}^{P}\{\mathbf{F}_{eq2}\}_p\langle\alpha_p\ \psi_j\rangle \tag{3.15}$$

Due to the orthogonality of the polynomials, most terms $\langle\alpha_p\ \psi_n\ \psi_m\rangle$ are zero. Indeed, we have

$$\langle\psi_i\ \psi_j\rangle_{i\neq j} = 0 \tag{3.16}$$

After resolution of algebraic system (3.14), the mean values and the variances of the dynamic response are given by the following relationships

$$E[\mathbf{u}_T] = \{\mathbf{u}_T(t+\Delta t)\}_0 \qquad \mathrm{Var}[\mathbf{u}_T] = \sum_{n=1}^{N}\Big(\{\mathbf{u}_T(t+\Delta t)\}_n\Big)^2\psi_j^2 \tag{3.17}$$

4. Equations of motion

The equations of motion describing the dynamic behavior of our system (Fig. 1) are obtained by applying Lagrange formulation, and are given by

$$\begin{aligned}
&m\ddot{x}_1 + k_1^x x_1 + \sin(\alpha)k(t)\langle L^\delta\rangle\mathbf{Q} = 0\\
&m\ddot{y}_1 + k_1^y y_1 + \cos(\alpha)k(t)\langle L^\delta\rangle\mathbf{Q} = 0\\
&m\ddot{x}_2 + k_2^x x_2 - \sin(\alpha)k(t)\langle L^\delta\rangle\mathbf{Q} = 0\\
&m\ddot{y}_2 + k_2^y y_2 - \cos(\alpha)k(t)\langle L^\delta\rangle\mathbf{Q} = 0\\
&I\ddot{\theta}_{(1,1)} + k_1^\theta(\theta_{(1,1)} - \theta_{(1,2)}) = Cm\\
&I\ddot{\theta}_{(1,2)} - k_1^\theta(\theta_{(1,1)} - \theta_{(1,2)}) + r^b_{(1,2)}k(t)\langle L^\delta\rangle\mathbf{Q} = 0\\
&I\ddot{\theta}_{(2,1)} - k_2^\theta(\theta_{(2,1)} - \theta_{(2,2)}) - r^b_{(2,1)}k(t)\langle L^\delta\rangle\mathbf{Q} = 0\\
&I\ddot{\theta}_{(2,2)} + k_2^\theta(\theta_{(2,1)} - \theta_{(2,2)}) = 0
\end{aligned} \tag{4.1}$$

where $\langle L^\delta\rangle$ is defined by

$$\langle L^\delta\rangle = [\sin(\alpha) \quad -\sin(\alpha) \quad \cos(\alpha) \quad -\cos(\alpha) \quad 0 \quad r^b_{(1,2)} \quad -r^b_{(2,1)} \quad 0] \tag{4.2}$$

(4.9) $r^b_{(1,2)}$, $r^b_{(2,1)}$ represent the base radius of gears, α is the pressure angle. $\mathbf{Q}(t)$ is the vector of generalized coordinates

$$\mathbf{Q}(t) = [x_1 \quad y_1 \quad x_2 \quad y_2 \quad \theta_{(1,1)} \quad \theta_{(1,2)} \quad \theta_{(2,1)} \quad \theta_{(2,2)}]^{\mathrm{T}} \tag{4.3}$$

5. Numerical simulation

The technological and dimensional features of the one-stage gear system are summarized in Table 1.

Table 1. System parameters

Material: 42CrMo4	$\rho = 7860\,\mathrm{Kg/m^3}$
Motor torque	$Cm = 200\,\mathrm{N\,m}$
Bearing stiffness	$k_j^x = 10^7\,\mathrm{N/m},\ \ k_j^y = 10^7\,\mathrm{N/m}$
Torsional stiffness of shaft	$k_j^\theta = 10^5\,\mathrm{N\,m/rad}$
Number of teeth	$Z(12) = 40,\ \ Z(21) = 50$
Module of teeth	$\mathrm{module} = 4.10^{-3}\,\mathrm{m}$
Contact ratio	$\varepsilon^\alpha = 1.7341$
The pressure angle	$\alpha = 20^\circ$

In this Section, numerical results are presented for the new formulations derived in Section 3. The polynomial chaos results are compared with Monte Carlo findings for 100000 simulations.

The mass m and the moment of inertia I of the gears are supposed to be random variables and defined as follows

$$m = m_0 + \sigma_m\xi \qquad I = I_0 + \sigma_I\xi$$

where ξ is the zero mean value Gaussian random variable, m_0 and I_0 are the mean values and σ_m and σ_I are the associated standard deviations.

The mean value and standard deviation of the dynamic component of the linear displacement of the first bearing in the two directions x and y have been calculated by the polynomial chaos

approach. The obtained results are compared with those given from Monte Carlo simulations for 100000 operations. The results are plotted in Figs. 3a, 4a, 5a and 6a for $\sigma_m = \sigma_I = 2\%$ and in Figs. 3b, 4b, 5b and 6b for $\sigma_m = \sigma_I = 5\%$.

These figures show that the obtained solutions oscillate around the Monte Carlo simulations which are the reference solution. It can be seen that for a small standard deviation $\sigma_m = \sigma_I = 2\%$, the polynomial chaos solutions in the second order polynomial provide a very good accuracy as compared with the Monte Carlo results. When the standard deviation increases, the error increases.

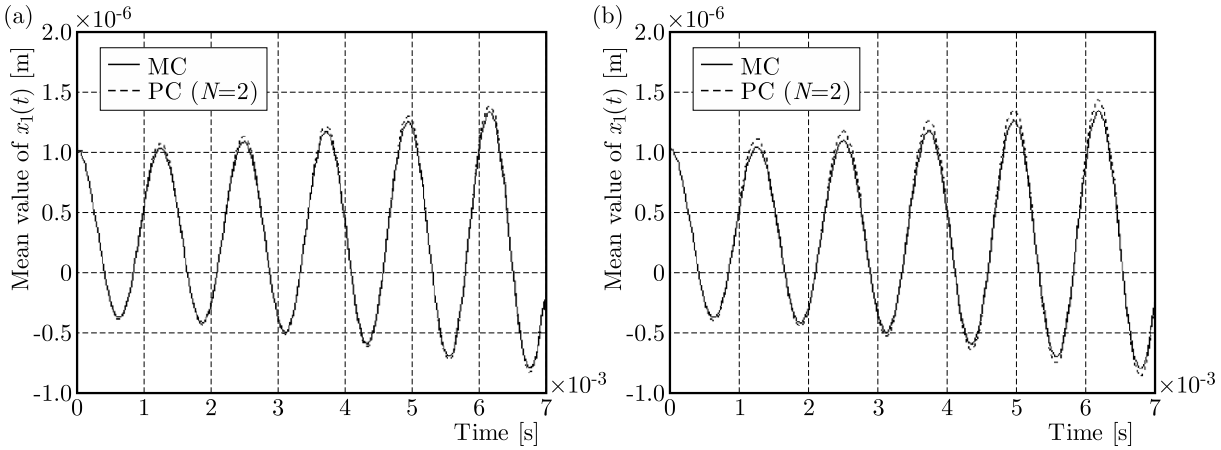

Fig. 3. Mean value of $x_1(t)$ for (a) $\sigma_m = \sigma_I = 2\%$ and (b) $\sigma_m = \sigma_I = 5\%$

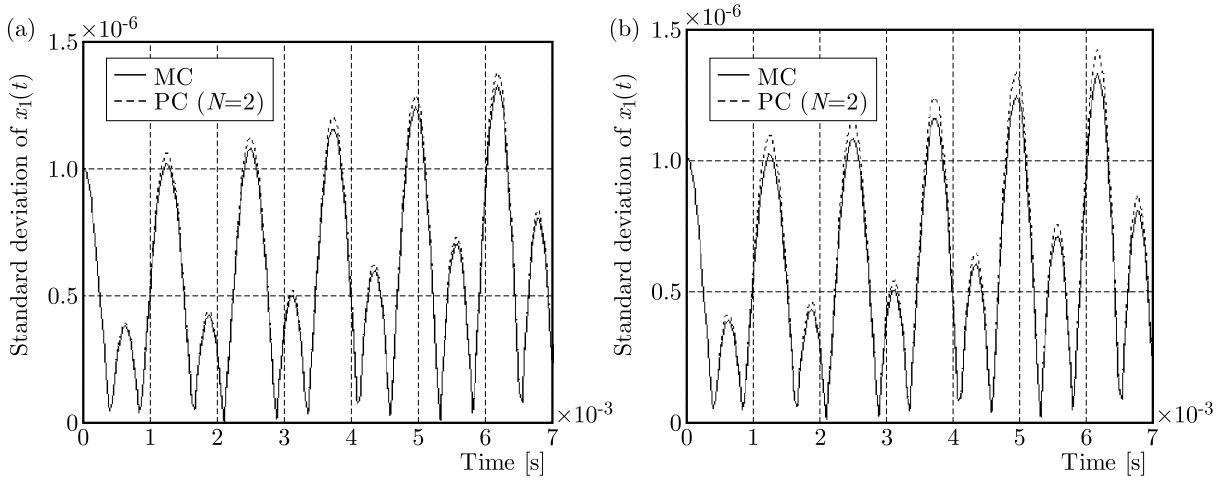

Fig. 4. Standard deviation of $x_1(t)$ for (a) $\sigma_m = \sigma_I = 2\%$ and (b) $\sigma_m = \sigma_I = 5\%$

The mean values of the dynamic component of the angular displacements $\theta_{(1,1)}$ and $\theta_{(2,1)}$ are presented in Figs. 7a and 7b for $\sigma_m = \sigma_I = 5\%$. The polynomial chaos results are compared with the Monte Carlo simulations for 100000 operations. The dynamic response of the angular displacement as predicted by polynomial chaos calculations matches exactly with that of the Monte Carlo analysis. $N = 8$ has been used for the PC model, and it is seen to be enough to capture the dynamic response of the angular displacement of our system.

The mean value and standard deviation of the dynamic component of the linear displacement of the second bearing in the two directions x and y are presented in Figs. 8 and 9 for $\sigma_m = \sigma_I = 10\%$.

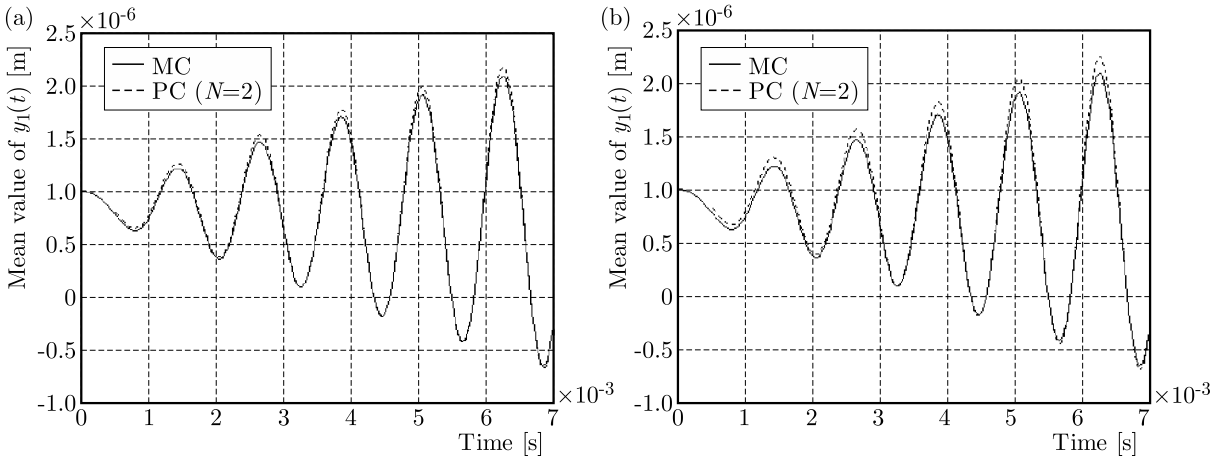

Fig. 5. Mean value of $y_1(t)$ for (a) $\sigma_m = \sigma_I = 2\%$ and (b) $\sigma_m = \sigma_I = 5\%$

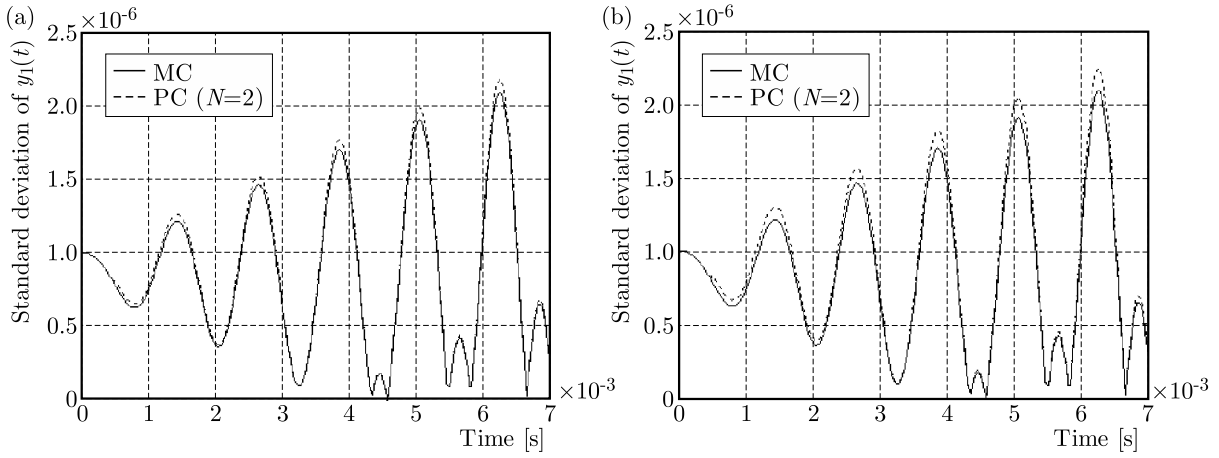

Fig. 6. Standard deviation of $y_1(t)$ for (a) $\sigma_m = \sigma_I = 2\%$ and (b) $\sigma_m = \sigma_I = 5\%$

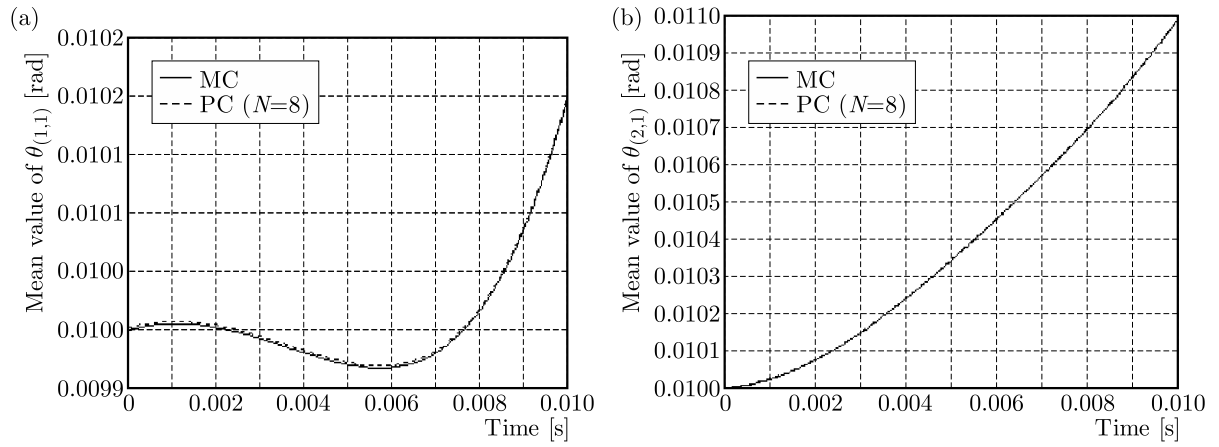

Fig. 7. Mean value of (a) $\theta_{(1,1)}(t)$ and (b) $\theta_{(2,1)}(t)$ for $\sigma_m = \sigma_I = 5\%$

The polynomial chaos results are compared with the Monte Carlo results for 100000 simulations. It is evident from these figures that the case $N = 2$ clearly has not enough chaos terms to represent the output. As N increases, the results seem to become better, and for $N = 8$, the dynamic response of the linear displacement of the second bearing with polynomial chaos values almost exactly match with the Monte Carlo simulation results.

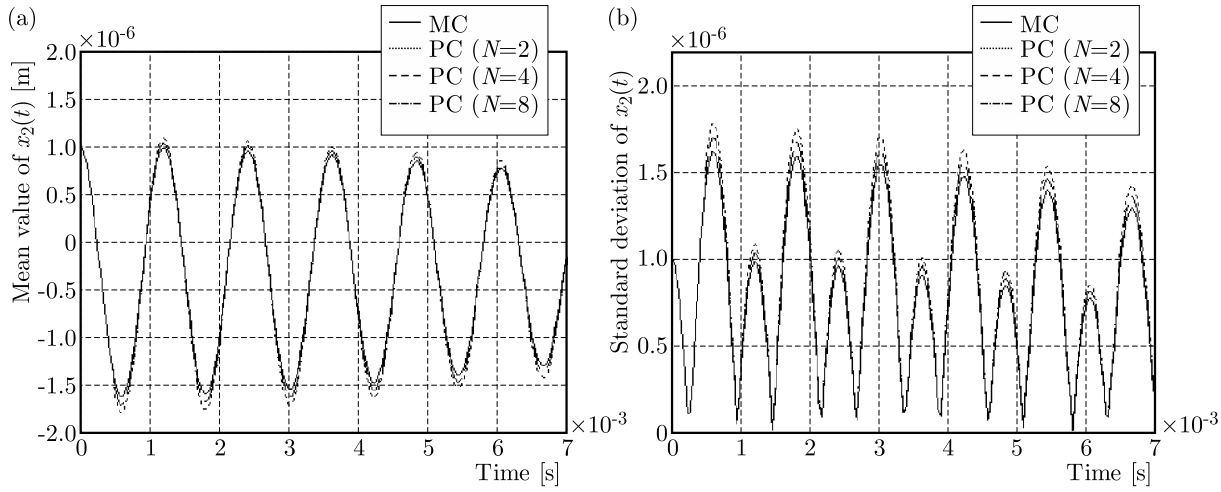

Fig. 8. (a) Mean value of $x_2(t)$ for $\sigma_m = \sigma_I = 10\%$, (b) standard deviation of $x_2(t)$ for $\sigma_m = \sigma_I = 10\%$

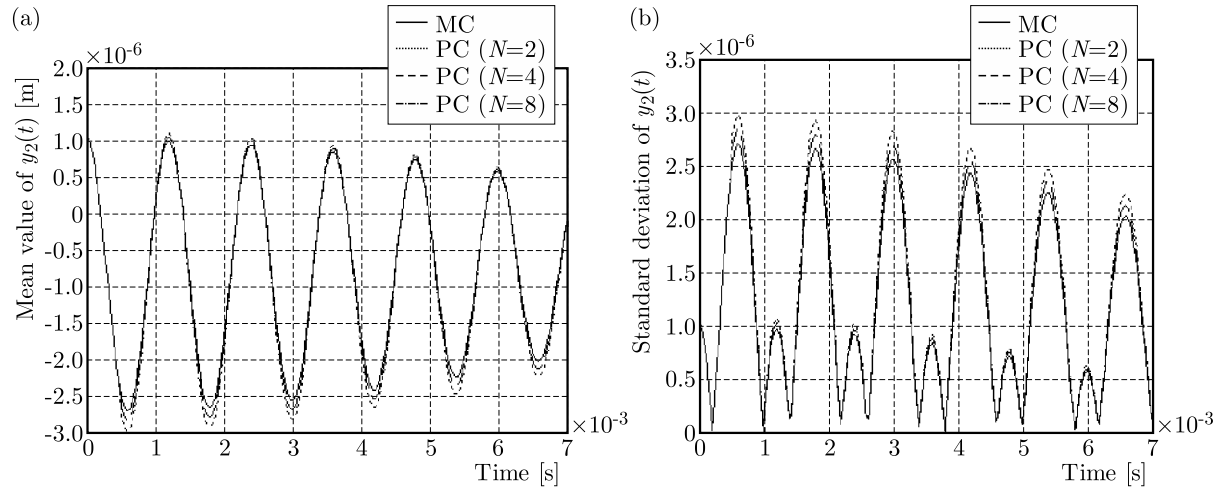

Fig. 9. (a) Mean value of $y_2(t)$ for $\sigma_m = \sigma_I = 10\%$, (b) standard deviation of $y_2(t)$ for $\sigma_m = \sigma_I = 10\%$

6. Conclusion

This paper has presents an approach to a one-stage gear system based on the polynomial chaos method while explicitly considering the uncertainty in parameters of the gear. The main results of the present study show that the polynomial chaos method may be an efficient tool to take into account the dispersions of the gear parameters. An interesting perspective is to apply this method to a system with higher degrees of freedom like an epicyclic gear system. Further work in this context is in progress.

References

1. Abo Al-kheer A., El-Hami A., Kharmanda M.G., Mouazen A.M., 2011, Reliability-based design for soil tillage machines, *Journal of Terramechanics*, **48**, 1, 57-64

2. Askey R., Wilson J., 1985, Some basic hypergeometric polynomials that generalize jacobi polynomials, *Memoirs of the American Mathematical Society*, **319**

3. Babuska I., Nobile F., Tempone R., 2007, A stochastic collocation method for elliptic partial differential equations with random input data, *SIAM Journal on Numerical Analysis*, **45**, 1005-1034

4. Babuska I., Tempone R., Zouraris G.E., 2004, Galerkin finite element approximation of stochastic elliptic partial differential equations, *SIAM Journal on Scientific Computing*, **24**, 619-644

5. Begg C.D., Byington C.S., Maynard K., 2000, Dynamic simulation of mechanical fault transition, *Proceedings of the 54th Meeting of the Society for Machinery Failure Prevention Technology*, Virginia Beach

6. Blanchard E., Sandu A., Sandu C., 2009, Parameter estimation for mechanical systems via an explicit representation of uncertainty, *Engineering Computations*, **26**, 5, 541-569

7. Cameron H., Martin W., 1947, The orthogonal development of nonlinear functional in series of Fourier-Hermite functional, *Annals of Mathematics*, **48**, 385-392

8. Crestaux T., Le Maitre O., Martinez J.M., 2009, Polynomial chaos expansion for sensitivity analysis, *Reliability Engineering and System Safety*, **94**, 1161-1172

9. Dalpiaz G., Rivola A., Rubini R., 1996, Dynamic modeling of gear systems for condition monitoring and diagnostics, *Congress on Technical Diagnostics*

10. El Hami A., Lallement G., Minottiand P., Cogan S., 1993, Methods that combine finite group theory with component mode synthesis in the analysis of repetitive structures, *International Journal Computers and Structures*, **48**, 975-982

11. El Hami A., Radi B., 1996, Some decomposition methods in the analysis of repetitive structures, *International Journal Computers and Structures*, **58**, 5, 973-980

12. El Hami A., Radi A., Cherouat A., 2009, The frictional contact of the shaping of the composite fabric, *International Journal of Mathematical and Computer Modelling*, **49**,7/8, 1337-1349

13. Fishman G.S., 1996, *Monte Carlo, Concepts, Algorithms and Applications*, First Ed. Springer-Verlag

14. Ghanem R.G., Spanos P.D., 1991, *Stochastic Finite Elements: A Spectral Approach*, Revised Ed. Springer Verlag

15. Guerine A., El Hami A., Fakhfakh T., Haddar M., 2015a, A polynomial chaos method to the analysis of the dynamic behavior of spur gear system, *Structural Engineering and Mechanics*, **53**, 819-831

16. Guerine A., El Hami A., Walha L., Fakhfakh T., Haddar M., 2015b, A perturbation approach for the dynamic analysis of one stage gear system with uncertain parameters, *Mechanism and Machine Theory*, **92**, 113-126

17. Isukapalli S.S., Roy A., Georgopoulos P.G., 1998a, Development and application of methods for assessing uncertainty in photochemical air quality problems, Interim Report for U.S.EPA National Exposure Research Laboratory

18. Isukapalli S.S., Roy A., Georgopoulos P.G., 1998b, Stochastic response surface methods (SRSMs) for uncertainty propagation: application to environmental and biological systems, *Risk Analysis*, **18**, 351-363

19. Le Maître O.P., Knio O.M., Najm H.N., Ghanem R.G., 2001, A stochastic projection method for fluid flow Basic formulation, *Journal of Computational Physics*, **173**, 481-511

20. Lindsley N.J., Beran P.S., 2005, Increased efficiency in the stochastic interrogation of an uncertain nonlinear aeroelastic system, *International Forum on Aeroelasticity and Structural Dynamics*, Munich, Germany

21. Papadrakakis M., Papadopoulos V., 1999, Parallel solution methods for stochastic finite element analysis using Monte Carlo simulation, *Computer Methods in Applied Mechanics and Engineering*, **168**, 305-320

22. Saad G., Ghanem R., Masri S., 2007, Robust system identification of strongly nonlinear dynamics using a polynomial chaos based sequential data assimilation technique, *Structural Dynamics and Materials Conference*, Honolulu, USA

23. Sandu A., Sandu C., Ahmadian M., 2006a, Modeling multibody dynamic systems with uncertainties. Part I: numerical application, *Multibody System Dynamic*, **15**, 369-391

24. Sandu C., Sandu A., Ahmadian M., 2006b, Modeling multibody dynamic systems with uncertainties. Part II: theoretical and computational aspects, *Multibody System Dynamic*, **15**, 241-262

25. Sarsri D., Azrar L., Jebbouri A., El Hami A., 2011, Component mode synthesis and polynomial chaos expansions for stochastic frequency functions of large linear FE models, *Computers and Structures*, **89**, 3/4, 346-356

26. Smith A.H.C., Monti A., Ponci F., 2007, Indirect measurements via a polynomial chaos observer, *IEEE Transactions on Instrumentation and Measurement*, **56**, 743-752

27. Walha L., Fakhfakh T., Haddar M., 2009, Nonlinear dynamics of a two-stage gear system with mesh stiffness fluctuation, bearing flexibility and backlash, *Mechanism and Machine Theory*, **44**, 1058-1069

28. Wiener N., 1938, The homogeneous chaos, *American Journal of Mathematics*, **60**, 897-936

29. Williams M.M.R., 2006, Polynomial chaos functions and stochastic differential equations, *Annals of Nuclear Energy*, **33**, 774-785

30. Xiu D., Karniadakis G.E., 2002, Modeling uncertainty in steady state diffusion problems via generalized polynomial chaos, *Computer Methods in Applied Mechanics and Engineering*, **191**, 4927-4948

31. Xiu D., Karniadakis G.E., 2003, Modelling uncertainty in flow simulations via generalized polynomial chaos, *Journal of Computational Physics*, **187**, 137-167

Manuscript received October 20, 2015; accepted for print February 12, 2016

JOURNAL OF THEORETICAL AND APPLIED MECHANICS
54, 3, pp. 1051-1062, Warsaw 2016
DOI: 10.15632/jtam-pl.54.3.1051

ON THE TURBULENT BOUNDARY LAYER OF A DRY GRANULAR AVALANCHE DOWN AN INCLINE. I. THERMODYNAMIC ANALYSIS

Chung Fang

National Cheng Kung University, Department of Civil Engineering, Tainan City, Taiwan
e-mail: cfang@mail.ncku.edu.tw

Characteristics of the turbulent boundary and passive layers of an isothermal dry granular avalanche with incompressible grains are studied by the proposed zero-order turbulence closure model. The first and second laws of thermodynamics are applied to derive the equilibrium closure relations satisfying turbulence realizability conditions, with the dynamic responses postulated within a quasi-static theory. The established closure model is applied to analyses of a gravity-driven stationary avalanche down an incline to illustrate the distributions of the mean solid content, mean velocity, turbulent kinetic energy and dissipation across the flow layer, and to show the influence of turbulent fluctuation on the mean flow features compared with laminar flow solutions. In this paper, detailed thermodynamic analysis and equilibrium closure relations are summarized, with the dynamic responses, the complete closure model and numerical simulations reported in the second part.

Keywords: closure model, dry granular avalanche, thermodynamics, turbulence

1. Introduction

Dry granular systems are collections of a large amount of dispersive solid particles with interstices filled with a gas. When in motion, the interactions among the solid grains result from short--term instantaneous elastic and inelastic collisions and long-term enduring frictional contact and sliding. They play a structural role in the macroscopic behavior, and are characterized as the *microstructural effect* (Aranson and Tsimring, 2009; Ausloos *et al.*, 2005; GDR MiDi, 2004; Mehta, 2007; Pöschel and Brilliantiv, 2013; Rao and Nott, 2008). Depending on dominant microstructural grain-grain interactions, the quasi-static, dense and collisional flow states are defined, by which the avalanche is classified as a flow with rapid speed (flow in collisional state) (Pudasaini and Hutter, 2007; Pöschel and Brilliantiv, 2013; Rao and Nott, 2008). The microstructural effect significantly depends on flow speed, leading to a dry granular avalanche exhibiting distinct rheological characteristics (Oswald, 2009; Pudasaini and Hutter, 2007).

A dry granular flow experiences fluctuations on its macroscopic quantities, a phenomenon similar to turbulent motion of Newtonian fluids in three perspectives: (i) it results from two-fold grain-grain interactions, in contrast to that of Newtonian fluids induced by incoming flow instability, instability in the transition region or flow geometry (Batchelor, 1993; Tsinober, 2009); (ii) it emerges equally at slow speed in contrast to that of Newtonian fluids, which is dependent significantly on flow velocity, characterized by the critical Reynolds number; and (iii) while turbulent fluctuation induces most energy production with anisotropic eddies and energy dissipation with fairly isotropic eddies at the scales similar to the integral and Kolmogorov length scales in Newtonian fluids, respectively. Granular eddies at the inertia sub-range or Taylor microeddies are barely recognized. These imply that a dry granular flow can be considered a rheological fluid continuum with significant kinetic energy dissipation. Turbulent fluctuation induces energy cascades from the stress power at the mean scale toward the thermal dissipation at the subsequent length and time scales (Pudasaini and Hutter, 2007; Rao and Nott, 2008).

Field observations suggest that turbulent intensity is responsible for the entrainment of geophysical mass transportation, and a dry granular avalanche is conjectured to consist of two distinct layers: a very thin *turbulent boundary layer* immediately above the base, and a relatively thick *passive layer* above the former (Pudasaini and Hutter, 2007; Wang and Hutter, 2001). In the turbulent boundary layer, the grains collide intensively one with another, resulting in reduced base friction so that the avalanche can travel unexpected long distance. On the contrary, the dominant grain-grain interaction in the passive layer is a long-term one, causing the grains to behave as a lump solid.

To take into account the effect of turbulent fluctuation on mean flow features, a conventional Reynolds-filter process is applied to decompose the variables into the mean and fluctuating parts to obtain the balance equations of the mean fields with ergodic terms. They need be prescribed as functions of the mean fields, known as the *turbulent closure relations*, to arrive at a mathematically likely well-posed problem. By different prescriptions of the closure relations, turbulence closure models of different orders can be established (Batchelor, 1993).

Studies on turbulent characteristics of dry granular systems are so far yet complete. Various models for slow creeping and dense laminar flows (e.g. Faccanoni and Mangeney, 2013; Fang, 2009a, 2010; Jop, 2008; Jop *et al.*, 2006; Kirchner, 2002) and for rapid laminar flows (e.g. Campell, 2005; Dainel *et al.*, 2007; Fang, 2008a, 2008b; Savage, 1993; Wang and Hutter, 1999) haven been developed. The turbulent models by Ahmadi (1985), Ahmadi and Shahinpoor (1983) and Ma and Ahmadi (1985) used Prandtl's mixing length to account for the turbulent viscosity, with applications to simple shear flows. Although the influence of velocity fluctuation on the linear momentum balance was accounted for by Reynolds' stress, the fluctuating kinetic energy was not taken into account. Effort has been made to account for the fluctuating kinetic energy by the granular temperature (e.g. Goldhrisch, 2008; Luca *et al.*, 2004; Vescoci *et al.*, 2013; Wang and Hutter, 2001). Only the equilibrium closure relations were obtained; numerical simulations of Benchmark problems compared with experimental outcomes were insufficient; the conjecture of a two-layered avalanche remains unverified systematically.

Recently, the granular coldness, a similar concept to the granular temperature, has been extended to account for the influence of weak turbulent fluctuation induced by two-fold grain--grain interactions (Fang, 2016a; Fang and Wu, 2014a). A kinematic equation was used to describe the time evolution of the turbulent kinetic energy, with the turbulent dissipation considered a closure relation or an independent field resulting respectively in zero- and first-order turbulence closure models. While the mean porosity and velocity coincided to the experimental outcomes, the turbulent dissipation was shown to be similar to that of conventional Newtonian fluids in turbulent boundary layer flows. Although the first-order model was able to account for the influence of turbulent eddy evolution, the zero-order model was sufficient to capture the turbulent kinetic energy and dissipation distributions (Fang and Wu, 2014b).

Thus, the goal of the study is to establish a zero-order closure model for isothermal dry granular avalanches with incompressible grains. The first and second laws of thermodynamics, specifically the Müller-Liu entropy principle, are used to derive the equilibrium closure relations with the dynamic responses postulated within a quasi-static theory. The established model is applied to analyses of a gravity-driven stationary avalanche down an incline, compared with laminar flow solutions to illustrate the distributions of turbulent kinetic energy and dissipation with their influence on the mean flow features, and to verify the characteristics of the turbulent boundary and passive layers with their similarities to those of Newtonian fluids. The study is divided into two parts. Analysis of the Müller-Liu entropy principle and derived equilibrium closure relations are summarized in this paper, with the complete closure model and numerical simulations reported in the second part (Fang, 2016b). The mean balance equations and turbulent state space are given in Section 2, followed by the thermodynamic analysis in Section 3.

The derived equilibrium closure relations are summarized in Section 4, with the work concluded in Section 5.

2. Mean balance equations and turbulent state space

2.1. Mean balance equations

Following the balance equations for laminar motion and the Reynolds-filter process, the mean balance equations for a turbulent flow are given by Batchelor (1993) and Fang (2009a, 2014a)[1]

$$0 = \dot{\bar{\gamma}}\bar{\nu} + \bar{\gamma}\dot{\bar{\nu}} + \bar{\gamma}\bar{\nu}\nabla\cdot\bar{\mathbf{v}} \tag{2.1}$$

$$bf0 = \bar{\gamma}\bar{\nu}\dot{\bar{\mathbf{v}}} - \operatorname{div}(\bar{\mathbf{t}} + \mathbf{R}) - \bar{\gamma}\bar{\nu}\bar{\mathbf{b}} \tag{2.2}$$

$$\mathbf{0} = \bar{\mathbf{t}} - \bar{\mathbf{t}}^{\mathrm{T}} \qquad \mathbf{0} = \mathbf{R} - \mathbf{R}^{\mathrm{T}} \qquad \mathbf{0} = \bar{\mathbf{Z}} - \bar{\mathbf{Z}}^{\mathrm{T}} \tag{2.3}$$

$$0 = \bar{\gamma}\bar{\nu}\dot{\bar{e}} - \bar{\mathbf{t}}\cdot\bar{\mathbf{D}} + \nabla\cdot(\bar{\mathbf{q}} + \mathbf{Q}) - \bar{\gamma}\bar{\nu}\varepsilon - \bar{\gamma}\bar{\nu}\bar{r} - \ell\bar{\mathbf{h}}\cdot\nabla\dot{\bar{\nu}} + \bar{\gamma}\bar{\nu}\bar{f}\ell\dot{\bar{\nu}} - \bar{\gamma}\bar{\nu}H \tag{2.4}$$

$$0 = \bar{\gamma}\bar{\nu}\dot{\bar{\eta}} + \nabla\cdot(\bar{\boldsymbol{\phi}} + \boldsymbol{\phi}') - \bar{\gamma}\bar{\nu}\bar{\sigma} - \bar{\pi} \tag{2.5}$$

$$0 = \bar{\gamma}\bar{\nu}\ell\ddot{\bar{\nu}} - \nabla\cdot(\bar{\mathbf{h}} + \mathbf{H}) - \bar{\gamma}\bar{\nu}\bar{f} \tag{2.6}$$

$$\mathbf{0} = \mathring{\bar{\mathbf{Z}}} - \bar{\boldsymbol{\Phi}} \qquad (\mathring{\bar{\mathbf{Z}}} \equiv \dot{\bar{\mathbf{Z}}} - [\bar{\boldsymbol{\Omega}}, \bar{\mathbf{Z}}]) \tag{2.7}$$

$$0 = \bar{\gamma}\bar{\nu}\dot{k} - \mathbf{R}\cdot\bar{\mathbf{D}} - \nabla\cdot\mathbf{K} + \bar{\gamma}\bar{\nu}\varepsilon \tag{2.8}$$

$$0 = \bar{\gamma}\bar{\nu}\dot{s} - \ell\mathbf{H}\cdot\nabla\dot{\bar{\nu}} - \nabla\cdot\mathbf{L} + \bar{\gamma}\bar{\nu}H \tag{2.9}$$

with the ergodic terms,

$$\begin{aligned}
&0 = R_{ij} + \bar{\gamma}\bar{\nu}\overline{v_i'v_j'} && 0 = H_j - \ell R_{ij}\frac{\partial\bar{\nu}}{\partial x_i} && 0 = \phi_j' - \bar{\gamma}\bar{\nu}\overline{\eta' v_j'}\\
&0 = Q_j - \bar{\gamma}\bar{\nu}\overline{e' v_j'} && 0 = \bar{\gamma}\bar{\nu}\varepsilon - \overline{t_{ij}'\frac{\partial v_i'}{\partial x_j}} && 0 = M_{ij} - \ell\overline{h_i' v_j'}\\
&0 = \bar{\gamma}\bar{\nu}k - \frac{1}{2}\bar{\gamma}\bar{\nu}\overline{v_i'v_j'} && 0 = K_j - \overline{t_{ij}'v_i'} - \frac{1}{2}R_{iij}\\
&0 = \bar{\gamma}\bar{\nu}s + \frac{1}{2}\ell^2 R_{ij}\frac{\partial\bar{\nu}}{\partial x_i}\frac{\partial\bar{\nu}}{\partial x_j} && 0 = \bar{\gamma}\bar{\nu}H - M_{ij}\frac{\partial^2\bar{\nu}}{\partial x_i x_j} - \bar{\gamma}\bar{\nu}d\\
&0 = R_{ijk} + \bar{\gamma}\bar{\nu}\overline{v_i'v_j'v_k'} && 0 = \bar{\gamma}\bar{\nu}d - \ell\left(\overline{h_i'\frac{\partial v_j'}{\partial x_i}} - \bar{\gamma}\bar{\nu}\overline{f' v_j'}\right)\frac{\partial\bar{\nu}}{\partial x_j}\\
&0 = L_j - M_{ji}\frac{\partial\bar{\nu}}{\partial x_i} - \frac{1}{2}\ell^2 R_{ijk}\frac{\partial\bar{\nu}}{\partial x_i}\frac{\partial\bar{\nu}}{\partial x_k}
\end{aligned} \tag{2.10}$$

in which $\bar{\nu}$ is the mean volume fraction defined as the total mean solid content divided by the volume of a representative volume element (RVE), and $\mathbf{A}\cdot\mathbf{B} \equiv \operatorname{tr}(\mathbf{A}\mathbf{B}^{\mathrm{T}}) = \operatorname{tr}(\mathbf{A}^{\mathrm{T}}\mathbf{B})$, $[\mathbf{A},\mathbf{B}] \equiv \mathbf{A}\mathbf{B} - \mathbf{B}\mathbf{A}$ for two arbitrary second-rank tensors $\mathbf{A}$ and $\mathbf{B}$. Variables and parameters arising in (2.1)-(2.10) are defined in Table 1, with KE and div abbreviations of kinetic energy and divergence, respectively. Quantities in (2.10), with the others shown later, are classified as closure relations.

Equations (2.1)-(2.5) are respectively the conventional mean balances of mass, linear momentum, angular momentum, internal energy and entropy for a fluid continuum in turbulent motion with the symmetry of the mean Cauchy stress demanded and the mean density $\bar{\rho}$ decomposed into $\bar{\rho} = \bar{\gamma}\bar{\nu}$. This introduces $\bar{\nu}$, considered an internal variable, with its time evolution

[1]It is equally possible to conduct the study by using the Naghdi-Green approach with original Reynolds' treatment, see e.g. Bilicki and Badur (2003).

Table 1. Variables and parameters in the mean balance equations

$\bar{\mathbf{b}}$	mean specific body force	$\bar{\mathbf{D}}$	symmetric part of $\bar{\mathbf{v}} \otimes \nabla$
$\bar{e}$	mean specific internal energy	$\bar{f}$	mean production associated with $\ell\dot{\bar{\nu}}$
$\bar{\mathbf{h}}$	mean flux associated with $\ell\dot{\bar{\nu}}$	H	specific turbulent dissipation of $\bar{\gamma}\bar{\nu}s$
$\mathbf{H}$	turbulent flux associated with $\ell\dot{\bar{\nu}}$	k	specific turbulent KE
$\mathbf{K}$	flux associated with $\bar{\gamma}\bar{\nu}k$	ℓ	constant internal length
$\mathbf{L}$	flux associated with $\bar{\gamma}\bar{\nu}s$	$\bar{\mathbf{q}}$	mean heat flux
$\mathbf{Q}$	turbulent heat flux	$\bar{r}$	mean specific energy supply
$\mathbf{R}$	Reynolds' stress	s	specific turbulent configurational KE
T	transpose	$\bar{\mathbf{t}}$	mean Cauchy stress
$\bar{\mathbf{v}}$	mean velocity	$\bar{\mathbf{Z}}$	mean internal friction
α	arbitrary quantity	$\bar{\alpha}$	time-averaged value of α
α'	fluctuating value of α	$\dot{\alpha}$	material derivative of α with respect to $\bar{\mathbf{v}}$
$\bar{\gamma}$	mean true mass density of solid grains	ε	specific turbulent dissipation of $\bar{\gamma}\bar{\nu}k$
$\bar{\eta}$	mean specific entropy	$\bar{\nu}$	mean volume fraction
$\bar{\pi}$	mean entropy production	$\bar{\sigma}$	mean specific entropy supply
$\bar{\boldsymbol{\phi}}$	mean entropy flux	$\boldsymbol{\phi}'$	turbulent entropy flux
$\bar{\boldsymbol{\Omega}}$	mean orthogonal rotation of RVE	∇	Nabla operator

described by the revised Goodman-Cowin model (2.6) for rapid flows (Fang, 2009a). It describes a self-equilibrated stress system, with constant internal length ℓ denoting the characteristic length of the grains (Fang, 2008a, 2009a; Wang and Hutter, 1999). Since the grain arrangements are assumed to be independent of motion of the granular body, variation in $\ell\dot{\bar{\nu}}$ provides extra energies to the internal energy balance, as indicated by $(-\ell\bar{\mathbf{h}} \cdot \nabla\dot{\bar{\nu}} + \bar{\gamma}\bar{\nu}\bar{f}\ell\dot{\bar{\nu}})$ in (2.4).

To account for the rate-independent characteristics, an Euclidean frame-indifferent, symmetric second-rank tensor $\bar{\mathbf{Z}}$ is introduced as an internal variable for the mean internal frictional and other non-conservative forces inside a granular microcontinuum (Svendsen and Hutter, 1999; Svendsen *et al.*, 1999), with $\mathring{\bar{\mathbf{Z}}}$ denoting the Zaremba-Jaumann corotational derivative of $\bar{\mathbf{Z}}$. It is a phenomenological generalization of the Mohr-Coulomb model for a granular material at low energy and high-grain volume fraction (see e.g. Fang, 2009b), with its time evolution described kinematically by (2.7). The mean internal friction $\bar{\mathbf{Z}}$ with its time evolution (2.7) are widely used for laminar and turbulent formulations (e.g. Fang, 2008a, 2009a, 2010; Fang and Wu, 2014a; Kirchner, 2002) and provide the foundation of a dry granular heap at an equilibrium state, when the grains are incompressible (Fang, 2009a).

Equation (2.8) is the evolution of the *turbulent kinetic energy*, $\bar{\gamma}\bar{\nu}k$, derived by taking the inner product of the velocity with the balance of linear momentum followed by the Reynolds--filter process. It is considered to account for the influence of the energy cascade in turbulent flows (Batchelor, 1993; Pudasaini and Hutter, 2007; Rao and Nott, 2008). The turbulent kinetic energy is generated by Reynolds' stress through mean shearing at the mean scale, transferred subsequently via the flux $\mathbf{K}$ at various length and time scales, and eventually dissipated at the smallest scale (the Kolmogorov scale) by the *turbulent dissipation*, $\bar{\gamma}\bar{\nu}\varepsilon$. Similarly, the fluctuation of the characteristic velocity $\ell\dot{\bar{\nu}}$ in (2.6) also contributes an additional turbulent kinetic energy, the *turbulent configurational kinetic energy*, $\bar{\gamma}\bar{\nu}s$, with its time evolution kinematically described by (2.9) with the flux $\mathbf{L}$ and *turbulent configurational dissipation*, $\bar{\gamma}\bar{\nu}H$ (Luca *et al.*, 2004). Thus, two turbulent kinetic energies appear: $\bar{\gamma}\bar{\nu}k$ for the turbulent fluctuation on the bulk material velocity, and $\bar{\gamma}\bar{\nu}s$ for that on the characteristic velocity of the grain configuration. Two-fold turbulent dissipations $\bar{\gamma}\bar{\nu}\varepsilon$ and $\bar{\gamma}\bar{\nu}H$ are considered closure relations, with their eventual thermal effects indicated in (2.4). Since the time evolutions of $\bar{\mathbf{Z}}$, k and s are described by using kinematic equations, their variations do not provide additional energy contributions in the internal energy balance equation.

2.2. Turbulent state space

With these, the quantities

$$\begin{aligned}\mathcal{P} &= \{\bar{\gamma}, \bar{\nu}, \bar{\mathbf{v}}, \bar{\mathbf{Z}}, \vartheta^M, \vartheta^T, \vartheta^G\}\\ \mathcal{C} &= \{\bar{\mathbf{t}}, \mathbf{R}, \bar{e}, \bar{\mathbf{q}}, \mathbf{Q}, \bar{\eta}, \boldsymbol{\phi}^T, \bar{\mathbf{h}}, \mathbf{H}, \bar{f}, \bar{\boldsymbol{\Phi}}, k, s, \mathbf{K}, \mathbf{L}, \varepsilon, H\}\end{aligned} \tag{2.11}$$

are introduced respectively as the primitive mean fields and closure relations, by which $\mathcal{C}$ should be constructed based on the turbulent state space given by

$$\mathcal{Q} = \{\nu_0, \bar{\nu}, \dot{\bar{\nu}}, \mathbf{g}_1, \bar{\gamma}, \mathbf{g}_2, \vartheta^M, \mathbf{g}_3, \vartheta^T, \mathbf{g}_4, \vartheta^G, \mathbf{g}_5, \bar{\mathbf{D}}, \bar{\mathbf{Z}}\} \qquad \mathcal{C} = \hat{\mathcal{C}}(\mathcal{Q}) \tag{2.12}$$

with $\mathbf{g}_1 \equiv \nabla\bar{\nu}$, $\mathbf{g}_2 \equiv \nabla\bar{\gamma}$, $\mathbf{g}_3 \equiv \nabla\vartheta^M$, $\mathbf{g}_4 \equiv \nabla\vartheta^T$, $\mathbf{g}_5 \equiv \nabla\vartheta^G$ and $\boldsymbol{\phi}^T \equiv \bar{\boldsymbol{\phi}} + \boldsymbol{\phi}'$. In $(2.11)_1$, ϑ^M is the *material coldness*, which can be shown to be the inverse of an empirical material temperature θ^M for simple materials (Hutter and Jöhnk, 2004). The turbulent kinetic energy is expressed conventionally by the *granular temperature* θ^T (Goldhirsch, 2008; Vescovi *et al.*, 2013; Wang and Hutter, 2001) or alternatively by the *granular coldness* ϑ^T (Fang and Wu, 2014a; Luca *et al.*, 2004).[2] In a similar manner, the turbulent configurational kinetic energy is expressed by the *granular configurational temperature* θ^G, or alternatively by the *granular configurational coldness* ϑ^G (Luca *et al.*, 2004). Two-fold granular coldnesses are used as implicit indices of the variations in $\bar{\gamma}\bar{\nu}k$, $\bar{\gamma}\bar{\nu}s$ and their dissipations.

State space (2.12) is proposed based on Truesdell's equi-presence principle and principle of frame-indifference, with ν_0 the value of $\bar{\nu}$ in the reference configuration, included due to its influence on the behavior of flowing granular matter (Luca *et al.*, 2004). The quantities ν_0, $\bar{\nu}$, $\dot{\bar{\nu}}$, $\mathbf{g}_1$, $\bar{\gamma}$ and $\mathbf{g}_2$ are for the elastic effect, corresponding to $\bar{\rho}$, $\dot{\bar{\rho}}$ and $\nabla\bar{\rho}$ for complex rheological fluids; ϑ^M and $\mathbf{g}_3$ represent temperature-dependency of physical properties; ϑ^T and $\mathbf{g}_4$ stand for influence of turbulent kinetic energy and dissipation; ϑ^G and $\mathbf{g}_5$ denote the effect of turbulent configurational kinetic energy and dissipation; while $\bar{\mathbf{D}}$ and $\bar{\mathbf{Z}}$ are for viscous and rate-independent effects, respectively. Since $\{\bar{\mathbf{t}}, \bar{\mathbf{q}}, \bar{\mathbf{h}}, \bar{\boldsymbol{\Phi}}\}$ are objective, and $\mathbf{v}'$ (the fluctuating velocity) is also objective, the quantities $\{\mathbf{R}, \mathbf{Q}, \mathbf{H}, \mathbf{K}, \mathbf{L}\}$ are equally objective, with which (2.3) is fulfilled.

3. Thermodynamic analysis

3.1. Entropy inequality

Turbulence realizability conditions require that during a physically admissible process, the second law of thermodynamics with a local form of non-negative entropy production, and all balance equations should be satisfied simultaneously (Rung *et al.*, 1999; Sadiki and Hutter, 2000). This can be achieved by considering the mean balance equations as the constraints of inequality (2.5) via the method of Lagrange multipliers, viz.[3]

[2]The simple relation between θ^M and ϑ^M does not hold for θ^T and ϑ^T in dry granular systems. Only the relation of $\vartheta^T = \hat{\vartheta}^T(\theta^T, \dot{\theta}^T)$ is understood, which holds equally for ϑ^G and θ^G. In addition, the coldness idea is more physically meaningful when materials exhibit no memory effect. Since a dry granular matter in rapid motion exhibits a relatively insignificant memory effect, the coldness is used as the first approximation.

[3]We follow the Müller-Liu approach, from our own experience it can deliver more possible findings than the classical Coleman-Noll approach for granular media thermodynamics. However, the classical Coleman-Noll approach is widely used to conduct thermodynamic analyses, see e.g. Cieszko (1996), Kubik (1986), Schrefler *et al.* (2009), Sobieski (2009), Wilmański (1996).

$$\begin{aligned}\bar{\pi} = {} & \bar{\gamma}\bar{\nu}\dot{\bar{\eta}} + \nabla\cdot\boldsymbol{\phi}^T - \bar{\gamma}\bar{\nu}\bar{\sigma} - \lambda^{\bar{\gamma}}(\dot{\bar{\gamma}}\bar{\nu} + \bar{\gamma}\dot{\bar{\nu}} + \bar{\gamma}\bar{\nu}\nabla\cdot\bar{\mathbf{v}}) - \boldsymbol{\lambda}^{\bar{\mathbf{v}}}\cdot\Big(\bar{\gamma}\bar{\nu}\dot{\bar{\mathbf{v}}} - \operatorname{div}(\bar{\mathbf{t}} + \mathbf{R}) - \bar{\gamma}\bar{\nu}\bar{\mathbf{b}}\Big)\\ & - \lambda^{\bar{e}}\Big(\bar{\gamma}\bar{\nu}\dot{\bar{e}} - \bar{\mathbf{t}}\cdot\bar{\mathbf{D}} + \nabla\cdot(\bar{\mathbf{q}} + \mathbf{Q}) - \bar{\gamma}\bar{\nu}\varepsilon - \bar{\gamma}\bar{\nu}\bar{r} - \ell\bar{\mathbf{h}}\cdot\nabla\dot{\bar{\nu}} + \bar{\gamma}\bar{\nu}\bar{f}\ell\dot{\bar{\nu}} - \bar{\gamma}\bar{\nu}H\Big)\\ & - \lambda^{\bar{\nu}}\Big(\bar{\gamma}\bar{\nu}\ell\ddot{\bar{\nu}} - \nabla\cdot(\bar{\mathbf{h}} + \mathbf{H}) - \bar{\gamma}\bar{\nu}\bar{f}\Big) - \boldsymbol{\lambda}^{\bar{\mathbf{Z}}}\cdot(\dot{\bar{\mathbf{Z}}} - [\boldsymbol{\Omega}, \bar{\mathbf{Z}}] - \bar{\boldsymbol{\Phi}})\\ & - \lambda^k(\bar{\gamma}\bar{\nu}\dot{k} - \mathbf{R}\cdot\bar{\mathbf{D}} - \nabla\cdot\mathbf{K} + \bar{\gamma}\bar{\nu}\varepsilon) - \lambda^s(\bar{\gamma}\bar{\nu}\dot{s} - \ell\mathbf{H}\cdot\nabla\dot{\bar{\nu}} - \nabla\cdot\mathbf{L} + \bar{\gamma}\bar{\nu}Ht) \geqslant 0\end{aligned} \tag{3.1}$$

with $\lambda^{\bar{\gamma}}$, $\boldsymbol{\lambda}^{\bar{\mathbf{v}}}$, $\lambda^{\bar{e}}$, $\lambda^{\bar{\nu}}$, $\boldsymbol{\lambda}^{\bar{\mathbf{Z}}}$, λ^k and λ^s being the corresponding Lagrange multipliers. Since $\{\dot{\vartheta}^M, \dot{\vartheta}^T, \dot{\vartheta}^G\}$ are not considered in $(2.11)_1$, it is assumed that (Hutter and Jöhnk, 2004)

$$\begin{aligned}&\lambda^{\bar{e}} = \vartheta^M \qquad \lambda^k = \vartheta^T \qquad \lambda^s = \vartheta^G\\ &\vartheta^M\psi^T \equiv \vartheta^M\bar{e} + \vartheta^T k + \vartheta^G s - \bar{\eta}\end{aligned} \tag{3.2}$$

with ψ^T the specific *turbulent Helmholtz free energy*. Since material behavior is required to be independent of external supplies, it follows $(-\bar{\gamma}\bar{\nu}\bar{\sigma} + \bar{\gamma}\bar{\nu}\boldsymbol{\lambda}^{\bar{\mathbf{v}}}\cdot\bar{\mathbf{b}} + \vartheta^M\bar{\gamma}\bar{\nu}\bar{r}) = 0$, an equation determining the mean entropy supply. Substituting (2.11)-(2.12) and (3.2) into (3.1) yields

$$\bar{\pi} = \mathbf{a}\cdot\boldsymbol{\mathcal{X}} + b \geqslant 0 \tag{3.3}$$

with $\boldsymbol{\mathcal{X}} = \{\dot{\bar{\mathbf{v}}}, \ddot{\bar{\nu}}, \dot{\bar{\gamma}}, \dot{\vartheta}^M, \dot{\vartheta}^T, \dot{\vartheta}^G, \dot{\mathbf{g}}_2, \dot{\mathbf{g}}_3, \dot{\mathbf{g}}_4, \dot{\mathbf{g}}_5, \dot{\bar{\mathbf{D}}}, \dot{\bar{\mathbf{Z}}}, \bar{\boldsymbol{\Omega}}, \nabla\nu_0, \nabla\dot{\bar{\nu}}, \nabla\mathbf{g}_1, \nabla\mathbf{g}_2, \nabla\mathbf{g}_3, \nabla\mathbf{g}_4, \nabla\mathbf{g}_5, \nabla\bar{\mathbf{D}}, \nabla\bar{\mathbf{Z}}\}$, and $\dot{\mathbf{g}}_1 = \nabla\dot{\bar{\nu}} - \mathbf{g}_1\nabla\bar{\mathbf{v}}$ has been used. Since the vector $\boldsymbol{\mathcal{X}}$ is the set of time- and space-independent variations of $\mathcal{Q}$, and the vector $\mathbf{a}$ and scalar b are only functions of (2.12), (3.3) is linear in $\boldsymbol{\mathcal{X}}$. Since $\boldsymbol{\mathcal{X}}$ can take any values, it would be possible to violate (3.3) unless

$$\mathbf{a} = \mathbf{0} \qquad \text{and} \qquad b \geqslant 0 \tag{3.4}$$

Equation $(3.4)_1$ leads to

$$\psi^T_{,\alpha} = \mathbf{0} \qquad \alpha \in \{\dot{\bar{\nu}}, \mathbf{g}_2, \mathbf{g}_3, \mathbf{g}_4, \mathbf{g}_5, \bar{\mathbf{D}}\} \tag{3.5}$$

for the restrictions on ψ^T; and

$$\begin{aligned}&\boldsymbol{\lambda}^{\bar{\mathbf{v}}} = \mathbf{0} \qquad \lambda^{\bar{\gamma}} = -\bar{\gamma}\vartheta^M\psi^T_{,\bar{\gamma}} \qquad \boldsymbol{\lambda}^{\bar{\mathbf{Z}}} = -\bar{\gamma}\bar{\nu}\vartheta^M\psi^T_{,\bar{\mathbf{Z}}}\\ &\boldsymbol{\lambda}^{\bar{\mathbf{Z}}}\bar{\mathbf{Z}} = \bar{\mathbf{Z}}\boldsymbol{\lambda}^{\bar{\mathbf{Z}}} \qquad \lambda^{\bar{\nu}} = -\vartheta^M\ell^{-1}\psi^T_{,\dot{\bar{\nu}}}\end{aligned} \tag{3.6}$$

for the Lagrange multipliers, determined with the prescribed ψ^T; and

$$\bar{e} = \psi^T + \vartheta^M\psi^T_{,\vartheta^M} \qquad k = \vartheta^M\psi^T_{,\vartheta^T} \qquad s = \vartheta^M\psi^T_{,\vartheta^G} \tag{3.7}$$

for three specific energies; and

$$\begin{aligned}\mathbf{0} &= \boldsymbol{\phi}^T_{,\nu_0} - \vartheta^M(\bar{\mathbf{q}} + \mathbf{Q})_{,\nu_0} + \vartheta^T\mathbf{K}_{,\nu_0} + \vartheta^G\mathbf{L}_{,\bar{\nu}_0}\\ \mathbf{0} &= \boldsymbol{\phi}^T_{,\dot{\bar{\nu}}} - \vartheta^M(\bar{\mathbf{q}} + \mathbf{Q})_{,\dot{\bar{\nu}}} + \vartheta^T\mathbf{K}_{,\dot{\bar{\nu}}} + \vartheta^G\mathbf{L}_{,\dot{\bar{\nu}}} + \ell(\vartheta^M\bar{\mathbf{h}} + \vartheta^G\mathbf{H}) - \bar{\gamma}\bar{\nu}\vartheta^M\psi^T_{,\mathbf{g}_1}\\ \mathbf{0} &= \boldsymbol{\phi}^T_{,\mathbf{A}} - \vartheta^M(\bar{\mathbf{q}} + \mathbf{Q})_{,\mathbf{A}} + \vartheta^T\mathbf{K}_{,\mathbf{A}} + \vartheta^G\mathbf{L}_{,\mathbf{A}}\\ \mathbf{0} &= \operatorname{sym}\Big(\boldsymbol{\phi}^T_{,\mathbf{g}} - \vartheta^M(\bar{\mathbf{q}} + \mathbf{Q})_{,\mathbf{g}} + \vartheta^T\mathbf{K}_{,\mathbf{g}} + \vartheta^G\mathbf{L}_{,\mathbf{g}}\Big)\end{aligned} \tag{3.8}$$

with $\mathbf{A} \in \{\bar{\mathbf{D}}, \bar{\mathbf{Z}}\}$ and $\mathbf{g} \in \{\mathbf{g}_1, \mathbf{g}_2, \mathbf{g}_3, \mathbf{g}_4, \mathbf{g}_5\}$. In obtaining (3.8), $\psi^T \neq \hat{\psi}^T(\cdot, \dot{\bar{\nu}})$ has been assumed, with which $\lambda^{\bar{\nu}}$ vanishes. This is motivated by that ψ^T is influenced significantly by the variations in $\bar{\nu}$, but not its time rate of change (Fang, 2009a; Kirchner, 2002; Luca *et al.*,

2004; Pudasaini and Hutter, 2007; Wang and Hutter, 1999) and justified for most dry granular systems in the collisional state.

Equation $(3.4)_2$ yields the residual entropy inequality, viz.

$$\begin{aligned}\bar{\pi} = &\Big(- \bar{\gamma}\bar{\nu}\vartheta^M\psi^T_{,\bar{\nu}} + \bar{\gamma}^2\vartheta^M\psi^T_{,\bar{\gamma}} - \bar{\gamma}\bar{\nu}\vartheta^M\bar{f}\ell\Big)\dot{\bar{\nu}} + \sum_g\Big(\boldsymbol{\phi}^T_{,g} - \vartheta^M(\bar{\mathbf{q}}+\mathbf{Q})_{,g} + \vartheta^T\mathbf{K}_{,g}\\ &+ \vartheta^G\mathbf{L}_{,g}\Big)\cdot\nabla g + \Big(\vartheta^M\bar{\mathbf{t}} + \vartheta^T\mathbf{R} + \bar{\gamma}\bar{\nu}\vartheta^M\psi^T_{,\mathbf{g}_1}\otimes\mathbf{g}_1 + \bar{\gamma}^2\bar{\nu}\vartheta^M\psi^T_{,\bar{\gamma}}\mathbf{I}\Big)\cdot\bar{\mathbf{D}}\\ &+ \bar{\gamma}\bar{\nu}\Big(\varepsilon(\vartheta^M-\vartheta^T) + H(\vartheta^M-\vartheta^G) - \vartheta^M\psi^T_{,\bar{\mathbf{Z}}}\cdot\bar{\boldsymbol{\Phi}}\Big)\geqslant 0\end{aligned} \tag{3.9}$$

with $\otimes$ denoting the dyadic product; $\mathbf{I}$ the second-rank identity tensor; and $g\in\{\bar{\nu},\bar{\gamma},\vartheta^M,\vartheta^T,\vartheta^G\}$.

3.2. Extra entropy flux

Define the extra entropy flux $\boldsymbol{\xi}$, viz.

$$\boldsymbol{\xi} \equiv \boldsymbol{\phi}^T - \vartheta^M(\bar{\mathbf{q}}+\mathbf{Q}) + \vartheta^T\mathbf{K} + \vartheta^G\mathbf{L} \tag{3.10}$$

Substituting (3.10) into $(3.8)_1$ and $(3.8)_{2,3}$, results respectively in

$$\mathbf{0} = \boldsymbol{\xi}_{,\nu_0} \qquad \mathbf{0} = \boldsymbol{\xi}_{,\mathbf{A}} \qquad \mathbf{0} = \operatorname{sym}(\boldsymbol{\xi}_{,\mathbf{g}}) \tag{3.11}$$

It follows from (2.12) and $(3.11)_{1-2}$ that $\boldsymbol{\xi} = \hat{\boldsymbol{\xi}}(\bar{\nu},\dot{\bar{\nu}},\bar{\gamma},\vartheta^M,\vartheta^T,\vartheta^G,\mathbf{g}_{1-5})$. Integrating $(3.11)_3$ one by one, yields (Wang, 1970, 1971; Wang and Liu, 1980)

$$\begin{aligned}\boldsymbol{\xi} &= \mathbf{A}_1\cdot\mathbf{g}_1 + \mathbf{B}_1\cdot\mathbf{g}_2 + \mathbf{C}_1\cdot(\mathbf{g}_1\otimes\mathbf{g}_2) + \mathbf{d}_1 = \mathbf{A}_2\cdot\mathbf{g}_2 + \mathbf{B}_2\cdot\mathbf{g}_3 + \mathbf{C}_2\cdot(\mathbf{g}_2\otimes\mathbf{g}_3) + \mathbf{d}_2\\ &= \mathbf{A}_3\cdot\mathbf{g}_3 + \mathbf{B}_3\cdot\mathbf{g}_4 + \mathbf{C}_3\cdot(\mathbf{g}_3\otimes\mathbf{g}_4) + \mathbf{d}_3\\ &= \mathbf{A}_4\cdot\mathbf{g}_4 + \mathbf{B}_4\cdot\mathbf{g}_5 + \mathbf{C}_4\cdot(\mathbf{g}_4\otimes\mathbf{g}_5) + \mathbf{d}_4 = \mathbf{A}_5\cdot\mathbf{g}_1 + \mathbf{B}_5\cdot\mathbf{g}_5 + \mathbf{C}_5\cdot(\mathbf{g}_1\otimes\mathbf{g}_5) + \mathbf{d}_5\end{aligned} \tag{3.12}$$

with $\{\mathbf{A}_{1-5},\mathbf{B}_{1-5}\}$ and $\mathbf{C}_{1-5}$ being respectively the second- and third-rank skew-symmetric tensors, and $\mathbf{d}_{1-5}$ the isotropic vectors. Since $\boldsymbol{\xi}$ is an isotropic vector, it follows that $\mathbf{0}=\mathbf{A}_{1-5}=\mathbf{B}_{1-5}$, and $\mathbf{0}=\mathbf{C}_{1-5}$, because there are no isotropic second- and third-rank skew-symmetric tensors. With these, equation (3.12) reduces to

$$\boldsymbol{\xi} = \hat{\boldsymbol{\xi}}(\bar{\nu},\dot{\bar{\nu}},\bar{\gamma},\vartheta^M,\vartheta^T,\vartheta^G) = \mathbf{0} \tag{3.13}$$

since there exist no isotropic vectors with only scalar arguments.

Equation (3.13) indicates that for rapid flows, the granular system as a whole and solid grains are moving in a way that combined contributions of two-fold turbulent kinetic energy fluxes are collinear with the entropy flux, a distinct result from that of dense flows (Fang and Wu, 2014a). For in rapid flows, the short-term grain-grain interaction is dominant, causing the grains to evolve in a more dispersive manner from the granular system. In dense flows, the long-term one dominates, resulting in more orientated grain arrangement from the granular body. With $\boldsymbol{\xi}=\mathbf{0}$, equation $(3.8)_2$ reduces to

$$\ell(\vartheta^M\bar{\mathbf{h}} + \vartheta^G\mathbf{H}) = \bar{\gamma}\bar{\nu}\vartheta^M\psi^T_{,\mathbf{g}_1} \qquad \mathbf{H} = \ell\mathbf{R}\mathbf{g}_1 \tag{3.14}$$

With (3.5)-(3.7) and (3.13)-(3.14), equation $(3.4)_1$ has been fully explored.

Residual entropy inequality (3.9) is recast, viz.

$$\begin{aligned}\bar{\pi} = &\Big(\vartheta^M\bar{\nu}\bar{p}\mathbf{I} + \vartheta^M\bar{\mathbf{t}} + \vartheta^T\mathbf{R} + \bar{\gamma}\bar{\nu}\vartheta^M\psi^T_{,\mathbf{g}_1}\otimes\mathbf{g}_1\Big)\cdot\bar{\mathbf{D}} + (\bar{\mathbf{q}}+\mathbf{Q})\cdot\mathbf{g}_3\\ &- \mathbf{K}\cdot\mathbf{g}_4 - \mathbf{L}\cdot\mathbf{g}_5 + \vartheta^M(\bar{p}-\bar{\beta}-\bar{\gamma}\bar{\nu}\bar{f}\ell)\dot{\bar{\nu}} + \bar{\pi}_{int}\geqslant 0\end{aligned} \tag{3.15}$$

with the internal dissipation $\bar{\pi}_{int}$

$$\bar{\pi}_{int} = \bar{\gamma}\bar{\nu}\varepsilon(\vartheta^M - \vartheta^T) + \bar{\gamma}\bar{\nu}H(\vartheta^M - \vartheta^G) - \bar{\gamma}\bar{\nu}\vartheta^M\psi^T_{,\bar{\mathbf{Z}}} \cdot \bar{\mathbf{\Phi}} \tag{3.16}$$

and the abbreviations

$$\bar{p} \equiv \bar{\gamma}^2\psi^T_{,\bar{\gamma}} \qquad \bar{\beta} \equiv \bar{\gamma}\bar{\nu}\psi^T_{,\bar{\nu}} \tag{3.17}$$

known respectively as the *turbulent thermodynamic pressure* and *turbulent configurational pressure*. They are extended versions of their counterparts in laminar flows (Fang, 2009a; Kirchner, 2002; Wang and Hutter, 1999).

4. Equilibrium closure relations

Thermodynamic equilibrium is defined to be a time-independent process with uniform vanishing mean entropy production, viz. (Hutter and Wang, 2003)

$$\bar{\pi}\Big|_{\mathrm{E}} = 0 \tag{4.1}$$

with the subscript E indicating that the indexed quantity is evaluated at thermodynamic equilibrium. In view of (2.12) and (3.15)-(3.16), equation (4.1) motivates the following equilibrium and dynamic state spaces, viz.

$$\begin{aligned} &\mathcal{Q}\Big|_{\mathrm{E}} \equiv (\nu_0, \bar{\nu}, 0, \mathbf{g}_1, \bar{\gamma}, \mathbf{g}_2, \vartheta^M, \mathbf{0}, \vartheta^T, \mathbf{0}, \vartheta^G, \mathbf{0}, \mathbf{0}, \bar{\mathbf{Z}}) \\ &\mathcal{Q}^D \equiv (\dot{\bar{\nu}}, \mathbf{g}_3, \mathbf{g}_4, \mathbf{g}_5, \bar{\mathbf{D}}) \end{aligned} \tag{4.2}$$

with the superscript D denoting the dynamic state space. The dynamic variables ($\dot{\bar{\nu}}$, $\mathbf{g}_3$, $\mathbf{g}_4$, $\mathbf{g}_5$, $\bar{\mathbf{D}}$) should vanish at the equilibrium state, with $\mathcal{Q}^D\Big|_{\mathrm{E}} = 0$. In addition, under sufficient smoothness, $\bar{\pi}$ has to satisfy

$$\bar{\pi}_{,a}\Big|_{\mathrm{E}} = 0 \qquad a \in \mathcal{Q}^D \tag{4.3}$$

and the Hessian matrix of $\bar{\pi}$ with respect to $\mathcal{Q}^D$ at the thermodynamic equilibrium should be positive semi-definite. Since the latter condition constrains the sign of the material parameters in the closure relations, only equations (4.1) and (4.3) will be investigated.

First, applying (4.1) and $(4.2)_1$ to (3.15) and (3.16), yields

$$0 = (\vartheta^M - \vartheta^T)\bar{\gamma}\bar{\nu}\varepsilon\Big|_{\mathrm{E}} + (\vartheta^M - \vartheta^G)\bar{\gamma}\bar{\nu}H\Big|_{\mathrm{E}} - \bar{\gamma}\bar{\nu}\vartheta^M\psi^T_{,\bar{\mathbf{Z}}} \cdot \bar{\mathbf{\Phi}}\Big|_{\mathrm{E}} \tag{4.4}$$

indicating that two-fold turbulent dissipations $\bar{\gamma}\bar{\nu}\varepsilon$ and $\bar{\gamma}\bar{\nu}H$ at the equilibrium state result from the internal friction, a justified result. It can be fulfilled with the assumptions

$$0 = \varepsilon\Big|_{\mathrm{E}} \qquad 0 = H\Big|_{\mathrm{E}} \qquad \mathbf{0} = \bar{\mathbf{\Phi}}\Big|_{\mathrm{E}} \tag{4.5}$$

for all productions cease at the thermodynamic equilibrium state.

Secondly, incorporating $(4.2)_2$ and (4.3) into (3.15) and (3.16), results respectively in

$$
\begin{aligned}
0 &= \vartheta^M(\bar{p}-\bar{\beta}-\bar{\gamma}\bar{\nu}\bar{f}\Big|_{\mathrm{E}}\ell) + (\vartheta^M-\vartheta^T)\bar{\gamma}\bar{\nu}\varepsilon_{,\dot{\bar{\nu}}}\Big|_{\mathrm{E}} + (\vartheta^M-\vartheta^G)\bar{\gamma}\bar{\nu}H_{,\dot{\bar{\nu}}}\Big|_{\mathrm{E}} \\
&\quad - \bar{\gamma}\bar{\nu}\vartheta^M\psi^T_{,\bar{\mathbf{Z}}}\cdot\bar{\mathbf{\Phi}}_{,\dot{\bar{\nu}}}\Big|_{\mathrm{E}} \\
\mathbf{0} &= (\bar{\mathbf{q}}+\mathbf{Q})\Big|_{\mathrm{E}} + (\vartheta^M-\vartheta^T)\bar{\gamma}\bar{\nu}\varepsilon_{,\mathbf{g}_3}\Big|_{\mathrm{E}} + (\vartheta^M-\vartheta^G)\bar{\gamma}\bar{\nu}H_{,\mathbf{g}_3}\Big|_{\mathrm{E}} - \bar{\gamma}\bar{\nu}\vartheta^M\psi^T_{,\bar{\mathbf{Z}}}\cdot\bar{\mathbf{\Phi}}_{,\mathbf{g}_3}\Big|_{\mathrm{E}} \\
\mathbf{0} &= -\mathbf{K}\Big|_{\mathrm{E}} + (\vartheta^M-\vartheta^T)\bar{\gamma}\bar{\nu}\varepsilon_{,\mathbf{g}_4}\Big|_{\mathrm{E}} + (\vartheta^M-\vartheta^G)\bar{\gamma}\bar{\nu}H_{,\mathbf{g}_4}\Big|_{\mathrm{E}} - \bar{\gamma}\bar{\nu}\vartheta^M\psi^T_{,\bar{\mathbf{Z}}}\cdot\bar{\mathbf{\Phi}}_{,\mathbf{g}_4}\Big|_{\mathrm{E}} \\
\mathbf{0} &= -\mathbf{L}\Big|_{\mathrm{E}} + (\vartheta^M-\vartheta^T)\bar{\gamma}\bar{\nu}\varepsilon_{,\mathbf{g}_5}\Big|_{\mathrm{E}} + (\vartheta^M-\vartheta^G)\bar{\gamma}\bar{\nu}H_{,\mathbf{g}_5}\Big|_{\mathrm{E}} - \bar{\gamma}\bar{\nu}\vartheta^M\psi^T_{,\bar{\mathbf{Z}}}\cdot\bar{\mathbf{\Phi}}_{,\mathbf{g}_5}\Big|_{\mathrm{E}} \\
\mathbf{0} &= \vartheta^M\bar{\mathbf{t}}\Big|_{\mathrm{E}} + \vartheta^T\mathbf{R}\Big|_{\mathrm{E}} + \bar{\nu}\vartheta^M\bar{p}\mathbf{I} + \bar{\gamma}\bar{\nu}\vartheta^M\psi^T_{,\mathbf{g}_1}\otimes\mathbf{g}_1 + (\vartheta^M-\vartheta^T)\bar{\gamma}\bar{\nu}\varepsilon_{,\bar{\mathbf{D}}}\Big|_{\mathrm{E}} \\
&\quad + (\vartheta^M-\vartheta^G)\bar{\gamma}\bar{\nu}H_{,\bar{\mathbf{D}}}\Big|_{\mathrm{E}} - \bar{\gamma}\bar{\nu}\vartheta^M\psi^T_{,\bar{\mathbf{Z}}}\cdot\bar{\mathbf{\Phi}}_{,\bar{\mathbf{D}}}\Big|_{\mathrm{E}}
\end{aligned}
\tag{4.6}
$$

While equation $(4.6)_1$ indicates that the internal friction and two-fold turbulent dissipations affect the evolution of $\bar{\nu}$ via two-fold pressures, justified in view of the microstructural grain-grain interactions, it also yields an equilibrium expression for $\bar{f}$. Equation $(4.6)_2$ delivers that the equilibrium mean and turbulent heat fluxes are related to the internal friction and two-fold turbulent dissipations, according to observations. It reduces to vanishing mean and turbulent heat fluxes for isothermal flows. Equation $(4.6)_3$ delivers an equilibrium expression for $\mathbf{K}$ in terms of the internal friction and two-fold turbulent dissipations. Since turbulent dissipation is (negative) production of $\bar{\gamma}\bar{\nu}k$, $(4.6)_3$ and (4.4) imply an energy cascade from the turbulent kinetic energy flux toward turbulent dissipation through the effect of internal friction in the presence of a non-uniform granular coldness gradient, a phenomenon similar to that of Newtonian fluids in turbulent shear flows (Batchelor, 1993; Tsinober, 2009). A similar situation is also found between $\mathbf{L}$ and $\bar{\gamma}\bar{\nu}H$, as indicated by $(4.6)_4$. Equations $(4.6)_3$ and $(4.6)_4$ also imply that $\mathbf{K}$ and $\mathbf{L}$ are mutually influenced, a result already indicated by (3.13). Lastly, equation $(4.6)_5$ yields an expression that should be satisfied by $\bar{\mathbf{t}}|_E$ and $\mathbf{R}|_E$ in terms of the internal friction, two-fold turbulent dissipations and the mean volume fraction gradient.

In the above, $\bar{\gamma}\bar{\nu}k$ and $\bar{\gamma}\bar{\nu}s$ are expressed respectively as functions of ϑ^T and ϑ^G; they are determined once ψ^T is prescribed. Thus, equations (3.5), $(3.7)_{2-3}$, (3.17), and (4.4)-(4.6) deliver implicitly the equilibrium closure relations for $\bar{\mathbf{h}}$, $\mathbf{H}$, $\bar{f}$, $\bar{\mathbf{t}}$, $\mathbf{R}$, $\mathbf{K}$, $\mathbf{L}$, ε, H and $\bar{\mathbf{\Phi}}$ in the context of the zero-order turbulence closure model.

Remarks

1. The derived equilibrium closure relations apply for both compressible and incompressible grains. For the incompressible grains, $\bar{p}$ is no longer determined by $(3.17)_1$, and should be computed from the momentum equation.
2. Equation (4.5) is made based on observations of Newtonian fluids in turbulent motion, with which equations (2.8) and (2.9) are automatically fulfilled, when $\mathbf{K}$ and $\mathbf{L}$ are assumed to depend explicitly on $\mathbf{g}_4$ and $\mathbf{g}_5$, respectively.
3. In the second part, a hypoplastic model is used for $\bar{\mathbf{\Phi}}$ with $\bar{\mathbf{\Phi}} = \hat{\bar{\mathbf{\Phi}}}(\bar{\nu}, \bar{\mathbf{D}}, \bar{\mathbf{Z}})$, with which equation $(4.5)_3$ is fulfilled, and equations (2.8) and (2.9) reduce to

$$
0 = \nabla\cdot\Big((\vartheta^M-\vartheta^T)\bar{\gamma}\bar{\nu}\varepsilon_{,\mathbf{g}}\Big|_E + (\vartheta^M-\vartheta^G)\bar{\gamma}\bar{\nu}H_{,\mathbf{g}}\Big|_E\Big) \qquad \mathbf{g} = \{\mathbf{g}_4, \mathbf{g}_5\} \tag{4.7}
$$

additionally restrictions that should be fulfilled by $\varepsilon|_{\mathrm{E}}$ and $H|_{\mathrm{E}}$.

4. Equation $(4.6)_5$, by using Truesdell's equi-presence principle, is decomposed into

$$\begin{aligned}\vartheta^M\bar{\mathbf{t}}\Big|_{\mathrm{E}} &= -\bar{\nu}\vartheta^M\bar{p}\mathbf{I} - \bar{\gamma}\bar{\nu}\vartheta^M\psi^T_{,\mathbf{g}_1}\otimes\mathbf{g}_1 + \bar{\gamma}\bar{\nu}\vartheta^M\psi^T_{,\bar{\mathbf{Z}}}\cdot\bar{\boldsymbol{\Phi}}_{,\bar{\mathbf{D}}}\Big|_{\mathrm{E}}\\ \vartheta^T\mathbf{R}\Big|_{\mathrm{E}} &= -(\vartheta^M-\vartheta^T)\bar{\gamma}\bar{\nu}\varepsilon_{,\bar{\mathbf{D}}}\Big|_{\mathrm{E}} - (\vartheta^M-\vartheta^G)\bar{\gamma}\bar{\nu}H_{,\bar{\mathbf{D}}}\Big|_{\mathrm{E}}\end{aligned} \tag{4.8}$$

in which $\bar{\mathbf{t}}\Big|_{\mathrm{E}}$ is generated through the mean fields, with $\mathbf{R}|_{\mathrm{E}}$ mainly induced via the quantities related to turbulent fluctuation (e.g. two-fold turbulent dissipations), a procedure widely used for Newtonian fluids in turbulent flows. For laminar flows, equation $(4.8)_2$ yields a vanishing $\mathbf{R}|_{\mathrm{E}}$, while equation $(4.8)_1$ delivers that a dry granular heap at the equilibrium state can be accomplished either by the internal friction or a non-uniform gradient of $\bar{\nu}$, coinciding with the previous works by Fang (2009a), Kirchner (2002), Wang and Hutter (1999).

5. Concluding remarks

The Reynolds-filter process is used to decompose the variables into the mean and fluctuating parts to obtain the balance equations of the mean fields. Two-fold granular coldnesses are introduced as primitive fields to index the variations in the turbulent kinetic and turbulent configurational kinetic energies, with their dissipations considered closure relations. The Müller-Liu entropy principle is investigated to derive the equilibrium closure relations.

Equations (3.13) and $(4.6)_{3,4}$ demonstrate that the flux of the turbulent kinetic energy and that of the turbulent configurational kinetic energy are mutually influenced. This implies that the turbulent fluctuation of the granular system as a whole tends to drive the grains to arrange and fluctuate in a way that their combined contributions provide the only deviation between the heat and entropy fluxes. This is justified, since laboratory experiments and field observations suggest that there exists a turbulent boundary layer immediately above the base, in which the grains collide one with another vigorously, resulting in a dominant short-term grain-grain interaction. On the other hand, this conclusion does not hold for dense flows with weak turbulent intensity, for only the collinearity between the fluxes of the turbulent kinetic energy and evolution of the mean volume fraction can be deduced.

The implementation of the closure model, and numerical simulation of an isothermal, isochoric, gravity-driven stationary dry granular avalanche with incompressible grains down an incline, compared with the laminar flow solutions are reported in the second part.

Acknowledgements

The author is indebted to the Ministry of Science and Technology, Taiwan, for the financial support through the project MOST 103-2221-E-006-116-. The author also thanks the editor and Professor Janusz Badur for detailed comments and suggestions which led to improvements.

References

1. Ahmadi G., 1985, A turbulence model for rapid flows of granular materials. Part I. Basic theory, *Powder Technology*, **44**, 261-268
2. Ahmadi G., Shahinpoor M., 1983, Towards a turbulent modeling of rapid flow of granular materials, *Powder Technology*, **35**, 241-248
3. Aranson I.S., Tsimring L.S., 2009, *Granular Patterns*, Oxford University Press, Oxford New York

4. Ausloos M., Lambiotte R., Trojan K., Koza Z., Pekala M., 2005, Granular matter: a wonderful world of clusters in far-from-equilibrium systems, *Physica A*, **357**, 337-349
5. Batchelor G.K., 1993, *The Theory of Homogeneous Turbulence*, Cambridge University Press, Cambridge New York
6. Bilicki Z., Badur J., 2003, A thermodynamically consistent relaxation model for turbulent binary mixture undergoing phase transition, *Journal of Non-equilibrium Thermodynamics*, **28**, 311-340
7. Campbell C.S., 2005, Stress-controlled elastic granular shear flows, *Journal of Fluid Mechanics*, **539**, 273-297
8. Cieszko M., 1996, Constitutive relations and internal equilibrium condition for fluid-saturated porous solids. Linear description, *Archive of Mechanics*, **48**, 911-923
9. Daniel R.C., Poloski A.P., Sáez A.E., 2007, A continuum constitutive model for cohesionless granular flows, *Chemical Engineering and Science*, **62**,1343-1350
10. Faccanoni G., Mangeney A., 2013, Exact solution for granular flows, *International Journal for Numerical and Analytical Methods in Geomechanics*, **37**, 1408-1433
11. Fang C., 2008a, Modeling dry granular mass flows as elasto-visco-hypoplastic continua with microstructural effects. I. Thermodynamically consistent constitutive model, *Acta Mechanica*, **197**, 173-189
12. Fang C., 2008b, Modeling dry granular mass flows as elasto-visco-hypoplastic continua with microstructural effects. II. Numerical simulations of benchmark flow problems, *Acta Mechanica*, **197**, 191-209
13. Fang C., 2009a, Gravity-driven dry granular slow flows down an inclined moving plane: a comparative study between two concepts of the evolution of porosity, *Rheologica Acta*, **48**, 971-992
14. Fang C., 2009b, A generalized Mohr-Coulomb criterion implied by the revised Goodman-Cowin theory, *Archive of Applied Mechanics*, **79**, 169-173
15. Fang C., 2010, Rheological characteristics of solid-fluid transition in dry granular dense flows: a thermodynamically consistent constitutive model with a pressure ratio order parameter, *International Journal for Numerical and Analytical Methods in Geomechanics*, **34**, 881-905
16. Fang C., 2016a, A k-ε turbulent closure model of an isothermal dry granular dense matter, *Continuum Mechanics and Thermodynamics* (in press, DOI: 10.1007/s00161-015-0454-1)
17. Fang C., 2016b, On the turbulent boundary layer of a dry granular avalanche down an incline. Part II. Closure model with numerical simulations, *Journal of Theoretical and Applied Mechanics* (in press)
18. Fang C., Wu W., 2014a, On the weak turbulent motions of an isothermal dry granular dense flow with incompressible grains. Part I. Equilibrium turbulent closure models, *Acta Geotechnica*, **9**, 725-737
19. Fang C., Wu W., 2014b, On the weak turbulent motions of an isothermal dry granular dense flow with incompressible grains. Part II. Complete closure models and numerical simulations, *Acta Geotechnica*, **9**, 739-752
20. GDR MiDi., 2004, On dense granular flows, *European Physics Journal E*, **14**, 341-365
21. Goldhirsch I., 2008, Introduction to granular temperature, *Powder Technology*, **182**, 130-136
22. Hutter K., Jöhnk K., 2004, *Continuum Methods of Physical Modeling*, Springer, Berlin Heidelberg
23. Hutter K., Wang Y., 2003, Phenomenological thermodynamics and entropy principle, [In:] *Entropy*, Greven A., Keller G., Warnecke G. (Eds.), 1st ed., Princeton University Press, 57-77
24. Jop P., 2008, Hydrodynamic modeling of granular flows in a modified Couette Cell, *Physics Review E*, **77**, 032301

25. Jop P., Forterre Y., Pouliquen O., 2006, A constitutive law for dense granular flows, *Nature*, **411**, 727-730

26. Kirchner N., 2002, Thermodynamically consistent modeling of abrasive granular materials. I: Non-equilibrium theory, *Proceeding of Royal Society London A*, **458**, 2153-2176

27. Kubik J., 1986, On internal coupling in dynamic equations of fluid-saturated porous solid, *International Journal of Engineering Science*, **24**, 981-989

28. Luca I., Fang C., Hutter K., 2004, A thermodynamic model of turbulent motions in a granular material, *Continuum Mechanics and Thermodynamics*, **16**, 363-390

29. Ma D., Ahmadi G., 1985, A turbulence model for rapid flows of granular materials. Part II. Simple shear flows, *Powder Technology*, **44**, 269-279

30. Mehta A., 2007, *Granular Physics*, Cambridge University Press, New York

31. Oswald P., 2009, *Rheophysics: The Deformation and Flow of Matter*, Cambridge University Press, New York

32. Pöschel T., Brilliantov N.V., 2013, *Granular Gas Dynamics*, Springer-Verlag, New York

33. Pudasaini S., Hutter K., 2007, *Avalanche Dynamics*, Springer Verlag, Berlin Heidelberg

34. Rao K.K., Nott P.R., 2008, *Introduction to Granular Flows*, Cambridge University Press, London New York

35. Rung T., Thiele F., Fu S., 1999, On the realizability of non-linear stress-strain relationships for Reynolds-stress closures, *Flow and Turbulent Combustion*, **60**, 333-359

36. Sadiki A., Hutter K., 2000, On thermodynamics of turbulence, *Journal of Non-equilibrium Thermodynamics*, **25**,131-160

37. Savage S.B., 1993, Mechanics of granular flows, [In:] *Continuum Mechanics in Environmental Sciences and Geophysics*, Hutter K. (Edit.), Heidelberg, Springer, 467-522

38. Schrefler B., Boso D., Pesavento F., Gawin D., Lefik F., 2009, Mathematical and numerical multiscale modelling, *CMM-2011-Computer Methods in Mechanics*, 1-4

39. Sobieski W., 2009, Momentum exchange in solid-fluid system modeling with the Eulerian multiphase model, *Dry Technology*, **27**, 653-671

40. Svendsen B., Hutter K., 1999, On the thermodynamics of a mixture of isotropic materials with constraints, *International Journal of Engineering and Science*, **33**, 14, 2021-2054

41. Svendsen B., Hutter K., Laloui L., 1999, Constitutive models for granular materials including quasi-static frictional behavior: toward a thermodynamic theory of plasticity, *Continuum Mechanics and Thermodynamics*, **14**, 263-275

42. Tsinober A., 2009, *An Informal Conceptual Introduction to Turbulence*, Springer, Heidelberg

43. Vescovi D., di Prisco C., Berzi D., 2013, From solid to granular gases: the steady state for granular materials, *International Journal for Numerical and Analytical Methods in Geomechanics*, **37**, 2937-2951

44. Wang C.-C., 1970, 1971, A new representation theorem for isotropic functions, Part I and Part II, *Archives of Rational Mechanics and Analysis*, **36**, 166-197, 198-223; Corrigendum, ibid. **43**, 392-395

45. Wang C.-C., Liu I.-S., 1980, A note on material symmetry, *Archives of Rational Mechanics and Analysis*, **74**, 277-296

46. Wang Y., Hutter K., 1999, A constitutive theory of fluid-saturated granular materials and its application in gravitational flows, *Rheologica Acta*, **38**, 214-223

47. Wang Y., Hutter K., 2001, Granular material theories revisited, [In:] *Geomorphological Fluid Mechanics*, Balmforth N.J., Provenzale A. (Edit.), Heidelberg, Springer, 79-107

48. Wilmański K., 1996, Porous media at finite strains. The new model with the balance equation of porosity, *Archives of Mechanics*, **48**, 4, 591-628

Manuscript received January 29, 2015; accepted for print February 23, 2016

INFORMATION FOR AUTHORS

Journal of Theoretical and Applied Mechanics (***JTAM***) is devoted to all aspects of solid mechanics, fluid mechanics, thermodynamics and applied problems of structural mechanics, mechatronics, biomechanics and robotics. Both theoretical and experimental papers as well as survey papers can be proposed.

We accept articles in English only. The text of a *JTAM* paper should not exceed **12 pages of standard format A4** (11-point type size, including abstract, figures, tables and references), short communications – **4 pages**.

The material for publication should be sent to the Editorial Office via electronic journal system: http://www.ptmts.org.pl/jtam/index.php/jtam

Papers are accepted for publication after the review process. Blind review model is applied, which means that the reviewers' names are kept confidential to the authors. The final decision on paper acceptance belongs to the Editorial Board.

After qualifying your paper for publication we will require LaTeX or TeX or Word document file and figures.

The best preferred form of figures are files obtained by making use of editorial environments employing vector graphics:

- genertaed in CorelDraw (*.cdr), AutoCad and ArchiCad (*.dwg) and Adobe Illustrator (*.ai). We require original fioles saved in the standard format of the given program.
- genertaed by calculation software (e.g. Mathematica) - we need files saved in *.eps or *.pdf formats.
- made in other programs based on vector graphics - we ask for *.eps, *.wmf, *.svg, *.psfiles.

Any figures created without application of vector graphics (scans, photos, bitmaps) are strongly encouraged to be supplied in *.jpg, *.tif, *.png formats with resolution of at least 300 dpi.

Requirements for paper preparation

Contents of the manuscripts should appear in the following order:

- Title of the paper
- Authors' full name, affiliation and e-mail
- Short abstract (**maximum 100 words**) and 3-5 key words (**1 line**)
- Article text (equations should be numbered separately in each section; each reference should be cited in the text by the last name(s) of the author(s) and the publication year)
- References in alphabetical order. See the following:

  1. Achen S.C., 1989, A new boundary integral equation formulation, *Journal of Applied Mechanics*, **56**, 2, 297-303
  2. Boley B.A., Weiner J.H., 1960, *Theory of Thermal Stresses*, Wiley, New York
  3. Canon W., 1955, Vibrations of heated beams, Ph.D. Thesis, Columbia University, New York
  4. Deresiewicz H., 1958, Solution of the equations of thermoelasticity, *Proceedings of Third U.S. National Congress of Applied Mechanics*, 287-305

- Titles of references originally published not in English, should be translated into English and formulated as follows:

  5. Huber M.T., 1904, Specific work of strain as a measure of material effort (in Polish), *Czasopismo Techniczne*, **XXII**, 3, 80-81

All the data should be reported in **SI units**.

Cena 35,00 zł (VAT 5%)

Contents